Development of Ultra-High Performance Concrete Against Blasts

From Materials to Structures

Chengqing Wu, Jun Li and Yu Su

WP
WOODHEAD
PUBLISHING

Development of Ultra-High Performance Concrete Against Blasts

Related titles

Wu and Eamon, Strengthening of Concrete Structures Using FRPs
(ISBN 978-0-081-00636-8)

Petrovic, Materials for Sustainable Built Environment
(ISBN 978-0-081-00707-5)

Alexander, Marine Concrete Structures
(ISBN 978-0-081-00905-5)

Woodhead Publishing Series in Civil and Structural Engineering

Development of Ultra-High Performance Concrete Against Blasts

From Materials to Structures

Chengqing Wu

Jun Li

Yu Su

For information on all Woodhead Publishing publications
visit our website at https://www.elsevier.com/books-and-journals

Working together
to grow libraries in
developing countries

www.elsevier.com • www.bookaid.org

Contents

Preface

In recent years scenarios involving terrorism activities continue to increase, structural protection against blast loads has been and will continue to be an important topic for engineering practitioners and researchers. Extensive research has been conducted to figure out the effective means to ensure the structural safety.

Recent advances in concrete admixtures and nanotechnology ensure the material durability, serviceability, and mechanical strength, which lead to the development of ultra-high performance concrete. Improvement in the concrete compressive strength leads to a significant reduction in structural member size and self-weight, which in turn results in project cost reduction and structural esthetic enhancement. Microreinforcement from steel fibers drastically improves the material ductility after cracking, which further elevates material energy absorption capacity. Despite these advantages, until now there is a lack of systematic study on ultra-high performance concrete to enlighten the community about the potential of this new construction material.

In this book, the development of UHPC materials and their application in protective structures are presented and discussed. The topics covering in this book range from material development to field blast tests, and to three-dimensional finite element modeling. This book compiles the most recent work in ultra-high performance concrete structures against blast loads. It is not intended to be an exhaustive treatise on ultra-high performance concrete, because ultra-high performance concrete technology and knowledge are evolving quickly. This book is primarily written to serve as a guide to engineers, researchers, and graduate students, to present the outstanding features of ultra-high performance concrete as a protective construction material.

This page intentionally left blank

Acknowledgment

This page intentionally left blank

Introduction

<div style="float:right">**1**</div>

1.1 Development of modern high strength concrete

High strength concrete (HSC) research began in the 1950s and has seen fast development ever since. Until now, there is no precise point of separation between HSC and normal strength concrete (NSC). According to the American Concrete Institute, HSC is defined as concrete having a compressive cylinder strength greater than 40 MPa. In the United Kingdom, BS EN 206-1 [1] defines HSC as concrete with a compressive strength class higher than C50/60. In Australia, HSC is defined as concrete with a characteristic of 28-day cylinder strength greater than 50 MPa, and up to 100 MPa.

In modern construction, HSC is favorable in high-rise buildings since it facilitates the design of smaller structural-member cross-sections for columns and walls, leaving more usable floor area. In marine structures, the low permeability characteristics of HSC reduce the risk of corrosion of steel reinforcement and improve the durability of concrete structures. HSC has also been used in design of safer structures because key supporting members are often designed to resist wind, seismic, and other impact forces [2,3]. After terrorist attack on September 11, 2001, the main building of the rebuilt World Trade Center complex, i.e., the One World Trade Center chose HSC. The supporting columns are made of steel and concrete ranging in strength from 59 to 97 MPa. Columns on the first 40 floors are made from 82 to 97 MPa concrete and the upper floors with 59−69 MPa mix designs. Fig. 1.1 shows some famous buildings in the world built with HSC.

Substantial work has been reported in the area of materials development for producing concrete with high strength. In the 1970s, concrete with higher compressive strength than NSC was used in the high-rise building construction, and these HSCs were made with the same technology as the NSC except carefully selected and controlled materials. In the late 1970s, when superplasticizer began to be developed and used to reduce the water/cement or water/binder ratio rather than being exclusively used to fluidize the usual concrete, it was found that concretes with a very low water/cement or water/binder ratio showed high compressive strength and at the same time they also had other improved characteristics such as higher flexural strength, lower permeability, improved abrasion resistance, and better durability. It had been revealed that a key factor influencing the concrete strength is the water/cement or water/binder ratio [4,5].

Besides superplasticizers, different kinds of cement replacement materials had also been developed and added to concrete mixtures. Silica fume is one of the most popular pozzolanas, whose addition to concrete mixtures results in lower porosity, permeability, and higher strength because their oxides (SiO_2) react with and consume calcium hydroxides (CH), which are produced by the hydration of ordinary
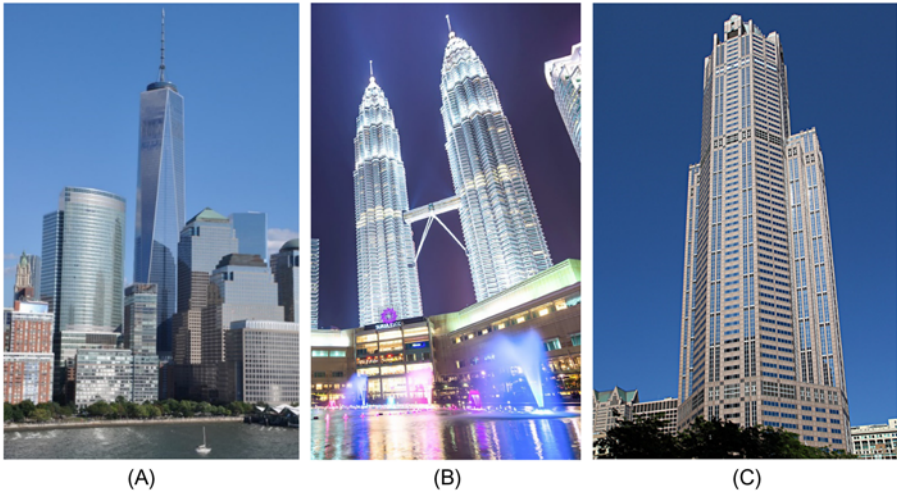
Figure 1.1 Buildings made of HSC. (A) One World Trade Center; (B) Petronas Towers; and (C) 311 South Wacker Drive.

Portland cement [6,7]. It is reported [8] that the optimum silica fume replacement percentage for obtaining the maximum 28-day strength of concrete ranged from 10% to 20%. Test results from Refs. [9,10] indicated that, when other mix design parameters remains constant, the optimum silica fume replacement percentage for 28-day compressive strength is not a constant but a function of the water/cement ratio of the mix. Regarding the tensile strength, it was observed that very high percentages of silica fume do not significantly increase the split tensile strengths, and the increase is almost insignificant beyond 15%. Of note, 5%−10% replacements considerably improve the split tensile strength with respect to control regardless of the water/binder ratio. It is [11] reported that incorporation of silica fume can effectively enhance the fiber−matrix interfacial properties in high strength steel fiber-reinforced concrete (SFRC), especially in fiber pull-out energy. In terms of the bond characteristics, the optimal silica fume content is between 20% and 30%.

1.2   Historical development of ultra-high performance concrete

The term "high-performance concrete" was a relatively new term for concrete, which is normally inclusive of the term "HSC." High-performance concrete is normally equipped with better material durability and abrasion resistance. Since there is no single best definition for the material known as high-performance concrete, it is preferable to define it as a low water/binder concrete which has an adequate curing with water [12]. In a low water/binder ratio mix, there are more cement grains and consequently less water per unit volume so that cement grains are much

closer to each other leading to reduced porosity. According to Griffith's theory [13], for the rupture of brittle materials with internal cracks, it is known that reduction of the particle dimension increases the strength.

In recent decades, concrete technology has made remarkable advances, and many works in this field had led to the development of ultra-high performance concretes (UHPC). UHPC is characterized by its material composition: fine-grained sand, silica fume, steel fibers, special blends of high-strength Portland cement, and an elimination of coarse aggregate. UHPC is normally characterized by compressive strengths in excess of 150 MPa. Reinforced by a small amount of steel fibers, UHPC becomes ductile and can reach direct tensile strength exceeding 15 MPa and flexural strength exceeding 50 MPa. For the first time, concrete material can be designed to accommodate tension. Conventional concrete contains a significant capillary porosity while UHPC has almost no capillary pores and is highly resistant to the water and ion penetration, therefore the durability of UHPC is much higher than conventional concrete. It can be used in harsh environments such as the wearing course of a bridge deck and pavements against chlorides, alkalis, or deicing salts.

The research of UHPC began in the 1980s when Danish researcher Hans Hendrik Bache [14] developed Compact Reinforced Concrete in which fine aggregates were used synergistically with fiber content. Bache's idea was taken by the French contractor Bouygues, who later cooperated with Lafarge to develop a new mix "Reactive Powder Concrete" (RPC) [15]. The concept of RPC continues to exist in the form of commercialized UHPCs such as "Ductal." The earliest application of UHPC was in Cattenom, France, where UHPC beams were used to replace the original steel beams in the cooling towers of a power station. It should be noted that in this case, UHPC was chosen not because of its high strength but rather because of its outstanding durability that can make the structure with a long service life in a highly corrosive environment.

1.2.1 Microstructural properties of ultra-high performance concrete

UHPC is more homogeneous than NSC due to optimized packing density and limited use of coarse aggregates. The size and strength difference between the matrix and the fine aggregates are so small that under external action, the unreinforced UHPC usually has crack propagation in a straight line, which highlights the brittleness of the unreinforced UHPC. Nevertheless, after reinforcement from small or microfibrous material, UHPC displays ductile material behavior and its tensile performance can be significantly improved.

The dense microstructure and high material strength of UHPC can be attributed to three important reasons. Firstly, UHPC mix is typically with a very low water/binder ratio, in which the binder is cement, silica fume and further reactive substances such as nanoparticles that will be discussed later in Chapter Two of this book. With low water/binder ratio (normally 0.25 or less), UHPC matrix has very low permeability. Secondly, the packing density of UHPC is optimized. Ultrafine
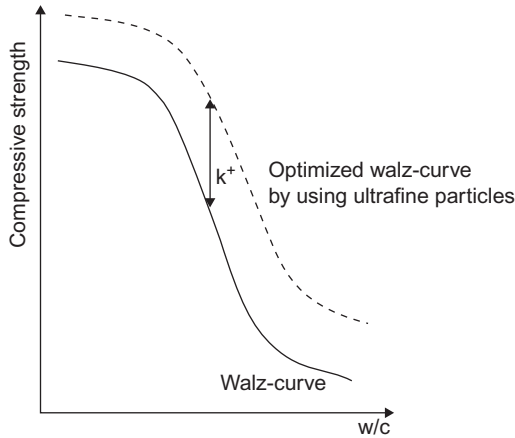
Figure 1.2 Effect of packing-optimized ultrafine particle combinations on UHPC compressive strength.

particles including cement, quartz powder, and silica fume are combined in an extremely tight way. Lastly, high pozzolanic material including silica fume reacts with free CH in the matrix forming additional calcium silicate hydrate leading to very high compressive strength.

Besides mass-based water/binder ratio, volume-based water/ultrafine particles ratio has also been established [16] for further improving the UHPC strength as shown in Fig. 1.2. It has been proven that given the same water/binder ratio, UHPC with volume-based optimization can get even higher strength enhancement.

Workability of UHPC places limits on optimizing the packing density. With a better/higher packing density, the pores between the particles are getting smaller, making the water hard to lubricate the particles. In addition, with large amount of ultrafine particles, the surface areas to be wetted increase significantly. Furthermore, the inter-particle forces between the ultrafine particles tend to attract nearby particles to form larger particles and therefore can no longer serve as optimum filler. These conflicts can be solved by high-performance superplasticizer that can deagglomerate and liquefy not only the cement but also all the other fine particles [17,18].

1.2.2 Curing of ultra-high performance concrete

Various versions of UHPCs have been developed and reported over the past decade [19−21]. However, most formulations were proprietary, expensive, and time/labor intensive. Among the difficult-to-achieve protocols are pressure and heat treatment processes required for curing the UHPC. Generally speaking, UHPC requires heat curing at $80°C−90°C$, and the high temperature promotes the pozzolanic effect of silica fume; the mechanical strengths are therefore higher and the microstructures are denser than ambient cured UHPC. For UHPC, the shrinkage only occurs during

the heat curing stage, and the heat curing process normally lasts for 48 hours and further time extension is not necessary for performance improvement. During the past 5 years, research has shown that it is possible to successfully make UHPC without complex and costly curing processes [22].

1.2.3 Material compositions

Material composition of UHPC differs from conventional concrete in many ways. In recent years, increasing research has been conducted to understand the influence of material compositions on UHPC performances [23−25].

1.2.3.1 Cement

For the design of UHPC mixtures, the choice of cement is a crucial step. Limited guidelines are found in the literature. The consumption of superplasticizer depends on the cement surface and thus the required superplasticizer dosage for the mix increases with the product of C_3A content and fineness, i.e., C_3A total surface area. According to Wille et al. [26], cement with a $d_{50} \approx 10\,\mu m$ is recommended for UHPC. Some authors state that in order to have an acceptable workability and suitable slump life, a cement with a low-alkali content (K_2O and Na_2O) has to be chosen [27].

Normally cement used in UHPC development is low-alkali Portland cements of strength class of 42.5 R and 52.5 R according to DIN EN 196. These cements are preferred because they can potentially provide high strength; the water requirement and chemical shrinkage are also limited, and the alkali−silica reaction is excluded. When selecting the cement, the water requirement should be carefully considered as it affects the water/binder ratio and also the adoption of the superplasticizer. It has been reported that even after heat treatment at $80°C−90°C$, about 30% of the cement remains unhydrated due to the low water content. The influence of cement type on mechanical strength and durability of UHPC has been studied [23].

1.2.3.2 Silica fume

Silica fume acts primarily on the matrix as microfiller due to its size in the concrete matrix as shown in Fig. 1.3. At high temperature $80°C−90°C$, silica fume contributes as pozzolanic material and promotes the hydration process creating more strength-forming hydration phases. Owing to its large specific surfaces of $100,000\,cm^2\,g^{-1}$, silica fume is the main factor in determining the water and superplasticizer requirements.

The influence of silica fume content on the performance of UHPC is widely studied [6,29]. They conclude that the compressive strength of UHPC is dependent on silica fume content since the additional amount of silica fume decreases the water demand which, in turn, needs more superplasticizer to make the concrete mix workable.

Specific surface area (m² kg⁻¹)
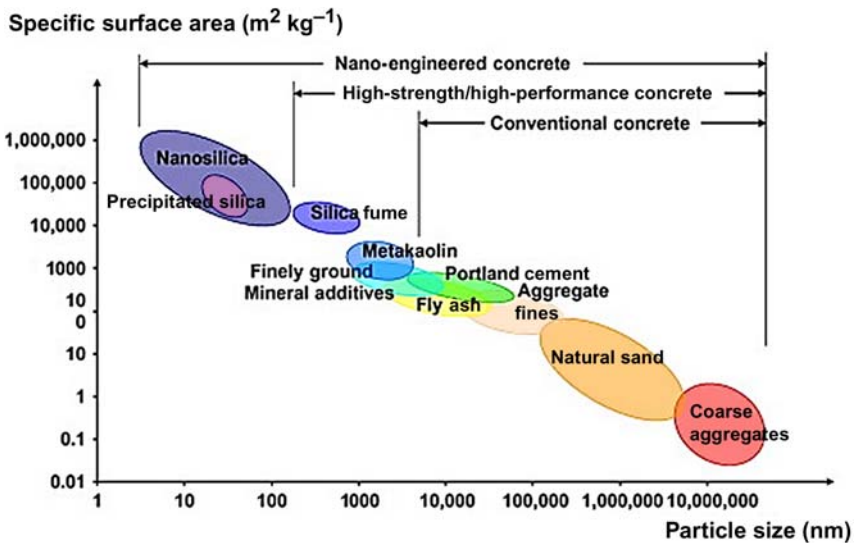
Figure 1.3 Particle size and specific surface area related to concrete materials.
Source: Adapted from F. Sanchez, K. Sobolev, Nanotechnology in concrete—a review, Construct. Build. Mater., 24 (2010) 2060−2071 [28].

Effective superplasticizers for UHPC are based on polycarboxylate ethers (PCE). Many different PCE superplasticizers are now available. However, most have to be optimized for their interaction with the different cements. Experience shows that for UHPC with a high quantity of silica fume, the superplasticizers that are particularly suitable are those that properly deagglomerate both the cement and the other fine particles. For example, testing individual cement and microsilica pastes revealed that the methacrylic acid ester (MPEG)-PCE disperses cement better than silica, whereas the allylether (APEG)-PCE fluidizes silica particularly well. The quantity required to reach a certain consistency in an individual case also depends on the quantity of active substances in the superplasticizer.

1.2.3.3   Fiber material

In the solid, dense, and homogeneous microstructure of UHPC, steel fibers can easily develop high bond stress. When matrix ruptures, the bonding and friction between the fiber and surrounding matrix effectively increase the material ductility. The selection of fiber material should consider both bonding and material workability. Generally speaking, fine fibers control opening and propagation of microcracks as they are densely dispersed in cement matrix. Longer fibers control larger cracks and contribute to increase the final strength of fiber-reinforced concrete (FRC) [30].

Investigation of the influence from varying fiber reinforcement type on the concrete performance had been conducted in the recent studies. Rigaud et al. [31] studied postcracking behavior of high-performance concrete containing glass

fibers, and the relationship between tensile strength and strain was extracted. Accelerated aging tests in 50° water were also conducted and the durability and ductility of such concrete material were verified. Zheng and Feldman [32] discussed characteristics of various synthetic fibers and the behavior of concrete reinforced with each of these fibers, and they reviewed research concerning the performance of synthetic FRC based on polyethylene, polypropylene, acrylics, poly (vinyl alcohol), polyamides, aramid, polyester, and carbon reinforcements. Alani and Beckett [33] presented results concerning the punching shear failure of a 6.00 m × 6.00 m × 0.15 m synthetic fiber-reinforced ground supported slab, and they concluded that the punching shear failure values obtained were comparable to values reported for the steel fiber slabs under similar conditions.

Among all fiber types, steel fibers are known to have higher modulus of elasticity than the concrete matrix which means they can enhance the load-carrying capacity, thus increase the tensile strength of the material. Concrete with steel fiber reinforcement has better impact, shatter, and abrasion resistance. Nowadays steel fibers are widely used as reinforcement in industrial floor slabs, standard reinforcing cage for tunnel segments, shotcrete, and prefabricated concrete products. Ye et al. [34] experimentally investigated the mechanical behavior of concrete reinforced by hybrid steel fibers with different shapes. The largest fracture energy and bending toughness were obtained with hybrid fibers, where the volume ratio of long ultrafine fiber was 1.5%, and the ratio of long end-hooked fiber was 0.5%. The hybrid fibers had generated positive intermixing effect. Kim et al. [35] examined the effects of twisted steel fiber on concrete flexural toughness, and three types of twisted fiber with different lengths and diameters were considered. Ryu et al. [36] found that concrete with twisted fiber reinforcement exhibited significantly improved mechanical characteristics compared to control concrete containing conventional straight fiber. Bindiganavile and Banthia [37] pointed out that under both static and low-rate impact loads, the predominant failure mode of SFRC material was the steel fiber pull out. To increase the bonding between the concrete and steel fiber material, Xu et al. [38] proposed spiral-shaped steel fibers, and the impact tests had demonstrated that FRC specimens reinforced with the spiral-shaped fibers displayed the largest ultimate compressive strength, the largest postfailure strength and the largest energy-absorption capacity among specimens reinforced with seven other types of fibers tested.

For SFRC, the most important factors affecting the concrete properties are fiber aspect ratio (ratio of steel fiber length over diameter) and volume fraction. Increasing fiber aspect ratio helps increasing the probability of heterogeneous distribution and flocculation in concrete. Fiber volume fraction significantly affects the workability of concrete. Yazıcı et al. [39] tested hooked-end bundled SFRC, and the influence of different aspect ratios and fiber volumes was discussed. They noted that split tensile strength and flexural strength of SFRC are improved with increasing aspect ratio and fiber volume fraction. Wang et al. [40] conducted experimental analysis on the effect of fiber aspect ratio on mechanical properties of SFRC, and the results revealed that the aspect ratio had an optimal value for strengths in every concrete batch. Beyond this value, the addition of steel fibers into concrete may have an effect of increasing the ductility rather than the strengths.
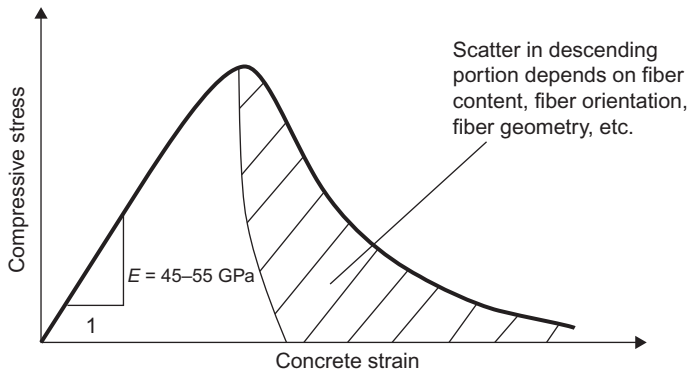
Figure 1.4 Fiber orientation influence on UHPC compressive behavior.

Besides fiber type, fiber content, and fiber geometry, fiber orientation has been recognized to be an important factor that affects the mechanical performance of UHPC as shown in Fig. 1.4. It should be remembered that the fiber orientation in a component can vary locally and be influenced by concreting activities. During concreting, the large majority of the fibers aligned with the direction of flow, primarily parallel with any nearby formwork surface. The postpeak behavior of UHPC which is dominant by the fiber material is therefore showing scattering. Due to the lack of standard testing procedures, different size components had been investigated in previous studies by different researchers, and the fiber content effect had been prominent with limited component size.

Due to the oxidation of steel fibers located at the surface of UHPC, some rust stain may be visible on the outer surface of the UHPC elements. However, it is claimed that the corrosion of steel fibers at the surface of the concrete is not structurally considerable [41]. Experimental investigations show that even in an aggressive environment with high potential of corrosion, rusting of steel fibers will not permeate beyond a depth of 2 mm from the concrete surface, and this is because UHPC matrix is impermeable (more than 20 times than conventional concrete), therefore, oxygen, moisture, and chloride ions are not able to penetrate deeper into the concrete.

1.2.3.4   Nanoparticles

Recently there has been a growing interest in the use of nanoscale materials in concrete to improve its performance [42−50]. With the development of nanotechnology, researchers noticed that several phenomena including statistically mechanical effects and quantum mechanical effects become pronounced as the size of the system decreases. Addition of nanoscale size particles results in significantly improved material properties without major changes of the material composition. Studies concerning properties of cement mortars with nano-SiO_2 addition were carried out [45]. The experimental results showed that the compressive strengths of mortars with nano-SiO_2 particles were higher than those of mortars containing silica fume

at 7 and 28 days. It was concluded that it was plausible to add nano-SiO_2 particles in order to make high-performance concrete. Similar observations [50] were obtained and it was also noticed that comparing with cement paste with silica fume addition, the cement paste mixed with nano-SiO_2 particles had obviously higher compressive strength, especially at early age. Nano-SiO_2 was believed to accelerate the cement hydration process. These findings proved that addition of nanomaterials can increase the hydration process and thus enable an early age workability of UHPC. Liu et al. [51] added nano-$CaCO_3$ (NC) into the cement paste and they observed a decreased flowability and shortened setting time of fresh cement paste, and they also noticed that compressive strength of UHPC increased with the addition of NC at 7 and 28 days. Similar observations were also made through experimental studies [52]. These findings indicate that the addition of small amount of nanomaterials can increase the mechanical performance of UHPC material. In the following chapters of this book, influences of nanomaterial additions on UHPC static and dynamic performances are to be discussed.

1.3 Application of ultra-high performance concrete in protective design

The use of UHPC in civil construction is seen worldwide and expands quickly. First UHPC footbridge spanning 120 m in the world was constructed in Seoul, South Korea in 2002. The Shawnessy Light Rail Transit (LRT) Station, constructed during fall 2003 and winter 2004, forms part of a southern expansion to Calgary's LRT system and is the world's first LRT system to be constructed with UHPC [53]. Subsequently, a motorway bridge was designed by VSL (Australia) at Shepherds Gully Creek, Australia, and was opened to traffic in 2005. Later applications of this material on pedestrian bridge in Germany [54], a cable stayed bridge in Korea [55], and a series of pedestrian bridges in New Zealand [56] have impressed the world with its great mechanical performance and durability. According to Federal Highway Administration (FHWA) tech-note [57], UHPC can be used in a broad range of highway infrastructure applications due to its high compressive and tensile strengths and its enhanced durability properties; thereby allowing a longer design/service life and thin overlays, claddings, or shells.

In the recent years, UHPC has been used in structural elements to resist extreme earthquake effects [58], and impact loads [59−61]. In more recent studies UHPC demonstrated high perforation resistance under high velocity impact loads [62,63]. The outstanding mechanical features of UHPC enable it to be used in the protective structure design against blast loads.

1.3.1 Blast loads and its effects on concrete structures

In contemporary society, concrete is the most widely used building material. Working together with steel reinforcement, concrete can provide a high level of

Figure 1.5 Structural progressive collapse induced by blast loads. Left: 1995 Alfred P. Murrah Federal Building (http://en.wikipedia.org/wiki/Alfred_P._Murrah_Federal_Building); Right: 1968 Ronan Point Building (http://en.wikipedia.org/wiki/Ronan_Point).

loading capacity which allows construction of high-rise buildings. During their service life, other than the design loads, reinforced concrete (RC) structures may experience extreme loads from impacts or explosions. Under these extreme loading conditions, instant response including flexural damage, shear damage, and concrete spall may occur on individual structural members. Subsequent damage to the entire building, which is known as progressive collapse (as shown in Fig. 1.5), can then be triggered after damage to one or several key load-carrying members occurs and there is insufficient redundant load paths. In recent years, the increase in terrorism activities highlights the importance of structural protection against blast loadings. Understanding the performance and remaining load-carrying capacities of structural columns after blast loadings is essential for structural protection.

Blast performance of structural members like concrete slabs, beams, and columns has been extensively investigated [64–67] in recent years. Under blast loading conditions, structural components may fail in multiple modes as shown in Fig. 1.6 [68]. At large scaled distances, flexural failure with ductile structural behavior and the maximum energy absorption may occur. With a decrease of scaled distance of blast scenarios, brittle damage modes like shear failure or combined shear and flexural failure may occur. When a blast occurs in close proximity to, or in contact with, concrete components, localized damage like concrete spall and cratering may happen.

When the blast scaled distance reduces, blast load magnitude is high and its rising time and duration is extremely short, flexure shear failure and direct shear failure could occur [69,70], and these failure modes, on the other hand, are abrupt and brittle so that they do not consume too much of the blast energy which severely
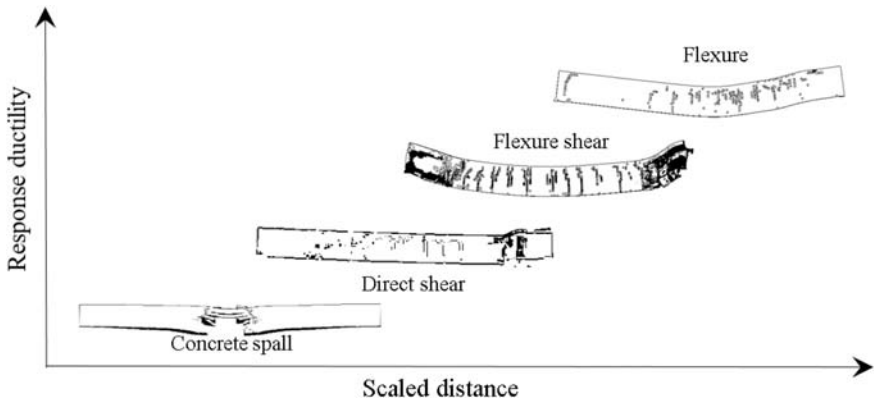
Figure 1.6 Structural-member failure modes under blast loads [68].

limit the loading capacity of the structural element. When an explosive detonation is in close proximity or even contact to the structure, material brittle spallation induced by stress wave propagation can be observed [64,71,72]. Given there is no sufficient structural redundancy, damage of individual component can cause the disproportional collapse of the entire structure [73,74] which is now an important concern for structural engineers and researchers.

Under blast loading conditions, assessing damage is of critical importance and significance for structural protective design. Pressure−impulse diagrams are widely adopted for evaluating blast induced damage. A pressure−impulse diagram ($P−I$ diagram) contains a series of iso-damage curves in which each iso-damage curve represents a structural damage level. Damage criterion for $P−I$ diagrams should be carefully chosen depending on the blast loading conditions and corresponding damage types. For structures which experience global deformations under blast loading conditions, the structural central deflections have been adopted as the damage criterion. According to this criterion, Fallah and Louca [75] derived pressure−impulse diagrams for elastic−plastic hardening and elastic−plastic softening single-degree-of-freedom (SDOF) systems under blast loads. Li and Meng [76] studied the pulse loading shape effects on the pressure−impulse diagram based on the maximum deflection damage criterion and the elastic SDOF model. When considering brittle shear damage, Li and Hao [65,77] used the shear slip close to the boundary to define the brittle shear damage level and generated $P−I$ diagrams. Although these parameters provide good quantifications of column damages subjected to blast loadings, they are indirect assessment of column conditions in relation to the functionality of structural columns. Since the primary function of a structural column is to carry vertical load, a damage criterion based on remaining load-carrying capacity of RC columns after blast loading was proposed by Shi et al. [78]. In the latter work, parametric studies were conducted to investigate the effects of column geometry, concrete strength, longitudinal and transverse reinforcement ratio on RC column capacity to resist blast loads. $P−I$ diagrams were developed

according to damage criteria defined with respect to the remaining load-carrying capacities. Based on the numerical results, analytical formulae to predict the $P-I$ diagrams for RC columns were derived. These $P-I$ diagrams give more direct and quantitative assessments of column functionality after blast loadings.

As discussed earlier, residual load-carrying capacity of columns plays a key role in the structural postblast performance. If residual load-carrying capacity is sufficient, then the threat of progressive collapse can then be minimized. Bao and Li [79] utilized a verified finite element model to study the residual load-carrying capacity of a column after a blast. An extensive parametric study was carried out on a series of 12 columns to investigate the effects of transverse reinforcement ratio, axial load ratio, longitudinal reinforcement ratio, and column aspect ratio on the residual load-carrying capacity. Roller et al. [80] observed that there is little research regarding the behavior of elements with one-dimensional load capacity like columns and their capacity under blast loading conditions. To provide more in-depth knowledge, they started a test program involving both standard RC columns and retrofitted concrete columns under blast loads first and then static loads. Remaining load-carrying capacities of blast-damaged columns were obtained through uniaxial compressive tests.

Generally speaking, there are two ways to enhance the blast resistance capacity of concrete columns. The first one is to retrofit concrete columns with fiber-reinforced polymer (FRP) composite laminates [81] and steel jackets [82,83]. Hao et al. [84] carried out reliability analysis of RC columns with FRP strengthening under explosive loading conditions, and demonstrated the effectiveness of FRP strengthening on structural protection. Through extensive numerical simulations, Mutalib and Hao [85] developed $P-I$ curves for assessing the damage of FRP retro-fitted concrete columns after blast loads. Wu et al. [86] conducted blast tests on two RC specimens: a plain RC specimen and an identical RC specimen retrofitted with near surface mounted carbon FRP plates. A number of unique behaviors of both specimens were observed, investigated, and analyzed. When designing steel jacket for the RC structures, the anchorage should be carefully considered as blast may trigger direct shear damage mode on the component that makes the retrofitting less efficient [87]. Unlike seismic retrofitting, when designing jacketing for a column against blast loads, it is preferable to provide no gap at the top or the bottom of the retrofit so as to provide continuity and maximize the resistance [88].

Another effective method to enhance the blast resistance of columns is to use high-performance concrete material such as FRC. Compared with NSC, FRC is known for its high strength, high ductility, and high durability. It allows construction of sustainable and economic buildings with extraordinarily slim designs. As a notable representative, UHPC has ultra-high strength and ductility which makes it an ideal construction material for bridge decks, storage halls, thin-wall shell structures, and highly loaded columns. Because UHPC is a relatively new concrete material, optimization of the material composition of UHPC is still widely studied in order to cater for the need of even better performance such as early age workability, impact and explosive resistance, fire and corrosion resistance, and aggressive chemical resistance. The development of UHPC is based on advancements in the

materials science. Considerable effort is required to transfer and implement the knowledge gained at the material level to structural engineering and design.

1.3.2 Ultra-high performance concrete members under blast loads

Published research data on the blast performance of UHPFRC structural components is focusing primarily on one-way panel components. The blast behavior of panel components made of Ductal, a commercial UHPC, has been investigated in a number of studies. As shown in Fig. 1.7, Ngo et al. [89] tested seven 2 m × 1 m Ductal panels having thicknesses which varied between 50 and 100 mm, under live explosives at standoff distances of 30−50 m and varying charge weights which resulted in reflected pressures of 400−2000 kPa. Overall, the UHPC panels showed high ductility, limited permanent deformations, and an ability to absorb substantial energy without fragmentation, in contrast to a companion panel constructed with conventional concrete.

Wu et al. [90] tested a further series of Ductal panels having dimensions of 2 m × 1 m × 0.1 m under "close-in" blast loads. The one-way panels were partially fixed and exposed to 1−20 kg of equivalent TNT at standoffs of 1−3 m. The UHPC panels showed increased hinge rotation capacity and an ability to sustain larger blast loads when compared to companion panels made of conventional RC. In a further study, four simply supported Ductal panels with dimensions of 3.5 m × 1.3 m × 100 mm were tested under larger charge weights of 100 kg of equivalent TNT at the University of Liverpool [91]. The first two panels contained conventional steel reinforcement, 2% steel fibers, and were tested at standoff distances of 7 and 9 m. The panels sustained large maximum displacements of 110 and 210 mm, but showed an ability to recover with residual displacements of 20 and 50 mm, respectively. The remaining two panels were unreinforced and contained a volume fraction of 2% and 4% steel fibers. The panels were tested at 12 m standoff and suffered large permanent displacements of 180 and 90 mm, respectively, with horizontal cracking across their full width. Nonetheless, the specimens showed no major fragmentation and remained standing after testing. Ellis et al. [92]

Figure 1.7 UHPC slab versus NSC slab under 5 ton Hexolite-RDX/TNT detonation at 40 m standoff distance.

tested four simply supported, unreinforced, one-way UHPC panels having dimensions 1.625 m × 0.864 m × 0.051 m under reflected impulse loads which varied between 0.77 and 2.05 MPa-ms using a shock tube. The study determined that the unreinforced panels failed at reflected impulse in between 0.97 and 1.47 MPa-seconds. The results were used to develop a hierarchical multiscale model which was then used to conduct a parametric study which demonstrated that factors that increase energy dissipation, such as fiber geometry, fiber packing, and fiber volume fraction, are critical to enhance the blast performance of unreinforced UHPC panels.

Published research on the blast performance of two-way UHPC panels is limited. Yi et al. [93] conducted "close-in" live explosive tests on three two-way panels constructed with NSC, HSC, and a proprietary UHPC. The 1 m × 1 m × 150 mm panels were clamped on all four sides and tested under charge weights of 4−16 kg of ammonium nitrate/fuel oil (ANFO) at a standoff of 1.5 m. When compared to the specimens made of HSC and NSC, the UHPC panel showed improved blast performance, reduced the maximum and residual displacements, more controlled cracking with reduced spalling.

Published research on the performance of UHPC columns is rather limited despite its importance. Under blast loads, columns of UHPC containing 4%−6% steel fibers produced very high blast resistance by reducing the maximum displacement, enhancing the damage tolerance, and eliminating secondary blast fragments. Aoude et al. [94] tested UHPC columns under simulated blast loads. As shown in Fig. 1.8, as part of the experimental program, nine full-scale columns constructed with compact reinforced composite (CRC), a proprietary UHPC, were tested under simulated blast loading and exposed to varying blast pressure−impulse combinations using a shock tube. While the fiber and steel reinforcement played important
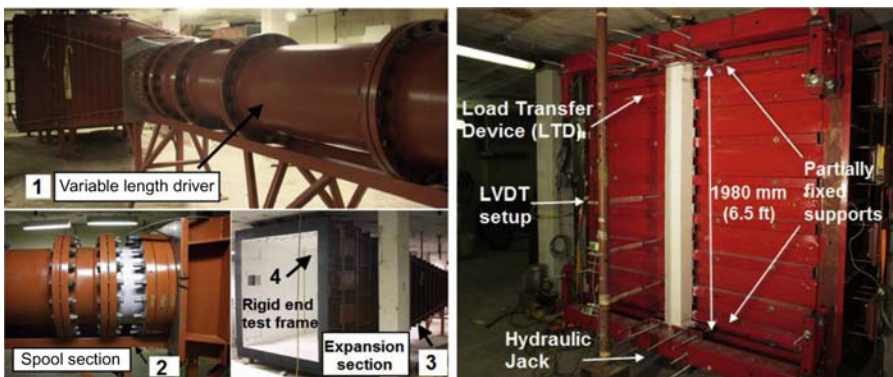

Figure 1.8 Shock tube testing on UHPC columns and sample photos of columns after application of blasts. (A) SCC-0%-75, (B) SCC-0%-38, (C) CRC-2%A-75, (D) CRC-6%A-75, (E) CRC-4%A-75, (F) CRC-2%A-38, (G) CRC-2%B-75, (H) CRC-2%C-75, (I) CRC-2%B-75-15 M, (J) CRC-2%C-75-15 M, and (K) CRC-2%C-38 [94].
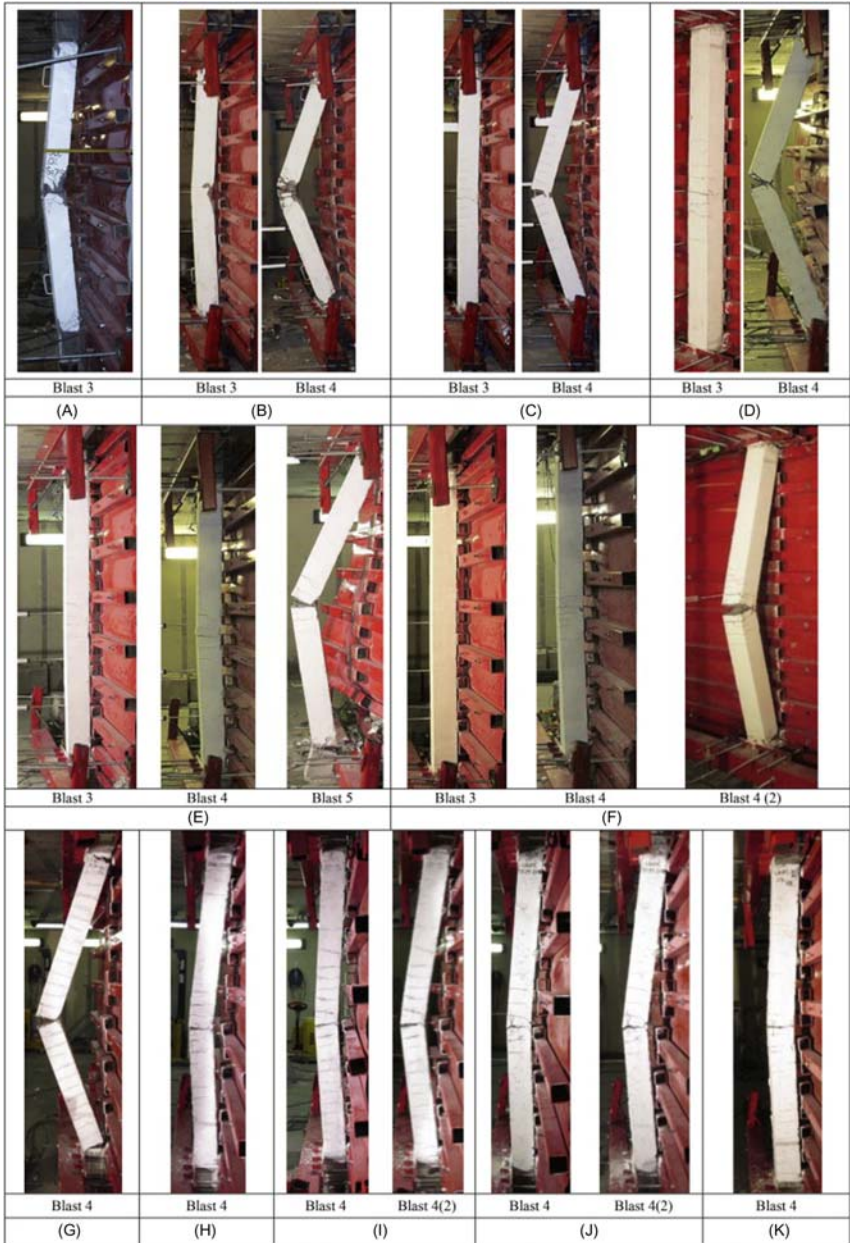
Figure 1.8 (Continued)

role in column performance, UHPC is found to significantly improve the column blast resistance and damage tolerance.

As evidenced in these limited blast tests, UHPC components with steel fibers reinforcement have high ductility, limited permanent deformations, and substantial energy absorbance without fragmentation under blast loads.

1.3.3   Ultra-high performance concrete filled steel tube columns against blast loads

In recent years, a new steel-concrete composite member, known as a concrete-filled double-skin steel tube (CFDST), has gained interest in the construction industry due to its attractive properties such as ease of construction, light weight, high strength, and good seismic resistance.

A CFDST member is simply made from two concentrically placed steel skins filled with concrete in between and it utilizes the advantages of both steel and concrete. Under axial compression, due to the different Poisson's ratio of steel and concrete, the concrete of a CFDST column is normally in a triaxially confined state and consequently the confining pressures can effectively enhance the strength and the ductility of the concrete which is known as the confinement effect. All of the previously mentioned studies indicate that CFDST members inherit the advantages of both steel and concrete and that they exhibit very ductile behavior under axial compressive as well as transverse loading. However, most existing studies are strictly limited to static loading only, thus the analytical models developed cannot be applied to evaluate situations where impact and blast loads are introduced. Therefore there is a need to evaluate the performance of CFDST members subjected to impact and blast loads. Furthermore, as CFDST members have been more and more commonly adopted in the field of civil engineering applications, large axial bearing capacity is required. Therefore by replacing NSC with UHPC in CFDST members, the cross-section area as well as the self-weight of the structural members can be further reduced.

In the following chapters, advanced UHPC materials with nanoparticle addition are presented, and the static and dynamic tests in the laboratory demonstrate their outstanding mechanical performance compared to NSC. Some field blast tests involving close-in and contact detonations are designed on concrete columns, slabs, and CFDST made/infilled by these materials. The results will further elaborate the effect of UHPC in protective design against catastrophic blast loads.

References

[1]   BS EN 206-1: 2000. Concrete. Specification, Performance, Production and Conformity, BSI, London, 2001.
[2]   E.G. Nawy, Fundamentals of High-Performance Concrete, John Wiley & Sons, New York, 2001.

[3] M.J. Shannag, High strength concrete containing natural pozzolan and silica fume, Cem. Concr. Compos. 22 (2000) 399−406.

[4] P.-C. Aïtcin, High Performance Concrete, CRC Press, Boca Raton, 2011.

[5] S. Popovics, Analysis of concrete strength versus water-cement ratio relationship, Mater. J. 87 (1990) 517−529.

[6] M. Mazloom, A.A. Ramezanianpour, J.J. Brooks, Effect of silica fume on mechanical properties of high-strength concrete, Cem. Concr. Compos. 26 (2004) 347−357.

[7] V. Yogendran, B. Langan, M. Haque, M. Ward, Silica fume in high-strength concrete, Mater. J. 84 (1987) 124−129.

[8] S.A. Khedr, M.N. Abou-Zeid, Characteristics of silica-fume concrete, J. Mater. Civil Eng. 6 (1994) 357−375.

[9] S. Bhanja, B. Sengupta, Influence of silica fume on the tensile strength of concrete, Cem. Concr. Res. 35 (2005) 743−747.

[10] F.A. Oluokun, Fly ash concrete mix design and the water-cement ratio law, Mater. J. 91 (1994) 362−371.

[11] Y.-W. Chan, S.-H. Chu, Effect of silica fume on steel fiber bond characteristics in reactive powder concrete, Cem. Concr. Res. 34 (2004) 1167−1172.

[12] P.C. Aïtcin, The durability characteristics of high performance concrete: a review, Cem. Concr. Compos. 25 (2003) 409−420.

[13] A.A. Griffith, The phenomena of rupture and flow in solids, Phil. Trans. R. Soc. Lond. Ser. A, Containing Papers of a Mathematical or Physical Character 221 (1921) 163−198.

[14] H.H. Bache, Compact Reinforced Composite Basic Principles, Aalborg, Portland, 1987.

[15] M. Cheyrezy, V. Maret, L. Frouin, Microstructural analysis of RPC (reactive powder concrete), Cem. Concr. Res. 25 (1995) 1491−1500.

[16] E. Fehling, M. Schmidt, J. Walraven, T. Leutbecher, S. Fröhlich, Ultra-High Performance Concrete UHPC: Fundamentals, Design, Examples, John Wiley & Sons, Marseille (France), 2014.

[17] T. Hirschi, F. Wombacher, Influence of different superplasticizers on UHPC, in: Proceedings of the Second International Symposium on Ultra High Performance Concrete, Kassel, Germany, 2008, pp. 77−84.

[18] C. Schröfl, M. Gruber, J. Plank, Preferential adsorption of polycarboxylate superplasticizers on cement and silica fume in ultra-high performance concrete (UHPC), Cem. Concr. Res. 42 (2012) 1401−1408.

[19] O. Bonneau, M. Lachemi, E. Dallaire, J. Dugat, P.-C. Aïtcin, Mechanical properties and durability of two industrial reactive powder concretes, ACI Mater. J. 94 (1997) 286−290.

[20] P. Acker, M. Behloul, Ductal® technology: a large spectrum of properties, a wide range of applications, in: Proceedings of the International Symposium on UHPC, Kassel, Germany, 2004, pp. 11−23.

[21] T.M. Ahlborn, D.L. Misson, E.J. Peuse, C.G. Gilbertson, Durability and strength characterization of ultra-high performance concrete under variable curing regimes, in: E. Fehling, M., Schmidt, S. Stürwald (Eds.), Proceedings of the Second International Symposium on Ultra High Performance Concrete, Kassel, Germany, 2008, pp. 197−204.

[22] K. Wille, A.E. Naaman, S. El-Tawil, Optimizing ultra-high performance fiber-reinforced concrete, Concr. Int. 33 (2011) 35−41.

[23] M. Alkaysi, S. El-Tawil, Z. Liu, W. Hansen, Effects of silica powder and cement type on durability of ultra high performance concrete (UHPC), Cem. Concr. Compos. 66 (2016) 47−56.

[24] B.A. Graybeal, Material Property Characterization of Ultra-High Performance Concrete, FHWA-HRT-06-103, Federal Highway Administration, Washington, DC, 2006.

[25] M. Alkaysi, S. El-Tawil, Effects of variations in the mix constituents of ultra high performance concrete (UHPC) on cost and performance, Mater. Struct. 49 (2016) 4185−4200.

[26] K. Wille, A.E. Naaman, S. El-Tawil, G.J. Parra-Montesinos, Ultra-high performance concrete and fiber reinforced concrete: achieving strength and ductility without heat curing, Mater. Struct. 45 (2012) 309−324.

[27] R.J. Flatt, Y.F. Houst, A simplified view on chemical effects perturbing the action of superplasticizers, Cem. Concr. Res. 31 (2001) 1169−1176.

[28] F. Sanchez, K. Sobolev, Nanotechnology in concrete−a review, Constr. Build. Mater. 24 (2010) 2060−2071.

[29] R. Duval, E. Kadri, Influence of silica fume on the workability and the compressive strength of high-performance concretes, Cem. Concr. Res. 28 (1998) 533−547.

[30] A.M. Brandt, Fibre reinforced cement-based (FRC) composites after over 40 years of development in building and civil engineering, Compos. Struct. 86 (2008) 3−9.

[31] S. Rigaud, G. Chanvillard, J. Chen, Characterization of bending and tensile behavior of ultra-high performance concrete containing glass fibers, in: G. Parra-Montesinos, H. Reinhardt, A.E. Naaman (Eds.), High Performance Fiber Reinforced Cement Composites 6, Springer, Netherlands, 2012, pp. 373−380.

[32] Z. Zheng, D. Feldman, Synthetic fibre-reinforced concrete, Prog. Polym. Sci. 20 (1995) 185−210.

[33] A.M. Alani, D. Beckett, Mechanical properties of a large scale synthetic fibre reinforced concrete ground slab, Constr. Build. Mater. 41 (2013) 335−344.

[34] Y. Ye, S. Hu, B. Daio, S. Yang, Z. Liu, Mechanical behavior of ultra-high performance concrete reinforced with hybrid different shapes of steel fiber, in: CICTP 2012: Multimodal Transportation Systems—Convenient, Safe, Cost-Effective, Efficient, Beijing, 2012, pp. 3017−3028.

[35] S.H. Kim, G.S. Ryu, K.T. Koh, Flexural behavior characteristics of UHPC according to twisted steel fiber, Adv. Mater. Res. 652 (2013) 1499−1504.

[36] G.S. Ryu, S.H. Kim, G.H. Ahn, K.T. Koh, Evaluation of the direct tensile behavioral characteristics of UHPC using twisted steel fibers, Adv. Mater. Res. 602 (2013) 96−101.

[37] V. Bindiganavile, N. Banthia, Polymer and steel fiber-reinforced cementitious composites under impact loading? Part 1: bond-slip response, ACI Mater. J. 98 (2001).

[38] Z. Xu, H. Hao, H. Li, Experimental study of dynamic compressive properties of fibre reinforced concrete material with different fibres, Mater. Des. 33 (2012) 42−55.

[39] Ş. Yazıcı, G. İnan, V. Tabak, Effect of aspect ratio and volume fraction of steel fiber on the mechanical properties of SFRC, Constr. Build. Mater. 21 (2007) 1250−1253.

[40] Z.L. Wang, J. Wu, J.G. Wang, Experimental and numerical analysis on effect of fibre aspect ratio on mechanical properties of SRFC, Constr. Build. Mater. 24 (2010) 559−565.

[41] B. Nematollahi, R.M. Saifulnaz, M.S. Jaafar, Y.L. Voo, A review on ultra high performance 'ductile' concrete (UHPdC) technology, Int. J. Civil Struct. Eng. 2 (2012) 994.

[42] J. Belkowitz, D. Armentrout, The Investigation of Nano Silica in the Cement Hydration Process, ACI Special Publication, 267 (2009), pp. 87−100.

[43] M. Berra, F. Carassiti, T. Mangialardi, A. Paolini, M. Sebastiani, Effects of nanosilica addition on workability and compressive strength of Portland cement pastes, Constr. Build. Mater. 35 (2012) 666−675.

[44] M. Jalal, M. Fathi, M. Farzad, Effects of fly ash and TiO_2 nanoparticles on rheological, mechanical, microstructural and thermal properties of high strength self compacting concrete, Mech. Mater. 61 (2013) 11−27.

[45] B.-W. Jo, C.-H. Kim, G.-h. Tae, J.-B. Park, Characteristics of cement mortar with nano-SiO_2 particles, Constr. Build. Mater. 21 (2007) 1351−1355.

[46] H. Li, H.-g. Xiao, J. Yuan, J. Ou, Microstructure of cement mortar with nano-particles, Compos. B Eng. 35 (2004) 185−189.

[47] A. Nazari, S. Riahi, The effect of TiO_2 nanoparticles on water permeability and thermal and mechanical properties of high strength self-compacting concrete, Mater. Sci. Eng. A 528 (2010) 756−763.

[48] A. Nazari, S. Riahi, The effects of ZrO_2 nanoparticles on physical and mechanical properties of high strength self compacting concrete, Mater. Res. 13 (2010) 551−556.

[49] A. Nazari, S. Riahi, The effects of SiO_2 nanoparticles on physical and mechanical properties of high strength compacting concrete, Compos. B Eng. 42 (2011) 570−578.

[50] Y. Qing, Z. Zenan, K. Deyu, C. Rongshen, Influence of nano-SiO_2 addition on properties of hardened cement paste as compared with silica fume, Constr. Build. Mater. 21 (2007) 539−545.

[51] X. Liu, L. Chen, A. Liu, X. Wang, Effect of nano-$CaCO_3$ on properties of cement paste, Energy Procedia 16 (Part B) (2012) 991−996.

[52] A. Nazari, S. Riahi, The effects of zinc dioxide nanoparticles on flexural strength of self-compacting concrete, Compos. B Eng. 42 (2011) 167−175.

[53] V. Perry, D. Zakariasen, First Use of Ultra-High Performance Concrete for an Innovative Train Station Canopy, Concrete Technology Today, 2004. <http://www. cement.org>.

[54] E. Fehling, K. Bunje, M. Schmidt, Gärtnerplatz − bridge over River Fulda in Kassel: multispan hybrid UHPC-steel bridge, Designing and Building with UHPFRC, John Wiley & Sons Inc., Marseille (France), 2013, pp. 0−136.

[55] W.J. Chin, Y.J. Kim, J.-R. Cho, J.S. Park, Dynamic characteristics evaluation of innovative UHPC pedestrian cable stayed bridge, Engineering 4 (12) (2012) 869−876.

[56] M. Rebentrost, G. Wight, Perspective on UHPCs from a specialist construction company, Designing and Building with UHPFRC, John Wiley & Sons Inc., Marseille (France), 2013, pp. 189−208.

[57] B. Graybeal, Ultra-high performance concrete. No. FHWA-HRT-11-038. 2011.

[58] G.J. Parra-Montesinos, S.W. Peterfreund, S.-H. Chao, Highly damage-tolerant beam-column joints through use of high-performance fiber-reinforced cement composites, ACI Struct. J. 102 (2005).

[59] V. Bindiganavile, N. Banthia, B. Aarup, Impact response of ultra-high-strength fiber-reinforced cement composite, ACI Mater. J. 99 (2002) 543−548.

[60] A. Bragov, Y.V. Petrov, B.L. Karihaloo, A.Y. Konstantinov, D. Lamzin, A. Lomunov, et al., Dynamic strengths and toughness of an ultra high performance fibre reinforced concrete, Eng. Fract. Mech. 110 (2013) 477−488.

[61] K. Habel, P. Gauvreau, Response of ultra-high performance fiber reinforced concrete (UHPFRC) to impact and static loading, Cem. Concr. Compos. 30 (2008) 938−946.

[62] J. Liu, C. Wu, X. Chen, Numerical study of ultra-high performance concrete under non-deformable projectile penetration, Construct. Build. Mater. 135 (2017) 447−458.

[63] T. Zhang, H. Wu, Q. Fang, T. Huang, Z. Gong, Y. Peng, UHP-SFRC panels subjected to aircraft engine impact: experiment and numerical simulation, Int. J. Impact. Eng. 100 (2017) 242−254.

[64] J. Li, H. Hao, Numerical study of concrete spall damage to blast loads, Int. J. Impact. Eng. 68 (2014) 41−55.

[65] T.S. Ng, A. Amin, S.J. Foster, The behaviour of steel-fibre-reinforced geopolymer concrete beams in shear, Mag. Concr. Res. 65 (2013) 308−318.

[66] W. Chen, H. Hao, S. Chen, Numerical analysis of prestressed reinforced concrete beam subjected to blast loading, Mater. Des. 65 (2015) 662−674.

[67] P.F. Silva, B. Lu, Blast resistance capacity of reinforced concrete slabs, J. Struct. Eng. 135 (2009) 708−716.

[68] J. Li, C. Wu, H. Hao, Y. Su, Z.-X. Li, A study of concrete slabs with steel wire mesh reinforcement under close-in explosive loads, Int. J. Impact. Eng. 100 (2017) 242−254.

[69] J. Li, H. Hao, Influence of brittle shear damage on accuracy of the two-step method in prediction of structural response to blast loads, Int. J. Impact. Eng. 54 (2013) 217−231.

[70] S. Menkes, H. Opat, Broken beams, Exp. Mech. 13 (1973) 480−486.

[71] J. Li, C. Wu, H. Hao, Z. Wang, Y. Su, Experimental investigation of ultra-high performance concrete slabs under contact explosions, Int. J. Impact. Eng. 93 (2016) 62−75.

[72] W. Wang, D. Zhang, F. Lu, S.-c. Wang, F. Tang, Experimental study and numerical simulation of the damage mode of a square reinforced concrete slab under close-in explosion, Eng. Fail. Anal. 27 (2013) 41−51.

[73] B. Luccioni, R. Ambrosini, R. Danesi, Analysis of building collapse under blast loads, Eng. Struct. 26 (2004) 63−71.

[74] J. Li, H. Hao, Numerical study of structural progressive collapse using substructure technique, Eng. Struct. 52 (2013) 101−113.

[75] A.S. Fallah, L. Louca, Pressure−impulse diagrams for elastic-plastic-hardening and softening single-degree-of-freedom models subjected to blast loading, Int. J. Impact. Eng. 34 (2007) 823−842.

[76] Q. Li, H. Meng, Pressure-impulse diagram for blast loads based on dimensional analysis and single-degree-of-freedom model, J. Eng. Mech. 128 (2002) 87−92.

[77] J. Li, H. Hao, Numerical and theoretical study of concrete spall damage under blast loads, Appl. Mech. Mater. 553 (2014) 774−779.

[78] Y. Shi, H. Hao, Z.-X. Li, Numerical derivation of pressure−impulse diagrams for prediction of RC column damage to blast loads, Int. J. Impact. Eng. 35 (2008) 1213−1227.

[79] X. Bao, B. Li, Residual strength of blast damaged reinforced concrete columns, Int. J. Impact. Eng. 37 (2010) 295−308.

[80] C. Roller, C. Mayrhofer, W. Riedel, K. Thoma, Residual load capacity of exposed and hardened concrete columns under explosion loads, Eng. Struct. 55 (2013) 66−72.

[81] O. Chaallal, M. Shahawy, M. Hassan, Performance of axially loaded short rectangular columns strengthened with carbon fiber-reinforced polymer wrapping, J. Compos. Construct. 7 (2003) 200−208.

[82] S. Fujikura, M. Bruneau, D. Lopez-Garcia, Experimental investigation of multihazard resistant bridge piers having concrete-filled steel tube under blast loading, J. Bridge Eng. 13 (2008) 586−594.

[83] K. Morrill, L. Malvar, J. Crawford, J. Ferritto, Blast resistant design and retrofit of reinforced concrete columns and walls, in: Proceedings of the 2004 Structures Congress−Building on the Past, Securing the Future, 22−26 May, Nashville, TN, 2004, pp. 1−8.

[84] H. Hao, Z. Li, Y. Shi, Reliability analysis of RC columns and frame with FRP strengthening subjected to explosive loads, J. Perform. Constr. Facil. (2015). 04015017.

[85] A.A. Mutalib, H. Hao, Development of PI diagrams for FRP strengthened RC columns, Int. J. Impact. Eng. 38 (2011) 290−304.

[86] C. Wu, D.J. Oehlers, J. Wachl, C. Glynn, A. Spencer, M. Merrigan, et al., Blast testing of RC slabs retrofitted with NSM CFRP plates, Adv. Struct. Eng. 10 (2007) 397−414.

[87] S. Fujikura, M. Bruneau, Dynamic analysis of multihazard-resistant bridge piers having concrete-filled steel tube under blast loading, J. Bridge Eng. 17 (2011) 249−258.

[88] L.J. Malvar, J.E. Crawford, K.B. Morrill, Use of composites to resist blast, J. Compos. Construct. 11 (2007) 601−610.

[89] T. Ngo, P. Mendis, T. Krauthammer, Behavior of ultrahigh-strength prestressed concrete panels subjected to blast loading, J. Struct. Eng. 133 (2007) 1582−1590.

[90] C. Wu, D. Oehlers, M. Rebentrost, J. Leach, A. Whittaker, Blast testing of ultra-high performance fibre and FRP-retrofitted concrete slabs, Eng. Struct. 31 (2009) 2060−2069.

[91] S. Barnett, S. Millard, A. Tyas, G. Schleyer, Briefing: blast tests of fibre-reinforced concrete panels, Proc. ICE −Construct. Mater. 163 (2010) 127−129.

[92] B. Ellis, B. DiPaolo, D. McDowell, M. Zhou, Experimental investigation and multi-scale modeling of ultra-high-performance concrete panels subject to blast loading, Int. J. Impact. Eng. 69 (2014) 95−103.

[93] N.-H. Yi, J.-H.J. Kim, T.-S. Han, Y.-G. Cho, J.H. Lee, Blast-resistant characteristics of ultra-high strength concrete and reactive powder concrete, Construct. Building Mater. 28 (2012) 694−707.

[94] H. Aoude, F.P. Dagenais, R.P. Burrell, M. Saatcioglu, Behavior of ultra-high performance fiber reinforced concrete columns under blast loading, Int. J. Impact. Eng. 80 (2015) 185−202.

This page intentionally left blank

Development, testing, and numerical simulation of ultra-high performance concrete at material level

<div style="text-align:right">**2**</div>

2.1 Introduction

Ultra-high performance concrete (UHPC) inherits positive aspects of ultra-high strength concrete (UHSC), and it is equipped with improved ductility as a result of fiber addition. Over the past several decades, a fast development is observed on high compressive strength concrete and high ductility concrete. High-strength concrete is designed to achieve a size efficiency of large structures and also provide extra strength safety margin. High ductility concrete, however, is mainly designed to overcome the material brittleness and ensure the material ductility and energy absorption capability of structural members under dynamic loads. The decoupled development of both resulted in exclusion of each other's desirable properties. Effort has been devoted to the development of new concrete with both benefits from high compressive strength and high material ductility.

Fiber material is known to be beneficial to ductility enhancement in cementitious matrix. The concept of using fibers as material reinforcement is not new. Fibers have been used as reinforcement since the mighty time of ancient Roman. Modern version of concrete fibers did not come into use until 1960s when steel fibers, glass fibers, and synthetic fibers took the stage. The use of fiber in concrete matrix can reduce the concrete permeability and enhance its crack control ability. Investigation of the influence from varying fiber reinforcement type on the concrete performance had been conducted in the recent studies. Among all fiber types, steel fibers are known to have higher modulus of elasticity than the concrete matrix, which means they can enhance the load carrying capacity, thus increase tensile strength of the material. Concrete with steel fiber reinforcement has better impact, shatter, and abrasion resistance.

Nowadays steel fibers are widely used as reinforcement in industrial floor slabs, standard reinforcing cage for tunnel segments, shotcrete, and prefabricated concrete products. Ye et al. [1] experimentally investigated the mechanical behavior of concrete reinforced by hybrid different shapes of steel fibers. The largest fracture energy and bending toughness were obtained with hybrid fibers, where the volume ratio of long ultra-fine fiber was 1.5%, and the ratio of long end-hooked fiber was 0.5%. The hybrid fibers had generated positive intermixing effect. Kim et al. [2] examined the effects of twisted steel fiber (TF) on concrete flexural toughness, and

three types of twisted fiber with different lengths and diameters were considered. Ryu et al. [3] found that concrete with twisted fiber reinforcement exhibited significantly improved mechanical characteristics compared to control concrete containing conventional straight fiber. Bindiganavile and Banthia [4] pointed out that under both static and low-rate impact loads, the predominant failure mode of steel fiber reinforced concrete material was the steel fiber pull-out. To increase the bonding between the concrete and steel fiber material, Xu et al. [5] proposed spiral-shaped steel fibers, and the impact tests had demonstrated that fiber-reinforced concrete specimens reinforced with this spiral-shaped fibers displayed the largest ultimate compressive strength, the largest post-failure strength and the largest energy-absorption capacity among specimens reinforced with seven other types of fibers tested.

For steel fiber—reinforced concrete, two of the most important factors that affect the concrete properties are fiber aspect ratio (ratio of steel fiber length over diameter) and volume fraction. Increasing fiber aspect ratio helps increasing the probability of heterogeneous distribution and flocculation in concrete. Fiber volume fraction significantly affects the workability of concrete. Yazıcı et al. [6] tested hooked-end bundled steel fibers reinforced concrete, and the influence of different aspect ratios and fiber volumes were discussed. They noted that split tensile strength and flexural strength of SFRC are improved with increasing aspect ratio and fiber volume fraction. Wang et al. [7] conducted experimental analysis on effect of fiber aspect ratio on mechanical properties of steel fiber reinforced concrete, and the results revealed that the aspect ratio had an optimal value for strengths in every concrete batch. Beyond this value, the addition of steel fibers into concrete may have an effect of increasing the ductility rather than the strengths.

Besides fiber material, the other fact that has profound impact on the UHPC performance is the pozzolanic material, and conventionally silica fume has been used due to its filling effect and reaction with calcium hydroxide in concrete. Recently, development of nanotechnology provided further improvement on UHPC. It was observed that several phenomena including statistically mechanical effects and quantum mechanical effects become pronounced as size of the system decreases. Due to their ultra-fine size, addition of nanoscale particles results in significantly improved material properties without much change of the material composition. As a consequence, researchers and engineers are exploring feasibility of reengineering many existing materials like concrete by adding nanoscale particles into the matrix to get new and novel material that has unprecedented performance.

Qing et al. [8] demonstrated that pozzolanic activity of nano-SiO_2 (NS) is much higher than that of silica fume, and the bond strength of the paste to aggregate interface is also higher than that of specimens with silica fume. Ji [9] also reported that NS has pozzolanic effect that can react with $Ca(OH)_2$ crystals, making the interfacial transition zone (ITZ) between the aggregate and the binding matrix denser. Experimental results showed that the compressive strengths of mortars with NS particles were all higher than those of mortars containing silica fume at 7 and 28 days [10, 8]. Liu et al. [11] added nano-$CaCO_3$ (NC) into cement paste, and the

experimental results showed that NC had no effect on water requirement of normal consistency of cement. However, with the increase of NC content, its flowability decreased and setting time of fresh cement paste was shortened. Flexural strength as well as compressive strength increased with the addition of NC at the age of 7 and 28 days. Nazari and his colleagues conducted series of experimental tests on different nanoscale additives mixed into concrete matrix [12−17]. Although their work had only been demonstrated in small samples, it was believed that if only it can scale up to larger quantities, it is possible to produce concrete four times stronger than the strongest existing commercial concrete mixes.

In Section 2.2, effect from nanomaterial addition on the mechanical performance of UHPC is investigated. Besides discussion on static and dynamic material properties, UHPC samples after Split Hopkinson Pressure Bar (SHPB) tests are analyzed under Scanning Electron Microscope (SEM) Analysis to explain the macro-failure in microscale. X-ray diffraction (XRD) analysis and X-ray fluorescence (XRF) analysis are carried out to further understand the failure element composition and strength development of this advanced material.

In Section 2.3, different fibers with varying geometries and volume fractions are considered in the UHPC design. Static tests including uniaxial compression, four-point bending as well as dynamic compressive tests using SHPB are conducted. Dynamic compressive strength and tensile strength of UHPC samples with varying fiber materials are compared and discussed. Dynamic increase factors that are important describing the material under high loading rate are generated and plotted in charts, and the influences of different fiber additions on the dynamic properties of UHPC material are discussed.

In Section 2.5, mesoscale numerical simulations on UHPC considering the explicit fiber distribution is conducted. Although concrete material can be treated as homogeneous at macroscopic scale, when observed at a smaller length scale, concrete like UHPC is heterogeneous and consists of constituents including aggregate, calcium hydroxide (CH) crystals, C-S-H gel, water, and fiber material. Existence of ITZs weakens the bonding between the fibers and concrete matrix. The bonding performance of SFRC is influenced by the fiber geometry [18−20], fiber orientation [21,22], and also the strength of the matrix; it is therefore critical to consider the ITZ effect in the performance of UHPC. In general, to investigate the ITZ effect on the fiber bonding properties, UHPC can be described as multiphase material consisting of the cement paste, aggregates, fibers, and ITZs among them. As can be noted in the literature, the mechanical behavior of SFRC is mainly investigated through experimental and associated analytical studies. Over the past several decades, with the development of computer power and computational mechanics, numerical simulation of material and structural behavior under both static and dynamic conditions are becoming increasingly popular. Fiber-reinforced concrete is studied as homogeneous material [23−28]. Besides these homogeneous models, mesoscale study considering the heterogeneity of concrete under static and dynamic loads can also be found in the literature. Research was carried out on plain concrete in mesoscale under dynamic loads [29−31]. Fang and Zhang [32] conducted three-dimensional modeling of steel fiber−reinforced concrete material under intense

dynamic loading, and their model well reproduced SFRC failure under contact deto-nations. Xu et al. [33] developed an axisymmetric mesoscale model with compo-nents of fiber, aggregate, and mortar to investigate the dynamic failure behavior of SFRC material under impact loading.

The mesoscale modeling of UHPC material is studied in this research in Section 2.5. Single-fiber pull-out tests are firstly carried out to provide information about the interfacial bonding between the fiber and concrete matrix. Then the bond-ing is modeled with sliding contact algorithm in the numerical model, the numerical model is then calibrated through static split tensile tests, and SHPB tests are finally investigated with the mesoscale model.

2.2   Ultra-high performance concrete development with steel fiber and nanomaterial addition

Like conventional concrete, UHPC is composed of a variety of constituents that are blended in a mixer to create a semifluid product that will develop a particular set of properties with time. The common constituents of UHPC include binders, chemical admixtures, fiber reinforcement, and water. UHPC formulations must be developed with a focus on performances and compatibility of constituent components. Dry components including Portland cement, silica fume, and fine aggregates comprise the majority of the UHPC constituents. The fine aggregates are proportioned and sized to allow a gradation of dry constituents that facilitates flowability of UHPC. A variety of fine aggregates can be appropriate for use in UHPC, including quartz, limestone, and basalt.

Steel fiber reinforcement is a critical component of UHPC when used in struc-tural elements or field-cast structural connections. Steel fiber reinforcement pro-vides superior crack-bridging capabilities compared with other lower stiffness fiber reinforcements. The steel fibers are typically made of high-strength steel to ensure that fiber tensile failure does not occur. The exceptional mechanical properties of UHPC can be largely attributed to the fiber reinforcement. Silica fume is another key component in UHPC because of its reactivity and its small particle size. In the recent years, with development in nanoscience and nanotechnology, using nano-scale particles as nanoscale reinforcement in cementitious materials is attracting increasingly more attentions. Nanoparticles hold the potential to act as fillers, pro-ducing denser materials, and they can also serve to enhance quality of the paste−aggregate interface leading to a reduced interfacial cracking; due to their large specific surface area, nanoparticles can serve as efficient pozzolanic material. As a result, much stronger and tougher concretes may be becoming possible. Jo et al. [10] experimentally investigated properties of cement mortars with NS addi-tion. The experimental results showed that the compressive strengths of mortars with NS particles were all higher than those of mortars containing silica fume at 7 and 28 days. They concluded that it was plausible to add NS particles to make high-performance concrete. Qing et al. [8] made similar observations, and they

noticed that comparing with cement paste with silica fume addition, the cement paste mixed with NS particles had obvious higher compressive strength, especially at early age. NS was believed to accelerate cement hydration process. Liu et al. [11] added NC into cement paste, and the experimental results showed that NC had no effect on water requirement of normal consistency of cement. However, with the increase of NC content, its flowability decreased and setting time of fresh cement paste was shortened. Flexural strength and compressive strength increased with the addition of NC at the age of 7 and 28 days. Nazari and his colleagues conducted series of experimental tests on different nanoscale additives mixed into concrete matrix [12−17]. Although their work had only been demonstrated in small samples, it was believed that if only it can scale up to larger quantities, it is possible to produce concrete four times stronger than the strongest existing commercial concrete mixes. Najigivi et al. [34] assessed workability and compressive strength of binary blended concretes mixed with different types of SiO_2 nanoparticles. It was concluded that SiO_2 nanoparticles played significant roles in mechanical properties of concrete by formation of additional calcium silicate hydrate gel during treatment, which played an important role in raising highly the compressive strength of binary blends. Mercury Intrusion Porosimetry (MIP) measurements revealed that the capillary pores of UHPC with 5% NS were 35% lower than that of the control mixture. SEM observation proved that nano-SiO_2 could efficiently improve the microstructure of ITZ between the aggregates and the cement paste [35]. Other benefits like self-cleaning, strain-sensing [36], and smog eating can be achieved by mixing different types of nanoparticles into concrete matrix.

All these pioneering work have demonstrated the effectiveness of nanoscale particles in improving concrete performances. As briefly introduced above, nanoparticles have very high surface area to volume ratio compared with other composites of concrete. At the same time, due to their high reactivity, they can act as pozzolanic material in cement phases, further promoting cement hydration. Furthermore, nanomaterials serve as nano-reinforcement and/or as filler, densifying the microstructure and the ITZ, thereby leading to a reduced porosity [37].

In this section, effects of steel fiber and nanoscale particles on the static mechanical performance of UHPC are to be presented through experimental investigations. Material compressive stress−strain relationships, strain energy absorption, the flexural strength, and fracture energy absorption of UHPC with different nanoscale materials and steel fibers are compared and discussed.

2.2.1 Experimental program

2.2.1.1 Materials

The main properties of materials used in producing UHPC in this study are presented in the following. To ensure consistency of concrete for all UHPC, the cement used in all mixes was Type SR Sulphate Resisting cement (namely 42.5

Figure 2.1 Different types of steel fibers.

Table 2.1 **Material properties of steel fibers**

Fiber types	Nominal diameter (mm)	Length (mm)	Fiber aspect ratio (L/D)	Volume fraction (%)	Tensile strength (MPa)
TF1	0.4	35	87.5	1	1480
TF2	0.4	35	87.5	2	1480
WF	0.5	30	60	1	>800
MF06	0.12	6	50	2.5	>4000
MF12	0.12	12	100	2.5	>4000

Grade) conforming to Chinese standard GB175-2007 [38]. The same types of nano-particles including NC, NS, Nano-Al$_2$O$_3$ (NA), and Nano-TiO$_2$ (NT) were used.

Three types of steel fibers including TF with diameter 0.4 mm and length 35 mm, waved steel fiber (WF) with diameter 0.5 mm and length 30 mm, and micro steel fibers (MF) with diameter 0.12 mm and lengths 6 mm and 12 mm, were incorporated into mix design of self-compacting concrete. Fig. 2.1 shows the different types of steel fibers used in this study. The mechanical properties of steel fibers are listed in Table 2.1. Volume fraction of the steel fibers varied from 1% to 2.5%. The dosage was determined on the basis of a series of preliminary tests, which confirmed that a reasonable increase in fiber content resulted in enhanced concrete performance.

2.2.1.2 Mixture design

The mixture proportions of UHPC are reported in Table 2.2. A total of five series of mixtures (plain concrete and four kinds of nanomaterials) were prepared in the laboratory trials. Five "ref" mixtures without fiber addition were used as control specimens. As seen from the table, except for the steel fibers all ingredients were kept constants. The same water to cement ratio (water/cement = 0.25) and the same weight of aggregates (with the sand percentage of 40% by weight), and a constant

Table 2.2 Mix proportions of UHPC (kg/m³)

Constituents	Pain	NC						NS						NT						NA					
	Ref	Ref	1	2	3	4	5	Ref	1	2	3	4	5	Ref	1	2	3	4	5	Ref	1	2	3	4	5
42.5 SR cement	750	750						750						750						750					
Silica fume	225	225						225						225						225					
Silica flour	190	190						190						190						190					
River sand	1030	1030						1030						1030						1030					
Superplasticizer	16	16						16						16						16					
Water	190	190						190						190						190					
Water/binder	16.3%	16.3%						16.3%						16.3%						16.3%					
Nano particles	—	21.7						21.7						21.7						21.7					
MF06	—	—	191	—	—	—	—	—	191	—	—	—	—	—	191	—	—	—	—	—	191	—	—	—	—
MF12	—	—	—	191	—	—	—	—	—	191	—	—	—	—	—	191	—	—	—	—	—	191	—	—	—
TF	—	—	—	—	79	158	—	—	—	—	79	158	—	—	—	—	79	158	—	—	—	—	79	158	—
WF	—	—	—	—	—	—	79	—	—	—	—	—	79	—	—	—	—	—	79	—	—	—	—	—	79

content of silica fume, silica flour, and binder were used for all the mixtures. For the mixtures with steel fibers and nanoparticles, the rows TF, WF, MF06, and MF12 were mixed with NC, NS, NA, and NT particles by the cement replacement of 3%, 1%, 2%, and 3% (63.1, 21.7, 45.4, and 63.1 kg) by weight, respectively. The dosages of TF are 1% and 2% (79 and 158 kg) by volume, respectively, the dosages of WF, MF06, and MF12 are 1%, 2.5%, and 2.5% (79, 191, and 191 kg) by volume, respectively.

Concrete mixtures were prepared in a laboratory concrete mixer. "Plain/Ref" mixture was plain concrete with neither nanomaterial nor steel fibers additions. Cubic specimens with dimension of 100 mm × 100 mm × 100 mm were made for uniaxial compressive tests and 100 mm × 100 mm × 400 mm beam specimens were made for flexural tests. After being cured in the humid room at a temperature of 20°C ± 5°C for 24 hours, the specimens were demolded and then cured in hot water at a temperature of 90°C for 48 hours. Then the specimens were cured in the first curing room again until they were tested. Both surfaces of the samples were properly leveled, sanded, polished, cleaned, and dried to attain smooth surfaces before testing.

2.2.1.3 Material testing

The test matrix devised for the material study was intended to cover a range of the basic behaviors of UHPC with and without different nanoscale additives. The types of tests performed can generally be grouped into two. Firstly, uniaxial compression tests that focused on the compressive strength, modulus of elasticity, compressive failure behaviors of UHPC specimens, and effect of nanoscale additives were carried out. Secondly, four-point bending tests were conducted to obtain flexural strength of UHPC specimens with and without nanoscale additives. Totally, 97 specimens were tested including 68 cubic specimens for compressive tests and 29 beam specimens for flexural tests.

2.2.1.4 Compressive testing

The experiments were carried out on a number of 100 mm × 100 mm × 100 mm cubes using a 3000 kN capacity computer-controlled electromechanical servo hydraulic pressure testing machine as shown in Fig. 2.2A. Testing procedure conformed to the China Standard GB/T 50081-2002. At both sides of the loading plate, there was an axially oriented linear variable displacement transformer (LVDT) to record the test data. In total, there were 68 specimens tested. All specimens were loaded via the hydraulically controlled machine at constant loading rate (0.2 mm/minute) until failure. In concrete compressive testing, all specimens were loaded via the hydraulically controlled machine at constant loading rate (0.2 mm/minute) until failure. Two parallel LVDTs were installed to measure the crosshead movement of the testing machine as shown in Fig. 2.2B.

Compressive strain measurement under uniaxial compression is difficult for UHPC material. Conventional method using electrical strain gauge is effective in
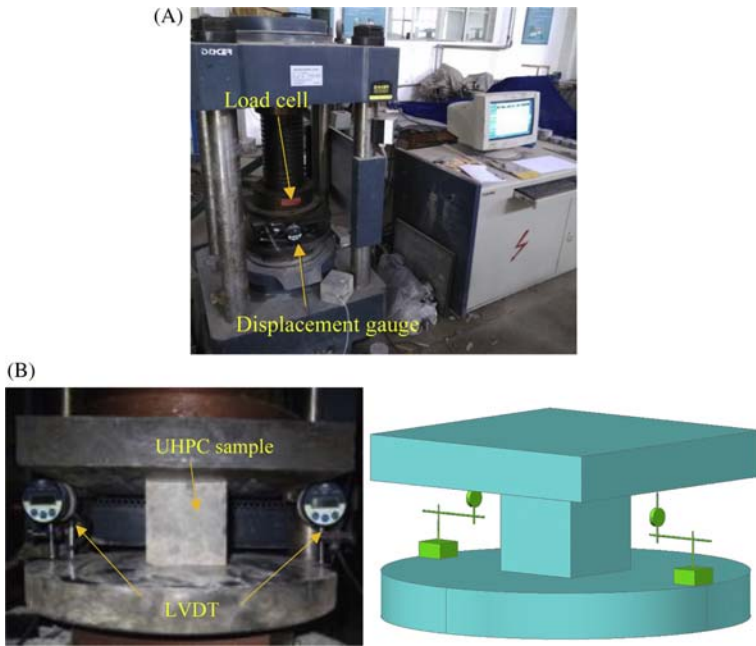
Figure 2.2 Testing setup for compression tests of cubic specimens. (A) YAW-3000 computer-controlled servo pressure testing machine. (B) Testing samples and displacement gauges installation.

measuring the static modulus of elasticity of UHPC, whereas it is unable to capture the postcracking behavior of the UHPC specimens because the strain gauges are normally detached from the surface and came off at peak strength due to concrete spalling. The second method, that is, in compliance with ASTM C469, uses two rigid circular rings, which are secured at approximately two-thirds the height of the specimen using clamping screws. Two LVDTs are introduced between the rings and positioned on opposite sides of the specimen. This method is also good at measuring the modulus and peak strength of UHPC specimens; however, this method is not suitable for capturing the post-peak softening branch because the clamping screws may rotate as the shear line failure occurs after peak. This test configuration is able to capture the peak strength and post-peak behavior of the specimens; however, crosshead displacement measurement does not eliminate the platen restraints from the testing machine, which leads to higher strain measurement and smaller value of the initial elastic modulus.

2.2.1.5 Flexural tests

Fiber material addition exerts profound influence on material tensile behavior. Many researchers have attempted to develop test methods for the assessment of the tensile performance of fiber-reinforced concretes. Test methods have

Figure 2.3 Setup of the flexural tests.

included both direct and indirect assessments, including some that have been standardized [39]. Direct testing method, i.e., the uniaxial tensile testing (UTT), is widely used in academia; this method is considered to be complicated and require advanced equipment and experimental skills. Splitting tensile test is generally carried out to obtain the tensile strength of concrete, and the stress field in the tests is actually a biaxial stress field with compressive stress three times greater than the tensile stress. In the case of fiber-reinforced concrete, previous studies have reported setting strain gages or LVDTs at the end surface of the specimen and obtaining the first cracking strength from the point at which displacement in the tensile direction increases remarkably. As a simple alternative to UTT, four-point bending test (FPBT) has been proposed [40] and widely adopted in the user community. It shall be noted that bending tests are not designed to determine the material tensile strain-hardening/ strain-softening behavior but rather to constrain the material tensile properties such as the tensile strain capacity and/or tensile strength. When using the FPBT for identifying a stress−strain constitutive law, an inverse analysis is necessary to determine the uniaxial tensile behavior [41−43].

In this flexural bending tests, beam specimens with dimension of 100 mm × 100 mm × 400 mm were tested to study the effect of the nanoparticles and steel fibers on their flexural strengths. The beam specimens were tested with a four-point bending loading configuration, and the space between load points is one-third of the clear span, which generates a region of no shear. As shown in Fig. 2.3, instrumentation for beam tests included LVDTs at mid-span and at the supports to measure deflection, as well as strain gauges along the depth of the beam at mid-span to generate an experimental curvature profile. The testing procedures conformed to the Chinese standard GB/T 50081-2002 [44]. In the tests, the specimens were subjected to pure bending between two loading points that were spacing at 100 mm. The specimens were supported by two metallic rollers spacing at 300 mm. A displacement-controlled load was applied at a constant rate of 0.2 mm/minute.

Figure 2.4 Failure of specimens from the compression tests.

2.2.2   Results and discussions

2.2.2.1   Samples after compressive tests

The static compressive tests for UHPC specimens with and without nano-additives were conducted. Fig. 2.4 shows the failure patterns of the plain and fiber-reinforced concrete specimens. It was observed that failure of plain concrete specimen occurred in a brittle manner. When steel fibers were mixed into cement, the specimens maintained their integrity and showed excellent crack control ability. This is because the steel fibers can bridge over the cracks and retard crack extension leading to high material ductility. The crack control ability increases with fiber volume fraction as evidenced in the comparison among samples with different fiber volume fractions. The specimen with 1 Vol% fibers had the most severe damage, whereas addition of 2.5 Vol% steel fiber provided exceptional crack control capacity in the sample.

2.2.2.2   Results from compression tests

A summary of the results from all of the compressive tests is shown in Table 2.3. It can be seen that when there is no steel fiber reinforcement, UHPC specimens with

Table 2.3 **Compression strength of UHPC with different nanoadditives (MPa)**

Fiber / Nano	NO	TF1	TF2	WF	MF06	MF12
NO	90.1	126		140.4	150.6	168.1
CaCO$_3$ 3%	108.4	144.3	150.9	136	137.3	–
SiO$_2$ 1%	107.2	142.3	131.2	139.2	152.5	139.1
TiO$_2$ 2%	95.7	124.1	160.8	136.9	156.1	168.3
Al2O$_3$ 3%	103.1	143.4	154.6	144.5	135.1	169.4

nano-additives displayed about 10% increase in peak stress as compared to the specimens without nano-additives.

When steel fibers were mixed, nanoadditives had less impact on the material strengths. For UHPC with 1 Vol% TF reinforcement, there was an average 12% strength increment except for the specimens with NT addition. To better illustrate the impact of nano-addition in TF fiber-reinforced UHPC, the compressive stress−strain curves of UHPC specimens (1 Vol% TF and 2 Vol% TF) with four different nanoparticles (Al$_2$O$_3$, CaCO$_3$, TiO$_2$, and SiO$_2$) are presented in Fig. 2.5, and all samples were picked up from the specimens at 7 days.

After addition of steel fibers in these four types of UHPC, significant changes occurred in the ascending and descending portions of the stress−strain curves. All these results well quantified the effect of steel fibers on material ductility enhancement. Increasing steel fibers from 1 Vol% to 2 Vol% affects the strain capacity and elastic deformation capability of the matrix in the preyielding zone considerably.

Except TF fiber-reinforced UHPC samples, there was only slight strength increase/decrease for other fiber-reinforced UHPC specimens (1 Vol% WF, 2.5 Vol% MF06, and 2.5 Vol% MF12) after nano-additions. The stress−strain curves for these samples are illustrated in Fig. 2.6. It is generally concluded that although nano-additives can increase the compressive strength of UHPC without fiber reinforcement, they have insignificant influence on the compressive strength of fiber reinforced UHPC specimens, despite post-yielding behavior may be influenced by different nano-additions.

The area under stress−strain curve is a measurement of energy absorption capacities of the material. Table 2.4 lists typical strain energy density of UHPC with and without fiber reinforcement and different nanoparticles. As shown, the energy absorption capacity of UHPC without any steel fiber has the smallest strain energy density. Steel fiber volume dosage plays an important role in material energy absorption. As can be noted from UHPC with 2% TF, its energy absorption is higher than UHPC with 1% TF. When the same volume dosage of steel fibers was mixed, the strain energy density increased with the fiber aspect ratio as seen from the comparison between 2.5 Vol% MF06 and 2.5 Vol% MF12.
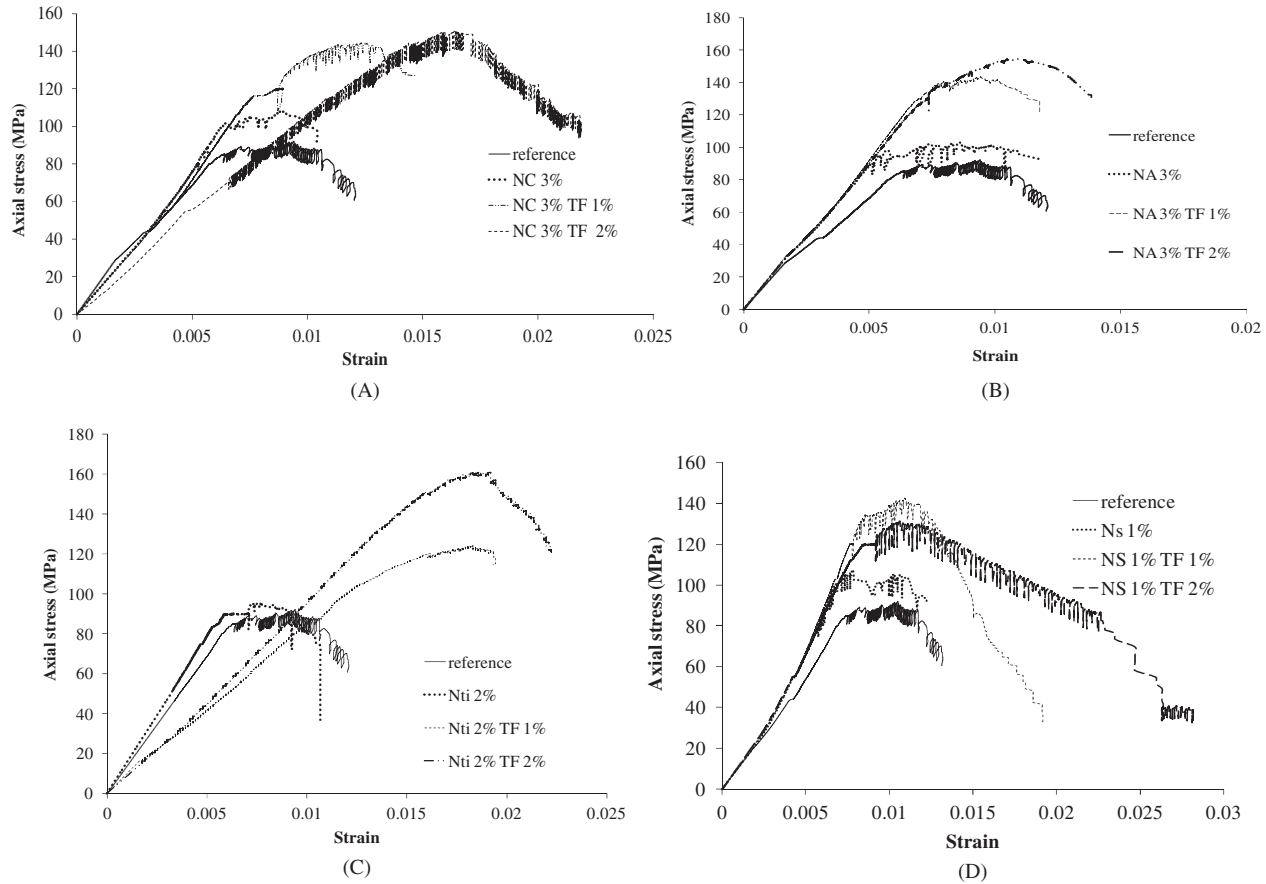
Figure 2.5 Comparison of compressive stress−strain curves of UHPC specimens (1 Vol% TF and 2 Vol% TF) with mixtures of (A) NC. (B) NA. (C) NT and (D) NS.
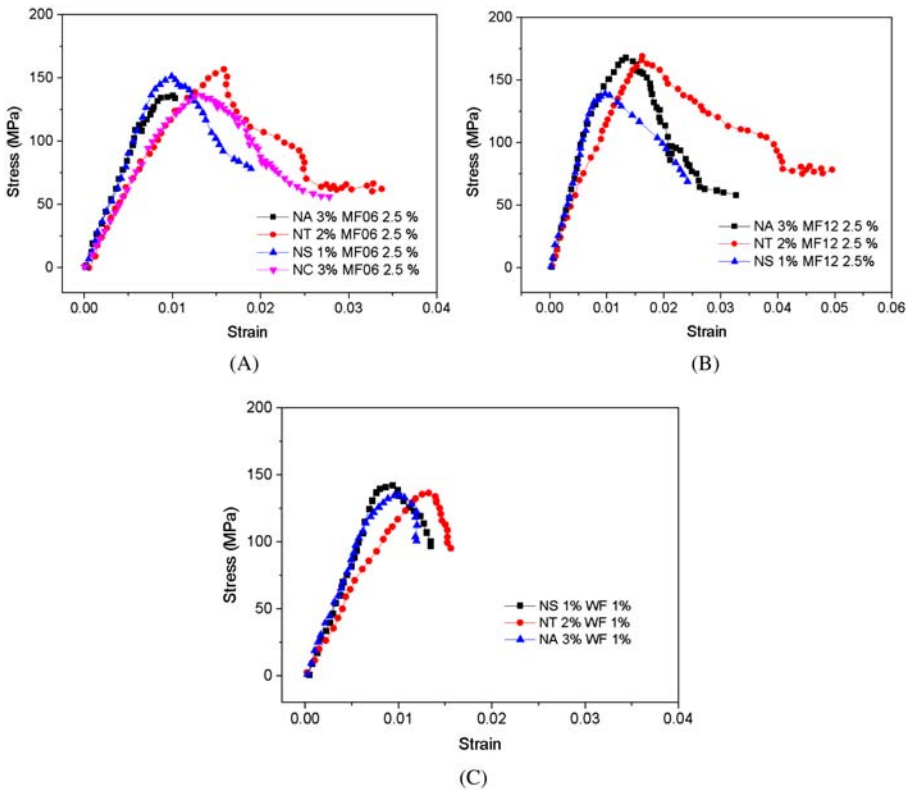
Figure 2.6 Comparison of compressive stress−strain curves of UHPC specimens of (A) MF06 samples with nano-addition. (B) MF12 samples with nano-addition. (C) WF samples with nano-addition.

Table 2.4 Compression strain energy density of UHPC with nano-additives (MJ/m^3)

Fiber / Nano	NO	TF1	TF2	WF1	MF06	MF12
NO	0.73	2.01	−	1.30	4.51	3.07
CaCO$_3$ 3%	0.73	1.39	1.24	1.30	2.67	3.38
SiO$_2$ 1%	0.85	1.61	2.63	1.10	3.30	2.94
TiO$_2$ 2%	0.71	1.90	4.42	3.33	3.14	5.45
Al$_2$O$_3$ 3%	0.92	1.13	1.46	1.31	3.25	3.42

2.2.2.3 Samples after flexural tests

It is well known that adding steel fibers will increase specimen toughness and the results of this study are no exception, but whether adding nanoparticles will also contribute to toughness is under investigation in this section.

In this study, four-point bending experiments on the UHPC specimens were performed. Mid-span deflections were recorded, and flexural strength and fracture energy were calculated for different specimens with varying nanoparticles.

Fig. 2.7 shows a comparison of failure modes of the UHPC specimens. As shown, for the specimen without fibers, the initial crack initiated from the beam
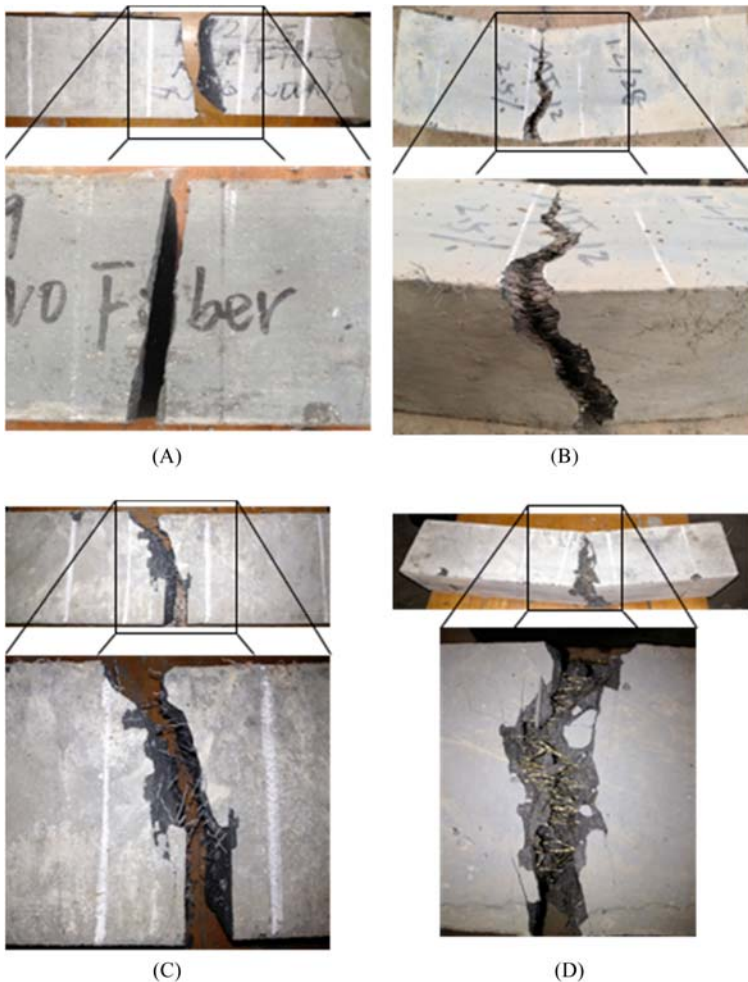
Figure 2.7 Failure modes of the UHPC specimens in flexural tests. (A) No fiber. (B) MF12 2.5%. (C) WF 1 Vol% and (D) TF 2 Vol%.
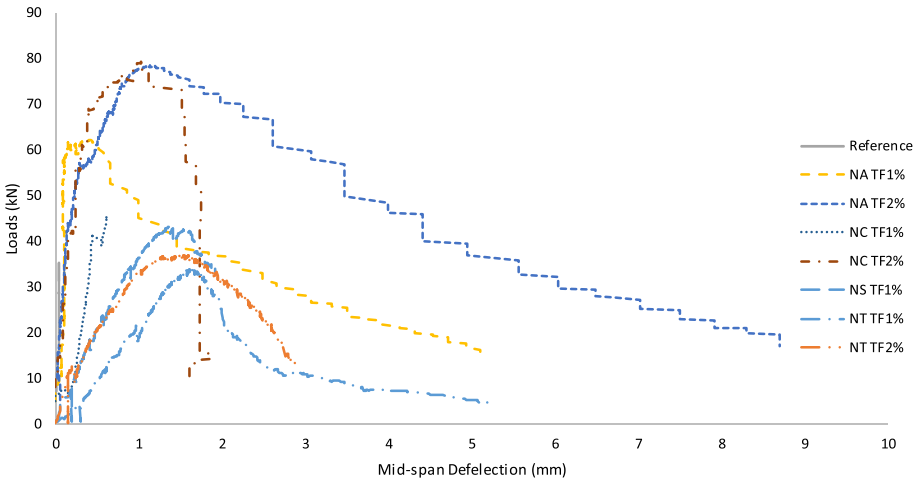
Figure 2.8 Flexural tests results.

bottom due to tensile stress, and then the specimen was split into two parts when the crack propagated towards the top. However, the fiber-reinforced UHPC specimens remained load carrying capacity after the first crack generated.

Typical load-deflection curves of the UHPC specimens are shown in Fig. 2.8. As expected, the load-displacement curve of the UHPC specimen without fiber reinforcement is linear up to the maximum and then failed in a brittle manner with a sudden drop, almost no material ductility can be observed. For UHPC specimens with the same nano-additives (NA), their peak load and material ductility both increased with fiber volume dosage from 1 Vol% TF to 2 Vol% TF. Similar observations were noted for other UHPC samples with NC and NT. Given the same volume dosage of TF fiber addition, addition of NA gives the best load and ductility enhancement.

Based on FPBTs, flexural strength was calculated from Eq. 2.1:

$$\sigma = \frac{3F(L - L_i)}{2bd^2} \tag{2.1}$$

where F is the total load as indicated in Fig. 2.8, L is the distance between two supports at bottom, L_i is the length of the loading span, b and d are the width and depth of the specimen, respectively.

Table 2.5 lists the data of the flexural strength of UHPC specimens with different nano-additives. It is very interesting to note that the specimens containing 1 Vol% WF have similar flexural strength when comparing with non-fiber reinforced UHPC specimens (10.8 vs 10.6 MPa). The addition of WF fiber in UHPC was not effective because 1 Vol% WF fiber with low tensile strength could not provide bridge effects after crack initiates.

Table 2.5 Flexural testing results (MPa)

Fiber / Nano	NO	TF1	TF2	WF1	MF06	MF12
NO	10.6	14.9	–	10.8	28.1	31.3
$CaCO_3$ 3%	12.1	14.9	23.7	11.0	20.3	34.2
SiO_2 1%	13.0	13.0	–	9.5	17.0	26.2
TiO_2 2%	12.3	10.2	11.1	12.4	22.4	21.9
Al_2O_3 3%	12.4	18.7	23.5	13.2	21.4	36.1

On the contrary, the inclusion of TF and MF fibers was useful for developing higher flexural strength. As mentioned in the previous sections, MF fiber had higher material strength, and also its volume percentage was larger. All of these guaranteed that MF fibers could provide effective bridging effect and postpone the final failure of the UHPC specimens. Comparing MF06 with MF12, it was noted that given a constant fiber volume dosage, fiber aspect ratio gave positive impact on material flexural strength, and this positive effect was also observed in material compressive strength tests.

Regarding TF fibers reinforced UHPC samples, NA addition seemed to provide exceptional flexural strength enhancement. One possible explanation is that alumina component effectively reacts with calcium hydroxide produced from the hydration of calcium silicates. The rate of the pozzolanic reaction is proportional to the amount of surface area available for reaction, and Brunauer−Emmett−Teller (BET) surface area measurement yields a smallest value of 20 nm for Al_2O_3.

As proposed by Bazant [45], the fracture energy may be uniquely defined as the energy required for crack growth in a specimen. The fracture energy was calculated from the following equations:

$$P_0 = \frac{4M_0}{S} \tag{2.2}$$

$$W_F = W_0 + 2P_0\mu_0 \tag{2.3}$$

where μ_0 is the maximum mid-span displacement, S is the distance between two supports at bottom, M_0 is the moment caused by the self-weight of the specimen, W_0 is the work done by the applied force, which is the area enclosed by the load-deflection curve. The fracture energy can be then obtained from Eq. 2.4:

$$G_f = \frac{W_F}{A} \tag{2.4}$$

where A is the cross-sectional area of the specimen.

Table 2.6 Fracture energy of UHPC with different nanoparticles (J/m³)

Fiber Nano	NO	TF1	TF2	WF1	MF06	MF12
NO	110.8	5029.1	–	3959.8	22,931.2	32,551
CaCO₃ 3%	–	7033.3	13031.9	2812.2	4809.6	38,773.1
SiO₂ 1%	987.6	5624.1	–	1781.4	7179.5	16,466.7
TiO₂ 2%	219.4	6988	7566.1	4268.7	13,746.5	17,715.8
Al₂O₃ 3%	877.8	17,060.8	39,538.3	4601	17,186.3	45,024.3

By using Eqs. 2.2−2.4, the fracture energies of all specimens were calculated and listed in Table 2.6, and fiber material again showed positive effects on increasing the fracture energy of UHPC. The additional fracture energy gained from fiber bridging effect can not only delay the crack propagation but also resist the friction and interlock at the crack surface.

Similar fracture energy was noticed for the specimens using different nanoparticles. However, for the fiber-reinforced UHPC specimens, the values from specimens with different nano-additions fluctuated significantly showing that the nanoparticles influenced the fracture energy of steel fiber-reinforced specimens more than non−fiber-reinforced specimens.

2.2.3 Conclusions

Based on compressive tests and FPBTs on UHPC samples, this study investigates the effects of incorporating nano-additives and different fiber types on the performance of UHPC. According to the compressive test results, UHPC specimens with different fiber types showed better performance than specimens without fiber reinforcement in terms of stress−strain relationship, compressive strength, and strain energy density. Among fiber-reinforced specimens, the specimens with 2.5% MF12 fibers showed the greatest improvement in the compressive tests.

The results obtained in the FPBT indicated that the fiber-reinforced UHPC beams outperformed the non−fiber-reinforced beams in terms of the ductility, flexural strength, and fracture energy. In contrary to the conclusion of the compressive test, the use of nano-additives affected the fracture energy of fiber-reinforced UHPC beams more than non−fiber-reinforced UHPC beams.

Reinforced UHPC components with selected material composition were tested under three-point bending, crack propagation process was recorded and discussed, and it was observed that fiber aspect ratio was influential on structural ductility.

2.3   Influences of nanoparticles on dynamic strength of ultra-high performance concrete

The effect of nanomaterial addition into UHPC matrix has been briefly discussed after static compressive and flexural bending tests in Section 2.2. In this section, a more comprehensive study on the effect of nano-addition is presented with a focus on the mechanical strength under dynamic loads. Dynamic compressive strength and tensile strength of these samples are compared and discussed. Dynamic increase factors that are important describing the material under high loading rate are generated and plotted in charts, and the influences of different nanomaterial additions and dosages on the dynamic properties of UHPC material are discussed. Furthermore, UHPC samples after SHPB tests are analyzed under microscopy SEM analysis to explain the macro-failure in microscale. XRD analysis and XRF analysis are carried out to further understand the failure element composition and early strength development after nano-addition into the UHPC matrix.

2.3.1   UHPC composition

The main properties of materials used in producing UHPC in this study are presented in the following. To ensure consistency of concrete for all UHPC, the cement used in all mixes was Type SR Sulphate Resisting cement (namely 52.5 Grade) conforming to Chinese standard GB175-2007 [38]. As for the aggregates, natural sand was used and the aggregate size was between 0.16 and 2.5 mm, and the specific gravity is 2.58 g/cm^3. Silica fume was used as a reactive material involving in the hydration of cement, and silica flour was used to fill in the voids that exist between the cement paste and aggregate matrix. To accelerate cement hydration process and provide even better filling effect at nanoscale, four types of nanoparticles including NC, NS, NA, and NT were used. The average particle size was determined from a BET surface area measurement, i.e., $40-80$ nm for $CaCO_3$, 20 nm for SiO_2, 30 nm for TiO_2, and 20 nm for Al_2O_3, and the specific surface area was more than 4 m^2/g for $CaCO_3$, $230-300$ m^2/g for SiO_2, 77.55 m^2/g for TiO_2, and 180 m^2/g for Al_2O_3. Nanomaterial in this study was mixed at a constant weight dosage of 3%. All specimens are reinforced by 2.5% volume fraction MF namely MF15. MF15 has a diameter of 0.12 mm and a length of 15 mm, and its yielding strength is 4200 MPa.

Table 2.7 shows the complete mix proportions of different UHPC formula.

All mixtures were mixed in dry condition for 5 minutes, and for another 3 minutes after adding approximate 70% water. Then superplasticizer was added before adding the remaining 30% water. The fibers were added after the mixing process continued for another 5 minutes. The fibers were manually dispersed and added to the mixer to avoid fiber clump. Slumps of fresh concrete were determined immediately to evaluate the workability. The concrete mixture and slump tests were conducted according to GB 2419-81 [46] to ensure consistency of concrete for all concrete specimens with and without nanoscale additives.

Table 2.7 Mix proportions of different UHPC formula (kg)

Constituents	MF15			
52.5 Cement	750			
Silica Fume	225			
Silica Flour	190			
Sand	1030			
Superplasticizer	16			
Water	190			
Water/Cement	25.30%			
Steel Fiber	191			
NC	63.1	–	–	–
NS	–	63.1	–	–
NA	–	–	63.1	–
NT	–	–	–	63.1

Slump tests were carried out to assess the workability of the UHPC material immediately after concrete mixing. It was noted that the concrete in this study had good workability with a slump exceeding 250 mm and slump spread exceeding 900 mm diameter.

After proper curing in wooden molds, specimens are prepared by cutting them to the specified length and thereafter grinded and measured. There are high requirements on the flatness of end surfaces to obtain an even load distribution in the load tests. The specimens used for static compression test were 100 mm cubes, and the samples used in the following split tensile and SHPB tests were cylinders with 75 mm diameter and 37.5 mm height.

2.3.2 Static tests

Uniaxial compression tests and split tensile tests were conducted to determine static uniaxial compressive strength and split tensile strength of UHPC.

2.3.2.1 Uniaxial compression test

The experiments were carried out on a number of 100 mm × 100 mm × 100 mm UHPC cubes using a 3000 kN capacity computer-controlled electromechanical servo hydraulic pressure testing machine as shown in Fig. 2.2.

Static compressive stress−strain curves obtained from samples with different nano-additions are shown in Fig. 2.9. It can be clearly observed that when the same steel fibers, i.e., MF15 were used as UHPC reinforcements, different nanomaterial additions had influence on the concrete compressive strength. UHPC with 3% of NT had the highest strength, which is about 14% higher than the lowest compressive strength measured from UHPC with NA. Addition of NC and NS provided slightly
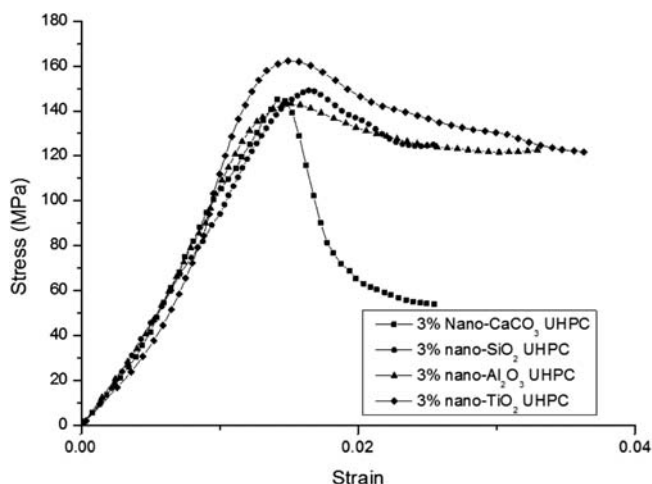
Figure 2.9 Stress−strain curves from quasi-static compressive tests.

Table 2.8 **Experimental results of different formula UHPC under static load**

	NC	NS	NA	NT
Compressive strength (MPa)	145.1	149.6	143.5	162.6
Standard deviation	16.59	17.47	16.15	20.37

higher compressive strength than NA. Among all the nanomaterials, UHPC mix with NC seemed to yield the lowest material ductility, post-peak compressive strength quickly dropped to around 60 MPa and then entered stress plateau. UHPC specimens with addition of other three nanomaterials exhibited prominent material ductility. Before entering the stress plateau, there was only slight stress loss from the peak.

The static compressive strengths for UHPC with different nano-additives are averaged and listed in Table 2.8.

2.3.2.2 Split tensile tests

Static split tensile tests were conducted on cylindrical UHPC specimens with diameter of 75 mm and height of 37.5 mm, as shown in Fig. 2.10.

The split tensile strength was calculated according to $\sigma = \frac{2P}{\pi DL}$ in which P is the load at failure and, D and L are the diameter and length of the specimen, respectively.

The static split tensile strengths for UHPC with different nano-additives are then averaged and listed in Table 2.9.

It is noted that all UHPC samples have greatly improved split tensile strength compared with their normal strength counterparts. UHPC sample with 3% volume

(A)   (B)

Figure 2.10 Split tensile tests. (A) Test setup. (B) Failure specimen.

Table 2.9 Static split tensile strength of different UHPC

UHPC	3% NC	3% NS	3% NA	3% NT
Strength (MPa)	22.2	13.9	15.4	17.7
Standard deviation	5.31	5.48	7.72	4.35

dosage NC addition has the highest split tensile strength and it is about 60% higher than the value obtained from UHPC with 3% NS. Addition of 3% NT gives the UHPC sample the second highest split tensile strength of 17.7 MPa.

From the uniaxial compressive and split tensile tests shown in the above sections, it is clearly observed that addition of different nanomaterials has a great influence on the mechanical properties of UHPC, given that UHPC samples have the same steel fiber material and fiber volume dosage. In general, UHPC material with nanomaterial addition outperforms the conventional strength concrete.

For cement-based material such as concrete, calcium silicate hydrate (C-S-H) is the main product during the hydration process and is primarily responsible for the material strength. Nanomaterials such as $CaCO_3$ and SiO_2 are typically highly effective pozzolanic materials and addition of such material into the cement paste will improve the microstructure of the paste and reduce calcium leaching as these materials react with CH and form additional C-S-H gel. The strength of hardened cement paste is thus increased.

2.3.3 SHPB test

Table 2.10 summarizes the number of SHPB compression and split tensile tests conducted for this study. In total, 41 compression SHPB tests and 53 split SHPB tests were conducted. Note that two more group tests were carried out to investigate the influence from different dosages of NC.

Table 2.10 **Number of SHPB compression and split tensile tests**

	L/D	Fiber	Nano	L (mm)	Compression test number	Split tensile test number
Effects of nanomaterial	0.5	MF15	3% $CaCO_3$	37.5	12	9
	0.5	MF15	3% SiO_2	37.5	7	8
	0.5	MF15	3% Al_2O_3	37.5	8	10
	0.5	MF15	3% TiO_2	37.5	7	10
Impact of nano-content	0.5	MF15	3% $CaCO_3$	37.5	12	9
	0.5	MF15	5% $CaCO_3$	37.5	4	8
	0.5	MF15	1% $CaCO_3$	37.5	3	8
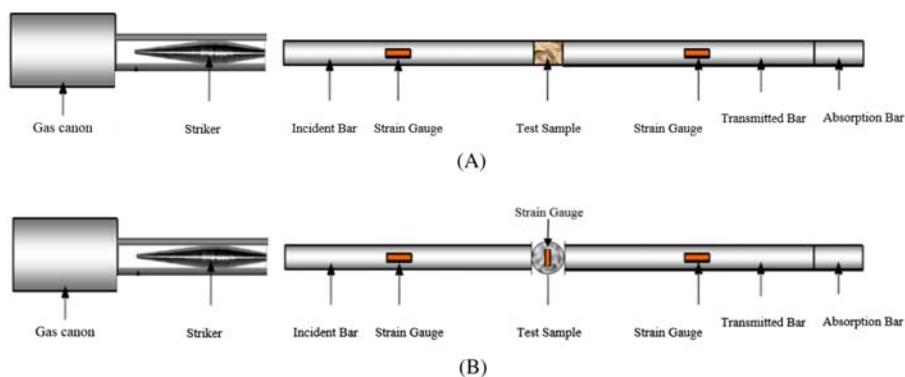
Figure 2.11 SHPB experimental system. (A) SHPB compression test setup. (B) SHPB split tensile test setup.

2.3.3.1 Test apparatus

In this study, the dynamic tests were conducted on SHPB test specimens with 75 mm diameter and 37.5 mm height. The experimental systems of SHPB compressive and split tensile tests are sketched in Fig. 2.11. It is worth noting that when determining the concrete tensile strength, traditional direct pull-out test is considered to be the best-suited method. However, the uniform stress−state idea in the specimen is rarely reached, and in practice, premature failure due to the stress concentration around grips is often observed. As an alternative and indirect method, SHPB split tensile test as shown in Fig. 2.11B can generate a tensile stress within the specimen by far-end compression, which is easier and more convenient in instrumentation than direct pull-out test.
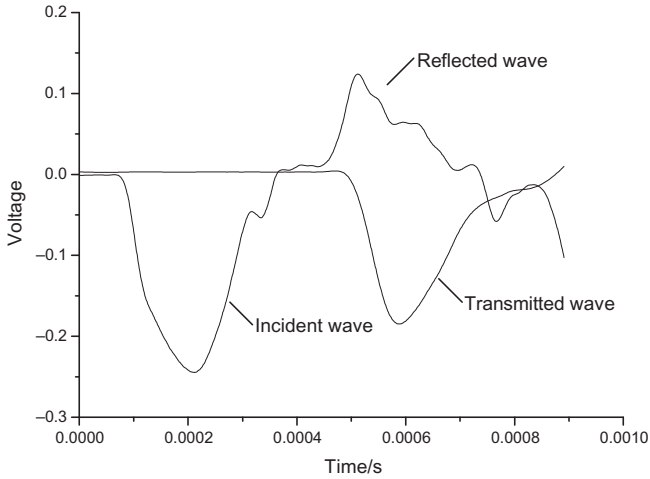
Figure 2.12 Typical waveform of compression test.

In SHPB tests, the specimens were placed between the ends of two straight bars, called the incident bar and the transmitted bar. At the end of the incident bar (some distance away from the specimen, typically at the far end), a stress wave is created, which propagates through the bar toward the specimen. This wave is referred to as the incident wave, and upon reaching the specimen, split into two smaller waves. One of them, the transmitted wave, travels through the specimen and into the transmitted bar, causing plastic deformation in the specimen. The other wave, called the reflected wave, is reflected away from the specimen and travels back down the incident bar. Strain gages were then placed on the bars to measure strains caused by the waves. Assuming deformation in the specimen is uniform, the stress and strain can be calculated from the amplitudes of the incident, transmitted, and reflected waves. Fig. 2.12 shows typical waves in SHPB compression test.

Based on one-dimensional stress wave propagation theory [47], the stress, strain, and strain rate in SHPB compressive test can be calculated using the following equations:

$$\sigma(t) = E\left(\frac{A}{A_s}\right)\varepsilon_T(t) \tag{2.5}$$

$$\varepsilon(t) = \int_0^T \dot{\varepsilon}(t)dt \tag{2.6}$$

$$\dot{\varepsilon}_c(t) = -\frac{2c_0}{L}\varepsilon_R(t) \tag{2.7}$$

where E, A, and C_0 are Young's modulus, cross-sectional area, and elasticity wave velocity of the SHPB bars, respectively; A_s and L are cross-sectional area and length of the test samples, respectively; ε_T and ε_R are incident strain and reflective strain, respectively.

For SHPB split tensile test, the compressive stress along the split bar length direction and tensile stress perpendicular to the bar length direction can also be calculated following the theory of elasticity.

$$\sigma_c = \frac{2P}{\pi DL} \frac{D^2}{r(D-r)} \tag{2.8}$$

$$\sigma_t = -\frac{2P}{\pi DL} \tag{2.9}$$

$$\dot{\varepsilon}_t(t) = \frac{\sigma_t}{E_s T} \tag{2.10}$$

where P is the loading force which can be calculated based on the stain measured on the split bar, D is the diameter, L is the thickness of the specimen, r is the distance measured from the loading point, E_s is the quasi-static Young's modulus of specimen, and T is the time lag between the start of the transmitted stress wave and the occurrence of the maximum transmitted stress.

2.3.3.2   Equilibrium check

In SHPB test, it is critical to conduct longitudinal stress equilibrium check. Eq. 2.11 is used to calculate the stress balance.

$$\sigma_T = \sigma_I + \sigma_R \tag{2.11}$$

where σ_T is the transmitted stress, σ_I is the incident stress, and σ_R is the reflected stress.

Fig. 2.13 shows stress equilibrium check on UHPC samples with different nanomaterial additions. The strain rates displayed in the figure are the highest strain rate reached in the SHPB tests. It can be concluded that under the highest strain rate, all specimens reached stress balance, which verified the accuracy of SHPB tests conducted in this research.

2.3.3.3   Compression test results

Fig. 2.14 shows the typical failure modes of UHPC samples with different nanomaterial additions after SHPB compression tests. It can be observed that, with the same steel fiber MF15 reinforcement, the samples failure modes are more or less the same regardless of the nanomaterial mixture. Except some visible cracks, most parts of the samples remain intact. This could be attributed to the effect of steel fiber, which bridges the cracks and retards crack extension.

Fig. 2.15 shows dynamic compressive stress−strain curves of UHPC specimens with different nanomaterial mixes. Comparing with static test results, it can be clearly observed that with the increase of strain rate from 0/s to 60/s and then 80/s,
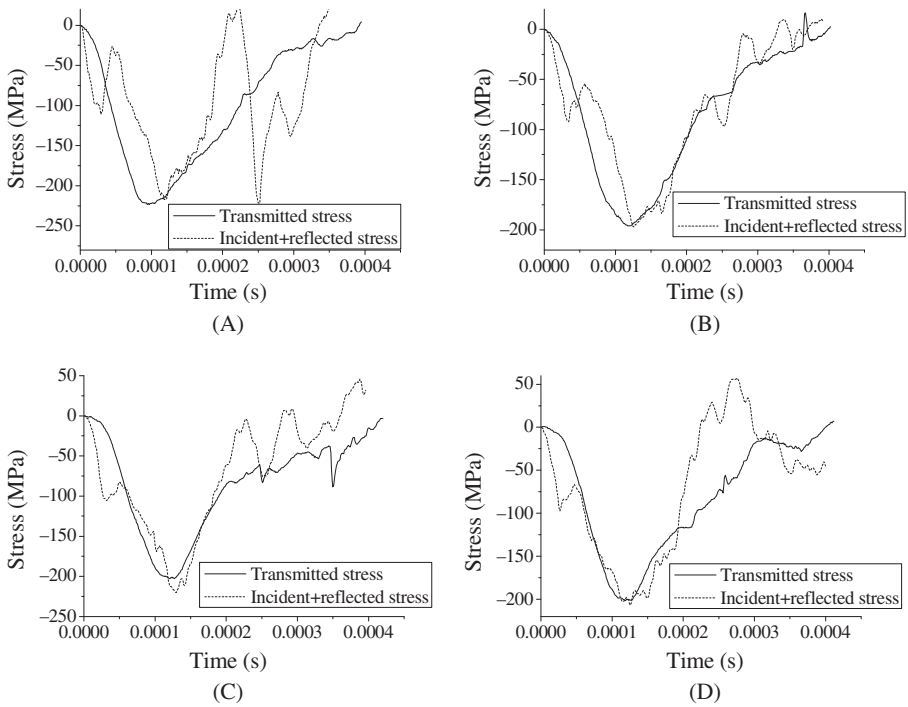
Figure 2.13 Stress equilibrium checks. (A) 3% NC (strain rate 93.74 1/s). (B) 3% NS (strain rate 79.72 1/s). (C) 3% NA (strain rate 85.45 1/s). (D) 3% NT (strain rate 90.35 1/s).

Figure 2.14 Failure patterns of specimens with different nanomaterials. (A) 3% NC. (B) 3% NS. (C) 3% NA. (D) 3% NT.
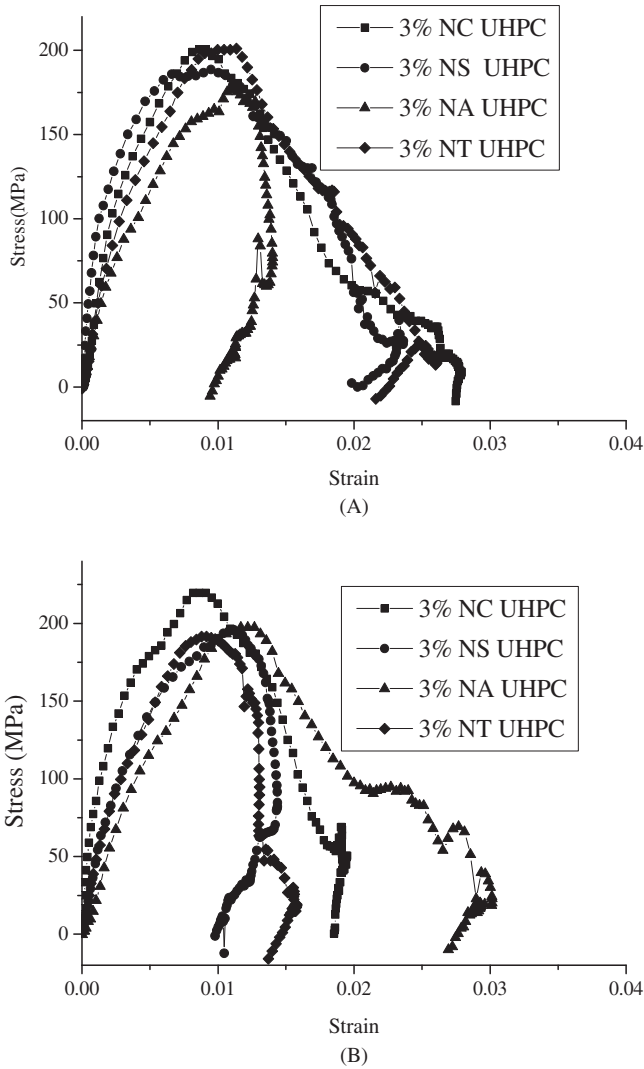
Figure 2.15 Comparison of stress−strain curves at different strain rates of different nanoparticles. (A) Strain rate 60/s. (B) Strain rate 80/s.

all UHPC samples display a strength enhancement. It can also be noticed that UHPC with NC addition is the most sensitive loading rate, which has the highest strength increment during the test.

Dynamic strengths of UHPC samples under various strain rates are plotted in Fig. 2.16. It can be observed all UHPC materials are sensitive to the strain rate ranging from 0/s to 80/s. The increase of loading rate favors the material compressive strength. When the strain rate exceeds 80/s, although strength increase can still be noticed in the UHPC material, the rate of strength increase gradually slows down.
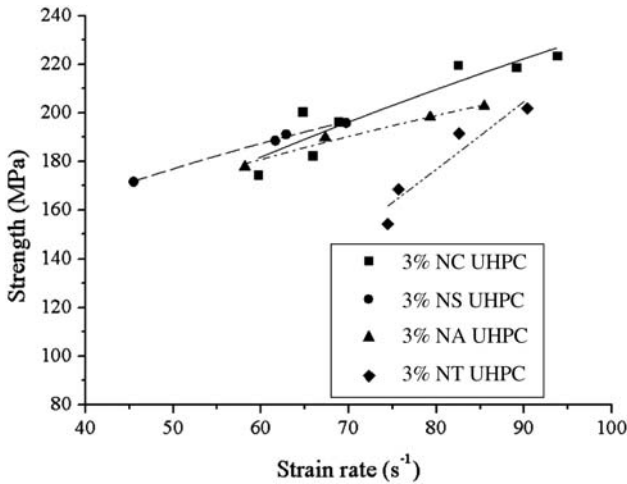
Figure 2.16 Dynamic strength of UHPC under various strain rates.
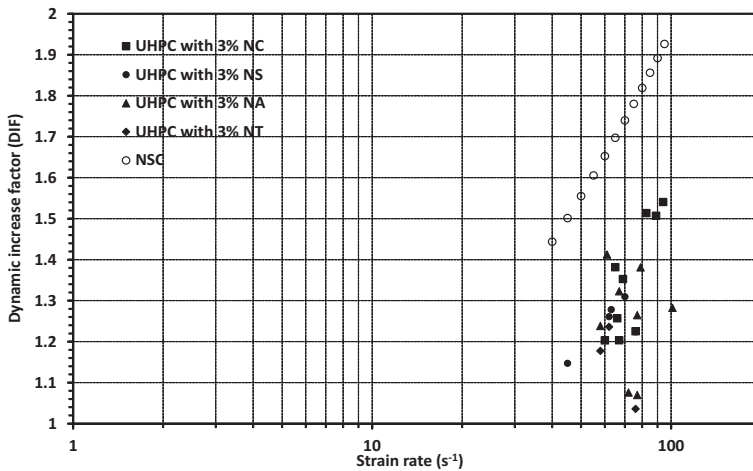
Figure 2.17 Comparison of DIF curves between NSC and UHPC.

The dynamic increase factors (DIF) for UHPC compressive strength including all test samples are plotted in Fig. 2.17. It should be noticed that, in this study, due to the lack of data at low strain rates, there are no DIF values ranging from 0 to 40/s. Further tests are required for a complete DIF curve fitting. In previous studies, CEB [48] assumed change of slope in DIF curves happens at 30/s for normal strength concrete (NSC). Marval et al. [49] proposed a formulation for DIF curves, which indicates a change of slope happens at 1/s for NSC. As shown in Fig. 2.17, a DIF of about 1.54 for UHPC with NC is obtained at the highest measured strain rate of 94/s.

Comparison is made between the NSC without fiber reinforcement and nanomaterial addition and UHPC material used in this study. For comparison, the NSC material has a static compressive strength of 52.5 MPa, and its DIF are calculated based on the formula discussed in Marval et al. [49], which is originated from CEB code [48].

For NSC compressive strength:

$$DIF = \frac{f_c}{f_{cs}} = \begin{cases} \left(\frac{\dot{\varepsilon}}{\dot{\varepsilon}_s}\right)^{1.026\alpha} & \text{for } \dot{\varepsilon} \leq 30 s^{-1} \\ \gamma_s \left(\frac{\dot{\varepsilon}}{\dot{\varepsilon}_s}\right)^{1/3} & \text{for } \dot{\varepsilon} > 30 s^{-1} \end{cases} \tag{2.12}$$

where f_c is the dynamic compressive strength at $\dot{\varepsilon}$, f_{cs} is the static compressive strength at $\dot{\varepsilon}_s$, $\dot{\varepsilon}$ is the strain rate in the range of 30×10^{-6} to 300 s^{-1}, $\dot{\varepsilon}_s$ is the static strain rate 30×10^{-6}; $\log \gamma_s = 6.156 \ \alpha \ - \ 2$; $\alpha = 1/(5 + 9f_{cs}/f_{co})$; $f_{co} = 10$ MPa.

As displayed in Fig. 2.17, NSC material has higher DIF values than UHPC with fiber and nanomaterial addition at the same strain rate. In fiber-reinforced concrete material, the fibers resist the lateral spreading of the cracks by bridging across regions of lower strength. Therefore, the beneficial effect of a restraint on lateral crack growth has already been partially accounted for by fiber reinforcement, resulting in higher failure strength under quasi-static loading. Subsequently, the influence of the higher loading rate on reducing lateral crack development would be lessened.

Low porosity microstructure is another possible reason for low rate sensitivity of UHPC. As listed in Table 2.7, the water/cement ratio for the current UHPC materials is 0.25, which is significantly smaller than conventional concrete that usually has a water/cement ratio around 0.4. Total porosity of UHPC is lower than normal concrete; although no clear relationship exists linking the DIF with porosity, indirect experimental evidences were noted from previous study proving that the strain rate sensitivity of compressive strength is more obvious for higher porosity specimens [50−52].

2.3.3.4 Split tensile results

After dynamic compressive tests, SHPB split tensile tests were carried out. Tension testing in a SHPB is more complex due to a variation of loading methods and specimen attachment to the incident and transmission bar [53]. Fig. 2.18A shows the SHPB split tensile test setup; the parallelism of the two flat ends of the UHPC specimen is important and hence should be checked carefully prior to the tests. Three strain gauges are glued perpendicular to the loading direction. Compared with the size of UHPC specimens, the strain gauge glued at the surface of the specimen is very small and thin, so the effects of crack bridging to the splitting crack by the gauges and the glue can be neglected.
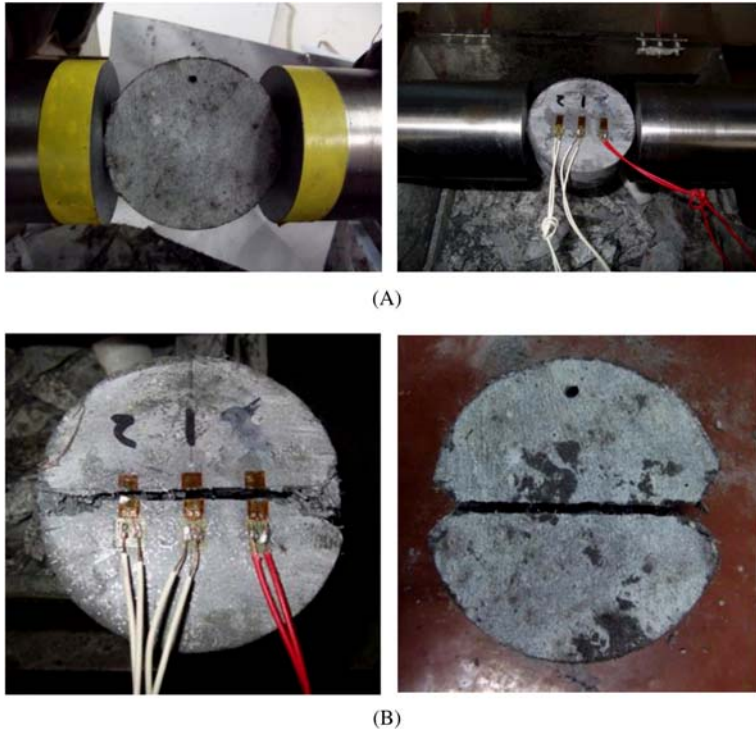
Figure 2.18 SHPB split tensile test. (A) Test setup. (B) Typical failure mode.

Fig. 2.18B shows the typical failure mode of UHPC material. It can be noticed that the crack propagation route and failure path is along the loading diameter at which position the strain can be recorded by the strain gauge attached on the sample surface.

The failure modes of the specimens are investigated from two perspectives. Firstly, it is necessary to check the location of crack initiation, whether the failure is initiated from the center of the disc is of vital importance. Secondly, the route of crack propagation is important, and the failure path should be along the loading diameter. To investigate these two phenomena, a high-speed camera was used in the SHPB split tensile tests, and sample responses at 155, 310, and 465 μs were captured. Based on trial tests, at these specified times, samples showed crack initiation, crack propagation, and end concrete crush. As depicted in Fig. 2.19, the crack initiated at the sample center where the maximum tensile stress existed and quickly propagated towards both ends, at about 310 μs, cracks reached the sample ends and end concrete crush started crushing. In general, the crack paths were all along the loading diameter in which the strain gauges could detect the response with accuracy. The comparison among UHPC with different nanomaterial additions showed that a mixture of 3% NS resulted in quicker crack generation and larger cracks while samples with NC mixture showed better crack confinement.

Fig. 2.20 gives the DIF values for dynamic tensile strength of UHPC with different nanomaterial additions. All samples have prominent tensile strength

t=0μs   t=155μs   t=310μs   t=465μs

3% Nano-CaCO$_3$

t=0μs   t=155μs   t=310μs   t=465μs

3% Nano-SiO$_2$

t=0μs   t=155μs   t=310μs   t=465μs

3% Nano-Al$_2$O$_3$

t=0μs   t=155μs   t=310μs   t=465μs

5% Nano-CaCO$_3$

t=0μs   t=155μs   t=310μs   t=465μs

1% Nano-CaCO$_3$
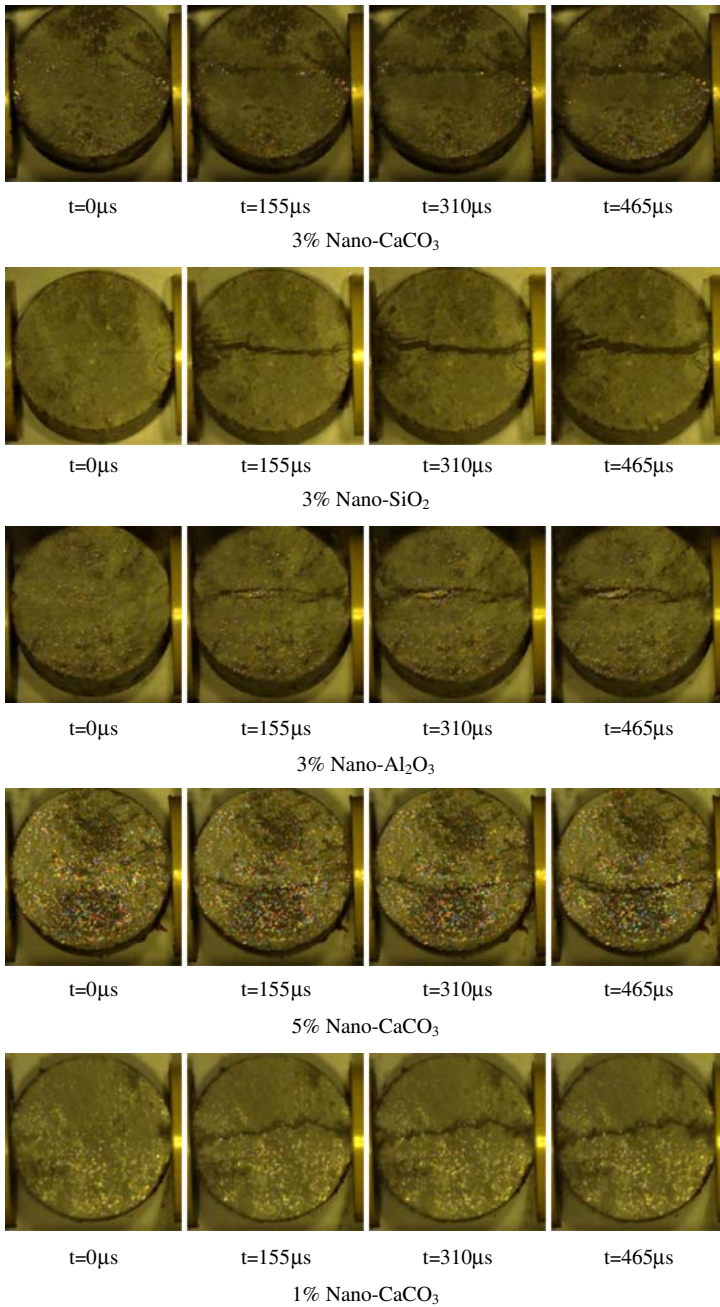
Figure 2.19 High-speed camera results of sample damage.
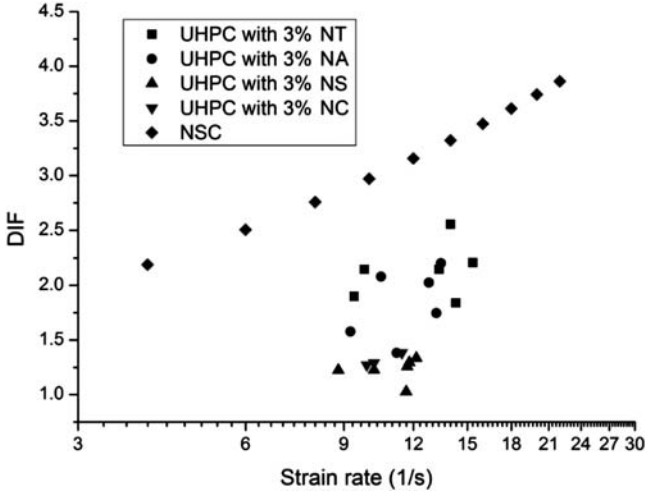
Figure 2.20 Comparison of DIF curves between NSC and UHPC.

enhancement during the tests. A largest DIF of about 2.55 was obtained in UHPC
with NT at the strain rate of 14/s. It can also be noted that different from the perfor-
mance under dynamic compressive test, UHPC with NC is relatively insensitive to
the high loading rate and its tensile DIF values are quite small around 1.3 even at
strain rate of 11/s.

Similar with SHPB dynamic compressive strength, the DIF values of the UHPC
materials are compared with those of the NSC material at the same loading rate.
The DIF of NSC which are obtained from formulae proposed by Malvar and
Crawford [49].

The DIF for NSC in tension can be calculated as:

$$
DIF = \frac{f_t}{f_{ts}} =
\begin{cases}
\left(\dfrac{\dot{\varepsilon}}{\dot{\varepsilon}_s}\right)^{\delta} & \text{for } \dot{\varepsilon} \leq 1s^{-1} \\[2mm]
\beta\left(\dfrac{\dot{\varepsilon}}{\dot{\varepsilon}_s}\right)^{1/3} & \text{for } \dot{\varepsilon} > 1s^{-1}
\end{cases}
\tag{2.13}
$$

where f_t is the dynamic tensile strength at $\dot{\varepsilon}$; f_{ts} is the static tensile strength at $\dot{\varepsilon}_s$; $\dot{\varepsilon}$
is the strain rate in the range of 1×10^{-6} to $160\ \text{s}^{-1}$; $\dot{\varepsilon}_s$ is the static strain rate
1×10^{-6}; $\log \beta = 6\delta - 2$; $\delta = 1/(1 + 8f_{cs}/f_{co})$; $f_{co} = 10$ MPa.

As shown in Fig. 2.20, similar with the observation made in the SHPB compres-
sion tests, the DIF of UHPC is constantly lower than the values of NSC. It is con-
sidered that the steel fiber reinforcement and nano-addition account for the major
strength increment of UHPC material and thus the contributions from the strain rate
effects are lessened. Also, as aforementioned, the porosity of UHPC is lower than
NSC, which has been experimentally proved to be influential to the dynamic perfor-
mance of concrete material.
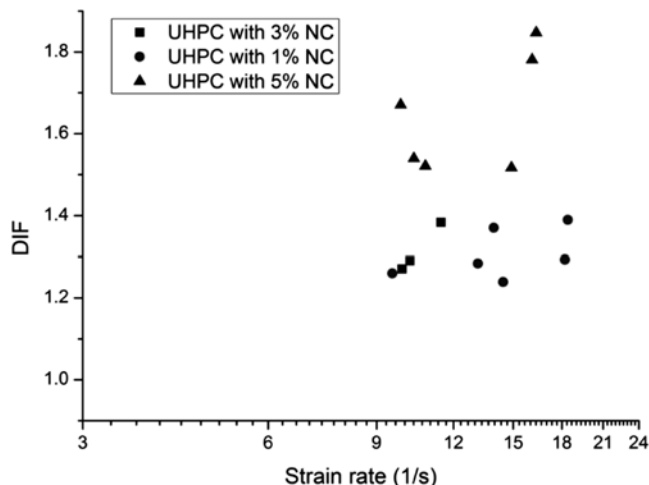
Figure 2.21 DIF influenced by the volume of NC in split tension SHPB tests.

In the split tensile test of this research, two more sets of UHPC samples with the same type of nanoparticle $CaCO_3$ addition but different dosages (1% $CaCO_3$ and 5% $CaCO_3$) were tested to investigate the influence of volume dosage of nanomaterial on the dynamic tensile strength of UHPC. In Fig. 2.21, influence of different nanomaterial $CaCO_3$ volume dosages on the dynamic tensile strength is plotted. According to available tests data, UHPC with 1% volume dosage of NC yields slightly lower DIF values than UHPC with 3% volume dosage of NC. However, great improvement is observed when the volume dosage increased to 5%. It can thus be concluded that increase of volume dosage could have positive influence on the dynamic tensile strength. However, further investigation is required to find out the optimal value of nanomaterial dosage to balance the strength requirement and workability.

After completing the SHPB tensile tests, it can be generally concluded that when compared with normal strength under dynamic tensile loads [49,53,54], UHPC with nanomaterial and fiber reinforcement has lower DIF, and this observation is consistent with the previous study [55,56].

2.3.4 Microscopy analysis

Microscopy analysis was conducted to provide explanation of macroscopic failure phenomenon at microscale. Morphology of the samples was observed by SEM using LEO 1550 Scanning Electron Microscope. XRD instrument Bruker D4 ENDEAVOR was used for phase analysis and semiquantitative analysis. Elemental analysis was conducted by XRF of Bruker Handheld XRF Spectrometry.

Specimens after SHPB split tensile tests were knocked into small pieces, soaked in ethanol for a week, and ethanol was renewed three times in this period, and then was put into a vacuum desiccator (about 40°C) for drying. Finally samples were stored in a desiccator with limestone inside to keep dry and anticarbonation.

2.3.4.1 SEM analysis of UHPC after SHPB split tensile tests

Pictures of matrix and ITZ taken from the SEM tests are listed in Fig. 2.22, consisting of four types of samples with different nano-additives and one without any nano-additive. Please note that all these photographs are taken from damaged samples after SHPB split tensile tests.

In Fig. 2.22A1, large number of well-developed calcium hydroxide $Ca(OH)_2$ plates can be observed, which implies that without nanoparticles addition, the porosity of the hardened UHPC is relatively large and $Ca(OH)_2$ has enough space to grow. In UHPC with nanoparticles addition as shown in Fig. 2.22B1, C1, D1, and E1, one can observe very dense structures with quite few air pores, and this observation confirmed the filling effect from the ultra-fine nanoparticles. Furthermore, after a close look into the cement matrix, one can notice that the main hydration product is the foil-like fine C-S-H gel, and no plate-shaped $Ca(OH)_2$ can be observed. These C-S-H gel are possibly generated from the pozzolanic reactions of nanoparticles with $Ca(OH)_2$.

The ITZs between the steel fiber and cement paste in post-damage UHPC samples are also shown in Fig. 2.22. Two major damage modes can be identified in the figure. In Fig. 2.22A2, C2, and D2, cement cracks around the ITZ are observed, and these cracks are generated by the stress transferred from steel fiber to the cement in dynamic tests, and cracks initiate in the cement because concrete cement has lower fracture strength than steel fiber. In Fig. 2.22B2 and E2, besides cement cracks, debonding and pulling out of steel fiber from cement paste can be observed. ITZs in these two figures are damaged and thus their widths are significantly larger than the other three scenarios.

2.3.4.2 XRF and XRD analysis

The XRF test results of UHPC samples are shown in Table 2.11. It is noted that CaO is the main component in UHPC with or without nano-addition, which is followed by SiO_2 and Fe_2O_3.

XRD analysis was used to identify the polycrystalline phases of cement and hardened cement paste through recognition of the X-ray patterns that are unique for each of the crystalline phases [57]. Comparing with SEM tests, a major advantage of the XRD technique is its speed and ease of measurement. Furthermore and perhaps more importantly, the different phases in the samples can be distinguished [58]. In this study, besides the investigation of UHPC with different nanomaterial compositions, UHPC samples of 28 and 500 days were analyzed to give information of long-term hydration process of UHPC.

Diffraction patterns were collected in the range of $10-80$ degrees 2θ, 0.02 degrees/step, 2 degrees/minute as continuous scans. After data collection, all patterns were processed through Jade 5.0 software.

Diffractograms are shown in Fig. 2.23, calcium hydroxide, $Ca(OH)_2$, peaks were identified on diffractograms of the UHPC mixture examined. It is noted that ettringite $(Ca_6Al_2(SO_4)_3(OH)_{12} \cdot 26H_2O)$ characteristic peaks are not seen in the diagram which confirms the SEM observation that ettringite needles are absent in UHPC with high pozzolanic effect. Similar observations were found in the previous UHPC development [59].
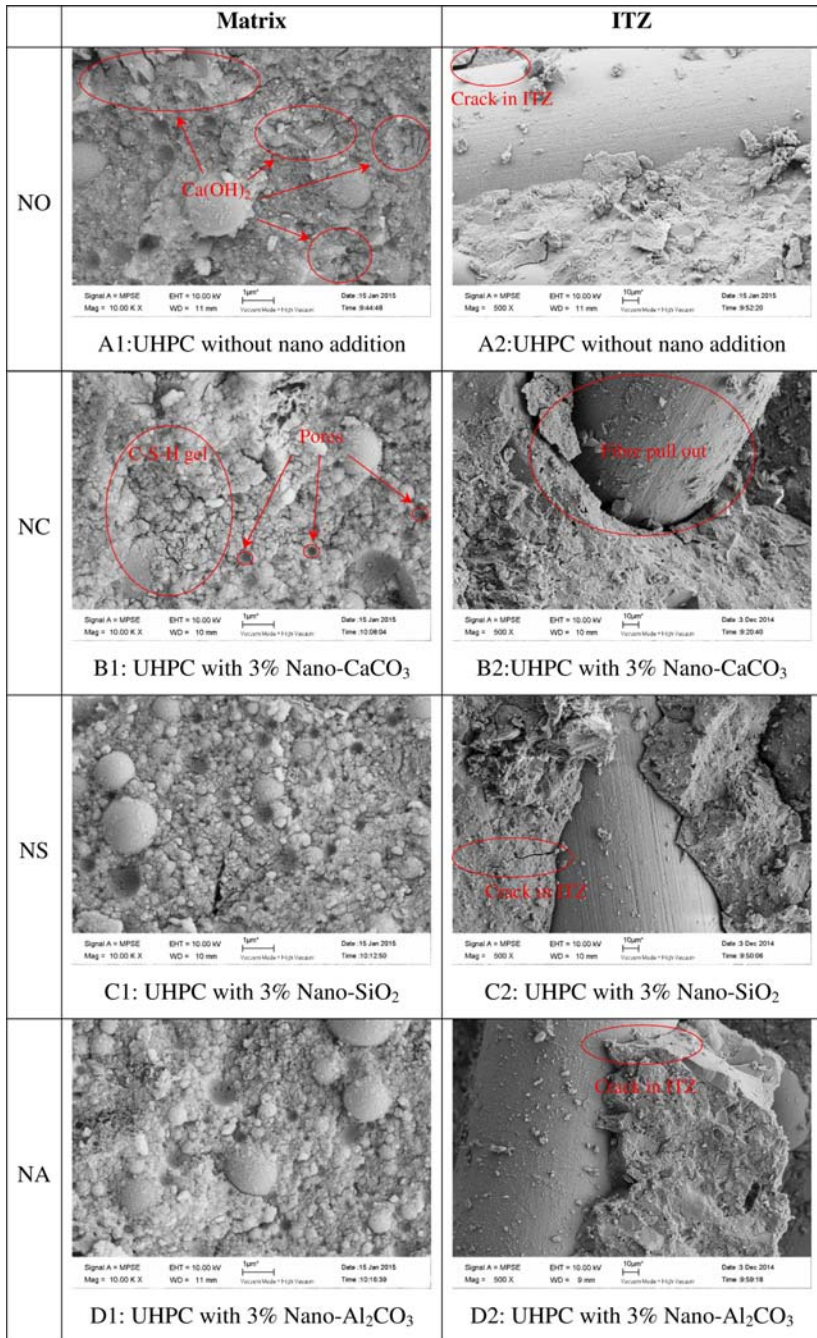
Figure 2.22 Pictures of motor matrix and ITZ from SEM analysis.
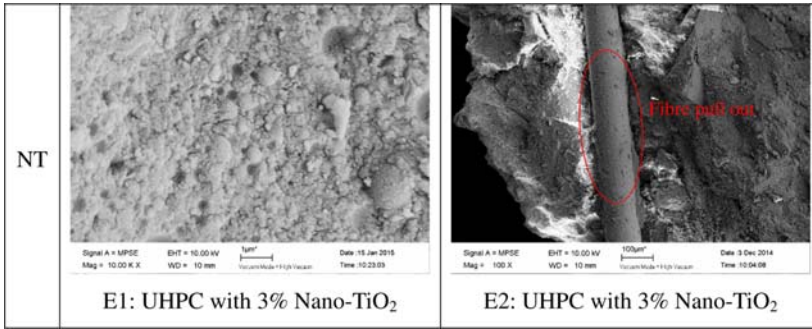
Figure 2.22 (Continued).

Table 2.11 Material semiquantitative analysis from XRF for UHPC with nano-additives

Material	Percentage			
	NC	NS	NA	NT
MgO	0.409	0.432	0.437	0.430
AL_2O_3	2.700	2.780	3.260	2.740
SiO_2	35.13	39.42	37.54	36.60
P_2O_5	0.783	0.788	0.768	0.746
SO_3	1.490	1.350	1.220	1.240
Cl	0.036			
K_2O	2.430	2.290	2.340	2.390
CaO	46.18	42.22	43.40	42.72
TiO_2	0.492	0.464	0.475	2.610
Cr_2O_3	0.099	0.129	0.095	
MnO	0.445	0.443	0.379	0.403
Fe_2O_3	8.983	8.209	8.994	9.152
CuO	0.120	0.133	0.135	0.139
ZnO	0.126	0.095	0.085	0.095
SrO	0.164	0.137	0.132	0.150
ZrO_2	0.037			
BaO	0.150			
WO_3	0.230	0.907	0.521	0.413

2.3.4.3 Influence of nano-additives on the properties of UHPC

Following Fig. 2.23, to quantitatively analyses the influence of nano-addition on the UHPC material hydration process, the reference intensity (RIR or K) or matrix flushing is adopted in this study. This technique was developed by Chung [60]. To guarantee the RIR method that can be used as a quantitative method, all phases in the sample being analyzed must be known; otherwise the method is at best semiquantitative. Secondly, to improve accuracy of the results, as many of the
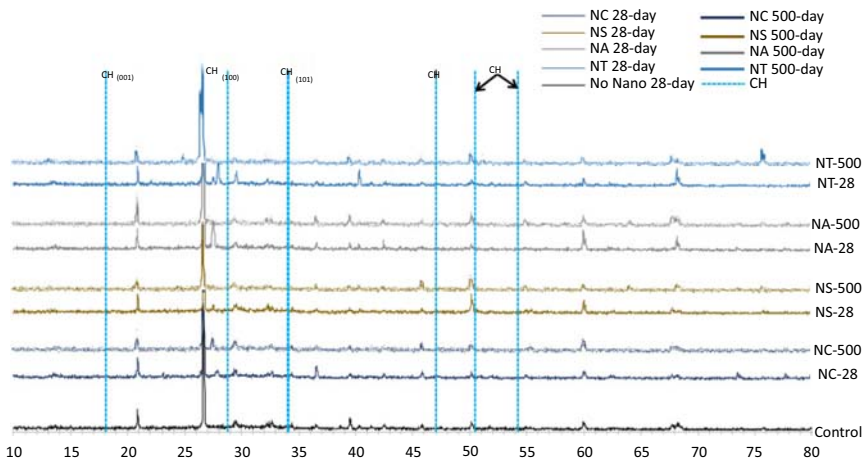
Figure 2.23 XRD analysis of UHPC with and without nano-additives.

variables as possible (the RIRs and the I_{rel} values) should be determined with the experimental set up used for specimen analysis.

Assuming n phases exist in the sample, the equation to calculate the weight fraction of a certain phase x is:

$$Wx = Ix/Kx \left(\sum_{i=1}^{n} Ii/Ki \right) \tag{2.14}$$

where Wx is the weight fraction of Phase x, Ix is the intensity (or intensity sum; IS) of Phase x in XRF analysis. Kx is the relative intensity (or RIR) for Phase x which can be found in PDF in XRF analysis.

Table 2.12 gives the measurement of intensity (PI) and full width at the half maximum (FWHM) of all Ca(OH)$_2$ peaks detected at 28 days, the IS of Ca(OH)$_2$ is also listed for UHPC with and without nanomaterial addition. It is noted for control sample without nanomaterial addition, CH phase IS is 33.7. For all UHPC samples with nanomaterial addition, IS decreases.

According to Eq. 2.14, the IS of a phase is proportional to its weight fraction in the sample. Based on this concept, it is noted given the same weight dosage nanomaterial was mixed in UHPC, the weight fraction of CH was significantly influenced by the nanomaterial type. NT and NS had lower IS of CH, which indicated more prominent pozzolanic reaction between CH and nanomaterial. The concrete strengths should be higher than the other two UHPCs with NC and NA additions. This assumption is confirmed with the compressive strength curve shown in Fig. 2.2 where UHPC with NT addition has the highest compressive strength (less CH in the paste and more CSH gel formed, whereas UHPC with NA has the lowest compressive strength.

The influence of nanomaterial addition on UHPC long-term hydration process is illustrated in Table 2.13 where XRD analysis on UHPC samples at 500 days is presented together with UHPC samples at 28 days. It is easily noted that all UHPC

Table 2.12 **CH measurement based on XRD analysis at 28 days**

Phase	d(Å)	Control			NC			NS			NA			NT		
		PI (cps)	FWHM	IS	PI (cps)	FWHM	IS	PI (cps)	FWHM	IS	PI (cps)	FWHM	IS	PI (cps)	FWHM	IS
CH	4.90	22	0.22	33.70	24	0.14	31.44	21	0.18	18.72	23	0.26	24.96	23	0.12	19.76
	3.10	27	0.14		26	0.20		28	0.16		28	0.12		23	0.12	
	2.63	21	0.90		26	0.58		22	0.16		26	0.32		31	0.04	
	1.93	18	0.24		22	0.24		11	0.12		14	0.26		17	0.44	
	1.81	17	0.06		14	0.14		28	0.16		21	0.06		17	0.26	
	1.70	14	0.06		14	0.04		19	0.06		15	0.16		11	0.10	

Table 2.13 CH measurement based on XRD analysis at 28 and 500 days

Phase	Time (Day)	d(Å)	NC			NS			NA			NT		
			PI (cps)	FWHM	IS	PI (cps)	FWHM	IS	PI (cps)	FWHM	IS	PI (cps)	FWHM	IS
CH	28	4.90	24	0.14	31.44	21	0.18	19.72	23	0.26	24.96	23	0.12	19.76
		3.10	26	0.20		28	0.16		28	0.12		23	0.12	
		2.63	26	0.58		22	0.16		26	0.32		31	0.04	
		1.93	22	0.24		11	0.12		14	0.26		17	0.44	
		1.81	14	0.14		28	0.16		21	0.06		17	0.26	
		1.70	14	0.04		19	0.06		15	0.16		11	0.10	
	500	4.90	21	0.08	18.16	21	0.16	18.5	18	0.48	22.46	18	0.18	17.24
		3.10	26	0.30		22	0.16		25	0.08		24	0.04	
		2.63	24	0.18		22	0.30		24	0.20		22	0.28	
		1.93	23	0.08		17	0.12		22	0.12		15	0.16	
		1.80	18	0.04		18	0.08		18	0.20		22	0.14	
		1.70	15	0.12		14	0.11		13	0.06		14	0.10	

samples with nanomaterial addition showed a decrease of IS of CH at 500 days. UHPC samples with NC had a most significant CH IS decrement that indicates a most prominent long-term strength increment for this material.

2.3.5   Conclusions

For the newly designed concrete materials with both steel fiber and nanomaterial additions, great static strength improvement was observed. SHPB tests were conducted to get full understanding of the material constitutive relationships especially under dynamic loading condition. It was observed that with the same fiber reinforcement, different nanomaterial additions seem to have insignificant influence on the material dynamic strengths. However, material strength could be increased with the increase of nanomaterial volume dosage. Comparing with the traditional NSC, UHPC with fiber and nanomaterial addition has less strength increment under the same loading rate when compared with NSC. In SEM tests on post-damage UHPC samples, different damage modes at ITZ are identified, XRD and XRF analysis confirmed the filling and pozzolanic effect of nanoparticles addition.

2.4   Effects of steel fibers on dynamic strength of ultra-high performance concrete

The work presented in Section 2.3 confirms the effect of nanoscale particle addition on the mechanical performance of the UHPC material, while Section 2.4 elaborated the impact from the steel fiber addition on the dynamic strengths and microstructure improvement on UHPC. Before proceeding to the utilization of the current UHPC material into protective design against blast loads, more study on the dynamic performance of UHPC with selected nano- and steel fiber is further studied in this section.

2.4.1   UHPC sample preparation

In this research, the complete mix proportion of UHPC is shown in Table 2.14. In UHPC, ultra-fine particle silica fume ($0.15-0.20\ \mu m$) instead of coarse aggregates is added to Portland concrete to improve its properties, in particular its compressive strength, bond strength, and abrasion resistance. These improvements stem from both the mechanical improvements resulting from the addition of a very fine powder to the cement paste mix as well as from the pozzolanic reactions between the silica fume and free calcium hydroxide in the paste. The addition of silica fume can also reduce the permeability of concrete material to chloride ions and thus protect the steel reinforcement against corrosion [61]. The workability of UHPC in coastal areas where the environment is chloride rich can be improved.

In this study, nanoparticles NC at a constant weight dosage is added into the UHPC specimens. The inclusion of NC into the UHPC matrix in this study is based on two considerations. Firstly, NC is proved to be effective in increasing concrete

Table 2.14 Mix proportion of UHPC (kg)

52.5 Cement	750			
Silica Fume	225			
Silica Flour	190			
River Sand	1030			
Superplasticizer	16			
Water	190			
Water/Binder	25.30%			
Nanoparticles	21.7			
MF15	191	—	—	—
MF06	—	191	—	—
TF03	—	—	191	—
TF05	—	—	—	191

Figure 2.24 Different types of steel fibers.

Table 2.15 Material properties of fibers

Type	Elastic modulus GPa	Tensile strength MPa	Diameter mm	Length mm	Aspect ratio
MF06	210	4295	0.12	6	50
MF15	210	4295	0.12	15	125
TF03	210	1500	0.3	30	100
TF05	210	1500	0.5	30	60

mechanical performance. Secondly, NC is a widely used nano-addition and its relatively low price promised its potential application in practical civil designs.

Fiber reinforcement including four different steel fibers, i.e. MF06, MF15, TF03, and TF05 as shown in Fig. 2.24 is mixed in the concrete material.

The mechanical properties and dimensions of the steel fibers are listed in Table 2.15.

Figure 2.25 Concrete wooden molds.

All UHPC samples were produced by mixing the silica fume, fine sand, and powder materials that consisted of cement and nanoparticles, in a laboratory concrete mixer. The mix procedure is similar to that described in Section 2.2.

Wooden molds as shown in Fig. 2.25 are prepared for curing of UHPC. The specimens were firstly cured in a humid room for 24 hours, and the temperature was controlled to be 20°C ± 5°C. The specimens were then demolded and cured in hot water at a temperature of 90°C for another 48 hours. At last, the specimens were placed in a room again at the ambient temperature until the commencement of the tests. Prior to any tests, samples were properly leveled, sanded, polished, cleaned, and dried to attain smooth surfaces.

After proper curing, the UHPC samples were drilled out using automatic core drilling machine. The specimens used for static compression test were 100 mm cubes, and the samples used in the static split tensile tests and the following SHPB tests were cylinders with 75 mm diameter with 37 mm or 75 mm height.

2.4.2 Static tests

Uniaxial compression tests and split tensile tests were conducted to determine static uniaxial compressive strength and split tensile strength of UHPC.

2.4.2.1 Uniaxial compression test

Static stress−strain curves representing all four kinds of samples are shown in Fig. 2.26. It can be clearly observed that with the addition of different steel fibers in UHPC, the static performance varies significantly. UHPC with 2.5% MF15 has the highest static strength around 150 MPa, which is about 30% higher than the lowest strength obtained in UHPC with 2.5% TF05 reinforcement.

For the two specimens reinforced by TFs as shown in Fig. 2.27A, it is noted TF03 (aspect ratio L/D = 100) has a higher compressive strength around 130 MPa, while TF05 (aspect ratio L/D = 60) has a relatively lower strength around 110 MPa. Given a same volume fraction, TF03 with a smaller diameter means a larger
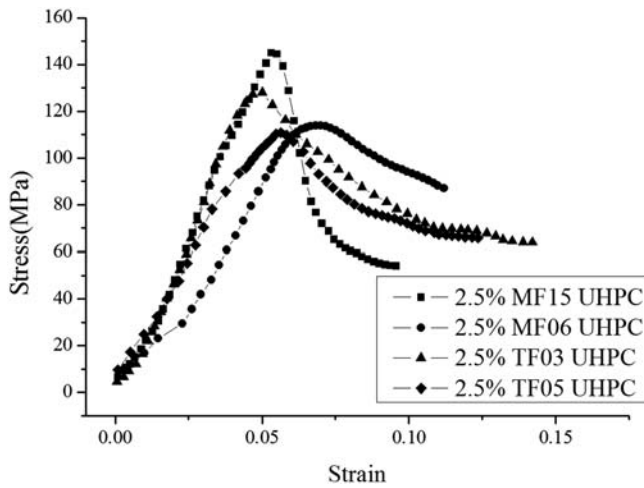
Figure 2.26 Stress−strain curves from quasi-static compressive tests.
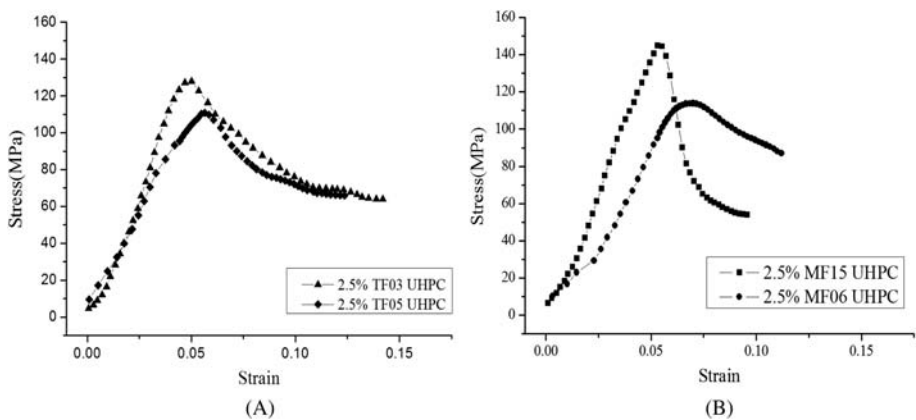
Figure 2.27 Influence from fiber aspect ratio on UHPC compressive strength. (A) TF fibre with different aspect ratio; (B) MF fibre with different aspect ratio.

number of fibers in the matrix and thus can effectively resist the cracking and improve the concrete strength.

For the two specimens reinforced by MFs as shown in Fig. 2.27B, it is easy to see that when the volume fraction is fixed, the fiber aspect ratio exerts significant influence on the stress−strain plots. Compared to smaller aspect ratio (MF06 in which L/D = 50), the peak strain decreases markedly but the compressive strength and elastic modulus (slope of initial straight line) increase for the larger aspect ratio (MF15 in which L/D = 125) case. Such observations can be attributed to the fact that fine fibers MF06 control opening and propagation of microcracks as they are densely dispersed in cement matrix, and longer fibers MF15 control larger cracks and contribute to increase the final strength of FRC.
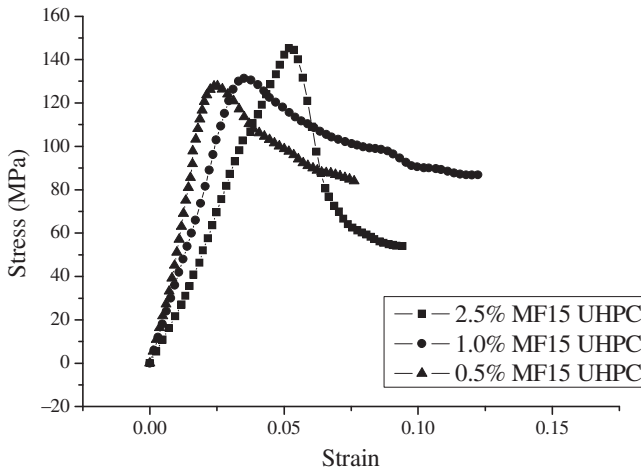
Figure 2.28 Compressive stress−strain curves for different fiber volume fractions.

Table 2.16 Experimental results of different formula UHPC under static compressive load

Fiber type	MF15	MF06	TF03	TF05
Strength (MPa)	145.12	114.51	132.29	113.05

The influence of fiber volume fraction is illustrated in Fig. 2.28. Three fiber volume fractions, i.e., 0.5%, 1.0%, and 2.5% are studied in the uniaxial compression test, and it can be noticed from the stress−strain curve that material peak compressive strength is increasing with fiber volume fraction. Furthermore, the material peak strain and ductility are also favored with an increasing fiber volume fraction. The results indicate that to obtain a better performance of UHPC material, a reasonably higher fiber volume fraction is essential given that the concrete workability can still be satisfied.

The static compressive strengths for UHPC with different fiber reinforcements are averaged and listed in Table 2.16.

2.4.2.2 Split tensile test

Split tensile test were conducted on UHPC cylinder specimens with a dimension of 75 mm diameter × 37 mm height as shown in Fig. 2.3. The test concrete cylinder was placed horizontally between the loading surfaces of compression testing machine (Fig. 2.3A). The compression load was applied diametrically and uniformly along the length of cylinder until the failure of the cylinder along the vertical diameter (Fig. 2.3B). To generate a uniform loading distribution and minimize the concentration of the high compressive stresses near the points of
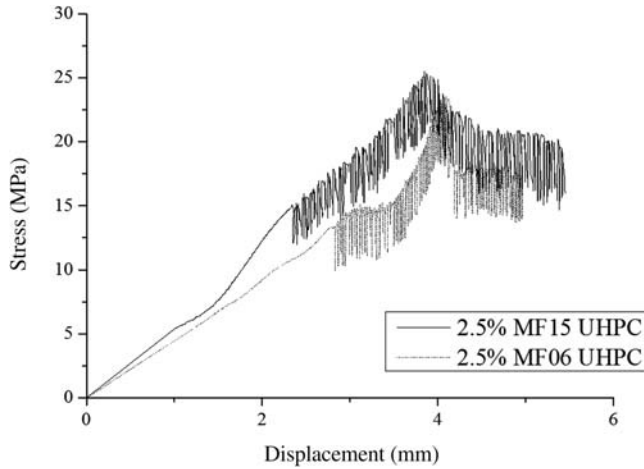
Figure 2.29 Stress−strain curves from static split tensile tests.

application, two strips of plywood were placed between the specimen and loading plates of the testing machine. Test stops until the concrete cylinder splits into two halves along the vertical diameter plane. The split tensile failure is induced by the indirect tensile stress form Poisson's effect.

The split tensile strength was calculated based on Eq. 2.15:

$$\sigma = \frac{2P}{\pi DL} \tag{2.15}$$

where P is the load at failure; D and L are the diameter and length of the specimen respectively.

Fig. 2.29 shows the static split tensile stress strain curve of two micro-fiber-reinforced UHPC. It is seen again that aspect ratio has positive influence on the material mechanical performance. Compared with MF06 reinforced UHPC, UHPC with MF15 reinforcement has higher peak tensile strength and higher ductility that indicates better energy absorption ability.

The influence of volume fraction on UHPC split tensile strength is shown in Fig. 2.30. It is observed that a slightly increased tensile strength is obtained in 1.0% MF15 UHPC comparing with 0.5% MF15 sample. A drastically increased strength is observed from 2.5% MF15 UHPC. In general, the ductility is also increasing with the fiber volume fraction.

The static split tensile strengths for UHPC with different fiber reinforcements are then averaged and listed in Table 2.17.

2.4.3 SHPB testing program

The dynamic tests were conducted on SHPB test machine with 75 mm diameter. The experimental system of SHPB is sketched in Fig. 2.4.
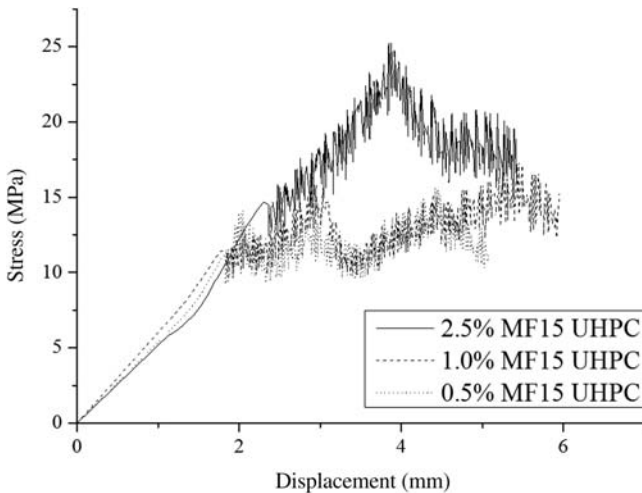
Figure 2.30 Tensile strength of UHPC with different fiber volume fractions.

Table 2.17 Split tensile strength of different formula UHPC under static load

Fiber type	MF15	MF06	TF03	TF05
Strength (MPa)	22.2	20.5	13.5	15.0

2.4.3.1 SHPB-compression

Dynamic compression test results are discussed in this section. Fig. 2.31 shows the failure modes of UHPC samples after the tests. It can be observed that under impact loads, different fibers addition has prominent influence on the samples failure modes. UHPC specimen with 2.5% MF15 fiber addition only has some visible cracks at the edge. However, UHPC sample with shorter length micro-fiber MF06 exhibits extensive cracks. For the two samples reinforced by twisted fibers TF03 and TF05, more extensive cracks can be found on the TF05 sample, which indicate the larger aspect ratio of length to diameter has positive influence on the crack control of UHPC.

From the dynamic compression tests, it can be concluded that fiber length and aspect ratio both have impact on the dynamic failure modes of UHPC sample, with the increase of fiber length or aspect ratio, the damage resistance of UHPC material increases. It can also be found that among all four steel fibers, MF15 has the best crack confinement ability in the dynamic compressive test.

Fig. 2.32 compares the dynamic compressive stress−strain curves obtained from all four UHPC specimens. Under the strain rate of 60 s^{-1}, UHPC with 2.5% MF15 fiber reinforcement has the highest dynamic strength that is about 200 MPa and UHPC with 2.5% TF05 fiber reinforcement has the lowest strength which is about

Figure 2.31 : Failure patterns of different types of fiber. (A) 2.5% MF15, (B) 2.5% MF06, (C) 2.5% TF03, and (D) 2.5% TF05.
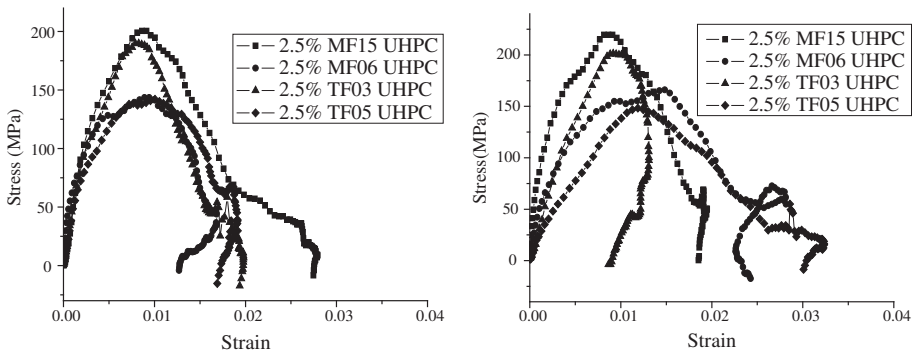
Figure 2.32 Comparison of stress−strain curves at different strain rates of different type fiber. (A) Strain rate 60 s^{-1}. (B) Strain rate 80 s^{-1}.

145 MPa. For UHPC specimens having the same type of reinforcements, it can be found that MF15 performs better than MF06, and TF03 performs better than TF05. It can be concluded that the increase of fiber length and aspect ratio favors the dynamic strength of UHPC material.

Under the strain rate of 80 s^{-1}, it is worth noting that although all four materials experience strength increase during the strain rate boost, UHPC with TF05, which always has the lowest dynamic strength, seems insensitive than the other three materials; however, a better ductility can be noticed for this material with increased strain rate.

Fig. 2.33 plots the dynamic strengths of UHPC materials with different fiber reinforcement. It can be noticed that UHPC with MF15 fiber reinforcement
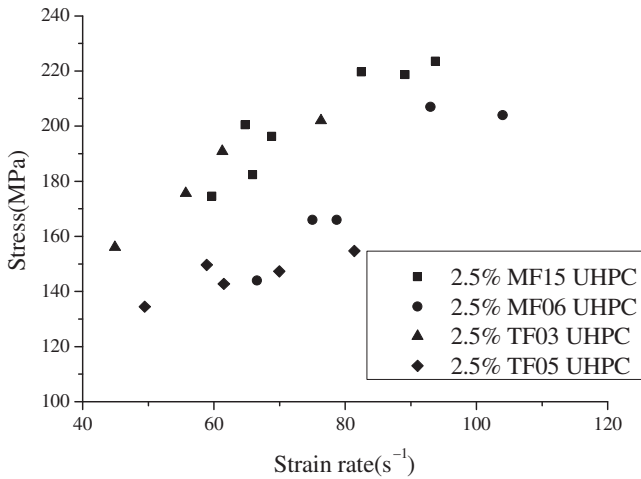
Figure 2.33 Strain rate−stress curves of UHPC with various types of fibers.
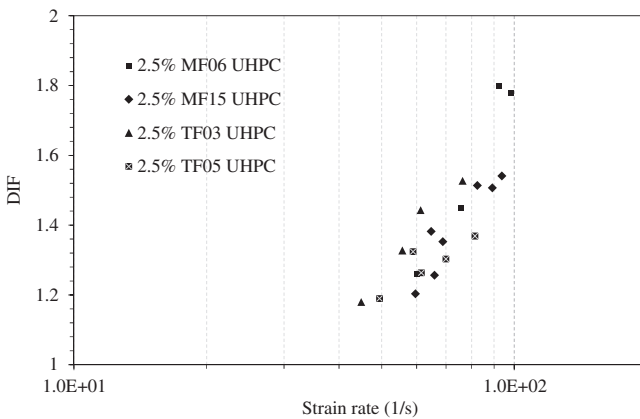
Figure 2.34 DIF curves of UHPC with various types of fibers.

can reach the highest strength exceeding 225 MPa at the strain rate of 93 s^{-1}. Micro-fiber reinforcement is more sensitive to the strain rate effect which can be noticed from the slope of the fitted trend curves. For all UHPC materials, when the strain rate exceeds 80/s, although strength increase can still be noticed in the UHPC material, the rate of strength increase gradually slows down. This can be seen from the convex trend curve shown the figure.

   Dividing by the static compressive strength, DIF curves for all these four materials are obtained and shown in Fig. 2.34. All UHPC specimens displayed a prominent strength enhancement under high strain loading condition, and the highest DIF of about 1.8 is obtained under strain rate of around 100 s^{-1} for UHPC with MF06 reinforcement.
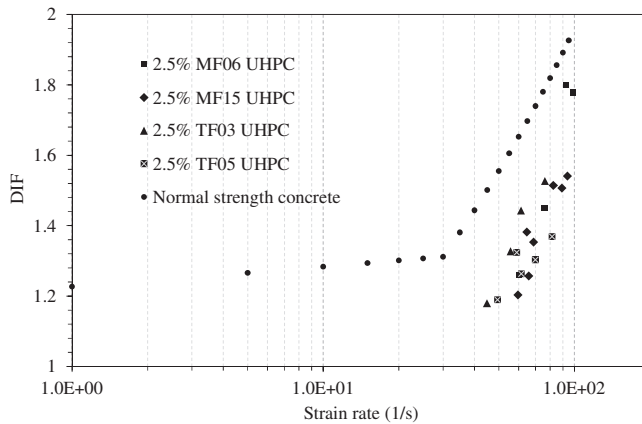
Figure 2.35 DIF of UHPC and NSC.

Comparison with conventional concrete without fiber reinforcement and nano-addition is made. DIFs for NSC ($fc = 52.5$ MPa) are obtained from empirical formulae proposed by Malvar et al. [49].

It can be seen from the comparison shown in Fig. 2.35 that NSC has constantly higher DIF values than UHPC material with different steel fiber enhancement. There are several possible explanations to such observation. Firstly, steel is known to be a more homogenous material with fewer defects than concrete. It was reported that the DIF of steel with ultimate strength of 860 MPa is lower than 1.1 at a strain rate of $10 \cdot s^{-1}$. Previous studies [62,63] revealed that the strain rate sensitivity of steel is decreasing with the increase of steel strength, and in this study, the tensile strengths for the micro-fiber and twisted fiber are 4295 and 1500 MPa, respectively. They are expected to have even lower strain rate sensitivity. With the inclusion of the steel fiber material, UHPC can have a low strength enhancement under high strain rate loading. Secondly, it was reported [64] that the presence of moisture in concrete appears to have a significant effect on the strength enhancement under high strain rate loading. It was found that strength increases in wet concrete greater than those exhibited by dry concrete. UHPC material in this study contains reactive powder ingredients that greatly reduce the water with in the concrete matrix and thus has a lower strain rate sensitivity than NSC. Finally, it is known that the crack velocity in concrete material increases with strain rate. Under similar strain rate loading, fiber-reinforced UHPC has a slower crack expansion than its normal strength counterpart and this results in a lower strength enhancement.

As shown in Fig. 2.35, a sharp increase in the slope of DIF curve happens at transition strain rate of 30 s^{-1} for NSC. Although without sufficient data, it can be predicted that such transition strain rate for UHPC material is higher than NSC. One possible explanation is that such transition stems from the increased lateral inertia effect, and in UHPC material, dispersed fiber material held together the concrete and reduced the lateral expansion which will postpone the sharp transition.

2.4.3.2 SHPB-tension

Results of SHPB tests on the UHPC dynamic tension are shown in this section.
Fig. 2.36 shows the damage modes of the UHPC specimens with different steel
fiber reinforcement, and influence from different fiber volume fraction is also
investigated. It can be seen that 2.5% MF15 reinforced UHPC has narrower crack
than 2.5% MF06 reinforced UHPC, and 2.5% TF03 reinforced UHPC has fewer
cracks than 2.5% TF05 reinforced UHPC. In general, higher fiber aspect ratio helps
resisting the crack extension. For the three UHPC samples reinforced by micro-
fiber, it is noticed that when the volume fraction is low at 0.5%, clear compressive
cracks can be seen at both ends of the sample. Such compressive concrete failure is
not seen in high volume fraction UHPC specimens, and with the increase of the
fiber dosage, the expansion of the crack is confined.

DIF values for materials with different steel fibers reinforcement are shown in
Fig. 2.37. It is noticed that under tensile tests, the twisted fiber-reinforced UHPC
outperforms the UHPC sample with microfiber reinforcement.

Fig. 2.38 shows the DIF values for UHPC material with the same steel fiber
type, i.e., MF15 but different volume fractions including 0.5%, 1.0%, and 2.5%. It
is noticed that increase of the steel fiber volume fraction gives opposite contribution
to the DIF value. The highest value of DIF is obtained in UHPC with 0.5% MF15
that is about 1.85 at around 200 s^{-1}. As discussed above, steel material is less sensi-
tive to the high strain rate loading, and UHPC material with higher dosage of steel
fiber can have less strength enhancement.

2.4.4 Conclusions

SHPB tests of newly developed UHPC materials are carried out. Test results are dis-
cussed and compared with static test results in this study. Influence of different fiber
reinforcements including MF and TF as well as fiber aspect ratio and fiber volume
fraction on the dynamic property of UHPC is investigated. The test results showed
the newly designed UHPC materials have outstanding mechanical performance and
ductility. The UHPC material with micro-fiber reinforcement generally gives better
dynamic strength when compared with the twisted fiber-reinforced UHPC specimen.
The increase of fiber length and aspect ratio has positive impact on the material
dynamic strength. Fiber volume fraction increase favors the UHPC material perfor-
mance. In the SHPC compression tests, the micro-fiber-reinforced UHPC is more
sensitive to the strain rate, whereas in the SHPB tensile test, twisted fiber−reinforced
UHPC has higher loading rate sensitivity. Comparing with NSC, UHPC material
developed in this study has relatively low sensitivity to the loading rate.

2.5 Meso-scale modeling of ultra-high performance concrete

2.5.1 Materials and single-fiber pull-out test

The material composition in this study is listed in Table 2.18, and high performance
steel fiber material used in this study has a diameter of 0.12 mm and a length of

t=0μs   t=155μs   t=310μs   t=465μs

2.5% MF15

t=0μs   t=155μs   t=310μs   t=465μs

2.5% MF06

t=0μs   t=155μs   t=310μs   t=465μs

2.5% TF03

t=0μs   t=155μs   t=310μs   t=465μs

2.5% TF05

t=0μs   t=155μs   t=310μs   t=465μs

1.0% MF15

t=0μs   t=155μs   t=310μs   t=465μs

0.5% MF15
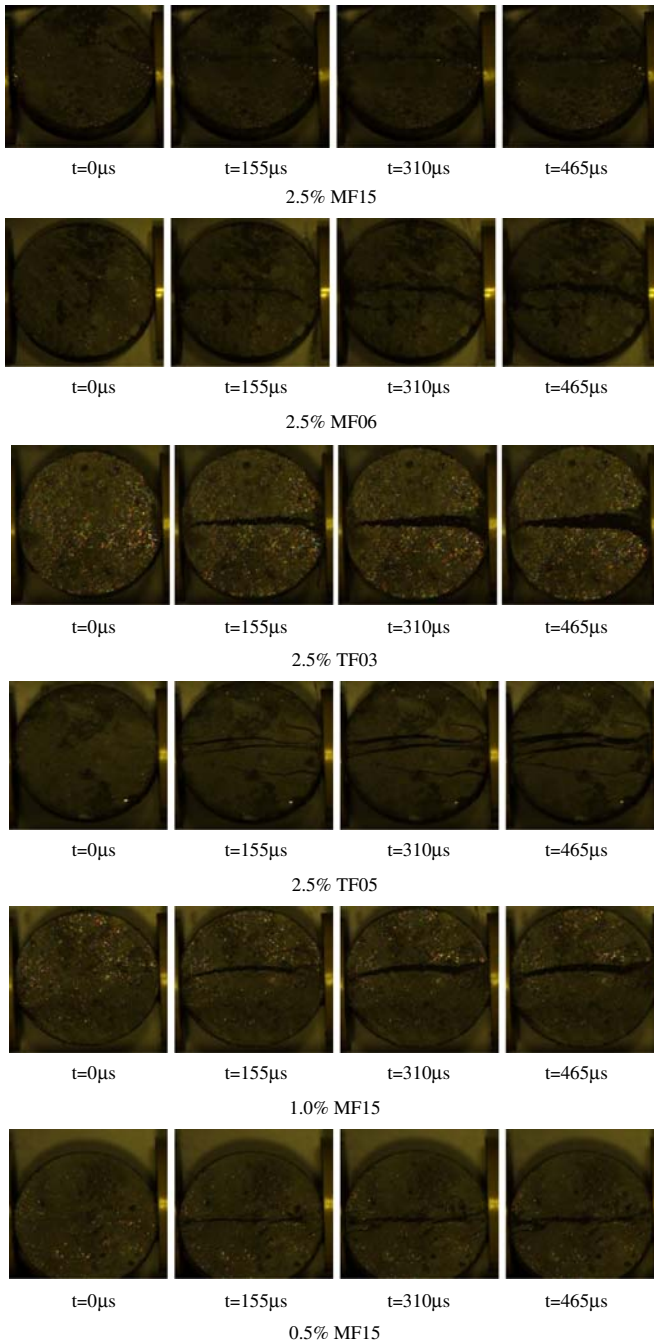
Figure 2.36 Damage modes of UHPC specimens under SHPB tension test.
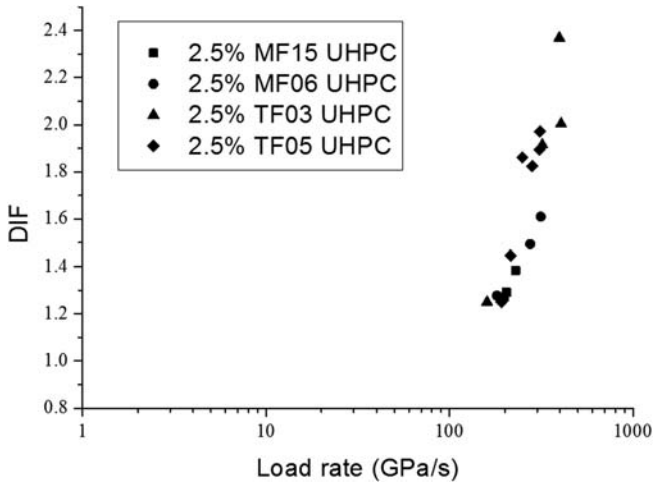
Figure 2.37 DIF of UHPC with different types of fibers in SHPB tests.
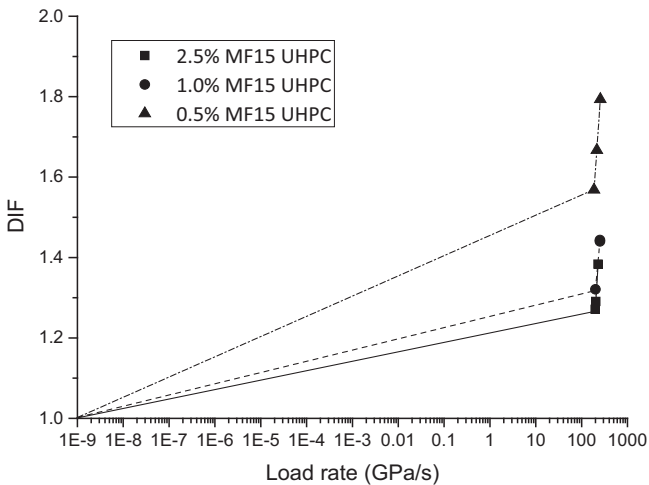
Figure 2.38 DIF influenced by the volume of MF15 in split tension SHPB tests.

15 mm with its yielding strength of 4200 MPa. Fiber volume fraction of 2.5 Vol% is considered a weight dosage of 2.5% NC is made in this study.

2.5.1.1   Single-fiber pull-out test

The primary reason behind the addition of fiber material into the concrete matrix is to delay and confine the crack. Although inclusion of fiber material is believed to enhance the concrete precracking strength, the effect of fiber addition becomes

Table 2.18 **Mix proportions of different UHPC formula (unit)**

Constituents	Proportions
52.5 Cement	750
Silica Fume	225
Silica Flour	190
Sand	1030
Superplasticizer	16
Water	190
Water/Cement	25.30%
Steel Fiber	2.5 Vol%
NC	63.1 (2.5 wt.%)
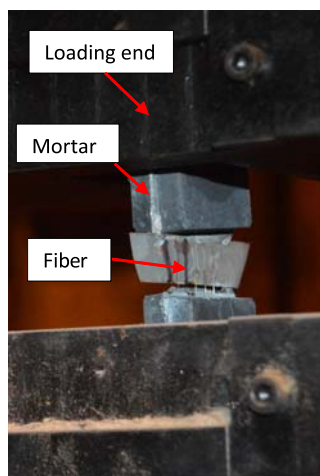
Figure 2.39 Setup of fiber pull-out test.

more prominent only after the crack initiates. Fibers bridge over the cracked parts, delaying the sudden failure of brittle concrete matrix. The fiber bridging effect is primarily related to the interfacial bonding strength which governs the postcracking material performance under external pull-out loads. It is therefore critical to understand the fiber pull-out behavior.

In this study, to obtain the interfacial bond properties between fibers and matrix, a series of fiber pull-out tests are conducted. As shown in Fig. 2.39, five embedding lengths, i.e., 20, 30, 40, 50, and 60 mm, are considered. In the test, displacement control is adopted with a constant loading speed of 1 mm/min. Test stops when the fiber is pulled-out or fractured. The fiber lengths after pull-out and fracture are measured.
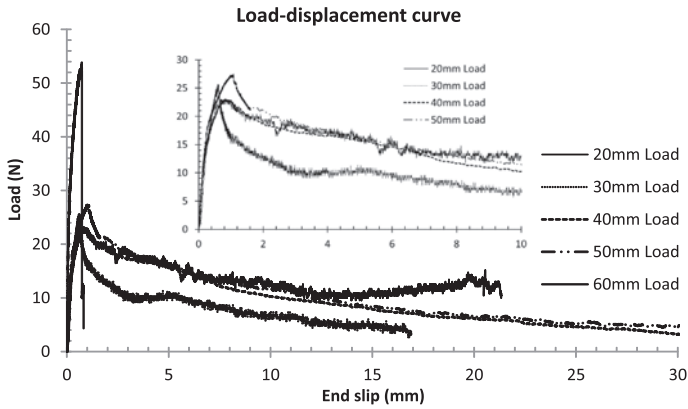
Figure 2.40 Load vs end-slip curves for different fiber embedding depths.
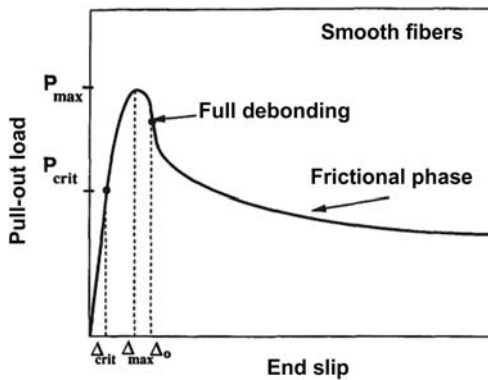
Figure 2.41 General fiber pull-out load vs. end slip curve.

Test results reveal that with the increase of fiber embedding length, the failure mode alters from fiber pull-out to fiber fracture. Fig. 2.40 shows the load vs slip curve for the given five fibers, and it is clear the peak load increases with the embedding length, however at a cost of post-peak ductility. When the embedding length is 60 mm, the peak load reached 54 kN while the peak load is only 22 kN for fiber with embedding length of 30 mm. The descending portion of the curve is rather steep for 60 mm embedding length indicating the fiber fracture.

For a smooth fiber with round cross-section, the whole process of fiber pull-out contains three stages as shown in Fig. 2.41. At the initial stage, the fiber−matrix interface remains intact and the corresponding segment of the curve is almost linear; when the external force reaches a critical value, an interfacial crack is initiated at the point where the fiber penetrates the matrix and starts propagating along the interface. In this stage, interfacial frictional force in the debonded zone is working

together with the adhesive force in the intact zone to resist the external force. With further increase of the external load, the frictional force increases proportionally in the debonded area, while the adhesive force in the intact zone progressively decreases. The force reaches its maximum when the embedded part of the fiber becomes too short. Full debonding occurs after the maximum force is reached. The force in the remaining segment is purely because of the frictional force between the fiber and matrix. It was found that this segment gradually deceases as the fiber is being pulled out from the matrix, but in microbond test in which the fiber−matrix contact area remains constant after the fully debonding, the recorded force is also constant.

Mathematical derivation of straight fiber pull-out from the matrix has been formulated by Naaman et al. [65]. Prior to end slip reaches a critical value of Δ_{crit}, the embedded fiber segment sticks with the surrounding matrix without any relative displacement. Within this stage, the pull-out load can be expressed as:

$$P = \Delta \frac{\lambda A_m E_m}{Q - 2} \frac{1 + e^{-\lambda l}}{1 - e^{-\lambda l}} \quad (\Delta \leq \Delta_{\text{crit}}) \tag{2.16}$$

where $Q = 1 + \frac{A_m E_m}{A_f E_f}$, A_f and E_f are the area and elastic modulus of the fiber, respectively, A_m and E_m are the area and elastic modulus of the matrix, respectively, $\lambda = \sqrt{KQ}$ in which $K = \kappa \psi / A_m E_m$ and κ is the bond modulus, ψ is the perimeter of the fiber, and l is the fiber embedded length.

It can be noted from the above equation that there is a linear relationship between the applied force and the displacement of the fiber-free end.

For debonding stage between $\Delta_{\text{crit}} \leq \Delta \leq \Delta_0$ and the fully debonded zone $\Delta \geq \Delta_0$, the theoretical solution of the pull-out load can be found in Naaman et al. [65].

2.5.2 Numerical study of single-fiber pull-out test and model validation

2.5.2.1 Material model

In the numerical simulation of the single-fiber pull-out tests, the matrix is modeled with a solid element and material model 72 Mat_CONCRETE_DAMAGE_Rel3 in LS-DYNA. This material model uses three shear failure surfaces and includes the damage and strain rate effects. This model provides model parameter generation capability that is based solely on unconfined compression strength of the concrete. The automatic generated model parameter can also be examined and modified by the user.

For the fiber material, Material model 98 Mat_SIMPLIFIED_JOHNSON_COOK is adopted, and fibers are modeled with truss element so as to avoid computational difficulties while maintaining reasonable accuracy.

Parameters used in the current numerical model are listed in Table 2.19.

Table 2.19 **Parameters used in numerical model**

Material	Model in LS_DYNA	Input parameter	Value
Mortar matrix	MAT_72R3	Density	2450 kg/m^3
		Unconfined compressive strength	140 MPa
		Poisson's ratio	0.19
Steel fibers	MAT_98	Density	7830 kg/m^3
		Young's modulus	210 GPa
		Poisson's ratio	0.28

2.5.2.2   Contact algorithm

It is worth noting that, in spite of the modeling efforts found in the literature [66], more advanced and comprehensive model is still required to predictively model the fiber−matrix bonding effect, including progressive interfacial debonding, unstable crack propagation, and post-debond frictional sliding. One such approach involves using tiebreak and cohesive zone models in the finite element analysis using commercial codes such as LS-DYNA. One viable material model offered in LS-DYNA for use with cohesive zone elements is *MAT_COHESIVE_MIXED_MODE, which is a bilinear mixed-mode traction separation constitutive law used to model interfacial failure [67]. However, this model requires establishment of solid element for the cohesive zone, which is impractical in this study considering the extremely small fiber diameter and large fiber number.

A feasible alternative contact modeling algorithm in LS-DYNA is Contact_1D. This one-dimensional contact algorithm, suitable for defining one-dimensional bonding and sliding mechanism between solid elements and truss elements in LS-DYNA, has been used to simulate the bonding, debonding, and sliding between the steel fiber and concrete matrix [32].

In this model, the slave node of a string of beam or truss elements, modeling the steel fiber, is forced to slide along a master line of nodes embedded in the solid mesh, which models the concrete matrix. This kinematic constraint is applied using a penalty function approach. Fictitious springs are inserted between slave nodes and their projections over the master lines. These springs produce internal forces along the rebar and are proportional to the distance between slave nodes and master lines, as shown in Fig. 2.42.

Considering the accumulative damage, the bond between fiber and concrete is represented in a two-phase constitutive model. In the elastic range, the bonding strength is linear proportional to the slip S. After reaching the maximum bonding strength τ_{max}, the bond shear stress will decay exponentially in the plastic range.

$$\tau = \begin{cases} G_s S, & S \leq S_{max} \\ \tau_{max} e^{-EXP \times D}, & S \leq S_{max} \end{cases} \tag{2.17}$$
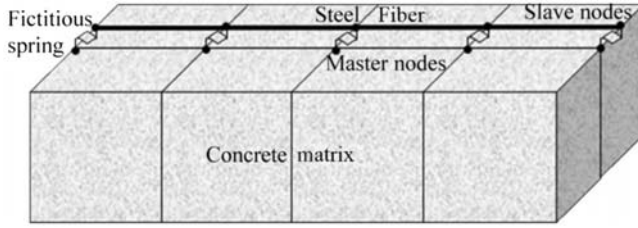
Figure 2.42 Fictitious spring between fiber and concrete matrix.
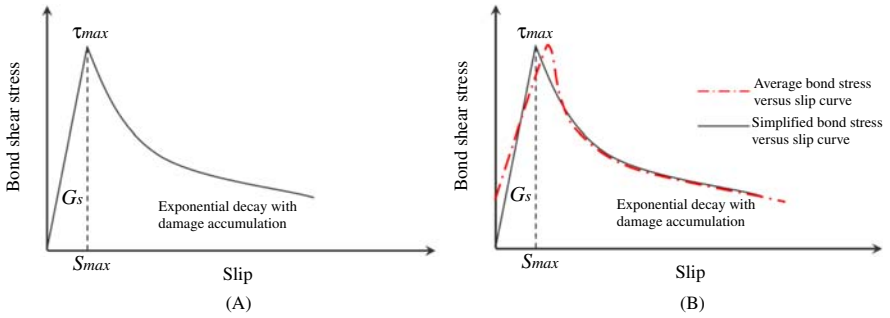
Figure 2.43 Bond shear stress−slip relationship for the one-dimensional slide line model. (A) Simplified bond stress-slip model; (B) Real bond stress-slip relation ship.

where G_s is bond shear modulus, *EXP* is the exponent in damage curve, and D is a damage parameter that is defined as the sum of the absolute values of the plastic displacement increments.

The shear force, acting on the bonding area A_s at step $n + 1$ is given as:

$$f_{n+1} = \min(f_n + G_s \times A_s \times \Delta S, \ G_s \times A_{s\times} \times S_{\max}) \tag{2.18}$$

Based on the above equations, the contact algorithm is defined as shown in Fig. 2.43A.

It is worth noting that this relationship is a simplified model for fiber−matrix interaction. In the real fiber pull-out test (as shown in Fig. 2.43B), there is no relative slip between concrete and steel fiber at the very beginning, and the stress transfer mechanism between them is represented by adhesion in this stage. In the simplified model, it is assumed that slip begins at the beginning of bond stress development. The shear modulus is assumed to be constant before reaching the peak bond stress $\tau_{\max}$. This assumption yields a less accurate model for the maximum elastic slippage but provides an accurate bond modulus. However, in the numerical simulation, the importance of the bond modulus overweighs the maximum elastic slip.

2.5.2.3 Contact parameters and modeling results

In this study, single-fiber pull-out tests were carried out, the relationship between the pull-out load and slip is now known for a given fiber, and the bond shear stress

Table 2.20 Parameters used in the contact definition

[a]CONTACT_1D				
ERR	SIGC	GB	SMAX	EXP
6E-5 m	1.4E8 Pa	2.393E9 Pa	1.25E-3	0.2

[a]*ERR* is the external radius of the fiber, *SIGC* is the compressive strength of the concrete.

vs slip curve can be theoretically obtained. Assuming that the curve is as described in Fig. 2.41 with the linear elastic ascending branch, followed by a deteriorating frictional zone, the whole curve can thus be described by three parameters: the bond modulus G_s, the bond strength τ_{max} or the slip S_{max}, and the decaying frictional parameter *EXP* describing the deteriorating frictional zone.

When determining the bond modulus, first of all, the slope of the linear ascending portion (P/Δ as shown in Eq. 2.16) of the pull-out curve is calculated graphically. The value of Q can be evaluated from the physical and mechanical properties of the fiber and the matrix. Only a fraction of the matrix cross-sectional area is effective if the proportion of the specimen's cross-sectional area to that of the fiber is relatively large; therefore, the area of the effective matrix requires evaluation. As pointed by Naaman et al. [65], the solution is not very sensitive to the value of A_m. Once Q and the slope are known, λ in Eq. 2.16 can be solved. Having found λ, the bonding modules can now be solved as

$$\kappa(\text{or } G_s) = A_m E_m K / \psi \tag{2.19}$$

The slip S_{max} can be approximately read graphically from the pull-out vs slip curve. The damage curve exponential coefficient *EXP* can be derived through the least squares fitting of the curve to the test data.

Previous study reveals that to prevent fiber fracture, the embedded length of fiber is limited by [68]:

$$L_e < \frac{\sigma_f D_f}{4\tau_{ult}} \tag{2.20}$$

where L_e is the maximum fiber embedded length, D_f is the fiber diameter, σ_f is the fiber tensile strength, and τ_{ult} is the interfacial shear strength, i.e., the IFSS.

Based on these experimental trails, the IFSS can be calculated as 2.1 MPa.

In this simulation, the parameter used in the contact algorithm for fiber with 20 mm embedding length is shown in Table 2.20.

The comparison between the simulation and the experimental results of 20-mm embedding length is shown in Fig. 2.44. It is seen that the simulation results coincide well with the experimental results, and the error in predicting the peak force is only 4%. The relatively accurate results indicate the effectiveness of the contact algorithm adopted in this study.
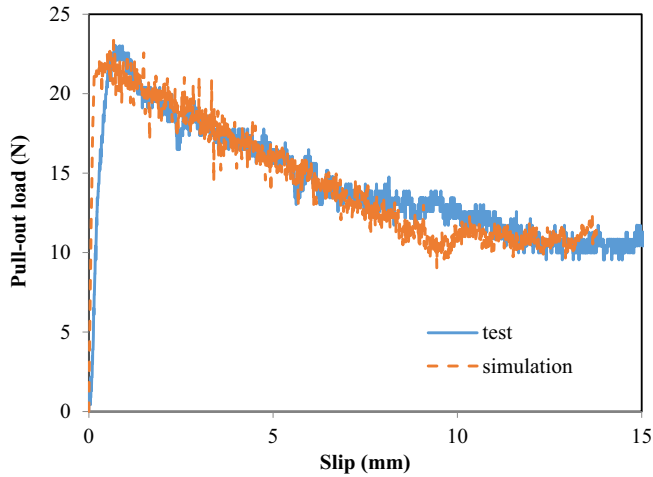
Figure 2.44 Comparison between test and simulation.

2.5.3 Static split tension test

After calibration with the experimental study, the bonding between the fiber materials with the base matrix is determined and simulated with contact algorithm, and in this section, static split tension test is numerically studied based on the 3D mesoscale model.

Static split tensile tests were conducted on cylindrical UHPC specimens with diameter of 75 mm and height of 37.5 mm as shown in Fig. 2.14.

In the numerical model, the steel fiber is assumed to be straight in the matrix with a predefined length L and diameter D, the total number of the fibers can be determined based on the fiber volume fraction and fiber dimension. The flow chart for the 3D mesoscale model establishment is shown in Fig. 2.45.

The established 3D mesoscale model contains 2,664,000 solid elements for concrete matrix and 291,342 truss elements for fiber phase, which are determined based on sensitivity analysis.

Comparison of the failure modes between the numerical model and experimental results is shown in Fig. 2.46, and reasonable accurate failure is predicted by the mesoscale model. It is clearly seen that the numerical model not only captures the cracking in the mortar matrix but also clearly demonstrates the bridging effect by the explicitly modeled steel fibers.

Comparing the splitting tensile stress displacement data as shown in Fig. 2.47, it is seen the simulation results collate well with the experimental study, and the peak stress from the simulation is around 22.5 MPa, while the average experimental result is around 20 MPa, and the error is 12.5%. The ascending and descending portion of the curves matches reasonably well.
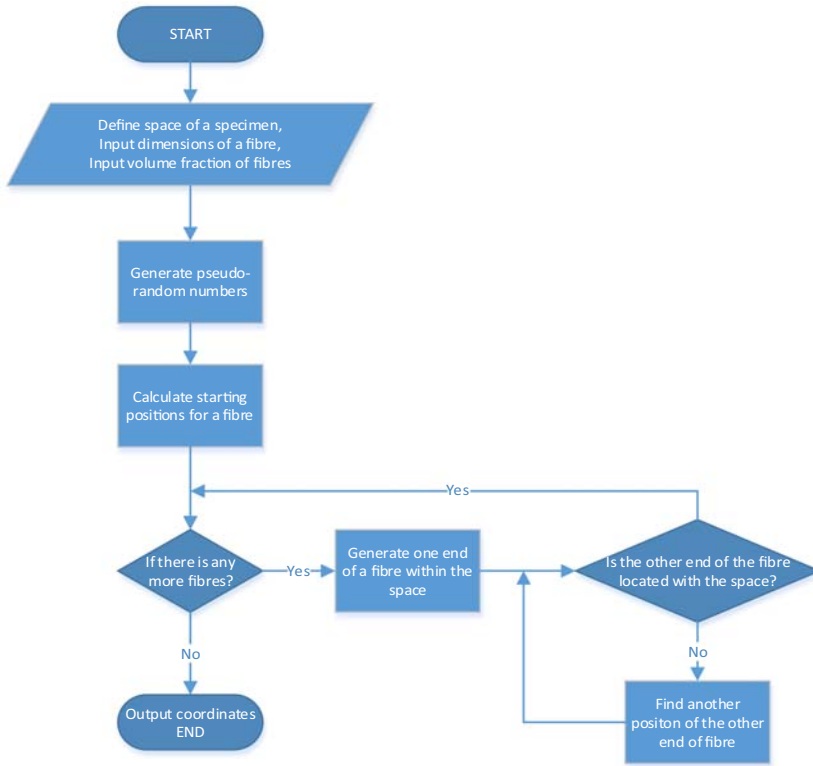
Figure 2.45 3D mesoscale model establishment.
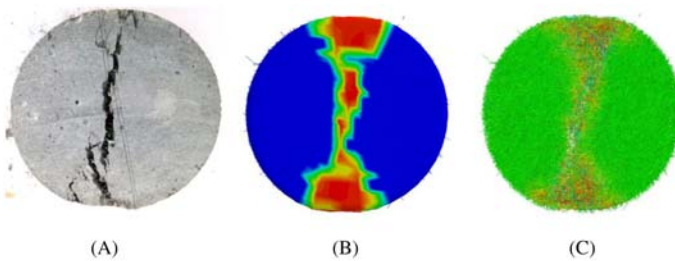
Figure 2.46 Comparison of the damage mode. (A) Test. (B) Damage in mortar. (C) Axial force in fibers.

2.5.4   Split Hokinson tension test

Concrete material is strain-rate sensitive, and the reason behind is ambiguous. Ross et al. [54] pointed out that the limiting crack velocity under increased strain rate would lead to an increase in ultimate strength and deformation capacity. Toutlemonde and Rossi [69] attributed the strength gain to an intrinsic viscous stress
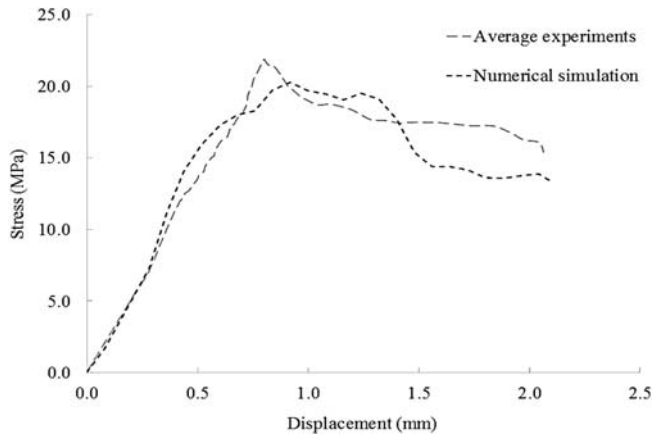
Figure 2.47 Split stress−displacement curve.

related to free-water movement within the nanopores instead of the coarser pores initially related to the water-cement ratio of the cement paste. Suaris and Shah [70] correlated the strain-rate effects on the mechanical behavior of concrete with the microcracking process and proposed an approach using a continuous damage concept. The strain-rate dependence of tensile microcrack growth has also been used by Bischoff and Perry [71] to explain the higher strength and compressive strain observed at high strain rates.

2.5.4.1 SHPB test setup

In this study, the dynamic tests were conducted on SHPB test specimens with 75 mm diameter and 37.5 mm height. The experimental systems of SHPB compressive and split tensile tests are sketched in Fig. 2.17B. SHPB split tensile test can generate a tensile stress within the specimen by far-end compression, which is easy and convenient in instrumentation.

When the striker impacts the incident bar, a one-dimensional compressive stress wave is generated. The stress wave (incident wave) propagates along the incident bar towards the specimen. When it reaches the interface between the incident bar and the specimen, the incident wave splits into two smaller waves. One of them, the transmitted wave, travels through the specimen and into the transmitted bar, causing plastic deformation in the specimen. The other wave, called the reflected wave, is reflected away from the specimen and travels back down the incident bar. Strain gages are then placed on the bars to measure strains caused by the waves. Assuming deformation in the specimen is uniform, the stress and strain can be calculated from the amplitudes of the incident, transmitted, and reflected waves.

The SHPB split tension setup is shown in Fig. 2.3. Both pressure bars in SHPB split tension tests have the same dimension of Ø75 mm and length of 2000 mm and the absorption bar is Ø75 mm and length of 500 mm. Strain gauges are attached at

the centers of the pressure bars. The bars are made of stainless steel with Young's modulus 210 GPa, density 7830 kg/m^3, elastic wave velocity 5547 m/s, and Poisson's ratio 0.3.

2.5.4.2 Numerical study

From the SHPB test, the typical stress−time relationship of UHPC from SHPB split tension test can be obtained.

Previous study had revealed the material dynamic performance of this advanced UHPC material, and influence of nanoparticles and steel fibers are discussed extensively [18,72]. In this study, the focus is numerical simulation of the SHPB split tensile test based on 3D mesoscale model. The numerical model consists of incident pressure bar, UHPC specimen, and transmitted pressure bar as shown in Fig. 2.8. The striker bar is not modeled. Instead, the incident dynamic stress generated by the impact of the striker bar is directly applied to the incident bar as a stress boundary. The steel pressure bars are modeled by MAT_RIGID, and the contact between the specimen and pressure bars is modeled by CONTACT_SURFACE_TO_SURFACE with default parameters in LS-DYNA (Fig. 2.48).

Adequate modeling of material under dynamic loads requires the information of strain rate effect, the DIF of NSC under tensile loads that are obtained from formulae proposed by Malvar and Crawford [49].

(A)

(B)   (C)
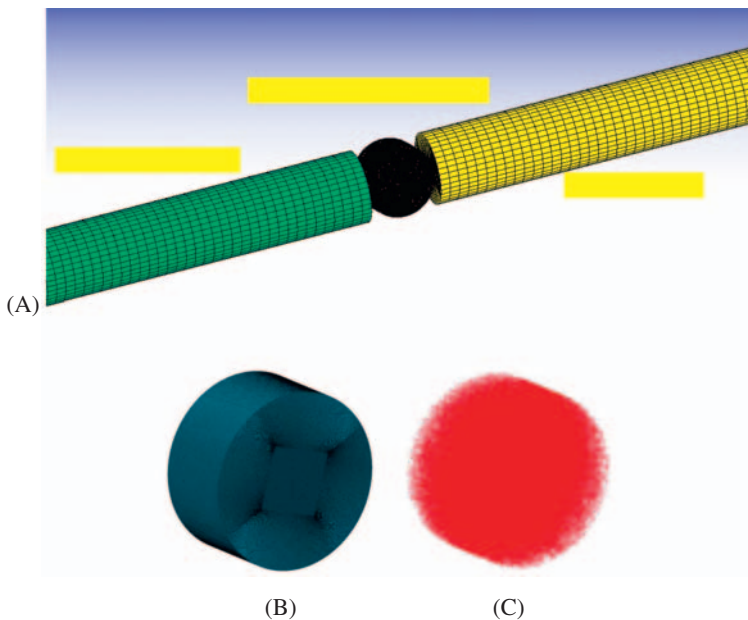
Figure 2.48 Finite element model of SHPB split tensile test. (A) 3D mesoscale UHPC sample. (B) Concrete matrix. (C) Embedded steel fibers.
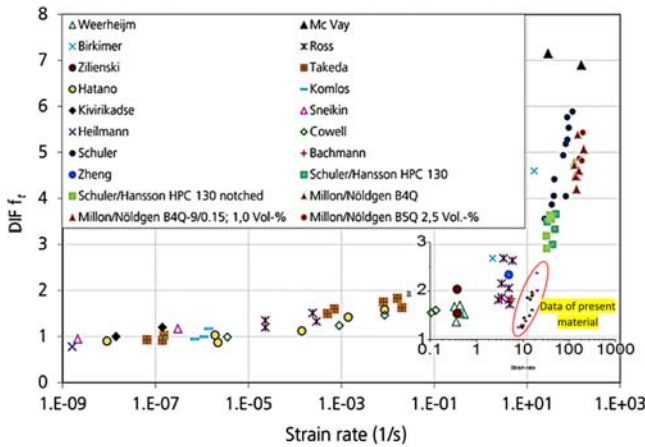
Figure 2.49 DIF for the tension strength of different concretes and UHPC in comparison.

Despite these well-established empirical equations for NSC, an analogous conclusion form normal concrete to UHPC is not adequate. With the alterations to the material composition, the failure mechanism changes, instead of progressive crack propagation and failure in NSC, fiber material in UHPC limits and confines the crack initiation and propagation that can significantly influence the inertia effect under high-rate loading condition. The low water−cement ratio in UHPC also warrants a much dense microstructure with less porosity (initial defects) and water content.

In the previous study conducted by the author, the rate effect is discussed through experimental study [18]. The results on material tensile strength, in combination with relevant study by other researchers, are presented in Fig. 2.49. The data points within the red circle are the results by the author. In general, with the increase of strain rate, the strength under tension loading also increases significantly. The increase is less pronounced with increasing concrete strength. It is clearly seen that the current material has lower strain rate effect than other concrete.

Material strain rate effect is less prominent under compressive loads, and this conclusion applies to UHPC as well [18]. In this study, the strain rate effect is considered for concrete phase only in 3D mesoscale model. The strain rate effect on the steel phase is neglected, although steel is also rate-dependent material, its rate sensitivity is lower than concrete, and also decreasing with the increase of steel strength. In this study, steel fiber has an ultra-high tensile strength 4200 MPa, its rate sensitivity is therefore much less than the concrete phase, which can be neglected. In addition, the previous study reveals that there are no additional overproportional increase of DIF between the UHPC specimen with and without fibers [73,74].

To provide in-depth comparison, homogenized model without modeling the steel fibers is also considered in this study. Teng et al. [75] and Wang et al. [7] developed homogenized numerical model based on MAT_ELASTIC_PLASTIC_ HYDRODYNAMIC to simulate the UHPC members subjected to dynamic loads, and their simulation results showed high accuracy when comparing with the experimental
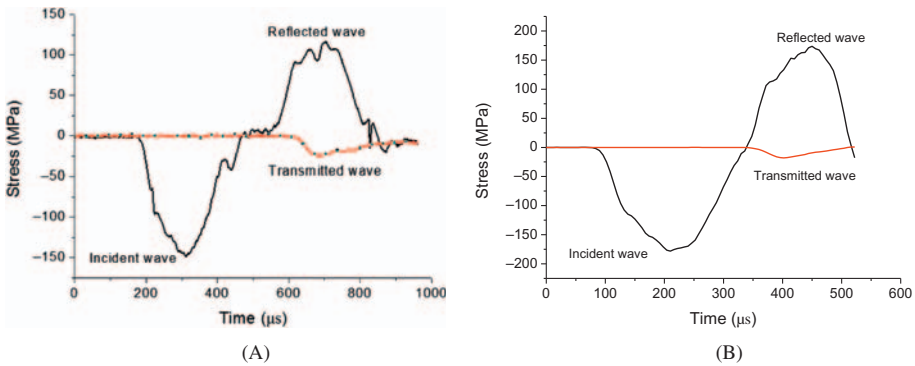
Figure 2.50 Comparison of stress histories from test and simulation. (A) Experiment. (B) 3D mesoscale model.
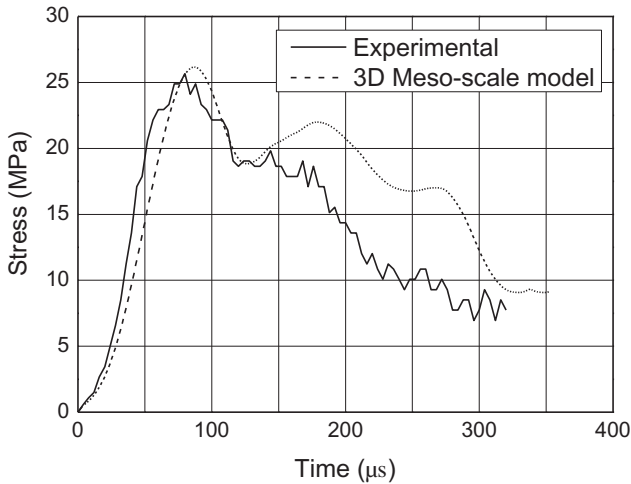
Figure 2.51 Comparison of stress−time curves obtained in the test and 3D mesoscale model.

observations. Similar procedures were also adopted when simulating blast-induced UHPC member response [26]. The parameter required for the material model is tabulated effective plastic stress vs effective plastic strain curve that can be straightforwardly obtained from uniaxial compressive tests.

In the tests, two strain gauges were attached on the incident pressure bar and transmitted pressure bar, and the measured stress histories under the applied impulse are shown in Fig. 2.50A. In the 3D mesoscale numerical simulation, stress histories of elements with the same locations as in the test are recorded for comparison, and the results are shown in Fig. 2.50B.

Fig. 2.51 shows the results of comparison between the 3D mesoscale simulation and test data. In this case study, the strain rate experienced in the

UHPC sample is 14.9/s. It can be noticed the stress−time history from the 3D mesoscale simulation coincides well with the laboratory test results, and both the peak value and softening behavior of the UHPC sample are in good agreement.

In the test, the high-speed camera photography was used to record the developing of crack of the UHPC specimen. The corresponding failure patterns from the test and 3D mesoscale numerical simulation are compared in Table 2.14. From the comparison of the failure patterns between testing results and simulation, it can be observed that under the same loading condition at the same time, the 3D mesoscale numerical simulation results yield good agreement with the test results in terms of the crack prediction. On the other hand, the homogenized model overpredicts the sample damage although it captures the crack initiation with reasonable accuracy.
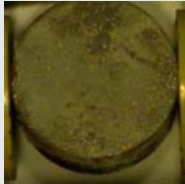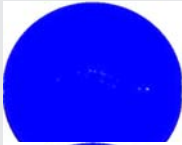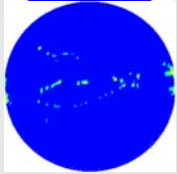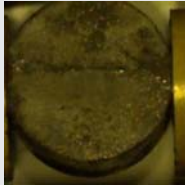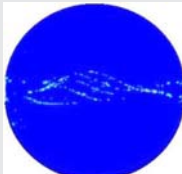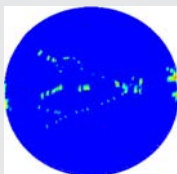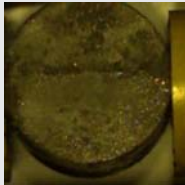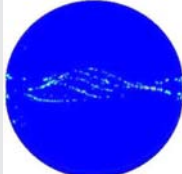
The fiber bridging effect can be interpreted by relating the crack propagation with the stress−time history curve as shown in Table 2.21. With wave propagation in the sample, damage accumulates and crack initiates in middle of the sample and the crack direction is parallel to the wave propagation direction. At time around 75 μs, major crack appears and there is a loss of the dynamic tensile stress, soon after that the stress increases again due to fibers bridging over the cracked parts and provide additional resistance. The fiber bridging effect prevails until the major crack reaches the sample edge at around 155 μs, and in the following stage, fiber bond-slip behavior dominates the sample resistance. As discussed in the previous sections, after full debonding occurs, pure fictitious load acts on the interface between the fiber and concrete matrix, and this fictitious load deteriorates almost exponentially with the slip.

Closer observation on the behaviors of embedded fiber is shown in Table 2.22. The contours in the table are axial stress within the fiber material, and it is noted at the very beginning when microcracks develop in the concrete matrix, there is no axial stress in the fibers; with the expanding of the microcrack, fiber axial load increases until the maximum pull-out load is reached at $T = 155$ μs. With explicitly modeled fiber material, the strain evolution during the dynamic loads can be clearly viewed and analyzed. The relatively accurate numerical results are promising, further study with the validated 3D mesoscale model can help ease the effort experiments that are costly and time-consuming.

2.5.5 Conclusion
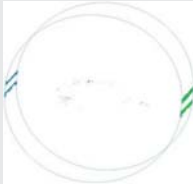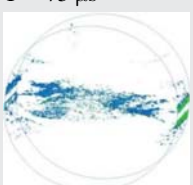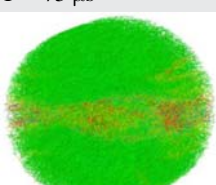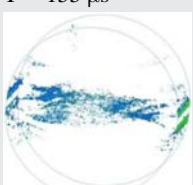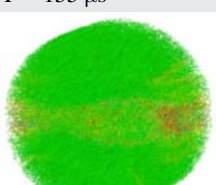
In this study, 3D numerical model, considering the random distribution of steel fibers, has been proposed to investigate the behavior of UHPC material under both static and intense dynamic loading. Random fiber distribution and orientation is considered in the model development. Fiber interaction with the concrete matrix is studied through single-fiber pull-out tests, and the results are used to establish the one dimensional bond-slip contact algorithm in the 3D model. Based on the proposed model, static split tensile test is simulated, and it is noted the proposed model

Table 2.21 Comparison of simulation results with high-speed camera observation

Test	Mesoscale model	Homogenized model
 T = 0 μs		
 T = 75 μs		
 T = 155 μs		
 T = 310 μs		

gives good prediction of material behavior under static load. In the simulation of the SHPB test, results from the proposed model correlate well with the experimental results, whereas the homogenized model without explicit modeling of steel fibers overpredicts the concrete damage. Compared with the frequently used homogeneous concrete model, the proposed 3D numerical model, considering the random distribution of steel fibers, could predict the responses of SFRC material subjected to intense dynamic loadings more realistically, especially in the postcracking phase. The dynamic stress−time history curve is interpreted with the aid of the proposed model, and the effect from fiber reinforcement can be clearly viewed in the 3D model.

Table 2.22 **Crack and axial force development in the numerical model**

Cracks in mortar	Axial force in fibers
T = 0 μs	T = 0 μs
T = 75 μs	T = 75 μs
T = 155 μs	T = 155 μs
T = 310 μs	T = 310 μs

References

[1] B. Daio, S. Hu, Y. Ye, S. Yang, Z. Liu, Mechanical behavior of ultra-high performance concrete reinforced with hybrid different shapes of steel fiber, in: CICTP 2012, pp. 3017−3028.

[2] S.H. Kim, G.S. Ryu, K.T. Koh, Flexural behavior characteristics of UHPC according to twisted steel fiber, Adv. Mat. Res. 652 (2013) 1499−1504.

[3] G.S. Ryu, S.H. Kim, G.H. Ahn, K.T. Koh, Evaluation of the direct tensile behavioral characteristics of UHPC using twisted steel fibers, Adv. Mat. Res. 602 (2013) 96−101.

[4] V. Bindiganavile, N. Banthia, Polymer and steel fiber-reinforced cementitious composites under impact loading? Part 1: bond-slip response, ACI Mat. J. 98 (2001).

[5] Z. Xu, H. Hao, H. Li, Experimental study of dynamic compressive properties of fibre reinforced concrete material with different fibres, Mater. Des. 33 (2012) 42−55.

[6] Ş. Yazıcı, G. İnan, V. Tabak, Effect of aspect ratio and volume fraction of steel fiber on the mechanical properties of SFRC, Constr. Build. Mater. 21 (2007) 1250−1253.

[7] Z.L. Wang, J. Wu, J.G. Wang, Experimental and numerical analysis on effect of fibre aspect ratio on mechanical properties of SRFC, Constr. Build. Mater. 24 (2010) 559−565.

[8] Y. Qing, Z. Zenan, K. Deyu, C. Rongshen, Influence of nano-SiO_2 addition on properties of hardened cement paste as compared with silica fume, Constr. Build. Mater. 21 (2007) 539−545.

[9] T. Ji, Preliminary study on the water permeability and microstructure of concrete incorporating nano-SiO_2, Cem. Concr. Res. 35 (2005) 1943−1947.

[10] B.-W. Jo, C.-H. Kim, G.-h. Tae, J.-B. Park, Characteristics of cement mortar with nano-SiO2 particles, Constr. Build. Mater. 21 (2007) 1351−1355.

[11] X. Liu, L. Chen, A. Liu, X. Wang, Effect of Nano-$CaCO_3$ on properties of cement paste, Energy Procedia 16 (Part B) (2012) 991−996.

[12] A. Nazari, S. Riahi, The effects of SiO_2 nanoparticles on physical and mechanical properties of high strength compacting concrete, Comp. Part B: Eng. 42 (2011) 570−578.

[13] A. Nazari, S. Riahi, The effects of zinc dioxide nanoparticles on flexural strength of self-compacting concrete, Comp. Part B: Eng. 42 (2011) 167−175.

[14] A. Nazari, S. Riahi, The effect of TiO_2 nanoparticles on water permeability and thermal and mechanical properties of high strength self-compacting concrete, Mater. Sci. Eng. A 528 (2010) 756−763.

[15] A. Nazari, S. Riahi, The effects of ZrO_2 nanoparticles on physical and mechanical properties of high strength self compacting concrete, Mater. Res. 13 (2010) 551−556.

[16] A. Nazari, S. Riahi, The effects of limewater on flexural strength and water permeability of Al_2O_3 nanoparticles binary blended concrete, J. Comp. Mater. 45 (2011) 1165−1172.

[17] A. Nazari, S. Riahi, The effects of ZnO_2 nanoparticles on split tensile strength of self-compacting concrete, J. Exp. Nanosci. 7 (2012) 491−512.

[18] Y. Su, J. Li, C. Wu, P. Wu, Z.-X. Li, Effects of steel fibres on dynamic strength of UHPC, Constr. Build. Mater. 114 (2016) 708−718.

[19] K. Holschemacher, T. Mueller, Y. Ribakov, Effect of steel fibres on mechanical properties of high-strength concrete, Mater. Des. 31 (2010) 2604−2615.

[20] R.S. Olivito, F.A. Zuccarello, An experimental study on the tensile strength of steel fiber reinforced concrete, Comp. Part B Eng. 41 (2010) 246−255.

[21] S.-T. Kang, J.-K. Kim, Investigation on the flexural behavior of UHPCC considering the effect of fiber orientation distribution, Constr. Build. Mater. 28 (2012) 57−65.

[22] S.J. Barnett, J.-F. Lataste, T. Parry, S.G. Millard, M.N. Soutsos, Assessment of fibre orientation in ultra high performance fibre reinforced concrete and its effect on flexural strength, Mater. Struct. 43 (2010) 1009−1023.

[23] L. Mao, S. Barnett, D. Begg, G. Schleyer, G. Wight, Numerical simulation of ultra high performance fibre reinforced concrete panel subjected to blast loading, Int. J. Impact. Eng. 64 (2014) 91−100.

[24] Z.L. Wang, L.P. Wu, J.G. Wang, A study of constitutive relation and dynamic failure for SFRC in compression, Constr. Build. Mater. 24 (2010) 1358−1363.

[25] J. Li, C. Wu, H. Hao, Investigation of ultra-high performance concrete slab and normal strength concrete slab under contact explosion, Eng. Struct. 102 (2015) 395−408.

[26] J. Li, C. Wu, H. Hao, An experimental and numerical study of reinforced ultra-high performance concrete slabs under blast loads, Mater. Des. 82 (2015) 64−76.

[27] J. Li, C. Wu, H. Hao, Residual loading capacity of ultra-high performance concrete columns after blast loads, Int. J. Protect. Struct. 6 (2015) 649−670.

[28] Z.L. Wang, H. Konietzky, R.Y. Huang, Elastic−plastic-hydrodynamic analysis of crater blasting in steel fiber reinforced concrete, Theor. Appl. Fract. Mech. 52 (2009) 111−116.

[29] X.Q. Zhou, H. Hao, Mesoscale modelling and analysis of damage and fragmentation of concrete slab under contact detonation, Int. J. Impact. Eng. 36 (2009) 1315−1326.

[30] Y. Lu, Z. Song, Z. Tu, Analysis of dynamic response of concrete using a mesoscale model incorporating 3D effects, Int. J. Protect. Struct. 1 (2010) 197−217.

[31] X. Wang, M. Zhang, A.P. Jivkov, Computational technology for analysis of 3D meso-structure effects on damage and failure of concrete, Int. J. Solid. Struct. 80 (2016) 310−333.

[32] Q. Fang, J. Zhang, Three-dimensional modelling of steel fiber reinforced concrete material under intense dynamic loading, Constr. Build. Mater. 44 (2013) 118−132.

[33] Z. Xu, H. Hao, H.N. Li, Mesoscale modelling of fibre reinforced concrete material under compressive impact loading, Constr. Build. Mater. 26 (2012) 274−288.

[34] J.E. Crawford, L.J. Malvar, K.B. Morrill, J.M. Ferritto, Composite retrofits to increase the blast resistance of reinforced concrete buildings, in: Symposium on Interaction of the Effects of Munitions with Structures, 2001.

[35] E. Ghafari, H. Costa, E. Júlio, A. Portugal, L. Durães, Optimization of UHPC by adding nanomaterials, in: Proceedings of the 3rd International Symposium on UHPC and Nanotechnology for High Performance Construction Materials, Kassel, Germany, 2012, pp. 71−78.

[36] H. Li, H.-g. Xiao, J. Yuan, J. Ou, Microstructure of cement mortar with nano-particles, Comp. Part B Eng. 35 (2004) 185−189.

[37] F. Sanchez, K. Sobolev, Nanotechnology in concrete—a review, Constr. Build. Mater. 24 (2010) 2060−2071.

[38] A. Neuberger, S. Peles, D. Rittel, Scaling the response of circular plates subjected to large and close-range spherical explosions. Part I: air-blast loading, Int. J. Impact. Eng. 34 (2007) 859−873.

[39] T. Rilem, 162-TDF. Test and design methods for steel fibre reinforced concrete, Mater. Struct. 35 (2002) 579−582.

[40] H. Stang, V.C. Li, Classification of fiber reinforced cementitious materials for structural applications, in: Proceedings of BEFIB, Varenna, Lake Como, Italy, September 2004, pp 197−218.

[41] J.L.A. de Oliveira e Sousa, R. Gettu, Determining the tensile stress-crack opening curve of concrete by inverse analysis, J. Eng. Mech. 132 (2006) 141−148.

[42] S. Qian, V.C. Li, Simplified inverse method for determining the tensile strain capacity of strain hardening cementitious composites, J. Adv. Concr. Tech. 5 (2007) 235−246.

[43] R. Walter, J.F. Olesen, Method for determination of tensile properties of engineered cementitious composites (ECC), in: Construction Materials: Proceedings of ConMat'05 and Mindess Symposium, Vancouver, The University of British Columbia, 2005, pp. 74

[44] Chinese standard GB/T 50081, (2002).

[45] Z.P. Bazant, Fracture mechanics of concrete structures. in: Proceedings of the First International Conference on Fracture Mechanics of Concrete Structures (FraMCoS1),

held at Beaver Run Resort, Breckenridge, Colorado, USA, 1−5 June 1992, Taylor & Francis, 1992.

[46] Chinese standard GB2419, (1981).

[47] S. Timoshenko, J.N. Goodier, Theory of Elasticity, 2nd Edition, McGraw-Hill book Company, 1951.

[48] C.E.-I.d. Béton, E.-I.C.f. Concrete, CEB., Concrete structures under impact and impulsive loading: synthesis report: contribution À la 26e Session Plénière Du C.E.B., Dubrovnik - Septembre 1988, CEB, Secrétariat Permanent, 1988.

[49] L.J. Malvar, J.E. Crawford, Dynamic increase factors for concrete, in, DTIC Document, 1998.

[50] D. Cusson, P. Paultre, High-strength concrete columns confined by rectangular ties, J. Struct. Eng. 120 (1994) 783−804.

[51] C. Roller, C. Mayrhofer, W. Riedel, K. Thoma, Residual load capacity of exposed and hardened concrete columns under explosion loads, Eng. Struct. 55 (2013) 66−72.

[52] H. Shin, Y. Yoon, S. Lee, W. Cook, D. Mitchell, Effect of steel fibers on the performance of ultrahigh-strength concrete columns, J. Mater. Civil Eng. 27 (2014). 04014142.

[53] T. Nicholas, Tensile testing of materials at high rates of strain, Exp. Mech. 21 (1981) 177−185.

[54] C.A. Ross, J.W. Tedesco, S.T. Kuennen, Effects of strain rate on concrete strength, ACI Mater. J. 92 (1995) 37−47.

[55] R. Chen, Y. Liu, X. Guo, K. Xia, F. Lu, Dynamic tensile properties of steel fiber reinforced concrete, in: T. Proulx (Ed.), Dynamic Behavior of Materials, Volume 1, Springer, New York, 2011, pp. 37−42.

[56] A.M. Weidner, Dynamic Properties of Concrete and Fiber Reinforced Concrete at Room and Elevated Temperatures, University of Utah, Utah, UT, 2013.

[57] J. Roncero, S. Valls, R. Gettu, Study of the influence of superplasticizers on the hydration of cement paste using nuclear magnetic resonance and X-ray diffraction techniques, Cem. Concr. Res. 32 (2002) 103−108.

[58] K.L. Scrivener, T. Füllmann, E. Gallucci, G. Walenta, E. Bermejo, Quantitative study of Portland cement hydration by X-ray diffraction/Rietveld analysis and independent methods, Cem. Concr. Res. 34 (2004) 1541−1547.

[59] M. Reda, N. Shrive, J. Gillott, Microstructural investigation of innovative UHPC, Cem. Concr. Res. 29 (1999) 323−329.

[60] F.H. Chung, Quantitative interpretation of X-ray diffraction patterns of mixtures. I. Matrix-flushing method for quantitative multicomponent analysis, J. Appl. Crystallogr. 7 (1974) 519−525.

[61] R.J. Detwiler, C.A. Fapohunda, J. Natale, Use of supplementary cementing materials to increase the resistance to chloride ion penetration of concretes cured at elevated temperatures, ACI Mater. J. 91 (1994).

[62] H. Fu, M. Erki, M. Seckin, Review of effects of loading rate on reinforced concrete, J. Struct. Eng. 117 (1991) 3660−3679.

[63] L.J. Malvar, Review of static and dynamic properties of steel reinforcing bars, ACI Mater. J. 95 (1998).

[64] C.A. Ross, D.M. Jerome, J.W. Tedesco, M.L. Hughes, Moisture and strain rate effects on concrete strength, ACI Mater. J. 93 (1996).

[65] A. Naaman, G. Namur, J. Alwan, H. Najm, Fiber pullout and bond slip. I: analytical study, J. Struct. Eng. 117 (1991) 2769−2790.

[66] Q.-S. Yang, Q.-H. Qin, X.-R. Peng, Size effects in the fiber pullout test, Comp. Struct. 61 (2003) 193−198.

[67] S. Sockalingam, G. Nilakantan, Fiber-matrix interface characterization through the microbond test, Int. J. Aeronaut. Space Sci. 13 (2012) 282−295.

[68] L. Yang, J.L. Thomason, Development and application of micromechanical techniques for characterising interfacial shear strength in fibre-thermoplastic composites, Polym. Test. 31 (2012) 895−903.

[69] F. Toutlemond, P. Rossi, Free water in concrete pores: an attempt of physical explanation of concrete dynamic behavior, Special Publication, 175 (1998) 261−280.

[70] W. Suaris, S.P. Shah, Constitutive model for dynamic loading of concrete, J. Struct. Eng. 111 (1985) 563−576.

[71] P. Bischoff, S. Perry, Compressive strain rate effects of concrete, MRS Proceedings, Cambridge University Press, 1985, p. 151.

[72] Y. Su, J. Li, C. Wu, P. Wu, Z.-X. Li, Influences of nano-particles on dynamic strength of ultra-high performance concrete, Comp. Part B Eng. 91 (2016) 595−609.

[73] T. Lok, P. Zhao, Impact response of steel fiber-reinforced concrete using a split Hopkinson pressure bar, J. Mater. Civil Eng. 16 (2004) 54−59.

[74] T. Lok, P. Zhao, G. Lu, Using the split Hopkinson pressure bar to investigate the dynamic behaviour of SFRC, Mag. Concr. Res. 55 (2003) 183−191.

[75] T.-L. Teng, Y.-A. Chu, F.-A. Chang, B.-C. Shen, D.-S. Cheng, Development and validation of numerical model of steel fiber reinforced concrete for high-velocity impact, Comput. Mater. Sci., 42 (2008) 90−99.

This page intentionally left blank

Ultra-high performance concrete slabs under blast loads

3

3.1 Introduction

Considerable research on the behavior of concrete slabs under blast loads has been conducted in recent years. Morales-Alonso et al. [1] conducted experiments that allow testing up to four concrete elements simultaneously under the same blast load. Twelve slabs of two different concrete types (normal strength concrete, NSC, and high strength concrete) were tested. A major conclusion from the close-in tests was that the ability of reinforced concrete (RC) structures of withstanding blast loads is primarily governed by their tensile strength. Thiagarajan et al. [2] studied behavior of high strength concrete (107 MPa) and NSC (27.6 MPa) slabs using the Blast Load Simulator, and it was observed that high strength concrete was very effective in reducing the level of response. In the close-in blast setup by Wang et al. [3], different damage levels and modes are observed by the detonations of 0.2−0.55 kg trinitrotoluene explosive located at a 0.4 m standoff above the slabs. An increase in the explosive charge was shown to gradually change the failure mode of RC slab from overall flexure failure to local punching failure.

Besides flexural and shear damage, concrete spall is another significant damage mode which is predominant in close-in or contact explosion scenarios. In such cases, blast imparts great amount of energy on the structure in the form of stress wave propagation. When the compression stress wave reaches the distal surface of the structural component, it will be reflected and then transformed into tensile stress wave. After superposition of the reflected and incident waves, if the net stress within the concrete material exceeds its dynamic tensile strength, spall damage happens [4−6]. Without evident structural deformation, spall damage reduces the cross-sectional area and thus reduces the element load-carrying capacity. Concrete spall also generates large amount of high speed flying fragments which impose threats to the personnel and equipment inside the structure.

Technical paper [7] details procedures for the collection, analysis, and interpretation of explosion-produced debris. It reports that a fragment with an impact kinetic energy of 79 J has a 31% probability of being lethal while an impact kinetic energy of 103 J would generate more than 50% probability of fatality. Later study in ref. [8] gives more discussions about lethality criteria for debris generated from accidental explosions. Clearly, characterization of debris would enable improvement of current guidelines on safe standoff distances from building undergoing demolition or terrorism attack. Fragments velocity and mass distribution are therefore of vital importance when analyzing fragment hazards of structures. Under blast loading environment, the concrete fracture and fragmentation result from both impulsive loading by stress waves and explosive gas-driven fracture propagation [9].

Brinkman [10] studied the fragmentation and projectile throwing process of brittle concrete-like material and concluded that stress waves generated by the detonation of an explosive charge are responsible for the development of a damage zone in the concrete material and the subsequent fragment size distribution, while the explosion gases are important in the separation of a crack that has already been formed during the passage of the stress wave, and in the subsequent launch of the fragments. Regarding the fragments mass and size distribution, a well-known analytical model of dynamic fragmentation [4] based on energetic criterion has found an extensive use in describing experimental data in a variety of solid materials. Wu et al. [11] carried out a sieve analysis to investigate the fragments size distributions from the concrete specimens under close-in detonations. It was found that the fragment size followed both a Weibull distribution and a Rosin−Rammler−Sperling−Bennet distribution.

Research on concrete spallation under blast environment had been carried out in the past several decades and mainly focused on RC slabs and/or pavements. Back to the 1970s, Kot et al. [12,13] proposed theoretical prediction methods for spall damage of concrete wall; however, these methods were limited to light and moderate bomb threats and were based on several simplified assumptions which compromised the calculation accuracy. Later in the 1980s, a series of concrete spall tests from different sources were summarized by McVay [5], and parameters affecting concrete spall were investigated and these parameters included scaled standoff distance, explosive charge weight, wall thickness, concrete strength, concrete additives, and reinforcement spacing. Based on the test results, an empirical approach for determining if and where a stress wave would cause the concrete to crack in tension was derived. In this method, the changes in the stress caused by stress waves traveling at different velocities, wave attenuation, and dispersion were neglected. The only change in the stress wave propagation that was taken into consideration was wave divergence. Nash et al. [14] developed a numerical model to predict spall damage to concrete walls from close-in explosions in air for cased and uncased munitions. The model was used to develop guidelines for designing concrete walls to prevent spallation. Recently, Wang et al. [3] carried out close-in explosion tests on square RC slabs and spall damage at different severities was observed, and the experimental results were used to verify their numerical model. Leppänen [15] conducted experimental and numerical analyses to examine the extent to which the concrete, at various distances, is affected by the blast wave and fragment impacts. The results showed that the damage in the concrete, from the blast wave and fragment impacts, is localized in the impact zone. The concrete below this zone, at a depth of approximately twice the depth of the maximum penetration, was hardly affected at all by the blast wave and fragment impacts. Based on a large database of empirical slab/wall tests, AFRL-MN-EG-TR-1998-7032 *Concrete Hard Target Spall and Breach Model* [16] details the development of a spall/breaching algorithm for RC slabs and walls.

Recent decades have witnessed an increasing demand of structural protection under explosive loads, and tremendous efforts have been dedicated to the development of new concrete material or concrete retrofitting technology. Ohtsu et al. [17]

experimentally and analytically investigated the dynamic failure of fiber-reinforced concrete (FRC) slabs, and it was observed that the averaged diameters and the volumes of the spall failure remarkably decreased with the increase in the flexural toughness of FRC concrete. Ohkubo et al. [18] conducted contact explosion tests on concrete plates reinforced by carbon or aramid fiber sheet, and it was noted that local spall damage had been significantly reduced with fiber sheet reinforcement; fiber sheets also had prevented concrete plates from fragmentation. Recently, Foglar and Kovar [19] plotted their experimental results on these spall and breach prediction curves, and they concluded that the observed spall damages in RC specimens agree with the spall and breach prediction curves according to UFC 3-340-02. However, they also noted the spall and breach prediction curves according to UFC 3-340-02 are not suitable for predicting the spall damage in FRC. Moreover, the spall damage severity is not clearly defined in UFC guideline. Therefore it can only predict the occurrence of spall damage in the wall slab under a blast load, but cannot quantify the damage levels.

Different from a slab or wall in which only the reflection of the blast-induced stress wave from the back surface needs be considered, stress wave in a column generated from a close-in detonation can be reflected from both the back and side faces which makes it a three-dimensional (3D) shock propagation problem. In NCHRP Report 645 [20], test results from 11 concrete columns were compiled and used to evaluate the performance of several design parameters and to determine the capacity and failure limit states of concrete highway bridge columns. Wu et al. [21] carried out contact explosion test on steel−concrete composite column and developed numerical model reproducing the spall damage. Based on extensive parametric study, Wu et al. [22] investigated the relationship between residual axial capacity and structural and loading parameters such as material strength, column detail, and blast conditions. In a recent study, Li and Hao [23] developed 3D numerical models to predict the concrete column spalling under blast loads. Intensive numerical simulations are carried out to investigate the influences of the column dimensions and reinforcement mesh on concrete spall damage.

Until now, there is limited systematic investigation on the performance of UHPC material under both static and blast loading condition. In Section 3.2, in-depth knowledge is obtained through a series of experimental tests ranging from contact detonation to close-in detonation on commercialized UHPC Ductal.

In Section 3.3, investigation is carried out on the new UHPC material that is discussed in Chapter 2, Development, testing, and numerical simulation of ultra-high performance concrete at material level. To investigate the concrete spall damage, especially the spall phenomena of ultra-high performance concrete (UHPC), contact explosion tests were carried out on seven slabs. In the seven slabs, two slabs were constructed with conventional concrete and the other five slabs were made of UHPC with different slab depths and longitudinal reinforcement spacing. The spall areas and crater areas are quantitatively analyzed and compared. Feasibility of utilizing existing theoretical and empirical methods predicting concrete spallation under blast loads is discussed. Furthermore, the fragments from each single test were collected for a sieve analysis, and the results are used for predicting fragments size distribution.

Although the merits of UHPC in protective designs have been well recognized and evidenced in the experimental and numerical tests shown earlier, when designing high-performance concrete component, high strength steel reinforcement is normally required due to higher concrete compressive strength and strain, and this inevitably increases the material cost. However, esthetic demand in modern society leads to increasingly more designs with thin cross-section and irregular curved structural shapes that limit the usage of conventional steel reinforcement. As an alternative, steel wire mesh (SWM) has been used in concrete members for strengthening and rehabilitation purpose over the past several decades. Comparing with conventional reinforcement, SWM can be easily adapted into different structural designs and maximize the workability of self-compacting concrete. In previous experimental studies, enhanced concrete compressive strength and failure strain were obtained after applying SWM reinforcement jacket to existing structures [24,25]. Regarding the performance of structural component with SWM reinforcement, El Debs and Naaman [26] studied bending behavior of mortar reinforced with steel meshes and polymeric fibers, and they concluded that this combination can satisfy the ultimate strength limit state through the steel mesh reinforcement (main reinforcement) and control cracking under service loads through fiber reinforcement (secondary reinforcement). It was noted that concrete with SWM reinforcement developed localized membrane effect when subjected to impact load and showed good scabbing resistance. Shear strength and energy absorption capacity of concrete slabs increased with the SWM reinforcement, and slab failure model altered from punching shear to flexure under dynamic impact loads [27]. Although SWM reinforcement technology showed good potentials in structural engineering, the study of utilizing it against blast load is quite limited in the open literature.

In Section 3.4, two blast-resistance slab designs, i.e., steel fiber-reinforced concrete (SFRC) slab and hybrid SWM and steel fiber (SWM-SF) RC slab are considered. Static tests were carried out in the laboratory to obtain the mechanical performance of concrete with different fiber additions. Beam samples with hybrid SWM-SF reinforcement were tested in static flexure to investigate the tensile performance and energy absorption capacity of this reinforcing scheme. In the field blast tests, behaviors of concrete slabs were experimentally investigated in close-in blast scenarios. Discussions about the performance and damage mechanism of these slabs are presented after the test results description. Numerical study based on multimaterial arbitrary Lagrangian−Eulerian (MMALE)−Lagrangian algorithm is also carried out to further investigate the blast effect and slab response in the field tests.

Previous studies found that contact detonation created large perforation damage of concrete slabs made of normal and high strength concrete even with strong reinforcements. To prevent perforation damage and to increase the capability of concrete slab to resist contact detonation, as shown in Section 3.5, SWM is proposed as additional reinforcements to concrete slab to resist blast loads. In the matrix formed by high strength self-compacting concrete, SWMs as well as the conventional steel reinforcement are embedded and serve as reinforcement. At the concrete cover layers, to improve the tensile crack resistance under both service load and dynamic load, microsteel fibers are mixed into the concrete matrix. Numerical

model based on a combined finite element (FE) and smoothed particle hydrodynamics (SPH) method is developed, and the contact detonation and fragmentation process are modeled. In the field test, contact explosion on the slab is carried out and the detonation and fragmentation process are captured by the high speed camera. Through image processing, the fragment velocities are identified, and the results are compared with the numerical predictions.

Until now, steel fiber is one of the most widely used fiber materials to enhance the concrete performance; however, just like conventional steel reinforcement, steel fibers are highly corrosive in nature which possibly leads to structural corrosion failure. A solution to this problem lies in the alternatives to traditional steel material. Since the 1970s, extensive research was carried out and many alternative fiber materials including glass fibers and synthetic fibers were developed. Among all fiber materials, those used for ballistic applications are typically carbon fiber, Kevlar (aramid fiber) and more recently the ultra-high molecular weight polyethylene (UHMWPE) fiber. Different to the conventional polyethylene fiber, low specific weight UHMWPE fibers possess extraordinary mechanical properties such as high modulus, high strength, high impact resistance, high cut, and abrasion tolerance. In the late 1970s, UHMWPE fibers were commercialized by DSM Dyneema, NL under the trade name Dyneema and more recently by Honeywell in the United States under the name Spectra.

Since the day of invention, one of the major interests in the application of UHMWPE fiber is in defense protection, and this material is found to be extensively used in the armor protection. Xu and Farris [28] developed matrix-free UHMWPE fiber-reinforced composite, and ballistic tests were carried out to investigate the composite under projectiles impact with different velocities. Test results reveal that UHMWPE composites performed better than Kelvar. Karthikeyan et al. [29] measured quasistatic and dynamic responses of laminated beams made from monolithic carbon fiber-reinforced polymer (CFRP) and UHMWPE. They observed that under quasistatic tests, UHMWPE beams had larger load-carrying capacity than CFRP beam, and similar observation was made under low velocity impacts. Karthikeyan et al. [30] also investigated the ballistic response of laminated composite plates made of 304 stainless steel, CFRP and UHMWPE. They found that on an equal areal mass basis, the UHMWPE plates had the highest ballistic limit. Mohagheghian et al. [31] experimentally studied the perforation of UHMWPE plate and the results were compared with those slabs cast with low-density polyethylene and high density polyethylene, and they noted that UHMWPE plates showed better perforation resistance under both quasistatic indentation and impact loading, and they ascribed such performance to UHMWPE's high strain hardening which delays the onset of localization. Russel et al. [32] developed test protocols for the tensile testing of laminates, yarns, and fibers made from UHMWPE, and had elucidated the relationship between the tensile properties of the laminate, yarn, and fiber for Dyneema SK76 over a wide range of strain rate.

Despite many researches on the UHMWPE laminate under static and dynamic loads, little work can be found in the open literature concerning the UHMWPE fiber mixed with concrete matrix. As reported by Xu and Farris [28], because of

chemical inertness and a lack of functional groups, UHMWPE fibers are difficult to bond to most materials, which makes it difficult to produce UHMWPE fiber-reinforced polymer (FRP) matrix composites. Several fiber pretreatments exist and they are proven to improve the bonding strength of UHMWPE fibers to matrix, however after treatment, fiber properties generally deteriorate. Among the quite few researches, Zhang et al. carried out experimental [33] and numerical [34] investigations on the projectile penetration into UHMWPE FRC, and their results showed UHMWPE fiber is of excellent effects to improve the tension strength and toughness of concrete, and penetration depth and cratering area under bullet penetration are decreased significantly compared with plain concrete. Ranade et al. [35] studied multiscale mechanical performance of high strength−high ductility concrete, and in their experiment, UHMWPE was used to reinforce the concrete material. Yamaguchi et al. [36] investigated polyethylene FRC slab under contact detonations, and they observed the improved spall and cratering resistance on the slab with fiber reinforcement. However, the polyethylene fiber material they used is high molecular weight polyethylene fiber not UHMWPE. Until now, in the open literature, no information was found on the blast resistance of UHMWPE RC.

In Section 3.6, UHMWPE fiber material is mixed into high strength concrete matrix, and static uniaxial compressive tests and third-point flexural bending tests are carried out to achieve the static mechanical properties of the RC material. As a comparison, plain concrete and hybrid steel fiber−UHMWPE FRC are also investigated. Field blast tests are carried out to investigate the blast resistance of concrete slabs made of above materials.

In Section 3.7, an advance moment rotation analysis model is incorporated into the finite difference (FD) procedure for the dynamic response analysis of reinforced UHPC slabs under blast loads. The accuracy of the FD analysis model which utilized the moment rotation analysis technique is validated using results from blast tests conducted on UHPC slabs.

3.2 Commercial ultra-high performance concrete slabs under blast loads

3.2.1 Blast test program with close-in detonations

3.2.1.1 Test samples

The blast program was designed to investigate the performance of reinforced UHPC slabs under close-in blast loading conditions. Test samples include UHPC slabs with various reinforcing ratios and different types of reinforcing steel. One additional normal strength slab which had pressure transducers attached to the surface was tested to determine the pressure loading distribution. All the slabs were constructed by VSL in their Melbourne Laboratory. The type of UHPC used in construction was Ductal and was identical for all four UHPC slabs. The concrete mix composition for Ductal is presented in Table 3.1. It is worth noting that for UHPC,

Table 3.1 Ductal mix proportions

Constituent	Amount
Cement	680 kg m^{-3}
Silica fume	204 kg m^{-3}
Silica flour	204 kg m^{-3}
Sand	974 kg m^{-3}
Steel fibers	156 kg m^{-3}
Superplasticizer	44 l m^{-3}
Water	150 l m^{-3}
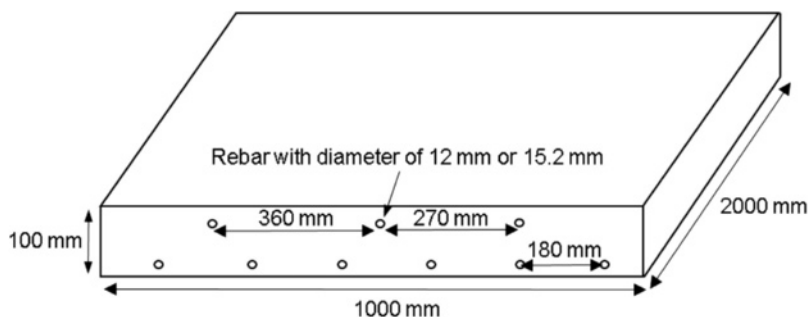
Figure 3.1 Slab dimension and reinforcement.

a normal steel fiber volume fraction ratio is between 2% and 6%, and this value is higher than high strength concrete discussed in the previous study. High strength concrete uses gravel as coarse aggregates; therefore the amount of steel fibers can be added is limited. UHPC (or reactive powder concrete) has no coarse aggregates. Instead, the ultrafine silica fume is added providing prominent pozzolanic effect and filling effect which can significantly improve material strength. Because there is no coarse aggregate, relatively high percentage of steel fibers can be added in UHPC. In this study, 2% volume fraction was adopted to balance the steel consumption and material performance. In the tests, both the NSC and UHPC slabs were erected vertically as 2000 mm × 2000 mm × 100 mm slabs and were later cut in half to generate two 2000 mm × 1000 mm × 100 mm slabs. The cross-section and reinforcement of the slabs are shown in Fig. 3.1. In all slabs, no stirrup rebars were used.

To determine the material properties like Young's modulus, Poisson's ratio, compressive strength, and the stress−strain relationship of the concrete, cylinder tests were carried out for both the NSC and UHPC conforming to Australian Standard 1012.17-1997. All concrete cylinders had a height of 200 mm and a diameter of 100 mm. Material parameters were obtained by attaching four strain gauges symmetrically about the mid-height of each cylinder, two longitudinally and two

transversely. The load was applied at a controlled rate of 15 MPa min^{-1}. Strain and the corresponding forces were recorded at constant intervals. In total, 10 NSC cylinders and 7 UHPC cylinders were tested and the results were averaged as shown in Table 3.2.

Fig. 3.2 shows the compressive stress−strain relationship for the UHPC material which is obtained from the above cylinder tests.

In the experiments, each of the four UHPC slabs was referenced with a unique identifier beginning with "D," followed by a number from 1 to 4. For UHPC-D3 slab, it is designed for two explosives, thus its name is followed by an ending of "A" and "B" to identify the blast scenarios. The properties and design considerations of the five slabs are summarized in Table 3.3. It should be made clear that when reference is made to the reinforcing ratio, this includes only the tensile steel, and does not take into account the layer of reinforcing closest to the extreme compression fiber. The blast scenarios considered in this research are also given in Table 3.3. It is deemed that the UHPC slabs under these blast loads may display

Table 3.2 Concrete material properties

Specimen	Young's modulus (MPa)	Poisson's ratio	Ultimate strength (MPa)	Ultimate strain	Density (kg m^{-3})
NSC	49195	0.24	56.6	0.0014	2440.5
UHPC	51503	0.20	128.9	0.0025	2424.9
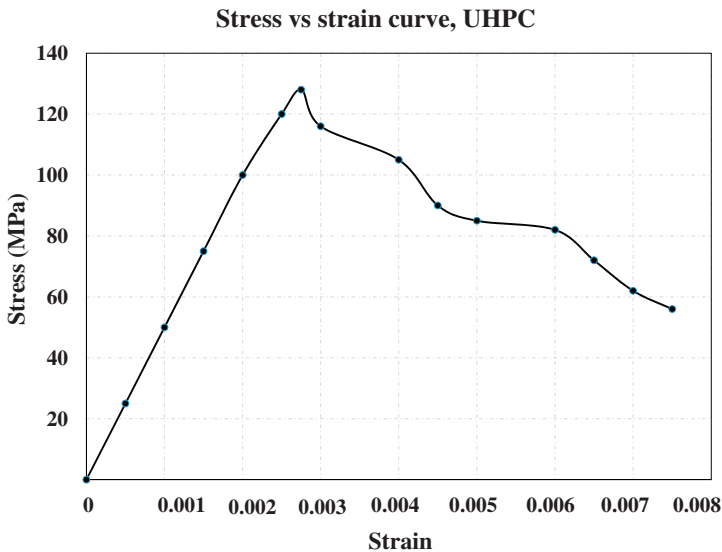
Figure 3.2 Stress−strain curve of UHPC material.
Averaged from a series of uniaxial tests.

Table 3.3 **Summary of test slabs and blast events**

Slab no.	Reinforcing ratio (%)	Steel type	Steel strength (MPa)	Charge weight (kg in TNT)	Scaled distance (m kg$^{-1/3}$)
UHPC-D1	0.8	Reo bar φ12 mm	600	14	0.41
UHPC-D2	1.4	High strength φ15.2 mm	1750	8	0.50
UHPC-D3A	0.8	Mild steel φ12 mm	300	1	3.05
UHPC-D3B	0.8	Mild steel φ12 mm	300	14	0.41
UHPC-D4	0.8	Mild steel φ12 mm	300	8	0.50
NSC-1	0.8	Reo bar φ12 mm	600	8	0.75

various response modes including elastic deformation, plastic deformation, and failure. In all the tests, the explosive used was Comp B. Comparing with TNT, Comp B has a relative effectiveness factor of 1.33. In the following study, the charge weights discussed are all TNT equivalents.

3.2.1.2 Testing system

The field blast testing system is shown in Fig. 3.3. The galvanized pipe frame was 5 m high and 3.7 m wide. The base plates were bolted to the concrete ground slab, and four cables were attached between the top of the frame and concrete blocks below to stabilize the frame. The two vertical members of the support frame were offset from the longitudinal axis of the concrete slab, and this was done to prevent damage to the frame caused by the highly directional blast acting along the same line as the longitudinal axis of the concrete slab. The explosive charge was suspended by a string over the slab at the specified height. Multiple guide strings were used when necessary to hold the charge in the correct location. One pressure sensor was erected to record the free air reflective pressure.

3.2.1.3 Data acquisition

Pressure transducers were used on all of the blast events to record the overpressure acting on the slab and in the free air. LVDTs were used to measure the vertical displacement at the center of the slab. The LVDTs had a stroke of up to 200 mm. All the LVDTs were attached to the bottom side of the slab using a Dynabolt and Plastibond. The sample rate for the LVDTs was 10,000 samples per second. For the pressure transducers, the sample rate was 2,000,000 samples per second.

Fig. 3.4 shows the sketch of the data acquisition system on the slab.
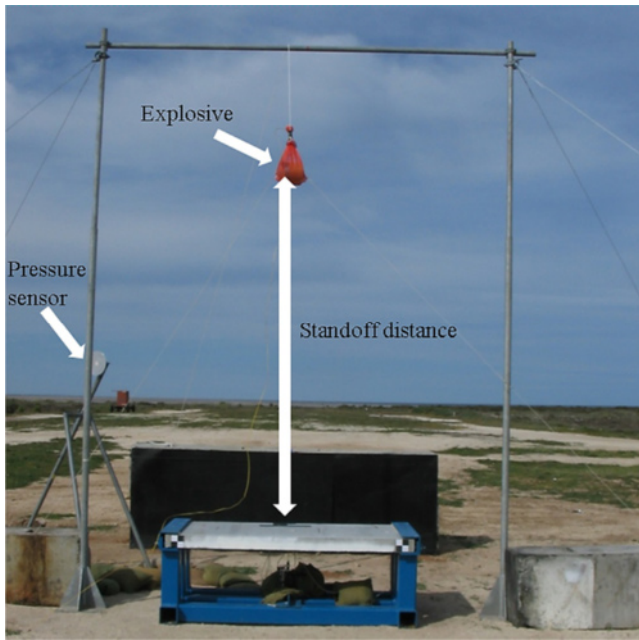
Figure 3.3 Testing system.
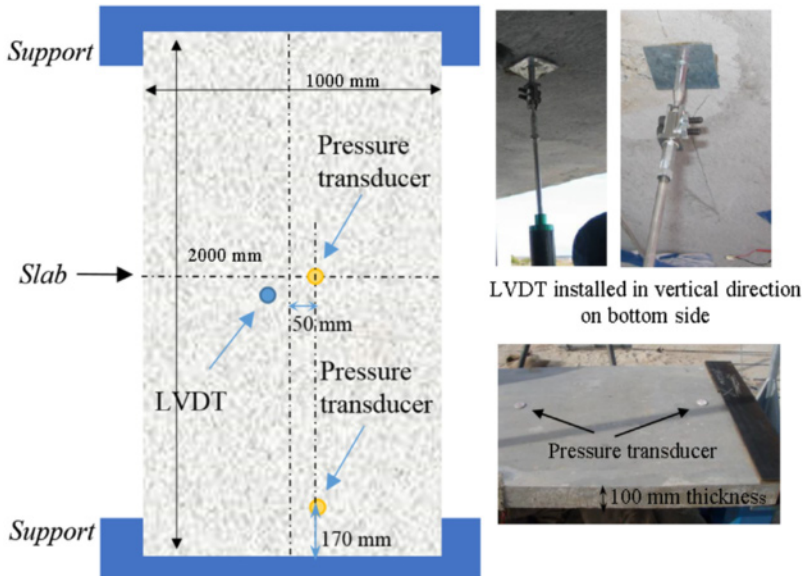
Figure 3.4 Data acquisition system.

3.2.1.4 Experimental results discussion

A synopsis of the experimental observations is presented in Fig. 3.5. It can be concluded from the comparison among UHPC-D3A, UHPC-D3B, and UHPC-D4 that the structural response is highly dependent on the blast scenarios. As the scaled distance decreases (meaning larger blast or closer range), in this experiment from 3.05 to 0.50 m kg$^{-1/3}$ and then to 0.41 m kg$^{-1/3}$, the permanent deflection of the members increases and the slab response shifts from the elastic range to plastic range and then to failure. The elastic range is characterized by no permanent deflection, where the plastic range shows a permanent deflection after the blast ceased. The slab is deemed to have failed when it has undergone significant deformation (UHPC-D3B).

Furthermore, from the comparison between UHPC-D1 and UHPC-D3B, it is noted that under the same blast scenario, the reinforcement plays a significant role in resisting the overall structural damage. With mild reinforcement of 300 MPa
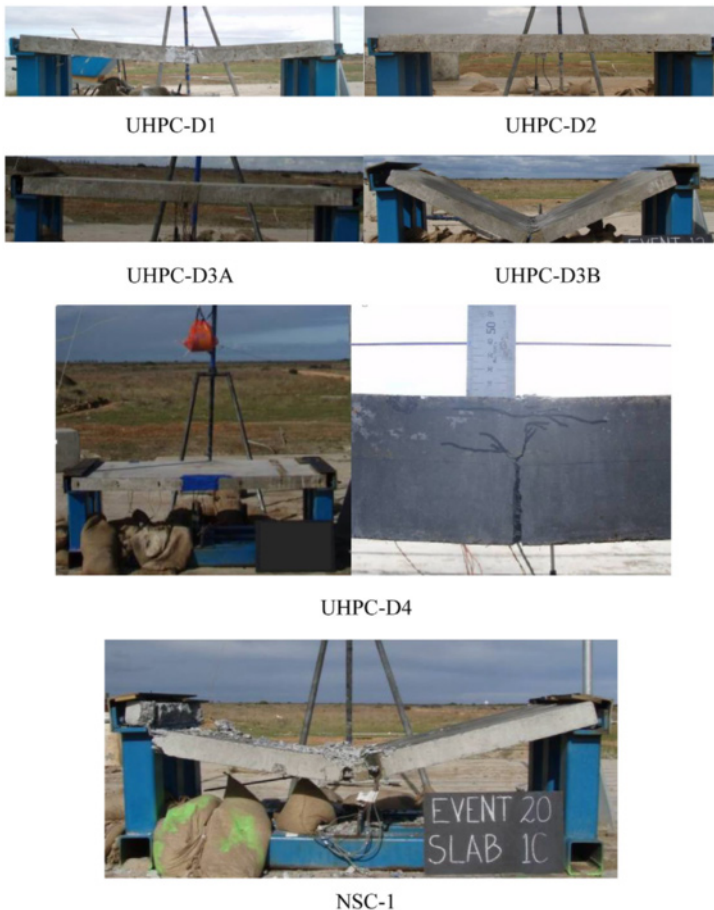
Figure 3.5 Slab responses after blast.

yielding strength, UHPC-D3B completely collapsed after the blast. With reinforcement of 600 MPa yielding strength, UHPC-D1 displayed plastic damage, but not a complete failure. The same conclusion can be drawn about UHPC-D2 with 1750 MPa steel reinforcement and UHPC-D4 with 300 MPa steel reinforcement. UHPC-D2 outperformed UHPC-D4 with almost no damage while UHPC-D4 experienced a plastic flexural damage with significant mid-span deflection.

For NSC slab NSC-1, even though the scaled distance was increased to 0.75 m kg$^{-1/3}$, the slab was completely destroyed with flexural damage at mid-span and brittle shear damage close to the support. The institutive experimental observations proved that the slabs constructed with UHPC material performed much better than the conventional NSC slab under extreme blast loading conditions.

After test on NSC-1 slab, it was noted that large amounts of fragments were generated at slab mid-span. These fragments are believed to be induced by the severe blast wave propagation. Under blast loading condition, on the slab proximal surface, concrete experiences compression and may fail under high compressive force and generate cratering. When the compressive stress wave interacts with the slab bottom free surface, it reflects and converts to a tensile wave. Under this condition, due to the low tensile resistance of NSC, crack will form if the net stress exceeds concrete dynamic tensile strength. Furthermore, if the trapped impulse is large enough to overcome the resistant forces such as the bond, shear around the periphery of the cracked portion, and the mechanical interlocking, concrete spallation happens and the cracked off parts displace from the backside of the structure at some velocity. These fragments can cause secondary injuries to the personnel shielded by the structures and therefore should be avoided in the protective design.

Concrete spall and fragments were not seen in UHPC-3B and UHPC-4 slabs which were subjected to even severe blast loads, and their enhanced spall resistance can be attributed to the bridging effect of the steel fibers. After initial crack happens on UHPC slabs, the steel fiber bridges over the cracks and retard crack extension. Steel fibers also have higher elasticity modulus than concrete which means during deformation they absorb large amount of energy and therefore reduce the stress transferred to the surrounding concrete matrix.

Table 3.4 lists the central deflection obtained from the LVDTs. Among all the slabs, UHPC-D2 with high strength steel reinforcement is deemed to have the best

Table 3.4 Central deflection of the slabs

Slab no.	Scaled distance (m kg$^{-1/3}$)	Maximum deflection (mm)	Permanent deflection (mm)	Response range
UHPC-D1	0.41	**	53.0	Plastic
UHPC-D2	0.50	41.0	0.0	Elastic
UHPC-D3A	3.05	1.0	0.0	Elastic
UHPC-D3B	0.41	**	**	Fail
UHPC-D4	0.50	72.0	40.0	Plastic
NSC-1	0.75	*	*	Fail

**Data faulty; *No data collected.

performance. Under blast load with $0.5 \, \mathrm{m \, kg^{-1/3}}$ scaled distance, UHPC-D2 restored its original state even after experiencing a maximum deflection of 41 mm during the blast.

Due to the missing of pressure data on the slab surface, Fig. 3.6 gives the comparison between the experimental data and UFC [37] prediction regarding the
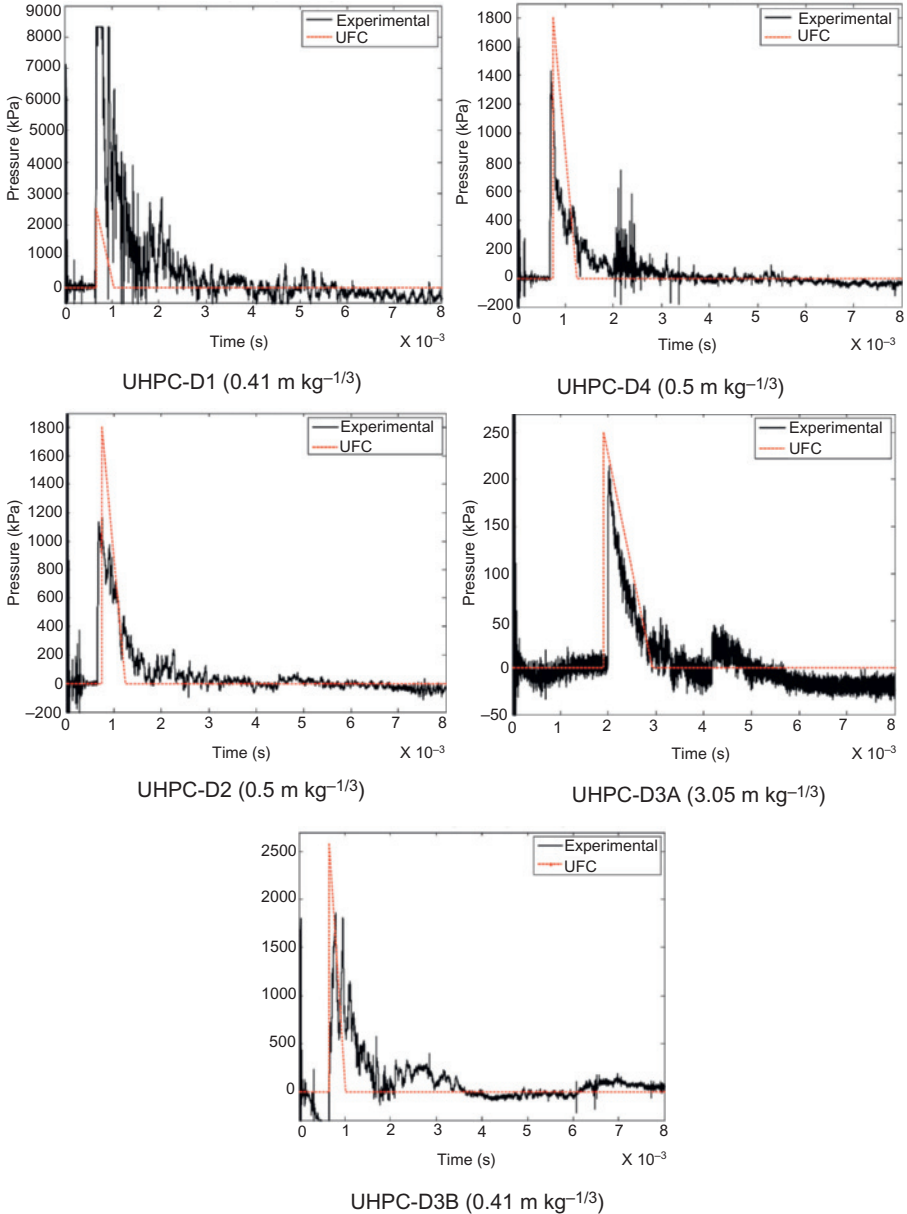
Figure 3.6 Free air pressure time history comparison.

pressure in the free air which is recorded by the pressure sensor in Fig. 3.3. It can be observed that when the scaled distance is relatively large as in UHPC-D3A test, UFC can give good predictions on both the peak pressure and positive blast duration. With the decrease of the scaled distance, UFC can give reasonable if not accurate predictions. The inconsistency between the experimental data with the UFC predictions when the scaled distance is small can be attributed to the fact that the test results in this study are obtained from limited and scattered tests which may contain sampling errors.

3.2.1.5   Numerical modeling

In this study, eight node hexahedron solid elements are employed for simulating the UHPC material. For the reduced integration elements, the Flanagan−Belytschko-based hourglass control option available in LS-DYNA was used with the hourglass coefficient set to 0.1. Hughes-Liu beam element with cross-section integration is used to model the steel reinforcement. In the present test observations, the primary response mode is global elastic or plastic response, and the damage is mainly flexural plastic damage at slab mid-span. After convergence test, two element sizes are used in this study to avoid excessive calculation time while retaining the simulation accuracy. As shown in Fig. 3.7, fine mesh size of 10 mm is used for the central part of the slab, while a relative coarse mesh size of 40 mm is used for the remaining part. At each end of the slab, nodes within a length of 100 mm is constrained in Z-axis.

In LS-DYNA, for NSC modeling, various material models such as Pseudo Tensor (MAT_16), Johnson Holmquist Concrete (MAT_111), and Concrete Damage Rel3 (MAT_72_REL3) have been widely used under dynamic loading condition.

In previous studies, for simulating the NSC, material model Concrete_Damage_ Rel3 was widely adopted. Concrete_Damage_Rel3 is a plasticity-based model, and it uses three failure surfaces which change shape according to the confinement pressure. The major advantage of this model is that it is based on a single user input parameter, i.e., the unconfined compressive strength. The remaining model parameters are automatically generated using a built-in algorithm and can also be modified by the user.

For UHPC material, Thiagarajan et al. [38] also used Concrete_Damge_Rel3 model to simulate its behavior under blast loads; however, it was noticed that this model showed a poor response predictions using the concrete parameters that were generated internally by LS-DYNA. To capture the UHPC material characterizing feature, i.e., nonlinear softening behavior after yielding, Teng et al. [39] and Wang et al. [40] developed numerical model based on MAT_Elastic_Plastic_ Hydrodynamic to simulate the UHPC members subjected to dynamic loads, and their simulation results showed high accuracy when comparing with the experimental observations.
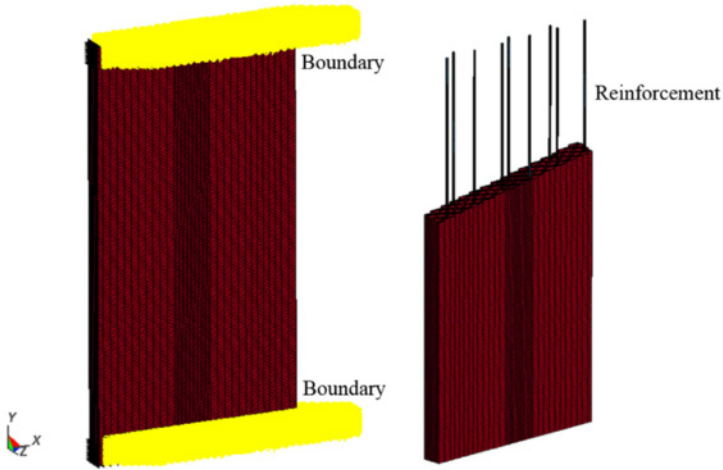
Figure 3.7 Numerical model of the slab.

Table 3.5 Effective stress-effective plastic strain data for describing UHPC hardening and softening

	Effective plastic strain	Effective stress (MPa)		Effective plastic strain	Effective stress (MPa)
Point 1	0	120	Point 9	0.003	102
Point 2	0.0002	122	Point 10	0.0035	96
Point 3	0.0004	124	Point 11	0.004	92
Point 4	0.0005	128	Point 12	0.0045	82
Point 5	0.00075	120	Point 13	0.005	72
Point 6	0.001	118	Point 14	0.00525	70
Point 7	0.0015	116	Point 15	0.0055	62
Point 8	0.002	108	Point 16	0.006	60

Source: Based on Fig. 3.2.

In this study, MAT_Elastic_Plastic_Hydrodynamic material model is adopted for modeling UHPC, and the elastic deformation phase is defined by Young's modulus of UHPC listed in Table 3.2. The material hardening and softening phase is defined by effective plastic stress versus effective plastic strain curve which is derived from the static cylinder test as shown in Fig. 3.2; in total, 16 effective plastic strain versus plastic strain values are input to represent the prominent postpeak softening of UHPC material as listed in Table 3.5. In addition, to describe the volumetric stress and strain associated with the blast pressure, an equation of state

Table 3.6 Parameters for the equation of state describing the UHPC

EOS	C_0	2100 m s^{-1}
	S_1	1.4
	γ_0	2

(EOS) for UHPC is also employed. In this study, the Gruneisen EOS is used. With cubic shock velocity−particle velocity, the Gruneisen EOS defines pressure for compressed material as:

$$p = \frac{\rho_0 C^2 \mu \left[1 + \left(1 - \frac{\gamma_0}{2}\right)\mu - \frac{a}{2}\mu^2 \right]}{\left[1 - (S_1 - 1)\mu - S_2 \frac{\mu^2}{\mu + 1} - S_3 \frac{\mu^3}{(\mu + 1)^2} \right]^2} + (\gamma_0 + a\mu)E \tag{3.1}$$

and for expanded material as:

$$p = \rho_0 C^2 \mu + (\gamma_0 + a\mu)E \tag{3.2}$$

where C is the intercept of the $V_s - V_p$ curve, S_1, S_2, and S_3 are the coefficients of the slope of the $V_s - V_p$ curve; γ_0 is the Gruneisen gamma; a is the first-order volume correction to γ_0; and $\mu = \rho/\rho_0 - 1$. The parameters used in the Gruneisen EOS are listed in Table 3.6.

Numerical erosion algorithm, i.e., Mat_Add_Erosion is adopted in the current simulation to capture the initiation and propagation of concrete material damage. When the user-defined criteria such as the principle stress or strain are reached, concrete element will be automatically deleted from the calculation. If the criterion is set improperly high, element distortion which is due to large element deformation happens; if the criterion is set improperly low, premature erosion and element deletion happens which violates the mass conservation and the results are no longer reliable. When choosing the erosion criterion for NSC and UHPC in this study, the primary concern is to avoid massive deletion of the elements and maintain the mass conservation. Ideally, erosion should not be used to delete elements. This, however, is not possible when modeling large deformation in the postfailure region. Therefore to avoid eroding elements prematurely, large strain is usually chosen as the erosion criterion. For NSC material, typical concrete strain at peak tensile stress under static loading is around 0.0002 (which is one-tenth of that peak compressive strain). Considering the softening phase, the concrete fracture strain may be assumed as $5 \times 0.0002 = 0.001$. Taken into consideration of other effects like strain rate effect (up to 7) and confinement effect from the reinforcement, this value can reach 0.01−0.02. In order to avoid massive deletion of the elements which breaches the mass conservation, a principle tensile strain value of 0.1 is taken as the erosion

Table 3.7 Material properties and erosion criterion

	NSC (MPa)	UHPC (MPa)
Young's modulus	49195	51,503
Compressive strength	56.6	128.9
Tensile strength	8.2	30
Failure principle strain	0.1	0.1

criterion. For UHPC material, as depicted in Fig. 3.2, UHPC has more or less the same peak compressive strain as NSC (around 0.002). Although UHPC has more prominent softening phase, its strain rate sensitivity is lower than NSC, an erosion criterion that is the same as the NSC is therefore adopted. Furthermore, considering that FE models for UHPC and NSC slabs have the same mesh density, uniform erosion criterion can give sound comparison on the crack propagation of the two materials.

Table 3.7 summaries the concrete material properties and erosion criterion in this study.

In this study, steel reinforcement is simulated by MAT_Piecewise_Linear_Plasticity (MAT_24). This model allows the definition of arbitrary stress versus strain curve and arbitrary strain rate curve. Also, failure based on a plastic strain or a minimum time-step size can be defined.

Material mechanical properties under high strain rate loading condition are significantly different from those under static loading condition. Previous studies indicate the strain rate effect in concrete is due to moisture at low strain rate and inertia effect at high strain rate. The strength enhancement under high loading rate conditions can be represented using dynamic increase factor (DIF). For NSC with compressive strength ranging from 20 to 70 MPa, their DIF can be calculated through equations proposed by Malvar and Crawford [41].

For NSC compressive strength:

$$\text{DIF} = \frac{f_c}{f_{cs}} = \begin{cases} \left(\dfrac{\dot{\varepsilon}}{\dot{\varepsilon}_s}\right)^{1.026\alpha} & \text{for} \quad \dot{\varepsilon} \le 30 \ \text{s}^{-1} \\ \gamma_s \left(\dfrac{\dot{\varepsilon}}{\dot{\varepsilon}_s}\right)^{1/3} & \text{for} \quad \dot{\varepsilon} > 30 \ \text{s}^{-1} \end{cases} \tag{3.3}$$

where f_c is the dynamic compressive strength at $\dot{\varepsilon}$; f_{cs} is the static compressive strength at $\dot{\varepsilon}_s$; $\dot{\varepsilon}$ is the strain rate in the range of 30×10^{-6} to $300 \ \text{s}^{-1}$; $\dot{\varepsilon}_s$ is the static strain rate 30×10^{-6}; $\log \gamma_s = 6.156 \ \alpha - 2$; $\alpha = 1/(5 + 9 f_{cs}/f_{co})$; $f_{co} = 10$ MPa.

For NSC tensile strength:

$$\text{DIF} = \frac{f_t}{f_{ts}} = \begin{cases} \left(\dfrac{\dot{\varepsilon}}{\dot{\varepsilon}_s}\right)^{\delta} & \text{for} \quad \dot{\varepsilon} \leq 1 \ \text{s}^{-1} \\[3mm] \beta\left(\dfrac{\dot{\varepsilon}}{\dot{\varepsilon}_s}\right)^{1/3} & \text{for} \quad \dot{\varepsilon} > 1 \ \text{s}^{-1} \end{cases} \tag{3.4}$$

For steel reinforcement

$$\text{DIF} = \left(\frac{\dot{\varepsilon}}{10^{-4}}\right)^{\alpha} \tag{3.5}$$

where for the yield strength, $\alpha = \alpha f_y = 0.074 - 0.04 f_y/60$; and for the ultimate stress, $\alpha = \alpha f_u = 0.019 - 0.009 f_y/60$.

As a relatively new material that varies in composition and fiber material dosage, research working on the strain rate effect of UHPC material is limited. Chen et al. [42] conducted dynamic tensile tests on steel FRC with various fiber volume fractions, and the largest DIF obtained was around 1.1 which is substantially smaller than NSC. Weidner [43] conducted a series of drop hammer tests on both plain concrete and fiber-reinforced high strength concrete, and it was observed that FRC specimens were less sensitive to the dynamic load as compared with NSC. Millard et al. [44] performed dynamic flexural tensile test on ultra-high strength concrete with different dosages of steel fiber. The results show that the strain rate enhancement of flexural strength for UHPC is reduced as the fiber percentage increases. It was explained that the fibers resist the lateral spreading of the cracks by bridging across regions of lower strength. Therefore the beneficial effect of a restraint on lateral crack growth has already been partially accounted for by fiber reinforcement, resulting in higher failure strength under quasistatic loading. Subsequently, the influence of the higher loading rate on reducing lateral crack development would be lessened.

Generally speaking, DIF of UHPC is under development and discussion, relevant study requires large number of repeated laboratory tests. The limited DIF data obtained in previous tests indicated that UHPC is less rate sensitive as compared to normal concrete. Because there is no sufficient data to appropriately model DIF of UHPC, and as it has been found less rate sensitive, in numerical study on dynamic performance of UHPC, usually no strain rate enhancement is assumed. Neeley et al. [45] developed the high strength concrete mix used in the dynamic experiments and modeled in the numerical simulations. The material strain rate enhancement effects in this model were not considered due to a lack of experimental data. The same consideration is also adopted in [2,40]. This assumption avoids overestimation of the dynamic performance of UHPC, but might slightly underestimate its dynamic strength. However, this conservation consideration is deemed necessary in protective design given no accurate DIF values are available yet.

In this study, strength enhancement in the UHPC material is not included in the numerical model due to the lack of test data.

3.2.1.6   Modeling results

In the modeling, the blast load was modeled using built-in *Load_Blast function in LS-DYNA. It is worth noting that such implementation is based on empirical models described in TM5-855-1 US army handbook, and it is limited to the treatment of hemispherical charges on the ground or spherical charges in the air. However, in real cases, the explosives used are not always in these shapes, and it was found that the detonation point within the explosive and the ratio of length to diameter in cylinder explosives can significantly influence the blast effects. In this study, based on the comparison discussed in Fig. 3.6 between the field test results and UFC handbook predictions, a relatively small difference is noticed and thus such shape and directional effects are not considered.

Among all the UHPC specimens tested, the primary damage mode is the flexural damage with plastic hinge at mid-span. This is the desired damage mode in practical design as such damage absorbs the most amount of energy. In Fig. 3.8, side view of the slab UHPC-D1 after blast load is shown. It can be noticed that on the distal surface, the concrete cracks formed and the cracks did not extend along the whole slab depth, and on the proximal surface concrete crush was clearly observed. Comparing with the experimental observation, the numerical simulation predicts the concrete damage with high accuracy although the crack orientation was not fully captured.

Fig. 3.9 shows the UHPC-D2 response simulation. Under blast load corresponding to a relatively large-scaled distance, i.e., $0.5 \, \mathrm{m \, kg^{-1/3}}$ in this case, the UHPC
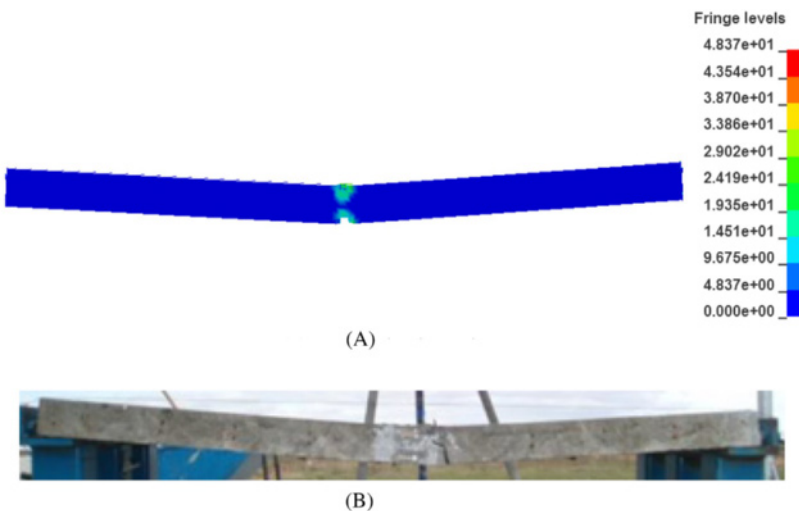
Figure 3.8 UHPC-D1 response: (A) numerical study and (B) experimental observation.
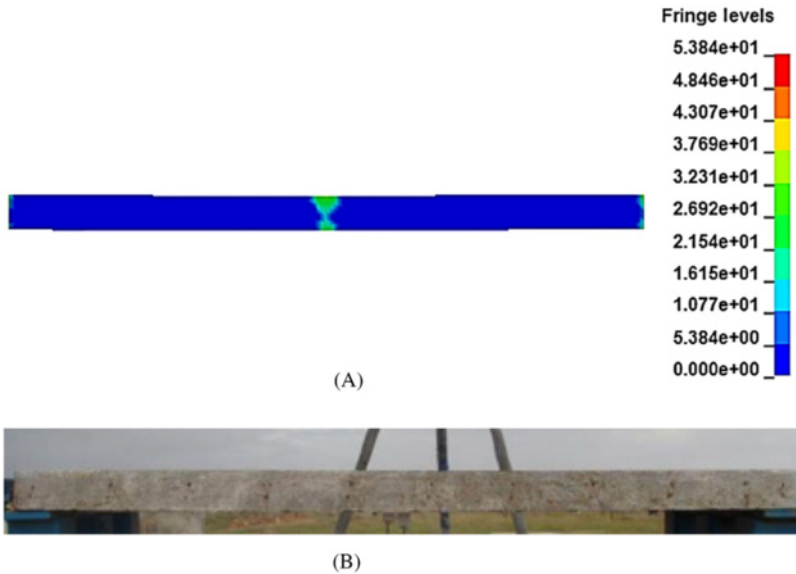
Figure 3.9 UHPC-D2 response: (A) numerical study and (B) experimental observation.

slab with high strength steel reinforcement had no visible cracks and remained intact. The numerical model captured the overall deformation of the slab with reasonable accuracy. However it can be seen that there is a stress concentration in the mid-span indicating a small plastic deformation. This small permanent deflection was not captured in the experiment.

Figs. 3.10 and 3.11 show the UHPC-D3 response simulation. This slab experienced two separate blast loads, i.e., UHPC-D3A under blast with scaled distance 3.05 m kg$^{-1/3}$ and UHPC-D3B under blast with scaled distance 0.41 m kg$^{-1/3}$. For the first blast scenario, the slab responded elastically, and no damage was recorded. For the second blast scenario, the slab completely collapsed and severe plastic damage was noticed at the mid-span. Numerical simulation reproduced the global deformation of UHPC-D3A while indicating a plastic stress concentration close to the support which was not observed from the field test. For UHPC-D3B, the numerical simulation gave highly accurate predictions on the slab deformation and damage.

Fig. 3.12 shows the simulation of UHPC-D4 under blast with 0.5 m kg$^{-1/3}$ scaled distance. In the experimental observation, concrete cracks extended to the half depth of the slab. Numerical model simulated the bottom cracks, and visible cracks on the upper surface are also noticed from the numerical simulation.

Fig. 3.13 shows the time history curve of the UHPC-D1 slab mid-span deflection from simulation, and comparison is made with the LVDT measurement of the slab permanent deflection. It can be seen that under the blast load, the slab deforms quickly and then bounces back and vibrates around a permanent deflection value of

(A)

(B)
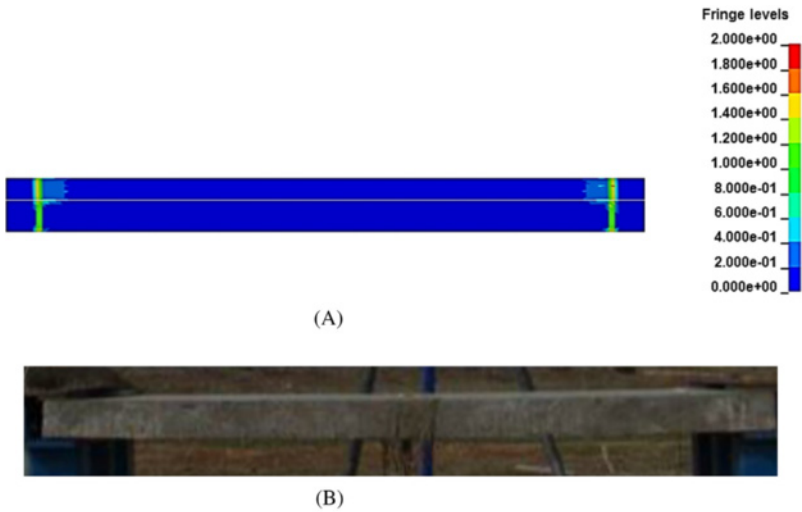
Figure 3.10 UHPC-D3A response: (A) numerical observation and (B) experimental observation.

(A)

(B)
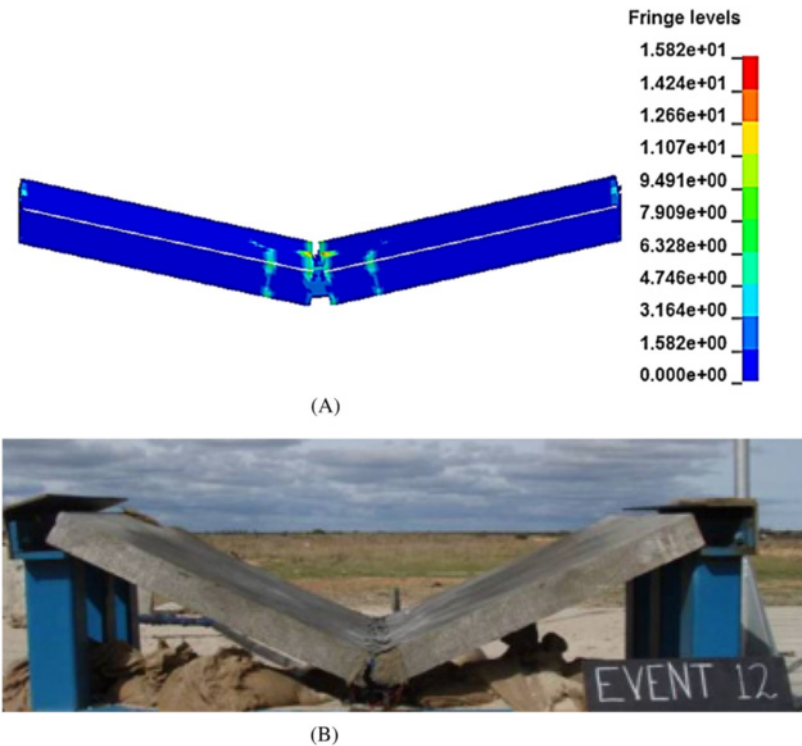
Figure 3.11 UHPC-D3B response: (A) numerical observation and (B) experimental observation.

Fringe levels

5.713e+01
5.142e+01
4.570e+01
3.999e+01
3.428e+01
2.856e+01
2.285e+01
1.714e+01
1.143e+01
5.713e+00
0.000e+00

(A)

(B)
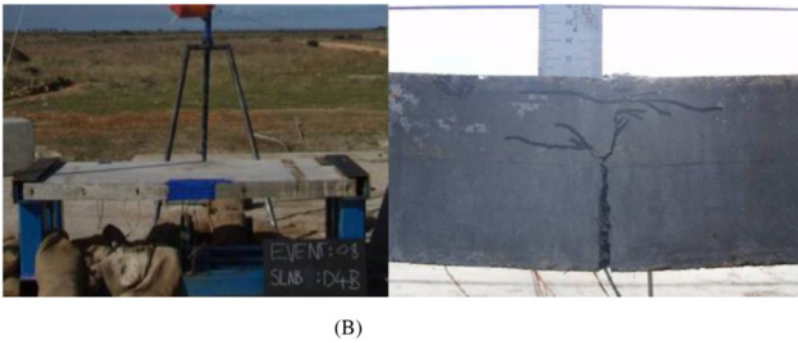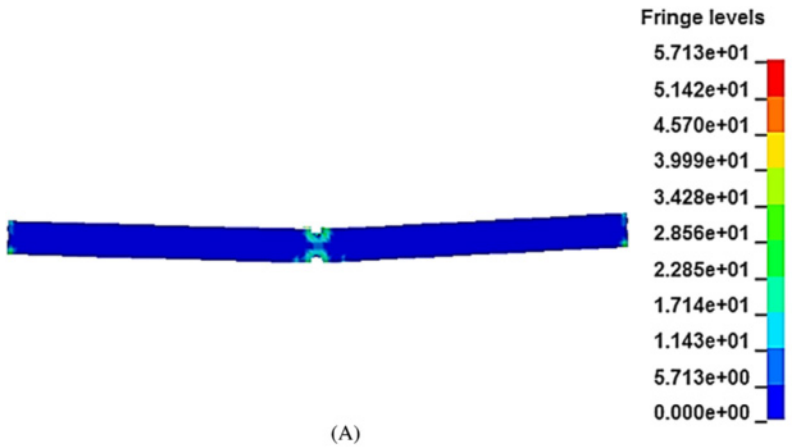
Figure 3.12 UHPC-D4 response: (A) numerical observation and (B) experimental observation.
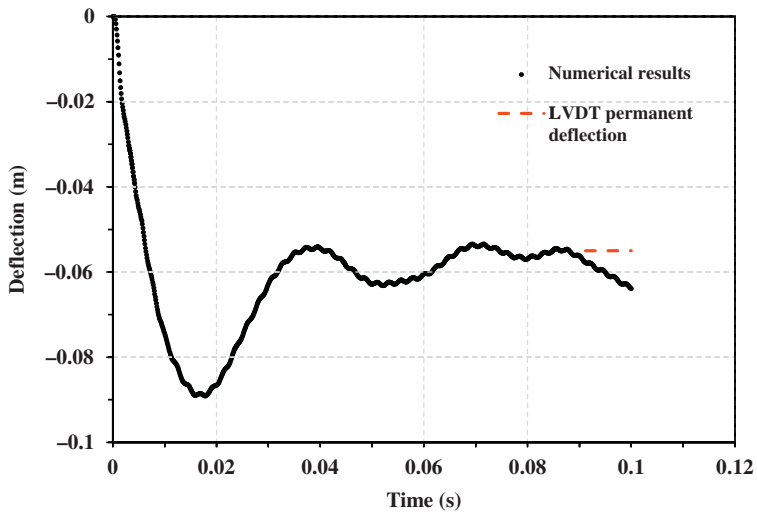
Figure 3.13 UHPC-D1 response.

about 58 mm. Although the deflection time history was not recorded in the test, the LVDT in the experiment recorded a permanent deflection value of about 53 mm. The numerical method yields a good prediction about the permanent deflection.

Fig. 3.14 compares the time history curve of the UHPC-D2 slab mid-span deflection. LVDT in the experiment gives a maximum deflection value of about 41 mm. The value obtained from the numerical simulation is 37 mm which slightly underestimates the maximum response. After the first period of vibration, the LVDT on the slab gave a faulty time history curve which was probably because the LVDT bolt connection was loosened by the blast load. However, the permanent deflection from the field measurement was 0 mm which is quite close to the numerical prediction, i.e., 4 mm.

Fig. 3.15 shows deflection time history curves for UHPC-D3 under two different blast scenarios. Due to the malfunction of the LVDT in these two tests, only the maximum and permanent deflections of UHPC-D3A were recorded. It can be noticed in Fig. 16A that the predictions from the numerical method correlate well with the experimental observations. The numerical simulation gives a maximum deflection value of 0.85 mm, while field test gives a value of 1 mm. The permanent deflections from both the numerical simulation and field observation are 0 mm indicating an elastic slab performance.

Fig. 3.16 shows comparison of the time history curves of UHPC-D4, and it is noticed that the numerical method not only gives good permanent deflection
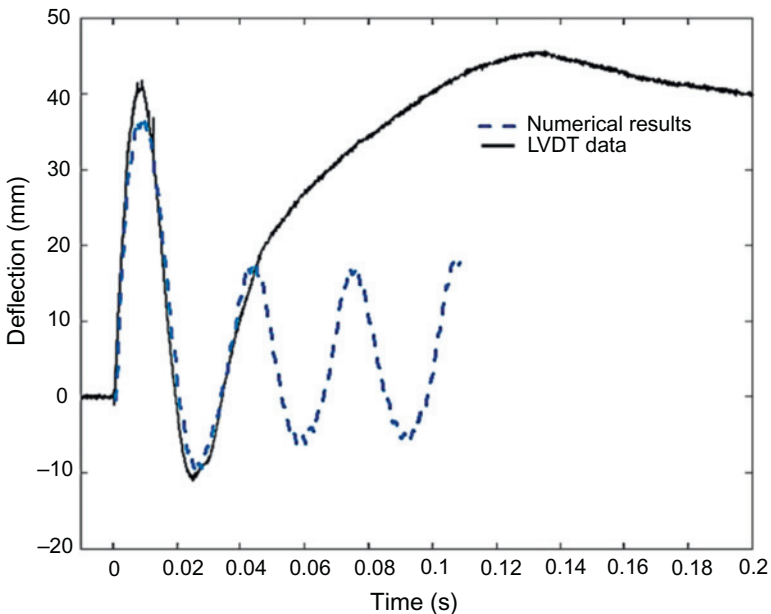
Figure 3.14 UHPC-D2 response.
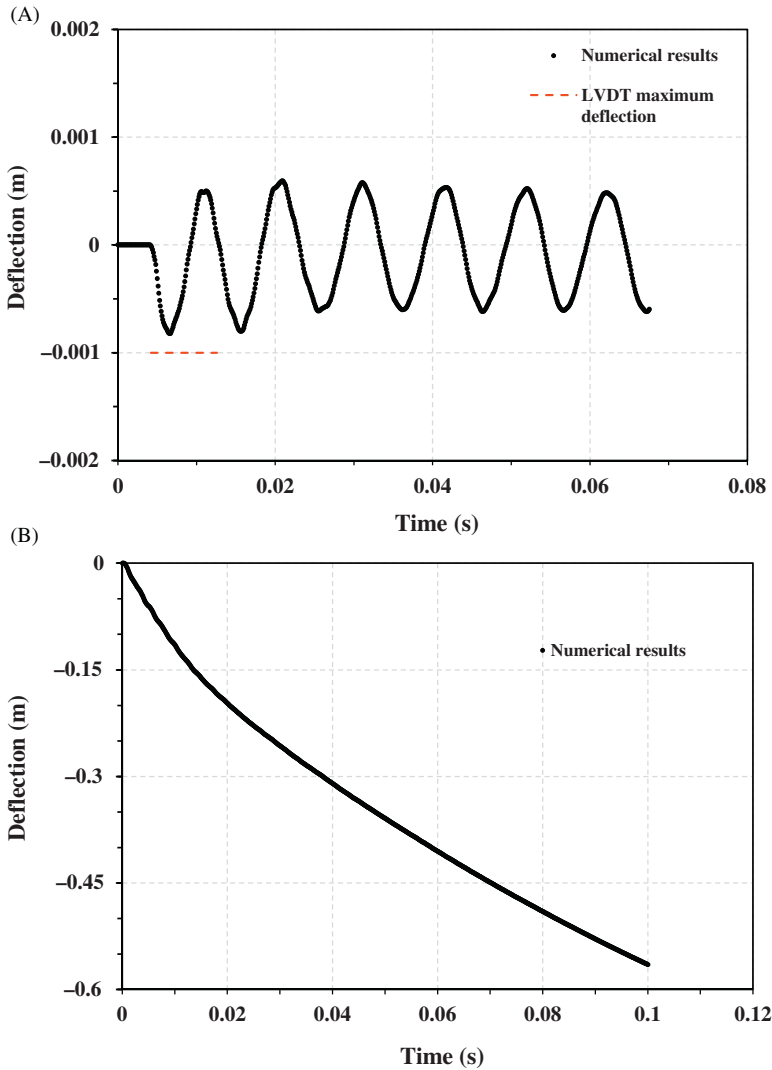
Figure 3.15 UHPC-D3 response: (A) UHPC-D3A and (B) UHPC-D3B.

prediction but also captures the maximum deflection with high accuracy. Generally speaking, the shape of the experimental deflection time history curve is captured by the numerical model.

3.2.1.7   Concluding remarks

A series of blast tests are carried out in the recent study on four UHPC slabs and one NSC slab. During the slab tests, various damage modes like flexural damage in UHPC slab and brittle shear damage in NSC slab are observed. Peak incident
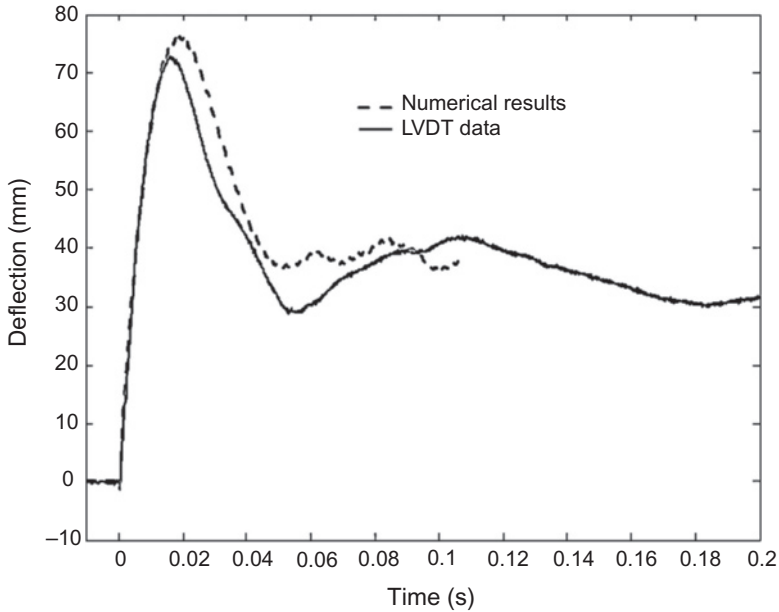
Figure 3.16 UHPC-D4 response.

pressures are compared with the UFC predictions and generally good correlations are obtained. Field measured mid-span maximum displacements and permanent deflections are used to verify the proposed numerical model analysis results. It is noticed that the FE model with predetermined material properties and boundary conditions can reasonably reproduce the structural damage under blast loads, and quantitative comparison regarding the mid-span deflection time histories further confirms the feasibility of the numerical model. However, it should be pointing out that the current numerical model neglects the strain rate effect on UHPC material, and this model can be further revised according to dynamic material tests to obtain more accurate predictions on the dynamic performance of UHPC.

3.2.2 Blast test program with contact detonations

3.2.2.1 Test setup

In these two contact blast tests, slab dimension is 2000 mm × 1000 mm × 100 mm. The NSC specimen was designed with both tension and compression reinforcement using a 12 mm diameter mesh, with a 10 mm concrete cover. The mesh bars were spaced at 100 mm centers in the major bending plane and 200 mm in the minor plane. This corresponds to a reinforcement ratio of 1.2%. Fig. 3.17 illustrates the configuration of the NSC slab.

UHPC slab shares the same dimension with the NSC slab but with no steel reinforcement. The confinement effect from the reinforcement mesh does not exist in
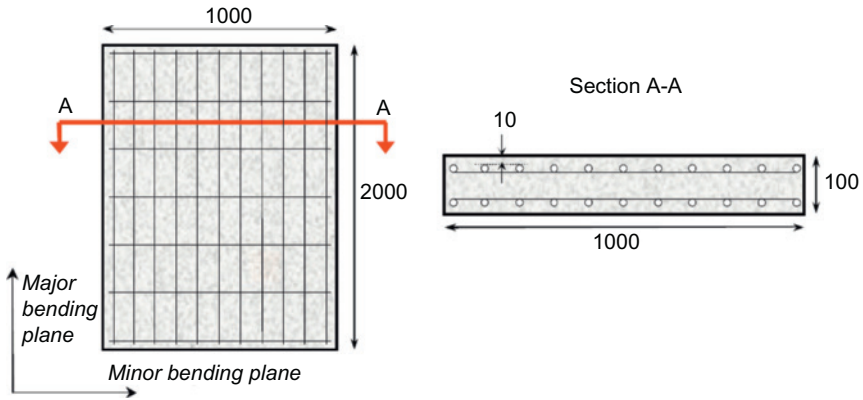
Figure 3.17 Dimension and reinforcement of NSC slab in contact explosion test.
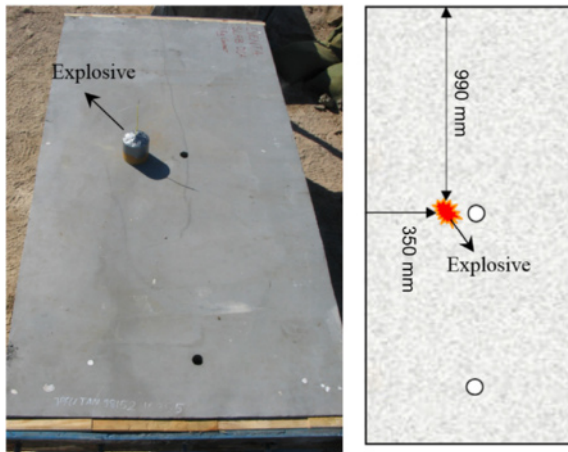
Figure 3.18 Contact explosion test.

UHPC slab, and the spall damage is solely resisted by the UHPC material. Of note, 1 kg explosive charge in the shape of cylinder with ratio of diameter to length 1 is placed on the upper surface of the slab specimens. Due to the predrilled holes in the slabs for the installation of pressure gauges, the charge is offset from the center as can be seen from Fig. 3.18.

Fig. 3.19 shows the field setup and steel rig supporting system for contact explosion test. The base steel plates are bolted to the concrete ground slab to stabilize the testing system, and the slab is placed on the steel rig with a simply support boundary.

The blast program is summarized in Table 3.8.

Figure 3.19 Test setup and supporting system.

Table 3.8 **Blast program**

Slab no.	Description	Rebar ratio	Standoff distance (m)	Scaled distance (m kg$^{-1/3}$)	Explosive charge (kg)
NSC	RC slab	1.2%	Contact explosion		1.0
UHPC	Unreinforced UHPC		Contact explosion		1.0

3.2.2.2 Test results

Fig. 3.20 shows the response of reinforced NSC slab NSC after 1 kg contact explosion. It can be noticed that the slab suffered a 390-mm diameter failure on the proximal surface as indicated in Fig. 3.20A, while the distal surface of the slab has a larger failure diameter of 710 mm as shown in Fig. 3.20B. This is a typical concrete spall and punching failure mode. Under contact loading condition, blast pressure directly impacts on the proximal surface, and this pressure easily exceeds the dynamic compressive strength of NSC which induces concrete punching failure. Blast load also generates severe stress wave propagation along the slab depth direction. Upon the interaction between the reflective stress and incident stress, if the resultant stress exceeds the dynamic tensile strength of the concrete, concrete spall occurs. It is worth noting that a wedge shape side failure was also observed on the NSC slab as shown in Fig. 3.20B. It is believed that such failure is caused by the stress wave propagation within the slab plane. As the explosives offset from the center to the side, the incident stress wave has a short distance to travel before it encounters the reflective stress wave from the free edge, only small amount of
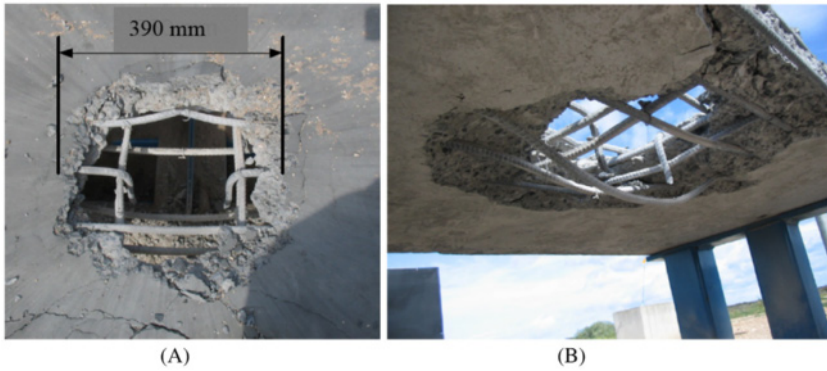
Figure 3.20 NSC response to contact explosion: (A) top face of slab and (B) bottom face of slab.
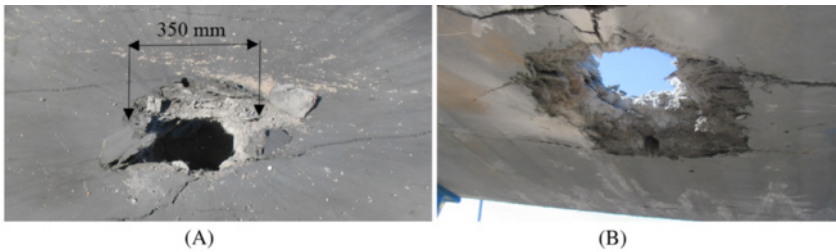
Figure 3.21 UHPC response to contact explosion: (A) top face of slab and (B) bottom face of slab.

energy has been dissipated before the wave superposition, and the resultant stress is still larger than the dynamic tensile strength of the concrete which brings damage to the free edge of the slab.

Fig. 3.21 shows the response of UHPC after 1 kg contact explosion. Similar damage mode as seen on the NSC slab is observed. However, after detailed measurement, the UHPC slab is found to have smaller damage diameter on both the top and bottom surfaces, i.e., 350 mm and 380 mm, respectively, and there is small difference between the upper and bottom damage area diameter. These observations could be explained by the two factors. Firstly, the steel fiber composites in UHPC slab can effectively prevent concrete cracking and even bridge over the concrete cracks to mitigate the bottom surface spall damage. Secondly, UHPC has ultra-high compressive strength and significant material ductility as shown in Fig. 3.2 which means it can absorb large amount of blast energy, thus reduce the concrete punching failure on the upper surface. It is worth noting that the UHPC slab in this contact explosion test does not have any steel reinforcement, and the spall damage can be further confined if reinforcement mesh is included.

Table 3.9 summarizes the spall damage diameters of both slabs.

Table 3.9 **Contact explosion-induced damage**

Slab no.	Damage diameters (mm)	
	d_{top}	d_{bottom}
NSC	390	710
UHPC	350	380

3.2.2.3 Numerical simulation

Contact explosion simulation is through the coupled FE and SPH methods. The SPH method was originally developed by Lucy [46] and Gingold and Monaghan [47]. Instead of FEs, this method uses discrete particles, interacting with each other via an interpolation function. Because this method is Lagrangian and mesh free, it is well suited to analyze large deformation events involving failure and fragmentation [48], and the utilization of using such method simulating the high explosive explosions is also found in the literature [49,50]. In this study, in order to simulate interaction of explosion wave with the slab, and capture large deformation of the explosive, the high explosive material is simulated through SPH particles and test slab is modeled with FEs as shown in the free air tests. MAT_High_Explosive is adopted to simulate the high explosive material, Mat_Concrete_Damage_Rel3 and Mat_Elastic_Plastic_Hydrodynamics are used to simulate the NSC slab and UHPC slab, respectively, and the MAT_Piecewise_Linear_Plasticity is used to model the steel reinforcement.

In total, 12,500 SPH particles are generated in cylinder shape to model the explosive. The SPH particles and test slab model are shown in Fig. 3.22.

Contact between the SPH particles and test slab is modeled through the LS-DYNA built-in algorithm *CONTACT_NODES_TO_SURFACE, and default value is used in the contact setup.

Fig. 3.23 shows the explosion phenomenon modeled in this study. The explosive expansion and corresponding blast wavefront pressure can be clearly observed in the figure.

Fig. 3.24 shows the top surface response of the target slab NSC. The punching and spall failure quickly expands with time. The damage extends quickly in the first 10 ms, and remains stable afterward. No global deformation can be observed which indicates that the slab response under contact explosion is highly localized.

It is even clearer to observe the spall damage from the bottom surface as shown in Fig. 3.25, comparing with the experimental observations of NSC on the bottom surface, the numerical model gives excellent predictions on the structural damage. Concrete spall, punching, and tearing of the steel reinforcement are all well simulated with high fidelity.
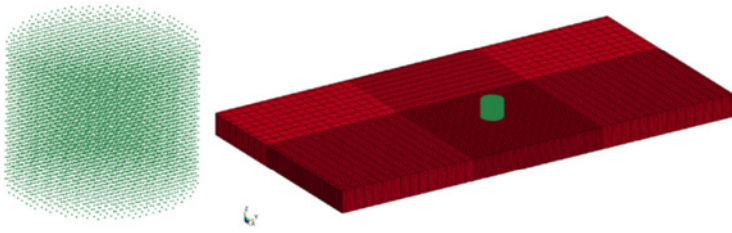
Figure 3.22 Coupled FE model and SPH particles.
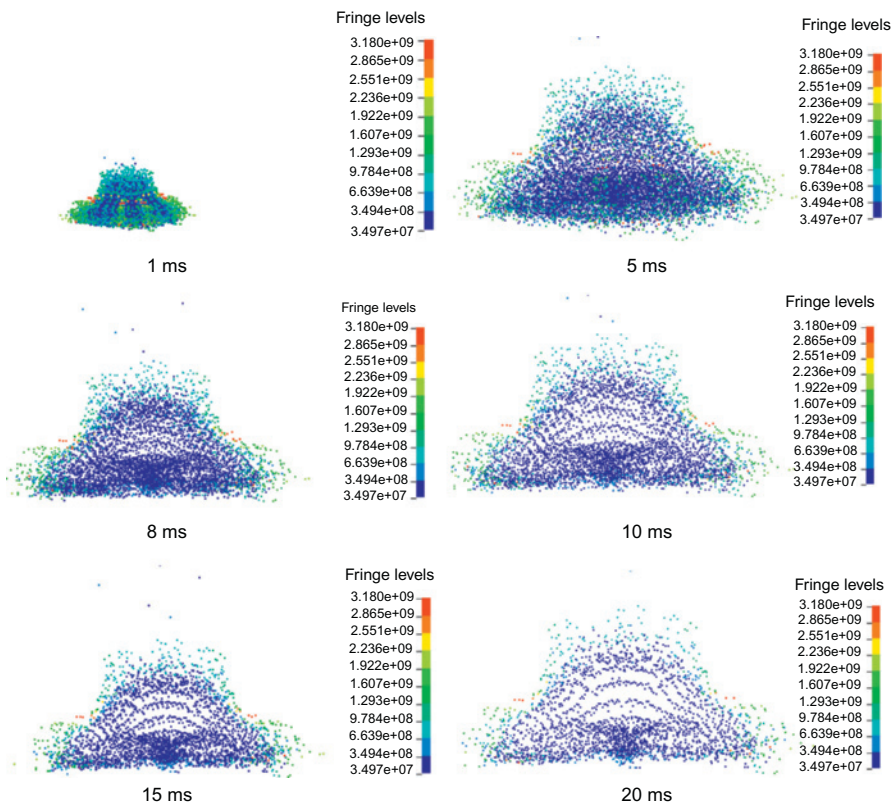
Figure 3.23 Explosion expansion.

Fig. 3.26 shows the UHPC slab under 1 kg contact explosion. Similar to the NSC slab, the concrete crush and spall is highly localized and the structure restores stability in a short period of time. Due to the high compressive strength, the concrete crush on the proximal face facing the explosive is significantly confined comparing with the NSC slab.
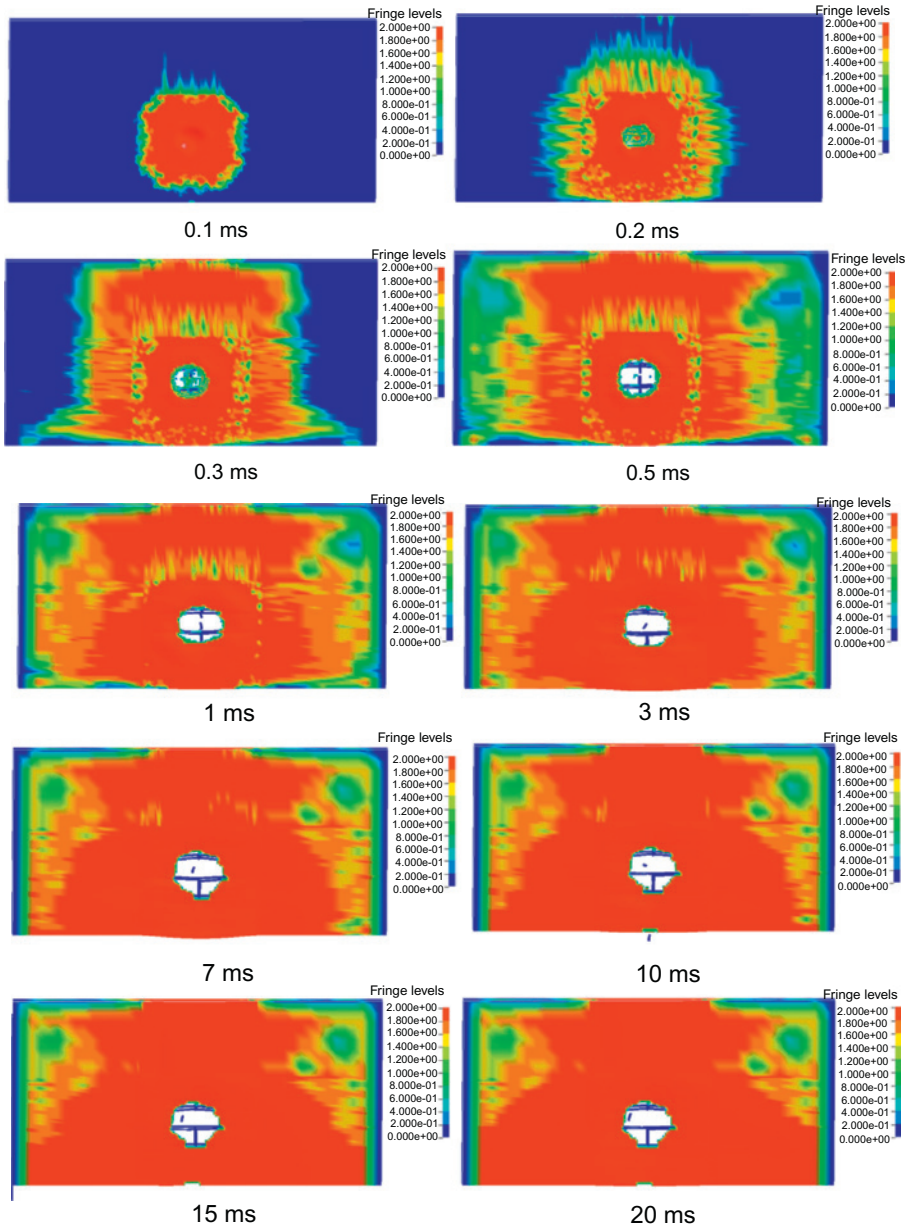
Figure 3.24 Slab NSC top surface response.
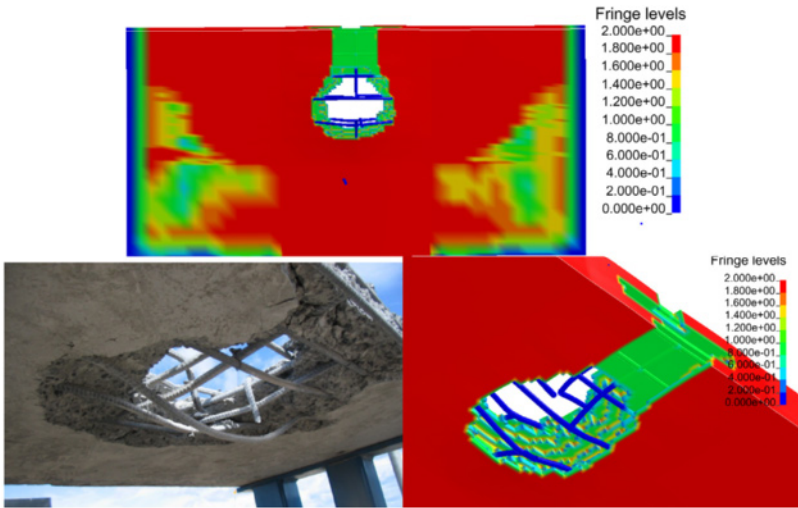
Figure 3.25 Slab NSC bottom response.
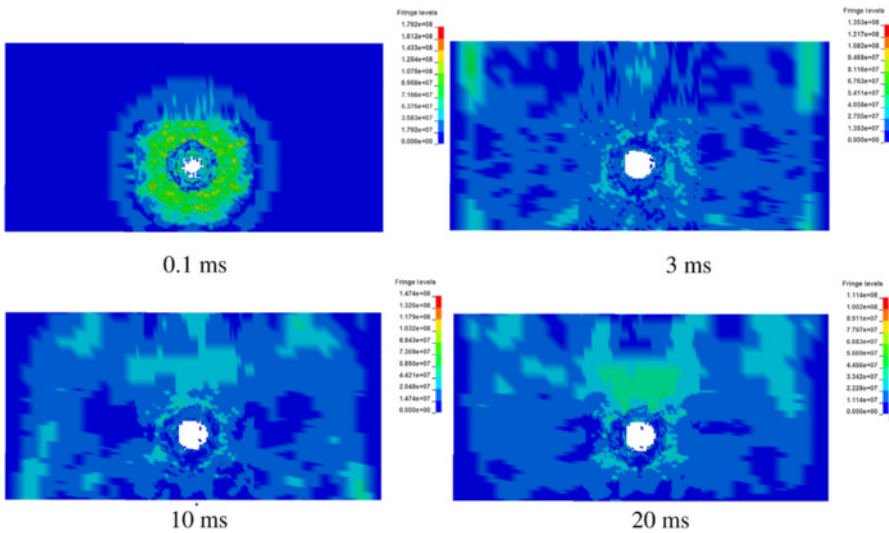
Figure 3.26 Slab UHPC top surface response.

On the distal face of the UHPC slab, concrete spall failure which is induced by the severe tensile wave propagation is again seen clearly as shown in Fig. 3.27. However, with the contribution from the steel fiber, the spall area is not as significant as seen on the NSC slab. It is worth noting that in this UHPC slab, no steel reinforcement is placed, and according to the previous study [5,51], with the inclusion of the steel reinforcement, the spall damage can be further mitigated.
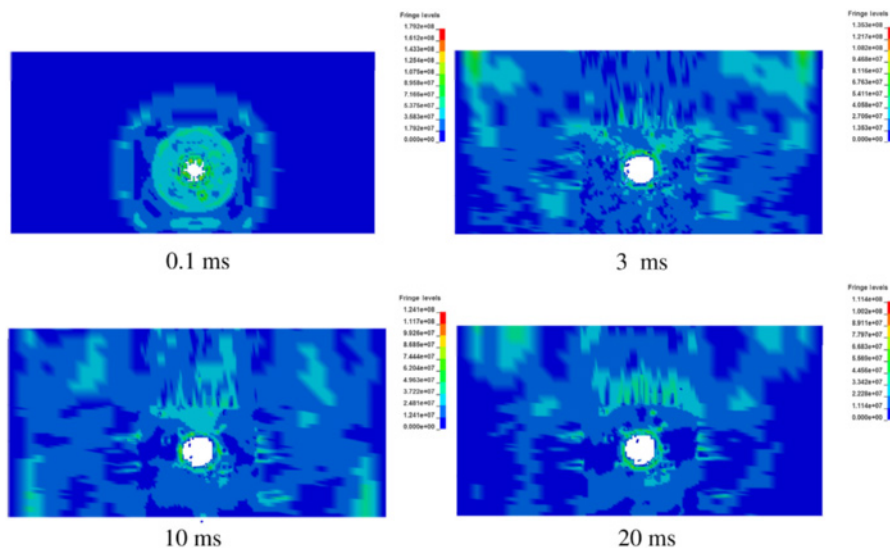
Figure 3.27 Slab UHPC bottom surface response.

Table 3.10 **Spall damage dimension comparison**

Slab	Damage diameters (mm)			
	Experimental top	**Experimental bottom**	**Numerical top**	**Numerical bottom**
NSC	390	710	360	700
UHPC	350	380	310	330

In the contact explosion tests, the minimum global flexural behavior was expected on the test slabs, thus no LVDT was installed on the slab for the deflection time history recording. Due to the lack of quantitative data of the test slab, only the failure mode and failure dimension are compared between the test slabs and numerical results, and the comparison is summarized in Table 3.10. It is noticed that the numerical method gives good prediction of the spall damage diameter. Again the superior blast-resistance capacity of UHPC slab is demonstrated.

3.2.2.4   Concluding remarks

In this section, experimental and numerical study are conducted on commercialized UHPC Ductal and NSC slabs under contact detonation. In NSC slab, severe concrete spallation is observed on the distal surface which is induced by the blast wave propagation. In UHPC slab, microsteel fibers effectively bridge over the crack and

retard the further expansion of the cracking, leading to confined spallation damage area. On the proximal surface, the compressive strength of the concrete material plays an important role in resisting the cratering under blast impact, and UHPC outperforms NSC with smaller damage area. The coupled SPH and FE method can well reproduce the structural response of NSC slab and UHPC slab under various blast loading conditions. The numerical results again demonstrated the superior blast-resistance capacity of UHPC material.

3.3 Investigation of ultra-high performance concrete slab and normal strength concrete slab under contact detonation

Following the study on commercial available UHPC material, in the subsequent chapters, more studies are conducted on the newly developed UHPC with nanomaterial modification.

3.3.1 Contact explosion tests on ultra-high performance concrete and normal strength concrete slabs

3.3.1.1 Explosive charges

TNT explosives with a thermal energy of $4521 \, \text{kJ} \, \text{kg}^{-1}$ and a density of $1.65 \, \text{g} \, \text{cm}^{-3}$ were used in the tests. Two major cylindrical charges with a mass of 0.1 and 1.0 kg were placed on the top center of the slabs. A detonator was wrapped to electrically activate the explosive charge. Fig. 3.28 illustrates the dimensions of the TNT explosives used in the tests.

3.3.1.2 Sample preparation

In total, seven slabs including two NSC slabs and five microsteel fiber-reinforced UHPC slabs were tested in the program. As shown in Fig. 3.29, the dimension of slabs is: 2000 mm long, 800 mm wide, and 100−150 mm thick. Slabs of different depths were designed to explore the depth influence on the mitigation of spall
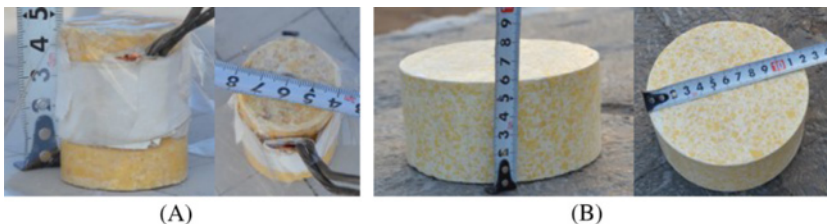
Figure 3.28 Cylindrical TNT explosives: (A) 0.1 kg and (B) 1.0 kg.
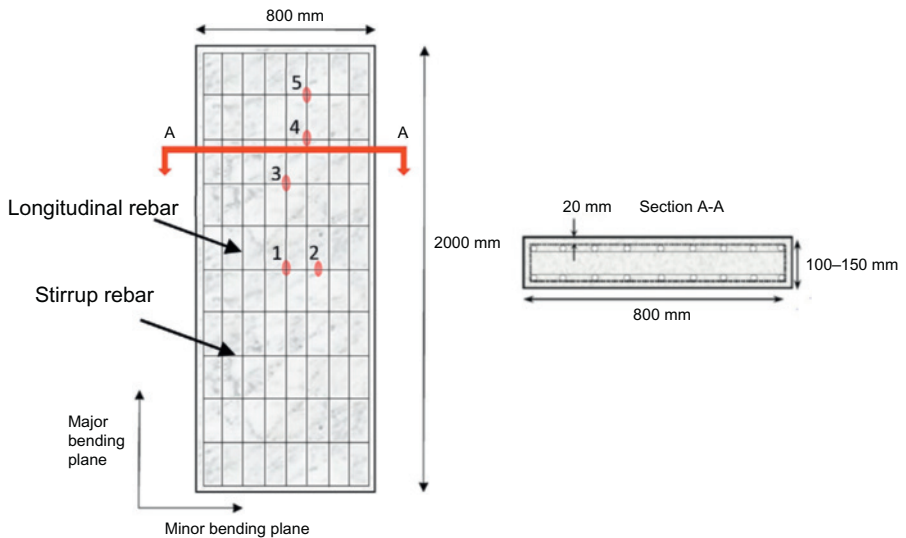
Figure 3.29 Slabs configuration.

damage. One of the five UHPC slabs was reinforced by less longitudinal reinforcement bars in which the rebar number in the compressive and tensile surface decreased from 9 each to 5. This modification was made to investigate the influence from longitudinal reinforcement spacing. The diameters of the longitudinal reinforcing rebar and stirrup rebar are 12 mm and 8 mm, respectively. Both of these two reinforcements are designed with 360 MPa yielding strength.

Two control NSC slabs were constructed by concrete with unconfined compressive strength of 40 MPa. UHPC with uniaxial compressive strength 145 MPa and tensile strength 22 MPa was used to build the UHPC slabs. For UHPC material, microsteel fibers with a length of 15 mm and diameter of 0.12 mm were mixed at a volume dosage of 2.5%, the tensile strength of the microsteel fiber is 4295 MPa. Typical stress−strain relationship obtained from uniaxial compression test and split tensile test are shown in Fig. 2.26 and Fig. 2.29, respectively.

During the sample preparation, strain gauges were attached to the reinforcement bars at different locations in each slab as indicated by red dots in Fig. 3.29. The positions where the strain gauges located were carefully grinded using electrical grinder, and later mopped using liquid acetone. These procedures were carried out to guarantee the contact between the strain gauge and reinforcing bar. These strain gauges were used to record the strain time history and the data obtained can be further used to derive the strain rate experienced by the slabs in each blast scenario.

3.3.1.3 Experimental setup

As depicted in Fig. 3.30, the slab was firstly placed on the steel rig using a crane, then both ends of the slab were bolt fixed with the angle steel cleats. In the previous

Steel support

Bolts and steel cleats
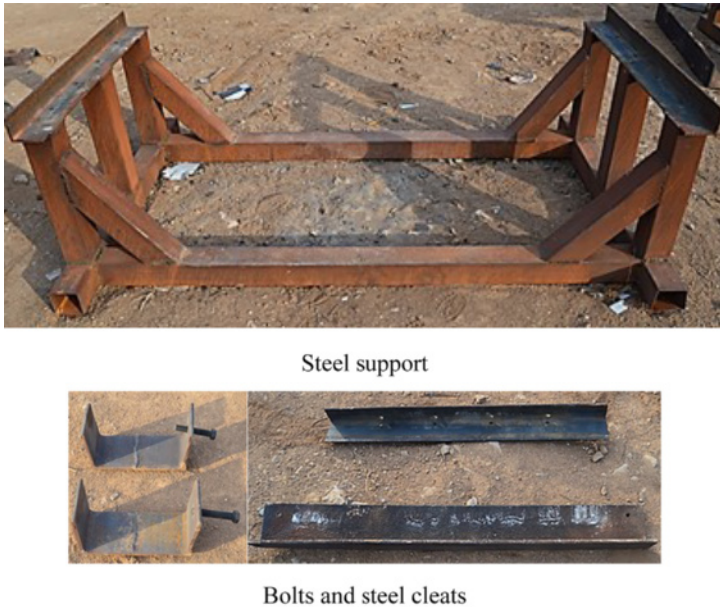
Figure 3.30 Supporting frame.

study carried out by Beppu et al. [52] and Ohkubo et al. [18], a simply supported boundary was adopted to study the contact explosion resistance of concrete slab reinforced with FRP laminates. It is deemed that contact explosion induces highly localized response and damage which is independent of the boundary condition.

3.3.1.4 Test program

In total seven shots were carried out in this study. In test events 1 and 2, two identical NSC slabs reinforced by 9 ϕ 12 mm longitudinal rebars and 11 ϕ 8 @ 200 mm stirrup rebars were subjected to contact explosions of cylindrical explosives of 0.1 kg and 1 kg, respectively, to obtain different levels of damages. In blast events 3 and 4, two UHPC slabs with the same reinforcements as the two reference NSC slabs were also subjected to the same blast scenarios in order to compare the blast resistances of NSC and UHPC slabs. The influence of the slab depth was investigated in blast events 4−6, in which three UHPC slabs with different thicknesses but the same reinforcements were subjected to 1 kg TNT contact explosion. To investigate the reinforcement mesh confinement effect on spalling damage, UHPC-7 slab in blast event 7 was made the same as slab 4 but with less number of the longitudinal reinforcements in both the compressive and tensile face, i.e., the number of longitudinal reinforcement bars is reduced to 5 from 9. The slab was also tested with 1.0 kg contact explosion. Comparison was made between UHPC-7 and UHPC-4 to investigate the influence of reinforcement mesh confinement effect on concrete crushing and spalling damages.

The test program is summarized in Table 3.11.

Table 3.11 **Test program**

Event no.	TNT charge weight (kg)	Slab specimen	Note
1	0.1	Normal (40 MPa) NSC-1	Depth 120 mm, 9 longitudinal rebar each side
2	1.0	Normal (40 MPa) NSC-2	Depth 120 mm, 9 longitudinal rebar each side
3	0.1	UHPC-3	Depth 120 mm, 9 longitudinal rebar each side
4	1.0	UHPC-4	Depth 120 mm, 9 longitudinal rebar each side
5	1.0	UHPC-5	Depth 100 mm 9 longitudinal rebar each side
6	1.0	UHPC-6	Depth 150 mm 9 longitudinal rebar each side
7	1.0	UHPC-7	Depth 120 mm 5 longitudinal rebar each side

3.3.2 Results and discussion

NSC-1 is a NSC slab with conventional steel reinforcement. Of note, 0.1 kg TNT was placed at the center of slab surface as shown in Fig. 3.31. After explosion, clear spall damage and concrete crater were observed on the bottom and top surfaces of the slab. The diameters of the concrete crater and spall were 20 cm and 33 cm, respectively. Neither perforation nor flexural damage was found at the slab mid-span.

In blast event 2, NSC slab NSC-2 was subjected to 1 kg TNT placing also at the center of slab surface. As can be noticed from Fig. 3.32, severe blast load induced perforation failure in the slab. Fracture happened on the central stirrup reinforcement. It is also noted that significant concrete cracking occurred along the two unsupported directions near the slab boundary. As no obvious slab deformation was observed, it was believed that these damages were also caused owing to stress wave propagation and reflection. Stress wave caused cracks along the two free ends because of the short propagation distance between the explosive and the free boundary, which generated large tensile stresses owing to wave reflection and hence cracking of concrete.

UHPC-3 was an UHPC slab with the same steel reinforcement as the two NPC slabs. Of note, 0.1 kg TNT was placed at the center of slab surface and detonated. After explosion, no spall damage was observed on the bottom surface of the slab, and a small concrete crater with a diameter of 90 mm and a depth of 27 mm was found on the top surface as shown in Fig. 3.33. Comparing with NSC-1 slab which has the same steel reinforcement and subjected to the same blast load, it is clear that UHPC material has much higher blast-resistance capacity.

Slab after test
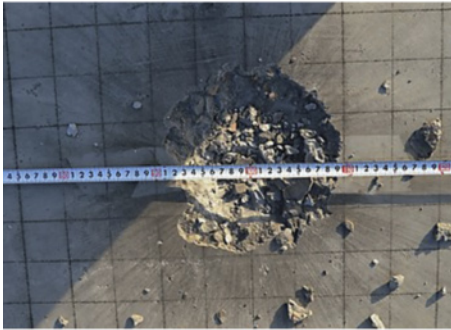
Top surface crater area diameter 200 mm　　　Bottom surface spall area diameter 330 mm

Figure 3.31 Blast event 1.

Top surface crater diameter 460 mm　　Bottom surface spall diameter 820 mm

Figure 3.32 Blast event 2.

UHPC-3 slab after test

Top surface concrete crater diameter and depth

Figure 3.33 Blast event 3.

UHPC-4 was tested with a 1 kg TNT detonated at its central surface. The slab was observed with spall and concrete crushing failure as shown in Fig. 3.34. Compared with NSC-2 slab under the same blast load, it was noted that UHPC-4 slab has better blast-resistance capacity. The top surface crater diameter and the bottom surface spall diameter were reduced from 460 and 820 mm to 230 and 450 mm, respectively. Moreover, no side concrete cracking as in NSC-2 was observed, and no reinforcement fracture was observed either. These comparisons clearly demonstrate the better blast loading resistance capacity of UHPC than normal concrete.

UHPC-5 was an UHPC slab with a depth of 100 mm. The reinforcements in the slab were kept the same as in the previous slabs. As shown in Fig. 3.35, subjected to 1 kg contact explosion, the slab suffered perforation failure. The stirrup and longitudinal reinforcements at mid-span were also fractured. Slight side concrete cracking which was similar to NSC-2 slab under 1 kg TNT was also noticed. Comparing with UHPC-4, the crater diameter and spall diameter both increased, indicating that slab depth played a positive role in resisting the contact explosion-induced damage, as expected.

Top surface crater diameter 230 mm   Bottom surface spall diameter 450 mm
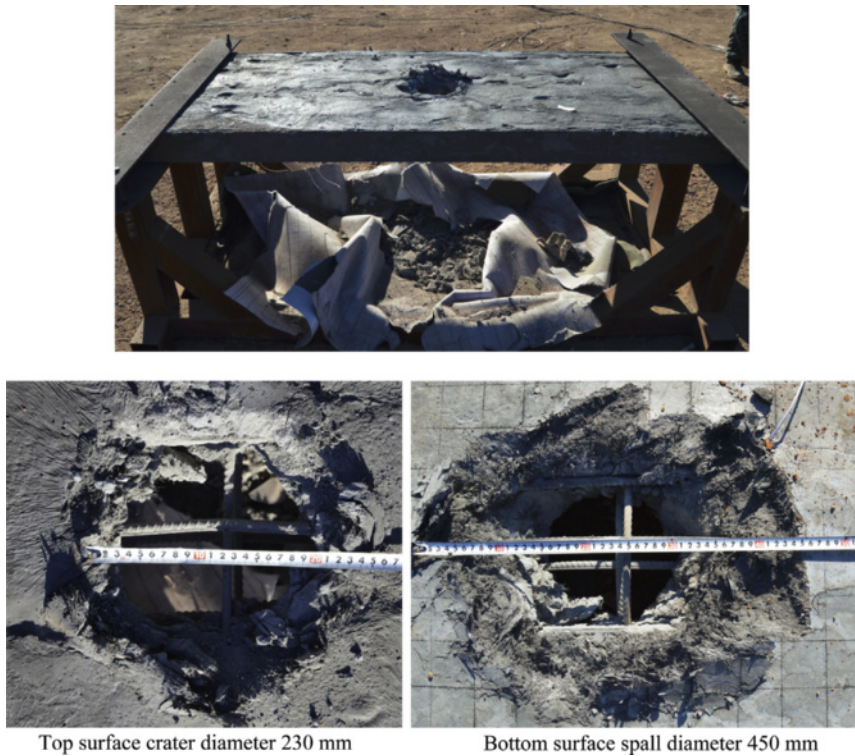
Figure 3.34 Blast event 4.

UHPC-6 was an UHPC slab with an increased depth of 150 mm subjected to 1 kg TNT contact explosion. Similar to the previous two trials, perforation failure was again observed as shown in Fig. 3.36. However the damage severity was reduced. Comparing with UHPC-5, the top surface crater diameter and bottom surface spall diameter dropped from 270 and 470 mm to 220 and 410 mm, respectively. Only one longitudinal rebar at the bottom side was fractured. No side concrete cracking was observed in this thicker slab.

As mentioned earlier, the UHPC-7 slab was made with less number of reinforcements. It was also subjected to the same 1 kg TNT explosion. After the test, severe perforation failure was observed as shown in Fig. 3.37. Comparing with UHPC-4, the top surface crater diameter and bottom surface spall diameter increased from 230 and 450 mm to 250 and 480 mm, respectively. Longitudinal reinforcement at mid-span experienced fracture failure that was not observed in UHPC-4. Generally speaking, the reinforcement mesh contributed to the resistance against the contact blast loads. However, in this particular case, the crater and spalling damage dimensions only slightly increased even when the number of reinforcement bars were almost reduced to half as compared to UHPC-4, indicating that the reinforcement confinement effect is not prominent. This observation nonetheless is based on only

UHPC-5 slab after 1 kg TNT contact explosion

Top surface crater diameter 270 mm

Bottom surface spall diameter 470 mm

Concrete scab

Side concrete scabbing
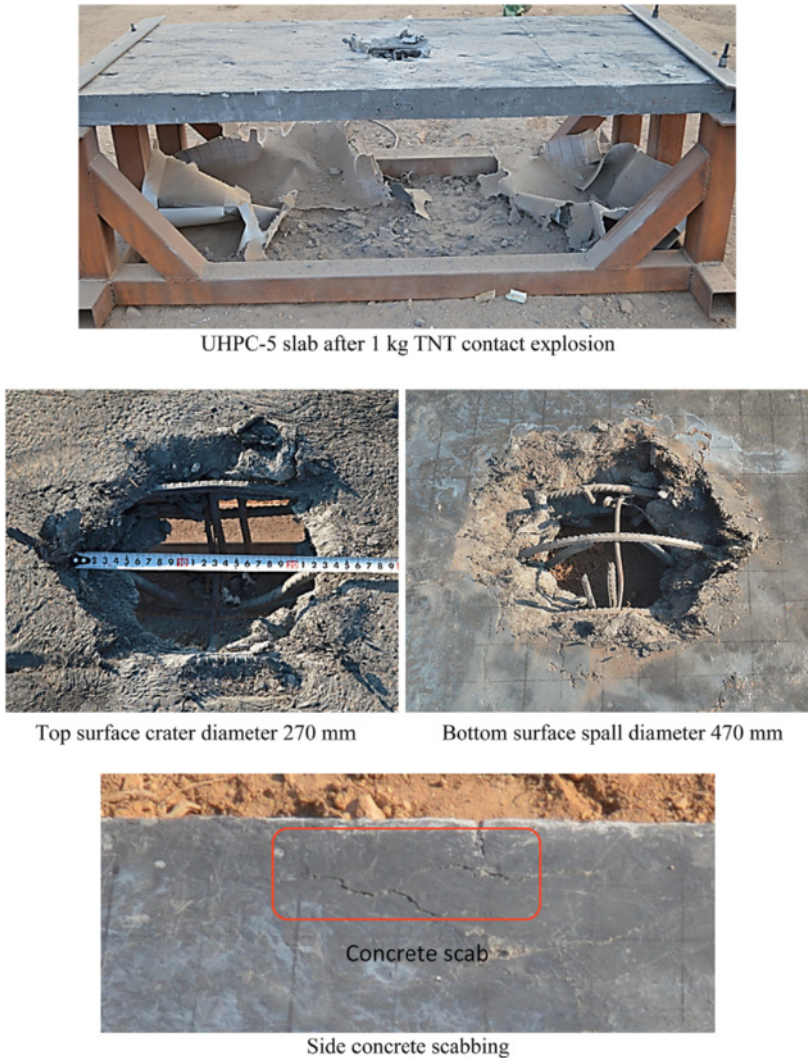
Figure 3.35 Blast event 5.

two types of reinforcement meshes. It is believed that if denser reinforcement mesh was used, its confinement effect on concrete would have been more prominent. More studies are deemed necessary to confirm and possibly quantify the reinforcement confinement effects on concrete materials subjected to blast loadings.

As observed from the earlier tests results, the failure modes of slabs under contact explosion can be classified into three categories, i.e., "crater only," "crater and spall," and "perforation." Table 3.12 summarizes the test results.

Fig. 3.38 shows the recorded strain time histories on refinement bars. It should be noted that no meaningful strain data were successfully recorded in slabs 3 and 5

UHPC-6 slab after 1 kg TNT contact explosion

Top surface crater diameter 220 mm   Bottom surface spall diameter 410 mm
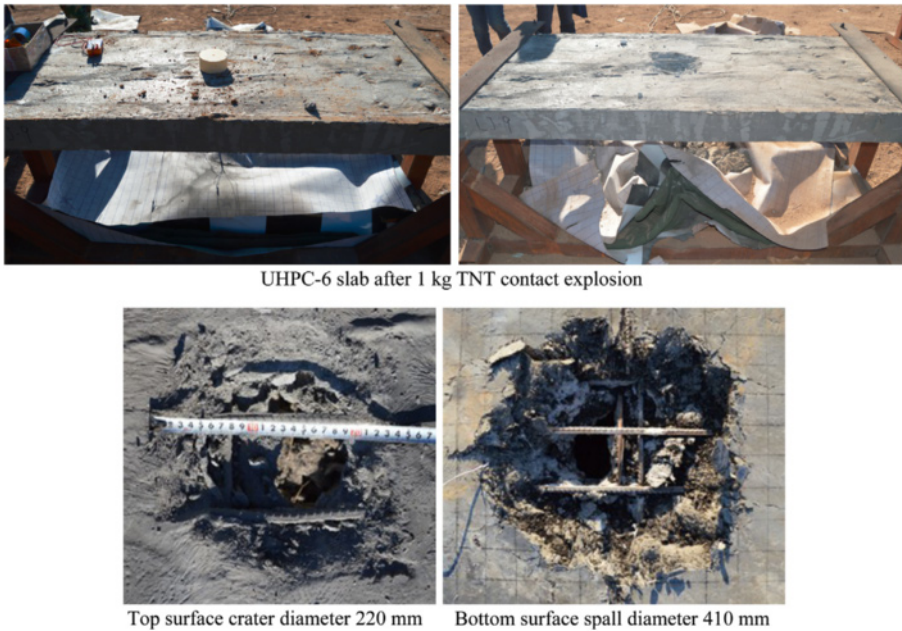
Figure 3.36 Blast event 6.

owing to malfunction of the sensor and/or equipment during these two tests. The strain time histories were recorded by resistance strain gauges provided by Jin-Li Sensor Company from China. The effective length of the gauge is 5 mm. The strain gauges were placed along the longitudinal direction of the rebars. Testing circuit was quarter-bridge strain gauge circuit with 2 V powering voltage and 100 amplification coefficient. The data were collected by high speed data collecting system TST5205 provided by Chengdu-Test company. The sampling rate was set at 1 million Hz in all the recordings.

Under contact explosion, the intense blast load is highly localized with extremely short duration. During the blast loading phase, the global structural response (shear and bending) is small because the time is too short for global structural response to develop. During the loading phase, explosion generates a stress wave propagating in the structure, which may cause concrete crushing and spalling damage, as observed in the tests presented in this study. After the action of blast loads, the structure continues to deform because significant explosion energy has been imparted into the structure and the global structural response modes and damage will be induced.

The measured strains as shown in Fig. 3.38 are associated with stress wave propagation in the initial stage and followed by global structural responses with lower frequency contents. Stress wave propagation results in rapid strain oscillations owing to wave reflection and refraction. The measured strain associated with stress wave propagation also decays quickly with respect to their distance to explosion. Taking NSC-1 as an example, the measured strain at gauge 1, which is buried
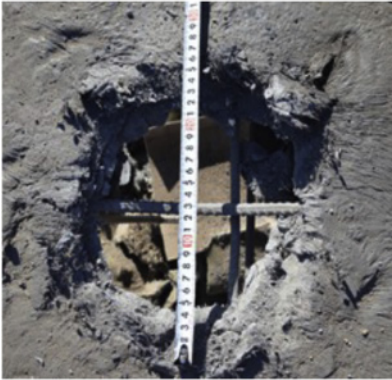
Top surface crater diameter 250 mm   Bottom surface spall diameter 480 mm
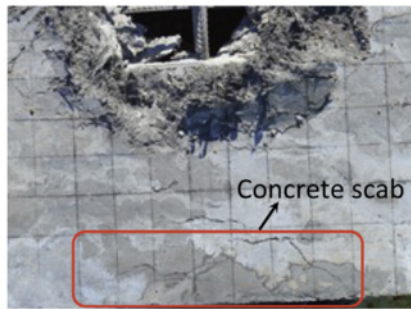
Concrete scab

Slight concrete scab

Figure 3.37 Blast event 7.

Table 3.12 Test results summary

Slab no.	Damage mode	Crater diameter (mm)	Spall diameter (mm)
NSC-1	Crater and spall	200	330
NSC-2	Perforation	460	820
UHPC-3	Crater only	90	0
UHPC-4	Perforation	230	450
UHPC-5	Perforation	270	470
UHPC-6	Perforation	220	410
UHPC-7	Perforation	250	480
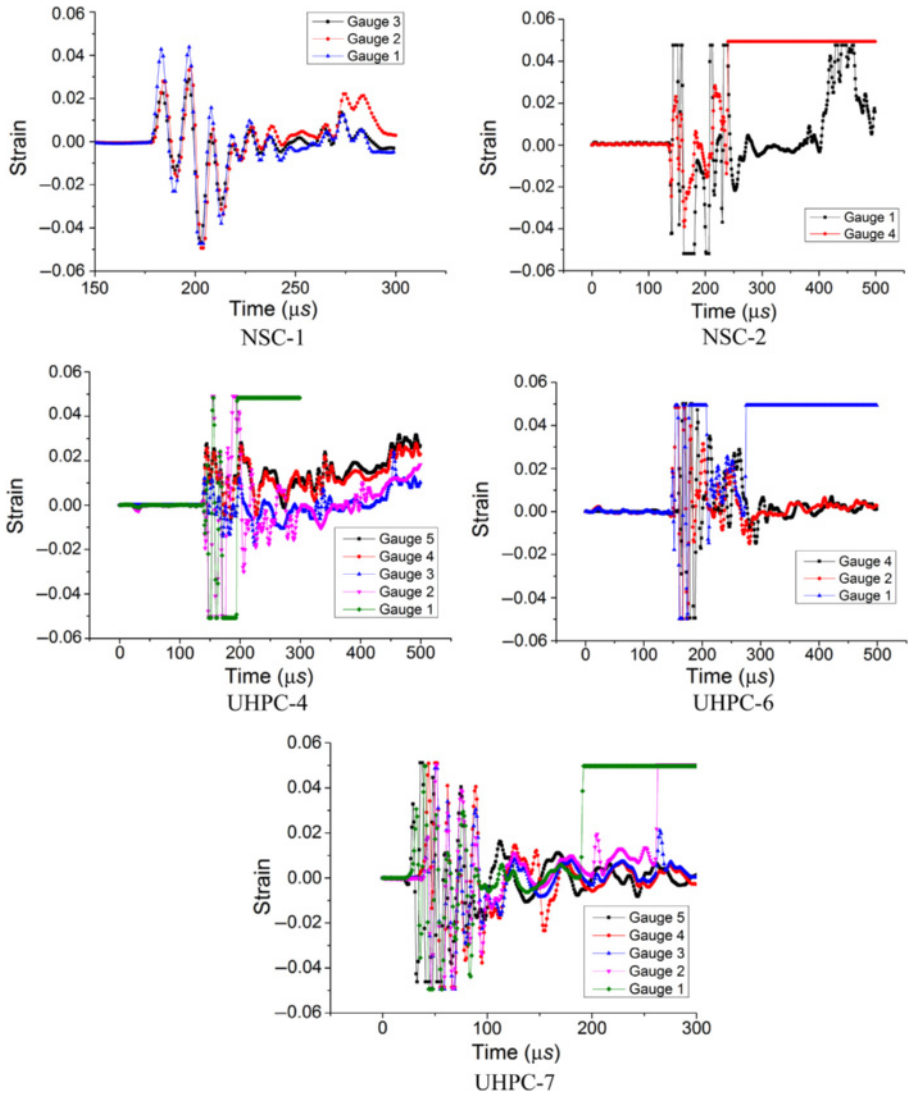
Figure 3.38 Strain time histories detected by the strain gauges.

directly underneath explosion, is larger than those at gauges 2 and 3. Moreover, the wave arrival time at gauge 1 is slightly earlier than that of gauges 2 and 3, which were placed further away from the explosion. These observations confirm that the measured strains are associated with stress wave propagation.

Some general observations can be made directly from these strain time histories. Firstly, comparing UHPC-4 with NSC-2, it is noted that the strain recorded in NSC-2 is higher than the strain obtained in UHPC-4, which indicates smaller deformation in the slab made with UHPC. Secondly, UHPC-6 with a depth of 150 mm has smaller strain in reinforcement bars as compared with data from UHPC-4,

indicating smaller deformation of thick slab as expected. Lastly, UHPC-7 with a sparse reinforcement spacing has higher strain as compared with data from UHPC-4, and this indicates that densely placed reinforcement can help to resist the contact explosion-induced slab deformation.

The strain rates in the all the tested slabs can be derived from the recorded strain time histories. In NSC-1, the explosive weight was 0.1 kg and the maximum strain rate reached $22,000 \text{ s}^{-1}$. When the explosive weight increased to 1.0 kg in NSC-2 slab, the maximum strain rate increased to $68,000 \text{ s}^{-1}$. For the UHPC slabs, strain rates around $50,000 \text{ s}^{-1}$ were noticed. These ultra-high strain rate values were caused because of contact explosions.

3.3.3 Failure predictions using existing methods

3.3.3.1 Theoretical prediction methods

Theoretical predictions on concrete spall damage is not straightforward because there are many unknown parameters and uncertainties such as the influence of charge geometry on blast loads, stress wave propagation, and attenuation rate in concrete, wave dispersion effects, dynamic compressive strength and tensile strength under high and varying strain rates. As a result, the existing theoretical methods have to be used with some assumptions and simplifications [12,13]. It was reported that [53] the theoretical methods do not necessarily give accurate predictions to concrete damage under close-in blast loads.

3.3.3.2 Empirical prediction methods

It is commonly acknowledged that empirical methods which are primarily based on large number of test trials are expensive to develop. Their application scopes are limited to situations similar to the data upon which the empirical methods were based.

In the widely used design guideline UFC 3-340-02, prediction of concrete spall under blast loading condition is discussed and spall test results have been compiled and plotted. Threshold spall and breach curves are plotted as approximate upper bounds to the spall and breach data points, and these curves may be used in practical analysis and design to approximately predict the concrete spall damage. However, it is noticed that the configurations in all these tests are different from this study and thus the empirical damage curves are not applicable for predicting the slab response in this study.

After reviewing test data from 334 field blast tests, McVay [5] compiled the test data and proposed empirical formulae to predict the local damage of concrete slabs subjected to bare explosive charges. As shown in Fig. 3.39, T is the slab thickness, R is the standoff distance, and for contact explosion, R is taken as one-half of the outer diameter of the cylindrical explosive charge, W is the charge weight, $T/W^{1/3}$ and $R/W^{1/3}$ are scaled slab thickness and scaled standoff distance, respectively. In McVay's method, the unit used is kg and m. Table 3.13 summarizes the corresponding parameters obtained from this study. After substituting these parameters
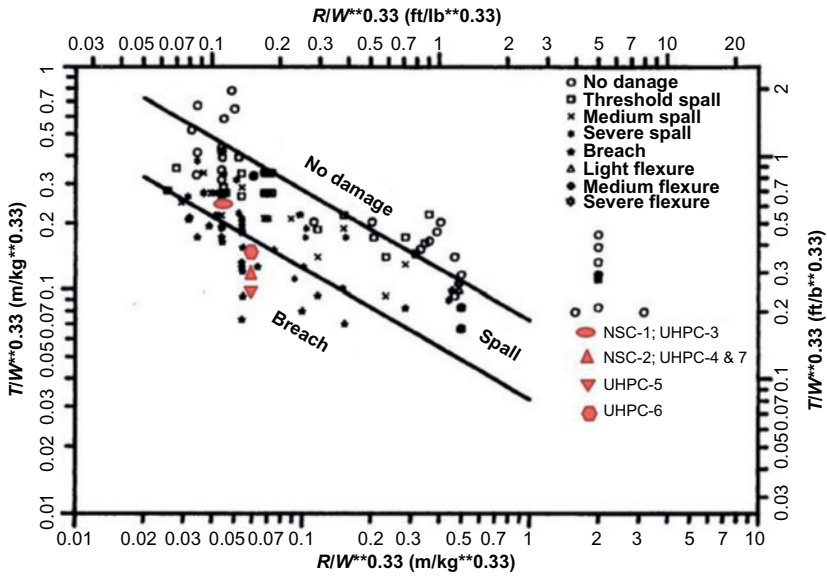
Figure 3.39 Empirical evaluations by McVay.

Table 3.13 Parameters for empirical predictions proposed by McVay

Slab no.	T	W	R	$T/W^{1/3}$	$R/W^{1/3}$
NSC-1	0.12	0.1	0.02	0.258532	0.043089
NSC-2	0.12	1	0.06	0.12	0.06
UHPC-3	0.12	0.1	0.02	0.258532	0.043089
UHPC-4	0.12	1	0.06	0.12	0.06
UHPC-5	0.1	1	0.06	0.1	0.06
UHPC-6	0.15	1	0.06	0.15	0.06
UHPC-7	0.12	1	0.06	0.12	0.06

into Fig. 3.39, it is noted that the empirical evaluation can give good prediction of spall damage of the two tested NSC slabs under contact explosion. For UHPC slab 3 which has the same scaled slab thickness and scaled standoff distance as NSC-1, empirical predictions derived by McVay underestimate its spall resistance capacity and give wrong prediction. For UHPC slabs 4 and 7, they have the same scaled slab thickness and scaled standoff distance as NSC-2; the observed spall damages, however, are substantially smaller, and these are not reflected from the empirical predictions. For UHPC slabs 5 and 6 with different slab depths as compared with NSC-2, empirical methods give sound predictions to the slabs perforation, however,

these predictions can still underestimate the performance of UHPC slab as these empirical methods are based on NSC and no control NSC slabs with the same dimensions were tested in this study.

Based on McVay's formulae and their own tests results, Morishita et al. [54] proposed new formulae to predict the contact explosion-induced concrete slab damage given as follows:

Limit of crater: $T/W^{1/3} > 3.6$ (3.6)

Limit of crater and spall: $2.0 \leq T/W^{1/3} \leq 3.6$ (3.7)

Limit of perforation: $T/W^{1/3} \leq 2.0$ (3.8)

The values of $T/W^{1/3}$ based on Morishita's method are given in Table 3.13 as well; the unit used in Morishita's formulae given above is cm/g$^{1/3}$. Applying the above formulae in this study, it is again noticed that although the NSC slabs damage modes are well predicted, the UHPC slabs performance are underestimated.

These comparisons demonstrate that the existing empirical methods, which were derived based on testing data on NSC slabs, can underestimate the performance of UHPC slab subjected to contact explosions. It should also be noted that these empirical predictions do not consider the influences of reinforcements, which certainly affect the spall damage of RC slabs. In future study, numerical tool will be adopted to investigate the UHPC slabs under contact explosions. The current test results will be used to calibrate the numerical model, and the verified numerical model will be used to conduct extensive contact explosion simulations.

3.3.4   Fragments distribution

Safety concern is always related with accidental explosions. The injuries under blast loading environment can be divided into five mechanistic types [55], in which secondary injuries induced by fragments under blast environment are of particular concerns.

- Primary injuries, which are mainly caused by excessive exposure to blast overpressure and likely to occur with thoracic organs and ears.
- Secondary injuries, which occur due to impacts from fragments of weapons and devices or from other structures such as containers or building components due to collapse.
- Tertiary injuries, which result from excessive blast overpressure that can throw the human body and cause skull fracture and whole body damage.
- Quaternary injuries, which take into account all the other types of injuries due to an explosion, such as flash burns, poisoning due to inhalation, and psychological trauma.
- Quinary injuries, which are caused by specific additives to the explosive device or munitions, such as bacteria and radiation.

As discussed well in the previous studies, contact explosion on brittle material like concrete can generate large number of fragments displacing from the material

surface at high velocities and these fragments are responsible for the human casualties and economic loss in those blast scenarios. It is thus important to investigate the fragment velocity, launching distance, and size distribution for concrete material. Unfortunately, the current test data only allow examining the fragment size distributions. Until now, although some work has been carried out identifying the fragments distribution of NSC material, no discussion or effort had been made to understand the size distribution of fragments from UHPC material under blast loading.

In this study, complete samples of fragments from both NSC slabs and UHPC slabs were collected and sieved. Six sieves with size range from 0.6 to 15 mm were used. The weights of fragments passing through each sieve had been measured as shown in Fig. 3.40.

Fragment samples of NSC and UHPC passing through each sieve are shown in Fig. 3.41. It is observed that fragments from NSC slabs have relatively more regular shapes, while the shapes of fragments from UHPC slab are more irregular due to the existence of the microfiber reinforcement.

A typical comparison between UHPC-4 slab and NSC-2 slab is made and shown in Fig. 3.42. As depicted in the figure, under the same blast loading condition, NSC slab generates more fragments than the UHPC slab and the fragments weight passing through every sieve level are all higher than the UHPC slab.

Under impact or blast loading condition, size distribution of fragments from brittle materials like rock and concrete is usually described by Weibull distribution which was suggested by Grady and Kipp [56]. Weibull distribution is suitable for handling characteristics of the cumulative distribution of fragment fractions. The cumulative density function is described by

$$P(<D) = 1 - \exp\left[-(D/D*)^n\right] \tag{3.9}$$

where $P(<D)$ is the cumulative weight percentage of all fragments with diameters smaller than D. The parameter D^* is defined as the scale parameter or characteristic

Figure 3.40 Sieve measurements.
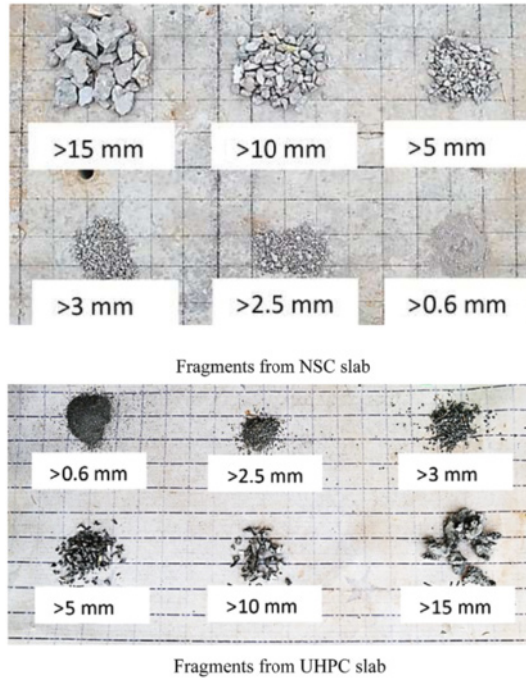
Figure 3.41 Samples of fragments with different sizes.
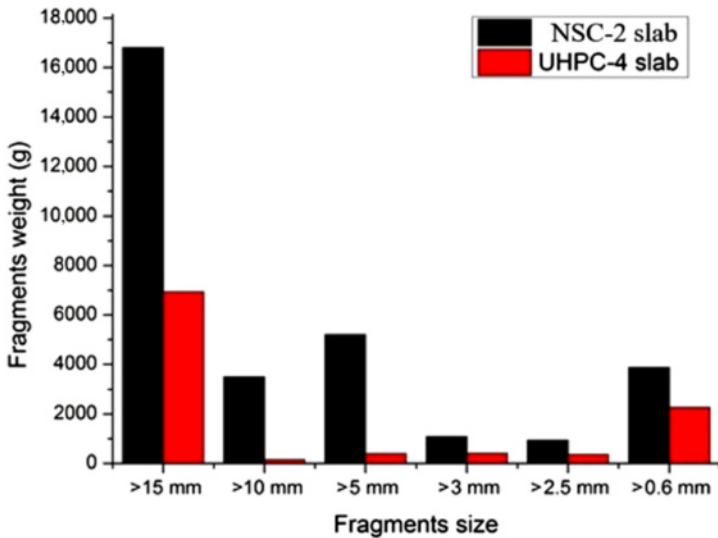
Figure 3.42 A typical comparison on fragments sizes.
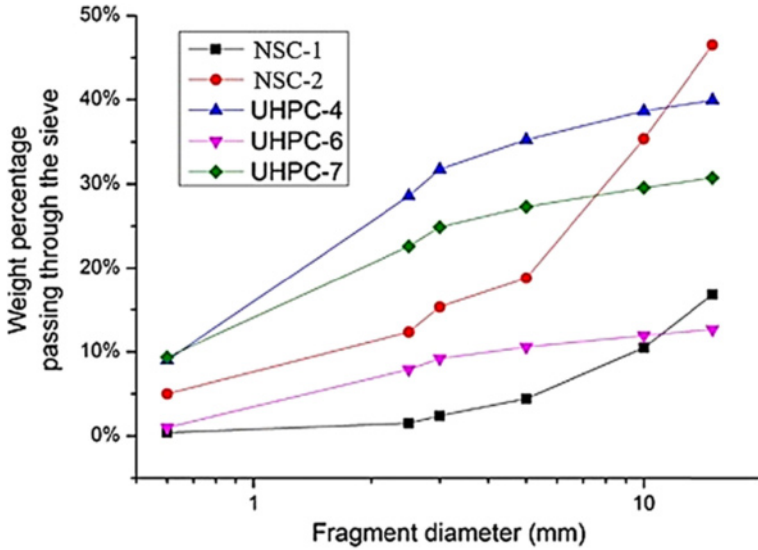
Figure 3.43 Size distribution of fragments from test specimens.

diameter which is referred to as the maximum mean diameter of the fragment, and *n* is a shape parameter which is referred to as the Weibull modulus.

Fig. 3.43 shows the standard size distribution of fragments from all the tested slabs except UHPC-3 and UHPC-5. Blast load only generated a small crater in UHPC-3 and no perforation. Therefore only very few fragments underneath the slab were collected. As shown in test results, blast flame caused fire which damaged the rug placed underneath the slab for fragments collection. This made the collection of fragments from UHPC-5 difficult. Therefore fragments from UHPC-3 and UHPC-5 are not included in the analyses here. It is obvious in Fig. 3.43 that the fragment size distributions from UHPC slabs differ from those from the two NSC slabs, indicating Weibull distribution is not a representative distribution type of the fragment sizes generated from UHPC slabs due to contact explosions.

Data from limited experimental observations suggested that the distribution parameter, i.e., *n* in Weibull distribution varies significantly. Direct impact experiments conducted by Shockey et al. [57] showed *n* with a range between 2 and 3. O'keefe and Ahrens [58] summarized fragment size distributions from nuclear and chemical explosions, and a value of *n* between 0.4 and 0.55 was noticed.

For the fragments generated from the contact explosion tests in this study, as depicted in Fig. 3.44, Weibull distribution with modulus of 1.63 and 0.67 can well represent the size distribution of fragments from NSC-1 and NSC-2 slabs. Residual sum of squares (R^2 values) are 0.976 and 0.95 for NSC-1 and NSC-2 slabs, respectively.
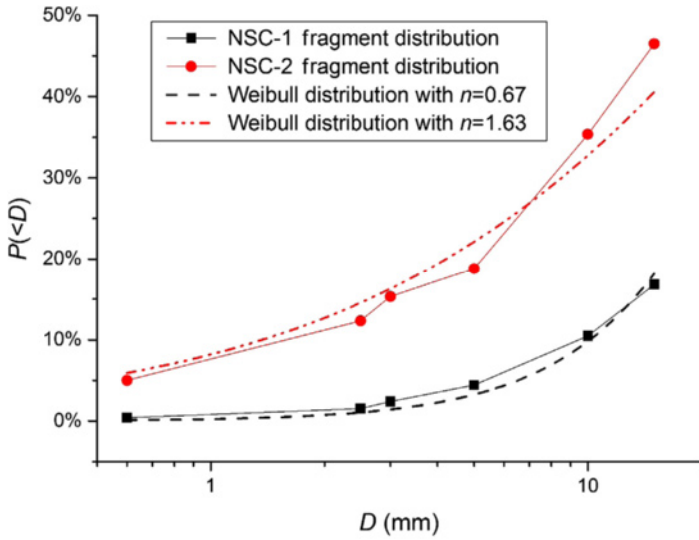
Figure 3.44 Weibull distribution for fragments from NSC specimens.
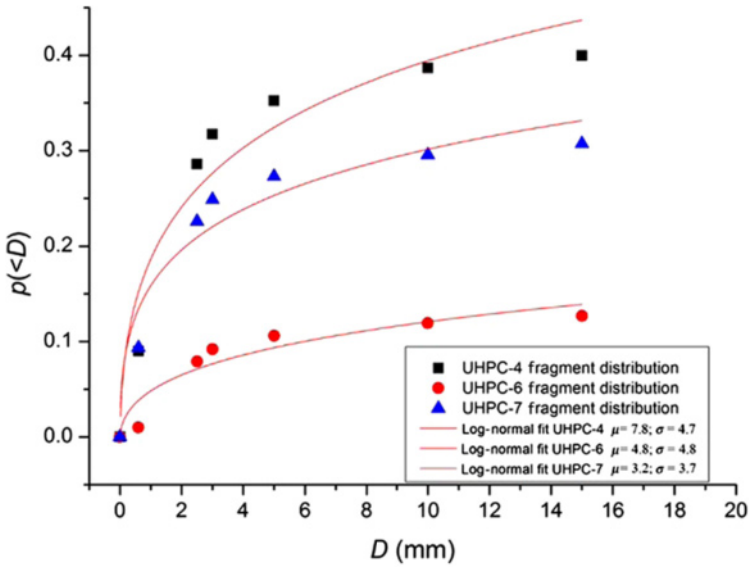
Figure 3.45 Log-normal distribution for fragments from UHPC specimens.

After careful examination, it is found that Log-normal distribution can well represent the size distributions of fragments from UHPC slabs. The cumulative distribution function is

$$P(<D) = \frac{1}{2}\left[1 + \text{erf}\left(\frac{\ln\ x - \mu}{\sigma\sqrt{2}}\right)\right] = \frac{1}{2}\text{erfc}\left(-\frac{\ln\ x - \mu}{\sigma\sqrt{2}}\right) = \phi\left(\frac{\ln\ x - \mu}{\sigma}\right)$$

(3.10)

where erf is an error function and erfc is the complementary error function, Φ is the cumulative distribution function of the standard normal distribution, μ is the location parameter, and σ is the scale parameter.

As depicted in Fig. 3.45, size distribution of fragments from UHPC slabs fits well the Log-normal distribution. Location parameters and scale parameters are plotted for each fitting. Residual sum of squares (R^2 values) are 0.89, 0.94, and 0.93 for UHPC-4, UHPC-6, and UHPC-7 slabs, respectively.

3.3.5   Conclusions

Concrete spall and crush are important damage modes under blast loading condition, and these phenomena become prominent when the explosives are detonated in close proximity to or in contact with the concrete structure. Concrete spall and crater cause severe loading capacity loss and fragments generated with spallation can eject from concrete surface with high velocity which will bring further threat to personnel and instruments shielded by the concrete structures. In this study, concrete slabs made with NSC material and UHPC material are tested under contact explosions. Spallation and cratering are observed and investigated quantitatively. UHPC slabs displayed significantly improved blast-resistance capacity than NSC slabs. Empirical methods developed based on large number of tests are adopted to evaluate the performance of slabs in this study and it is noted that these empirical methods can give good predictions on concrete spallation of NSC slabs but can significantly underestimate the spall resistance of UHPC slabs. Size distributions of fragments are investigated and it is noted that Weibull distribution can be used to represent the fragment sizes from NSC slabs, while fragments from UHPC slabs can be fitted to Log-normal distributions.

3.4   A study of concrete slabs with steel wire mesh reinforcement under close-in explosive loads

3.4.1   Material composition and mechanical properties

Table 3.14 summaries the material compositions for steel FRC used in this study. It can be noted that two steel FRC materials were developed. In the first material mix, steel fibers had a length of 6 mm and diameter of 0.12 mm (aspect ratio is 50). The fibers had a tensile strength of 4200 MPa, and the volume fraction in the mix design

Table 3.14 **Steel fiber-reinforced concrete composition (unit: kg m^{-3})**

Cement	Silica fume	Silica flour	Sand	Water	Superplasticizer	Steel fiber		Nano-CaCO$_3$
1155	437	178	823	305	40	230 for SFRC slab	153 for SWM-SF slab	57.8

was 3.0%. This material was used to cast the SFRC slab in the field blast test. In the second material mix design, steel fibers with 12 mm length and 0.12 mm diameter (aspect ratio is 100) were mixed at a volume fraction of 2.0%, the tensile strength of the fiber was 4200 MPa, and this fiber material was used to reinforce the protective layers of the SWM-SF slab.

In this study, nanoparticles nano-CaCO$_3$ was added into the concrete matrix at a constant volume fraction. Previous study in Chapter 2, Development, testing, and numerical simulation of ultra-high performance concrete at material level, revealed that addition of nanosize particles into the concrete matrix favors the material mechanical performance because nanoparticles provide nanoscale filling effect and prominent pozzolanic effect. The nanomaterial addition also improves the interfacial bonding between the fiber/SWM and concrete matrix.

3.4.2 Static tests on steel fiber-reinforced concrete

Quasistatic uniaxial compression tests were carried out on a number of 100 mm cubes using a 3000-kN capacity computer-controlled electromechanical servo hydraulic pressure testing machine. The testing procedure conformed to the Chinese Standard GB/T 50081-2002. Fig. 3.46A illustrates the testing setup. At both sides of the loading plate, there was an axially oriented linear variable displacement transducer (LVDT) to record the loading plate movement.

Fig. 3.46B shows the compressive stress−strain curves for the concrete material used in SFRC slab. In these samples, steel fiber had a length of 6 mm, diameter of 0.12 mm, and the volume fraction was 3.0%. An improved compressive strength of 83 MPa was achieved after fiber addition (vs 57 MPa obtained from the sample without fiber addition) and the material postpeak ductility was also enhanced significantly.

Four-point bending tests setup is shown in Fig. 3.46C, and beam samples with dimension of 400 mm × 100 m × 100 mm (effective span 300 mm) were tested under pure bending to study the material tensile performance. From Fig. 3.46D, it is noted that, flexural strength of the concrete composite with fiber addition reached 14 MPa which was much higher than conventional high strength concrete of which the flexural strength was around 2.5 MPa. SFRC also showed prominent postpeak tensile ductility.
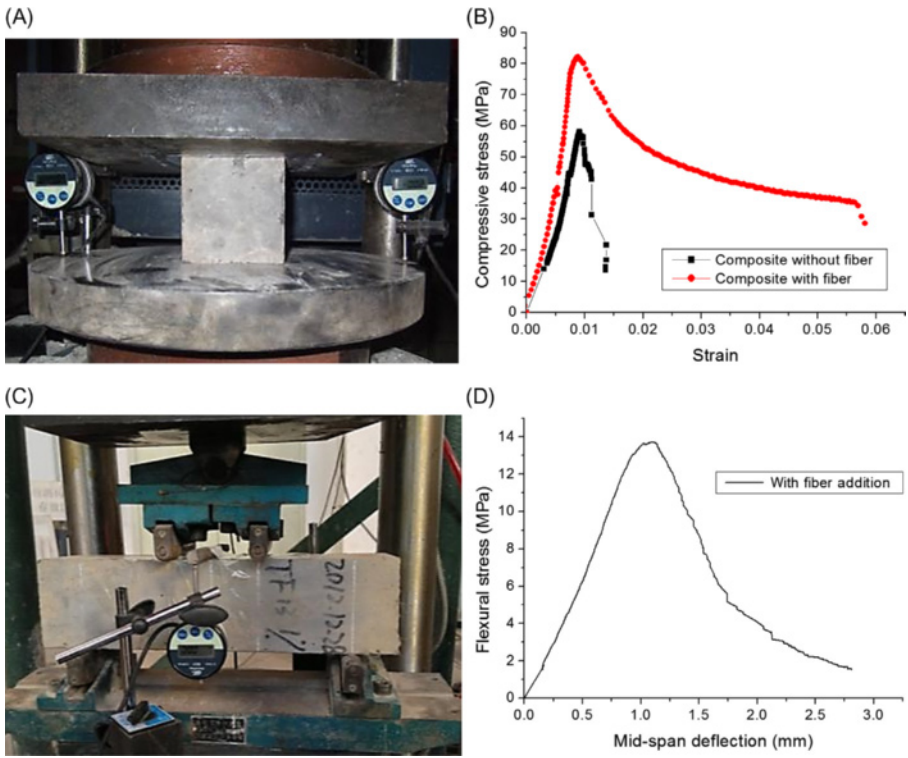
Figure 3.46 Static performance of concrete composite reinforced with 6 mm fiber 3.0% volume fraction: (A) uniaxial compression tests setup, (B) compressive stress−strain curve, (C) four-point bending tests setup, and (D) flexural strength.
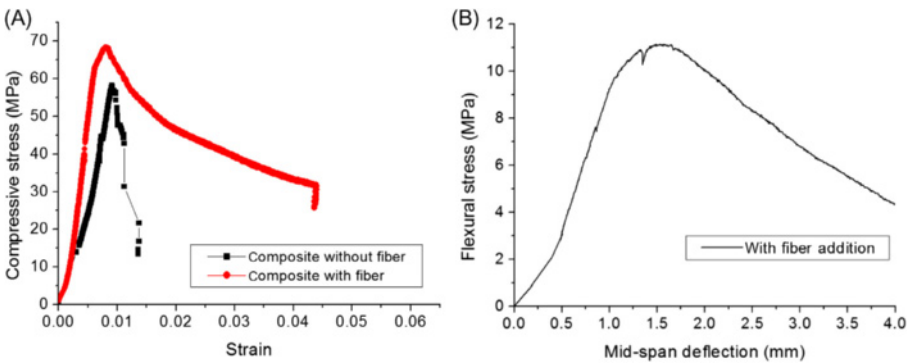
Figure 3.47 Static performance of concrete composite reinforced with 2.0% 12 mm fiber: (A) compressive stress−strain curve and (B) flexural strength.

Similarly, static material properties of SFRC used in the protective layer of SWM-SF slab are shown in Fig. 3.47. In this material composition, steel fiber had 12 mm length, 0.12 mm diameter, and 2.0% volume fraction. From the comparison shown in Fig. 3.46A, it is noted that this material achieved a higher compressive strength and better ductility when compared with unreinforced counterpart. However, the improvement was not as prominent as 6 mm fiber reinforcement at 3% volume fraction (as shown in Fig. 3.45B). Although material performance can be enhanced by either increasing fiber aspect ratio or fiber volume fraction, the effect from fiber volume fraction overweighted the fiber aspect ratio in this study.

As denoted in Fig. 3.47B, due to a lower fiber volume fraction (2% vs 3%), this material had lower flexural strength than previous composition shown in Fig. 3.46D (11.5 MPa vs 14 MPa). However, the material was equipped with better tensile ductility due to larger fiber aspect ratio (100 vs 50). When mid-span deflection exceeded 4 mm, the material preserved a flexural strength over 4 MPa.

Material static test results are summarized in Table 3.15.

Concrete samples after the static tests are shown in Fig. 3.48. Without fiber addition, failures of concrete in uniaxial compression and flexure bending tests were abrupt and catastrophic. The addition of fiber material confined and bridged over the concrete cracks, and therefore led to ductile material damage. Under external loads, the interaction between fibers and concrete matrix is mainly characterized as chemical bonding and frictional bonding, and the contact area significantly influences the fiber pull-out mechanism. In the present material tests, due to longer fiber embedding length of 12 mm steel fiber, the stress developed in the fiber material effectively transferred into surrounding concrete matrix under external loads. Therefore 12 mm 2.0% volume fraction FRC showed good material ductility and the sample developed multiple cracks in the flexural tests indicating good energy absorption capability.

3.4.3 Static tests on hybrid steel wire mesh-steel fiber-reinforced concrete beams

In the following experimental study, concrete beams with SWM reinforcement were studied under static flexural bending tests. As shown in Fig. 3.49A, these beam samples had a dimension of 400 mm × 100 mm × 100 mm with a protective

Table 3.15 Material static tests results

Material	Uniaxial compressive strength (MPa)	Flexural strength (MPa)
No fiber addition	57	2.5
SFRC with 6 mm fiber 3.0% volume fraction (in SFRC slab)	83	14
SFRC with 12 mm fiber 2.0% volume fraction (in SWM-SF slab)	69	11.5
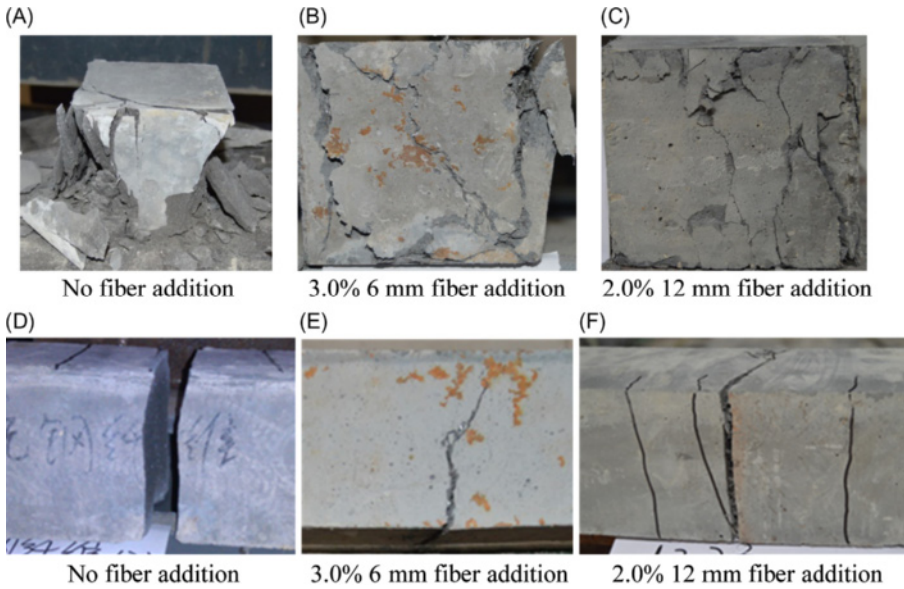
Figure 3.48 Concrete samples after static tests. (A)−(C) Uniaxial compression tests; (D)−(F) flexural bending tests.

layer of 10 mm thickness on both compressive and tensile surfaces. The spacing between loading points was set to be 1/3 of the beam effective span. Within the zone between the loading points, the specimen was subjected to pure bending. The mid-span deflection of the beam element was measured through a LVDT device.

In the intermediate layer of the beam sample, 20 layers of SWMs were embedded with uniform layer gap. In each mesh layer, the dimension of the SWM is illustrated in Fig. 3.49B. These wire meshes were made of 304 stainless steel with a tensile strength of 500 MPa. The ultimate strain of the SWM was 0.15.

Two series of the bending tests were conducted. In the first series, beam samples were solely reinforced by the SWMs in the intermediate layer, and in the second series, besides the SWM in the intermediate layer, 12 mm steel fiber with 2.0% volume fraction was used to reinforce the beam sample in the protective cover layer. The performances of beams from these two series were compared.

3.4.3.1 Steel wire mesh beam sample without fiber addition

In the first stage tests, no steel fibers were mixed in these beam samples, and only SWMs reinforcement was used in the intermediate layer of the beam sample. Fig. 3.50A−C shows the failure modes of the tested beams. As can be noted beams with high degree of reinforcement (20 and 30 layers) did not fail in the intended flexural mode but by shearing. The increment in the beam flexural stiffness outweighed the shear capacity increment, and therefore the beams' failure became
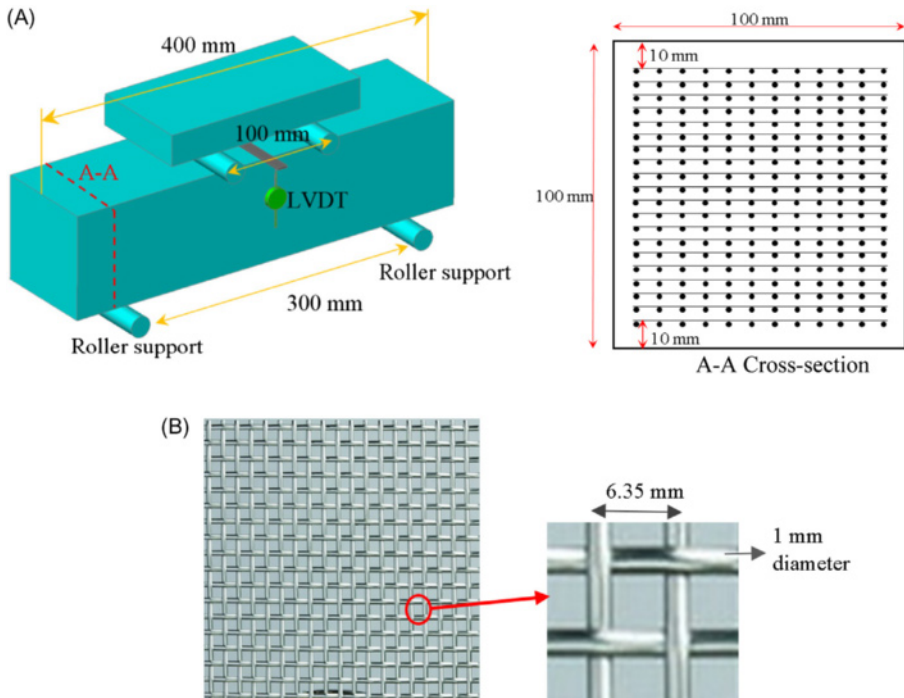
Figure 3.49 Setup of SWM beam sample tests: (A) beam dimensions and cross-section in bending tests and (B) SWM reinforcement dimension.

shear critical. It can also be seen from Fig. 3.50D that the beam with 10 layers of SWM reinforcement showed enormous plastic deformation. After reaching the elastic limit in the bending mode, the beam developed multiple cracks and deformed further before failure. However, heavily reinforced beams (20 and 30 layers of SWM) failed at significantly lower deflections. Both of them failed at lower external forces than the beam with 10 layers of SWM. In Fig. 3.50D, obvious drop in the load can be observed when the mid-span deflection reached 2.5 and 6 mm corresponding to the shear damage. The nonductile shear failure did not take full advantage of the element flexural capacity.

The earlier observations indicate that providing more layers of SWM might have an adverse effect. It may result in reductions in both the load-carrying capacity and ductility. Similar observations were also made by other researchers based on experiments on commercially available SWM RC structure. Adding more SWMs changes the failure mode of the beam from flexural failure to shear failure. Premature shear failures were observed even on slender concrete beams reinforced with SWMs. These results indicate that improvement on the shear capacity of the SWM RC structures is critical for its practical applications.
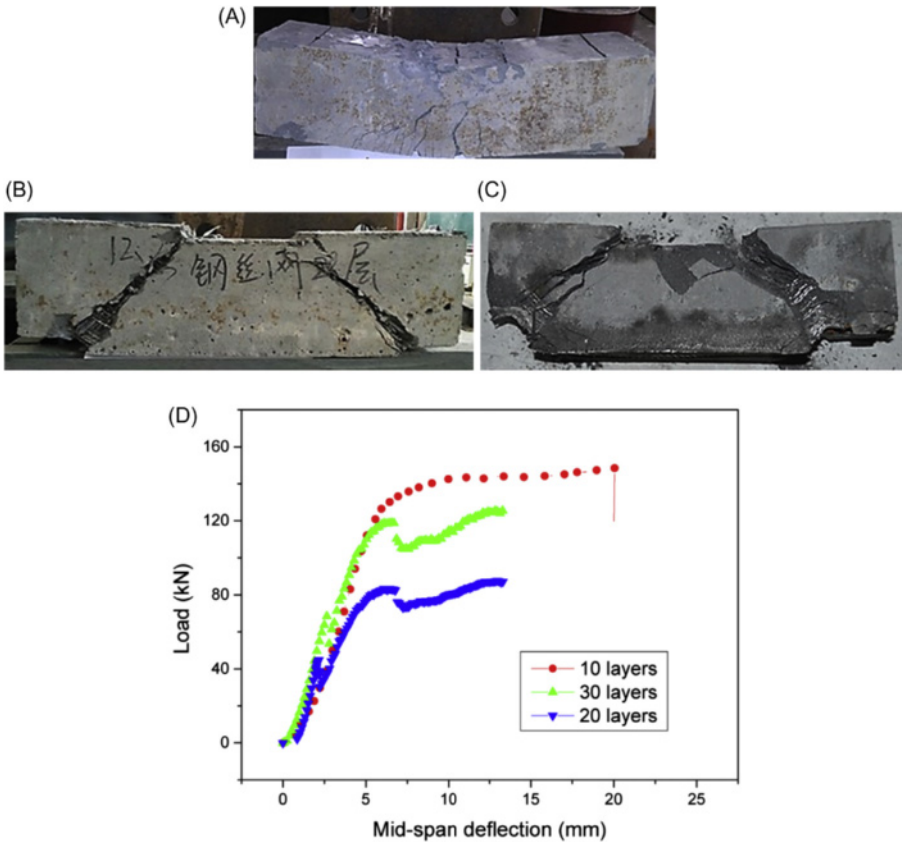
Figure 3.50 Four-point bending tests on beam samples: (A) beam with 10 layers of steel wire mesh, (B) beam with 20 layers of steel wire mesh, (C) beam with 30 layers of steel wire mesh, and (D) force versus mid-span deflection curves.

3.4.3.2 Steel wire mesh beam samples with fiber addition

With fiber material addition into the protective cover layer of beam with 20 layer SWM reinforcement, flexural bending tests were carried out to investigate the flexural tensile performance of hybrid SWM-SF reinforced beam sample.

On contrary to the previous test results, the improved material performance resulted in the desired flexural failure of the beam as shown in Fig. 3.51A,B, and the sample sustained much greater mid-span deflection with excellent crack control. From the force−deflection curves shown in Fig. 3.51C,D, it can be straightforwardly calculated that the new composite beam has an improved flexural tensile strength, and the energy absorption capacity was more than four times higher than the beam sample made of concrete material without microfiber strengthening the cover layers.

Generally speaking, adding steel fibers mixture into SWM slab provided several benefits. With addition of the microsteel fibers into the high strength self-compacting
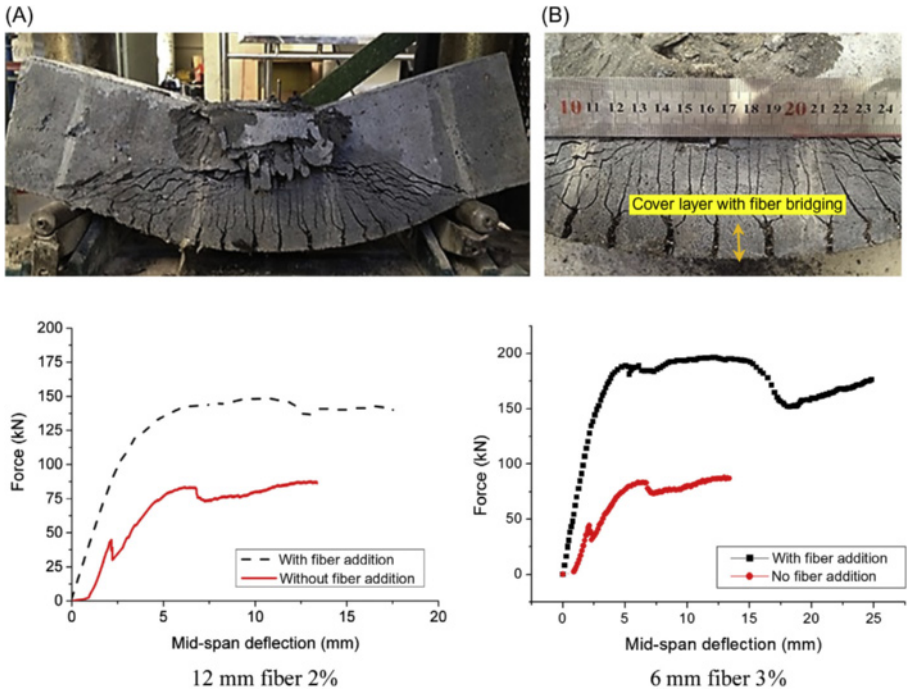
Figure 3.51 Four-point bending tests on 20 layers steel wire mesh-reinforced samples with and without fiber addition. (A-B) Flexural failure on the sample; (C-D) Force-displacement curve.

Table 3.16 Beam samples with different reinforcements under flexural bending

Beam sample	Ultimate flexural load (kN)
Steel wire mesh reinforcement	85
SWM-SF reinforcement 12 mm fiber 2%	150
SWM-SF reinforcement 6 mm fiber 3%	190

concrete, the composite receives enhanced compressive and tensile strength, good anti-abrasion, and energy absorption capacity. Due to the microbridging effect from the fiber material, after initial cracking, the stress is allowed to transfer from concrete matrix to fibers which significantly reduces the crack propagation [59].

Test results of beam sample tests are summarized in Table 3.16.

3.4.4 Field blast tests on reinforced concrete slabs

To further investigate the effectiveness of hybrid SWM-SF reinforcing scheme, field blast tests were carried out. As shown in Fig. 3.52, all the slabs designed for
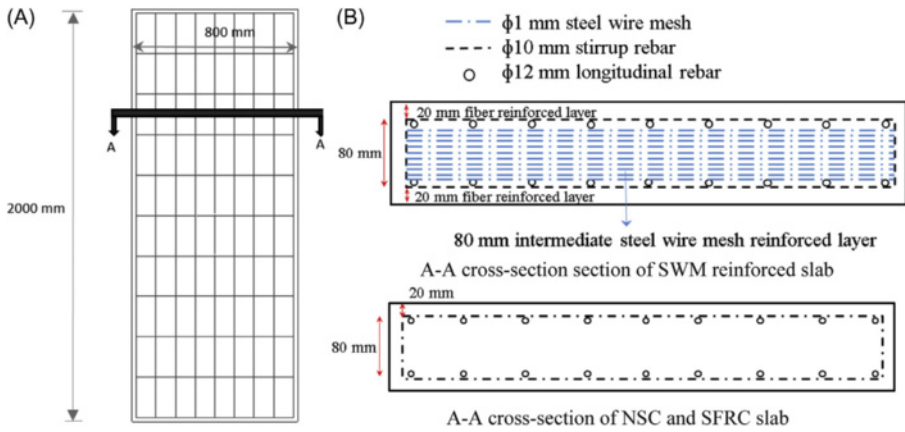
Figure 3.52 Dimension and reinforcement of slabs in contact explosion test: (A) slab dimension and (B) slab cross-section with different reinforcement.
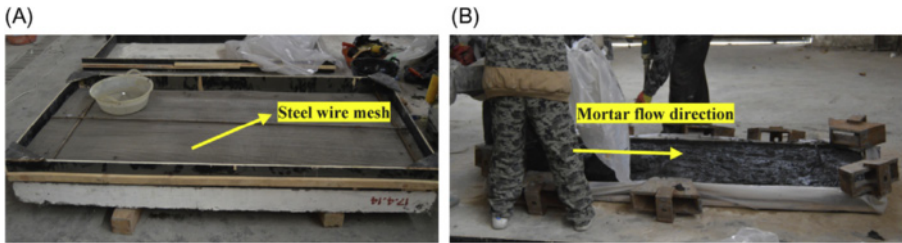
Figure 3.53 Slab preparation: (A) SWM reinforcement in the slab and (B) mortar flow in slab casting process.

the blast tests were cast with the same size, i.e., 2000 mm long, 800 mm wide, and 120 mm thick. The diameters of the longitudinal rebar and stirrup rebar were 12 mm and 10 mm, respectively. The yielding strengths for the longitudinal rebar at the proximal and distal surfaces were 270 MPa and 960 MPa, respectively. The stirrup reinforcement had a yielding strength of 270 MPa. A reference concrete slab made of conventional concrete with compressive strength 40 MPa was also prepared as a control specimen. In total, 20 layers of the SWMs were placed in the intermediate layer of the slab, while 12 mm fiber at 2% was mixed in the slab protective layer.

During the construction of the SWM-reinforced self-compacting concrete slab, the liquid self-compacting mortar was poured into a wooden mold with SWM cage (Fig. 3.53A and 3.53B). Due to the high flowability of the self-compacting mortar, no vibration and compaction plus leveling of the surface were required. When constructing the protective cover layer, the FRC mortar was poured from the edge of the slab and the mortar flowed along the slab length direction due to gravity. This kind of casting method influenced the fiber orientation [60,61] and most of the

fibers would be positioned horizontally in the protective layer leading to a better flexural performance under external loads.

3.4.4.1 Field testing setup

The material properties and static performance of both the SFRC and the SWM RC were obtained from the earlier static experiments. Outstanding compressive and tensile properties as well as improved energy absorption capability were noted from the results. In the following study, field blast tests were designed and carried out. Blast resistances of these slabs under close-in detonations were observed and compared with each other.

Testing apparatus and TNT explosive used in the close-in explosion are shown in Fig. 3.54A. Bolts clamping system was used to stabilize the slab during the tests. Due to low blast resistance of NSC slab, an 8 kg TNT explosive was adopted in the test scheme, while a 12 kg TNT explosive was designed for both the SFRC and SWM-SF reinforced slabs. The standoff distances in these cases were set as 1.5 m, and the scaled blast distances were 0.75, 0.655, and 0.655 m kg$^{-1/3}$ for NSC slab, SFRC slab, and SWM-SF slab, respectively. A linear variable displacement transducer (LVDT in Fig. 3.54A) was installed on the distal surface of the slab to acquit the slab deflection time history.

It is worth noting in this study that cylindrical TNT explosives were used in the tests with its axis perpendicular to the slab surface (see Fig. 3.54B). The charge shape and orientation were found to play important roles in the blast peak pressure and impulse distribution [62,63]. In the case of cylindrical charges with length-to-diameter (*L/D*) ratio greater than 1, the overpressure is the highest in the radial direction. By contrast, for *L/D* ratios lower than 1, it is the highest in the axial direction. In this
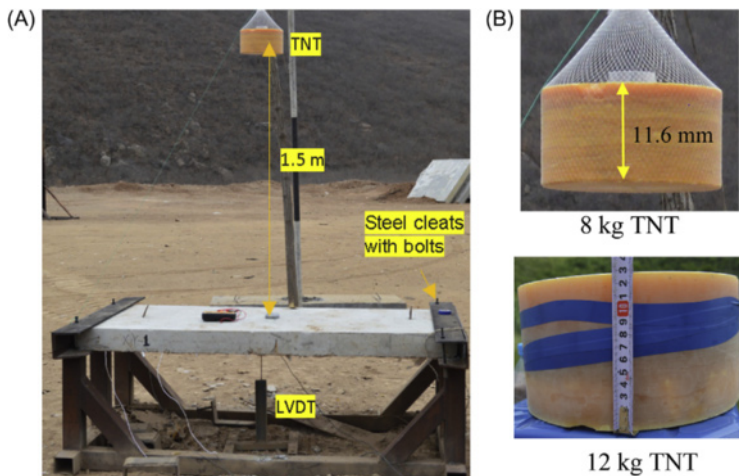
Figure 3.54 Close-in detonation setup and clamping system: (A) testing system and (B) TNT explosives.

Table 3.17 **Field blast test matrix**

Slab no.	Cylindrical TNT charge weight (kg)	Standoff distance (m)	Scaled distance (m kg$^{-1/3}$)
SFRC slab	12	1.5	0.655
SWM-SF slab	12	1.5	0.655
Normal strength concrete slab ($f_c = 40$ MPa)	8	1.5	0.750
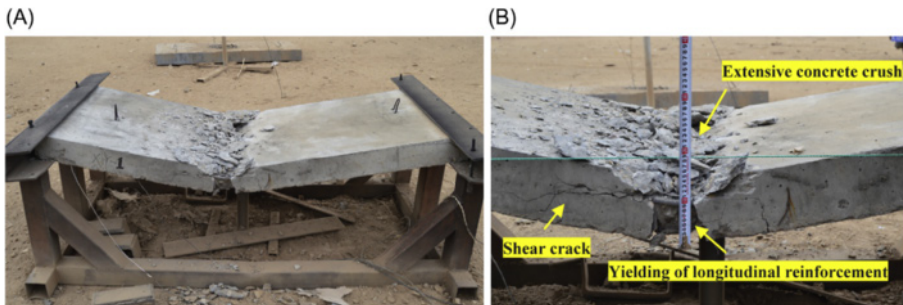
Figure 3.55 NSC slab after 8 kg TNT detonation from 1.5 m standoff distance: (A) NSC slab damage profile and (B) measurement of the permanent deflection.

study, cylindrical explosives with L/D ratio equal to 0.5 were used and the explosives were detonated from the center of the top surface, therefore the blast effect in the axial direction pointing downward should be larger. In the previous tests concerning the shape and orientation of the explosive, it was found that, for the cylindrical charge with the axis oriented vertically, the reflected pressures were highly directional, and the peak pressures were constantly larger than the empirical values given by UFC 3-340-02. A discussion on the blast pressure is presented later in the numerical study.

A summary of the field blast test matrix is shown in Table 3.17.

3.4.4.2 Close-in detonation testing results

Fig. 3.55 shows the NSC slab after 8 kg TNT detonation at 1.5 m above the slab center, and the slab failed completely with a permanent deflection of 190 mm which was manually measured after the test. Although some shear cracks can be observed, the failure of the NSC slab was predominantly flexure with a major crack in the slab mid-span. After the blast load impinged upon the slab, tensile crack was initiated on the slab distal surface. With the increase of the slab deflection, longitudinal reinforcement started yielding and the slab failed after concrete crush on the slab proximal surface.

Fig. 3.56 shows the SFRC slab after 12 kg TNT detonation at 1.5 m standoff distance above the slab center. Despite being under an increased blast load, SFRC slab experienced flexural deformation with a ductile damage mode. A permanent deflection of 70 mm was measured at slab mid-span which was even smaller than that
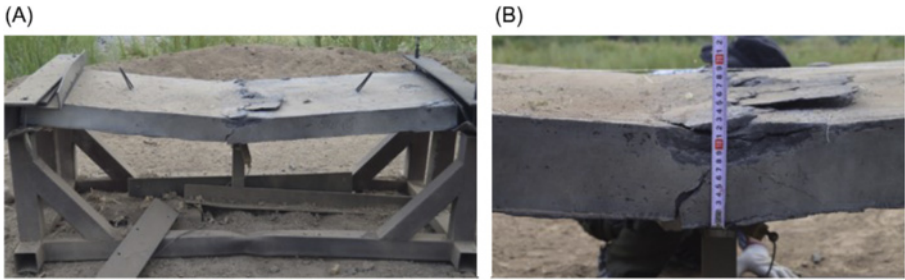
Figure 3.56 SFRC slab after 12 kg TNT detonation from 1.5 m standoff distance: (A) SFRC slab damage profile (B) and measurement of the permanent deflection.
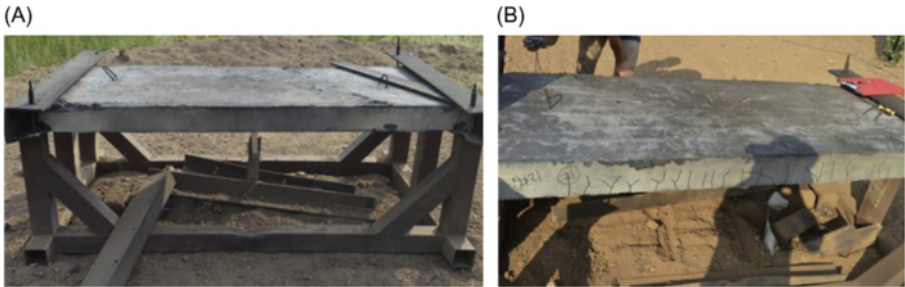
Figure 3.57 SWM-SF slab after 12 kg TNT detonation from 1.5 m standoff distance: (A) SWM-SF slab after test and (B) crack distribution on the slab.

observed on the NSC slab. When flexural deflection occurred, steel fibers effectively bridged over the cracks and retarded crack propagation. A certain amount of blast energy was consumed by fibers extension and pull-out from the concrete matrix. Similar to the NSC slab, concrete crush on the top surface was also observed and such failure was caused by the formation of the plastic hinge.

Performance of SWM-SF reinforced slab is shown in Fig. 3.57. The slab responded in a flexural mode with almost no permanent deflection after the test. Hairline cracks were observed from the side of the slab which indicated the slab experienced flexure greater than the cracking capacity; however, as only hairline cracks were present, it can be assumed that the internal moment was approaching, but did not reach the yield moment capacity. It was also noted that these cracks were widely distributed along the slab major bending plane. This kind of extensive crack distribution was different from the NSC slab and SFRC slab in which the cracks concentrated in the mid-span. It is believed that the SWM reinforced the slab in both the major and minor bending planes, and they significantly enhanced structural bending and shearing strength. The cracks in the covering area were further confined by the steel fiber material. Upon slab interaction with the blast load, a uniform deformation occurred on the slab and large amount of the blast energy was consumed by the deformation of SWMs.

The effect of the different reinforcement schemes can also be observed from the slabs distal surface cracks. As shown in Fig. 3.58, NSC slab had multiple cracks
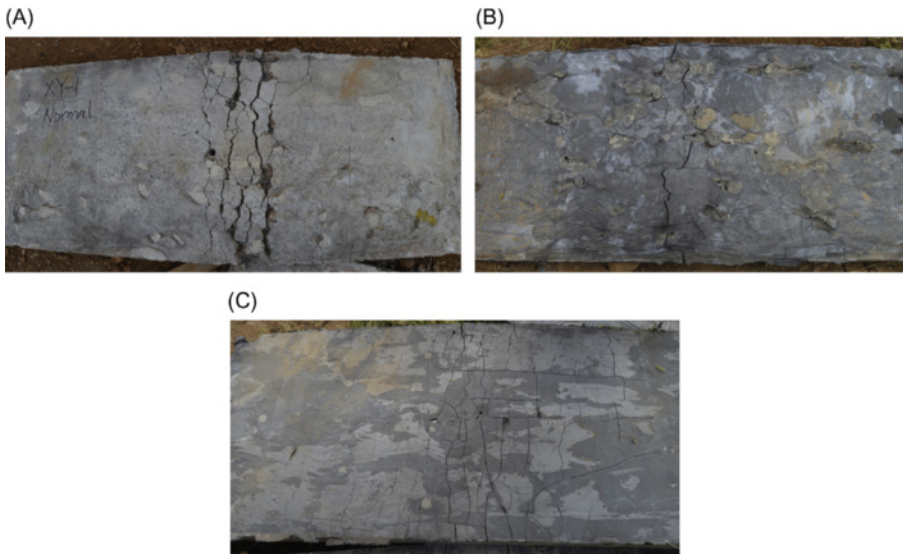
Figure 3.58 Damages on the distal surface of the slabs after blast tests: (A) NSC slab 8 kg 1.5 m, (B) SFRC slab 12 kg 1.5 m, and (C) SWM-SF slab 12 kg 1.5 m.

localized in the mid-span, and the crack opening size was larger than 20 mm. Small area of concrete peeling was observed and such failure can be possibly caused by the severe stress wave propagation. On the back surface of SFRC slab, no concrete spallation was noted and only one major crack was observed, and the cracking width is less than 8 mm. The SWM-SF slab had much smaller crack opening (less than 3 mm), and the cracks distributed in a wide range. The SWM developed localized membrane effect when small slab deflection occurred; although such effect improved slab resistance, difference in the tensile strain capacity of the SWM and concrete material caused the cracks and the possible debonding between the SWM and concrete matrix.

3.4.5 Numerical study of slab response

To better understand the blast load distribution and also the behavior of slabs under close-in blast loads, numerical models are established in commercial hydro-code LS-DYNA to reproduce the field blast tests.

For close-in free air test simulation, the explosive shape is known to have a significant influence on the blast load distribution, and to account for such influence, TNT explosive is explicitly modeled in the subsequent numerical simulation. A coupled algorithm involving MMALE and Lagrangian formulations is adopted. As shown in Fig. 3.59, the explosive and air are explicitly modeled with arbitrary Lagrangian−Eulerian elements while slab is modeled in Lagrangian elements. The blast wave propagation and interaction with the slab is modeled with
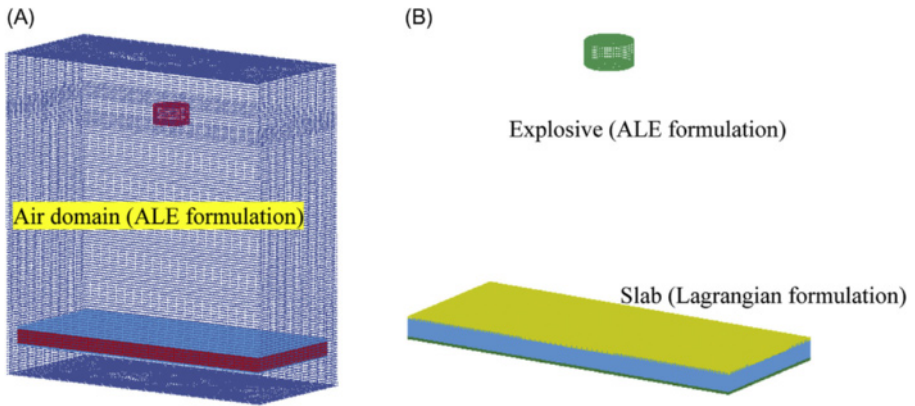
Figure 3.59 Numerical model of slab against blast load: (A) numerical model of TNT, air, and slab and (B) numerical model of TNT and slab.

fluid-structure interaction which is realized based on *Constrained_Lagrange_in_Solids function in LS-DYNA.

Mat_High_Explosive_Burn with EOS_JWL is adopted to model the TNT explosive, Mat_Null with EOS_Linear_Polynomial is used to model the ambient air. To mitigate the boundary effects, the air domain has a larger dimension than the slab, and the slab is engulfed within the air. The boundary of the air domain is set as nonreflecting boundary to avoid any wave reflection.

Material models and parameters used in the simulation of SWM-SF slab against blast loads are summarized in Table 3.18. For SFRC slab, the concrete is homogeneous material modeled with *Mat_Elastic_Plastic_Hydrodynamic, and the input effective stress−plastic strain curve is obtained from compression tests. For NSC slab simulation, *Mat_Concrete_damage_REL3 is adopted with single compressive strength $f_c = 40$ MPa input to model the concrete material. All the other parameters including the steel material, TNT explosive, and air remain the same as the SWM-SF slab simulation.

The equations of states associated with the material model are summarized in Table 3.19.

The major disadvantage of MMALE−Lagrangian algorithm is the large air domain that needs to be included in the simulation to accommodate the target structure and minimize the boundary effect, and the computational difficulty is further aggravated by the requirement of small Eulerian mesh size to precisely capture the blast wave magnitude and propagation, and also the small Lagrangian element to convert the blast energy into the structure and capture the localized response. Previous study [64] has pointed out that mesh density significantly influences the blast pressure in the Eulerian mesh.

In this study, mesh convergence test is firstly carried out to achieve a balance between computational effort and accuracy of the results. The reinforced slab is

Table 3.18 **Material model and parameters**

Material	Material model	Input values	Magnitude
Cover layer fiber-reinforced concrete	Mat_Elastic_Plastic _Hydrodynamic	Tabulated compressive stress−strain curve from uniaxial compression test	
Core concrete in refined mesh zone	Mat_Concrete_damage _REL3	Uniaxial compressive strength	60 MPa
Core concrete in coarse mesh zone	Mat_Pseudo_Tensor	Uniaxial compressive strength for concrete and volume fraction for mesh reinforcement	57 MPa/4%
Steel reinforcement	Piecewise_linear_plasticity	Mass density	7800 kg m^{-3}
		Elastic modulus	2.0 E + 11 Pa
		Poisson's ratio	0.3
		Yield stress	270/960 MPa
		Failure plastic strain	0.15
Steel wire mesh	Piecewise_linear_plasticity	Same with steel reinforcement but with 500 MPa yield strength	500 MPa
TNT explosive	Mat_High_Explosive_Burn	Materia density	1630 kg m^{-3}
		Detonation velocity	6930 m s^{-1}
		C-J pressure	2.1 E + 10 Pa
Air	Mat_Null	Density	1.29 kg m^{-3}

Table 3.19 **EOS for material model in the simulation**

EOS	Material	Input values	Magnitude
Linear_Polynomial	Mat_Null (air)	C4	0.4
		C5	0.4
		E_0	250,000 Pa
JWL	Mat_High_Explosive_Burn (TNT)	a	3.738 E + 11 Pa
		b	3.747 E + 9 Pa
		R1	4.15
		R2	0.90
		Omega	0.35
		E_0	6.0 E + 9 J m^{-3}
		V_0	1
Gruneisen	Mat_Elastic_Plastic_Hydrodynamic (fiber-reinforced concrete)	C	3100 m s^{-1}
		S1	1.4
		Gamma	1.69

meshed with small element in the central area while relative coarse mesh is adopted for the remaining model. In the refined mesh zone, the SWMs are explicitly modeled while in the other area a smeared concrete model considering the SWM
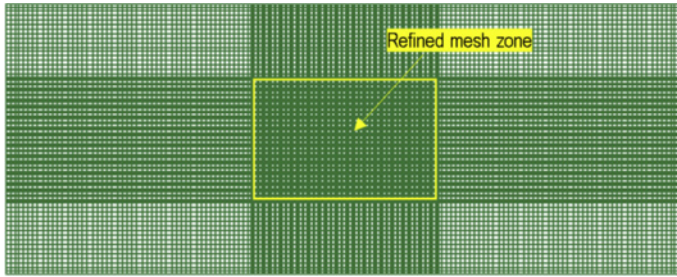
Figure 3.60 Numerical model of SWM-1 slab under close-in detonation.
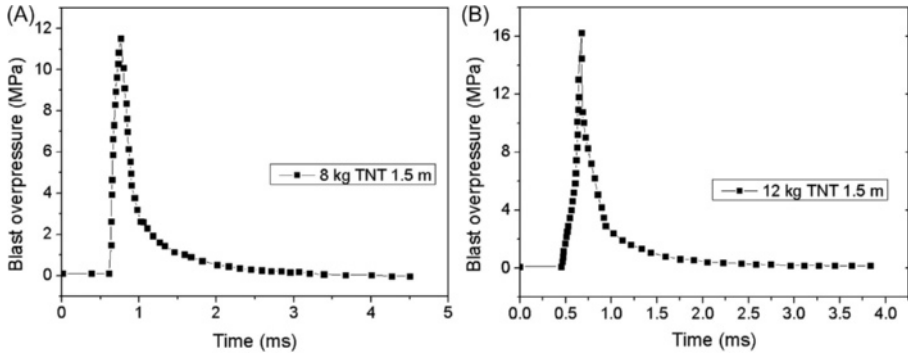
Figure 3.61 Blast overpressure at slab mid-span: reflected overpressure of (A) 8 kg TNT and (B) 12 kg TNT.

reinforcement ratio is established through Mat_Pseudo_Tensor. After convergence test, the refined element size is determined as 5 mm while the coarse mesh size is taken as 8 mm (as shown in Fig. 3.60). Regarding the Eulerian mesh of the air and explosive, a mesh size of 10 mm (sweep mesh) is used for the TNT and 20 mm is used for the air domain. In total, 390,000 elements are used for the slab construction, 6500 and 980,000 elements are used for the explosive and air modeling.

The calculated reflective blast pressures at slab center are shown in Fig. 3.61, and it is seen the calculated blast pressure for 8 kg TNT at 1.5 m standoff distance (NSC slab case) is 11.5 MPa, and this value is a bit higher than UFC 3-340-2 prediction which is 10.5 MPa. The calculated impulse is 4.6 kPa s while empirical result from UFC is merely 1.6 kPa s. Despite similar blast overpressure, the large impulse in the simulation indicates that the empirical curves in UFC 3-340-2 are not adequate for analyzing structural response under nonspherical explosive detonation at close-in range. Similar observation was noted from the blast calculation on 12 kg TNT detonation at 1.5 m standoff distance (SWM-SF slab and SFRC slab case). These findings correlate well with the previous experimental investigations,
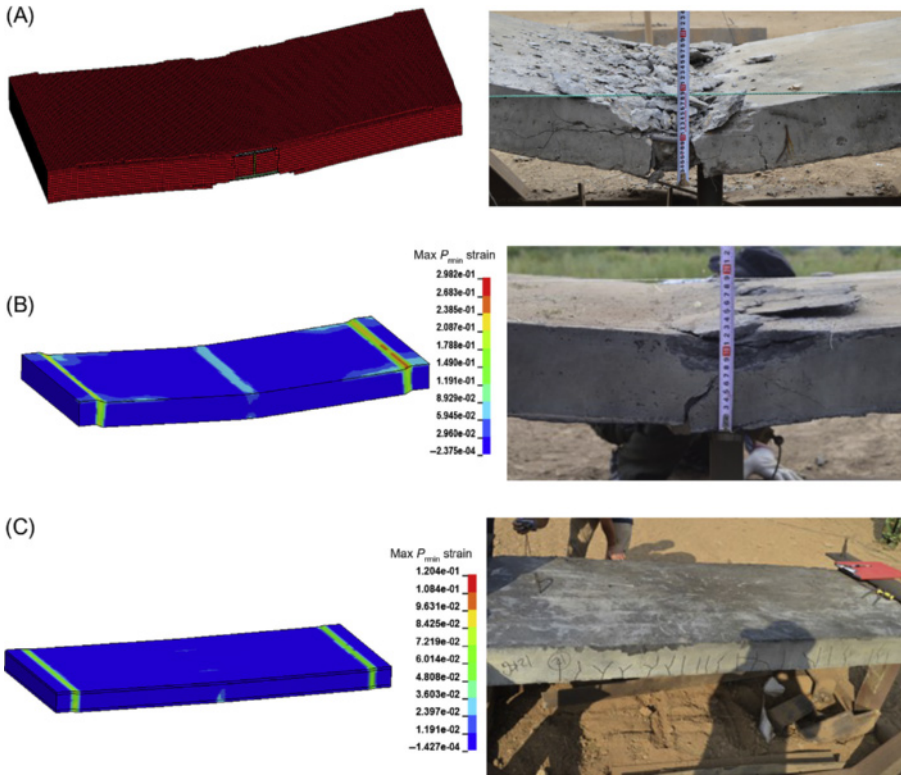
Figure 3.62 Numerical modeling results of slabs after blast test: (A) NSC slab damage, (B) SFRC slab damage, and (C) SWM-SF slab damage.

and the difference highlights the explosive shape effect which should be carefully treated during the analysis.

Response of NSC slab after detonation is shown in Fig. 3.62A; the proposed MMALE−Lagrangian method well reproduces the damage mode; and the flexural damage and the side concrete spallation are captured with reasonable accuracy. Concrete principle strain distribution of SFRC slab is shown in Fig. 3.62B, and it is noted that at slab mid-span, the concrete strains in both the proximal and distal surfaces are larger than the material compressive and tensile capacity. The results show good correlation with field observation. For the SWM-SF slab, the maximum concrete principle strain at mid-span occurs in the tensile surface and the value is about 0.03, indicating some concrete tensile cracking. However, in the compressive face of the slab, almost no damage is observed which matches well with the experimental results.

Due to the recording system malfunction, the LVDT data for NSC and SWM-SF slabs are not available for comparison with numerical simulation. For the SFRC slab, mid-span deflection is compared with the field test results. As shown in
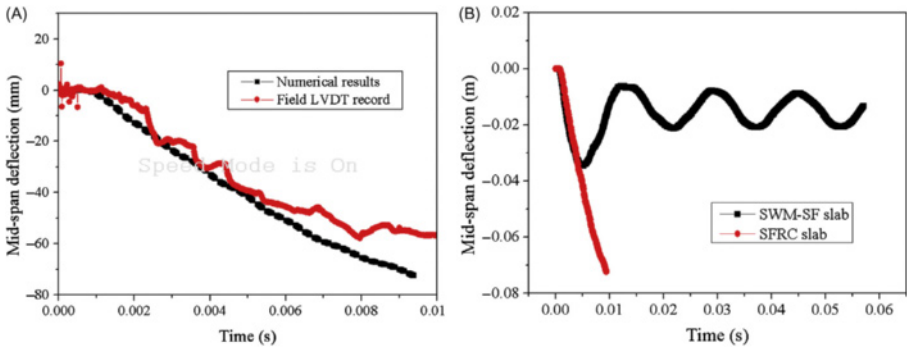
Figure 3.63 Mid-span deflection comparison: (A) SFRC slab and (B) SFRC and SWM-SF slab.

Fig. 3.63A, the numerical simulation gives a sound prediction of the slab deflection time history despite some minor discrepancy being observed after 7 ms. The comparison between the SFRC and SWM-SF slab is shown in Fig. 3.63B, and it is noted the SWM-SF slab shows an elastic response and the peak deflection is about 35 mm.

3.4.6 Conclusion

In this study, toward a blast-resistance design under close-in detonations, concrete slab reinforced by hybrid SWM-SF was investigated. Static test results showed promising mechanical properties of hybrid SWM-SF design. Concrete composite with SWM-SF reinforcement displayed greatly improved material strength and ductility under both compression test and flexural tests.

In the subsequent field blast tests, performance of slab with hybrid SWM-SF reinforcement was investigated under 12 kg TNT detonation at 1.5 m standoff distance and comparison was made against SFRC slab. A control slab made of NSC was tested under smaller blast load from 8 kg TNT detonation from 1.5 m standoff distance. NSC slab experienced complete failure while SFRC slab showed plastic deformation with plastic hinge formed at slab mid-span. SFRC slab had small post-blast deflection and multiple cracks at slab mid-span due to enhanced material ductility from fiber addition. Under the same blast load as SFRC, SWM-SF slab responded in an elastic mode and showed no permanent deflection, and only hairline cracks were observed. Compared with SFRC slab, these cracks are distributed in a wider area, and it is considered that under close-in detonation, SWM provided good blast resistance due to localized membrane effect, and the close spacing SWM effectively reduces the blast wave propagation leading to less structural damage. Numerical simulation adopting the MMALE−Lagrangian algorithm confirmed the explosive shape effect on the blast load magnitude, and the slab responses and damage were captured by numerical model with good accuracy.

3.5 Experimental and numerical study on steel wire mesh-reinforced concrete slab under contact explosion

In this section, performance of SWM-SF slab under contact detonation is investigated. In Section 3.3, it has been demonstrated that concrete with ultra-high compressive strength has excellent antispall capacity under contact detonation. In this chapter, SWM-SF material provide 3D microreinforcement to concrete matrix. SWMs reinforce the slab intermediate layer and steel fibers reinforce the slab protective layers. Based on the laboratory study shown in Section 3.4, 6 mm 3% steel fiber provides higher compressive strength and toughness to the concrete when compared with 12 mm fiber at 2% volume fraction, 6 mm 3% steel fibers are used in the slab protective layer to provide higher blast resistance. Detailed compressive tests about the materials are discussed in Section 3.4.2 and not to be repeated herein.

3.5.1 Design of slabs with steel wire mesh reinforcement

The earlier material tests and beam sample tests have proved that high strength self-compacting mortar with SWM reinforcement and fiber addition in the protective layer achieved high material strength and energy absorption capacity. In this section, design of slabs utilizing this reinforcing method is discussed.

As shown in Fig. 3.64, the dimension of slabs considered is: 2000 mm long, 800 mm wide, and 120 mm thick. The diameter of the longitudinal reinforcing rebar and stirrup rebar is 10 mm. Both of these two reinforcements are plain round steel bars with 360 MPa yielding strength. The slab is designed with 20 mm concrete cover which is cast with high strength self-compacting concrete with 3 vol.-% fiber addition. The fiber material has a length of 6 mm and diameter of 0.12 mm, and
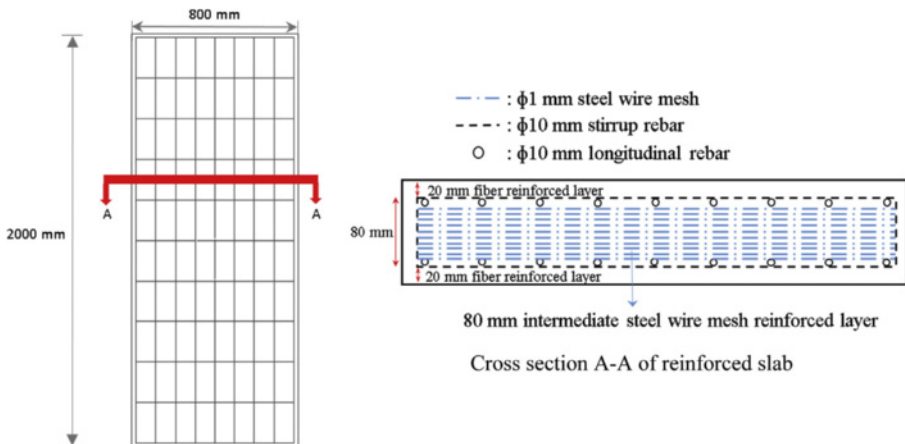
Figure 3.64 Dimension and reinforcement of slabs considered in the study.

its tensile strength is 4200 MPa. The intermediate layer of the slab is reinforced by SWM.

Prior to experimental study, preliminary numerical study is carried out in Hydro-code LS-DYNA, and three different volume fractions of the SWM are considered, i.e., 2 vol.-% (10 layers), 4 vol.-% (20 layers), and 6 vol.-% (30 layers). The considered blast loading scenario is 1 kg TNT contact detonation.

3.5.1.1 Numerical model development

In this study, hybrid FE and SPH method is utilized to simulate the damage and associated fragmentation during the contact detonation. It is widely acknowledged that a key issue with the Lagrangian grid-based FE model for blast loading is the incapability of modeling large element deformations, which can cause singular Jacobi matrices, leading to high inaccuracy and ultimately the computational over-flow. To overcome this problem, so-called erosion algorithm is widely adopted and elements are eroded when user-defined failure criterion is reached. This method is easy to be used, but lacks physical background as it violates mass conservation, and the criterion must be carefully defined to minimize such influence as premature deletion of elements in the simulations.

To better address this problem, numerical methods including interfacial ele-ment method and meshfree methods have been developed. One of the most widely used meshless methods is the SPH method. Conventional SPH method requires intensive computational effort and therefore it is usually used in conjunction with FE method. There are several benefits from this combination. Firstly, due to its Lagrangian formulation, SPH nodes can be straightforwardly linked to standard FE. Secondly, SPH method allows tracking of material deformation and the time-varying behavior. Complex material models that are used in traditional FE model can still be allocated to SPH model. Last but not least, this method allows track-ing of blast-induced fragments formation. In a previous study, Johnson and Stryk proposed a method to resolve the FE mesh distortion problem using coupled SPH and FE method. This method simply converts highly distorted elements into meshless particles during the dynamic response simulation [65]. This approach is suitable for problems involving severe localized distortion such as contact detonation-induced structural response, as in such cases effect of the distorted ele-ments to the remaining structure may be rather significant, and with a particle conversion and the associated contact algorithms such an effect could be well preserved [66].

Adopting this hybrid method, numerical model in this study is shown in Fig. 3.65A. Concrete material is modeled with solid element, while SWM and steel reinforcement are modeled with beam element. The TNT explosive is modeled with SPH particles. Contact detonation induces localized structural response and damage. To save computational effort, refined mesh size of 5 mm is used in the center part of the slab (0.5 m in width direction $\times$ 0.6 m in length direction), while a coarse mesh size of 10 mm is used for the remaining part. SWM is explicitly modeled in the refined mesh zone.
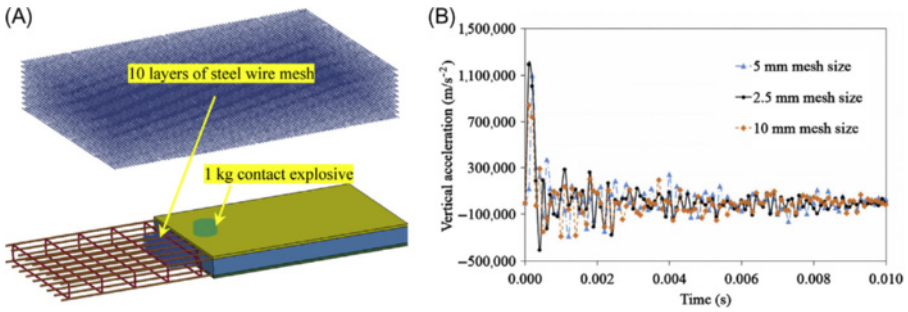
Figure 3.65 Numerical model (A) and convergence test results (B).

Mesh size in this study is determined based on convergence test. As shown in Fig. 3.65B, simulation of slab with 2 vol.-% (10 layers) SWM under 1 kg TNT contact detonation is carried out with three mesh sizes for the central part of the slab, i.e., 10, 5, and 2.5 mm. As shown the central nodal acceleration converges with a decreasing element size; however, 2.5 mm element size requires enormous computational resources and time. When modeling the slab with 6 vol.-% (30 layers) SWM with the 2.5 mm mesh size, the computer memory and calculation are beyond the current computer power (workstation with 4 core 3.0 GHz processor and 16 g memory). In this study, mesh size of 5 mm is adopted. At both ends of the slab, nodes within 100 mm from the free edge are constrained to achieve a fully fixed boundary in the simulation.

To explicitly model the fragmentation process, the method discussed by Johnson and Stryk is adopted, and solid elements with large distortion is converted into meshless particles in the numerical simulation. These particles carry velocity and mass of original element, and they are defined with the same material properties. This algorithm does not violate the mass conservation, and can simulate the fragmentation process. Table 3.20 summarizes the material models adopted in this study.

To use the Material Elastic_Plastic_Hydrodynamic, an EOS is required. In this study, the Gruneisen EOS is adopted. With cubic shock velocity−particle velocity, the Gruneisen EOS defines pressure for compressed material as:

$$p = \frac{\rho_0 C^2 \mu \left[1 + \left(1 - \frac{\gamma_0}{2}\right)\mu - \frac{a}{2}\mu^2 \right]}{\left[1 - (S_1 - 1)\mu - S_2 \frac{\mu^2}{\mu + 1} - S_3 \frac{\mu^3}{(\mu + 1)^2} \right]^2} + (\gamma_0 + a\mu)E \qquad (3.11)$$

and for an expanded material as:

$$p = \rho_0 C^2 \mu + (\gamma_0 + a\mu)E \qquad (3.12)$$

Table 3.20 **Material model in the numerical simulation**

Material	Material model	Input values	Magnitude
Cover layer fiber-reinforced concrete	Mat_Elastic_Plastic _Hydrodynamic	Tabulated compressive stress−strain curve from uniaxial compression tests	
Core concrete in refined mesh zone	Mat_Concrete_damage _REL3	Uniaxial compressive strength	60 MPa
Core concrete in coarse mesh zone	Mat_Pseudo_Tensor	Uniaxial compressive strength for concrete and volume fraction for mesh reinforcement	60 MPa/2%, 4%, 6% reinforcement ratio
Steel reinforcement	Piecewise_linear_plasticity	Mass density Elastic modulus Poisson's ratio Yield stress Failure plastic strain	7800 kg m^{-3} 2.00E + 11 0.3 360 MPa 0.15
Steel wire mesh	Piecewise_linear_plasticity	Same with steel reinforcement but with 500 MPa yield strength	500 MPa
TNT Explosive	Mat_High_Explosive_Burn	Material density Detonation velocity C-J pressure	1630 kg m^{-3} 6900 m s^{-1} 2.1E + 10 Pa

where C is the intercept of the V_s-V_p (shock velocity vs particle velocity) curve, E is the specific internal energy. S_1, S_2, and S_3 are the coefficients of the slope of the V_s-V_p curve, and as the relationship of the shock wave velocity and particle velocity is often linear, only S_1 is considered in this study; γ_0 is the Gruneisen gamma; a is the first-order volume correction to γ_0; and $\mu = \rho/\rho_0 - 1$.

In addition, a widely adopted Jones−Wilkens−Lee (JWL) EOS model for TNT explosive is used in this study to model the detonation process. JWL EOS models the pressure generated by chemical energy in an explosive. It can be written in the following form.

$$p = A\left(1 - \frac{\omega}{r_1 V}\right)e^{-r_1 V} + B\left(1 - \frac{\omega}{r_2 V}\right)e^{-r_2 V} + \frac{\omega E}{V} \tag{3.13}$$

The values of the constants A, r_1, B, r_2, and ω for many common explosives have been determined from dynamic experiments. These values should be considered as a set of interdependent parameters. The parameters in JWL EOS for

Table 3.21 Parameters for the equation of state

EOS_ Gruneisen [39]	C_0	2600
	S_1	1.4
	γ_0	2
EOS_JWL [67,68]	A	3.71 E + 11
	B	3.23 E + 9
	r_1	4.15
	r_2	0.95
	ω	0.3
	E_0	7 E + 9
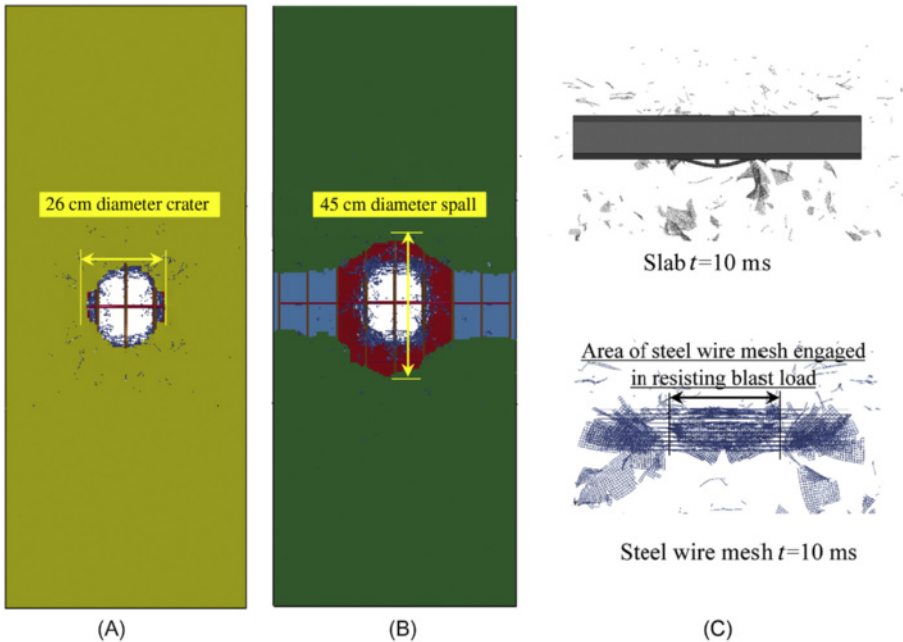
Figure 3.66 Slab with 2 vol.-% (10 layers) steel wire mesh reinforcement: (A) top view $t = 10$ ms, (B) bottom view $t = 10$ ms, and (C) side view.

TNT used in this study are listed in Table 3.21, in which E_0 is initial C−J (Chapman−Jouguet) energy per volume as the total chemical energy of TNT.

The parameters in the EOS used in this study are shown in Table 3.21.

3.5.1.2 Numerical simulation results

Figs. 3.66−3.68 show the damage of slabs with different SWM reinforcements. When slab is reinforced by 2 vol.-% (10 layers) SWM, severe concrete cratering and spalling can be observed on proximal and distal surfaces, respectively. Due to the fracture of all the SWMs, slab perforation failure occurs. The steel
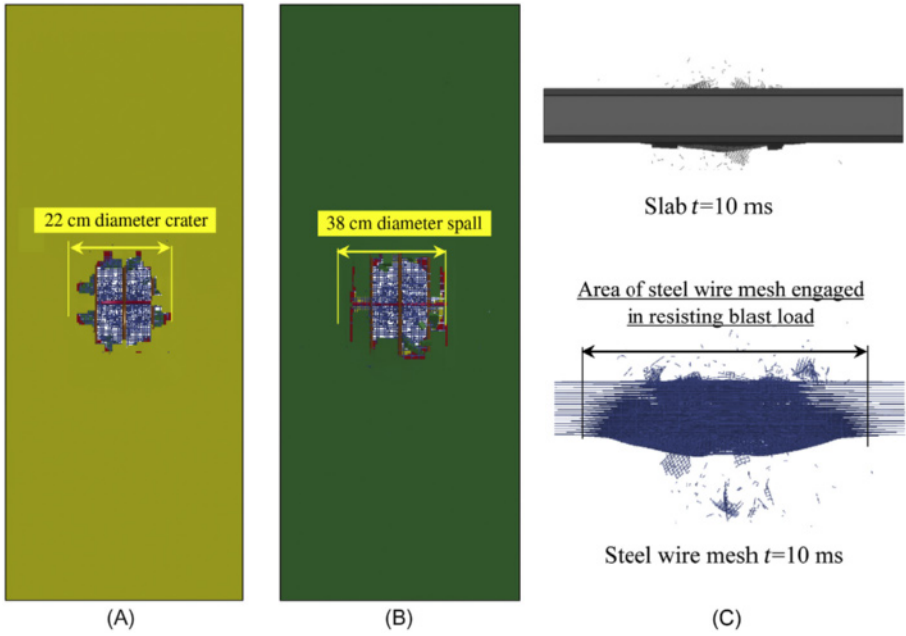
Figure 3.67 Slab with 4 vol.-% (20 layers) steel wire mesh reinforcement: (A) top view $t = 10$ ms, (B) bottom view $t = 10$ ms, and (C) side view.
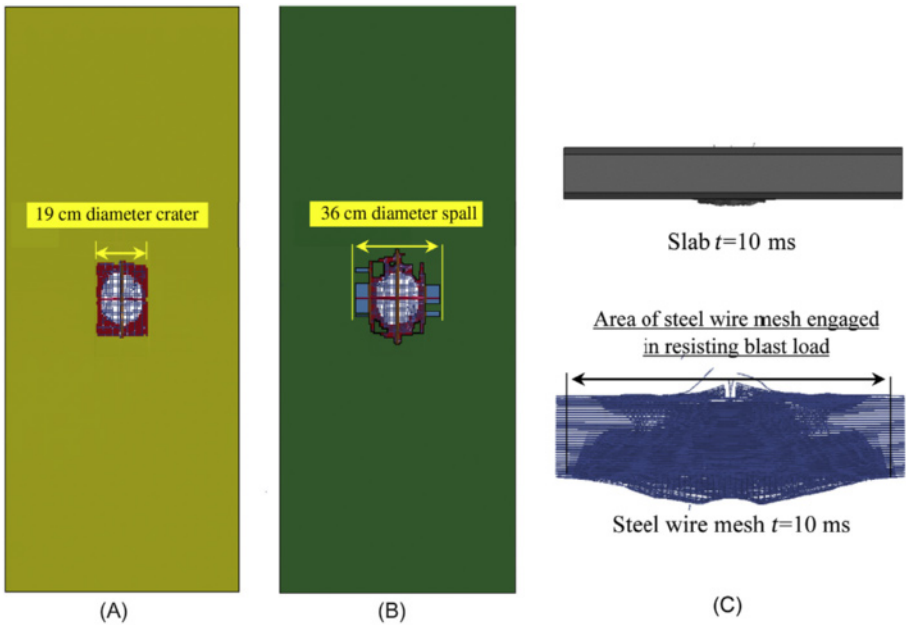
Figure 3.68 Slab with 6 vol.-% (30 layers) steel wire mesh reinforcement: (A) top view $t = 10$ ms, (B) bottom view $t = 10$ ms, and (C) side view.

reinforcement at slab mid-span also experiences significant deformation. With increment of the SWM to 4 vol.-% (20 layers), the concrete crater and spall areas are smaller than the 2 vol.-% (10 layers) SWM-reinforced slab, no slab perforation is observed due to the bridging effect from SWM. With 6 vol.-% (30 layers) SWM, the slab damage is further reduced, no perforation occurs, and a close examination shows that only the outmost layers of the SWMs experience fracture.

Effect of SWM on confining the concrete damage is shown in Figs. 3.66C, 3.67C, and 3.68C. It is observed from Fig. 3.66C that when 2 vol.-% (10 layers) steel mesh is used, the area of SWM engaged in resisting blast load is limited, all layers of the steel meshes experience fracture and large deformation occurs on steel reinforcement. With the increase of the SWM volume percentage, tensile membrane effect takes place and more obvious confining effect can be observed. Localized tensile membrane action develops in the SWM-reinforced panels at large deflections caused by contact detonation. It is a self-equilibrating mechanism comprising a tensile net in the central region surrounded by a peripheral compressive ring of concrete. Tensile membrane action is not a common phenomenon and only occurs in severe conditions such as explosion, and this mechanism is able to provide alternate load path in mitigating blast effects. The engagement of more SWM effectively transfers the blast energy into the elastic and plastic strain energy of the steel meshes, and therefore less concrete damage occurs. Besides consuming blast energy due to steel mesh fracturing, the close-spaced SWMs and rebars also provide shock reflections and shock wave interference that effectively reduce the blast energy propagating within the slab, leading to reduced damage.

The slab central part which consists of the SWMs experiences the most significant deformation and damage under the contact blast loads. The following plots illustrate the energy evolution with respect to time for the SWMs in the three slabs. For the internal energy, it is indicating that increasing SWM reinforcement results in an increase of the internal energy of SWMs. Unlike the other two cases, the kinetic energy of 2 vol.-% SWMs does not drop to zero, and this is because in this case the fractured SWMs preserve a certain amount of kinetic energy as shown in Fig. 3.69. In the slabs with 4 and 6 vol.-% SWMs reinforcement, the kinetic energy drops back to zero as the movement of SWMs stops soon after the blast loads. It is worth noting that the deceleration of the movement in 6 vol.-% SWMs is higher than 4 vol.-% SWMs. Due to the fact that SWMs are only explicitly modeled in the central region of the slab, the energy evolution plot cannot serve as an indication of the energy absorbed by the SWM. However, it can be used to indicate the sensitivity of the internal energy absorption to the SWM volume fraction changes in each design case.

Fragmentation process is simulated for the slab with 6 vol.-% (30 layers) SWM reinforcement. As shown in Fig. 3.70, failed elements transform into SPH particles and fly with high velocity. These SPH particles inherit all the properties of the Lagrangian element, e.g., mass, constitutive relations, and kinetic variables. In this model setup, mass of each failed element is 0.35 g, depending on the SPH particle size, which is a shortcoming of particle method in simulating fragmentation process of structures because the fragment size and shape depend on the predefined particles. However, the approach does not erode away elements and therefore the mass and energy conservation are maintained. The maximum horizontal velocity of the
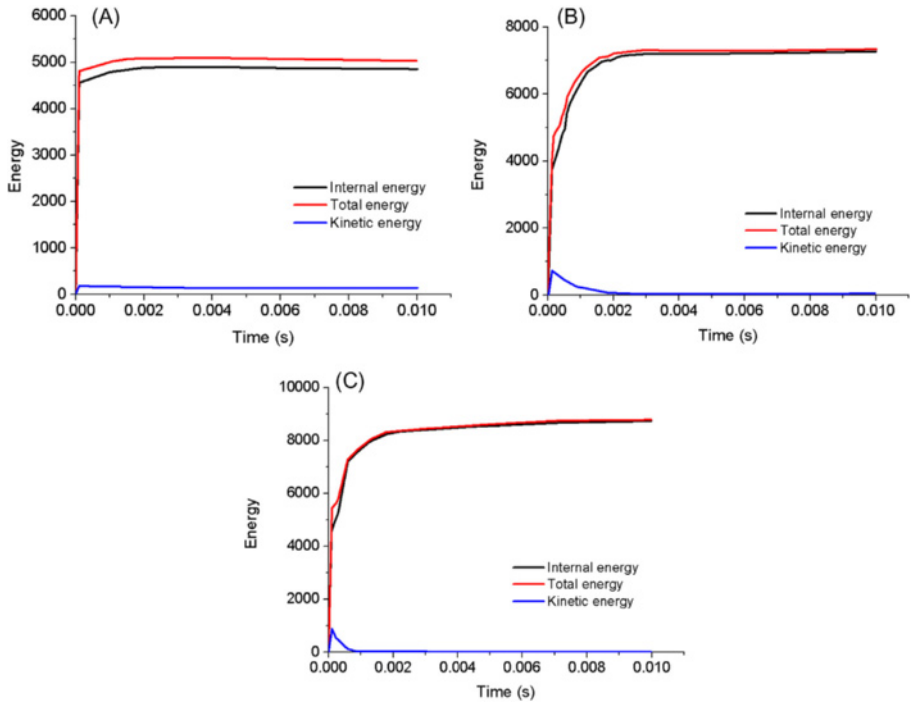
Figure 3.69 Energy evolution in slabs with varying steel wire mesh reinforcements: (A) 2 vol.-% (10 layers) steel wire mesh (B) 4 vol.-% (20 layers) steel wire mesh, and (C) 6 vol.-% (30 layers) steel wire mesh.

$t = 0.5$ ms $t = 1$ ms $t = 3$ ms $t = 10$ ms
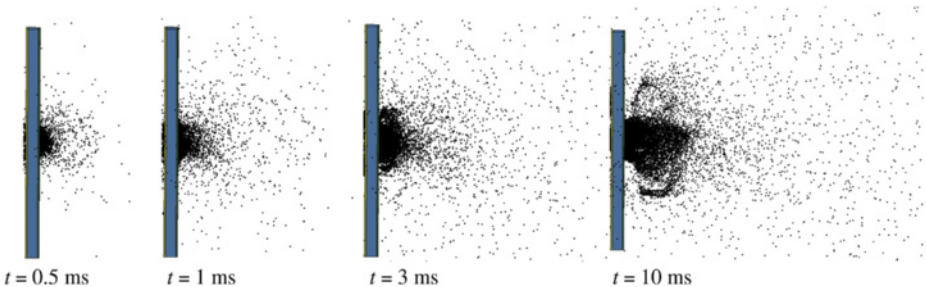
Figure 3.70 Concrete fragment simulation and velocity prediction.

fragment in the simulation is measured to be around 600 m s^{-1}. It should be pointed out that, due to the missing of the air domain and inaccurate prediction of the fragment shape, the air drag force which is related to the particle shape and velocity is not modeled in this study, and this leads to an over prediction of the fragment velocity.

Steel support

Bolts and steel cleats

Figure 3.71 Supporting frame.

3.5.2 Experimental study of slab with steel wire mesh reinforcement

In the experimental verification, slab was cast with 6 vol.-% (30 layers) SWM reinforcement. Apparatus used in the contact explosion are shown in Fig. 3.71. Bolting clamping system was used to stabilize the slab during the test. Besides direct compressive failure in the proximal surface beneath the charge, contact detonation also induces 3D shock wave propagation within the slab. Upon reaching the boundaries where shock impedance mismatch exists, e.g., the distal slab surface, side surface in the free edge and the fixed end, and also the SWMs and rebar, shock wave reflects and interacts with the upcoming wave. Material spallation occurs if the net stress magnitude is larger than the material dynamic tensile strength. In this study, major damage is anticipated to be directly beneath the contact explosion including both material crush and spallation.

After the slab was firmly clamped, the whole system was elevated and stabilized into the vertical position as shown in Fig. 3.72, and both sides of the slab were painted with different colors. According to the original plan, fragments after the test would be collected and grouped according to the projectile distance and color, however, due to the site limitation including unleveled sandy ground and bushes, the collection process was not successful. Cylindrical TNT explosive with height of 60 mm and diameter of 120 mm was placed with its end on the center of the slab. High speed camera (Photron SZ) was used to record the fragmentation process, and the frame rate was set to 10,000 fps (frames per second), and the data were postanalyzed through Photron Fastcam Analysis (PFA) software.

In the test, the supporting frame was covered with dark green canvas cloth, and the gap between the slab and canvas cover was carefully sealed. The setup was to prevent overexposure in the high speed camera image. Upon detonation, fire with strong light could cause overexposure that made the image in the high speed camera
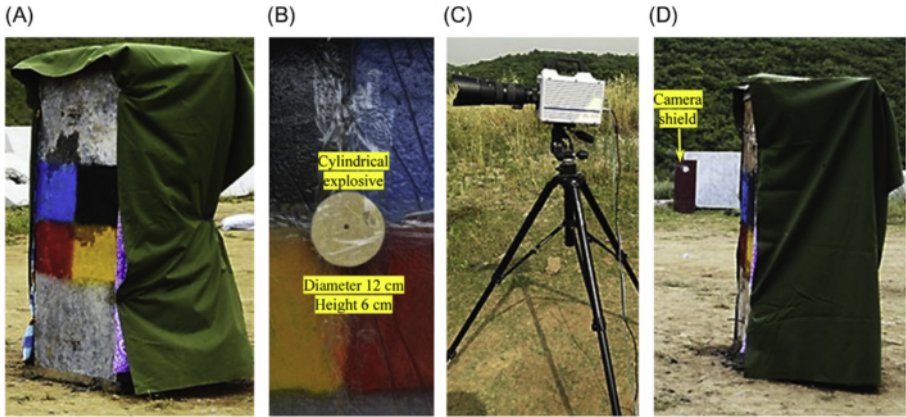
Figure 3.72 Test setup and high speed camera: (A) frame with canvas cover, (B) 1 kg TNT, (C) Photron SZ, and (D) slab ready for test.

too bright to be analyzed. As shown in Fig. 3.72, the camera was placed 30 m away from the slab center with shooting angle parallel to the slab surface.

The TNT explosive was electrically initiated through a detonator. The detonator was bonded in the core of the TNT explosive through predrilled hole as shown in Fig. 3.72. The detonation point is of key importance in directing the explosive wave, and this experimental setup is consistent with the previous numerical investigation in which the detonation was initiated in the core of the TNT. The explosive in the detonator is Hexogen (RDX) with TNT equivalence of 1.58. One detonator contains 0.4−0.6 g RDX with net explosive quantity less than 1 g TNT per detonator. Comparing with the explosive charge weights used in the current test, the effects from the detonator are deemed not prominent and can be neglected.

The energy releasing process of a high explosive detonation is almost instantaneous. To determine the parameters of explosive loading, a system of differential equations describing the conservation laws of mass, momentum, and energy as well as material EOS under high pressure needs to be solved using numerical integration techniques [69] and specialized computer programs, e.g., LS-DYNA, AUTODYN, SAP, and SHARC.

Simplified engineering-level relationships for explosive loads hypothesized that detonation is an instantaneous process where the volume, initially occupied by the condensed matter, is filled instantaneously by hot, highly compressed detonation product gases. The mean detonation pressure within the charge can be determined as:

$$P_0 = \frac{\rho_0 D_0^2}{2(k+1)} \tag{3.14}$$
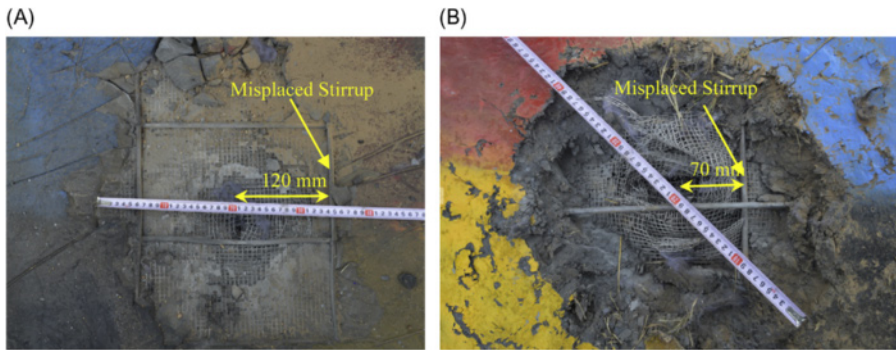
Figure 3.73 Steel wire mesh-reinforced concrete slab after detonation: (A) top surface crater diameter 200 mm and (B) bottom surface spall diameter 400 mm.

where ρ_0 is the density of explosive; D_0 is detonation velocity; k is the polytrophic exponent of the detonation products. The polytrophic exponent typically used is $k \approx 3$. The exact value of k lies within the range of $2.54 \leq k \leq 3$, depending on the kind of explosive.

In contact detonation case, the pressure acting on the structure equals to the mean detonation pressure, which in this case is as high as 9 GPa. Under such high explosive loads, concrete in contact with the explosive failed under compression as shown in Fig. 3.73A. The remaining portion of the explosive energy continued propagating in the structure in the form of stress wave causing localized structural response, upon deformation, SWM developed localized tensile membrane action which enhanced the local blast resistance. In this experiment, though the stress wave propagation was partially mitigated by the close-spaced SWM, the remaining stress wave continued propagating within the slab and caused the concrete spall-ation in the distal surface as shown in Fig. 3.73B.

Fracture of SWM on both surfaces was also observed in the test. The spall diam-eter on the distal surface was 400 mm which was slightly larger than that predicted by the numerical simulation. The SWM fracture on the distal surface was not well predicted by the numerical simulation. This could be because the simulation time is insufficient. The simulation stops at 10 ms, which well captures the forced response phase of the slab but not the free-vibration phase, because it is extremely time con-suming to perform such simulations. Primary damages at the center of the slab caused by direct contact explosion are captured by the simulation because they occur quickly in the 10 ms duration. Free vibration might cause further damage on SWM. Another reason is the insufficient confinement from the steel reinforcement owing to the poor workmanship in casting the test specimen. Figs. 3.68B and 3.68C show that the excessive deformation of SWM on the distal surface is restrained by the longitudinal and stirrup steel rebar. Nevertheless, as can be noted from Fig. 3.73, due to inadequate workmanship, the stirrup reinforcement shifted 120 and 70 mm from the designated location on the proximal and distal surfaces, respectively. The missing of the stirrup reinforcement had a direct influence on the
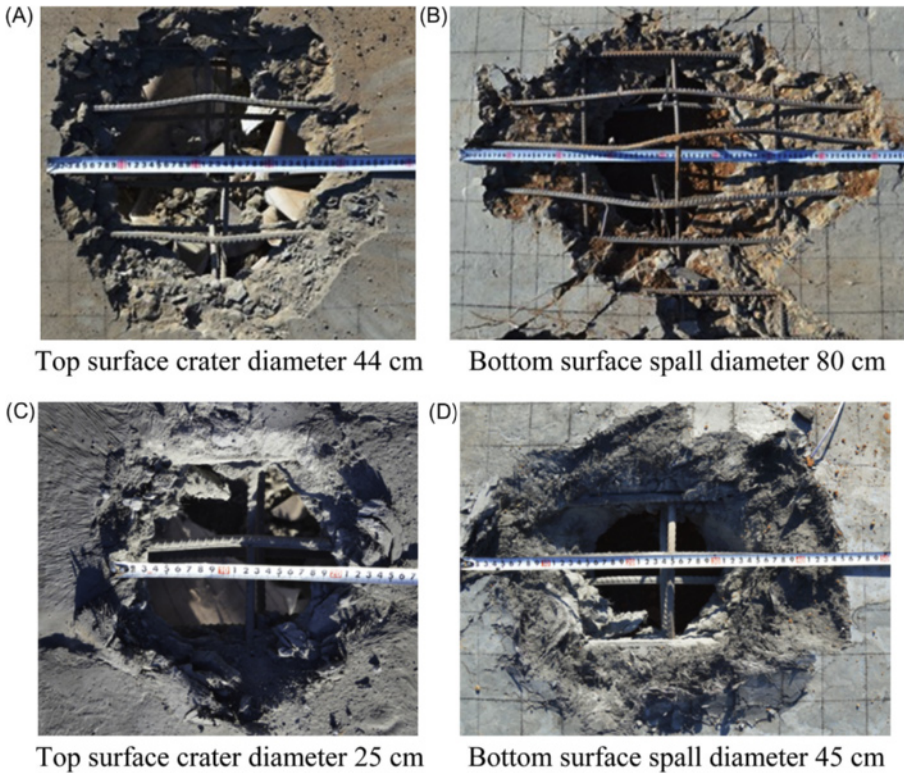
Figure 3.74 Response to 1 kg contact explosion (A, B) normal strength concrete slab and (C, D) ultra-high performance concrete slab.

SWM deformation. Contact detonation induces highly localized damage and response, and the dislocation of the steel reinforcement made the passive confinement of SWM less effective and therefore more fractures were observed. In addition, in the numerical simulation, failed concrete elements are transformed into SPH particles, and these SPH particles inherit all the properties of the Lagrangian element, e.g., mass, constitutive relations, and kinetic variables. However, due to the limitation of SPH algorithm, they are incapable of transmitting the tensile stress wave caused by impedance mismatch at material boundaries (between SWM and concrete, steel rebar and concrete) afterward. This may lead to underestimation of the responses.

Under contact detonation, SWM RC slab with steel fiber in the concrete cover area performs better than NSC and UHPC as presented in the previous study. Fig. 3.74 shows the comparison of slab damage after an identical 1 kg TNT contact detonation. Both the NSC and UHPC slabs have the same dimension as the present slab shown in Fig. 3.73. It is clearly observed that perforation failure occurred on

both NSC and UHPC slabs. In addition, the crater and spall area on these two slabs are larger than those on the SWM RC slab presented in this study.

The improvement mainly comes from the following aspects. Firstly, during the wave propagation in the SWM-reinforced slab, due to shock impedance mismatch at the material boundaries (SWM/concrete, steel rebar/concrete), the closely spaced SWMs effectively dispersed the stress wave which in turn retarded wave propagation. Secondly, kinetic energy of particle movement was transferred to slab deformation and fracture of SWM absorbed energy leading to reduced damage. Finally, when local large deformation occurred, the tensile membrane effect from multi-layers of the SWM increased the scab and spall resistance.

Fig. 3.75 shows the high speed camera images which were obtained with the PFA software by Photron. A thin and very light layer of aluminum foil was placed 10 m in front of the test slab. This setup was aiming at monitoring the arrival time for calculation of the propagation speed of the shock wave. Upon interacting with the shock front, aluminum foil which is thin and light would deform and reflect light into the camera so that the arrival time can be determined. Close examination of the video footage indicates a transparent shock front with compressed air layer interacted with the aluminum foil at 14.2 ms after detonation. The shock front velocity is therefore determined as 704 m s^{-1}.

Upon detonation, the slab was engulfed firstly by the strong light followed by fireball, and the fire lasted around 50 ms. TNT has the fuel and oxidizer built in, when TNT explodes

$$2CH_3C_6H_2(NO_2)_3(s) \rightarrow 3N_2(g) + 5H_2O(g) + 7CO(g) + 7C(s) \tag{3.15}$$
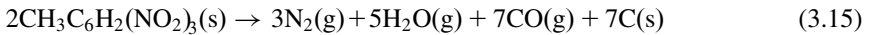
It is seen that the products include lots of gases, and it is incomplete combustion as CO is formed rather than CO_2, and unburnt carbon forms the black cloud which is clearly seen in the figure.

The analysis on concrete fragment velocity is a complex problem as it involves many uncertainties. In a previous report [7], based on field tests, one empirical method was proposed. The following equation can be used to estimate the ejection velocity of the concrete fragments in a blast scenario.

$$V_{\text{fragment}} = A_m e^{(B_m \times R)} \tag{3.16}$$

where $A_m = 5.41 + 1.79 \times [\ln(M)] + 0.049 \times ([\ln(M)])2$, $B_m = 0.053 \times M^{-0.304}$, M = mass of the fragment in grams, and R = range in meters from the center of the detonation to the fragments found in field.

Given that the fragment flying distance and weight are known, the above equation can give crude estimation on the initial velocity of the fragment. However, it is noted that, the fragment generated in blast scenario can be distributed in a wide range with a diameter of several hundred meters; the collecting process could be very time and resource consuming.
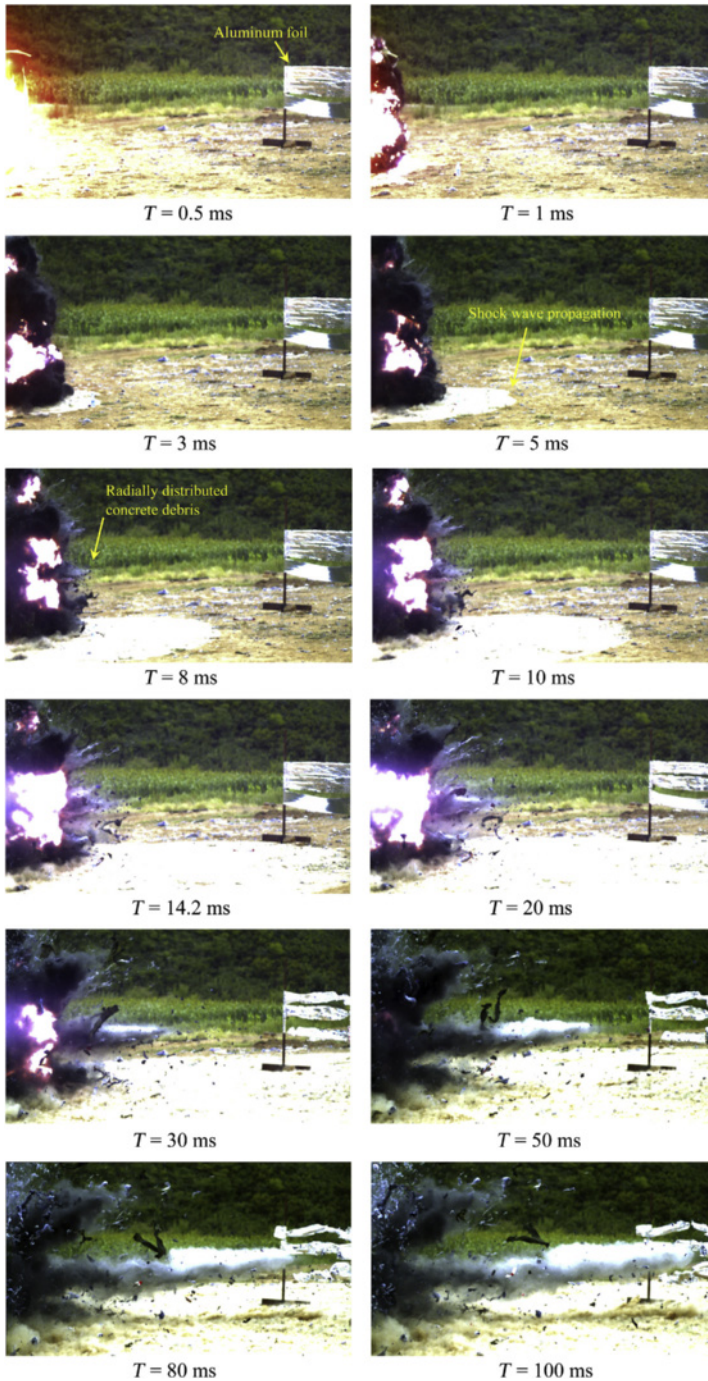
Figure 3.75 Blast test recorded in high speed camera.

(A)
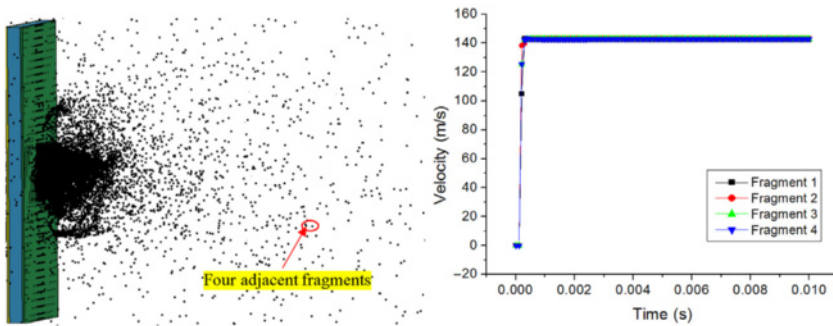
(B)

Figure 3.76 Fragment velocity determination: (A) image analysis in PFA system and (B) fragment velocity from numerical simulation.

In this study, the particle-based numerical approach provides an alternative to estimate the ejecting velocity of the debris, and its feasibility is validated through comparison with the high speed camera results from the field.

As shown in Fig. 3.76A, concrete fragments started to become visible in the camera from 8 ms. Through the image analysis in PFA software, the fragments can be identified and tracked. For instance, the speed of the fragment which is located 1.2 m away from the slab as shown in Fig. 3.76A is calculated as 120 m s^{-1}. The length of the fragment can be approximately determined from the recorded images in test as 20 mm, and this size equals to four FEs in the numerical model. Based on this assumption, four adjacent elements in the same location in the numerical model

are selected and their velocities are plotted in Fig. 3.76B, and it is noted that numerical prediction yields a fragment velocity around 145 m s^{-1} (averaged from the four adjacent fragments) which is higher than the test observation. As discussed earlier, numerical simulation does not consider the air drag force which is related to the fragment shape and velocity; therefore it will overestimate the actual fragment velocity.

3.5.3   Conclusions and discussions

In this study, an advanced design of SWM RC slab is proposed. Although high strength concrete contributes to the enhanced resistance against dynamic compressive loads, it is prone to fail in a more brittle manner than conventional concrete. In addition, to achieve a balanced cross-section design, i.e., concrete crushes at the same time when tensile rebar yields, high strength steel rebar is required to work together with high strength concrete. To overcome the material brittleness and reduce the material cost, in this study, SWM is used as additional reinforcement in high strength self-compacting concrete slab, and steel fibers are mixed into concrete and applied to the cover layer to provide microbridging effect. Static test results showed promising mechanical properties of this advanced design. Considering different volume fractions of the SWM, numerical simulation of slabs under contact detonations is carried out and the results are validated with the field blast tests. Key findings in the present research include:

1. SWM reinforcement provides additional spall and crater resistance due to the localized membrane effect, also closely spaced SWM effectively reduces the blast wave propagation leading to less perforation and concrete spall.
2. Numerical simulation based on coupled FE and SPH methods captures the test observations, and yields reasonably accurate fragment velocity predictions. However, improvement should be made in the future study to include air domain in the numerical study to consider the drag force. In addition, the fragment size prediction should be considered in the numerical simulation process.
3. High speed camera analysis provides useful information including shock front velocity and fragment velocity. It can be used as a powerful tool for validating the numerical results.

3.6   Blast resistance of concrete slab reinforced with high-performance fiber material

3.6.1   Experiment method

3.6.1.1   Materials and mix proportions

Table 3.22 shows the concrete material compositions in this study. Coarse aggregates in conventional concrete design are replaced by ultrafine silica fume. Silica fume can provide high pozzonalic effect that promotes the concrete strength growth, especially at the early age. Silica fume with small size (less than 1 μm) can

Table 3.22 Material compositions for fiber-reinforced concrete (kg m^{-3})

Composition	UHMWPE fiber concrete	Hybrid UHMWPE-steel fiber concrete
P.O 52.5 Cement	1155.60	1155.60
Silica fume	437.50	437.50
Nano-CaCO3	57.80	57.80
Microbead	111.50	111.50
Silicon powder 500	110.30	110.30
Silicon powder 325	68.20	68.20
Fine sand	334.50	334.50
Medium sand	278.80	278.80
Coarse sand	211.90	211.90
Water reducer	55.47	55.47
Water	294.67	294.67
Fiber	24.30 UHMWPE fiber	14.6 UHMWPE fiber
		76.4 Steel fiber
Antifreeze fluid	16.50	16.50

Table 3.23 Fiber material properties

Type	Density	Length	Diameter	Strength	Elasticity modulus	Elongation (fracture strain)
UHMWPE fiber	970 kg m^{-3}	10 mm	0.012 mm	3000 MPa	100 GPa	4%–6%
Steel fiber	7900 kg m^{-3}	12 mm	0.12 mm	4295 MPa	200 GPa	15%

also fill the voids to generate low-porosity concrete matrix. Nanoparticles nano-CaCO$_3$ is added into the concrete matrix at a constant volume fraction. These particles can provide nanoscale filling effect, and previous study revealed that inclusion of nanosize particles into the concrete matrix favors its mechanical performance.

Two different fiber materials, i.e., steel fiber and UHMWPE fiber are used in the current design. Material properties of these two fibers are listed in Table 3.23. From the hybrid-fiber reinforcement design, it is anticipated that the stronger and stiffer steel fiber improves the ultimate strength, while the more flexible and ductile UHMWPE fiber leads to improving toughness and strain capacity in the postcrack zone [70].

Maalej et al. [71] proposed a hybrid-fiber reinforcement for concrete material, and hybrid-fiber engineered cementitious composites containing a combination of high-modulus steel fibers and relatively low-modulus polyethylene fibers were adopted to achieve a desired balance between the ultimate strength and the strain capacity of the material required for impact- and blast-resistant structures.

The effect of using steel and polyethylene fibers together in concrete has been investigated by Kobayashi and Cho [72], and they found the first-crack strength of
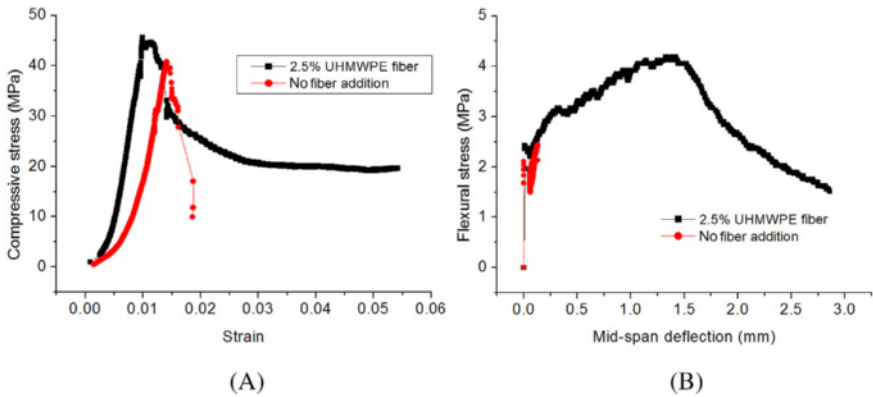
Figure 3.77 Static test results on concrete with and without UHMWPE fiber reinforcement: (A) uniaxial compressive test results and (B) third-point bending test results.

a hybrid composite was about the same as that for SFRC, and moreover, it was possible to achieve a toughness such that there was little reduction in strength after extensive deformation.

In this study, for mono UHMWPE FRC, the fiber volume fraction is 2.5 vol.-% while the hybrid FRC, UHMWPE fiber is 1.5 vol.-% and steel fiber is 1.0 vol.-%.

3.6.1.2 Material static tests

Static uniaxial compression and third-point bending tests are conducted to investigate the mechanical properties of concrete reinforced with fiber material proposed in this study. Testing procedure conforms to the China Standard GB/T 50081-2002. Fig. 3.77A shows the compressive stress−strain curve for the concrete material with 2.5 vol.-% UHMWPE fiber addition, and the curve is averaged from a series of uniaxial compression tests on 100 mm cubic samples. Compared with plain concrete without fiber material, material stiffness and ductility are significantly enhanced, however, material compressive strength is less influenced by the UHMWPE fiber addition.

To investigate the tensile performance and ductility of concrete material after UHMWPE fiber reinforcement, three-point bending tests are carried out on beam samples with a dimension of 400 mm × 100 m × 100 mm. The spacing between the two loading points is 100 mm which is 1/3 of the clear (outer) span. Within the loading points, no shear acted and the specimens are solely subjected to bending moments. The displacement of the beam element is measured in the center of the free span through a LVDT device. Fig. 3.77B shows the flexural bending test results, and it can be observed that plain concrete has a relatively low strength of 2.5 MPa while UHMWPE RC has an enhanced flexural strength of 4.2 MPa. The tensile strain capacity is significantly improved with UHMWPE fiber addition.

Regarding the hybrid-fiber reinforcement, uniaxial compression test is carried out and comparison is made among plain concrete, mono UHMWPE FRC and hybrid FRC. As shown in Fig. 3.78, improvement of both material ductility and
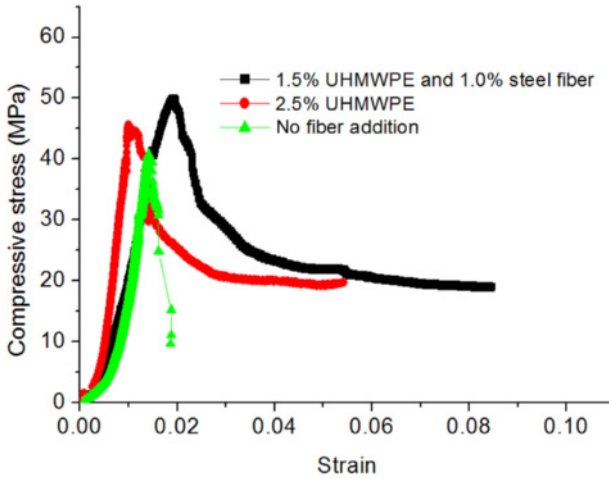
Figure 3.78 Hybrid fiber-reinforced concrete under uniaxial compression.
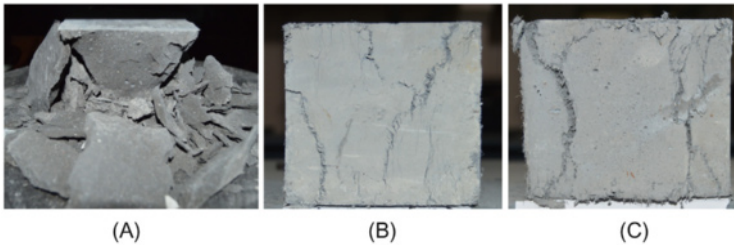
Figure 3.79 Concrete samples after uniaxial compression test: (A) plain concrete, (B) UHMWPE concrete, and (C) hybrid-fiber concrete.

strength is observed on the sample with hybrid-fiber reinforcement. Using the concept of hybridization with two different fibers incorporated into a common cement matrix, the hybrid composite can offer more attractive engineering properties because the presence of one fiber enables the more efficient utilization of the potential properties of the other fiber [73]. As observed in this study, the inclusion of steel fiber and UHMWPE fiber effectively enhances the material strength and tensile capacity which is favorable for the next stage blast-resistance design.

Concrete samples after uniaxial compression tests are shown in Fig. 3.79, where plain concrete failure is in a progressive brittle mode while the fiber-reinforced samples showed ductile failure, and bridging effect from fiber material can be clearly observed. After initiation of crack, fiber material bridges over cracks and retards crack propagation which helps improve the material ductility and strength.

3.6.2   Blast testing program

3.6.2.1   Slab preparation

In the present test matrix, all slabs were built with the same size. As depicted in Fig. 3.80, the dimensions of the slabs are: 2000 mm long, 800 mm wide, and 120 mm thick. The diameter of the longitudinal reinforcing rebar and stirrup rebar is 12 mm and 10 mm, respectively. The longitudinal and stirrup spacing is 95 mm and 196 mm, respectively. The yielding strength for the longitudinal and stirrup rebar is 270 MPa.

The material properties and static performance of both the mono UHMWPE FRC and the hybrid FRC material are obtained from the above static experiments. Improved compressive and tensile properties as well as energy absorption capability are noted from the fiber addition. In the following study, field blast tests on mono UHMWPE FRC slabs and hybrid steel-UHMWPE FRC slabs are carried out. Blast resistances of these slabs under close-in detonations are observed and compared with each other.

For mono UHMWPE FRC slabs, two blast events are considered. A 6 kg TNT explosive is used in the first event on UHMWPE-1 slab in which an elastic slab deformation is expected. The data acquisition system is composed of pressure transducer and linear variable displacement transducer (LVDT). As shown in Fig. 3.81, two pressure sensors (PT1 and PT2) with 1 MHz sampling rate are installed on the slab proximal surface to record the blast pressure: PT1 is installed on the slab center and PT2 is installed close to the free edge. A LVDT with effective stroke distance of 300 mm ($+150$ to -150 mm) is installed beneath the slab on the distal surface to record the slab mid-span deflection history. In the second event, a 12 kg TNT
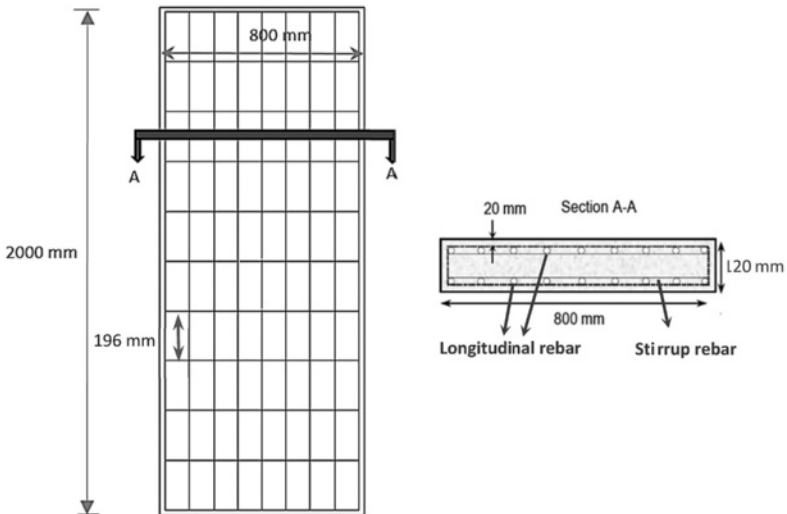
Figure 3.80 Dimension and reinforcement of slabs in close-range explosion tests.
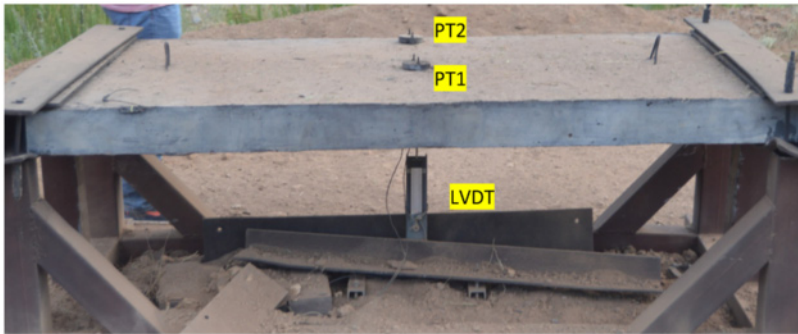
Figure 3.81 Pressure sensor installation on the UHMWPE-1 slab under 6 kg TNT at 1.5 m standoff distance.

Table 3.24 **Field blast test matrix**

Slab no.	TNT charge weight (kg)	Standoff distance (m)	Scaled distance (m kg$^{-1/3}$)	Data acquisition
UHMWPE-1	6	1.5	0.825	Blast pressure Slab deflection
UHMWPE-2	12	1.5	0.655	Slab deflection
Hybrid-1	6	1.5	0.825	Slab deflection
Hybrid-2	12	1.5	0.655	Slab deflection
Plain concrete slab	8	1.5	0.750	Slab deflection

explosive is used on UHMWPE-2 slab. To avoid possible damage, no pressure sensor is installed.

For hybrid fiber-reinforced slabs, the same blast loading scenarios are considered. A 6 kg TNT at 1.5 m standoff distance is employed for Hybrid-1 slab, while 12 kg TNT at 1.5 m standoff distance is used for Hybrid-2 slab. Only LVDT is installed on these two slabs for deflection measurement.

For comparison purpose, slab made of plain concrete is tested under 8 kg TNT detonation at 1.5 m above the slab center. Slab failure is anticipated for plain concrete slab under this loading scenario. It is worth noting that though the inclusion of plain concrete slab cannot provide quantitative comparison with fiber-reinforced slabs, its performance can qualitatively demonstrate the effectiveness of the FRC against blast load.

Test matrix in this study is summarized in Table 3.24.

3.6.2.2   Testing setup

Test setup is shown in Fig. 3.82. In this test study, the slab is placed on a precast steel frame with a height of 600 mm above the ground. The slab is clamped at its

Figure 3.82 Close-in detonation setup and clamping system.
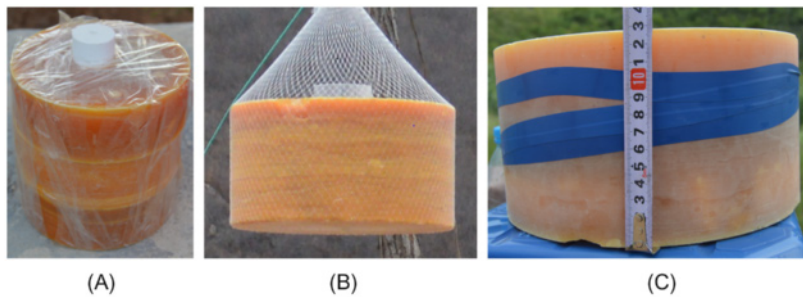
Figure 3.83 Explosives used in the current blast tests: (A) 6 kg TNT, (B) 8 kg TNT, and (C) 12 kg TNT.

both ends with steel cleats and bolts. This setup is an idealized fix end boundary which prevents slab from rebounding under severe blast loads. It is also worth noting that, as the distance between the slab and ground is not sufficiently large, blast pressure that reflects from the ground may generate negative bending moment on the slab. It is believed that such blast reflection may help increase the slab blast-resistance performance, however, this part is beyond the scope of current study, and therefore not discussed herein.

It is worth noting that in this study, cylindrical TNT explosive is used in the tests with its axis perpendicular to the slab surface (see Fig. 3.83), and detonator is used to electrically activate the explosive.

The charge shape and orientation play important roles in the blast peak pressure and impulse [62,74]. In the present setup, the detonator is positioned at the top of the cylinder causing the blast to propagate along the axis of the cylinder, focusing the pressure of the charge to the center of the slab. Also the geometry of the charge may cause a concentration of blast energy to emanate from the end of the charge. In the previous tests concerning the shape and orientation of the explosive, it was

found that for the cylindrical charge with the axis oriented vertically, it can be seen that the reflected pressure was highly directional, and the peak pressure was approximately 200% larger than the theoretical value given by UFC 3-340-02, and then drops below the theoretical value at the edges of the slab.

3.6.3 Field blast tests results and discussion

Fig. 3.84 shows the UHMWPE-1 slab after 6 kg TNT detonation at 1.5 m standoff distance. It can be clearly noted that UHMWPE-1 slab suffered no damage and no permanent deflection can be observed. The clamped boundary effectively resisted the blast load and rebound of the slab was prevented. Due to the pressure sensor system malfunction, the pressure time history data in the present test were not properly recorded. The peak blast overpressures given by PT1 and PT2 are 9.5 MPa and 7.7 MPa, respectively, which are more than 20% higher than the empirical predictions by UFC 3-340-02.

The deflection time history of the UHMWPE-1 slab is shown in Fig. 3.85. During the blast loading phase (within several milliseconds), slab responds promptly and after the blast loading phase the slab enters into a free-vibration period, and the maximum deflection at slab mid-span is around 27 mm.

UHMWPE-2 fiber-reinforced concrete slab was subjected to a 12 kg TNT detonation at the same standoff distance, and it is noted from Fig. 3.86 that flexural failure occurred at the slab mid-span. Mid-span crack can be observed but not throughout the whole cross-section. Slab mid-span deflection was not completely measured in the test owing to the deflection that went beyond the measurement range of the LVDT as shown in Fig. 3.87. The slab maximum deflection was measured to be more than 95 mm and its permanent deflection was 50 mm obtained manually with a ruler and string after test.

Fig. 3.88 shows the Hybrid-1 slab after 6 kg TNT detonation at 1.5 m standoff distance, and the slab shows some hairline cracks but no permanent deflection,

Figure 3.84 UHMWPE-1 fiber-reinforced concrete slab after 6 kg TNT from 1.5 m standoff.
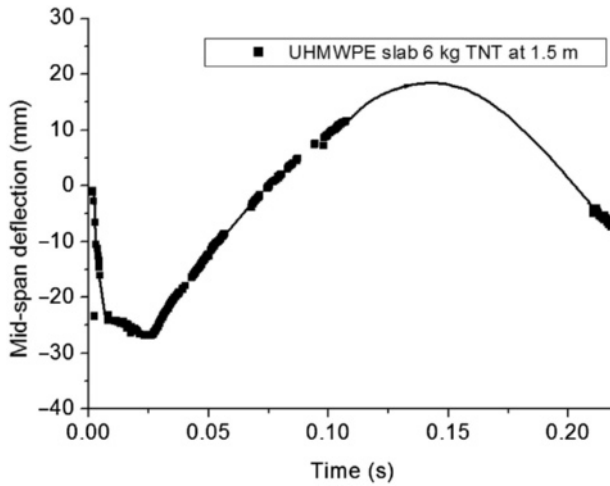
Figure 3.85 Deflection time history of UHMWPE slab under 6 kg TNT at 1.5 m.
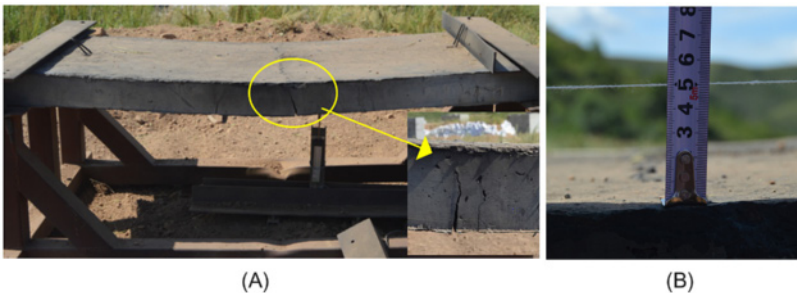
Figure 3.86 UHMWPE-2 fiber-reinforced concrete slab after 12 kg TNT detonation from 1.5 m standoff distance: (A) slab flexural crack and (B) residual deflection.

thanks to the fiber material addition. Due to the LVDT system malfunction, no data were collected for slab mid-span deflection.

For Hybrid-2 slab which was loaded with the same blast as UHMWPE-2 slab, similar flexural failure was observed with a major crack located on the slab mid-span as shown in Fig. 3.89. The crack depth was about 70 mm which was smaller than UHMWPE-2 slab. According to LVDT measurement, the maximum slab deflection was about 72 mm as shown in Fig. 3.90. The slab permanent deflection was manually measured as 34 mm. Both the maximum deflection and permanent deflection of Hybrid-2 slab are smaller than UHMWPE-2 slab. Such improvement can be ascribed to the combination of both fiber materials, and steel fiber contributes more to the strength enhancement while UHMWPE fiber helps more with the material ductility.
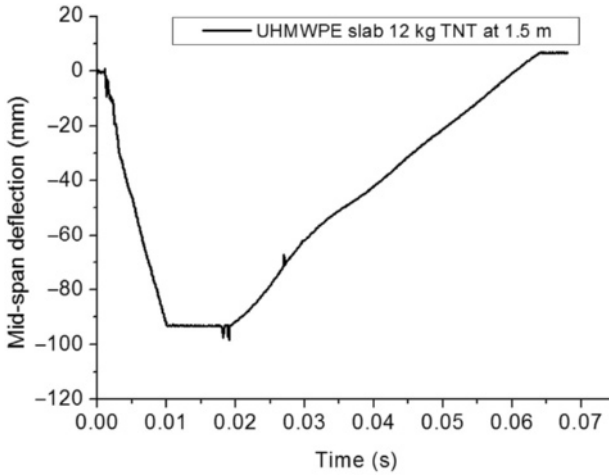
Figure 3.87 Deflection time history of UHMWPE slab under 12 kg TNT at 1.5 m.

Figure 3.88 Hybrid-1 fiber-reinforced concrete slab after 6 kg TNT detonation from 1.5 m standoff distance.

A close investigation on the mid-span cracks on UHMWPE-2 fiber-reinforced slab and Hybrid-2 fiber-reinforced slab is shown in Fig. 3.91. It is noted that Hybrid-2 slab develops multicracks along the slab depth. During the crack opening, steel fibers with higher tensile strength effectively bridge over the major cracks; the elongation and pull-out of the steel fiber transfer stress into the surrounding concrete matrix and develop more refined cracks, and these microcracks can be further confined by both steel and UHMWPE fibers. For mono UHMWPE fiber-reinforced slab UHMWPE-2, due to the lower fiber strength and modulus, and also the weaker

(A)   (B)

Figure 3.89 Hybrid-2 fiber-reinforced concrete slab after 12 kg TNT detonation from 1.5 m standoff distance: (A) slab flexural crack and (B) residual deflection.
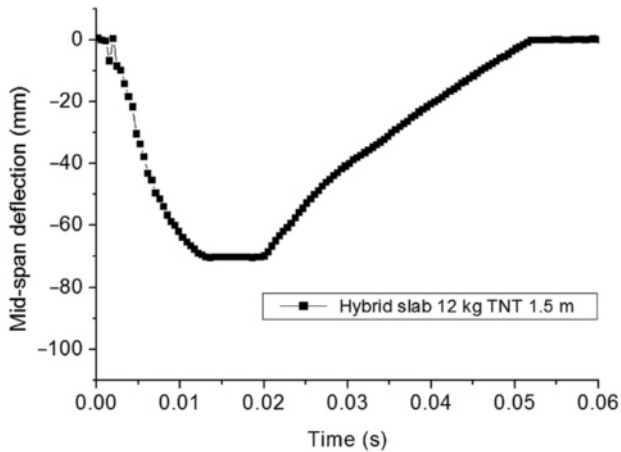
Figure 3.90 Deflection time history of Hybrid-2 slab under 12 kg TNT at 1.5 m.

bonding between UHMWPE fiber and concrete matrix [28], the bridge effect is less prominent than hybrid FRC slab.

Fig. 3.92 shows the plain concrete slab after 8 kg TNT detonation at 1.5 m above the slab center, and the slab fails completely with a permanent deflection of 190 mm which is manually measured after the test. Although some shear cracks can be observed, the failure of the plain slab is predominantly flexure with a major crack in the slab mid-span. After the blast load impinged upon the slab, tensile crack was initiated on the slab distal surface. With the increase of the slab deflection, longitudinal reinforcement started yielding and the slab failed after concrete crush on the slab proximal surface. In addition, some side concrete spallation can be observed on the slab free edge, and this kind of failure is induced by stress wave propagation. It is clearly seen that plain concrete is less blast resistant than FRC discussed earlier.
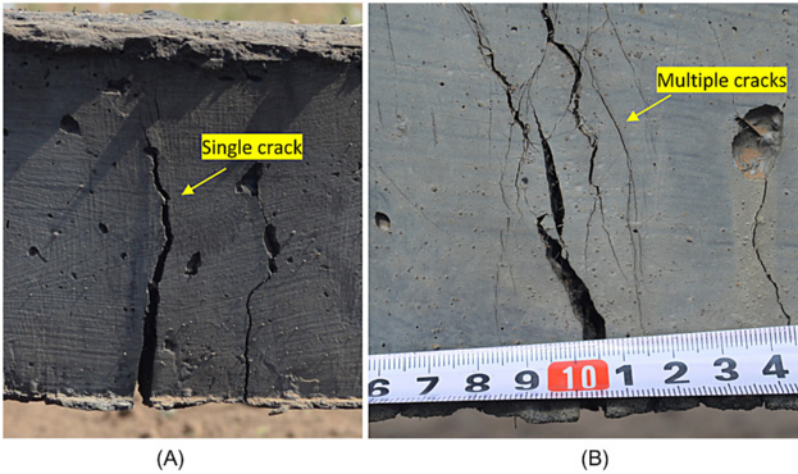
Figure 3.91 Crack development on (A) UHMWPE-2 slab and (B) Hybrid-2 slab.

Figure 3.92 Plain concrete slab after 8 kg TNT detonation from 1.5 m standoff distance: (A) slab failure and (B) residual deflection.

3.6.4 Conclusion

In this research, an experimental study on the high-performance FRC is carried out. UHMWPE fiber material is featured with low density but equipped with high material tensile strength and modulus. Previous study reveals that UHMWPE composites have excellent antiimpact capability. In this study, concrete material with UHMWPE fiber reinforcement is developed, and static test results show that addition of UHMWPE fiber material has profound influence on concrete tensile performance, and both concrete tensile strength and strain capacity receive enhancement after UHMWPE fiber addition. However, material compressive strength is less sensitive to the UHMWPE fiber addition. A hybrid-fiber addition, i.e., steel fiber and UHMWPE fiber is also investigated, and the static test results show that hybrid-fiber addition can further enhance concrete strength and also provide better tensile strain capacity. Field blast tests on concrete slabs demonstrated the feasibility of

using these FRC materials against blast loads. Under severe blast loads from 12 kg TNT detonations at 1.5 m standoff distance, the slabs made of UHMWPE fiber and hybrid-fiber material experienced much less damage and smaller structural deformation as compared to the normal RC slab.

3.7 Derivation of normalized pressure−impulse curves for flexural ultra-high performance concrete slabs

In this section, an advanced moment rotation analysis model for simulating the behavior of the plastic hinge of a UHPC member is incorporated into the FD procedure for the dynamic response analysis of reinforced UHPC slabs under blast loads. The accuracy of the FD analysis model that utilized the moment rotation analysis technique was validated using results from blast tests conducted on UHPC slabs. The validated FD model was then used to generate pressure−impulse ($P-I$) curves. Parametric studies were then conducted to investigate the effects of various sectional and member properties on $P-I$ curves. Based on the simulated results, two equations were derived which can be used to normalize a $P-I$ curve. Further numerical testing of the normalization equations for UHPC members was then undertaken. The generated normalized $P-I$ curve, accompanied by the derived normalization equations, can be used for the purposes of general UHPC blast design.

3.7.1 Finite difference model for ultra-high performance concrete against blast loads

Until now, little research has been conducted to analytically investigate the dynamic performance of UHPC members under blast loads. Due to the significant difference in mechanical properties of UHPC, conventional analytical methods, such as single-degree-of-freedom (SDOF) models, FD, and FE models, need to be extended to accommodate UHPC. It has been proven that the FD analysis method is an accurate and fast running method suitable for the prediction of the behavior of NSC members subjected to high intensity, short duration dynamic loads such as those associated with impacts and explosions. It is expected that the FD model can also be used for the dynamic analysis of UHPC members subjected to blast loads.

The FD model incorporates the variation of blast loading distribution and mechanical properties of the cross-section along the member, and accommodates shear and flexural deformations with strain rate effects. Such a model has been developed [75] to predict the behavior of NSC members subjected to blast and impulsive loading. Within this FD model, a moment curvature relationship, determined assuming full interaction between the steel bar and concrete, for NSC members is utilized. When analyzing an RC beam in flexure, once the elastic limit is reached, it is assumed that a plastic hinge region forms in which a large amount of rotation occurs over a discrete region, known as the hinge length. The hinge length is determined empirically and there is no general agreement on the value or even

which parameters to use to find the hinge length. Traditionally, the rotation is found by multiplying the hinge length by the curvature obtained from the moment curvature relationship and, due to this, is deemed only to be an empirical method. Recently, an advanced mechanics-based approach was developed [76] to determine the rotation of an NSC section taking into account the slip characteristics of the reinforcing steel and the softening wedge of concrete. Based on this, it is possible to derive a more accurate moment rotation relationship for the plastic hinge of an NSC member. However, due to the addition of small steel fibers into the UHPC mix, while NSC is assumed to have no tensile strength in analyses, UHPC has a flexural tensile strength of approximately 30 MPa. To accommodate such differences, the moment rotation model developed for NSC members needs to be extended for UHPC members.

Pressure−impulse ($P-I$) diagrams based on the equivalent SDOF approach and numerical approaches have been adopted for use during building design in order to assess the effects of blasts on structures. The formulae are normally based on an SDOF system with a bilinear resistance deflection curve, i.e., elastic−plastic hardening, elastic−plastic softening, or elastic−perfectly plastic. Although the use of the bilinear resistance deflection curve is more appropriate, the SDOF model cannot consider a spatially and temporally varying distribution of blast loading, and is incapable of allowing for variations of mechanical properties of the cross-section along the member. Shi et al. [77] attempted to derive analytical formulae that can be used to derive a normalized $P-I$ diagram for RC columns. The analytical formulae are functions of the properties of the member, such as reinforcing ratio and depth of the member. The formulae are limited by the small range of parameters that were investigated in the parametric study. For example, the effects of steel bars with strain hardening properties and also the effects of higher strength (above 50 MPa) concretes were not investigated.

In this section, the FD model for NSC members is extended to accommodate UHPC members by incorporating the properties of the blast load and the advanced moment rotation model into the analysis. The extended FD model is validated using data from blast tests conducted on UHPC members. With the validated FD model, parametric studies are carried out to derive $P-I$ diagrams, which have been widely used in the design of conventional RC structures against blast loads, for UHPC members. Using the simulated results, two equations, which can be used to normalize a $P-I$ curve for an UHPC member, have been identified and tested. A normalized $P-I$ curve has been derived which, when accompanied by the two normalization equations, can be used for the generic assessment of structures to establish safe response limits for given blast loading scenarios.

3.7.2 Moment rotation analysis of ultra-high performance concrete members

An advanced approach to incorporate the uncracked tension force of UHPC, steel fibers, and steel forces in the cracked section, and a softening wedge in the
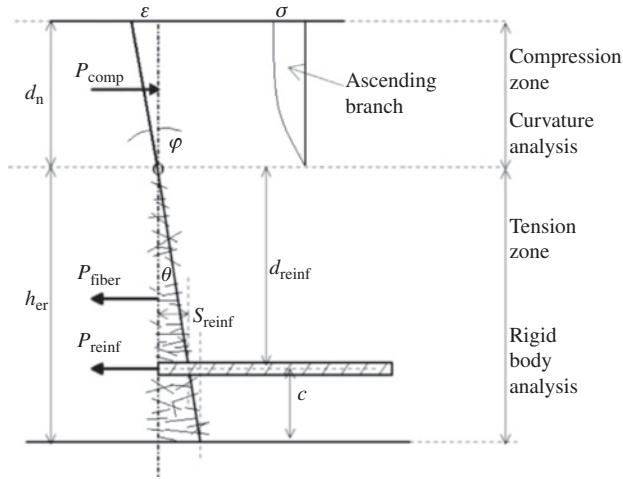
Figure 3.93 Moment rotation analysis.

compression zone into the rigid body rotation analysis as shown in Fig. 3.93, was developed to determine the moment rotation relationship for UHPC members. The steel fibers are responsible for a significant increase in the tensile strength of UHPC. The tensile force contributed by the fibers in UHPC is obtained through an experimental stress-crack width relationship using a slice approach [78]. This approach, usually referred to as the layered capacity method [79], involves splitting the cracked tensile zone, as seen in Fig. 3.93 into thin horizontal slices. Each slice has a given crack width, and thus has a given stress which can be determined using the above-mentioned stress-crack width relationship. For each slice, these stresses can then be converted to forces which contribute to the overall moment. To incorporate an uncracked and cracked tensile force, due to the steel fibers, the method developed by Haskett et al. [76] had to be modified by assuming a linear strain profile. This allowed the model to determine a moment rotation relationship and a moment curvature relationship for a given section. The incorporation of steel fibers within this type of analysis enabled more accurate moment rotation curves to be determined.

The new model was divided into four stages to incorporate the uncracked tension force of UHPC, effects of steel fibers, steel forces in the cracked section, and softening wedge in the compression zone. The four stages are stage 1: prior to cracking; stage 2: crack below the reinforcement; stage 3: before formation of softening wedge; and stage 4: after formation of softening wedge. In stage 1, because the tensile region is uncracked, all forces in the compression and tensile region can be obtained by the assumption of a linear strain profile. The curvature and moment can be obtained by achieving force equilibrium. In stage 2, when a crack forms below the reinforcement, additional forces within this cracked region due to the steel fibers in the cracked section are calculated based on the stress-crack width

relationship. All other forces are obtained based on the linear strain profile assumption as mentioned earlier. Now that a crack has formed, a moment, curvature, and a rotation can be determined for this stage and all subsequent stages. In stage 3, the crack apex is above the steel reinforcement, therefore a slip exists between the steel reinforcement and the concrete on the inside crack face, denoted by S_{reinf} in Fig. 3.93. Partial interaction theory is used to determine the tension force of steel reinforcement based on a given slip. The partial interaction model [80] is the method in which a local bond stress−strain relationship, between the steel reinforcement and concrete, is used to determine a global load slip relationship. The same procedures as in stage 2 are used to determine all other forces. Stage 3 ends when the strain in the top fiber of the slab reaches the crushing strain. In stage 4, a softening wedge forms as the strain in the top fiber of the slab has exceeded the crushing strain. In this stage, the concrete compressive force is divided into two parts. The first is the ascending region, which is calculated using Hognestad's concrete stress−strain model and acts below the wedge. The second is the softening force due to the formation of the softening wedge. The rest of the forces are calculated using the procedures discussed in stage 3. In any stage, the analysis stops when a failure mechanism of bar fracture, bar debonding, or wedge failure occurs.

The moment rotation analysis was used to determine a moment curvature and moment rotation relationship for UHPC slab D2B. The reinforced UHPC slab, D2B, has a span of 2000 mm, width of 1000 mm, and a thickness of 100 mm [81]. It is reinforced with a 12.7 mm diameter mild steel mesh with yield strength of 600 MPa that is spaced at 100 mm centers in the major bending plane (0.8%) and at 200 mm centers in the minor plane. The UHPC had an average compressive strength of 175 MPa, tensile capacity of 22 MPa, and Young's modulus of 47 GPa. The moment curvature and moment rotation relationships were used to derive a theoretical load deflection relationship which was compared to the experimental load deflection relationship of slab D2B in Fig. 3.94.
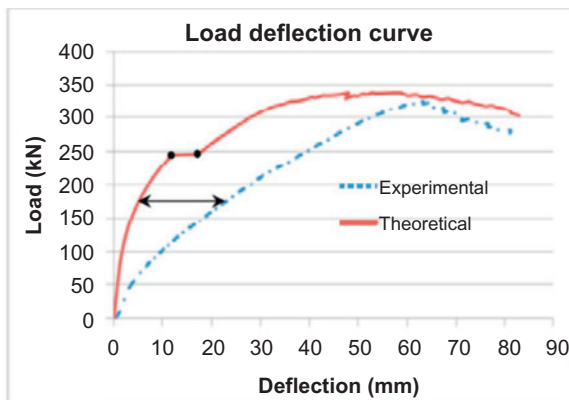
Figure 3.94 UHPC slab D2B load deflection relationship.

Although the dynamic response model as a whole is primarily interested in the behavior of UHPC members at or near ultimate state, Fig. 3.94 helps to justify why it is worth modeling the sectional behavior at the early stages of cracking. For an NSC section, cracking typically occurs at a very low moment. However, for an UHPC section, cracking occurs at a moment which can be up to 70% of its ultimate moment capacity. This is due to the addition of fibers in the UHPC material, which causes the material to have a significantly larger tensile strength that cannot be ignored. This can be seen in Fig. 3.94 as the horizontal portion, at approximately 250 kN, represents the point at which cracking occurs. As this region influences the dynamic behavior of members against large blasts which cause failure, it is deemed important to model this region more accurately. From Fig. 3.94, it can be seen that there are large discrepancies between the theoretical and experimental curves in the rising branch, shown by the horizontal arrow, but the results are much more reasonable at ultimate conditions. As the stress-crack width relationship [78] was used, this is attributed to the difference in material properties between the UHPC material used in this study and that used in their study. Therefore the deflections caused by larger loads are quite accurate, whereas the deflections caused by smaller loads are not as accurate. The above moment rotation analysis model provides moment curvature and moment rotation relationships which are inputs for the FD model for determining the dynamic response of UHPC members against blast loads. Although the model is not fully accurate, what is most important is the concept of modeling the response of the plastic hinge via a moment rotation relationship in a dynamic model.

3.7.3   Finite difference analysis of ultra-high performance concrete members

The Timoshenko Beam Theory accounts for shear deformation and rotational inertia, being solved for in the FD model. The dynamic equilibrium equations are as follows:

$$\frac{\partial M}{\partial x} - Q = -\rho_m I \frac{\partial^2 \beta}{\partial t^2} \tag{3.17}$$

$$\frac{\partial Q}{\partial x} + q + P_a \frac{\partial \beta}{\partial x} = \rho_m A \frac{\partial^2 v}{\partial t^2} \tag{3.18}$$

where M = bending moment, Q = shear force, q = load acting transverse to the beam, P_a = axial load in the beam, A = cross-sectional area, I = moment of inertia of the beam, ρ_m = mass density of the beam, β = rotation, and v = transverse displacement.

3.7.3.1 Numerical method

The response of the member is determined using the FD method. Eqs. 3.19 and 3.20 show how the rotation and displacement, respectively, of node i at time $t + 1$ are calculated.

$$\beta_i^{t+1} = 2\beta_i^t - \beta_i^{t-1} - \frac{\mathrm{d}t^2}{\rho_{\mathrm{m}} I_i} \left[\frac{M_{i+1}^t - M_{i-1}^t}{2\mathrm{d}x} - Q(i) \right] \tag{3.19}$$

$$\nu_i^{t+1} = 2\nu_i^t - \nu_i^{t-1} + \frac{\mathrm{d}t^2}{\rho_{\mathrm{m}} A_i} \left[\frac{Q_{i+1}^t - Q_{i-1}^t}{2\mathrm{d}x} + q(i) \right] \tag{3.20}$$

To calculate the rotation and displacement for the new time step using Eqs. 3.19 and 3.20, respectively, the shear force at each node must be known. The shear force at each node is calculated as a function of shear strain. The shear strain, seen in Eq. 3.21, is calculated by converting the partial derivative into FD form.

$$\gamma_{xzi}^t = \frac{\partial v}{\partial x} - \beta = \frac{v_{i+1}^t - v_{i-1}^t}{2\mathrm{d}x} - \beta_i^t \tag{3.21}$$

To calculate the rotation for the new time step, the bending moment at each node must be known. At the nonplastic hinge regions, the bending moment of a node is calculated as a function of curvature using the moment curvature relationship. At the plastic hinge region, the bending moment of a node is calculated as a function of its rotation using the moment rotation relationship. The moment curvature relationship and moment rotation relationship of a member are both derived using the moment rotation model. The curvature, seen in Eq. 3.22, is also calculated by converting the partial derivative into FD form.

$$\varphi_i^t = -\frac{\partial \beta}{\partial x} = -\frac{\beta_{i+1}^t - \beta_{i-1}^t}{2\mathrm{d}x} \tag{3.22}$$

The plastic hinge region was modeled in such a way that the discrete rotation of the plastic hinge occurred between two adjacent nodes. Therefore by knowing the rotation of the adjacent nodes, β_{left}^t and β_{right}^t, the discrete rotation of the plastic hinge can be calculated and can be seen in Eq. 3.23.

$$\theta_i^t = -\frac{\beta_{\mathrm{right}}^t - \beta_{\mathrm{left}}^t}{2} \tag{3.23}$$

It is important to note that modeling of the plastic hinge begins at the onset of cracking of a particular node. This was done by calculating the curvature in which cracking occurs, so that when the curvature of the node reaches the cracking curvature, moment rotation is then used to model that region as a plastic hinge. A plastic hinge was assumed to only form at the center for a simply supported member, and

they were assumed to form at the ends and the center for a member fixed at both supports.

The FD method allows an arbitrary blast load to be applied on each node of the member as a function of time. This allows one to determine the structural response of a member due to a pressure time history which has been derived by codes, equations, or measured directly through experiments. However, due to the assumption of the positions in which the plastic hinges form, only blast loads which are symmetrical about the mid-span can be applied.

3.7.3.2 Shear behavior

Linear shear stress−strain theory was used to calculate the shear force, Q, from the shear strain, as can be seen from Eq. 3.24.

$$Q = KA\sigma_{xz} = KAG\gamma_{xz} \tag{3.24}$$

where G = shear stiffness, σ_{xz} = shear stress, γ_{xz} = shear strain, and K = correction factor that is used to take into account the constant cross-sectional shear stress assumption. $K = \pi^2/12$ for rectangular cross-sections.

3.7.4 Validation of structural response model

As can be seen from Table 3.25, two blast events involving UHPC slabs with a span of 2000 mm, 1000 mm wide, and 100 mm thick were chosen for validation; events 1 and 2 [81]. During event 1, slab D2B was subjected to a blast from a cylindrical charge, whereas during event 2, slab D3B was subjected to a blast from a cylindrical charge. Both cylindrical charges were oriented in the radial direction, meaning the primary axis of the cylindrical charge was directed parallel to the plane of the slab. No overpressure time history data were obtained from these tests, so they had to be estimated. This involved converting the peak reflected overpressure and impulse predicted by UFC guidelines (UFC-3-340-02 2008) for a spherical charge to that of a cylindrical charge of the same scaled distance in the radial direction. It should be emphasized that the predicted pressure time history will have a significant influence on the results, so it should be considered when evaluating the suitability of the structural response model.

Table 3.25 **Charge properties and slab models used in blast events for validation**

Event no.	Slab no.	Charge mass (kg)	Standoff distance (m)	Scaled distance (m kg$^{-1/3}$)	Charge shape
1	D2B	14	1	0.4	Cylindrical
2	D3B	8	1	0.5	Cylindrical

During the validation process, it had to be decided whether to model the response under pinned or fixed end support conditions. From the blast tests, it was observed that the end restraints, which each consisted of two steel equal angles bolted together to act as a clamp, could not be considered to be fully fixed or fully pinned. They witnessed that for large blasts, which caused large deflections, the clamps would give way, but for small blasts, causing small deflections, the clamps would remain fully intact. Therefore it was deduced that when the moment developed at the ends of the slab was believed to be large, due to a large blast causing large deflections, the restraint could be considered pinned. Conversely, for small developed moments at the ends of the slab, due to small blasts causing small deflections, fixed end conditions could be considered more suitable. This ideology was adopted when undertaking the validation.

Fig. 3.95 shows the deflection time history for event 6. This response is of slab D2B subjected to a blast with a small-scaled distance, which caused the member to collapse. The model correctly predicts that the member fails. It also roughly estimates at what time and deflection collapse of the member occurs. The discrepancy due to the increased initial stiffness of the theoretically developed moment curvature relationship can be observed, as the theoretical deflection occurs with a greater frequency than the experimental deflection.

Fig. 3.96 shows the deflection time history for event 2. This is the response of slab D3B under a charge which caused a significant deflection. It can be seen that the model reasonably predicts the maximum deflection in this case. The discrepancy in the time to reach the maximum deflection can be accredited to the increased initial stiffness of the theoretically developed moment curvature and moment rotation relationships of slab D3B. The discrepancy in the falling branch can not only be described by the increased initial stiffness, but also because of the fact that the structural response model does not attempt to model the postpeak behavior of the member response. Therefore the unloading curve of the member response may not be correct. The correct postpeak behavior was not modeled as only the first peak of
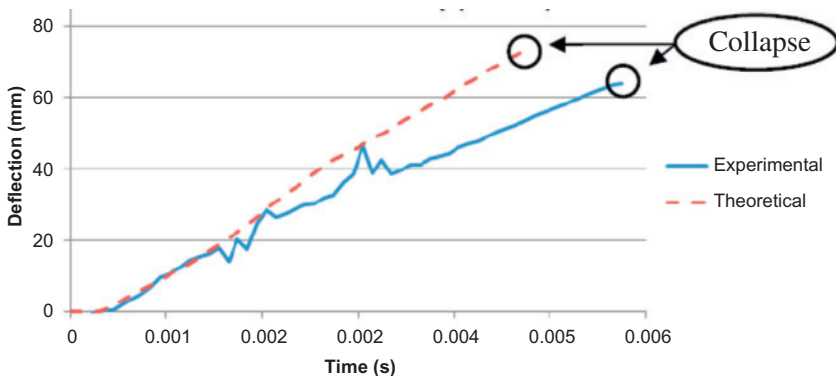
Figure 3.95 Deflection time history for event 1.
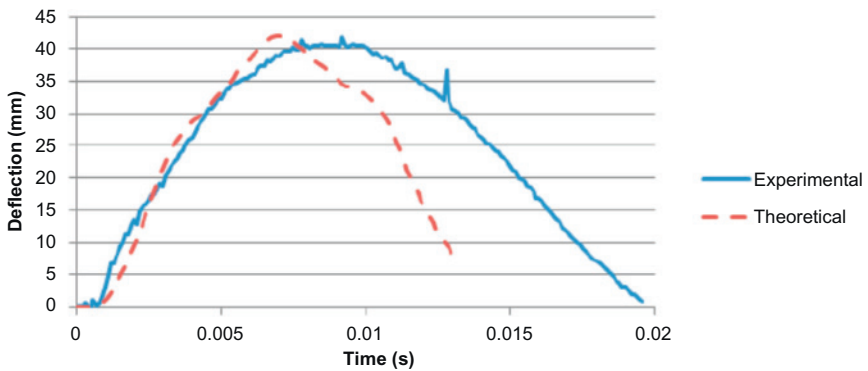
Figure 3.96 Deflection time history for event 2.

the deflection time history was required for this research and because modeling of the postpeak response can be very difficult.

After observing the comparison, it can be seen that for larger blast loads, and thus larger deflections, the differences in the results are quite small. This is because the inaccuracy of the moment rotation model in the elastic region, thus before cracking occurs, has a negligible effect on the response of structural members near ultimate state. As this research is more interested in the response of structural members under large blasts, which cause large deflections, the model was considered to be appropriate.

3.7.5   Overpressure impulse curve

Various blasts which produce various peak reflected overpressures and impulses can cause failure. A $P{-}I$ curve is the envelope of all overpressure time histories, plotted on axes of impulse and peak reflected overpressure, which cause failure. The $P{-}I$ curve can be used as a tool to design members against blast loads, if the peak reflected overpressure and impulse of the blast are known.

3.7.5.1   P$-$I *curve generation*

This ultimate rotation of the plastic hinge was used as the failure criteria. The $P{-}I$ curve developed for slab D3B can be seen in Fig. 3.97. To generate a $P{-}I$ curve, the minimum peak reflected overpressure and a very large impulse, altered by manipulating t_d, had to be chosen. They had to be chosen such that it was known those two parameters for a particular blast load would cause failure for the given member. The program then decreases the impulse, by decreasing t_d, without changing P_r and runs the structural response simulation. This process is iterated until it is found that the member survives a simulation. The peak reflected overpressure and impulse of this particular overpressure time history is then plotted on the $P{-}I$
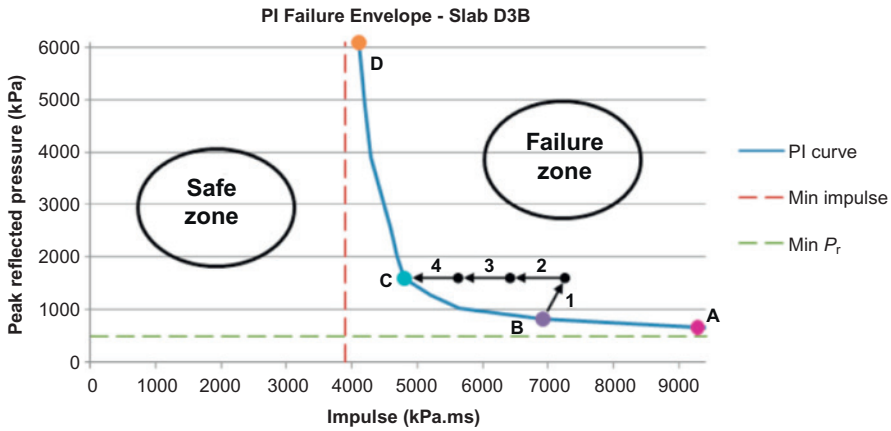
Figure 3.97 $P-I$ curve for slab D3B.

diagram axes. The peak reflected overpressure is then increased, which in turn also increases the impulse of the blast load as t_d is not changed. For example, in Fig. 3.97, if point B was known, to find the next point on the $P-I$ curve, the structural response model would first increase P_r without changing t_d, seen as arrow 1. Then it would incrementally reduce the impulse, seen as arrows 2, 3, and 4, until point C has been located. That is the next point in which the member survives a simulation. The above process is repeated such that many points are plotted on the $P-I$ diagram. These points then form the $P-I$ curve.

Fig. 3.97 shows how for large impulses, the peak reflected overpressure of the $P-I$ curve converges to a minimum value, P_{rmin}. It also shows that for large peak reflected overpressures, the impulse of the $P-I$ curve converges to a minimum value, I_{min}. Finally, between these extremes lies a transition zone, for example point C. A blast load which lies in the lower right hand side of the $P-I$ diagram, for example point A in Fig. 3.97, can be thought of as an explosion from a large charge weight and a large standoff distance. This is because such a blast will cause a pressure time history with a small peak reflected overpressure, a large duration, t_d, and also a large impulse. Conversely, a blast load which lies in the upper left hand side of the $P-I$ diagram, for example point D in Fig. 3.97, can be thought of as an explosion from a small charge weight but a small standoff distance. This is because such a blast will cause a pressure time history with a large peak reflected overpressure, a small duration, t_d, and also a small impulse. Fig. 3.97 also displays the safe zone and failure zone of the $P-I$ curve of slab D3B, which shows whether the member will fail or survive under any given external blast load. The structural response model assumes that the overpressure time history is uniformly distributed on the slab. Therefore the effects of angle of incidences along the slab are ignored, and the effects of time of arrival differences along the slab are also ignored. As the angle of incidence increases, the pressure time history typically becomes less

damaging. Therefore as long as the maximum pressure time history is assumed to act on the entire slab, the developed $P-I$ curve can be thought of as conservative.

3.7.6 Normalization of P–I curves

The structural response model can be used to generate $P-I$ curves for a given member for collapse. Using this data, the normalization of $P-I$ curves will take place. This includes understanding what factors affect the $P-I$ curve of given members so that empirical equations of proportionality or empirical normalization equations, for slabs with pinned supports, can be developed. This allows the designer to quickly draw a $P-I$ curve based on the member and sectional properties of the slab.

3.7.6.1 Methodology

The effects of member and sectional properties on $P-I$ curves were investigated. The members' properties investigated included span and depth, whereas the sectional property investigated was the moment rotation relationship. As this study only applies to one-way slabs, the effects of the width of the slab on the $P-I$ curve were not investigated as the width of a one-way spanning slab has no effect on its response.

To normalize the $P-I$ curves the effects of member and sectional properties on the minimum impulse, I_{min}, and minimum peak reflected overpressure, P_{rmin}, asymptotes were studied. Therefore the concept of a control specimen had to be introduced. When manipulating a property, for example the span of the member, the asymptotes had to be factored up or down from that of the control specimen to understand how it affected P_{rmin} and I_{min}. It should be noted that the aim of this section is to determine equations for P_{rmin} and I_{min} only. Any $P-I$ curve, with asymptotes of unity, can be used in conjunction with the equations developed in this study to determine the $P-I$ curve of a given member.

3.7.6.2 Span of a member

To normalize the span of a member, a section with a certain width, depth, and moment rotation relationship was chosen. The span was then altered to find the effects of this parameter on P_{rmin} and I_{min}. $P-I$ curves for slabs of varying spans can be seen in Fig. 3.98. From Fig. 3.98, P_{rmin} and I_{min} values can be determined for each span. The ratio of these two values, for each span, to those of the control specimen ($P_{rmin,o}$ and $I_{min,o}$, respectively) can be plotted to find how the span affects the $P-I$ curve. In this case, the slab with length 1.78 m is the control specimen. The plots can be seen in Fig. 3.98 for P_{rmin} and I_{min}.

Fig. 3.99A shows that P_{rmin} is inversely proportional to L^2. For slabs with the same moment capacity subjected to static uniform overpressures, the overpressure capacity is also inversely proportional to L^2. Fig. 3.99B shows that I_{min} is proportional to $L^{-0.25}$. This is different as other additional factors are affected by the slabs
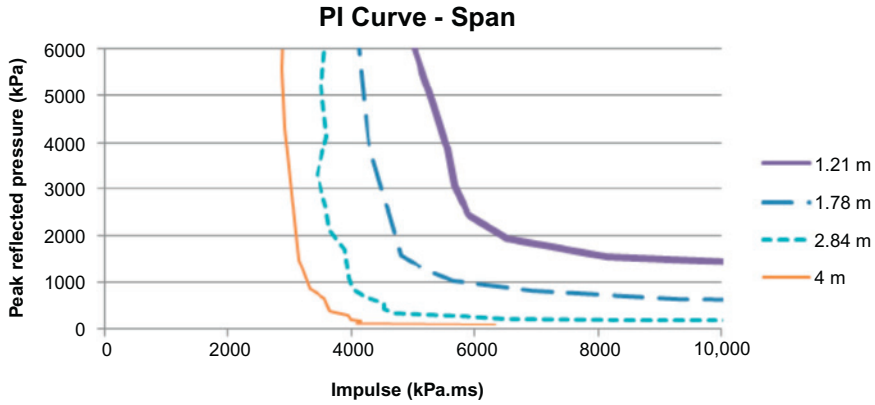
PI Curve - Span

Figure 3.98 $P-I$ curves for slabs of varying spans.

(A)   (B)
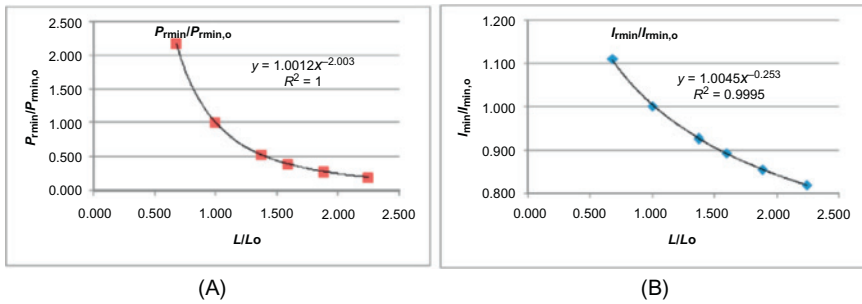
Figure 3.99 Effects of span on P_{rmin} (A) and I_{min} (B).

span, such as its total mass and its ability to absorb energy. These additional factors also affect the slabs ability to resist impulse controlled blasts.

3.7.6.3 Moment rotation relationship

To understand how the shape of the moment rotation relationship affected P_{rmin} and I_{min}, a control slab was chosen, and $P-I$ curves were determined for many slabs with moment rotation relationships which differ from the control slab. All slabs contained UHPC, reinforced with high strength steel bars, with an ultimate strength of 1800 MPa, in the tensile region only. To produce different moment rotation relationships, the reinforcing ratio, from 1% to 3.5%, and bond stress characteristics between the steel bars and concrete were changed.

Using the structural response model, $P-I$ curves were determined for each of the slabs with differing moment rotation relationships. From these $P-I$ curves, P_{rmin} and I_{min} were determined. The aim was then to develop equations which can be used to determine P_{rmin} and I_{min} based on any moment rotation relationship. To

Table 3.26 Quantification of the effects of the moment rotation relationship on P_{rmin}

Properties							$P_{rmin}/P_{rmin,o}$		
n bars	k_τ	k_{yp}	$k_{yp}/k_{yp,o}$	k_{duc}	$k_{duc}/k_{duc,o}$	M/M_o	Numer.	Theor.	Error (%)
5b	2.2	0.913	0.946	0.240	0.905	0.779	1.500	1.500	0.000
5b	1.25	0.991	1.026	0.269	1.017	0.676	1.430	1.418	0.870
5b	0.9	0.993	1.029	0.280	1.056	0.637	1.460	1.445	1.011
8b	1.25	0.966	1.001	0.266	1.003	0.888	1.120	1.122	0.166
5b	0.5	0.992	1.027	0.306	1.155	0.587	1.430	1.435	0.348
10b	1.25	0.966	1.000	0.265	1.000	1.000	1.000	1.000	0.000
15b	1.25	0.951	0.985	0.277	1.046	1.261	0.750	0.770	2.605
18b	1.25	0.953	0.987	0.302	1.142	1.363	0.660	0.651	1.359
		kyp,power		kduc,power				Average	0.908
		0.29256		0.16817					

do this, it was necessary to identify the main points on the moment rotation relationship which affected P_{rmin} and I_{min}. As all moment rotation relationships were of bilinear shape, after careful analysis, three values, corresponding to two points on the moment rotation relationship, were recognized as having influence over P_{rmin} and I_{min}. These values were the ultimate moment (M_u), yield moment (M_y), and the ultimate rotation (θ_u).

When investigating the effects of the moment rotation relationship on P_{rmin}, it was observed that P_{rmin} was proportional to the product of three terms. The first term is the ultimate moment which has the most influence over P_{rmin}. The other two terms were factors derived from the three influential moment rotation relationship values. The two factors were named, Yield Factor (Pressure) (Eq. 3.25) and Dynamic Ductility Shape Factor (Eq. 3.26):

$$k_{yp} = \left(M_y/M_u\right)^{0.293} \tag{3.25}$$

$$k_{duc} = \left(\theta_u/M_u\right)^{0.168} \tag{3.26}$$

Therefore if the control specimen was denoted with subscript "o," the analyses resulted in the following:

$$\frac{P_{rmin}}{P_{rmin,o}} = \frac{k_{yp}k_{duc}M_u}{k_{yp,o}k_{duc,o}M_{u,o}} \tag{3.27}$$

The derivation of Eqs. 3.25−3.27 can be seen in Table 3.26. $k_{yp,power}$ and $k_{duc,power}$ represent the exponents used in k_{yp} and k_{duc}, respectively. The exponents were determined using a goal seek method to minimize the average error and the average of the errors squared.

Using the same approach for P_{rmin}, I_{min} was found to be proportional to the square root of one term and inversely proportional to the square root of another term. The first term was named the Energy Absorption Capacity Factor (Eq. 3.28) and the second term was named the Yield Factor (impulse) (Eq. 3.29):

$$W = M_u\theta_u \tag{3.28}$$

$$k_{yi} = M_y/M_u \tag{3.29}$$

Similarly, denoting the control specimen with subscript "o," the analyses resulted in the following:

$$\frac{I_{min}}{I_{min,o}} = \sqrt{\frac{W/k_{yi}}{W_o/k_{yi,o}}} \tag{3.30}$$

Table 3.27 **Quantification of the effects of the depth of the member on P_{rmin}**

Depth	$k_{yp}/k_{yp,o}$	$k_{duc}/k_{duc,o}$	M_u/M_{uo}	$(D/D_o)^{Dp,power}$	$P_{rmin}/P_{rmin,o}$		Error (%)
					Theor.	Numer.	
100	1.000	1.000	1.000	1.000	1.000	1.000	0.000
135	0.976	0.815	2.271	1.192	0.464	0.455	2.011
170	0.967	0.705	4.029	1.363	0.267	0.270	1.128
205	0.968	0.626	6.265	1.521	0.173	0.175	1.122
240	0.963	0.573	9.128	1.667	0.119	0.118	0.874
				$D_{p,power}$		Average	1.284
				0.584			

Table 3.28 **Quantification of the effects of the depth of the member on I_{min}**

Depth	$k_{yi}/k_{yi,o}$	W/W_o	$(D/D_o)^{Di,power}$	$I_{min}/I_{min,o}$		Error (%)
				Theor.	Numer.	
100	1.000	1.000	1.000	1.000	1.000	0.000
135	0.976	1.531	1.447	0.645	0.650	0.740
170	0.967	2.036	1.922	0.477	0.490	2.599
205	0.968	2.428	2.420	0.391	0.380	2.797
240	0.963	3.047	2.938	0.313	0.315	0.576
			Di,power		Average	1.678
			0.616			

The derivation of Eqs. 3.28−3.30 can be seen in Table 3.26. $k_{yi,power}$ represents the exponent used in k_{yi}. The exponents were determined using a goal seek method to minimize the average error and the average of the errors squared.

Finally, it was necessary to define ultimate moment, yield moment in such a way that the width of the slab had no effect on P_{rmin} and I_{min}. Therefore M_u and M_y were defined as ultimate moment per unit width and yield moment per unit width, respectively.

3.7.6.4 Depth of a member

Manipulating the depth of a member affects both the moment rotation relationship and the member's total mass. Therefore it affects P_{rmin} and I_{min} both at the sectional

and member levels. When changing the depth of the slab, the cover to the center of the reinforcing bars was held constant, say 30 mm. As the moment rotation relationship for each depth was known, Eqs. 3.27 and 3.30 were used to normalize P_{rmin} and I_{min}, respectively, at the sectional level. For both P_{rmin} and I_{min}, it was observed that further manipulation was required to normalize the $P{-}I$ curves based on depth. The results indicated that P_{rmin} was also proportional to $D^{0.586}$ and that I_{min} was also proportional to $D^{0.616}$. This additional proportionality is how the depth affects the $P{-}I$ curve at the member level, due to the addition of mass.

The effects of the depth of the member on P_{rmin} are quantified in Table 3.27. The exponent, $D_{p,power}$, was determined using a goal seek method to minimize the average error and the average of the errors squared. In Table 3.27, columns $2{-}4$ represent the effects of the moment rotation relationship that occurs when a change in depth is chosen. This had to be normalized before the effects of the depth could be determined.

The effects of the depth of the member on I_{min} are quantified in Table 3.28. The exponent, $D_{i,power}$, was determined using a goal seek method to minimize the average error and the average of the errors squared. In Table 3.28, columns 2 and 3 show the effects of the moment rotation relationship that occurs when a change in depth is selected. This had to be normalized before the effects of the depth could be determined.

3.7.7 Normalization equations

As the effects of the span, depth, width, and moment rotation relationship had been identified, they were then combined to produce normalization equations for P_{rmin} (Eq. 3.31) and I_{min} (Eq. 3.32).

$$\frac{P_{rmin}}{P_{rmin,o}} = \frac{k_{yp}k_{duc}D^{0.584}L^{-2}M_u}{k_{yp,o}k_{duc,o}D_o^{0.584}L_o^{-2}M_{u,o}} \tag{3.31}$$

$$\frac{I_{min}}{I_{min,o}} = \sqrt{\frac{WD^{1.231}L^{-0.5}/k_{yi}}{W_oD_o^{1.231}L_o^{-0.5}/k_{yi,o}}} \tag{3.32}$$

if $P_{rmin,o}$ and $I_{min,o}$, and all the discussed parameters of the control specimen and the desired specimen are given, P_{rmin} and I_{min} for the desired specimen can be calculated. For all parameters used in Eqs. 3.31 and 3.32, any units can be used.

Table 3.29 Parameters of the control specimen

L_o	D_o	$M_{u,o}$	$M_{y,o}$	$\theta_{u,o}$	$I_{min,o}$	$P_{rmin,o}$
(m) 2.07	(mm) 100	(kNm/m) 215.2	(kNm/m) 191.4	(rad) 0.0795	(kPa ms) 3550	(kPa) 340

However, the same units used for a parameter with a subscript "o" should also be used for its corresponding parameter without a subscript "o". The equations are valid for one-way slabs with a span between 1 and 4 m and a depth between 100 and 240 mm. Also, the equations are valid for an ultimate hinge rotation of less than 0.23 rad or 13°. This is significantly large considering that ASCE Guidelines suggest that 8° is a high level of rotation. As the entire $P-I$ curve, for a typical RC slab subjected to an external blast, can be defined by P_{rmin} and I_{min}, this allows one to determine the $P-I$ curve for any desired RC slab, based on member and sectional properties, for the purpose of preliminary design. Although the equations are not completely based on structural dynamics principles, but are purely empirical, they can still be used to gain insight into how slabs resist various types of blast loads. Also, they can be used as a starting point for deriving normalization equations for $P-I$ curves based on structural dynamics principles.

To derive a normalized $P-I$ curve based on Eqs. 3.31 and 3.32, a control specimen with a given I_{min} and P_{rmin} is required. The parameters of the control specimen are shown in Table 3.29. After substituting all the parameters of the control specimen into Eqs. 3.31 and 3.32, a normalized $P-I$ curve, seen in Fig. 3.100, with corresponding normalized $P-I$ curve equations, seen as Eqs. 3.33 and 3.34, can be developed. Due to the nature of Eqs. 3.33 and 3.34, the units used for parameters in Eqs. 3.33 and 3.34 should correspond with that used for the control specimen parameters, as shown in Table 3.29.

$$\rightarrow P_{rmin} = 1.80\left(k_{yp}k_{duc}D^{0.584}L^{-2}M_u\right) \tag{3.33}$$

$$\rightarrow I_{min} = 57.04\sqrt{WD^{1.231}L^{-0.5}/k_{yi}} \tag{3.34}$$
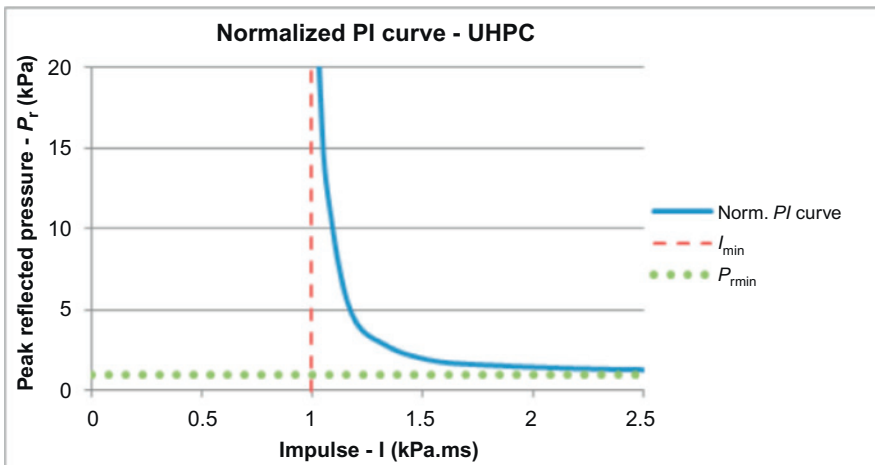
Figure 3.100 Normalized $P-I$ curve.

Eqs. 3.33 and 3.34 can be used in the normalized $P-I$ curve, shown in Fig. 3.100, where the coordinates, P_r and I, should be scaled up by P_{rmin} and I_{min} as given earlier, respectively. The shape and equation of the normalized $P-I$ curve in Fig. 3.100 is that of a typical RC slab subjected to an external blast load. This normalized $P-I$ curve can be replaced with any other normalized $P-I$ curve, with vertical and horizontal asymptotes of unity.

When studying the effects of sectional properties on P_{rmin} and I_{min}, it was observed that the cracking moment had very little effect on the results, therefore it was ignored. Also, the initial stiffness of the moment curvature relationship was ignored as this would have very little effect on the structural response due to large blasts, causing nearly ultimate deflections. Also, although the Timoshenko Beam Equations take into account deflections due to shear using a linear shear stress–strain relationship, the effects of shear properties were not considered in our investigation. This is because most span to depth ratios of conventional slabs, designed against blasts, range from 10 to 50, so the effects of shear properties were considered insignificant. However, it is known that, even for slabs with larger span to depth ratios, for large blasts with a small standoff distance, shear behavior can influence the response. This type of blast corresponds to the impulse controlled region of the $P-I$ diagram. Therefore the use of the normalized $P-I$ curve for blasts within this region should only be used if it is known that shear behavior has no dominant influence on the response of the slab to such blasts. Also, this approach is not suitable for blasts with extremely small standoff distances as local damage of the slab can occur. This is because the structural response model can only simulate the global response of the member and not the local damage of the material itself due to concentrated effects of the blast.

3.7.8 Numerical testing of normalization equations

Although numerically derived results for many different slabs were used to produce the normalization equations, further numerical testing of the equations was
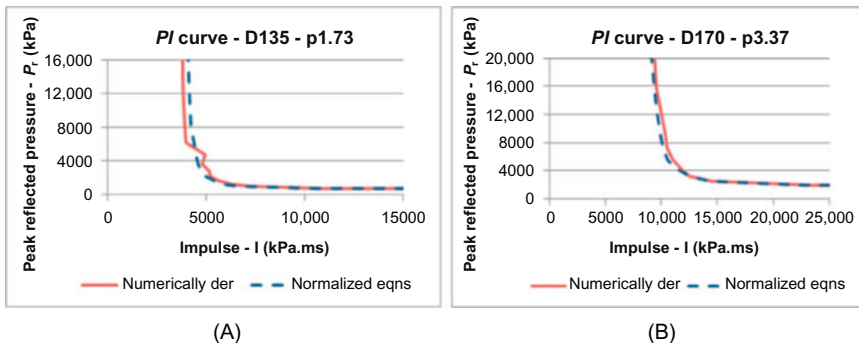
Figure 3.101 Numerically derived and theoretical $P-I$ curves for two separate specimens. (A) $P-I$ curve of slab with depth of 135 mm; (B) $P-I$ curve of slab with depth of 170 mm.

undertaken. This was done by generating $P-I$ curves for slabs with varying depths and reinforcing ratios, using both the normalization equations and the structural response model, and comparing them. Fig. 3.101 shows $P-I$ curves for two slabs which differ in depth and reinforcing ratio, in comparison to that of the control slab. It can be seen that the results are quite good as P_{rmin}, I_{min} and the transition zone match up quite well for both cases.

In the tests shown in Fig. 3.101, the maximum error of the asymptotes, P_{rmin} and I_{min}, between the numerically derived results and that obtained through the normalization equations, is 5%. It can be seen that the instability within the structural response model can sometimes occur and can sometimes cause noticeable errors within the transition zone of the generated $P-I$ curves. However, it should be noted that the aim of this section is to only derive normalization equations for the asymptotes, P_{rmin} and I_{min}. It can be seen that at the extremes of the generated $P-I$ curves, toward P_{rmin} and I_{min}, the instability, which is represented by zig-zagging, decreases significantly. This is why the maximum errors experienced, when calculating P_{rmin} and I_{min}, are only 5%. These errors are attributed to the uncertainty involved in determining P_{rmin} and I_{min} for various UHPC slabs used to derive the normalization equations. Also, as a moment rotation relationship is never exactly bilinear, the errors are also attributed to the judgment which should be used when determining the moment at yield, M_y.

3.7.9 Conclusion

An innovative approach was developed to predict the sectional behavior of a reinforced UHPC member accurately. The approach used modified rigid body analysis, curvature analysis and incorporated a stress−strain/crack width relationship to develop a new moment rotation relationship. The moment rotation and moment curvature relationships were incorporated into a FD model which was validated using blast test data. With the validated FD model, the entire dynamic structural response model was recreated and also extended to generate $P-I$ curves. From an extensive parametric study, a normalized $P-I$ curve, accompanied by two equations for the asymptotes, was also derived. This was done by developing empirical equations of proportionality for various sectional and member properties, which can be used to generate a $P-I$ curve for any given member.

References

[1] G. Morales-Alonso, D.A. Cendón, F. Gálvez, B. Erice, V. Sánchez-Gálvez, Blast response analysis of reinforced concrete slabs: experimental procedure and numerical simulation, J. Appl. Mech. 78 (2011) 051010.
[2] G. Thiagarajan, A.V. Kadambi, S. Robert, C.F. Johnson, Experimental and finite element analysis of doubly reinforced concrete slabs subjected to blast loads, Int. J. Impact Eng. 75 (2015) 162−173.

[3] W. Wang, D. Zhang, F. Lu, S.-c Wang, F. Tang, Experimental study and numerical simulation of the damage mode of a square reinforced concrete slab under close-in explosion, Eng. Failure Anal. 27 (2013) 41−51.

[4] D. Grady, The spall strength of condensed matter, J. Mech. Phys. Solids 36 (1988) 353−384.

[5] M.K. McVay, Spall damage of concrete structures, DTIC Document, 1988.

[6] M. Foglar, R. Hajek, M. Kovar, J. Štoller, Blast performance of RC panels with waste steel fibers, Construct. Build. Mater. 94 (2015) 536−546.

[7] M.M. Jr.Swisdak, J.W. Tatom, C.A. Hoing, Procedures for the collection, analysis and interpretation of explosion-produced debris-revision 1, DTIC Document, 2007.

[8] J. Henderson, Lethality criteria for debris generated from accidental explosions, DTIC Document, 2010.

[9] K. Xu, Y. Lu, Debris velocity of concrete structures subjected to explosive loading, Int. J. Numer. Anal. Methods Geomech. 30 (2006) 917−926.

[10] J.R. Brinkman, Separating shock wave and gas expansion breakage mechanisms, in: Second International Symposium on Rock Fragmentation by Blasting, Keystone, CL, 1987, pp. 6−15.

[11] C. Wu, R. Nurwidayati, D.J. Oehlers, Fragmentation from spallation of RC slabs due to airblast loads, Int. J. Impact Eng. 36 (2009) 1371−1376.

[12] C. Kot, R. Valentin, D. McLennan, P. Turula, Effects of air blast on power plant structures and components, Argonne National Laboratory, IL, 1978.

[13] C. Kot, Spalling of concrete walls under blast load, Structural Mechanics in Reactor Technology, 1977.

[14] P.T. Nash, C. Vallabhan, T.C. Knight, Spall damage to concrete walls from close-in cased and uncased? Explosions in air, ACI Struct. J. 92 (1995).

[15] J. Leppänen, Experiments and numerical analyses of blast and fragment impacts on concrete, Int. J. Impact Eng. 31 (2005) 843−860.

[16] K.A. Marchand, B.T. Plenge, Concrete hard target spall and breach model, US air force research laboratory, Munitions Directorate, Lethality & Vulnerability Branch, 1998.

[17] M. Ohtsu, F.A. Uddin, W. Tong, K. Murakami, Dynamics of spall failure in fiber reinforced concrete due to blasting, Construct. Build. Mater. 21 (2007) 511−518.

[18] K. Ohkubo, M. Beppu, T. Ohno, K. Satoh, Experimental study on the effectiveness of fiber sheet reinforcement on the explosive-resistant performance of concrete plates, Int. J. Impact Eng. 35 (2008) 1702−1708.

[19] M. Foglar, M. Kovar, Conclusions from experimental testing of blast resistance of FRC and RC bridge decks, Int. J. Impact Eng. 59 (2013) 18−28.

[20] E.B. Williamson, O. Bayrak, G.D. Williams, C.E. Davis, K.A. Marchand, A.E. McKay, et al., Blast-resistant highway bridges: design and detailing guidelines, Transportation Research Board, Washington, DC, 2010.

[21] K.-C. Wu, B. Li, K.-C. Tsai, The effects of explosive mass ratio on residual compressive capacity of contact blast damaged composite columns, J. Construct. Steel Res. 67 (2011) 602−612.

[22] K.-C. Wu, B. Li, K.-C. Tsai, Residual axial compression capacity of localized blast-damaged RC columns, Int. J. Impact Eng. 38 (2011) 29−40.

[23] J. Li, H. Hao, Numerical study of concrete spall damage to blast loads, Int. J. Impact Eng. 68 (2014) 41−55.

[24] A.B.M.A. Kaish, M. Jamil, S.N. Raman, M.F.M. Zain, M.R. Alam, An approach to improve conventional square ferrocement jacket for strengthening application of short square RC column, Mater. Struct. 49 (2016) 1025−1037.

[25] B. Kondraivendhan, B. Pradhan, Effect of ferrocement confinement on behavior of concrete, Construct. Build. Mater. 23 (2009) 1218−1222.

[26] M. El Debs, A. Naaman, Bending behavior of mortar reinforced with steel meshes and polymeric fibers, Cem. Concr. Compos. 17 (1995) 327−338.

[27] H.M. Ibrahim, Experimental investigation of ultimate capacity of wired mesh-reinforced cementitious slabs, Construct. Build. Mater. 25 (2011) 251−259.

[28] T. Xu, R.J. Farris, Comparative studies of ultra high molecular weight polyethylene fiber reinforced composites, Polym. Eng. Sci. 47 (2007) 1544−1553.

[29] K. Karthikeyan, B. Russell, N. Fleck, M. O'Masta, H. Wadley, V. Deshpande, The soft impact response of composite laminate beams, Int. J. Impact Eng. 60 (2013) 24−36.

[30] K. Karthikeyan, B. Russell, N. Fleck, H. Wadley, V. Deshpande, The effect of shear strength on the ballistic response of laminated composite plates, Eur. J. Mech.-A Solids 42 (2013) 35−53.

[31] I. Mohagheghian, G.J. McShane, W.J. Stronge, Impact perforation of monolithic polyethylene plates: projectile nose shape dependence, Int. J. Impact Eng. 80 (2015) 162−176.

[32] B.P. Russell, K. Karthikeyan, V.S. Deshpande, N.A. Fleck, The high strain rate response of ultra high molecular-weight polyethylene: from fibre to laminate, Int. J. Impact Eng. 60 (2013) 1−9.

[33] Y.W. Zhang, L.H. Yan, L. Zhu, S. Zhang, L.F. Li, Experiment research on mechanical properties and penetration performance of UHMWPE fiber concrete, in: Q.F. Zhang, S.Z. Cai, X.P. Xu, D.H. Hu, Y.M. Qu (Eds.), Advanced Materials Research, Trans Tech Publ, 2014, pp. 961−965.

[34] Y.W. Zhang, L.H. Yan, L.F. Li, Numerical simulation of projectile penetration into UHMWPE fiber reinforced concrete, in: K.M. Li, M.R. Xue, M.H. Lee, X.Y. Zhang (Eds.), Applied Mechanics and Materials, Trans Tech Publ, 2014, pp. 513−516.

[35] R. Ranade, W.F. Heard, B.A. Williams, Multi-scale mechanical performance of high strength-high ductility concrete, in: B. Song, L. Lamberson, D. Casem, J. Kimberley (Eds.), Dynamic Behavior of Materials, Volume 1: Proceedings of the 2015 Annual Conference on Experimental and Applied Mechanics, Springer International Publishing, Cham, 2016, pp. 93−101.

[36] M. Yamaguchi, K. Murakami, K. Takeda, Y. Mitsui, Blast resistance of polyethylene fiber reinforced concrete to contact detonation, J. Adv. Concrete Technol. 9 (2011) 63−71.

[37] UFC, Structures to resist the effects of accidental explosions, Department of Defense, Unified Facilities Criteria 3-340-02, Washington, DC, 2008.

[38] G. Thiagarajan, A.K. Vasudevan, S. Robert, Numerical modeling of concrete slabs reinforced with high strength low alloy vanadium steel bars subjected to blast loads, ACI Special Publication, 281, 2011.

[39] T.-L. Teng, Y.-A. Chu, F.-A. Chang, B.-C. Shen, D.-S. Cheng, Development and validation of numerical model of steel fiber reinforced concrete for high-velocity impact, Comput. Mater. Sci. 42 (2008) 90−99.

[40] Z. Wang, J. Wu, J. Wang, Experimental and numerical analysis on effect of fibre aspect ratio on mechanical properties of SRFC, Construct. Build. Mater. 24 (2010) 559−565.

[41] L. Malvar, J. Crawford, Dynamic increase factors for concrete, Naval Facilities Engineering Service Center, Port hueneme CA, 1998.

[42] R. Chen, Y. Liu, X. Guo, K. Xia, F. Lu, Dynamic tensile properties of steel fiber reinforced concrete, Dynamic Behavior of Materials, vol. 1, Springer, New York, 2011, pp. 37−42.

[43] A.M. Weidner, Dynamic properties of concrete and fiber reinforced concrete at room and elevated temperatures, The University of Utah, Salt Lake City, 2013.

[44] S. Millard, T. Molyneaux, S. Barnett, X. Gao, Dynamic enhancement of blast-resistant ultra high performance fibre-reinforced concrete under flexural and shear loading, Int. J. Impact Eng. 37 (2010) 405−413.

[45] B.D. Neeley, M.I. Hammons, D.M. Smith, The development and characterization of conventional-strength and high-strength portland cement concrete mixtures for projectile penetration studies, US Army Engineer Waterways Experiment Station, 1991.

[46] L.B. Lucy, A numerical approach to the testing of the fission hypothesis, Astron. J. 82 (1977) 1013−1024.

[47] R.A. Gingold, J.J. Monaghan, Smoothed particle hydrodynamics: theory and application to non-spherical stars, Mon. Notices Royal Astron. Soc. 181 (1977) 375−389.

[48] T. Rabczuk, J. Eibl, Simulation of high velocity concrete fragmentation using SPH/MLSPH, Int. J. Numer. Methods Eng. 56 (2003) 1421−1444.

[49] M.B. Liu, G.R. Liu, Z. Zong, K.Y. Lam, Computer simulation of high explosive explosion using smoothed particle hydrodynamics methodology, Comput. Fluids 32 (2003) 305−322.

[50] M.B. Liu, G.R. Liu, K.Y. Lam, Z. Zong, Meshfree particle simulation of the detonation process for high explosives in shaped charge unlined cavity configurations, Shock Waves 12 (2003) 509−520.

[51] J. Li, H. Hao, Numerical study of concrete spall damage to blast loads, Int. J. Impact Eng. 68 (2014) 41−55.

[52] M. Beppu, T. Ohno, K. Ohkubo, B. Li, K. Satoh, Contact explosion resistance of concrete plates externally strengthened with FRP laminates, Int. J. Prot. Struct. 1 (2010) 257−270.

[53] J. Li, H. Hao, Numerical and theoretical study of concrete spall damage under blast loads, Appl. Mech. Mater. 553 (2014) 774−779. Trans Tech Publ.

[54] M. Morishita, H. Tanaka, T. Ando, H. Hagiya, Effects of concrete strength and reinforcing clear distance on the damage of reinforced concrete slabs subjected to contact detonations, Concr. Res. Technol. 15 (2004) 89−98.

[55] S. Lord, R. Nunes-Vaz, A. Filinkov, G. Crane, Airport front-of-house vulnerabilities and mitigation options, J. Transport. Secur. 3 (2010) 149−177.

[56] D. Grady, M. Kipp, Dynamic rock fragmentation, Fract. Mech. Rock 475 (1987).

[57] D.A. Shockey, D.R. Curran, L. Seaman, J.T. Rosenberg, C.F. Petersen, Fragmentation of rock under dynamic loadsElsevier Int. J. Rock Mech. Min. Sci. Geomech. Abstr., 11, 1974, pp. 303−317.

[58] J.D. O'Keefe, T.J. Ahrens, Impact and explosion crater ejecta, fragment size, and velocity, Icarus 62 (1985) 328−338.

[59] K. Holschemacher, T. Mueller, Y. Ribakov, Effect of steel fibres on mechanical properties of high-strength concrete, Mater. Design 31 (2010) 2604−2615.

[60] D.-Y. Yoo, N. Banthia, S.-T. Kang, Y.-S. Yoon, Effect of fiber orientation on the rate-dependent flexural behavior of ultra-high-performance fiber-reinforced concrete, Compos. Struct. 157 (2016) 62−70.

[61] D.-Y. Yoo, S.-T. Kang, Y.-S. Yoon, Effect of fiber length and placement method on flexural behavior, tension-softening curve, and fiber distribution characteristics of UHPFRC, Construct. Build. Mater. 64 (2014) 67−81.

[62] C. Wu, G. Fattori, A. Whittaker, D.J. Oehlers, Investigation of air-blast effects from spherical-and cylindrical-shaped charges, Int. J. Protect. Struct. 1 (2010) 345−362.

[63] C. Wu, D.J. Oehlers, M. Rebentrost, J. Leach, A.S. Whittaker, Blast testing of ultra-high performance fibre and FRP-retrofitted concrete slabs, Eng. Struct. 31 (2009) 2060−2069.

[64] J. Wang, Simulation of landmine explosion using LS-DYNA3D software: benchmark work of simulation of explosion in soil and air, DTIC Document, 2001.

[65] G.R. Johnson, R.A. Stryk, Conversion of 3D distorted elements into meshless particles during dynamic deformation, Int. J. Impact Eng. 28 (2003) 947−966.

[66] Y. Lu, Modelling of concrete structures subjected to shock and blast loading: an overview and some recent studies, Struct. Eng. Mech. 32 (2009) 235−249.

[67] J.-H. Kim, H.-C. Shin, Application of the ALE technique for underwater explosion analysis of a submarine liquefied oxygen tank, Ocean Eng. 35 (2008) 812−822.

[68] G.W. Ma, H. Hao, Y.X. Zhou, Modeling of wave propagation induced by underground explosion, Comput. Geotech. 22 (1998) 283−303.

[69] C.E. Needham, Blast wave propagation, Blast Waves, Springer, Berlin, 2010, pp. 87−99.

[70] Z. Zheng, D. Feldman, Synthetic fibre-reinforced concrete, Progr. Polym. Sci. 20 (1995) 185−210.

[71] M. Maalej, S. Quek, J. Zhang, Behavior of hybrid-fiber engineered cementitious composites subjected to dynamic tensile loading and projectile impact, J. Mater. Civil Eng. 17 (2005) 143−152.

[72] K. Kobayashi, R. Cho, Flexural characteristics of steel fibre and polyethylene fibre hybrid-reinforced concrete, Composites 13 (1982) 164−168.

[73] W. Yao, J. Li, K. Wu, Mechanical properties of hybrid fiber-reinforced concrete at low fiber volume fraction, Cem. Concr. Res. 33 (2003) 27−30.

[74] J. Li, H. Hao, Influence of brittle shear damage on two-step method prediction of structural response to blast loads, in: Fifth International Conference on Protection of Structures Against Hazards, Singapore, 2012, pp. 243−251.

[75] J. Jones, C. Wu, D. Oehlers, A. Whittaker, W. Sun, S. Marks, R. Coppola, Finite difference analysis of simply supported RC slabs for blast loadings, Eng. Struct. 31 (2009) 2825−2832.

[76] M. Haskett, D.J. Oehlers, M.M. Ali, C. Wu, Rigid body moment−rotation mechanism for reinforced concrete beam hinges, Eng. Struct. 31 (2009) 1032−1041.

[77] Y. Shi, H. Hao, Z.-X. Li, Numerical derivation of pressure−impulse diagrams for prediction of RC column damage to blast loads, Int. J. Impact Eng. 35 (2008) 1213−1227.

[78] J. Jungwirth, A. Muttoni, Structural behavior of tension members in ultra high performance concrete, in: International Symposium on Ultra High Performance Concrete, Kassel, 2004.

[79] C. Wu, D.J. Oehlers, I. Day, Layered blast capacity analysis of FRP retrofitted RC member, Adv. Struct. Eng. 12 (2009) 435−449.

[80] M. Haskett, D.J. Oehlers, M.M. Ali, Local and global bond characteristics of steel reinforcing bars, Eng. Struct. 30 (2008) 376−383.

[81] J. Ciccarelli, A. Henderson, K. Jordans, B. Noack, D. Oehlers, C. Wu, Resistance Against Explosive Loading of Metal Foam Retrofitted and Ultra High Strength Concrete Structural Members, University of Adelaide, Adelaide, 2008.

This page intentionally left blank

Ultra-high performance concrete columns

4

4.1   Introduction

Accidental and intentional events involving blast effects on structures are attracting increasingly more public concerns nowadays. A large number of casualties and countless property loss could be induced by unexpected blast loads. While immediate structural damage and casualties are normally caused by blast overpressure released in an explosion, progressive failures of structures and their components result in the majority of casualties and damages. Despite widely spreading concerns about this issue, most structures including iconic and public buildings were and are still being constructed without considering these extreme loading scenarios.

In a structural system, failure of one or several key load-carrying columns may trigger large-scale disproportionate structural progressive collapse. A progressive collapse can be initiated for many reasons, including design and construction errors and load events that are outside the normal structural design basis that is seldom considered by the structural engineers. Documentation of such disastrous failure has a long history tracked back in the 1900s on stonemasonry structures. In modern construction, although steel-frame or steel-reinforced concrete (RC) structures are adopted to provide enhanced ductility and redundancy, structural progressive collapses might still occur. Extensive study on structural progressive collapse has been carried out in recent decades. Sasani [1] analytically studied the response of a six-story RC infilled-frame structure after removal of two adjacent columns, and identified the major mechanism in load redistributions after the loss of columns. Woodson and Baylot [2] verified the importance of in-fill walls in affecting the load applied on the structural column, and concluded that collapse would have occurred if slab edge beams failed to carry dead weight when load-carrying columns incurred severe damage. With high-fidelity physics-based computer program, the vulnerability of structures to progressive collapse was numerically studied [3,4]. In all these studies, failure of columns was identified as the most critical cause for triggering a structural collapse.

Due to easy accessibility, perimeter columns in modern structures may be targeted by terrorists using improvised explosive devices such as VBIED (vehicle-borne improvised explosive device) and suitcase bombs. To prevent initiation of progressive collapse, it is necessary to investigate failure mechanism of an individual column in a frame structural system and provide adequate protections. Under blast loading environments, concrete structural members may fail in brittle modes like shear punching and concrete spall rather than desired flexural mode. According

to UFC 3-340-2, if the structural response is ductile, which means the plastic/permanent deflection absorbs blast energy, concrete structural members are capable of attaining six degrees support rotation. This damage criterion, however, is not suitable for describing brittle damage modes of columns. Hao [5] discussed possible failure modes and applicable damage criteria of structures subjected to dynamic loads of various loading rates. A concrete beam or column could suffer localized crushing/spalling damage, direct shear, diagonal shear, ductile flexural damage, or combined damage of these damage modes depending on the explosion standoff or loading rates. Hao et al. [6] recently conducted a review of the current practices in blast-resistant analysis and design of concrete structures. The methods that lead to more reliable predictions of concrete structures to blast loads are discussed. For concrete columns, in particular Shi et al. [7] adopted residual loading capacity of RC columns after blast loading as the damage criterion to generate pressure−impulse (P−I) curves. Based on parametric studies, analytical formulae to predict pressure−impulse diagrams for RC columns were proposed. Later in the study carried out by Bao and Li [8], residual strength of RC columns after small standoff blast loads was investigated, and the formulae which were capable of estimating column residual strength were provided. The validity range of these formulae was later refined through the experimental results obtained by Li et al. [9]. In their experimental setup, the columns were loaded with three horizontal actuators to simulate the actual blast loads. Wu et al. [10] carried out experimental and numerical studies on the residual axial compression capacity of RC columns after localized blast effects. The relationship between residual axial capacity and structural and loading parameters such as material strength, column detailing, and blast conditions was investigated through numerical parametric studies. Roller et al. [11] observed that there was just little knowledge about the behavior of elements with one-dimensional (1D) load capacity like columns under blast loading conditions. To provide in-depth knowledge, they started a test program involving both standard RC columns and retrofitted concrete columns under blast loads first and then static loads. Remaining load-carrying capacities of blast-damaged columns were obtained through uniaxial compressive tests.

Structural behavior during an explosion is highly dependent on the materials used in the construction. Upon hitting the face of a building, the shock front from an explosion is instantly reflected. This impact with the structure imparts momentum to exterior components of the building. The associated kinetic energy of the moving components must be absorbed or dissipated in order for them to survive. Generally, this is achieved by converting the kinetic energy of the moving component to strain energy in resisting elements and fracture energy of the concrete material. The understanding of deflection and response modes of RC members is therefore essential in the blast analysis and design of civil and defense structures.

High-strength concrete (HSC) members is undergoing widespread usage in civil engineering and construction processes and ultra-high performance concrete (UHPC) is deemed to be a promising material due to its high ductility, impact resistance, and energy absorption capacity, and it has drawn intense interests in the blast-resistant design of structures. This chapter presents experimental and numerical study of

failure modes of high-strength reinforced concrete (HSRC) members and ultra-high performance fiber-reinforced concrete (UHPFRC) members under explosion loads.

A blast testing program on UHPFRC and HSRC columns is presented in this chapter and finite element (FE) model is then adopted for further investigations, due to its inherent accuracy and stability despite its numerically efficiency. Firstly, experimental study on blast resistance of ultra-high performance twisted steel fiber RC and HSRC columns is conducted. Then, a detailed investigation of the capabilities of ultra-high performance microsteel fiber RC columns and HSRC columns against close-in blasts is given. To achieve this objective, a series of blast tests were conducted to investigate the behavior of UHPFRC and HSRC columns subjected to blast loading. Postblast behavior of UHPC columns is also investigated afterward. Finally, numerical method is used to accurately analyze the response of UHPFRC and HSRC columns subjected to blasts.

This chapter deals with a broad range of topics in analyzing the static and dynamic responses of structural members including RC members, HSRC and UHPFRC columns. The static loading regimes include the flexural response. The dynamic loading regimes include impulse loading due to real blast experiments. The failure modes under blast loading conditions and postblast behavior have been addressed in great details in experimental study. Numerical models for simulating responses and residual strengths of the UHPC columns after blast loadings are also developed in commercial hydro-code LS-DYNA. Simplified finite difference model is also used to analyze UHPFRC columns under blast loads.

4.2   Blast resistance of ultra-high performance concrete columns

4.2.1   The mechanical properties of the ultra-high performance concrete

Mix proportions of the UHPC are given in Table 2.2. In the current research, nanoparticles nano-$CaCO_3$ were mixed in the concrete matrix to provide nanoscale filling effect and also facilitate hydration process. Two types of steel fiber material, i.e., twisted fiber (TF) and microfiber (MF) were mixed at a volume dosage of 2.5% to provide additional tensile and crack resistance.

The columns are classified into three categories based on the fiber additions.

1. Twisted steel fiber (TF) (as shown in Fig. 2.1) that has a tensile strength of 1480 MPa, a diameter of 0.3 mm, and a length of 30 mm.
2. Microsteel fiber (MF) (as shown in Fig. 2.1) that has tensile strength of 4250 MPa, a diameter of 0.12 mm, and a length of 15 mm.
3. No fiber material addition.

Compressive stress−strain relationships from cylinder tests and force−displacement curves from flexural tests of UHPC with different fiber reinforcements are shown in Fig. 4.1. Stress−strain relationships for the two UHPCs are obtained from
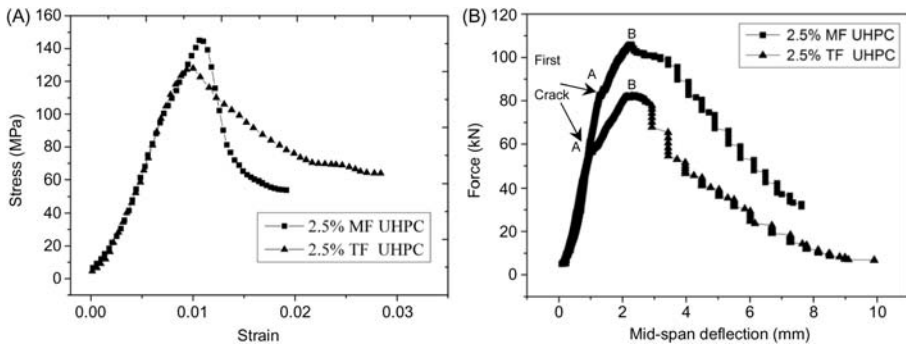
Figure 4.1 Mechanical properties of UHPC. (A) UHPC under compression; (B) UHPC under flexural tension.

uniaxial compression tests. The addition of MF and TF reinforcements gives a compressive strength of 148 MPa and 130 MPa, respectively. Flexural force−deflection relationships are obtained from four-point bending test. In flexural bending tests, two flexural strength values are commonly reported. One, termed the first-crack flexural strength, corresponds to the load at which the load−deformation curve departs from linearity (point A in Fig. 4.1B). The other corresponds to the maximum load achieved, commonly called the ultimate flexural strength or modulus of rupture (point B in Fig. 4.1B). The samples in four-point bending tests (FPBTs) have a length of 400 mm with cross-section of 100 × 100 mm, clear span and loading span are 300 mm and 100 mm, respectively. Ultimate flexural strengths (32 MPa and 25 MPa for MF- and TF-reinforced UHPC, respectively) are calculated from the corresponding load using the formula for modulus of rupture given in ASTM C 78, although the linear stress and strain distributions on which the formula is based no longer apply after the matrix has cracked.

4.2.2 Blast resistance of ultra-high performance fiber-reinforced concrete columns

4.2.2.1 Experimental program

Blast tests were conducted on columns constructed with the advanced UHPC and HSC. Emulsion explosive charge weights ranging from 1.4 to 70 kg were placed at 1.5 m height above the specimens. The nominal TNT equivalent factor for emulsion explosive charge is 0.71. Fig. 4.2 shows the emulsion explosive used in the column blast tests.

Blast tests matrix is given in Table 4.1. The columns with prefix "U" were constructed with UHPC and columns with prefix "H" were built with the same material composition but without fiber reinforcement.

Trial test utilizing 14 kg explosive (10 kg TNT equivalence) at 1.5 m standoff distance did not cause any visible cracks on UHPC column U5A. To observe column response and possible damage at more advanced stages, blast tests involving

Figure 4.2 Emulsion explosive used in the tests.

17.5 or 35 kg TNT equivalence with the same standoff distance were carried out for UHPC columns U1A−U5B, while TNT equivalence of 25 kg were detonated for U5C. For HSRC columns, less severe blast loads with TNT equivalence of 8 or 17.5 kg were applied. In all the tests, standoff distances were kept the same as 1.5 m, and blast scaled distances investigated in this study ranged from 0.46 to 0.75 m kg$^{-1/3}$.

It is worth noting that, after conducting test on column U4A against 35 kg TNT equivalent explosion, only minor damage was observed at column mid-span. It was planned to increase the explosive weight to 50 kg TNT equivalence for U4B, however, the blast load generated from 50 kg TNT equivalent explosion exceeded the capacity of the test field and could destroy the test apparatus and cause serious safety concerns, thus a 35 kg TNT equivalent explosion was repeated on U4B to verify the previous blast results.

Axial loads on columns play a critical role in influencing their performance especially when large flexural deformations occur. However, axial loads on columns were sometimes overlooked in previous blast tests due to the difficulty of application and also the safety concern. In this study, effects of axial loads on columns are studied. For comparison as listed in Table 4.1, four UHPC columns and two HSRC columns were tested without axial loads.

For columns with axial loads, prior to blast detonation, axial load was applied through a pneumatic jack located at column end. For typical ground floor column in a low-to-medium rise building, its axial load ratio (service load vs loading capacity) is from 0.2 to 0.4. Considering the high mechanical performance of UHPC and its comparable density to normal strength concrete, in this study, an axial load of 1000 kN which equals to approximately 20% of the load capacity of the column

Table 4.1 **Blast test matrix**

UHPC specimen with microfiber reinforcement	Charge weight (kg)	Axial load (kN)	UHPC specimen with twisted fiber reinforcement	Charge weight (kg)	Axial load (kN)	HSRC specimen with no fiber reinforcement	Charge weight (kg)	Axial load (kN)
U1A	1.4	0	U3A	1.4	0	H7A	1.4	0
U1A	48	0	U3A	48	0	H7A	25	0
U1B	1.4	0	U3B	1.4	0	H7B	1.4	0
U1B	25	0	U3B	25	0	H7B	11.2	0
U2A	1.4	1000	U4B	48	1000	H8A	25	1000
U2A	48	1000	U5A	1.4	1000	H8B	11.2	1000
U2B	1.4	1000	U5A	14	1000	H9A	35	500
U2B	25	1000	U5B	25	1000			
			U5C	35	1000			
			U6A	70	1000			
			U6B	25	1000			

was applied during the tests and was kept constant for all UHPC samples. For comparison purpose, HSRC columns H8A and H8B were loaded with the same axial load, i.e., 1000 kN which equals to their 50% load capacity, and HSRC column H9A was loaded with a 500 kN axial force which equals to 25% of its axial loading capacity. It should be noted that when designing the columns in the blast tests, no material reduction factor was considered in the column axial loading capacity calculation, and both the contribution of steel and concrete were considered in the column axial loading capacity.

4.2.2.2 Test specimen descriptions

As shown in Fig. 4.3, the columns had a square cross-section of 200 mm × 200 mm and a total height of 2500 mm. The longitudinal reinforcement consisted of 8-Φ16 mm bars (bar yield stress and ultimate strength are 1450 and 1600 MPa) and had 90° hooks extending 75 mm at each extremity to ensure full development of reinforcement into the support region. The transverse reinforcement consisted of roller steel 8 mm diameter ties (f_y = 300 MPa) with 135° hook extensions and the clear concrete cover was kept as a constant of 35 mm. The dimension and reinforcement arrangement of UHPC and HSRC columns is shown in Fig. 4.4.

4.2.2.3 Test setup and instrumentation

A specified 2600 mm × 400 mm × 1000 mm steel frame as shown in Fig. 4.5 was built with a clamping system to ensure that a column was firmly placed inside the frame and no uplifting happened. The whole system was then lowered into the ground. Two strips of rubber sheet were used to cover gaps between the column and ground support so as to prevent blast wave passing through the gaps, which might not only destroy the testing instruments beneath the column, but also result in shock waves engulfing the column specimen. Three linear variable differential transformers (LVDTs) were installed under the column using Dynabolts for
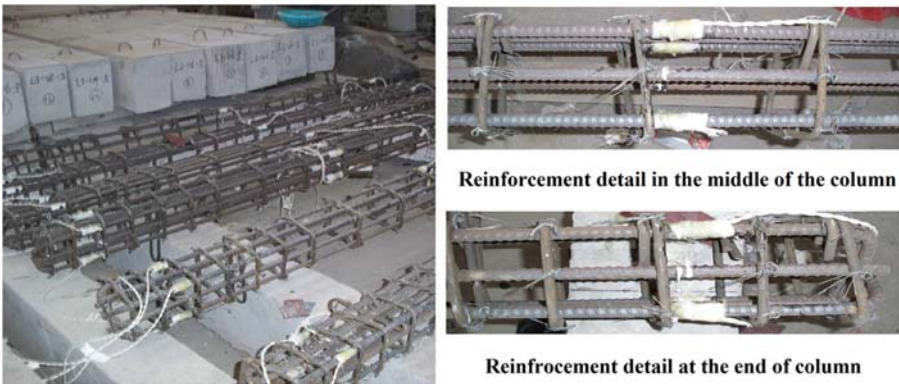
Figure 4.3 Column reinforcement details.
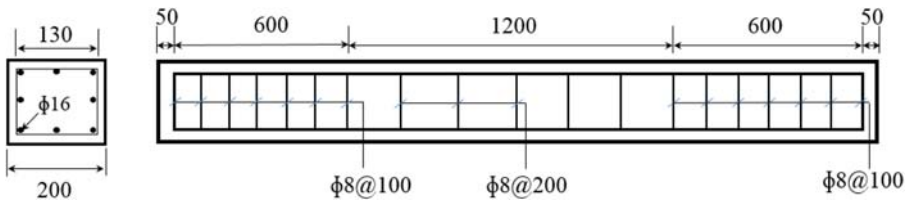
Figure 4.4 Dimension and reinforcement arrangement of UHPC and HSRC columns.
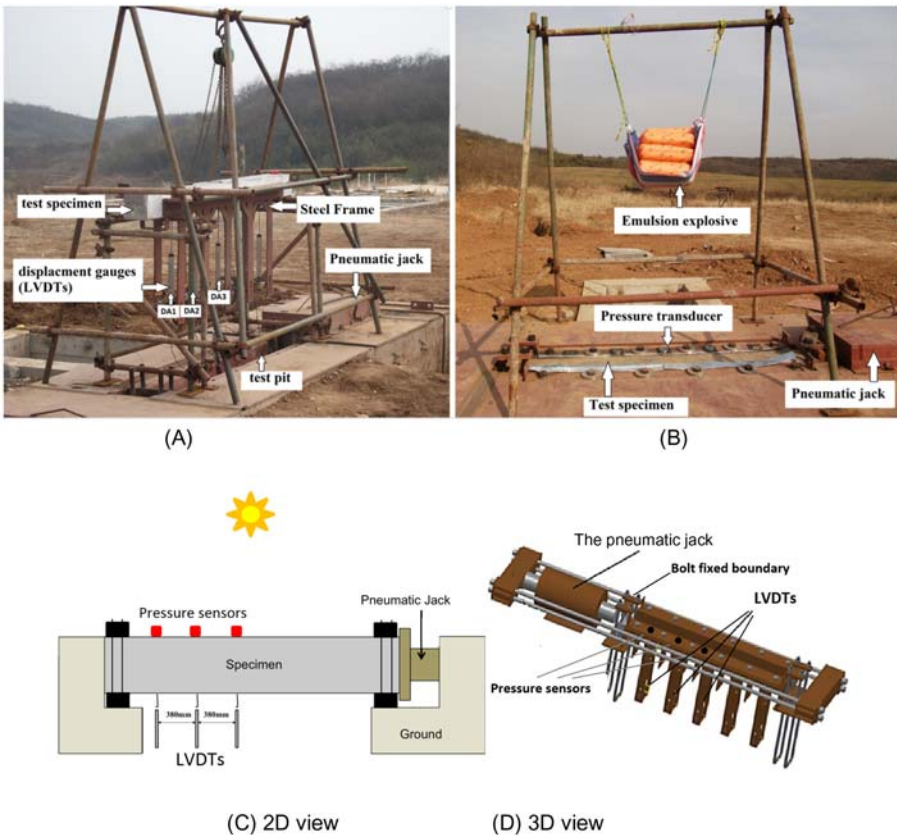
Figure 4.5 Blast test setup (A) before, (B) after the specimen being installed into the test pit, (C) 2D view of test, and (D) 3D view of the test.

deflection measurement, DA3 was located at the center, DA2 was located at 550 mm away from the center, and DA1 was located at 1100 mm away from the center of the specimen. Before testing columns, axial load was slowly increased to 1000 kN by using a pneumatic jack, which was installed at one side of the test column. When the designed axial load was reached, the pneumatic jack maintained a constant load to make sure the axial load applied to the column remained constant

during the blast test period. The pressure-time history was recorded by blast pressure transducers installed on top surface of the specimens at distance of 0, 380, and 760 mm away from center of the specimen, which were labeled as P3, P2, and P1, respectively. It should be noted that the pressure measurement accuracy depends on the sensitivity of the blast pressure transducers. The voltage signals from LVDTs and pressure sensors were recorded by data acquisition system. The unit had a maximum recording frequency of 0.2 MHz per channel: there were three channels for pressure recording and three channels for displacements recording simultaneously during the blast tests.

4.2.2.4   Test procedure

All specimens were tested under combined with/without static axial loading and blast loads; a clear distance between charge center and center of specimen is 1.5 m. Each column was tested by the following procedures:

1. The first step of the experiment was to place the specimen on top of the steel frame, connect all the LVDTs, and check connections and functionality.
2. The whole frame with specimens is needed to be placed in a horizontal position and lowered into the testing frame, to make sure that the top surface of the column at the same level as the ground surface.
3. Then make sure the designed steel yokes are performed well to let specimen free-standing at two lateral sides of the test position. The other support is connected with the pneumatic jack which is located at the same level with the column to make sure that the axial load could be transferred from the pneumatic jack to the column.
4. Afterward, the pressure transducers are needed to be properly installed and checked.
5. Explosive was placed on the normal line passing through the center of the column 1.5 m above the column.
6. Finally, the detonation was triggered and the test data were recorded.

4.2.3   Results and discussion

The measured blast testing data were processed in order to have a better understanding of the dynamic response of UHPC and HSRC columns to blast loads. The raw data included peak pressure and duration, column deflections.

4.2.3.1   Blast pressure measurements

Blast overpressure time history curves were recorded by center pressure gauge. Empirical prediction on the peak blast overpressure is based on UFC 3-340-2 [12]. Based on the comparison between the experimental and empirical blast pressure-time histories as shown in Fig. 4.6, it is generally concluded that empirical method can give reasonable overpressure decay prediction. Although it underestimates the peak values of the blast overpressure for all the blast scenarios, the empirical prediction is still able to provide a good prediction of the trend of the blast overpressure experimental results, especially the trend of the blast overpressure.

Column deflection results for UHPC and HSRC columns are listed in Table 4.2.
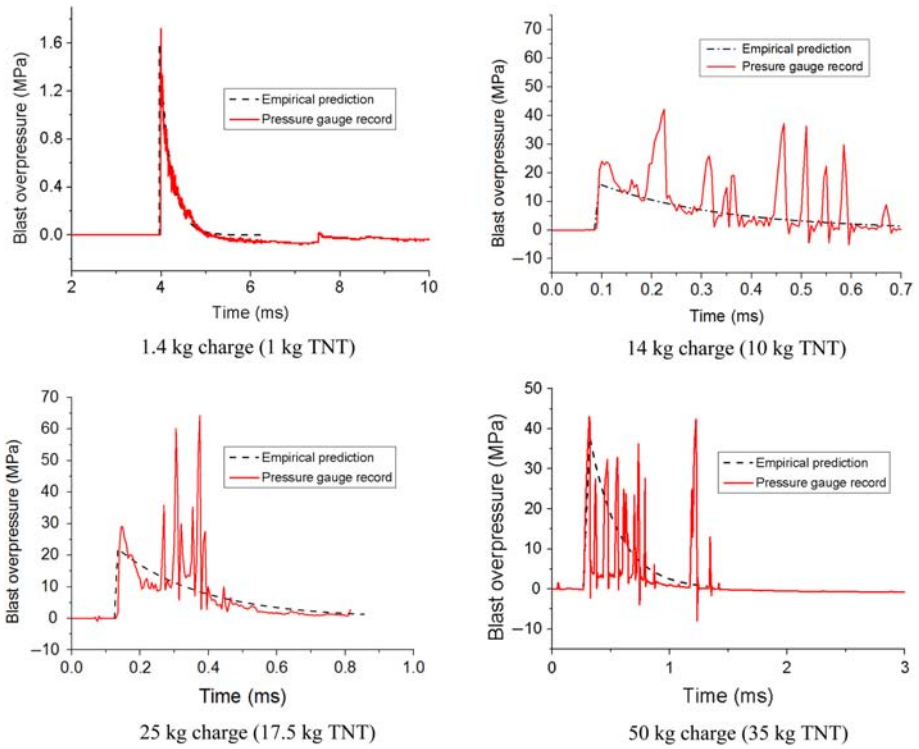
Figure 4.6 Blast pressure-time histories measured by center pressure gauge.

Table 4.2 Summary of UHPC and HSRC series test results

Specimen	Charge weight (kg)	Axial load (kN)	Maximum deflection (mm)	Residual displacements (mm)
U1A	1	0	2.0	0
U1A	35	0	—	21
U1B	1	0	2.0	0
U1B	17.5	0	63	18.5
U2A	1	1000	—	0
U2A	35	1000	68	23
U2B	1	1000	1.2	0
U2B	17.5	1000	29.3	4
U5B	24	1000	27.2	0
U5C	35	1000	51.1	0
U6A	70	1000	—	12
U6B	24	1000	—	3
H7A	24	0	82.6	2
H8A	24	1000	56.0	12
H8B	11.2	1000	32.2	2
H9A	35	500	—	100

4.2.3.2   Deflection versus time profile of ultra-high performance concrete columns reinforced by microfiber

The displacement-time profiles recorded by LVDTs at different locations were compared and shown in Fig. 4.7. As mentioned earlier, LVDTs were placed at three different positions for recording the displacements with the legend of DA1, DA2, and DA3; DA1−DA3 represented the LVDTs placed at 1/6th, 1/3rd, and 1/2 (mid-span) of the distance along the column, respectively. Figs. 4.7A and 4.7B show the mid-span deflections of MF-reinforced UHRC specimens U1B and U2B under the 1.4 kg charge (1 kg TNT equivalence) detonation. U1B showed slight vibration with a peak mid-span deflection around 2 mm, U2B showed less deflection response with the peak value less than 1.5 mm. Both columns responded in an elastic manner and a clear inclusion of axial force effectively reduced column deflection.

The results of specimens U1B and U2B under the 25 kg explosive (17.5 kg TNT equivalence) detonation are shown in Figs. 4.7C and D. Clear plastic response was noted from U1B column in which the mid-span deflection exceeded 60 mm. With inclusion of axial load, U2B showed much less deflection with less than 30 mm mid-span deflection, and the column responded in an elastic manner.

4.2.3.3   Deflection versus time profile of ultra-high performance concrete columns reinforced by twisted fiber

More severe blast loading scenarios were employed in TF-reinforced UHPC columns, and it can be noted from the mid-span deflection-time history shown in Fig. 4.8 that, UHPC column maintained high level of blast resistance, and column U4B showed an residual deflection of 24 mm after 48 kg explosive detonation.

Fig. 4.9A−C present the measured deflections of specimens U5A and U5B under the 1.4 kg to 14 kg and finally 24 kg blasts, respectively. U5A column has the maximum mid-span deflection of merely 1.18 mm under 1.4 kg blast loading, while 14 kg blast loading leads to the maximum mid-span deflection of 16.6 mm. Furthermore, the maximum mid-span displacement of U5B under 24 kg blast loading is 27.2 mm.

4.2.3.4   Deflection versus time profile of high-strength reinforced concrete columns

Response mode of HSRC columns was primarily shear controlled in a brittle manner. Concrete crack on the bottom side of the column made some deflection data not available. Fig. 4.10 shows the H7B and H8B column under 11.2 kg explosive (8 kg TNT equivalence) detonation. Clearly, compared with UHPC column with fiber reinforcement, HSRC showed much larger deflection. Inclusion of axial force again showed beneficial effect in terms of deflection reduction.
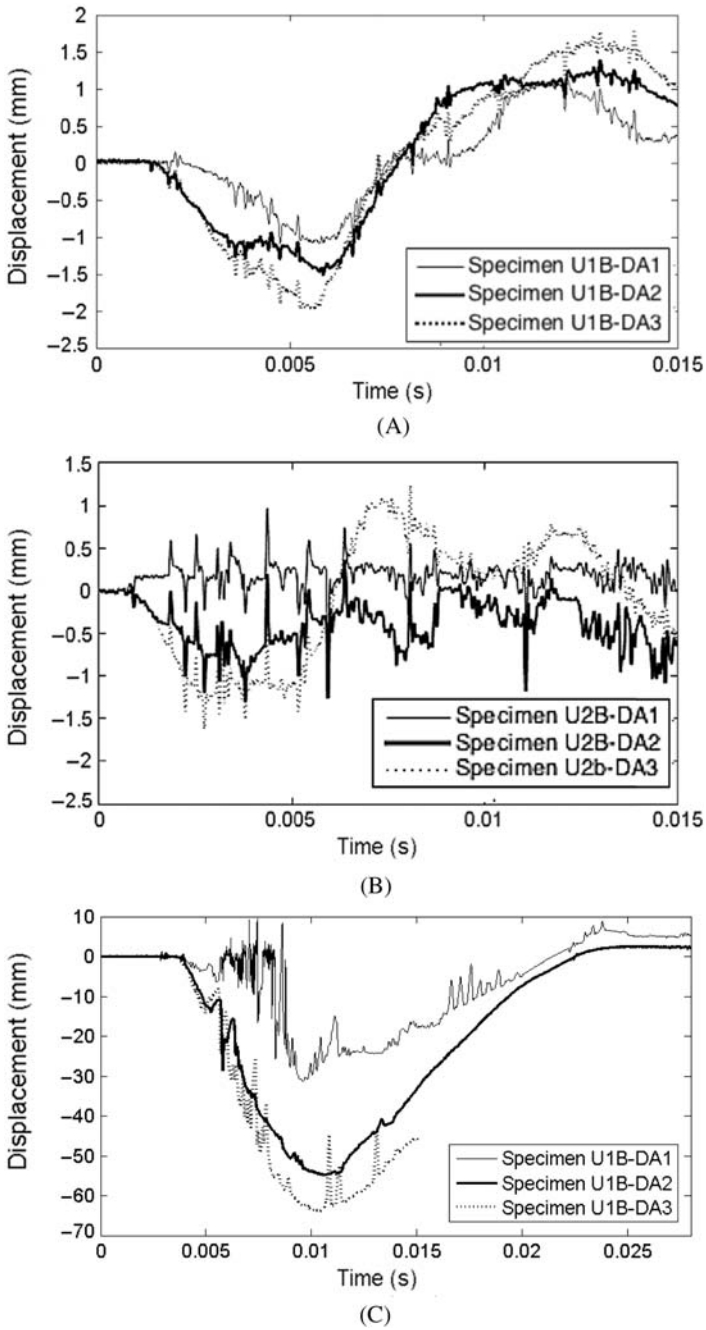
Figure 4.7 Deflection-time profiles recorded on UHPC columns with MF reinforcement. (A) 1.4 kg explosive on U1B. (B) 1.4 kg explosive on U2B. (C) 25 kg explosive on U1B, and (D) 25 kg explosive on U2B.
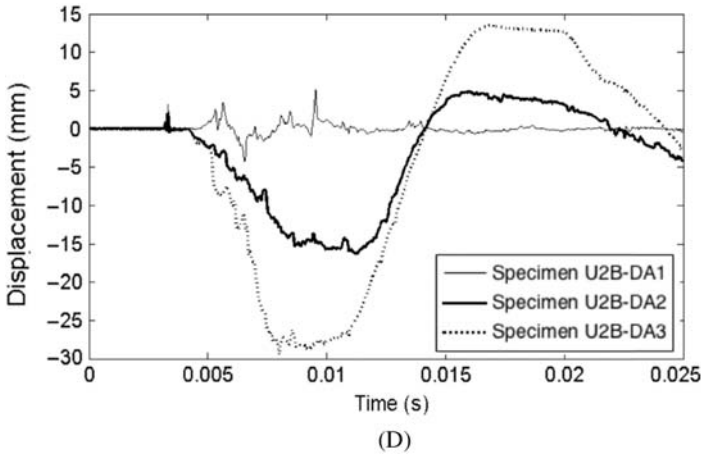
Figure 4.7 (Continued)

4.2.3.5 Axial load effects and comparison between high-strength reinforced concrete and ultra-high performance concrete columns

4.2.3.5.1 Axial load effect

Fig. 4.11 shows the effect of axial load on UHPC columns. With axial load acting on column, it results in an increase in its moment capacity and its nominal shear strength. However, the reduction in mid-height displacement would only occur before the impulse and its corresponding displacement reaches a critical value (i.e., balance condition). Once this critical value is exceeded, the mid-height displacement would increase greatly with the increase of axial load. This is expected for columns with flexural behavior. When columns experience large deflection and plastic hinges formation occurs at mid-span and fixed ends, axial loads will amplify the lateral deflection and internal moment due to the $P-\Delta$ effect. As the deflection increases, the column will transit from a gradual stiffness and strength degradation to a rapid loss of strength due to the buckling of the longitudinal reinforcement.

Another possible reason for the strength enhancement is the membrane effect. In this study, axial loads application provides lateral restrain to the column, and compressive membrane action may occur. A small initial deflection may cause a migration of the neutral axis which is accompanied by in-plane expansion of the column at its boundaries. If this expand is restrained, in this case by the axial load application, the development of arching action enhances the strength of the column.

4.2.3.5.2 Comparison of ultra-high performance concrete and high-strength reinforced concrete under blast loadings

Comparing the results of UHPC and HSRC columns under the same 24 kg blast loading as shown in Fig. 4.12, the results clearly demonstrated that the use of twisted steel fiber (U5B) in columns substantially reduced the mid-span
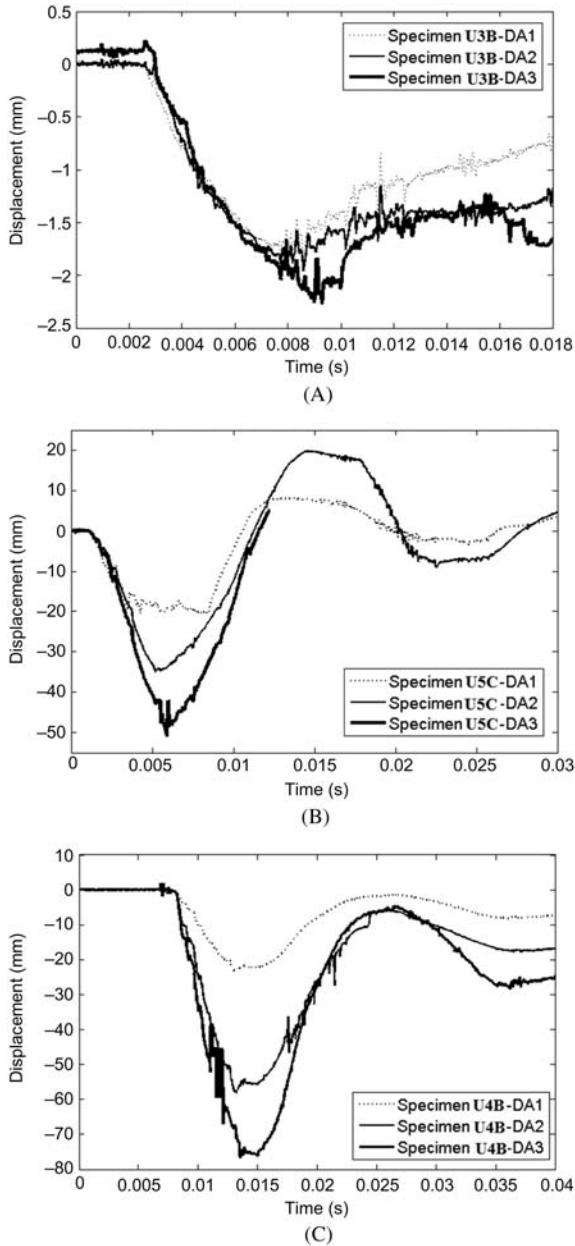
Figure 4.8 Deflection-time profiles recorded on UHPC columns with TF reinforcement. (A) 1.4 kg explosive on U3B. (B) 35 kg explosive on U5C, and (C) 48 kg explosive on U4B.
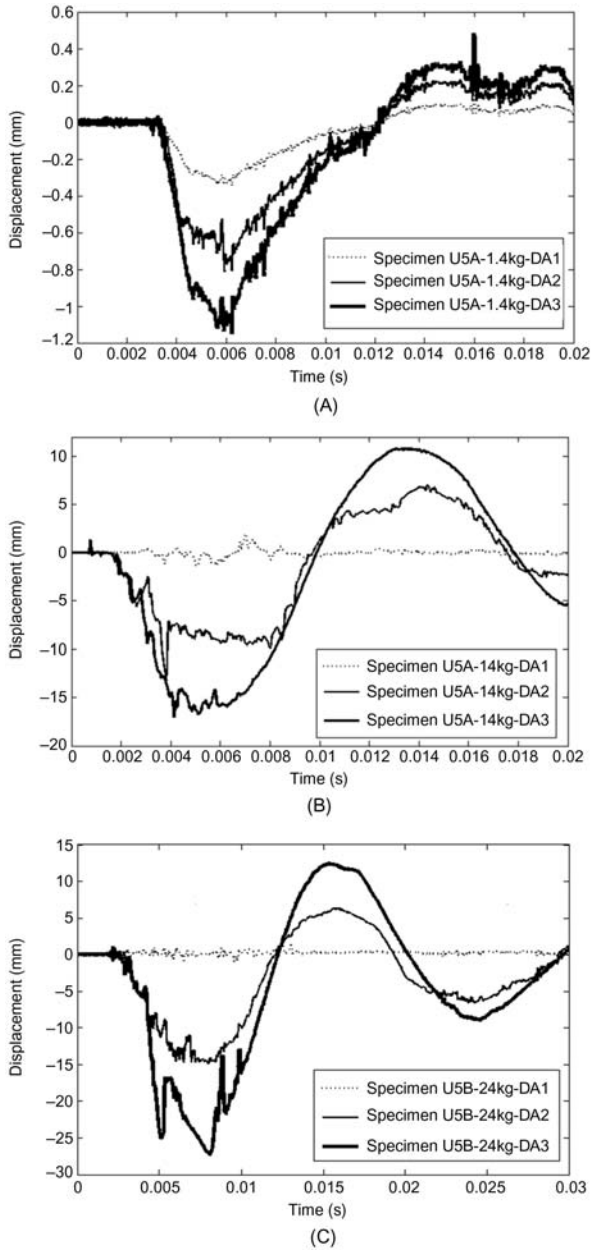
Figure 4.9 Deflection-time profiles recorded on U5A and U5B. Displacement-time history of specimen U5A under (A) 1.4 kg blast loading, (B) 14 kg blast loading, and (C) 24 kg blast loading.
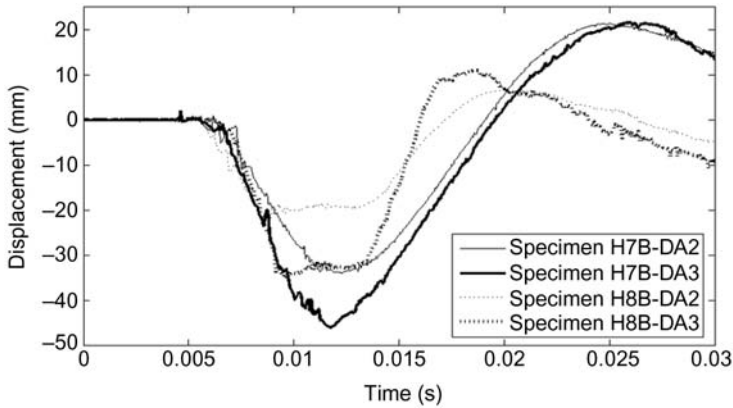
Figure 4.10 Displacement-time profiles of HSRC specimens under the 8 kg charge weight loads.
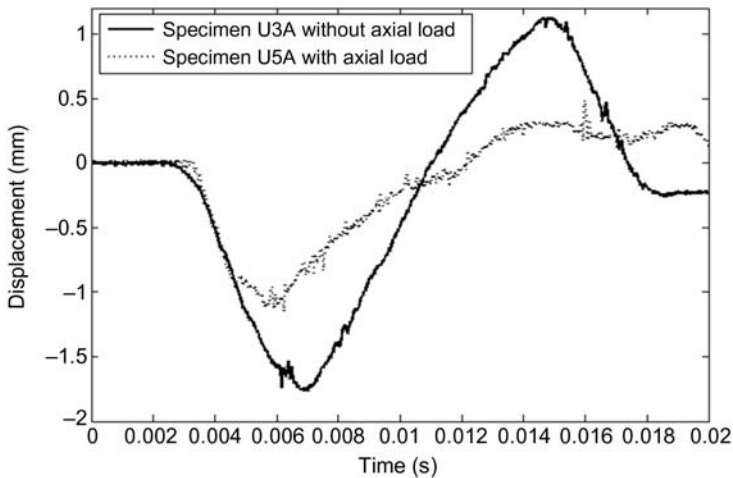
Figure 4.11 Displacement-time histories at mid-span (DA3) of UHPC specimen U3A (without axial loading) and U5A (with 1000 kN axial loading) under the same 1.4 kg blast loading.

displacements when compared to a typical HSRC column (H8A). This is due to the fact that UHPC has drastically greater compressive and tensile strengths, as well as ductility due to high steel fiber contents. The results of H7A and H8A in Fig. 4.12 show that there is a 28% decrease in deflection when the axial load was applied to the column specimen H8A.
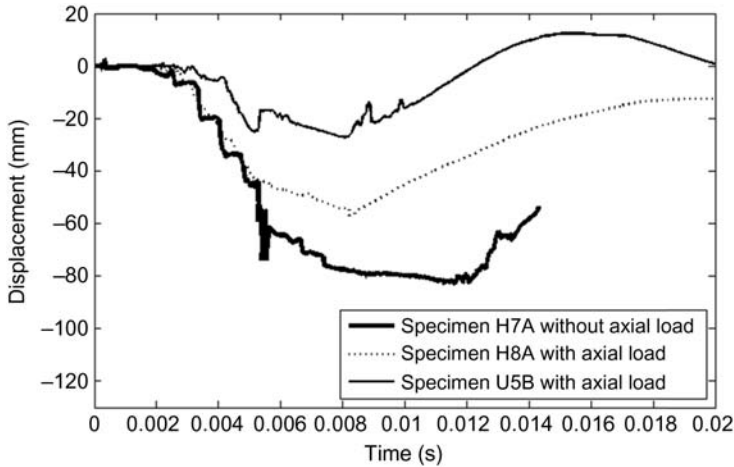
Figure 4.12 Displacement-time histories at mid-span (DA3) of H7A (without axial load), H8A (with axial load), and U5B (with axial load) under the same 24 kg blast loading.

4.2.4 Crack patterns and failure modes

Postblast crack patterns of UHPC and HSRC specimens are briefed in this section. Detailed descriptions of typical crack profile together with classification of the failure modes are presented. Generally speaking, four levels of damage have been characterized to describe the postblast specimens, which are light, moderate, heavy, and severe.

For light damage, column is in good service condition with almost no lateral deflection, only hairline cracks can be observed. When moderate damage occurs, the formation of cracks can be found at the distal face and the crack width cannot exceed 5 mm. Following that, heavy damage is defined when concrete crushing at proximal surface is observed together with massive cracking of concrete at distal surface; the crack width is more than 5 mm.

As shown in Fig. 4.13, UHPC columns suffered much less damage than HSRC columns. All UHPC specimens were in light or moderate damage level; however, HSRC specimens suffered heavy to severe damage under similar or smaller blast loading. The response mode of UHPC columns is shown to be primarily flexural, while HSRC columns tend to fail under shear with significant fragmentation extensively. Two major factors account for the present damage of HSRC columns. Firstly, during the blast loading phase, when blast load hits the column, the column experiences only minimum movement and the blast load is balanced primarily by inertial resistance. Shear force magnitude/distribution in this stage is primarily determined by the shape of inertia force distribution along the column. The maximum shear is located at the mid-span of the column, rather than at the supports in the static loading condition. If the column lacks sufficient shear reinforcement, brittle shear damage occurs. Secondly, due to the nature of the blast loads, i.e., extremely short rising time (in the range of μs) and very short load duration (in the
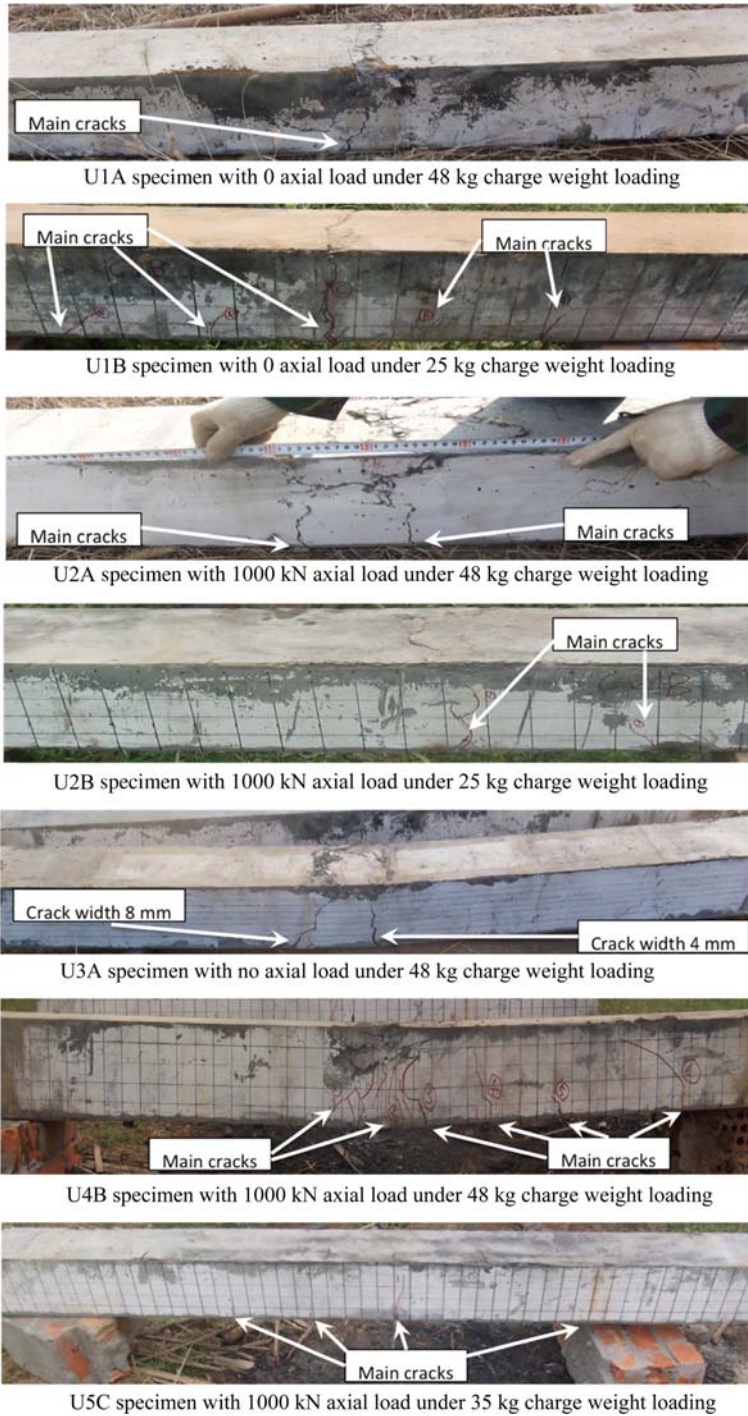
Figure 4.13 Postblast column damage.
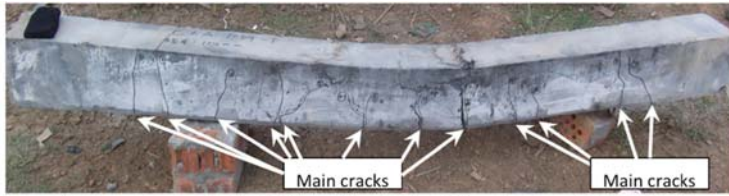
U6A specimen with 1000 kN axial load under 70 kg charge weight loading

U6B specimen with 1000 kN axial load under 24 kg charge weight loading

H7A specimen with no axial load axial load under 24 kg charge weight loading
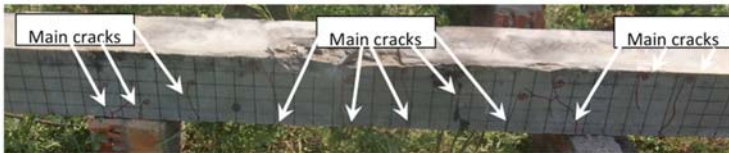
H7B specimen with no axial load under 11.2 kg charge weight loading

H8A specimen with 1000 kN axial load under 24 kg charge weight loading

H8B specimen with 1000 kN axial load under 8 kg charge weight loading

Figure 4.13 (Continued)

range of ms), structural columns subjected to blast load will experience higher modes of vibration after blast loading phase. The amplitudes of the higher modes are relatively small and their contributions to the overall deformations are limited. However, the higher vibration modes will give rise to larger shear forces in the element. It has been demonstrated in previous experimental and analytical work that the local shear forces close to the mid-span are several times higher in relation to the static mode. In the present experiment, the rising of the shear force led to premature shear failure in the HSRC column as the shear resistance provided by the HSC was much less than the UHPC due to fiber reinforcement.

The influence of axial loading on the damage of the specimens was also under investigation. The results on columns tested with axial loading ranging from 0 to 1000 kN showed that axial loading can affect the postdamage scenario. When observing the postdamage scenario of HSRC columns, columns with axial loading exhibit more severe damage in comparison to the specimens without axial loading. For example, for specimen H7B without axial loading, typical thin cracks with limited spalling of concrete from the surfaces of the column were observed; although the diagonal splitting width of H7B was 2 mm and the crushing width was 300 mm, the column remains intact. In contrast, there are several diagonal slitting developed from the bottom of the specimen H8B (with 1000 kN axial load) and extend to the top of the column, and also massive crushing of compression concrete was observed; the large diagonal crack with 15 mm width tends to disengage the column into different pieces. This situation may be due to the fact that axial compression strain and flexural compression strain from the blast load exceed the ultimate strains of the columns at the supports. Under the combination force of blast and axial loading, the concrete material is under a complex three-dimensional stress state, and increasing of axial loading increases the load applied on the concrete element and thus leading to more severe damage. The addition of axial loading may reduce the capacity of the column to withstand blasts as a result of the precompressed concrete being close to material failure.

Generally speaking, UHPC columns displayed less damage and smaller mid-span permanent deflection. Under very large blast loading, UHPC columns developed cracking around mid-span; however, the cracking was effectively restrained by the steel fibers on all UHPC columns. A comparison of UHPC columns against different blasts is divided into two groups. Firstly, under the same 48 kg blast loading, the comparison between U3A and U4B columns is made. Although it is mentioned in the previous discussion that adding axial loading can effectively reduce the maximum deflection, the column with axial loading (U4B) exhibited more cracks at mid-span in comparison to U3A without axial loading. This situation may be due to the fact that under the combined blast and axial loading, the concrete material is under a complex three-dimensional stress state, and addition of axial loading increases the load applied on the concrete element, thus leading to more severe damage. Second comparison is focusing on the postfailure performances of UHPC columns under the 35 and 70 kg blasts. U5C showed a typical flexural failure pattern with small cracks distributed near the specimen center. For U6A column under the 70 kg blast load, this severe blast loading resulted in fracturing of the

concrete on the bottom face. Although some major cracks tended to split the concrete specimen from top to bottom, the steel fibers still held the parts of UHPC column together. These observations indicated that UHPC columns could resist severe blast pressures.

Compared with HSRC columns, UHPC columns can effectively resist the overpressures and shock waves resulted from high explosive loads, reducing the maximum and residual displacements when subjected to similar blast loads, and enhancing the blast-resistant capacity substantially.

4.2.5 Conclusions

This section achieves the aims of characterizing the dynamic performance of UHPC and HSRC columns under blast loads. Explosive loading with explosive weights ranging from 1.4 to 70 kg at standoff distance 1.5 m was employed in field blast tests. Based on the findings of this study, the following conclusions can be made:

- Results from the blast experimental program show that both the twisted and microsteel fibers in UHPC enhanced the blast resistance of columns, resulting in reducing the maximum displacements of columns subjected to blast loads.
- UHPC specimens can effectively resist the overpressures and shock waves resulted from high explosives, reducing the maximum and residual displacements of columns when subjected to similar blast loads, and enhancing the blast-resistant capacity substantially. In all blast tests, UHPC columns showed flexural response, while HSRC columns failed in brittle shear mode.
- Inclusion of axial load can reduce the deflection of the column when the blast loading and corresponding column deformation are small. For larger blast loading and column deformation situation, the axial load increases the deflection of the columns under the blast loads. Investigation into the effect of axial loading on columns subjected to blasts has been performed and the results show that the axially loaded specimens have smaller deflections for UHPRC members. The axial loading changes the column boundary condition and limits the end rotation, and the influence from boundary change outweighs the P-Δ effect which results in a reduced mid-span deflection.

4.3 Postblast residual load-carrying capacity of ultra-high performance concrete columns

Until now, no systematic study on UHPC columns against blast loads and their corresponding postblast behaviors are found in the open literature. Systematic experimental results on UHPC columns under blast loads were reported in the "Blast resistance of ultra-high performance concrete columns" section, and the capability of UHPC columns to resist the blast loads was demonstrated both qualitatively and quantitatively. To observe responses of UHPC columns in more advanced stages, in this section, laboratory residual load-carrying capacity tests on postblast columns are presented and discussed.

4.3.1 Laboratory residual load-carrying capacity tests

To obtain the residual load-carrying capacities of these blast-tested UHPC and HSRC columns, columns were shipped back to the laboratory and tested under static axial loads until failure.

4.3.1.1 Residual loading capacity test setup

The hydraulic testing system as shown in Fig. 4.14 is capable of providing a maximum axial load of 10,000 kN (1000 ton). During the static test, the column was placed on the steel column supports, and two-step loading scheme was conducted. In the first step, an axial load was applied gradually on column ends with a controlled loading rate until a constant value of 500 kN was reached. Then, the axial load was maintained for 60 seconds before increased to 1000 and 2000 kN. At each of these loading levels, the constant load was maintained for 60 seconds as shown in Fig. 4.15. In the second loading phase, the axial load was increased at a constant loading rate until column failure. This two-step testing procedure was made to conform the safety regulation and also guarantee that the hydraulic load cell was in firm contact with the column ends.

In the residual loading tests, the column was placed in the horizontal position on the steel supports owing to the restriction of the testing equipment. This arrangement makes the specimen more like a simply supported beam subjected to an axial force instead of a column, and the two supports would generate some constraints to the specimen which reduced the free span length of the column. In order to minimize the influence of support reactions during the residual loading tests, the column was intentionally placed with its compression surface on the supports, and though this setup, under axial loads, the column would deflect upward as shown in Fig. 4.16.
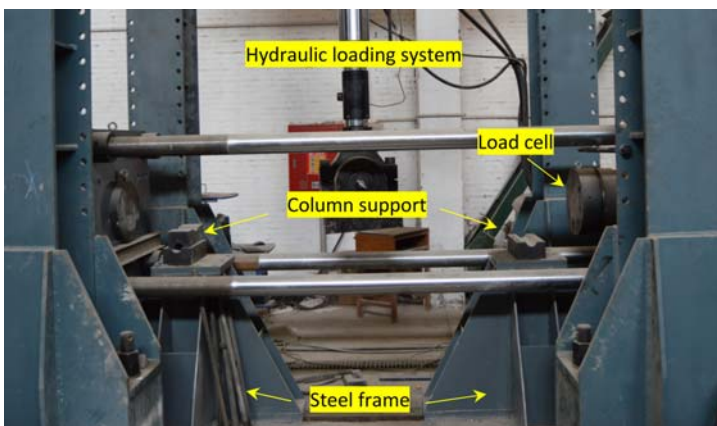
Figure 4.14 Axial load-carrying capacity testing system.
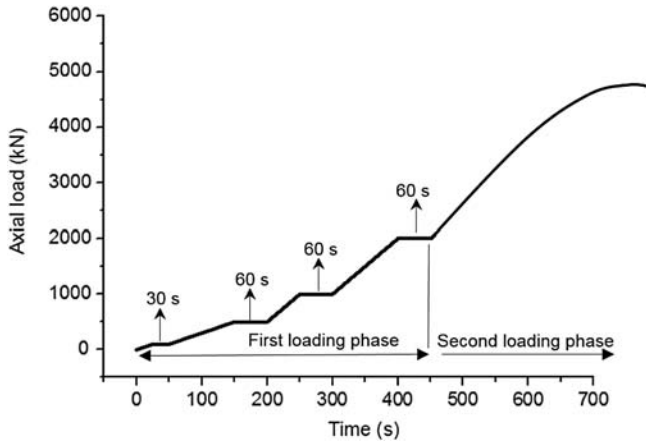
Figure 4.15 Loading scheme in the residual tests.
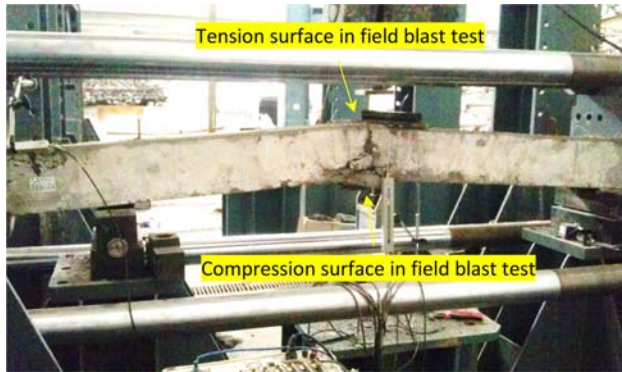
Figure 4.16 Column on the test machine.

Upon starting the test, there was an initial friction force between the supports and the column in the axial direction which reduces the axial force within the clear loading span, i.e., between the two steel supports. The resultant axial force can be simply derived as:

$$F = P - W\mu/2 \tag{4.1}$$

where F is the resultant axial load, P is the axial load at column ends, W is the column self-weight, and μ is the static friction coefficient between steel and concrete which depends on the steel surface roughness.

In this study, column self-weight is around 2500 N, static coefficient between steel supports and concrete is roughly taken as 0.2, and the friction force at a steel support is 250 N. Compared to the failure axial load which is around 5800 kN, the influence from the supports is small and can be neglected.

4.3.1.2 Benchmark test on undamaged ultra-high performance concrete column

Undamaged column specimens including an HSRC column and two UHPC columns, respectively, with MF and TF fiber reinforcements were tested to provide the benchmark load-carrying capacity. Under uniaxial compression loads, short concrete columns usually fail under material compressive failure, while slender columns usually experience buckling due to instability. It is necessary to check intermediate-length columns like those columns in this study to determine the governing failure mode.

The critical load indicating the equilibrium stability of a column can be calculated based on Euler formula as:

$$P_{cr} = \pi^2 EI/(kL)^2 \tag{4.2}$$

where E is the material elasticity modulus, I is the average moment of inertia of the cross-section of the column, L is the unsupported length of the column, and k is the column effective length factor. For benchmark columns, the existence of the support reduced the unsupported length of the column, and column boundary was more close to a fixed boundary without end rotation and displacement, therefore $k = 0.5$ was used in the calculation.

After simple calculation based on Eq. (4.2), it is found that the critical stress to induce buckling failure is larger than the material compressive strength. The failure of undamaged columns in this study is therefore determined to be controlled by material compressive strength.

Failures of undamaged UHPC column (MF reinforcement) and HSRC column are shown in Fig. 4.17. Under axial loading condition, column lost load-carrying capacity owing to the concrete fracture at the column support. No flexural damage at the column mid-span was observed. With damage and cracking only distributed over the column surface and where the provision of fibers prevented cover spalling, superior damage tolerance was observed in UHPC column. HSRC column lacked fiber reinforcement and therefore its failure is quite brittle and extensive.

In this test on the undamaged UHPC columns, upon column failure, axial loads for column with MF and TF reinforcements are 5900 kN and 5010 kN, respectively. For HSRC column, the ultimate axial load is 2970 kN. Axial load−strain relationships of undamaged UHPC column (with MF fiber) and HSRC column which are derived based on LVDT data are given in Fig. 4.18 It is clear that UHPC column is more ductile and able to sustaining a larger axial load while the failure of HSRC column is abrupt.

In a previous publication and ACI-318 code, the following equation was used to assess the maximum axial load-carrying capacity of an undamaged RC column:

$$P_{code} = 0.85f'_c(A_g - A_s) + f_y A_s \tag{4.3}$$
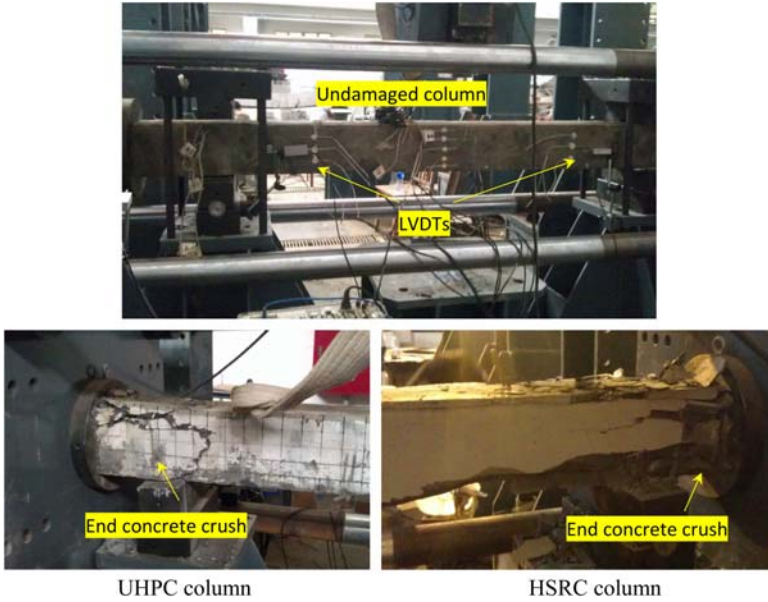
Figure 4.17 Concrete crush near the supports of the undamaged UHPC column and HSRC column.
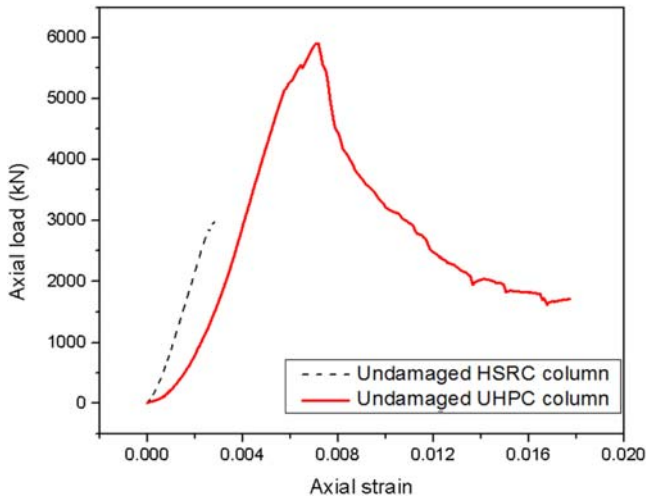
Figure 4.18 Axial load−strain relationships of undamaged columns.

where f'_c is the compressive strength of concrete, f_y is the yield strength of the longitudinal reinforcement, A_g is the gross area of the column cross-section, and A_s is the area of the longitudinal reinforcement.

It is noted that the axial capacity of UHPC columns remains well above the nominal capacity predicted by the ACI-318 code. Similar observation is found in ref. [13]. Regarding the UHPC column under pure axial loading condition, extensive research was carried out to examine the impacts from factors like longitudinal reinforcement, stirrup reinforcement, fiber material addition on short [14] and slender UHPC [15] columns, and analytical models describing the ductile load−strain curve was proposed and discussed. Because it is beyond the scope of this study, it is not discussed in this study.

4.3.1.3 Test results of blast-damaged columns

The damage index D for postblast UHPC columns is defined as [7]:

$$D = (1 - P_{\text{residual}}/P_{\text{max}}) \times 100\% \tag{4.4}$$

Residual load-carrying capacity test results of UHPC columns and one HSRC column are summarized in Table 4.3. The other HSRC columns are not in the list because they were completely failed in the field blast tests.

Due to the higher material compressive strength, residual loading capacities of columns with MF fiber reinforcement are higher than the columns with TF fiber reinforcement. It is also clearly noted that columns subjected to higher blast loads maintained lower residual axial loading capacity.

When studying the influence from the axial load during the field blast test on postblast behavior of UHPC columns, it is interesting to note that for columns U1A versus U2A and U3A versus U4B (all of them were subjected to 35 kg TNT equivalence detonated at 1.5 m), axial load seems to exert negative effect on column residual loading strength. However, based on the observations made after the blasting tests, axial load application actually reduced mid-span deflection of UHPC columns during the field tests. These observations indicate that application of axial load reduced the column lateral deflection, but increased column damage and hence reduced its residual loading capacity. This is because axial load application introduced compressive membrane effect which enhanced the column flexural resistance. However, when compressive membrane effect occurred, rotation of column ends would inevitably reduce the contact area between the column and the axial load cell and boundary confinement which generated some compressive cracks as shown in Fig. 4.19. When residual loading tests were carried out, the damage at the column ends effectively reduced the column axial loading resistance. It is worth pointing out that such observation is not seen in cases where less severe blast loads were employed. For example, after the 17.5 kg TNT explosion at 1.5 m standoff distance, the TF-reinforced UHPC column U3B had lower postblast axial loading strength when compared with U5B which was subjected to the same blast load but with axial load application during the field tests. These results are also consistent with the observations made in a study of posttensioned RC beam subjected to blast load [16]. In the latter study, it was observed that applying posttension force was beneficial in reducing the beam response when the response was governed by the

Table 4.3 **Residual load-carrying tests results**

Column number	Fiber material	TNT equivalence (kg)	Standoff distance (m)	Axial load (kN)	Residual strength (kN)	Damage, D (%)
U1A	Microfiber	35	1.5	0	5535	6.2
U1B	Microfiber	17.5	1.5	0	5825	1.3
U2A	Microfiber	35	1.5	1000	4540	23
U2B	Microfiber	17.5	1.5	1000	5660	5
U3A	Twisted fiber	35	1.5	0	3595	28
U3B	Twisted fiber	17.5	1.5	0	3806	24
U4B	Twisted fiber	35	1.5	1000	3068	39
U5B	Twisted fiber	17.5	1.5	1000	4799	4
U5C	Twisted fiber	25	1.5	1000	4830	4
H7B	Nil	8	1.5	0	1146	60

Figure 4.19 Boundary cracks on U2A.

MF reinforcement   TF reinforcement
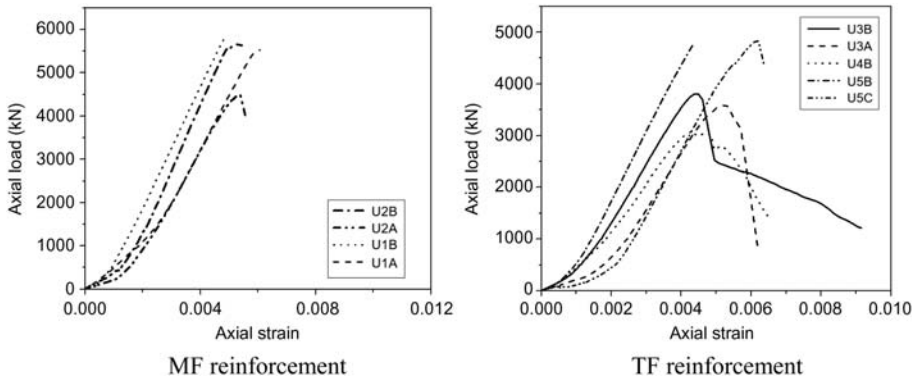
Figure 4.20 Axial load−strain curves for UHPC columns.

flexural mode associated with relatively small blast load. When the blast load was large that shear failure governed the beam damage mode, posttensioning force actually resulted in severe damage because the shear stress in the beam was larger owing to the axial posttensioning force.

Generally speaking, even after the most severe blast event (35 kg TNT equivalence detonated at 1.5 m) in this study, UHPC columns (U1A, U2A, U3A, and U4B) preserved most of their axial loading capacity. On the contrary, HSRC column lost 60% of its loading capacity although it was subjected to smaller blast load, i.e., 8 kg TNT equivalence at 1.5 standoff distance.

Postblast axial load−strain relationships for UHPC columns are shown in Fig. 4.20. Firstly, it is noted that TF-reinforced UHPC columns showed some

ductility in the residual load capacity tests while MF-reinforced UHPC columns showed more brittle postblast behavior. As demonstrated in the earlier discussion, the axial loading capacity of the columns in this study is governed by the material compressive strength, and the postpeak ductility is influenced by the fiber material. Although UHPC with TF additions has lower material compressive strength, its material ductility after yielding is more prominent than MF-reinforced UHPC (Fig. 4.20A), and the ductile performance stems from the better bond between TF and concrete matrix after initiation of cracks. Secondly, it is noticed that after UHPC column was subjected to larger blast loads, its axial stiffness decreases, and this trend exists for columns with and without axial load application. Such differences in axial stiffness can be attributed to the damages imposed by blast loads, UHPC columns exposed to higher blast loads suffered more damage which reduced its axial load-carrying performance.

Damage mode of each column is shown in Fig. 4.21. U3B, U5B, and U5B only suffered slight blast damage, and their damage modes in residual load-carrying capacity tests are quite similar to the undamaged column. Although concrete cover spalling happened near the column end, the cover remained on the specimens throughout testing due to the bridging effect of steel fiber material. This behavior contrasts with the brittle and explosive cover failure reported by numerous researchers for traditional high-strength concrete columns, and it illustrates the enhanced damage tolerance of UHPC.

The damage modes of the other columns are significantly different from the undamaged UHPC column. This is because blast load caused significant flexural damage at the column mid-span as shown in previous column blast tests. The less confinement to reinforcement bars at the mid-span due to concrete damage and plastic deformation of the reinforcements by blast load reduced the capacity of the section at the mid-span. As a result, failure occurred at the mid-span due to concrete crushing and reinforcement buckling when the axial load was applied.

4.3.2 Conclusion

In this study, residual load-carrying capacities of postblast UHPC columns are experimentally evaluated. In previous field blast tests, UHPC columns demonstrated high blast-resistant capability and the performance stems not only from the ultra-high mechanical properties but also from the bridging effects of steel fibers. The postblast columns were taken back to the laboratory and subjected to static loads to determine the column residual loading capacity. While benchmark columns failed under end crush, postblast columns suffered buckling failure at column mid-span. The test results reveal that the UHPC columns retain most of their loading capacity after blast loads. UHPC column that is cast with microsteel fiber reinforcement preserved more than 70% of its loading capacity after 35 kg TNT detonation at 1.5 m standoff distance, while HSRC column only maintained 40% loading capacity after 8 kg TNT detonation at 1.5 m standoff distance.
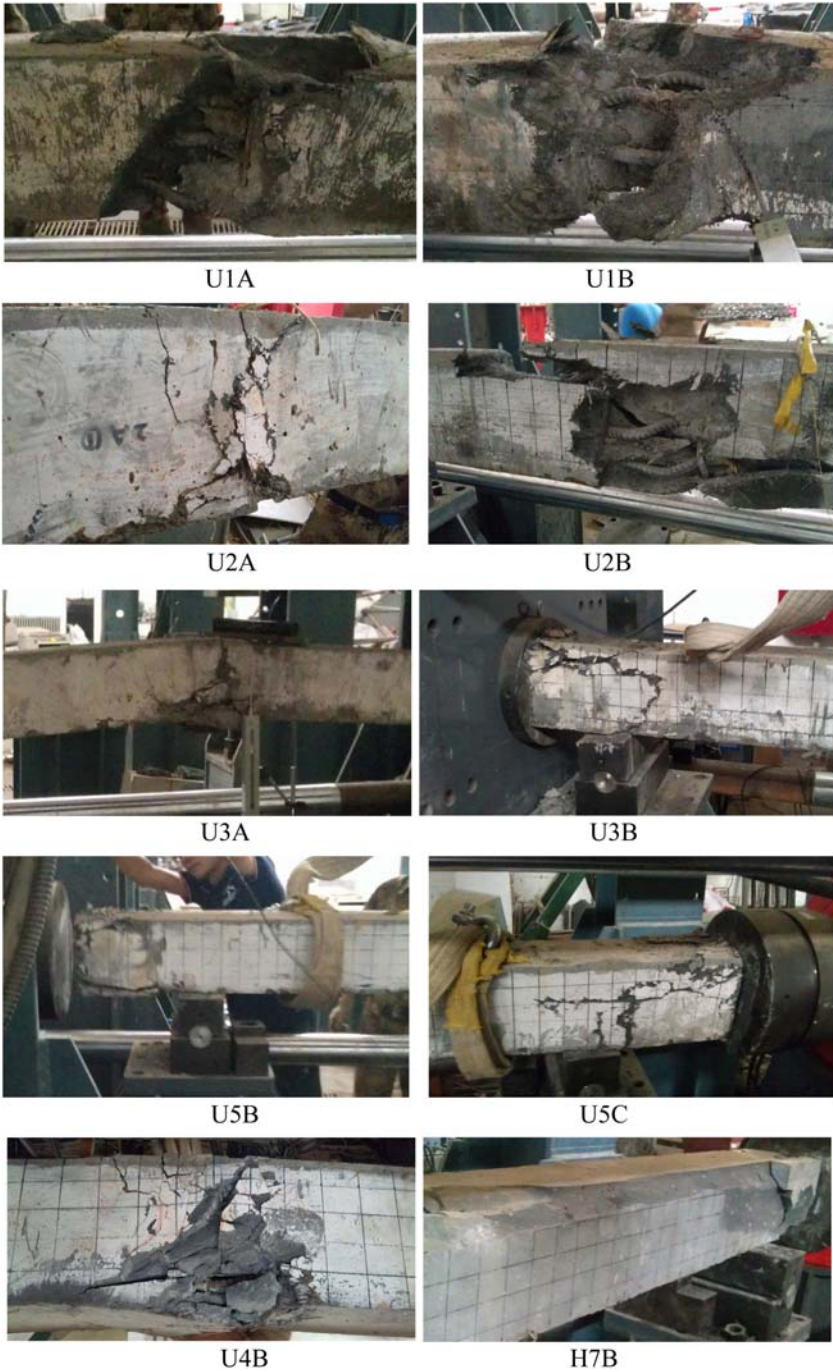
Figure 4.21 UHPC columns after residual loading test.

4.4 Numerical simulation of ultra-high performance concrete columns

4.4.1 Numerical model

In this study, numerical models aiming to reproduce the field blast tests and residual load-carrying capacity tests are developed in LS-DYNA. Parameters used for UHPC concrete and steel reinforcement are listed in Table 4.4.

To use the Material Elastic_Plastic_Hydrodynamic, an equation of state (EOS) is required. In this study, the Gruneisen EOS is defined. The parameters in the EOS used in this study are given in Table 4.5.

4.4.2 Numerical results

In this study, two cases, i.e., U1B and U2B under 1 kg TNT equivalence and 17.5 kg TNT equivalence, are simulated using the proposed numerical model. FE model with mesh size 0.01 m is created in LS-DYNA and shown in Fig. 4.22, and

Table 4.4 Material model and properties

Material	LS-DYNA model	Input parameters	Magnitude
UHPC	Elastic_Plastic_Hydrodynamic	Tabulated effective plastic stress versus strain obtained from uniaxial compression tests	
Steel	Erosion criterion Piecewise_linear_plasticity	Principal tensile strain	0.1
		Mass density	7800 kg m^3
		Elastic modulus	2.00E + 11
		Poisson's ratio	0.3
		Yield stress	1350 MPa
		Failure plastic strain	0.15

Table 4.5 Parameter for the equation of state

EOS_Gruneisen	C_0	2100 m s^{-1}
	S_1	1.4
	γ_0	2
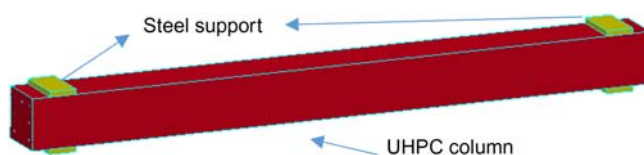
Figure 4.22 Finite element model.

steel support is simulated through Mat_Rigid_Body. Contact_Automatic_Surface_to_Surface is used to describe the contact between the column and support. Default values in LS-DYNA are used to define the contact.

Fig. 4.23 compares the mid-span deflection-time history curve of U1B column under 1 and 17.5 kg TNT equivalent explosions. It is noted that for 1 kg TNT equivalent explosion, the numerical model captures the maximum deflection and reproduces time history curve quite well until the first peak. The slight inconsistence afterward can be explained by the fact that in the real blast test, the blast energy can be dissipated in multiple ways like column free vibration, friction

(A)

No cracks

$T = 5.2$ ms when U1B has maximum deflection

(B)
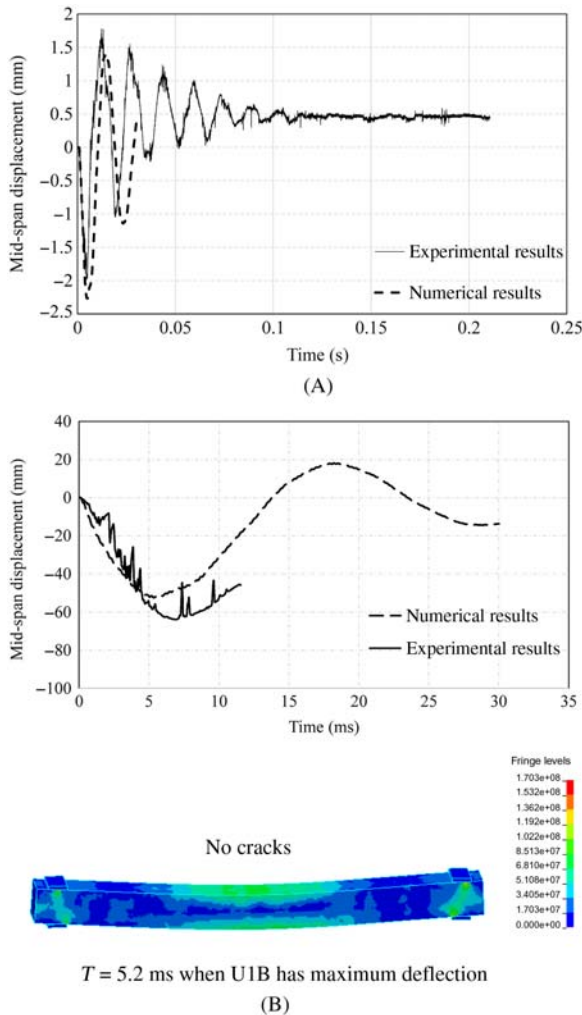
Figure 4.23 Comparison of deflection-time history curve for U1B. (A) U1B under 1 kg TNT equivalent explosion and (B) U1B under 17.5 kg TNT equivalent explosion.

between the column and boundary or surrounding medium. As shown the simulated peak response is slightly higher than the recorded one and the free vibration period is slightly longer than the column specimen, indicating that the stiffness of the numerical model is probably slightly smaller than the real column. Nonetheless, the numerical model gives reasonably good predictions of the column responses under blast loadings.

For the 17.5 kg TNT equivalent explosion test, experimental observation gives a maximum deflection of 63.74 mm, while the numerical simulation underestimates the maximum mid-span deflection of around 56 mm. The inaccurate numerical prediction can be attributed to the modeling of mid-span flexural cracks. As can be noted from the test results, hairline cracks, although not significant, can be found on the bottom side of the column, and these cracks are quite narrow with a width less than 2 mm. In numerical simulation based on LS-DYNA, element erosion is commonly used to avoid mesh distortion under severe blast effects. However, it shall be noted that erosion algorithm does not have any physical background and thus shall be used with caution. To avoid premature element deletion, conservative erosion criteria are usually used. For example, in this study, a tensile strain of 0.1 is used to model UHPC material damage, i.e., crack. In reality, tensile UHPC crack might occur at a smaller strain. Furthermore, to generate small cracks with width less than 2 mm, very fine element size should be used. This requirement makes the simulation extremely time and resource consuming. If a more appropriate erosion criterion and smaller elements were used in the numerical model, larger mid-span deflection could be predicted. The current prediction underestimates the recorded deflection with an error of 12%.

For U2B column tested with 17.5 kg TNT equivalent explosion, 1000 kN axial load was applied on the UHPC column. In the numerical simulation, a static pressure of 25 MPa which equals to a 1000 kN axial load on column end cross-section is applied on one end of the column and lasts for the entire simulation. The first 10 ms is used to stabilize the column under axial load. Due to the very high axial stiffness, after 10 ms the axial velocity of the column is very small approaching zero. Therefore, the effect of axial load application can be deemed negligible. Fig. 4.24 shows the column maximum deflection at around 7.5 ms. Similar to the tested column, it is noted that at the end of simulation, no visible flexural crack is observed at the column mid-span.

Fig. 4.25 displays the time history curve comparison for U2B column, and it can be noted that the numerical model yields a reasonably accurate maximum deflection and good time history curve prediction.

Fig. 4.26 shows the simulation results of the undamaged UHPC column under uniaxial loading (fringe level of plastic strain is given). It should be noted that the both ends of the column model are assumed to be fully fixed except axial direction, and the simple supports in the laboratory test are not included in the numerical model due to their minimal influence on the residual tests. In the simulation, a linearly increased axial load is applied on the column until its failure. The extremely high axial stiffness and slow axial loading guarantee that there is no any axial vibration or velocity induced during the residual loading capacity test simulation. It is

Maximum deflection

Residual deflection
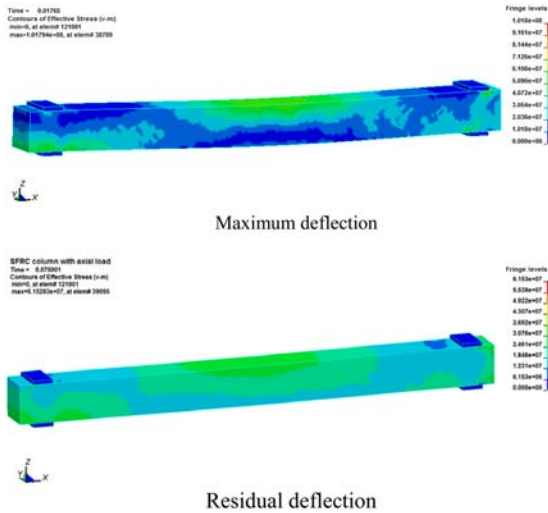
Figure 4.24 Deflection of U2B under 17.5 kg TNT.
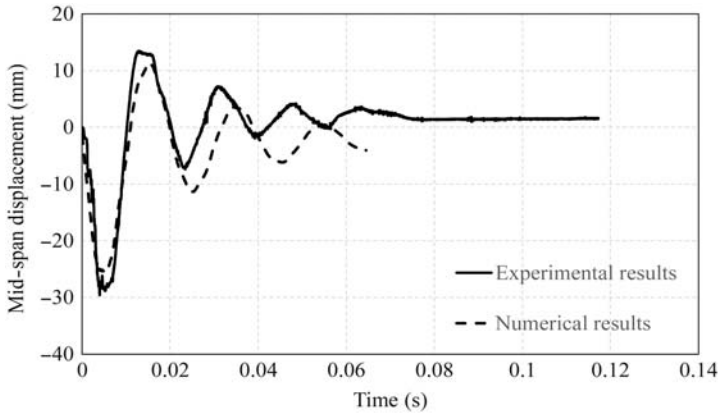
Figure 4.25 Comparison of deflection-time history curve for U2B under 17.5 kg TNT.

noted that the numerical simulation gives reasonable reproduction of the laboratory observation, and failure of the undamaged UHPC column initiates at the columns ends.

Column residual loading capacity test of U1B column is simulated after the simulation of blast-induced structural response. The simulation consists of two steps: the first is the blast response simulation as described earlier; and then static response simulation starts after the column residual velocity in the first step simulation becomes very small around $0.02 \, \text{m s}^{-1}$. A linearly increased axial load is applied on the column where failure occurs. The column residual loading capacity
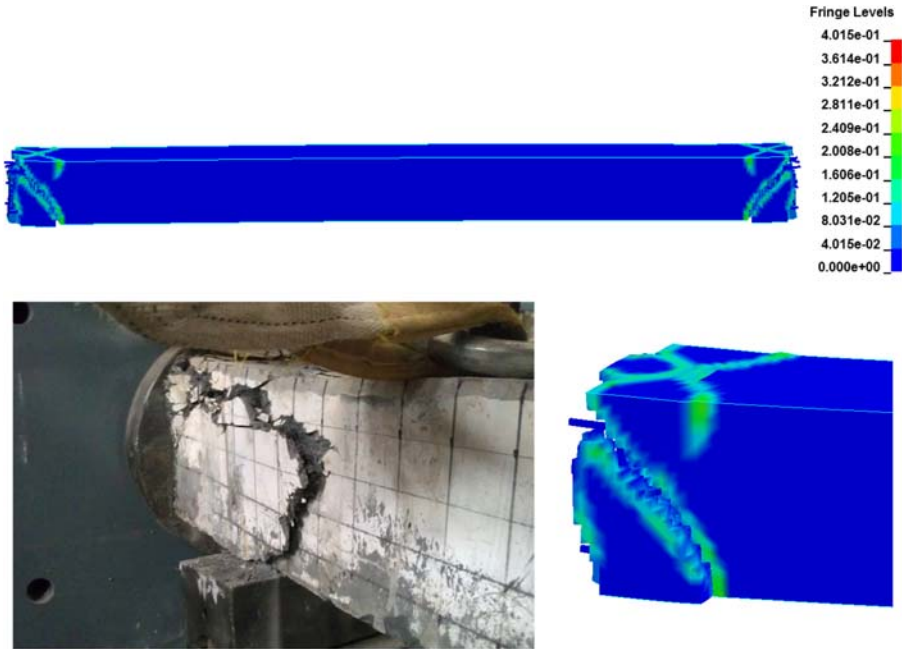
Figure 4.26 Simulation of undamaged UHPC column in residual load-carrying test.
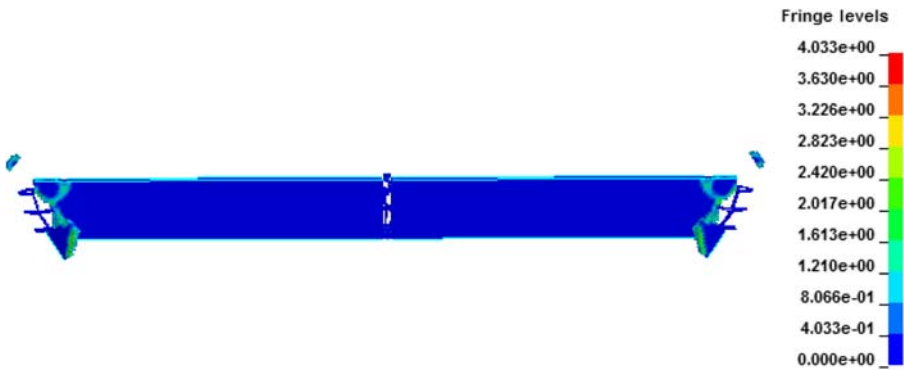
Figure 4.27 Failure mode of U1B column in the simulation.

can then be determined. Fig. 4.27 shows the failure mode of UHPC column U1B under residual load-carrying test simulation, and it is noted that U1B failure initiates at the column ends which is similar to the undamaged column. Column lost its loading capacity when its mid-span reinforcement buckled.

As shown in Fig. 4.28, comparing with its laboratory test result, the numerical simulation of U1B column slightly overestimates the loading capacity after blast loading. This can be attributed to the fact that in the blast test simulation prior to
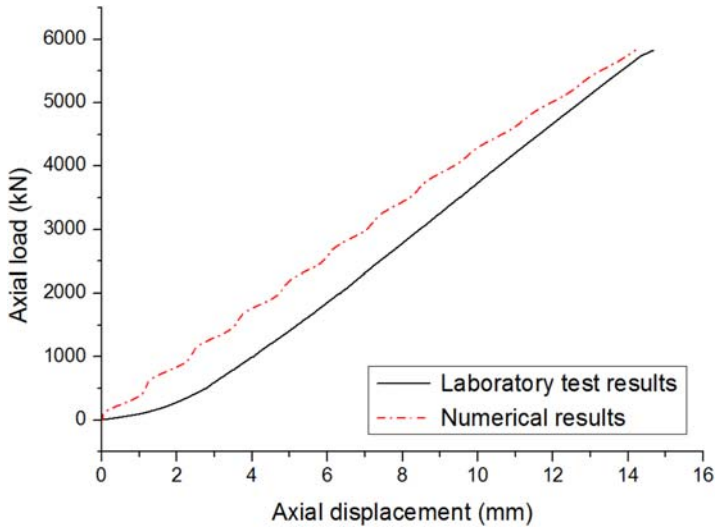
Figure 4.28 Axial load−displacement curve for U1B column.
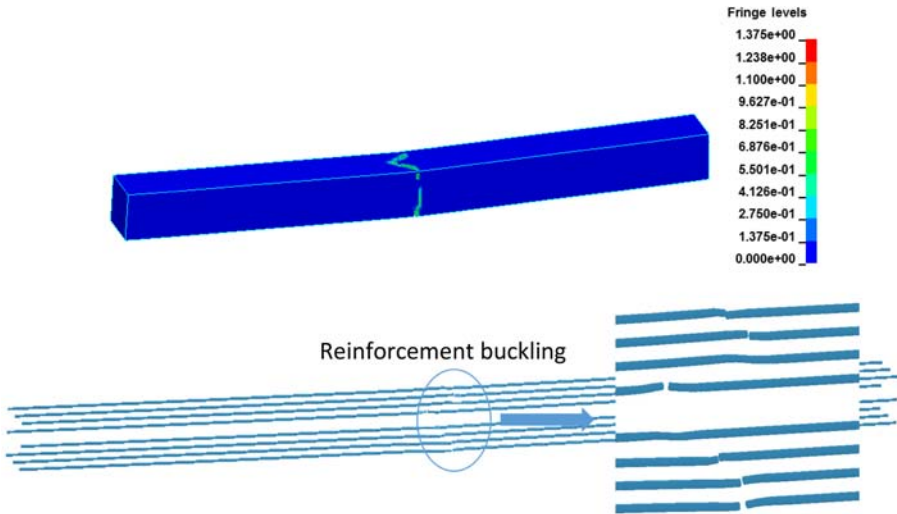
Figure 4.29 Failure of U2B column in residual load-carrying test simulation.

the residual load-carrying capacity simulation, the flexural cracks at column mid-span are not reproduced, and these cracks influence the structural integrity and reduce loading capacity. However, it is worth noting that the numerical simulation gives accurate prediction of column residual capacity which is close to 5800 kN.

Similarly, residual loading capacity test of U2B column is simulated in LS-DYNA. Fig. 4.29 demonstrates the failure mode of UHPC column U2B under residual load-carrying test simulation, and it is seen that clear concrete failure happens
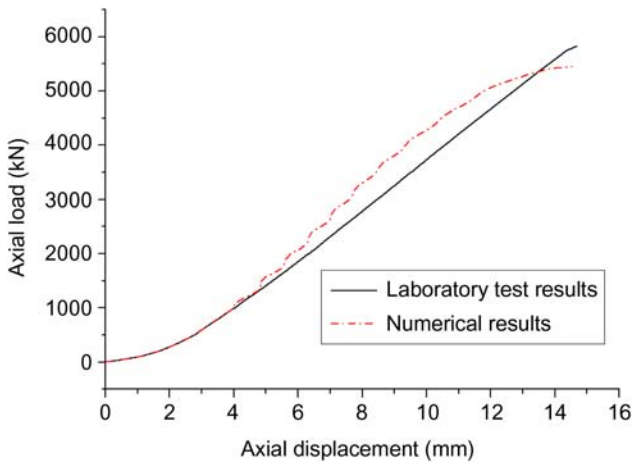
Figure 4.30 Axial load—displacement curve for U2B column.

at the column mid-span which follows the reinforcement buckling, and there is no concrete cracking at the column ends. Axial load—displacement curve shown in Fig. 4.30 demonstrates that comparing with laboratory test results, the numerical simulation gives good predictions of the remaining load-carrying capacity of UHPC column after blast loading. In the simulation, the column fails at around 5500 kN, and comparing with the test result which is 5660, the deviation is −2.8% (positive value indicates overestimation in numerical simulation).

4.4.3 Conclusion

Preliminary numerical study on UHPC columns under close-in detonation and post-blast loading capacity is presented in this section. Due to the missing data in uniaxial tensile and triaxial compression/tension, the FE model is deemed to have some limitation in prediction UHPC behavior and damage, despite reasonable results are obtained. In the next section, more numerical study is presented based on revised UHPC model.

4.5 Damage evaluation of ultra-high performance concrete columns

Following the numerical study presented in last section, extensive numerical study aiming at evaluating generic UHPC columns under blast loads is carried out.

In most numerical model for concrete, uniaxial tensile strength and strain capacity are required rather than flexural tensile strength as discussed in Chapter 2, Development, testing, and numerical simulation of ultra-high performance concrete at material level. Therefore an inverse analysis on the FPBTs are carried out based

on Japan Concrete Institute (JCI) Standard JCI-S-003-2007 [17]. By adopting this method, it is assumed that the stress distribution on the compression side is triangular, and the stress distribution on the tension side is uniform.

$$\varepsilon_{tu,b} = \phi_u \cdot D \cdot (1 - x_{nl}) \tag{4.5}$$

$$f_{t,b} = 0.5 \cdot E \cdot \phi_u \cdot D \cdot x_{nl}{}^2 / (1 - x_{nl}) \tag{4.6}$$

where

$$x_{nl} = -1 + 2\cos(\theta/3)$$

$$\theta = \arccos(-1 + 6m^*)$$

$$m^* = M_{max} / (E \cdot \phi_u \cdot B \cdot D^3)$$

$$x_{nl} = x_n / D$$

where x_n is the distance from compressive edge to neutral axis (mm); D is the depth of test specimen (100 mm); M_{max} is the maximum moment $= P_{max}/2 \times l/3$; ϕ_u is the curvature at the maximum load; and B is the width of the specimen (100 mm).

The curvature measurement in the JCI method is based on two staggered (lower and upper) LVDTs on the specimen side. In this study, curvature is expressed in relation with the mid-span deflection as $\phi = 216\delta/(23L^2)$ in which δ is the mid-span deflection and L is the clear span between the supports.

After inputting all parameters into Eqs. (4.5) and (4.6), the uniaxial tensile strength and ultimate strain for TF-reinforced UHPC are calculated, and presented in Fig. 4.31. The parameters shown in this figure are to be applied in the subsequent FE analysis.

4.5.1 Material dynamic performance

As a relatively new material which varies in composition and fiber material mixture, dynamic material behavior of UHPC is still under discussion. While some tests data showed that UHPC exhibits similar increases in strength to normal strength concrete for strain rates in the range of $100-1000 \text{ s}^{-1}$ [18]. More test data reveal that UHPC is less rate sensitive than conventional concrete material. Chen et al. [19] conducted dynamic tensile tests on steel fiber RC with various fiber volume fractions, and the largest DIF obtained was around 1.1 which is substantially smaller than the normal strength concrete. Weidner [20] conducted a series of drop hammer tests on both plain concrete and fiber-reinforced HSC, and it was observed that fiber RC specimens were less sensitive to the dynamic load as compared with normal strength concrete. Millard et al. [21] performed dynamic flexural tensile test on ultra-HSC with different dosages of steel fiber. The results show that the strain rate enhancement of flexural strength for UHPC is reduced as the fiber percentage
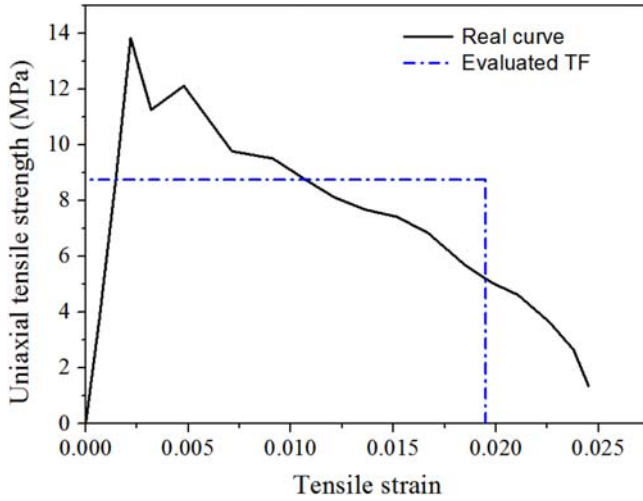
Figure 4.31 Inverse analysis on FPBTs.
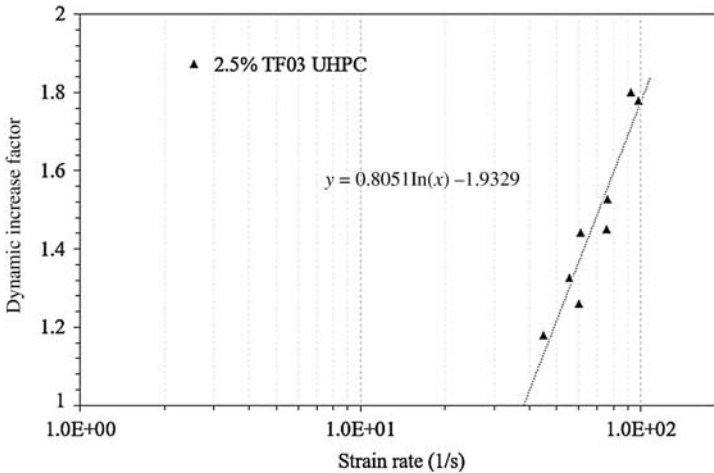
Figure 4.32 DIFs for UHPC under compression.

increases. It was explained that the fibers resist the lateral spreading of the cracks by bridging across regions of lower strength. Therefore the beneficial effect of a restraint on lateral crack growth has already been partially accounted for by fiber reinforcement, resulting in higher failure strength under quasistatic loading. Subsequently, the influence of the higher loading rate on reducing lateral crack development would be lessened.

In this study, the DIFs for the UHPC under compression and tension are obtained though Split-Hopkinson-Pressure-Bar (SHPB) tests on cylinder samples and are shown in Fig. 4.32 and Fig. 4.33, respectively [22,23]. Generally speaking, UHPC
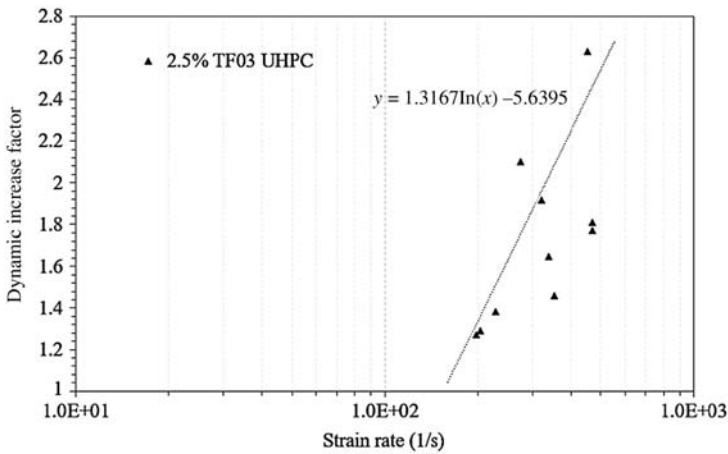
Figure 4.33 DIFs for UHPC under tension.

developed in this study is rate dependent but the rate sensitivity is lower than the conventional concrete. In addition, for conventional concrete, according to the empirical formulae proposed by Malvar and Crawford [24] and Malvar and Ross [25], a sharp increase in the slope of DIF curve happens at transition strain rate of $30 \, s^{-1}$ and $1 \, s^{-1}$ for compression and tension, respectively. Although without sufficient data, it can be predicted that such transition strain rate for UHPC material is higher than the normal strength concrete. One possible explanation is that such transition stems from the increased lateral inertia effect, and in UHPC material, dispersed fiber material held together the concrete and reduced the lateral expansion which will postpone the sharp transition. In the subsequent study, the DIFs for TF-reinforced UHPC under compression and tension are considered in the numerical modeling of blast effects on UHPC elements.

4.5.2 Numerical study on ultra-high performance concrete elements under and after blast loads

Under blast loads, columns of UHPC containing steel fibers produced very high blast resistance by reducing the maximum displacement, enhancing the damage tolerance, and eliminating secondary blast fragments.

For the present UHPC material, field blast tests on columns with a span length of 2.5 m and a cross-section of 0.2 m $\times$ 0.2 m were carried out in recent study as shown in the "Blast resistance of ultra-high performance concrete columns" section. With a fixed standoff distance of 1.5 m, blast loads generated from 1 kg TNT equivalence to 35 kg TNT equivalence were designed in the tests; in addition, the effect of the axial load was also investigated. It is concluded that UHPC columns had high blast resistance and all of them showed flexural response and ductile failure while conventional HSC column showed brittle shear damage and concrete

spallation. The detailed information including the test setup, blast loads, column deflection-time history can be found in previous publication [26].

In this study, the numerical simulations on the UHPC columns under and after blast loads are carried out, and the analysis is performed in commercial hydro-code LS-DYNA. LS-DYNA provides a variety of concrete constitutive models including Mat_Pseudo_Tensor (MAT016), Mat_Geologic_Cap_Model (MAT025), Mat_Concrete_Damage (MAT072) (KCC model), Mat_Soil_Concrete (MAT078), Mat_Winfrith_Concrete (MAT084), Mat_Brittle_Damage (MAT096), Mat_Johnson_Holmquist_Concrete (MAT111), and Mat_CSCM_Concrete (MAT159). Each of these models has its own merits and limitations. In previous studies concerning concrete structural modeling and testing, a number of plasticity-based [12,27] and tensor-based [28,29] models have been developed and these concrete models typically have an unconfined compressive strength less than 40 MPa. Due to its unique properties, there is no constitutive model that is suitable in first-principle FE analysis for UHPC. In some pioneering numerical work, Mat_Concrete_Damage (MAT072) (KCC model) was adopted to simulate the UHPC under static [30] and dynamic loads [31], and the model features automatic parameter generation that is achieved by inputting concrete unconfined compression strength. KCC model also allows user-defined material strain rate curve for dynamic analysis. However, it shall be noted that KCC model was developed based on normal strength concrete with uniaxial compressive strength of 45.4 MPa, whereas the strength and postyielding behaviors of UHPC are significantly different. Therefore the parameters generated by KCC concrete model shall be modified/updated based on available UHPC tests before they can be applied to model the behaviors of UHPC elements.

Based on the available tests data, the modification on the KCC default parameters is presented. The modified parameters involve: f_t, which is the uniaxial tensile strength; b_1, which governs the compressive damage and softening behavior; and *wlz*, which governs the fracture energy of each element. Single element tests in accordance with mesh size used in the structural analysis was first simulated with the default parameters. The area under the postpeak portion of the stress−strain curves are then computed and compared to the experimental stress−strain curve. The calibration involves several iterations to equalize the area and the resultant was utilized as the input for the relevant material data.

Without losing generality, the TF fiber-reinforced UHPC and their components are discussed in the following study.

4.5.2.1 Single element test

The basic performances of the UHPC element built by KCC model are examined through single element simulations subjected to stress paths similar to that done in the material static tests. It is worth noting that the single element size shall be consistent with the subsequent structural analysis as element size is influential on the damage features of the KCC model.

Single element under unconfined uniaxial tensile tests was firstly performed and the results are shown in Fig. 4.34. As the uniaxial tension test data were not
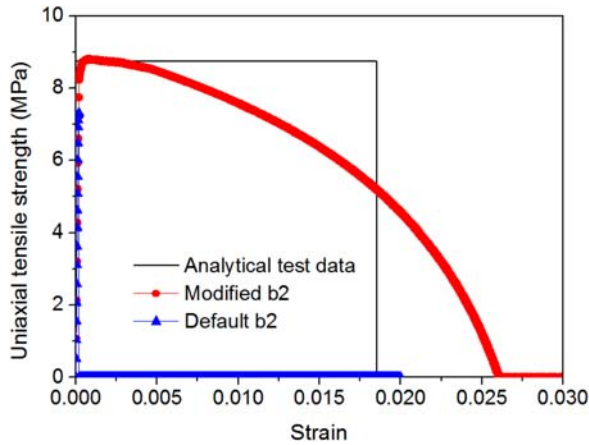
Figure 4.34 Single model under UUT test.
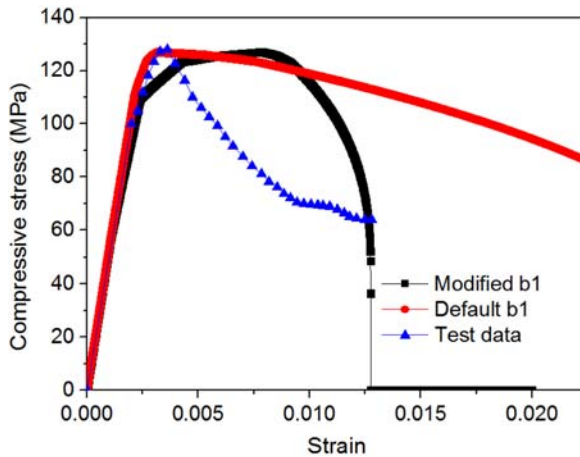
Figure 4.35 Single model under UCC test.

available, the model was calibrated with the analytical results from the inverse analysis on the FPBTs as shown in previous chapter. A value of b_2 is first chosen and boundary motion is prescribed on the single element to simulate uniaxial tension loading. This process is repeated by changing the value of b_2 and rerunning the analysis until Gf/h coincides with the area under the FE stress−strain curve, where Gf is the strain energy and h is the single element length. After updating the parameter b_2 from 1.35 to −5.5, a better curve fitting result on the material uniaxial tensile performance is obtained as shown in Fig. 4.34.

The stress−strain curves for single element unconfined uniaxial compression tests are shown in Fig. 4.35. It is noted that KCC model with default parameters showed excessive postyielding behavior. After updating the b_1 from 1.6 to 1.0,

Table 4.6 **Parameters in KCC model for UHPC**

Model parameter	Default value	Updated value
f_c	127 MPa	No update
f_t	7.6 MPa	8.8 MPa
B_1	1.6	1.0
B_2	1.35	-5.5
wlz	25.4 mm	6.00 mm

material softening behavior was better modeled despite some discrepancy being observed.

The parameters before and after update are shown in Table 4.6.

4.5.2.2 Model validation by field blast tests

Under high strain rate loading condition, the DIFs for both UHPC and steel tendon shall be considered in the material model. For UHPC materials, the tests data shown in Figs. 4.32 and 4.33 are adopted. For stirrup steel tendon with 300 MPa yielding strength in the field tests [26], the formulae proposed by Malvar [32] are used for generating the DIFs versus different strain rates. It is worth noting that Malvar's formulae are applicable for steel with yield strengths varying from 42 to 103 ksi (290−710 MPa); therefore they cannot be used for the longitudinal tendon with 1400 MPa yielding strength in the present tests. To the authors' best knowledge, there is no reliable DIF data for the high-strength steel tendon in the open literature; considering the rate dependence of steel reduces with the increase of the steel yielding strength, no dynamic increase factor is considered for the high-strength longitudinal tendon; and this assumption is deemed reasonable and conservative.

The numerical setup for the UHPC under field blast test is shown in Fig. 4.36: the column is constrained by the rigid steel clamps at both ends, and two circular steel plates with a diameter of 400 mm were placed at the column ends to simulate the air jack. Solid elements of 10 mm cube with a single integration point were used to model the concrete, and 10 mm beam elements were used for the reinforcement bars and the stirrups. Numerical convergence study showed that further decrease of the mesh size has a limited effect on the numerical results but leads to an excessive calculation time. Therefore a mesh size of 10 mm is used in the study. It is worth noting that the same element size shall be used in the single element calibration for damage characteristics of UHPC.

The axial load is applied using the LOAD_NODE_SET function. The air blast load is simulated by the empirical LOAD_BLAST. It is worth noting that such implementation is based on empirical blast load models described in TM5-855-1 US army handbook, and it is limited to the treatment of hemispherical TNT charges on the ground or spherical TNT charges in the air. However, in real cases, the explosives used are not always in these shapes, and it was found that the detonation point within the explosive and the ratio of length to diameter in cylinder explosives can
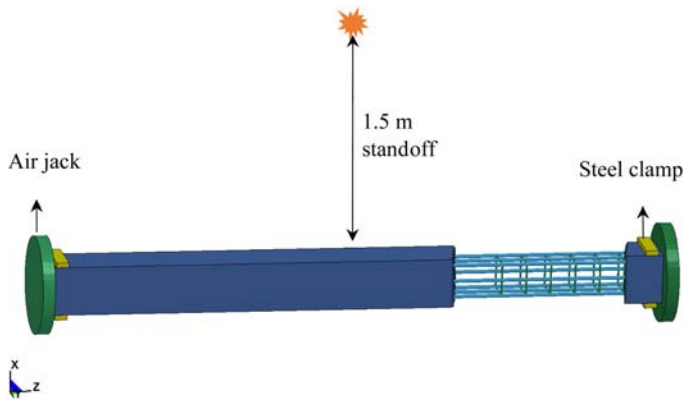
Figure 4.36 FE mode of UHPC column under blast loads.

significantly influence the blast effects. In this study, both the longitudinal and stirrup tendon are simulated by MAT_PIECEWISE_LINEAR_PLASTICITY (MAT24). This model allows the definition of arbitrary stress versus strain curve and arbitrary strain rate curve. Also, steel failure based on a plastic strain of 0.15 is defined.

The first model calibration is performed on UHPC column under 10 kg TNT equivalence detonation in which no damage was observed in the field test (see Fig. 4.37A and B shows the column after 50 ms from detonation, and the effective plastic strain contour shown in the plot represents the damage level in the UHPC material). The column suffers minimal damage around the mid-span while primary damage occurs at the column boundary due to the contact with the steel clamp and axial loading plate.

Mid-span deflection-time history is compared with the field measurement as shown in the Fig. 4.38. It is noted that the numerical model underestimates the peak mid-span deflection despite the residual deflection is captured with good accuracy (around 2 mm), and the predicted vibration frequency is higher than the field test measurement. There are two reasons accounting for these inaccurate predictions. Firstly, the material model for the UHPC is not complete; despite some calibrations being carried out based on the available uniaxial compression and flexural test data, the behavior of UHPC under direct tensile and confinement (triaxial tests) is not well established. In addition, the shear dilatancy is not understood in UHPC material, it is known that geomaterials including concrete subjected to deviatoric loading exhibit dilatancy, and this behavior is engendered by local failures due to distributed microcracking and formation of shear bands. However, in most UHPC material including the present formation, coarse aggregates are omitted and fibers are included throughout cementitious matrix which leads to difficulty in understanding the material dilatancy behavior. The other reason for the inaccurate peak deflection prediction and vibration frequency prediction is the boundary setup. In the field blast tests, the clamps are hand-fixed by the steel bolts. Under severe blast loading, the bolts fixture became loose, leading to a boundary setup more close to simply support, and this explains why the first negative peak from the numerical model is

(A)

Time =   0.05
Contours of effective plastic strain
min=-0.000329858, at elem# 127284
max=2, at elem# 7

Effective plastic strain

2.000e+00
1.800e+00
1.600e+00
1.400e+00
1.200e+00
9.998e-01
7.998e-01
5.998e-01
3.997e-01
1.997e-01
−3.299e-04

(B)
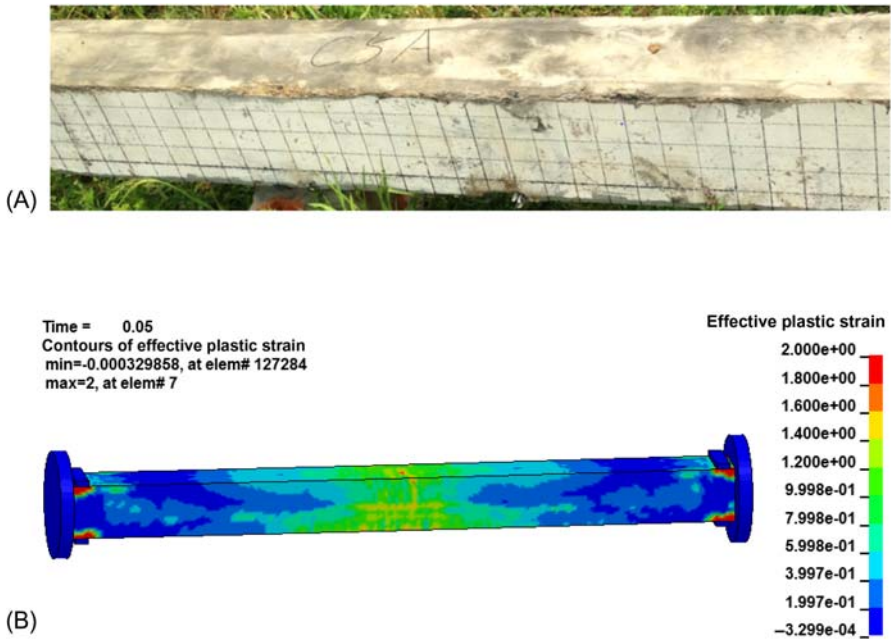
Figure 4.37 Column damage after 10 kg TNT equivalence detonation at 1.5 m standoff. (A) Field observation; (B) Numeircal result.
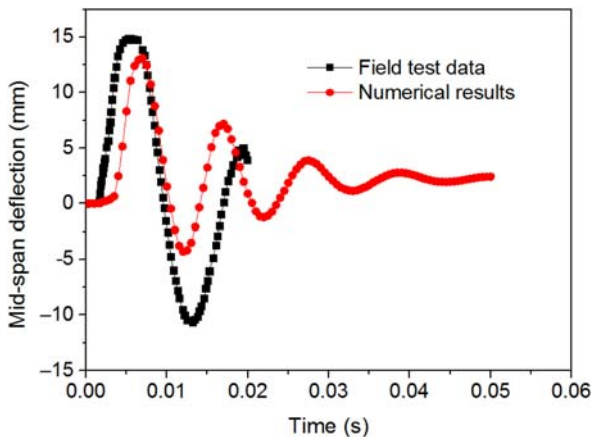
Figure 4.38 Mid-span deflection under 10 kg TNT detonation.

clearly smaller than the field record. Due to the incomplete knowledge in the UHPC material and difficulty in FE model to precisely reproduce the column boundary setup, the present model is deemed acceptable in predicting UHPC columns under blast loads.

(A)

(B)

Figure 4.39 Column damage after 35 kg TNT equivalence detonation at 1.5 m standoff.
(A) Field damage observation and (B) Numerical damage prediction.

The other model calibration is performed on UHPC column under 35 kg TNT equivalence detonation in which combined damage including major flexure and minor shear was observed in the field test (see Fig. 4.39A). It is observed that numerical model yields reasonable damage prediction on the UHPC column.

Due to the excessive blast loads from 35 kg TNT detonation at 1.5 m standoff distance, the LVDT at mid-span was knocked off in the test, and only the LVDT that located 490 mm away from the boundary survived after the detonation. Comparison to the column deflection at that location is shown in Fig. 4.40, it is noted that numerical results yielded reasonable accurate peak and residual deflection, and the discrepancies are deemed to be engendered by the same reasons explained in last case study.

4.5.2.3 Residual load-carrying capacity of ultra-high performance concrete column

To quantitatively study the structural damage after blast loads, damage criterion based on single-degree-of-freedom (SDOF) models and component deflections
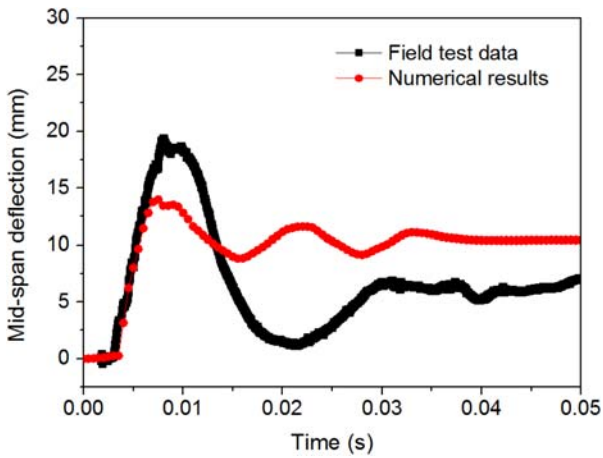
Figure 4.40 Column deflection under 35 kg TNT detonation.
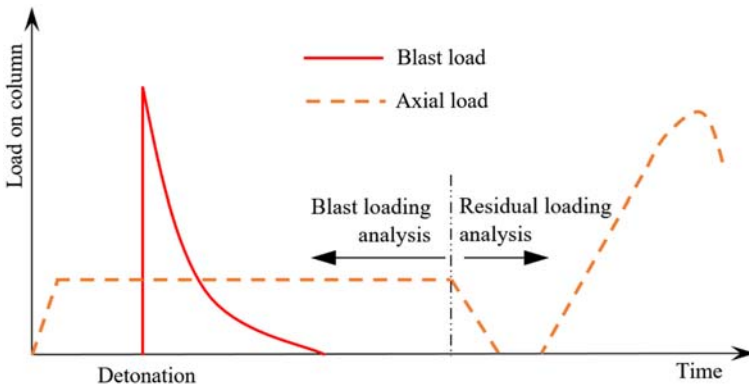
Figure 4.41 Schematic loading on UHPC column.

were widely adopted [33]. However, these criteria may not be accurate when describing structural damage under close-in blast loads in which structural component could suffer combined damage including concrete spallation, shear, and excessive flexure. To better describe the structural damage, a performance-based damage evaluation method was proposed by Shi et al. [7] in which column residual loading capacity was picked as the damage index.

The damage index D for postblast UHPC columns is defined as [7]:

$$D = (1 - P_{\text{residual}}/P_{\text{max}}) \times 100\% \tag{4.7}$$

Following this damage evaluation method, residual load-carrying capacity of the postblast column is simulated using the present numerical model. The loading scheme in the numerical analysis is shown schematically in Fig. 4.41.

UHPC columns in the postblast axial loading tests are shown in Fig. 4.42: the column that experienced 10 kg TNT equivalence in the field remains straight and intact until sudden failure occurs on the boundary elements, and the load-carrying capacity is 95% of the precinct column. For the column that underwent 35 kg TNT equivalence in the field tests, damage initiates at mid-span where flexure damage

(A)

(B)
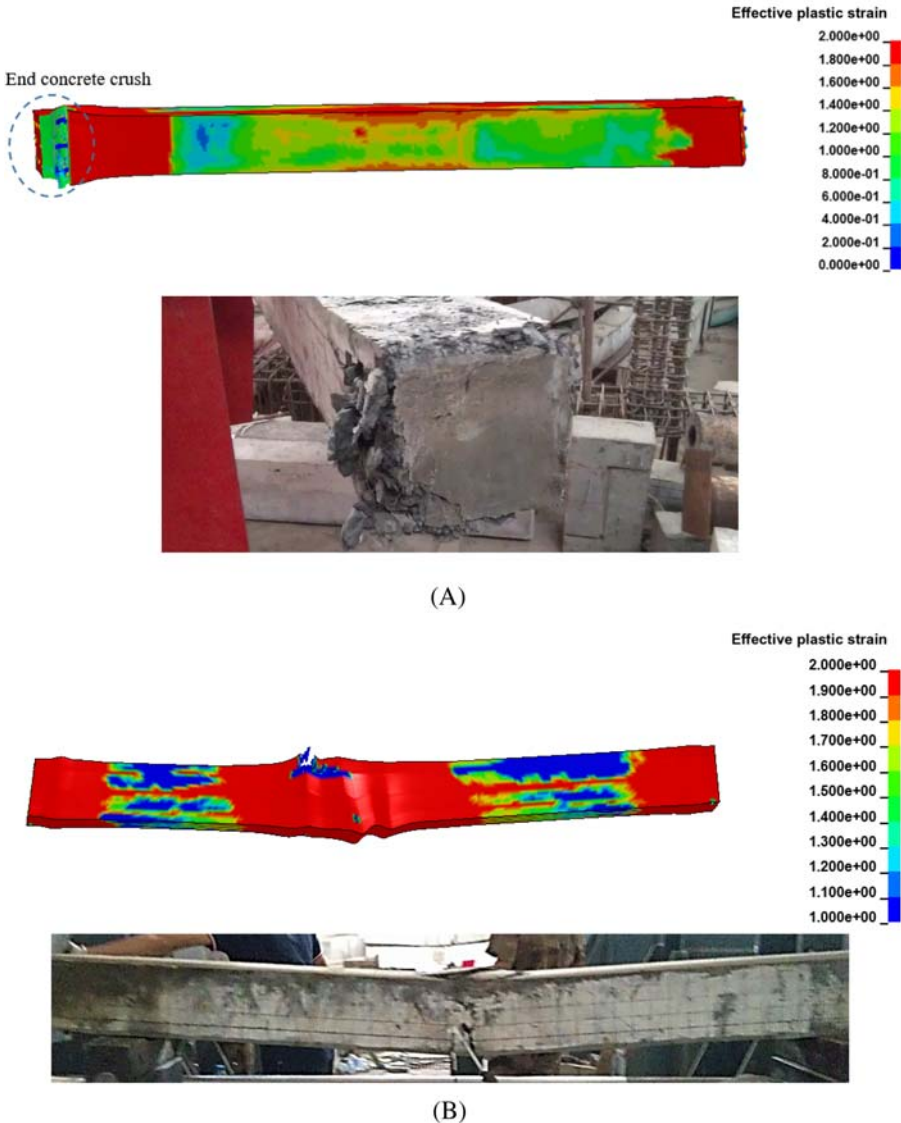
Figure 4.42 Column damage in residual loading tests. (A) Column that experienced 10 kg TNT equivalence explosion. (B) Column that experienced 35 kg TNT equivalence explosion.

was observed in the blast test, and the column preserved 76% of its original load-carrying capacity. Both the numerical results agree well with the test results reported in ref. [34].

4.5.2.4 Pressure−impulse diagram for the ultra-high performance concrete column

For a given blast loading scenario, pressure−impulse (P−I) diagrams are commonly used for quick evaluation of the structural damage. A P−I diagram is composed of a series of iso-damage curves defining different damage levels. In this study, column damage based on residual loading capacity is adopted and three damage levels, i.e., 20%, 40%, and 60% are considered. It should be mentioned that as it is difficult to obtain the exact critical damage for damage boundaries, the numerical data obtained in a range are used for the curve fitting. For example, all the data around $D = 40\%$ are used to get the curve for $D = 40\%$. The range of the data around the aimed damage degree is decided by trial and error, so that the derived pressure−impulse curves are the approximate upper bounds of the simulated data for the respective damage levels.

After examination of the fitted pressure−impulse curves, it is found that they can be expressed analytically as:

$$(P - P_0) \times (I - I_0) = \alpha(P_0 + I_0)^{\beta} \tag{4.8}$$

where P_0 is the pressure asymptote for individual damage level, and I_0 is the impulsive asymptote for individual damage level. α and β are constants, which are related to the column configuration and degree of damage.

For the UHPC columns tested in the field tests, the P−I diagrams are shown in Fig. 4.43, and the parameters α and β are shown in Table 4.7. It is worth noting
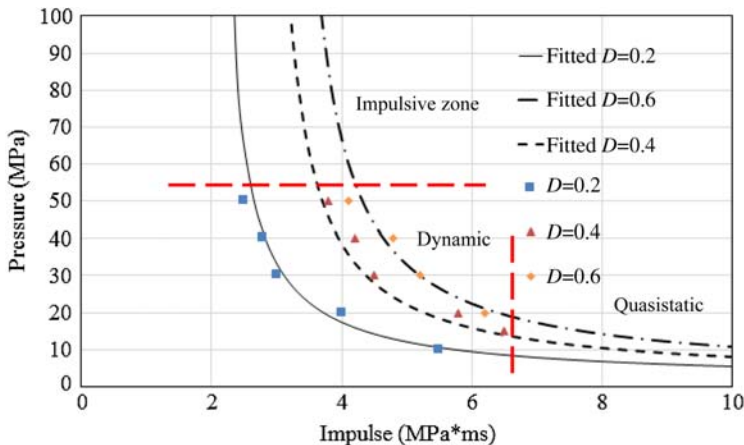
Figure 4.43 P−I diagram for the present UHPC column.

Table 4.7 **Value of the parameters α and β**

D	P_0 (MPa)	I_0 (MPa ms)	α	β
0.2	1.5	2	5.3	1.3
0.4	1.8	2.75	5.5	1.4
0.6	2.4	3.1	5.5	1.35
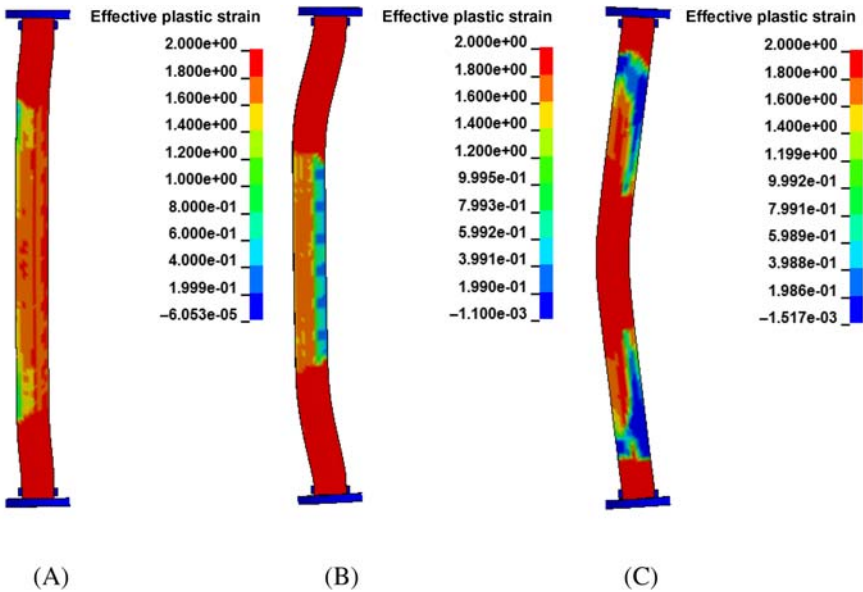
Figure 4.44 Damage modes of UHPC column. (A) impulsive load. (B) dynamic load, and (C) quasistatic load.

that it is extremely difficult to obtain the accurate damage level on the column, and therefore pressure and impulse combinations that yield damage around the predetermined damage level are taken into the curve fitting process.

Three distinctive zones can be characterized in the $P-I$ diagram, i.e., the impulsive zone, dynamic zone, and quasistatic zone. $P-I$ combination that lies in each of these zones induces different damage on the same column. In impulsive zone, column tends to fail under shear, and in the quasistatic zone, column is prone to flexural failure, and in the dynamic zone, a combined shear and flexure failure is commonly seen. These damage modes are shown in Fig. 4.44.

It is noted that damage constants α and β are almost independent of the damage level, and therefore averaged values of α and β from $D = 0.4$ are tested for the other two damage levels, and comparison is shown in Fig. 4.45 in which very minor difference is noted.
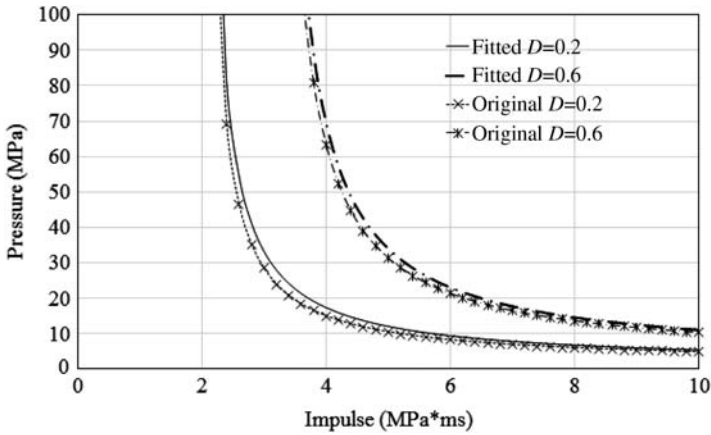
Figure 4.45 $P{-}I$ diagram with different damage constants.

Table 4.8 Range of the parameters studied

Cross-section side length (mm)	Height, H (mm)	Concrete strength fc′ (MPa)	Reinforcement (ratio ρ)
200	2500	127	0.040
250	3000	140	0.023
300	3500	160	0.010

4.5.3 Parametric studies on postblast loading capacity of ultra-high performance concrete columns

Based on the above numerical model, parametric studies on UHPC columns considering different concrete strengths, column sizes, and reinforcement configurations are carried out. Pressure−impulse diagrams representing three structural damage levels, i.e., 20%, 40%, and 60% are presented. In all columns, the preblast axial load application is assumed to be 20% of undamaged column loading capacity. Table 4.8 summarizes the parameters investigated in this study.

4.5.3.1 Column cross-section size

In order to investigate the effect of column size on the UHPC column pressure−impulse diagram, the pressure−impulse diagrams of three UHPC columns with different column cross-section sizes, i.e., 200, 250, and 300 mm are derived using the proposed method.

Table 4.9 shows the pressure asymptotes and impulsive asymptotes of the pressure−impulse curves, from which one can see that increasing the column size results in an increment on both the pressure and impulse asymptotes of the pressure−impulse curve. This is because increasing the column size will increase the mass, shear

Table 4.9 Effect of column cross-section size on pressure and impulsive asymptotes

Cross-section side length (mm)	D = 0.2		D = 0.4		D = 0.6	
	P_0 (MPa)	I_0 (MPa ms)	P_0 (MPa)	I_0 (MPa ms)	P_0 (MPa)	I_0 (MPa ms)
200	1.5	2	1.8	2.75	2.4	3.1
250	2.3	2.6	3	3.35	3.2	5
300	3	3	3.7	3.5	3.9	5.5

Table 4.10 Effect of concrete strength on pressure and impulsive asymptotes

Concrete strength (MPa)	D = 0.2		D = 0.4		D = 0.6	
	P_0 (MPa)	I_0 (MPa ms)	P_0 (MPa)	I_0 (MPa ms)	P_0 (MPa)	I_0 (MPa ms)
127	1.5	2	1.8	2.75	2.4	3.1
140	1.7	2.2	2.1	2.95	2.45	3.3
160	2	2.5	2.4	3.15	2.7	3.45

strength, and the bending strength of the column. Despite the blast loads acting on the column will also increase due to the increase in the loading surface, the increment of the blast resistance overweights the increment in the external loading.

4.5.3.2 Concrete strength

Columns with concrete strength of 127, 140, and 160 MPa are analyzed to generate the corresponding pressure−impulse diagrams. The pressure asymptotes and impulsive asymptotes of the pressure−impulse curves are given in Table 4.10. It shows that increasing the concrete strength will increase both the pressure and the impulsive asymptotes of the pressure−impulse curve. This can be explained by the fact that the concrete strength contributes to both the shear and bending strength of the column.

4.5.3.3 Longitudinal reinforcement ratio, ρ

The comparisons of the pressure asymptotes and impulsive asymptotes of pressure−impulse curves for UHPC columns with different longitudinal reinforcement ratios are given in Table 4.11. It indicates that with the increase of the longitudinal reinforcement ratio, the pressure asymptote of the pressure−impulse curve will increase, which is expected. It is also noted that the impulsive asymptote is less influenced by the reinforcement ratio. This is because increasing the longitudinal reinforcement ratio can significantly increase the bending strength of the UHPCC column, but has little contribution to the shear strength.

Table 4.11 Effect of reinforcement ratio on pressure and impulsive asymptotes

Reinforcement ratio	D = 0.2		D = 0.4		D = 0.6	
	P_0 (MPa)	I_0 (MPa ms)	P_0 (MPa)	I_0 (MPa ms)	P_0 (MPa)	I_0 (MPa ms)
0.040	1.5	2	1.8	2.75	2.4	3.1
0.023	1.2	2.1	1.5	2.8	2.1	2.9
0.010	1.0	2	1.3	2.65	2	3

Table 4.12 Effect of column height on pressure and impulsive asymptotes

Column height (mm)	D = 0.2		D = 0.4		D = 0.6	
	P_0 (MPa)	I_0 (MPa ms)	P_0 (MPa)	I_0 (MPa ms)	P_0 (MPa)	I_0 (MPa ms)
2500	1.5	2	1.8	2.75	2.4	3.1
3000	0.9	1.4	1.05	2.25	1.2	2.9
3500	0.7	1.0	0.95	2.05	1	2.6

4.5.3.4   Column height, H

The pressure−impulse diagrams for another three columns with different column heights are derived to examine the column height effect. Table 4.12 shows the pressure asymptotes and impulsive asymptotes of the pressure−impulse curves, from which one can see that both the pressure asymptote and impulsive asymptote decrease with the column height. This result is consistent with the fact that when the column is higher, the blast load on its surface increases and column is more prone to damage, especially when the blast load is quasistatic. However, it should be noted that this result is obtained based on the assumption of uniformly distributed blast loads on the column. If blast load is very close to column base or surface, concrete spall will be dominating the structural damage [35].

4.5.3.5   Analytical formulae to generate pressure−impulse diagram

Based on the numerical results, analytical formulae are developed to predict the pressure asymptotes and impulsive asymptotes for the pressure−impulse curves when the degree of damage equals 0.2, 0.4, and 0.6, which are the critical values between different damage levels defined in this study.

Using the least-squares fitting method, the pressure asymptote $P_0(D)$ and impulsive asymptote $I_0(D)$ are derived from numerical simulation data as a function of longitudinal reinforcement ratio ρ, concrete strength fc', column height H, column cross-section size W. They are

$$P_0(0.2) = -0.864H/1000 + 0.0157fc' + 15.4W/1000 + 16.39\rho - 2.1 \quad (4.9)$$

$$I_0(0.2) = -1.05H/1000 + 0.0149fc' + 10.3W/1000 - 1.15\rho + 0.716 \qquad (4.10)$$

$$P_0(0.4) = -0.979H/1000 + 0.0189fc' + 20.0W/1000 + 16.89\rho - 2.82 \qquad (4.11)$$

$$I_0(0.4) = -0.782H/1000 + 0.0119fc' + 8.18W/1000 + 2.52\rho + 1.47 \qquad (4.12)$$

$$P_0(0.6) = \exp(-1.06H/1000 + 0.00345fc' + 5.01W/1000 + 6.44\rho + 1.84) \quad (4.13)$$

$$I_0(0.6) = -0.551H/1000 + 0.0091fc' + 26.1W/1000 + 7.71\rho - 2.15 \qquad (4.14)$$

4.5.4   Conclusions

In this research, a numerical study to analyze the UHPC column damage under blast loads is conducted. The material model is calibrated with the available material tests data, and the structural model is calibrated with the field test data. The results show that KCC model, which is popular in use for prediction concrete damage under blast loads, shall be carefully modified before applying on ultra-high performance fiber RC. It is also worth pointing out that more extensive experimental studies on the material uniaxial and triaxial behavior shall be studied to complete the material model in numerical analysis.

Performance−based criteria for UHPC columns are defined based on the residual axial load-carrying capacity. The pressure−impulse diagrams for UHPC column tested in the field blast experiments are derived from the numerical simulations. Following the numerical analysis, analytical equations for the pressure−impulse diagrams for this particular column are proposed.

Parametric studies are carried out to study the effect of column height, cross-section size, concrete strength, and reinforcement ratio on the pressure−impulse diagram of the UHPC column. Based on the numerical results, analytical formulae to predict the pressure asymptotes and impulsive asymptotes for the pressure−impulse curves are derived.

4.6   Simplified finite element method analysis of ultra-high performance fiber-reinforced concrete columns under blast loads

For carrying out dynamic analysis of structural members against blast loads, there are two common approaches: SDOF method and FE method. Although SDOF method is computational efficient and easy to implement, it lacks accuracy. Comparatively, commercial FE software package typically requires implementation of a three-dimensional meshing with quite a number of degrees of freedom, and hence, it requires significant computational effort [36]. To achieve both accuracy

and computational efficiency, in Section 3.7, a fast-running 1D FE approach is presented to determine response of RC members subjected to blast loading and this method has been successfully performed on normal RC slabs [37]. The present research effort is intended to extend applicability of the previous research into the realm of the new advanced UHPC columns.

The first step is to experimentally obtain reliable load−displacement relationships of UHPC columns. The load−displacement relationships of both HSRC and UHPC columns are then incorporated into a computational efficient 1D FE model utilizing Timoshenko beam theory for further dynamic analysis. Finally, the real experimental testing data of HSRC and UHPC columns under blast loading are used to validate the 1D FE model for undertaking the dynamic analysis.

4.6.1 Static experimental program for testing flexural behavior of ultra-high performance fiber-reinforced concrete columns

The experimental program was designed to derive moment curvature relationships of UHPC and HSRC columns, and hence, it allowed investigation of their flexural behaviors with and without axial loading.

4.6.1.1 Test specimens

The same size specimens as those discussed in the "Blast resistance of ultra-high performance concrete columns" section are used in this study. The dimensions and reinforcement can be referred in Fig. 4.4.

4.6.1.2 Quasistatic bending test setup

As shown in Fig. 4.46, columns were tested under electromechanical servo hydraulic pressure testing machine by displacement control in 3000 kN capacity testing machine [38], with the standard procedures conforming to the Chinese standard GB/T 50081−2002 test method [39]. The 2500 mm long specimen was tested in flexure with a 2400 mm clear span. The column was loaded in three-point bending, with the point load located at mid-span as shown in Fig. 4.46A for the specimen without axial loading and Fig. 4.46B for the specimen with axial loading. The supported conditions were best described as simply supported with one edge under pure axial load. The simple support was designed to restrain the lateral movement. The axial loading was applied using hydraulic jacks located axially to the specimen.

Instrumentation for the flexural test is shown in Fig. 4.46A. LVDT with a stroke of 100 mm was installed to measure the central deflection during the test. Load was applied through displacement control at a speed of 1/1500 of the specimen span length (2400 mm) per minute. In addition strain gauges were installed to obtain strain profile along height direction of column, and hence, curvature of cross-section could be determined and then used in the "Structural response using a finite
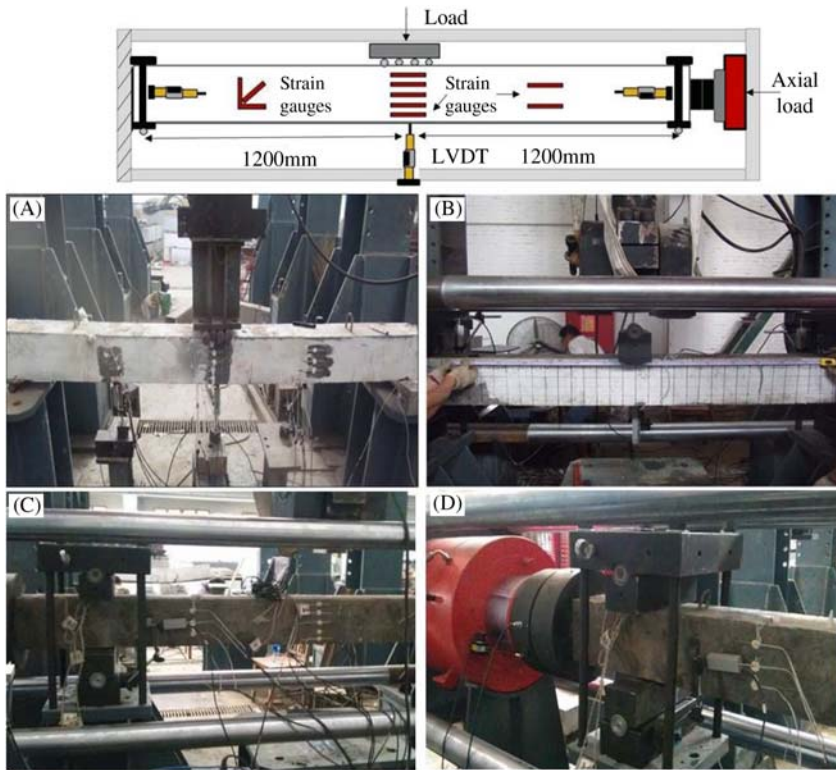
Figure 4.46 Test setup. (A) testing without axial loading. (B) testing with axial loading. (C) support of specimen, and (D) axial loading equipment.

difference model" section from the strain profile. The deformations occur when a cross-section is subjected to axial force and bending moment will be planar on elastic regime, and hence, it is customary to assume that the deformations remain planar after yielding has occurred. Therefore the curvature could be determined by using the strain profile results [40].

4.6.1.3 Static testing results

Due to the increased tensile capacity of cementitious composite matrix and crack-bridging behavior of fiber reinforcement, UHPC exhibits significant, sustained post-cracking flexural tensile capacity prior to crack localization, fiber pull-out, and loss of tensile capacity [41]. The current section will discuss the flexural behavior by analyzing the experimentally obtained load−displacement curves.

The force−displacement relationships describing nonlinear inelastic response of UHPFRC columns with and without axial loading are shown in Fig. 4.47. The bending response of UHPC columns is characterized by a pronounced nonlinear behavior due to multi-micro cracking and propagation of macrocracks at failure.
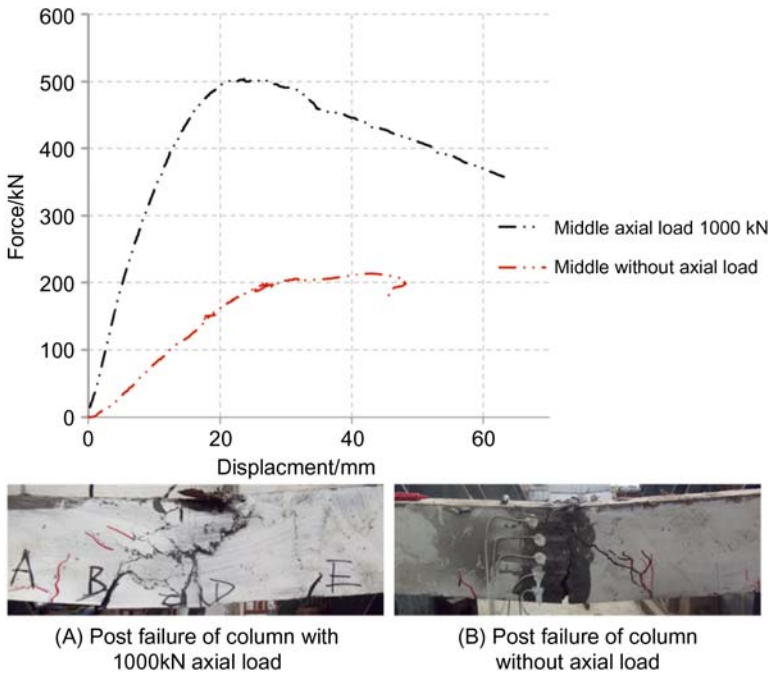
Figure 4.47 Force−displacement behaviors of UHPFRC columns, postfailure crack pattern of UHPFRC column (A) with 1000 kN axial load and (B) without axial load.

Two groups of UHPC columns were tested and each group contained three curves that represented the response at middle of the specimen. First of all, based on the deformation states of the critical section, the overall shape of load−displacement curves of UHPC columns is primarily characterized as four behavior regimes: (1) linear-elastic behavior; (2) nonlinear inelastic behavior before macrocrack opening; (3) nonlinear behavior with macrocrack opening, and increase in load-bearing capacity; (4) postpeak behavior. For regime (1), there was no significant crack pattern or surface appearance observed under the loading. Afterward, the nonlinear phase before macrocrack opening (regime 2) was characterized by the presence of multi-micro cracking. Beyond the level of deformations corresponding to macrocrack opening, deformations continued to increase with a very slight change in the force level, indicating that the crack opening allows a plastic like behavior to develop. Finally, regime 4 showed very ductile postpeak behavior after formation of a major crack, with fibers bridging the crack helping the column to sustain load as a crack opened and the fiber were slowly pulled out.

For mid-span load−deflection curves of columns with and without axial loads in Fig. 4.47 at loads below approximately 90 kN (for specimen without axial loads) and 150 kN (for specimen with axial load), the cracks on column were not visible. Significant visible cracking showed up when loads reached 150 and 250 kN for specimens without and with 1000 kN axial loads, respectively. Column with axial load

application sustained a peak load of 502 kN at a deflection of 24 mm before entering into a softening regime. Both column displayed ductile flexural behavior and no abrupt drop in the loading curve as observed, and this is primarily because of the steel fiber reinforcement. During the pseudo-static lateral loading process, strong bond between the steel fiber and concrete matrix effectively retards the crack initiation, and after the crack is initiated, over the cracks and the fibers pull-out and fracture consume large amount of energy and therefore enhance the structural ductility. The column with axial loading exhibited significantly additional load-carrying capacity after initial cracking. Two reasons can be accounted for this observation. Firstly, axial load application generated an initial compressive stress state within the column, and therefore a large lateral force was required to induce sufficient tensile strain on the column bottom surface and initiate concrete cracking. Secondly, the application of axial load changed boundary condition of the column in the current test setup, when the column was loaded with axial force, and the end restrains could generate compressive membrane effect when column lateral deformation was small, and this effect was beneficial for enhancing column lateral resistance.

From the postfailure cracking patterns, it was noticed that one obvious large crack existed for the column without axial loading, and the fiber played an important role in bridging two crack surfaces during the crack propagation. For column with axial load, more severe damage was observed at column mid-span, compressive membrane action effectively enhanced column flexural capacity and column sustained larger mid-span deflection during the lateral loading, due to the secondary P-Δ effect, the axial load generated additional bending moment on the column and thus more severe damage was observed.

The load−displacement behavior of HSRC column was observed to be significantly different from UHPC columns, and the summary of comparison is shown in Table 4.13. In general, under the same 1000 kN axial loading, UHPC specimen was able to develop approximately 13.4% higher load level over HSRC specimen. Both UHPC specimens with/without axial load displayed a very ductile behavior in Fig. 4.48 where the specimen continued to carry load up to displacement far greater than the displacement corresponding to peak load. For HSRC column, it showed a linear behavior up to cracking; however, soon after the maximum load (432 kN) was reached, a sudden drop in load occurred which was induced by brittle compressive failure of concrete in contact with the lateral load cell. The lateral load resistance then rebounded due to the contribution from the longitudinal reinforcement.

Table 4.13 **Summary of results from three-point bending tests**

Specimen	Axial loading (kN)	Peak load	Peak displacement (mm)	Crack width at failure (mm)
UHPFRC	0	231	28	7.8
UHPFRC	1000	502	21	2.79
HSRC	1000	432	4.5	21
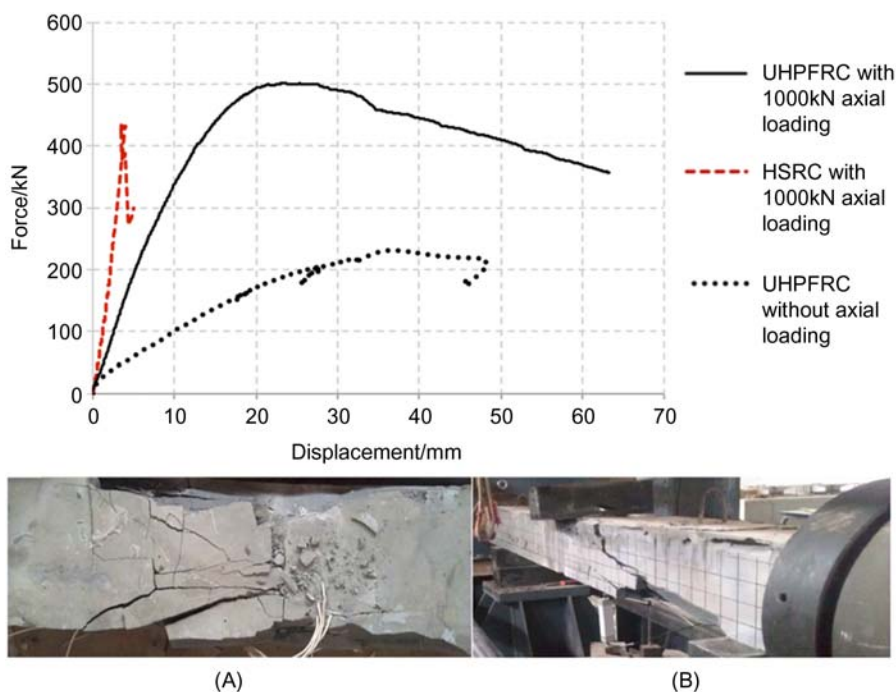
Figure 4.48 Force−displacement behaviors of HSRC and UHPC columns. (A) Top and (B) Side views of the postfailure crack pattern of the HSRC column.

Regarding the postfailure photographs of UHPC and HSRC columns, two distinct failure modes were observed in the tests. HSRC specimen displayed a very brittle behavior with a catastrophic failure after the peak load was reached. There was no warning before collapse and the specimen lost its integrity and broke into several pieces. However, UHPC specimens failed in a more ductile manner, in which diagonal cracks at the failure plane were developed, and due to the fiber bridging effect, no fragments were found on UHPC columns.

All the above static tests were conducted at the Structures Laboratory at TCU-UA (Tianjin Chengjian University−University of Adelaide) Joint Research Centre on Disaster Prevention and Mitigation. As a summary, the results from three-point bending tests of UHPC and HSRC columns are listed in Table 4.13.

4.6.2   Structural response using a finite difference model

Similar to finite difference model on UHPC slabs in Section 3.7.3, a simplified FE model has been developed to simulate dynamic response of UHPC and HSRC columns against blast loads in this section. The structural response along the column was modeled by considering the column to be comprised of a series of segment elements developed based on Timoshenko's beam theory. Timoshenko's beam theory

considers both shear deformation and bending deformation as well as rotational inertia, as shown in Eqs. (4.15) and (4.16) and this theory has been demonstrated useful for blast loading problem by previous researchers in the literature [42].

$$\frac{\partial M}{\partial x} - Q = -\rho_{m} I \frac{\partial^2 \rho}{\partial t^2} \tag{4.15}$$

$$\frac{\partial Q}{\partial x} + q + P_{a}\frac{\partial \beta}{\partial x} = \rho_{m} A I \frac{\partial^2 v}{\partial t^2} \tag{4.16}$$

where M is the applied bending moment, Q is the applied shear force, q is the distributed blast loading acting transverse to the beam, P_a is the column axial load, A is the cross-sectional area, I is the moment of inertia of the beam, ρ_m is the mass density of the beam, β is the rotation, and v is the transverse displacement. The FE method solves Eqs. (4.15) and (4.16) in their weak forms. The governing weak form equation can be expressed in matrix form as:

$$([K] + P_{a}[K_{G}])\{\delta\} + [M]\{\ddot{\delta}\} = \{P\} \tag{4.17}$$

where $[K]$ is the stiffness matrix, P_a is the axial load on column, $[K_G]$ is the geometric stiffness matrix, $[M]$ is the mass matrix, $\{\delta\}$ is the displacement vector, $\{\ddot{\delta}\}$ is the acceleration vector, and $\{P\}$ is the load vector. Eq. (4.17) is solved using Newmark method at each time interval. It should be noted that P_a is negative, thereby, reducing stiffness of column via $P - \Delta$ effect.

For solving displacement at each time step of Eq. (4.17), Newmark's method was implemented. By using this approach, the solution process is step by step in nature, and this implies that at each discrete time interval within the solution time domain, the stiffness matrix [K] and mass matrix [M] both in the global level needs to be specified first. To achieve a high accuracy while maintaining an appropriate level of calculation efficiency, a three-node isoperimetric beam element which maps into axis system (ξ) ranging from -1 to $+1$ having a quadratic shape functions is adopted. At each time integral, the mass and stiffness matrices are determined at the element level by using the principle of virtual work and then assembled them to the global level by undertaking the Gauss quadrature [36]. The stiffness matrix and mass matrix at the element level can be shown in Eqs. (4.18) and (4.19).

$$[K] = \int_{-1}^{1} [B]^{\mathrm{T}}[D][B]|J|\partial\xi \tag{4.18}$$

$$[M] = \int_{-1}^{1} [N_{m}]^{\mathrm{T}}[R_{m}][N_{m}]|J|\partial\xi \tag{4.19}$$

where

$$[R_{\mathrm{m}}] = \begin{bmatrix} \rho_{\mathrm{m}}A & 0 \\ 0 & \rho_{\mathrm{m}}I \end{bmatrix}$$

where $[B]$ is the strain displacement quadratic shape matrix, $[N_{\mathrm{m}}]$ is the quadratic shape matrix for the mass matrix, $|J|$ is the Jacobian determinant which is equal to half the length of the beam element, $[D]$ is the elasticity matrix, ρ_{m} is the density, A is the cross-sectional area, and I is the moment of inertia.

In order to determine the stiffness matrix at each time interval, the nonlinear curvature-dependent flexural rigidity and linear shear rigidity need to be known for calculating the elasticity matrix [D]. For determining flexural rigidity, moment curvature relationships are directly applied for loading phases. For unloading phases, it is assumed that the unloading curve has a slope same as the elastic region of moment curvature relationship. For shear rigidity, a linear shear stress–strain theory is applied as shown in Eq. (4.20). This linear shear strain relationship is considered sufficient because this study is dealing for the members with large span to depth ratio, where failure is usually governed by flexural damage.

$$Q = KA_w\sigma_{xz} = KA_wG\gamma_{xz} \tag{4.20}$$

where σ_{xz} is the shear stress, γ_{xz} is the shear strain, G is the shear stiffness, and A_w is the cross-sectional area. Timoshenko beam theory relies on the assumption that the distribution of shear stress over the cross-section is a constant. To account for the fact that the distribution of shear stress along the depth of the section is parabolic, Eq. (4.20) contains a correction factor, K, where $K = \pi^2/12$ for rectangular cross-sections [43].

It is necessary to determine the moment-curvature relationship to model the blast-induced structural response using a 1D FE model. As discussed in the previous section, many previous studies have not adequately characterized UHPC resistance model. In the present research, it is achieved toward derivations of resistant capability of UHPC by using static testing. By taking into account mechanics of concrete cracking and softening behavior, flexural response of UHPFRC columns can be derived. Therefore following up the next section, our research is devoted to simulating UHPC specimens under different blast experimental tests by incorporating the derived moment curvature relationships into the 1D FE model.

4.6.3 Blast experiments

The experimental results described later were obtained from previous sections in this chapter. The experimental results were used to calibrate and validate the 1D FE simulation code that aimed at stimulating large-scale UHPC and HSRC events and better designing protective structures.

The selected blast scenarios are from Table 4.1 and are provided in Table 4.14.

Table 4.14 Summary of results from three blast tests with various charge weights

Column name	Description	Axial force (kN)	Scaled distance	TNT equivalent charge weight
			$(\text{m kg}^{-1/3})$	(kg)
U1A	UHPC	0	1.5	1
H8B	HSRC	1000	0.75	8
U1B	UHPC	0	0.58	17.5
U1A	UHPC	0	0.46	35

4.6.4   Validation of the 1D finite element model

To evaluate the reliability of the 1D FE model, the results of FE model are compared with the measured displacement histories obtained from UHPC and HSRC columns under blast testing. There are two main input data that need to be defined first before running the program, the blast loading and structural material properties. As discussed previously, the approximation of pressure-time histories by using UFC 3-340-02 shown in the "Blast resistance of ultra-high performance concrete columns" section is within the acceptable tolerance range; thus in the FE simulation, the blast load applied to the surface as a time-dependent boundary load was considered as an idealized triangular pressure-time history for the analysis and solution procedures. When considering the material properties as input data, in order to obtain the moment curvature relationship from the experimental results, it is necessary to transform the load to moment and to determine the curvature of the model. Individual gauges were used until their readings became unreliable due to cracking in the underlying concrete. The process required comparing the pressure-time histories produced from the 1D FE model and the experimental results obtained from the LVDTs, which were attached to measure the central deflection of the column. In the modeling of support, because there is no special element used to relieve the uplift forces during rebound, for this reason, in the comparison process between modeling and test results, the deflection and reaction force time histories are only presented up to the first peak.

The mid-span displacement-time histories of UHPC and HSRC columns against blast loading from the experiment are presented in Figs. 4.49–4.51 together with the calibrated FE model simulation results. In the first phase of validation, the same UHPC columns against 1 and 17.5 kg charge weight were analyzed under different levels of axial loads. Generally, the FE model curve shows a good agreement with the experimental results up to the peak response. Although there was a slight discrepancy between the FE and experimental data at the peak displacements, the magnitude of the discrepancy was less than 10% for charge weight 1 kg and 20% for
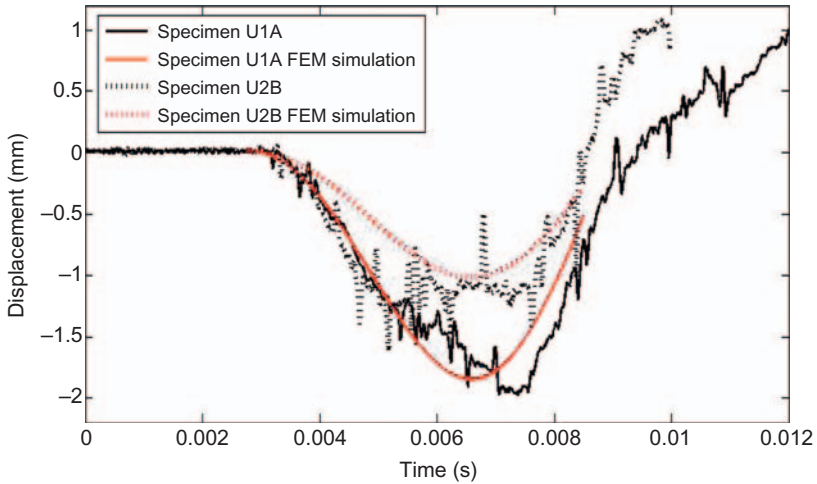
Figure 4.49 Deflection-time histories of experimental data and FE prediction of UHPFRC columns under 1 kg charge weight.
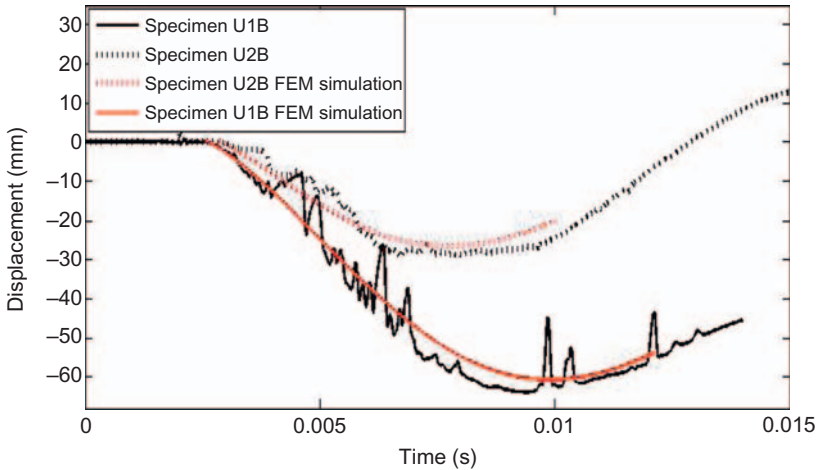
Figure 4.50 Deflection-time histories of experimental data and FE prediction of UHPFRC columns under 17.5 kg charge weight.

charge weight of 17.5 kg, respectively. Thus, it is believed that the results obtained from the 1D FE model are reasonably accurate. It was noted that there was a better agreement between the peak displacements calculated by the 1D FE model in the blast cases, which had the smaller level of axial load. Whereas the largest discrepancy between the peak displacements predicted by the FE model and the experimental data was as high as 17% in the case of a 1000 kN axial load and a transverse blast loading with a peak pressure of 29.01 MPa.
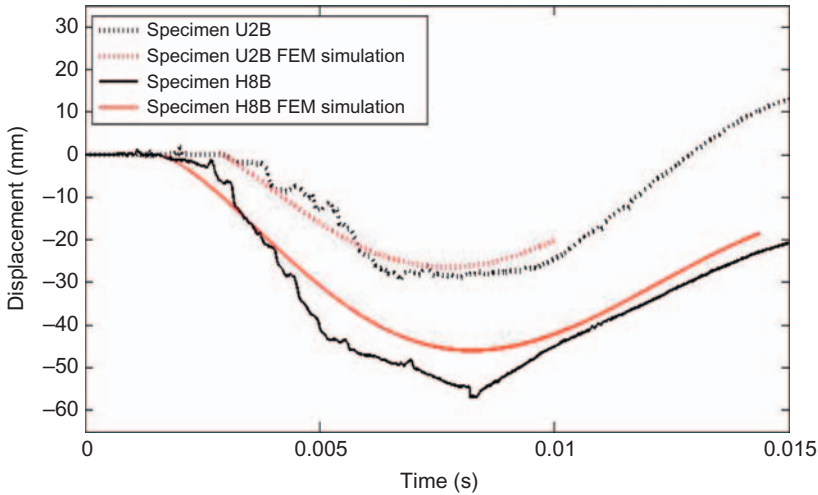
Figure 4.51 Deflection-time histories of experimental data and FE prediction of UHPC and HSRC columns under 17.5 kg charge weight.

Table 4.15 **Validation of the 1D FE model with experimental program**

Specimen	Charge weight (kg)	Axial load (KN)	Experimental maximum deflection (mm)	FEM modeling max deflection (mm)	Error %
U1A	1	0	1.96	1.84	5.1
U1B	17.5	0	63.74	59.2	7.1
U2A	1	1000	1.14	1.04	8.7
U2B	17.5	1000	29.27	24.3	17
H8B	17.5	1000	56.04	45.6	18.6

Fig. 4.51 shows further validation of the results obtained from UHPC and HSRC columns. It focuses on predicting both UHPC and HSRC columns under the same axial and blast loading condition. As shown in the figure, the period of oscillation predicted by the 1D FE model also has a good agreement with the period of the column determined from the experimental data for both UHPC and HSRC columns. However, the maximum deflection discrepancy between the FE simulation and the experimental results of HSRC column was 18.6%. This may be attributed to both the inability of the material model developed from the previous static tests in the 1D FE model to capture the hysteretic behavior of HSRC column and the idealization of the blast pressure; thereby it needs to highlight the potential underestimation of the results predicted by FE simulation for HSRC column in this section.

For comparison purposes, the peak mid-span displacements from both experimental and FE simulation are shown in Table 4.15. Generally, the FE simulation results follow the experimental results closely; the discrepancy of the results was less than 20% from

the measured peak displacements. The peak displacement calculated by the 1D FE model was slightly smaller. One possible reason is that the blast loading shapes on the structures has been simplified into a triangular shape based on the UFC 3-340-02, and hence, it underestimates shock velocity, pulse duration, and the time to the end of impulse.

4.6.5 Application of the 1D finite element model for rest of columns

During the experimental testing, due to the recording system malfunction, the displacement data were not recorded for the specimen under charge weights of 8 and 35 kg. With the FE model calibrated and validated against the experimental data in the previous section, it was then possible to predict their response using the validated FE model for different charge weights. The previous experimental peak overpressure, impulse, and overpressure duration were used as the input data and the effects of adding external axial loading can be further studied.

Figs. 4.52 and 4.53 present the deflections of UHPC and HSRC specimens generated under charge weights 8 kg and 35 kg loading, respectively. It is obvious that the curves are quite similar to the previously discussed responses where the data of HSRC and UHPC columns without axial loading have similar displacement magnitudes, and UHPC column with 1000 kN axial loading has the smallest magnitude of displacement.

Comparing with the average deflections of U1B and U2B in Fig. 4.52, the average displacement of U2B is approximately 57% less than that for the U1B as axial loads can effectively reduce the mid-span deflections. Comparing the results of U2B with H1A in Fig. 4.53, it is obvious that with the steel fiber and magnitude of the axial loading, it dramatically increases the blast resistance. Also, U2B specimen
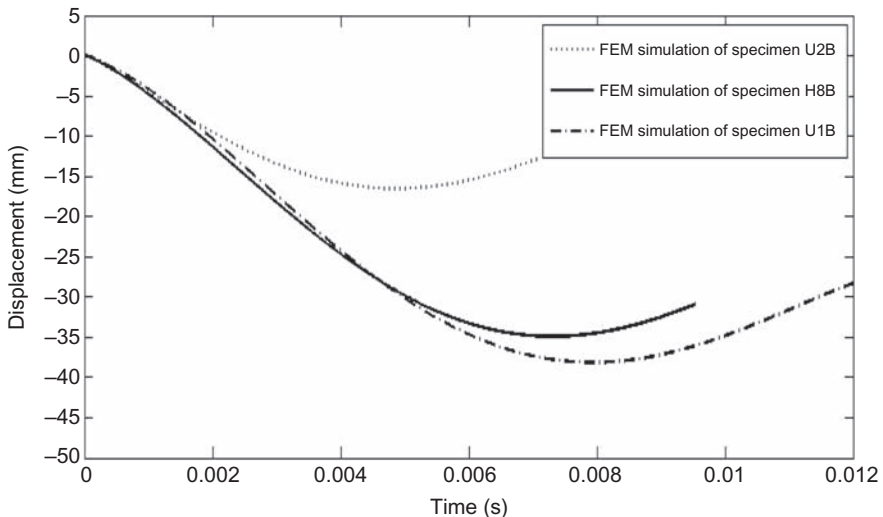
Figure 4.52 Deflection-time histories of FEM prediction of UHPC and HSRC columns under 8 kg charge weight.
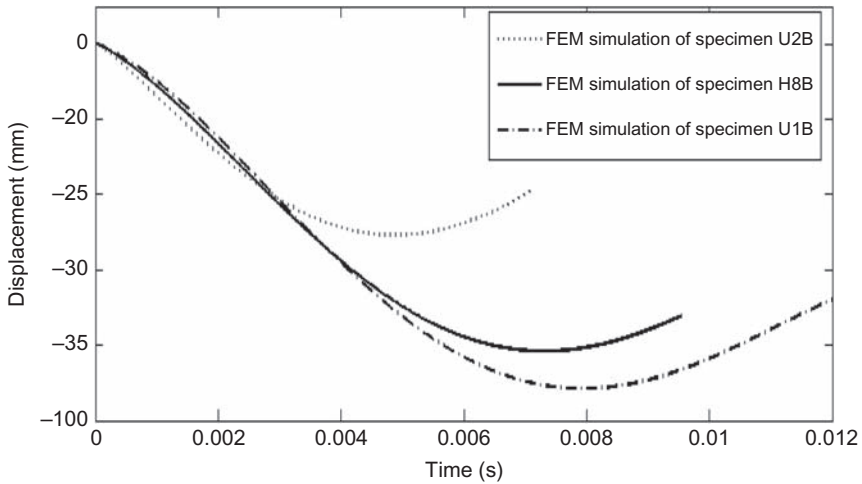
Figure 4.53 Deflection-time histories of FEM prediction of UHPFRC and HSRC columns under 35 kg charge weight.

performs extremely well in the 35 kg blast, in which it has the smallest deflection magnitude (48 mm). HSRC column H8B with 1000 kN axial loading and data of UHPC column U2B without axial loading display a similar peak displacement of 81 mm and 87 mm, respectively.

4.6.6   Conclusions

This study characterizes response of HSRC and UHPC columns through both static and dynamic analysis. The resistance deflection curves of UHPC columns with and without axial loads have been studied by using a quasistatic bending test, and the dynamic response of UHPC columns under blast loads has been simulated using the 1D FE model. The study leads to the following conclusions:

- Static testing results show that addition of axial loading produces enhancement of flexural properties of UHPC columns.
- The computational efficient 1D FE model was validated by simulating dynamic response of columns against blasts and the simulated results had a good agreement with the experiment data.
- The validated 1D FE model developed based on Timoshenko's beam theory could be used to predict the behavior of UHPC columns under blast loads.

References

[1] M. Sasani, Response of a reinforced concrete infilled-frame structure to removal of two adjacent columns, Eng. Struct. 30 (2008) 2478−2491.
[2] S.C. Woodson, J.T. Baylot, Structural collapse: quarter-scale model experiments, DTIC Document, 1999.

[3] J. Li, H. Hao, A simplified numerical method for blast induced structural response analysis, Int. J. Protect. Struct. 5 (2014) 323−348.

[4] Y. Shi, Z.-X. Li, H. Hao, A new method for progressive collapse analysis of RC frames under blast loading, Eng. Struct. 32 (2010) 1691−1703.

[5] H. Hao, Predictions of structural response to dynamic loads of different loading rates, Int. J. Protect. Struct. 6 (2015) 585−606.

[6] H. Hao, Y. Hao, J. Li, W. Chen, Review of the current practices in blast-resistant analysis and design of concrete structures, Adv. Struct. Eng. 19 (2016) 1193−1223.

[7] Y. Shi, H. Hao, Z.-X. Li, Numerical derivation of pressure−impulse diagrams for prediction of RC column damage to blast loads, Int. J. Impact Eng. 35 (2008) 1213−1227.

[8] X. Bao, B. Li, Residual strength of blast damaged reinforced concrete columns, Int. J. Impact Eng. 37 (2010) 295−308.

[9] B. Li, A. Nair, Q. Kai, Residual axial capacity of reinforced concrete columns with simulated blast damage, J. Perform. Construct. Facil. 26 (2012) 287−299.

[10] K.-C. Wu, B. Li, K.-C. Tsai, Residual axial compression capacity of localized blast-damaged RC columns, Int. J. Impact Eng. 38 (2011) 29−40.

[11] C. Roller, C. Mayrhofer, W. Riedel, K. Thoma, Residual load capacity of exposed and hardened concrete columns under explosion loads, Eng. Struct. 55 (2013) 66−72.

[12] L.E. Schwer, Y.D. Murray, A three-invariant smooth cap model with mixed hardening, Int. J. Numer. Anal. Method. Geomech. 18 (1994) 657−688.

[13] M.M. Hosinieh, H. Aoude, W.D. Cook, D. Mitchell, Behavior of ultra-high performance fiber reinforced concrete columns under pure axial loading, Eng. Struct. 99 (2015) 388−401.

[14] S. Sugano, H. Kimura, K. Shirai, Study of new RC structures using ultra-high-strength fiber-reinforced concrete (UFC)-the challenge of applying 200MPa UFC to earthquake resistant building structures, J. Adv. Concr. Technol. 5 (2007) 133−147.

[15] B. Aarup, L.R. Jensen, H.-C. ApS, P. Ellegaard, Slender CRC columns, Nordic Concr. Res. 34 (2005) 80−97.

[16] W. Chen, H. Hao, S. Chen, Numerical analysis of prestressed reinforced concrete beam subjected to blast loading, Mater. Des. 65 (2015) 662−674.

[17] T. Kanakubo, Tensile characteristics evaluation method for ductile fiber-reinforced cementitious composites, J. Adv. Concr. Technol. 4 (2006) 3−17.

[18] J.E. Crawford, J.M. Magallanes, A. Whittaker, T.R. Brewer, Modeling of pristine and damaged UHPFRC materials for use in performing blast and projectile penetration analyses, 4th International Conference on Protective Structures (ICPS4), Beijing, China, Oct 2016.

[19] R. Chen, Y. Liu, X. Guo, K. Xia, F. Lu, Dynamic tensile properties of steel fiber reinforced concrete, Dynamic Behavior of Materials, vol. 1, Springer, New York, 2011, pp. 37−42.

[20] A.M. Weidner, Dynamic properties of concrete and fiber reinforced concrete at room and elevated temperatures, The University of Utah, Salt Lake City, 2013.

[21] S. Millard, T. Molyneaux, S. Barnett, X. Gao, Dynamic enhancement of blast-resistant ultra high performance fibre-reinforced concrete under flexural and shear loading, Int. J. Impact Eng. 37 (2010) 405−413.

[22] Y. Su, J. Li, C. Wu, P. Wu, Z.-X. Li, Influences of nano-particles on dynamic strength of ultra-high performance concrete, Compos. Part B Eng. 91 (2016) 595−609.

[23] Y. Su, J. Li, C. Wu, P. Wu, Z.-X. Li, Effects of steel fibres on dynamic strength of UHPC, Construct. Build. Mater. 114 (2016) 708−718.

[24] L.J. Malvar, J.E. Crawford, Dynamic increase factors for concrete, DTIC Document, 1998.

[25] L.J. Malvar, C.A. Ross, Review of strain rate effects for concrete in tension, Mater. J. 95 (1998) 735−739.

[26] J. Xu, C. Wu, H. Xiang, Y. Su, Z.-X. Li, Q. Fang, H. Hao, Z. Liu, Y. Zhang, J. Li, Behaviour of ultra high performance fibre reinforced concrete columns subjected to blast loading, Eng. Struct. 118 (2016) 97−107.

[27] L.J. Malvar, J.E. Crawford, J.W. Wesevich, D. Simons, A plasticity concrete material model for DYNA3D, Int. J. Impact Eng. 19 (1997) 847−873.

[28] Z.P. Bažant, F.C. Caner, I. Carol, M.D. Adley, S.A. Akers, Microplane model M4 for concrete. I: formulation with work-conjugate deviatoric stress, J. Eng. Mech. 126 (2000) 944−953.

[29] G. Cusatis, Z.P. Bažant, L. Cedolin, Confinement-shear lattice CSL model for fracture propagation in concrete, Comput. Method. Appl. Mech. Eng. 195 (2006) 7154−7171.

[30] J. Magallanes, Y. Wu, J. Crawford, K. Morrill, Feasibility studies of a plasticity-based constitutive model for ultra high performance fiber-reinforced concrete, MABS, 21, 3−8.

[31] F. Zhang, C. Wu, X.-L. Zhao, A. Heidarpour, Z. Li, Experimental and numerical study of blast resistance of square CFDST columns with steel-fibre reinforced concrete, Eng. Struct. 149 (2016) 50−63.

[32] L.J. Malvar, Review of static and dynamic properties of steel reinforcing bars, Mater. J. 95 (1998) 609−616.

[33] G. Mays, P.D. Smith, Blast effects on buildings: design of buildings to optimize resistance to blast loading, Thomas Telford, London, 1995.

[34] J. Li, C. Wu, H. Hao, Z. Liu, Post-blast capacity of ultra-high performance concrete columns, Eng. Struct. 134 (2017) 289−302.

[35] J. Li, H. Hao, Numerical study of concrete spall damage to blast loads, Int. J. Impact Eng. 68 (2014) 41−55.

[36] J. Dragos, P. Visintin, C. Wu, D. Oehlers, A numerically efficient finite element analysis of reinforced concrete members subjected to blasts, Int. J. Protect. Struct. 5 (2014) 65−82.

[37] C. Wu, D. Oehlers, M. Rebentrost, J. Leach, A. Whittaker, Blast testing of ultra-high performance fibre and FRP-retrofitted concrete slabs, Eng. Struct. 31 (2009) 2060−2069.

[38] J. Xu, C. Wu, Experimental study on blast resistance of ultra high performance fiber reinforced concrete columns, Cement Concr. Compos. (2016), under review.

[39] J.E. Crawford, L.J. Malvar, K.B. Morrill, J.M. Ferritto, Composite retrofits to increase the blast resistance of reinforced concrete buildings, in: Proceedings of the Tenth International Symposium on Interaction of the Effects of Munitions with Structures, 1−13 May, San Diego, CA, 2001.

[40] I.H. Yang, C. Joh, B.-S. Kim, Structural behavior of ultra high performance concrete beams subjected to bending, Eng. Struct. 32 (2010) 3478−3487.

[41] B.A. Graybeal, Flexural behavior of an ultrahigh-performance concrete I-girder, J. Bridge Eng. © ASCE 13 (2008) 602−610.

[42] C. Wu, H. Sheikh, A finite element modelling to investigate the mitigation of blast effects on reinforced concrete panel using foam cladding, Int. J. Impact Eng. 55 (2013) 24−33.

[43] T. Krauthammer, A. Assadi-Lamouki, H. Shanaa, Analysis of impulsively loaded reinforced concrete structural elements—I. Theory, Comput. Struct. 48 (1993) 851−860.

Ultra-high performance concrete-filled steel tubular columns

5

5.1 Introduction

In the past decades, thousands of lives have been lost all over the world due to terrorist activities. Much research has been carried out, aiming to improve the reliability of vulnerable structures so as to reduce the number of human casualties. A number of studies have discussed retrofitting techniques to protect existing structures [1−3], while others have proposed innovative structures and materials to construct new buildings [4−7]. In recent years, new steel-concrete composite members, known as concrete-filled steel tubes (CFSTs) and concrete-filled double-skin steel tubes (CFDSTs), have gained increasingly more interests in the construction industry due to their attractive properties such as ease of construction, light weight, high strength, and good seismic resistance.

A CFST column consists of a thin-walled hollow steel tube filled with concrete. The tube can effectively restrain the lateral expansion of concrete, resulting in a confining pressure which can greatly enhance the strength and ductility of concrete. The concrete filler, in turn, improves the geometric stability of steel tube so that the local buckling of steel is postponed, if not prevented at all. In recent years, CFST columns have been more and more commonly used in the construction industry due to their attractive properties such as high strength, advanced plasticity, fatigue resistance, high temperature resistance, and impact resistance [8,9]. A number of studies have showed that the overall axial load capacity of a CFST column is considerably greater than the sum of the individual components acting independently, and the ductility of a CFST column under axial load and flexural load can also be significantly enhanced [10−12].

Apart from studies on the axial behaviors of CFST columns, the knowledge of their structural behaviors under lateral impact and blast loads is quite limited. Wang et al. [13] experimentally studied the behaviors of CFST columns subjected to lateral impact loads. It was observed that there were generally two types of failure modes: specimens with large constraining factors (i.e., area of steel/area of concrete) showed behavior in a ductile manner while those specimens with low constraining factors were found to behave in a brittle manner. Deng et al. [14] studied the use of posttensioned and steel-fiber reinforced CFST columns to alleviate lateral impact loads. It was reported that prestressing strands and steel-fiber concrete-filled steel tube column delayed concrete tension cracks, hence effectively reducing the column deflection under transverse impact load.

Different to CFST, a CFDST member is made from two concentrically placed steel skins filled with concrete in between, and it utilizes the advantages of both steel and concrete. Under axial compression, due to the different Poisson's ratio of

steel and concrete, the concrete of a CFDST column is normally in a triaxially confined state and consequently the confining pressures can effectively enhance the strength and the ductility of the concrete which is known as the confinement effect. Wei et al. [10] reported the investigation on 26 circular CFDST stub columns under axial compression and it was found that the axial load capacity of a CFDST stub column was usually 10%−30% larger than the simply superposed capacity of the steel tubes and core concrete when acting alone. Following references [15,16], the failure mode of CFDST stub columns under axial compression was also investigated: the most dominant failure mode was found to be local buckling of the outer steel tube associated with concrete shear failure; also, the outer diameter to steel-tube-thickness ratio had the most significant influence on the failure mode. Analytical models have also been derived, based on a large number of experiments, to predict the behavior of CFDST members under axial compression and these have showed good agreement with the test results [17−19].

However, studies have also been carried out to examine the performance of CFDST members under transverse cyclic load [20,21]. In the experiments, different cross-sectional geometries were compared and it was found that the energy-absorbing ability of the CFDST columns with circular cross-sections was superior to those of the specimens with square cross-sections. From the test results, an analytical model was also developed to predict the response of CFDST beam-columns under combined axial load and cyclically increasing flexural load. Efforts were also put into studying the tensile behavior [22,23], torsional behavior [24], and fire resistance of CFDST columns [25]. Experiments and numerical analyses were also carried out to explore the behavior of tapered CFDST members under concentric and eccentric axial compression [26,27].

All of the previously mentioned studies indicate that CFDST members inherit the advantages of both steel and concrete and that they exhibit very ductile behavior under axial compressive and transverse loadings. However, most existing studies are strictly limited to static loading only, thus the analytical models developed cannot be applied to evaluate situations where impact and blast loads are introduced. Therefore there is a need to evaluate the performance of CFDST members subjected to impact and blast loads. Furthermore, as CFDST members have been more and more commonly adopted in the field of civil engineering applications, large axial bearing capacity is required. Therefore by replacing normal strength concrete by UHPC in CFDST members, the cross-sectional area as well as the self-weight of the structural members can be further reduced, owing to its much higher strength and ductility. In addition, for UHPC mixed with fibers, crushing and spalling damage of the concrete can be well restrained thus can further delay the buckling of the steel tubes. Moreover, CFDST columns are becoming more and more commonly seen in high rise buildings and bridge piers where large axial capacity is required; therefore, by replacing the normal strength concrete filler by UHPC, the axial load capacity and ductility can be further enhanced while the cross-sectional area and the self-weight of the column can be reduced. Additionally, for UHPC mixed with fibers, crushing and spalling damage of the concrete can also be restrained; consequently, the buckling of the steel tubes can be delayed or prevented.

There are three types of how blast loading could be applied to a structure in terms of the distance from the explosives to the surface of the structure, i.e., near-field blast (e.g., [28,29]), close-range blast (e.g., [1,3]), and direct contact (e.g., [30,31]). This study presents an experimental investigation on ultra-high performance concrete-filled double-skin tubes (UHPCFDST) subjected to close-range blast loading.

In this chapter, firstly the experimental study is conducted on CFST and CFDST columns under blast loading. The blast experiment aims to examine the blast resistance of CFST and CFDST specimens, including square cross-section and circular cross-section. The parameters that are investigated during the blast experiment include cross-sectional geometry, steel tube thickness, explosive charge weight, and magnitude of axial load. After the experiment, postdamage UHPC-filled tube specimens are transported back to the laboratory for residual axial load-carrying capacity tests. The proposed CFDST columns are able to retain more than 60% of its axial load-carrying capacity even after being subjected to close-range explosion.

As blast experiments are often costly and associated with potential safety concerns, numerical tools have been adopted by increasingly more researchers. Therefore numerical approaches in modeling the dynamic behavior of CFST and CFDST columns under blast loading are presented. The numerical models are validated against the results of the blast experiment and good agreement is achieved. Parametric studies on the effect of column dimensions and material properties are also discussed through intensive numerical simulations.

Finally, a numerical method to generate pressure−impulse diagrams for CFDST columns is proposed which uses a damage criterion involving the residual axial load-carrying capacity. Based on the numerical method, pressure−impulse diagrams for different column configurations are derived and analytical expressions of deriving pressure−impulse diagrams for CFDST columns are also developed through regression analysis.

5.2 Experimental study of concrete-filled steel tube/concrete-filled double-skin steel tube columns against close-range blasts

5.2.1 Experimental program of concrete-filled steel tube columns

5.2.1.1 Specimen preparation

All CFST specimens were made 2500 mm long and the steel tubes were either 2.8 or 3.8 mm thick. Prior to concrete pouring, one steel plate (400 mm × 500 mm × 16 mm) was firstly welded to one end of the empty steel tube. The tube was then set up straight followed by pouring concrete from the top. For consolidation purposes, concrete vibrator was also used. Each specimen was cured at room temperature for 28 days. At last, each specimen was leveled and polished before welding the other steel plate to the end.

Table 5.1 **Material experimental parameters of steel tube**

Geometry	Thickness (mm)	Yield strength (MPa)	Tensile strength (MPa)	Elongation (%)	Elasticity modulus (GPa)
Circular	2.8	311.5	414.0	22.1	203.6
Square	2.8	358.1	437.7	21.3	202.6
Circular	3.8	471.9	535.4	25.4	226.3
Square	3.8	484.7	535.2	20.8	215.9

C40 grade concrete was used to manufacture all specimens. Compressive tests were carried out on a number of 100 mm × 100 mm × 100 mm cubic specimens to determine the compressive strength. The average cubic compressive strength obtained from the tests was 47.4 MPa with the elastic modulus being 34 GPa and the concrete tensile strength being 2.6 MPa.

The strengths of steel tubes were determined by direct tensile test using a high-capacity hydraulic machine. The average strengths of the steel tubes obtained from the direct tensile test are listed in Table 5.1.

5.2.1.2 Three-point bending test

Three-point bending tests were carried out to investigate the static behaviors of CFST columns subjected to combined axial and lateral loads. As shown in Fig. 5.1, the test specimen was simply supported during the test.

In total, three CFST columns were tested including one square CFST column and two circular CFST columns. Table 5.2 summarizes the experimental results of three-point bending tests and their corresponding theoretical values calculated from theoretical equations as given in the following [32]:

If $N/A_{sc} \geq 0.2 \left[1 - \left(\frac{V}{V_0} \right)^2 \right]^{0.5} f_{sc}$, then

$$\left(\frac{N}{N_0} + \frac{M}{1.07M_0} \right)^{1.4} + \left(\frac{V}{V_0} \right)^2 \leq 1 \tag{5.1a}$$

Otherwise,

$$\left(\frac{N}{1.4N_0} + \frac{M}{M_0} \right)^{1.4} + \left(\frac{V}{V_0} \right)^2 \leq 1 \tag{5.1b}$$

where N is the applied axial load and N_0 is the designed axial load capacity:

$$N_0 = A_{sc}f_{sc} \quad \text{and} \quad f_{sc} = \left(1.212 + B\xi + C\xi^2 \right) f_{ck} \tag{5.2}$$
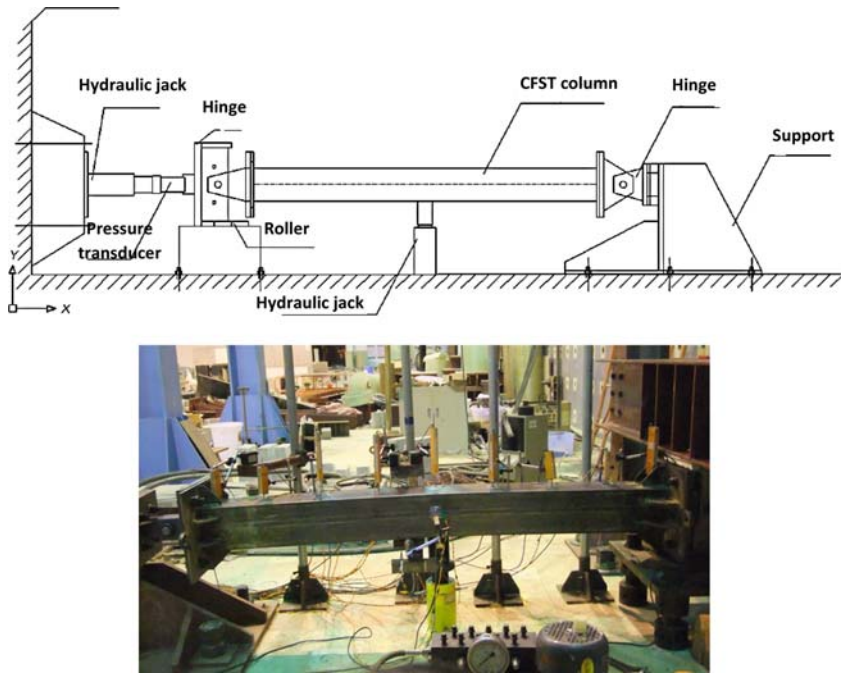
Figure 5.1 Experimental setup for three-point bending test.

Table 5.2 Results of the three-point bending tests

Column no.	Cross-section	Applied axial load (kN)	Lateral load (kN)		Error (%)
			Test	**Theoretical**	
TS1	Square (200 mm × 200 mm)	514	168	181	7.7
TC1	Circular (194 mm diameter)	414	95	96	0
TC2	Circular (194 mm diameter)	0	88	109	19.2

in which

$$B = \begin{cases} 0.1759f_y/235 + 0.974 & \text{(circular cross-section)} \\ 0.131f_y/235 + 0.723 & \text{(square cross-section)} \end{cases}$$

$$C = \begin{cases} -0.1038f_{ck}/20 + 0.0309 & \text{(circular cross-section)} \\ -0.07f_{ck}/20 + 0.0262 & \text{(square cross-section)} \end{cases}$$

M is the applied moment and M_0 is the designed moment capacity:

$$M_0 = r_m W_{sc} f_{sc} \text{ and } r_m = -0.4832\xi + 1.9264\xi^{0.5}, W_{sc} = \begin{cases} \dfrac{\pi r^3}{4} \text{(circular)} \\ \\ \dfrac{b^3}{6} \text{(square)} \end{cases} \quad (5.3)$$

V is the applied shear force and V_0 is the designed shear capacity:

$$V_0 = r_v A_{sc} f_{sc} \text{ and } r_v = -0.2953\xi + 1.2981\xi^{0.5} \quad (5.4)$$

A_{sc} is the cross-sectional area of the CFST column; A_s and A_c are the cross-sectional areas of the steel tube and the concrete, respectively.

f_y and f_{ck} are the yield strength of the steel tube and the characteristic strength of the concrete, respectively.

ξ is the restraining factor and $\xi = \frac{A_s f_y}{A_c f_{ck}}$

For both axially loaded specimen TS1 and TC1, the theoretical formulae can well predict the experimental results, whereas for axial-load−free specimen TC2, the theoretical prediction was 19.2% larger than the experimental results and this might be due to variation of concrete strength.

Fig. 5.2 depicts the force−displacement histories of the three-point bending tests. It is evident that the tested square specimen TS1 exhibited a larger lateral load capacity than the circular specimen TC1 due to a larger plastic moment capacity. Also, the axially loaded specimen TC1 showed slightly larger lateral load capacity but less ductile behavior than its axial-load−free counterpart TC2.
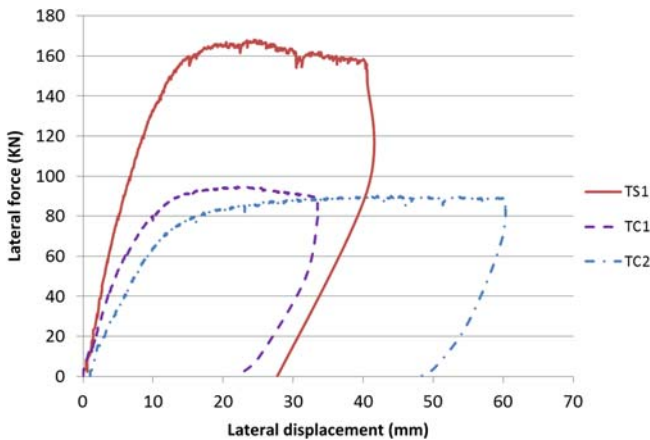
Figure 5.2 Force−displacement histories of the three-point bending tests.

Table 5.3 **Configuration of each specimen**

Specimen	Section size (mm)	TNT equivalence (kg)	Tube thickness (mm)	Axial load (kN)
C1	∅194	25	2.8	500
C2	∅194	35	2.8	500
C3	∅194	25	3.8	562
C4	∅194	50	3.8	562
S5	200 × 200	35	2.8	500
S6	200 × 200	25	2.8	500
S7	200 × 200	35	3.8	562
S8	200 × 200	40	3.8	562

Note: *C*, circular specimen; *S*, square specimen.

5.2.1.3 Blast program

A total of eight CFST specimens, including four circulars and four squares, were used during the blast program. All specimens were 2500 mm in length and the thickness of steel tubes was either 2.8 or 3.8 mm. For all specimens, the explosive was placed 1500 mm away. It should be mentioned that emulsion explosive was used in this research which has an average TNT conversion factor of 0.7 [33]. Table 5.3 lists the details of each specimen.

In practice, the axial load ratio on columns is usually 40%−65% of the ultimate axial capacity [34]. In this study, the applied axial load during the blast test corresponds to 40% of the axial capacity.

The blast experiment was conducted using the same testing facility as discussed in Chapter 4, Ultra-high performance concrete columns. Fig. 5.3 compares the measured pressure−time histories to values predicted by ConWep and reasonable agreement was achieved. Table 5.4 lists the measured peak pressure and impulse for each blast event along with the comparisons to values predicted by ConWep.

For S6 and S7, the pressure−time histories from 1.4 kg emulsion explosive were also used for a comparison.

Fig. 5.4 shows the typical displacement−time histories of test specimens and Table 5.5 summarizes the maximum and residual deflections. It should be noted that all deflection−time histories are only shown up to 50 ms after detonation for easy-reading purpose, whereas the actual free vibration of the test specimens did not stop until at least 150 ms. As mentioned previously, LVDT1 is located at the mid-span of the test specimen, while LVDT2 and LVDT3 are located 380 and 760 mm away from LVDT1, respectively.

Fig. 5.5 compares the mid-span deflections of test specimens under different blast loads. It is evident that the mid-span deflection increased substantially with explosive charge weight. However, this effect appears to be more noticeable on square CFST specimens than circular ones: the mid-span deflection was increased by more than 200% for square CFST specimen with just a 10% increase in the
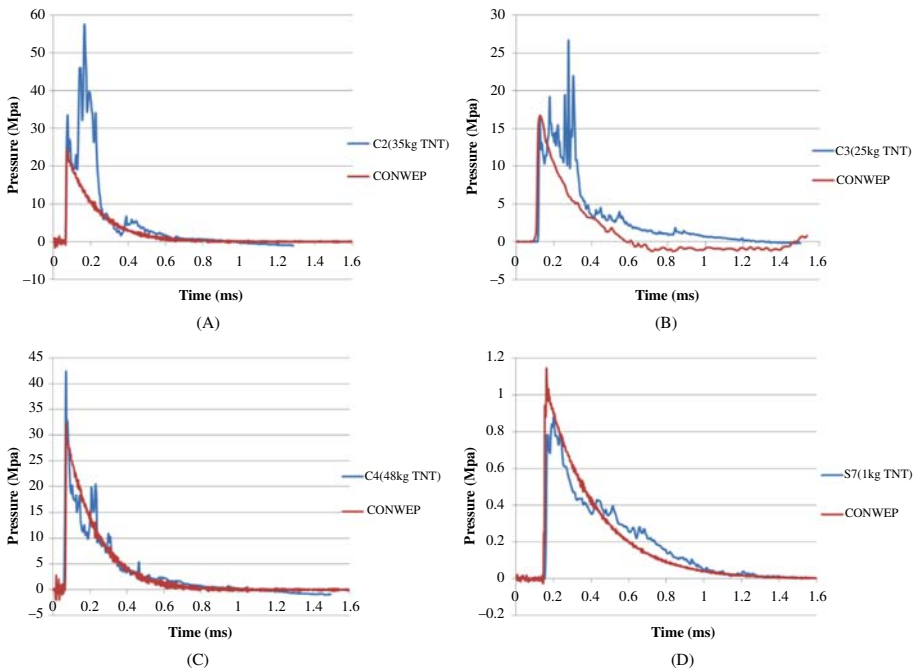
Figure 5.3 Typical pressure−time histories (A) 35 kg TNT, (B) 25 kg TNT, (C) 48 kg TNT and (D) 1 kg TNT.

charge weight. This might be because CFST specimens are more sensitive to blasts due to its large frontal surface.

Fig. 5.6 manifestly indicates that the steel tube thickness has a significant impact on blast resistances of CFST columns. By thickening the steel tube from 2.8 to 3.8 mm, the peak mid-span deflection was effectively reduced by 67% and 50% for circular and square specimens, respectively. Although the effect of varying concrete strength was not investigated during the blast tests, it is believed that for CFST members under lateral loading, the steel tube is the main contributor to the moment capacity as concrete is knowingly weak in tension [12,35,36].

A number of studies have suggested that the effective confinement obtained from a square cross-section is much less than that from a circular cross-section [37−39]. However, according to Fig. 5.7 in terms of blast load resistance, the square specimen S5 still yielded a much smaller deflection than its circular counterpart C2 when subjected to the same blast loading. This indicated that the confinement effect benefits circular CFST specimens more under axial loading rather than under lateral loading.

5.2.1.4 Residual axial load capacity

After the blast experiment, test specimens C1, C3, S6, and S7 were transported back to the structural laboratory for the residual axial load capacity tests.

Table 5.4 Peak pressure and impulse values

Specimen	Explosive weight (kg)	Peak pressure			Peak impulse		
		Measured (kPa)	ConWep (kPa)	Error (%)	Measured (kPa ms)	ConWep (kPa ms)	Error (%)
C1	35 (25)	—	—	—	—	—	—
C2	50 (35)	33,460	24,500	27	6954	3758	−46
C3	35 (25)	16,514	16,700	−1	4365	1960	−55
C4	70 (50)	41,852	32,200	23	4506	4980	11
S5	50 (35)	—	—	—	—	—	—
S6	1.4 (1)	967	1138	−18	285	281	−1
	35 (25)	—	—	—	—	—	—
S7	1.4 (1)	883	1138	−29	286	281	−2
	50 (35)	9690	24,500	−153	3370	3758	12
S8	56 (40)	47,180	23,900	49	8860	3429	−61

Note: Values in the bracket mean the equivalent TNT charge weight.
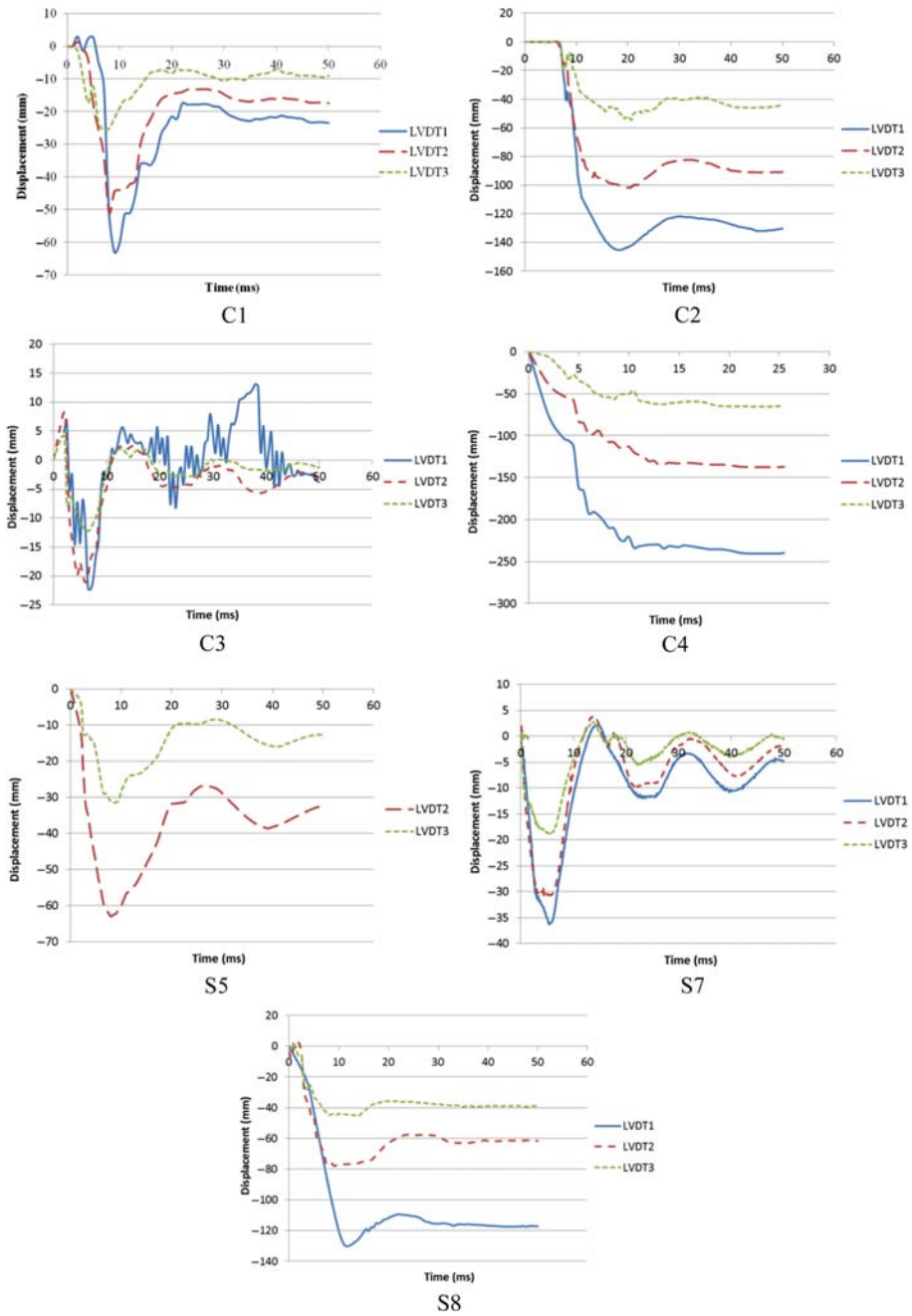
Figure 5.4 Displacement−time histories.

Table 5.5 **Maximum mid-span deflection**

Specimen	Explosive weight (kg)[a]	Standoff distance (mm)	Tube thickness (mm)	Peak deflection (mm)	Residual deflection (mm)
C1	35 (25)	1500	2.8	64.4	25.4
C2	50 (35)	1500	2.8	145.8	126.4
C3	35 (25)	1500	3.8	24.1	3.4
C4	70 (48)	1500	3.8	244.7	233
S5	50 (35)	1500	2.8	60+	33
S6	35 (25)	1500	2.8	–	8[b]
S7	50 (35)	1500	3.8	36.2	5.3
S8	56 (40)	1500	3.8	130.6	116.2

[a]Values in the parentheses mean the equivalent TNT charge weight.
[b]LVDT reading for S6 was lost, residual deflection was manually measured.
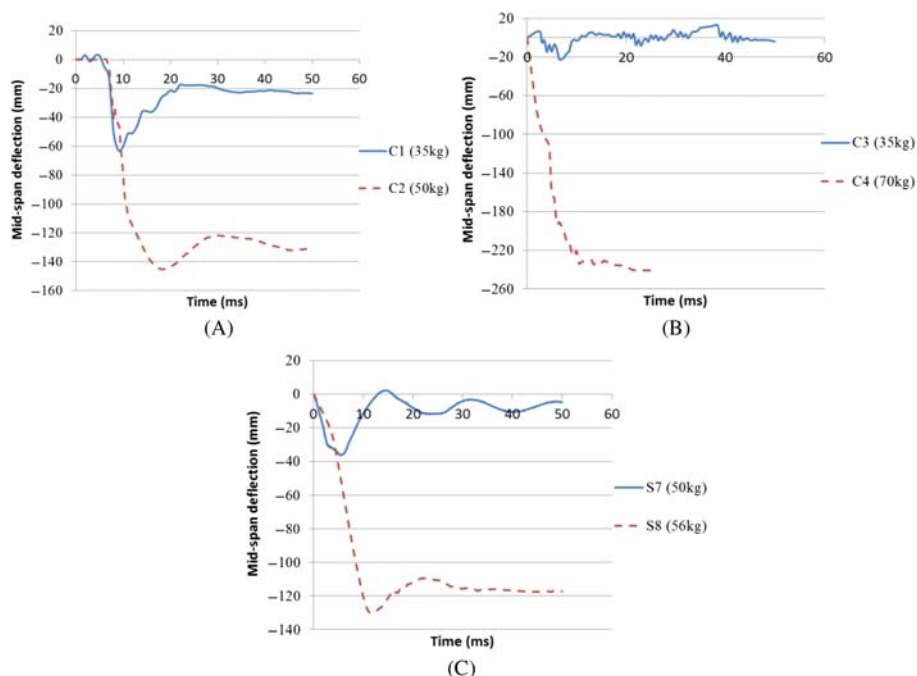
Figure 5.5 Effect of charge weight (A) C1 versus C2, (B) C3 versus C4 and (C) S7 versus S8.

The experiment was carried out by the equipment depicted in Fig. 5.8 whose load capacity is up to 10,000 kN. Knife-edge hinge supports were attached to both ends of the test specimen to simulate simply supported condition.

During the experiment, a three-step loading scheme was used: (1) before the steel yielding, each loading increment was 100 kN and the loading rate was
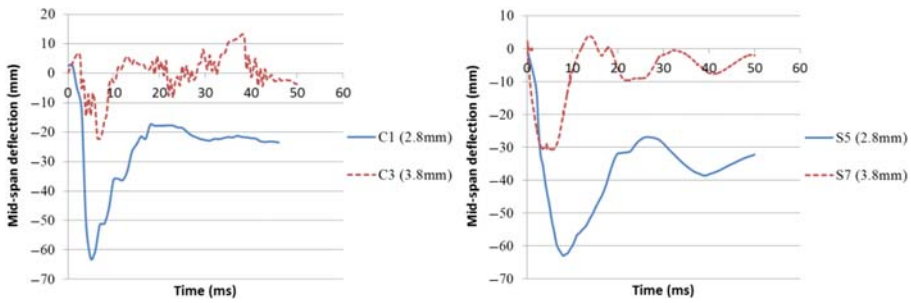
Figure 5.6 Effect of steel tube thickness.
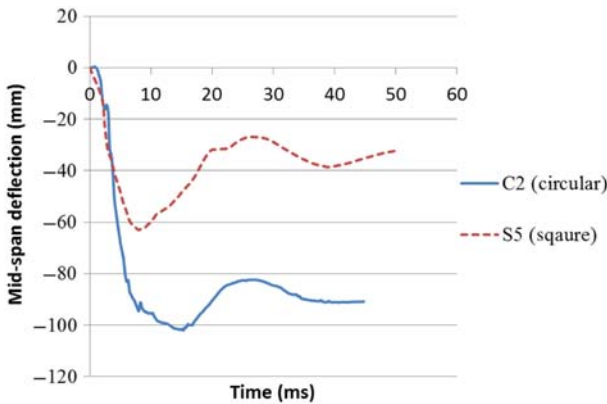
Figure 5.7 Effect of cross-sectional geometry.

0.33 kN s^{-1}; between each loading increment, the load was sustained for 1 minute for stability purpose. (2) Once the steel tube started to yield, the loading rate was reduced to 0.1 kN s^{-1} with the loading increment remained unchanged. (3) Once signs of failure appeared, the loading increment was reduced to 50 kN along with the loading rate reduced to 0.05 kN s^{-1}; during this stage, the load was sustained for 2 minutes instead of 1 minute between loading increments. Thus, actual "residual capacity" in this study should be stability capacity.

Table 5.6 lists the experimental residual axial capacities along with the axial capacities of undamaged specimen calculated from Eq. (5.2). It can be seen that CFST columns were still able to retain relative high residual axial capacities after close-range blast loads. In general, specimens with thicker steel tubes had larger $N2/N1$ ratios than those with thinner steel tubes; square specimens not only had larger designated axial load capacity, but they also showed larger $N2/N1$ ratios over circular specimens under the same blast loads.

It is evident from Figs. 5.9 and 5.10 that the failure modes of all specimens were mainly global flexural failure due to excessive lateral bending. Until failure, there was no sign of local buckling on the two circular columns, whereas it was observed on the two square columns. The reason for local buckling not forming on the circular columns
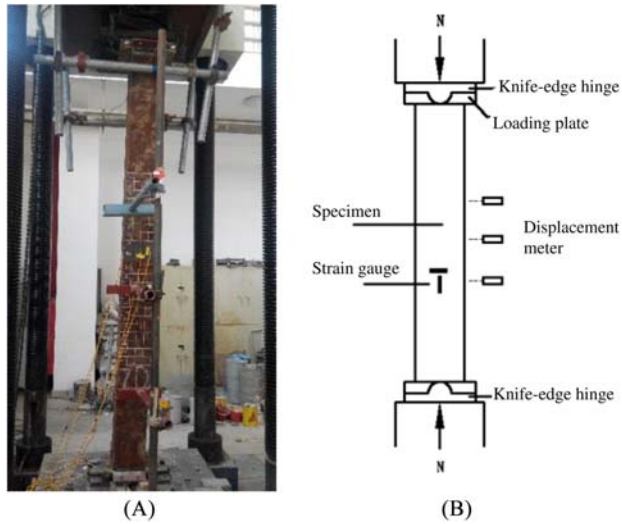
Figure 5.8 Experimental scheme for residual capacity test: (A) experimental setup and (B) experimental instrument.

Table 5.6 **Results of the residual capacity test**

Label	TNT equivalence (kg)	Steel tube thickness (mm)	Residual deflection (mm)	Theoretical axial load capacity, $N1$ (kN)	Residual axial load, $N2$ (kN)	$N2/N1$
C1	25	2.8	25.4	2320	947	0.41
C3	25	3.8	3.4	2531	1623	0.64
S6	35	2.8	8	3018	1672	0.55
S7	25	3.8	5.3	3264	1981	0.61

Figure 5.9 Overall deformed shapes after residual capacity test.
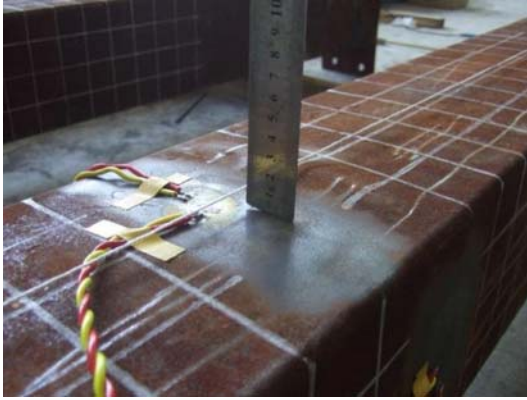
Figure 5.10 Local buckling on square specimens.

Figure 5.11 Split of circular columns (A) C1 (top) and (B) C3 (bottom).

could be due to the circular cross-section resulting in better confinement effect than the square counterparts, thus delaying and/or preventing the occurrence of local buckling.

After the tests, steel tubes of all test specimens were removed to investigate the failure mode of concrete filler. From Figs. 5.11 and 5.12, it can be observed that both square columns exhibited clear signs of concrete crushing and spalling, whereas both circular columns were split into three segments horizontally. The differences in failure modes could be due to circular cross-sections having better confinement to concrete filler than square cross-sections. However, after steel tubes being removed, the confinement no longer existed, which resulted in the cracking energy in circular specimens dissipating more intensely than that in square specimens. As a result, the concrete confined in circular columns was split into several segments.

It can be seen from Figs. 5.11 and 5.13 that under blast loads, the compressive wave in the CFST columns propagated to the back of columns thus forming a

(A) S6

(B) S7

Figure 5.12 Blast surface (A) of S6 and side surface (B) of S7.

(A) c2

(B) c4

Figure 5.13 Split of circular columns (A) C2 and (B) C4 after blast test.

strong tensile wave; meanwhile, due to the spring back displacement trend of CFST columns, concrete fillers in the CFST columns exhibited a number of weak areas. During the residual axial capacity tests, as the lateral displacement increased, the concrete filler was then split into several segments at these weak areas.

5.2.1.5 Conclusion remarks

Based on the tests on CFST columns, some conclusions are made here:

1. The peak reflected pressures and impulses measured by the pressure transducers during the blast experiment showed reasonable agreement with ConWep predictions, yielding 22% and 11% error on average, respectively.

2. The maximum mid-span deflection increased significantly with the increase of explosive charge weight. However, with the increase of steel tube thickness, the maximum mid-span deflection decreased. As for the effect of cross-sectional geometry, the confinement effect benefits circular CFST specimens more under axial loading rather than under lateral loading.
3. During the residual capacity tests, differences in the failure modes for circular and square specimens were observed: square columns failed due to concrete crushing and spalling, whereas circular columns failed due to concrete filler splitting into three segments horizontally at the weak areas caused by blast loads.
4. Test results suggested that CFST specimens were still able to retain up to 60% of its axial capacity after close-range blast loading. In general, specimens with thicker steel tubes had larger residual axial load ratios, and square specimens showed larger axial load ratios over circular specimens under the same blast loads.

5.2.2 Experimental program of concrete-filled double-skin steel tube columns

5.2.2.1 Specimen preparation

Ten CFDST specimens, including five specimens with SHS (square hollow section) outer and SHS inner and five circular specimens with CHS (circular hollow section) outer and CHS inner were tested. In addition, one square and one circular concrete-filled steel tube (CFST) specimens were also investigated to check the dissimilarities, in terms of their structural response subjected to blast loading, when compared with their double-skinned counterparts.

  All specimens measured 2500 mm in length with outer diameter/width $D_{\mathrm{o}} = 210$ mm, inner diameter/width $D_{\mathrm{i}} = 100$ mm and both steel tubes' thickness $t_{\mathrm{si}} = t_{\mathrm{so}} = 5$ mm. The steel tubes were made of hot-rolled seamless steel conforming to Chinese Standard GT/B 8162-2008 [40]. For ease of concrete pouring, a steel plate was first welded to one end of the empty steel tube prior to pouring concrete, making sure that both their geometric centers were aligned. The empty tube was then set up straight and concrete was poured from the top with concrete vibrators being used for compaction. All specimens maintained at room temperature for 28 days and then leveled and polished before any tests.

  The cross-sectional classification of the test specimens was determined in accordance with AS4100 [41]. A cross-section can be classified as compact, noncompact, or slender based on the section slenderness which can be calculated as

$$\lambda = \frac{B - 2t}{t} \sqrt{\frac{f_{\mathrm{y}}}{250}} \text{ for square cross-section} \tag{5.5a}$$

$$\lambda = \frac{D}{t} \frac{f_{\mathrm{y}}}{250} \text{ for circular cross-section} \tag{5.5b}$$

where B is the outer length of the square cross-section, D is the outer diameter of the circular cross-section, t is the thickness of the outer tube, and f_{y} is the yield stress of the outer tube.

For unfilled square hollow tube, the plastic limit, λ_p, is 82, whereas for unfilled circular hollow tube, λ_p is 50. According to Elchalakani et al. [42], the concrete filler in CFST/CFDST specimens increases the plastic limit by about 50%. As a result, λ_p for the square and circular CFDST columns in this study are 123 and 75, respectively. By using Eqs. (5.5a) and (5.5b), the section slenderness for the square and circular cross-sections is 48 and 60.5, respectively, which are both less than their corresponding plastic limits; therefore, the square and circular CFDST specimens used in this study can be classified as compact sections.

Fig. 5.14 shows the typical cross-sections of the CFDST specimens used in the blast tests and Table 5.7 presents detailed information for each of the tested specimens.
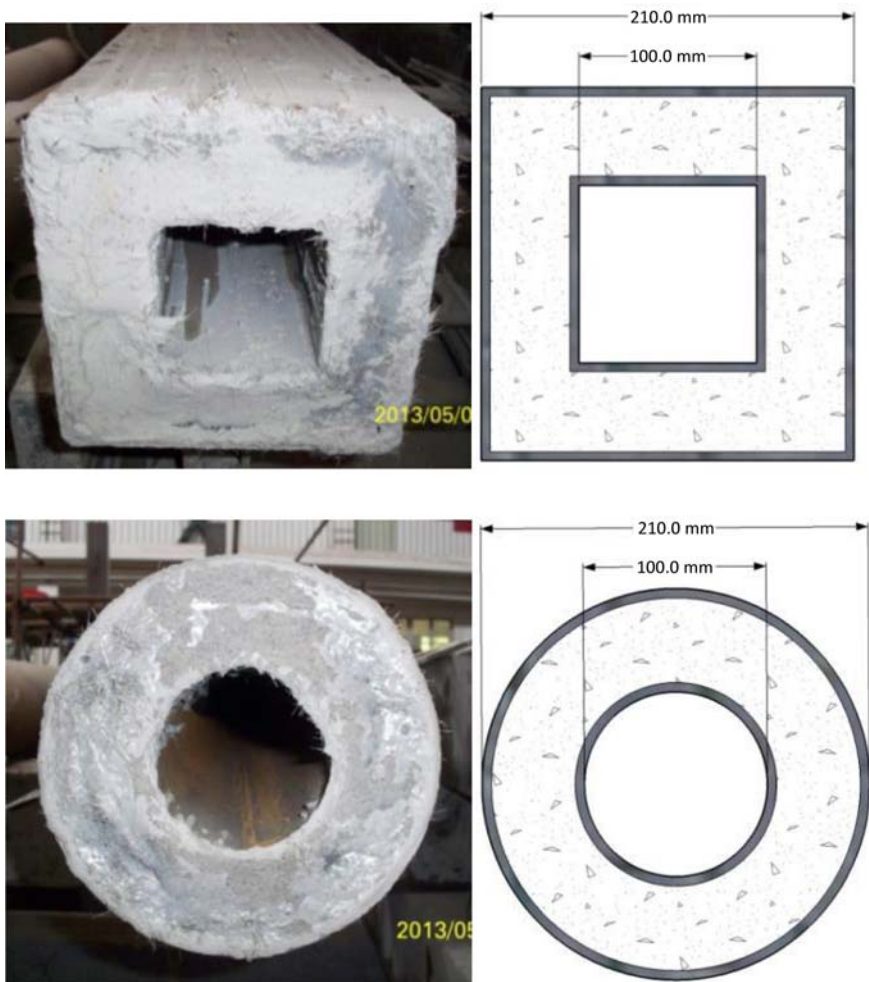
Figure 5.14 Cross-sections of a square and a circular CFDST specimen.

Table 5.7 The characteristics of each test specimen

Cross-section	Label	Test setup	L (mm)	Nominal outer dimensions ($D \times t_{so}$ mm)	Nominal inner dimensions ($D \times t_{io}$ mm)	χ	TNT (kg)[a]	Axial load (kN)	Maximum Δ (mm)	Residual Δ (mm)
Square	S1A	a	2500	210 × 5	110 × 5	0.5	35	—	41	16
	S1B	a	2500	210 × 5	110 × 5	0.5	50	—	49	22
	S2A	a	2500	210 × 5	110 × 5	0.5	35	1000	36	8
	S2B	a	2500	210 × 5	110 × 5	0.5	50	1000	—	14[b]
	S3A	a	2500	210 × 5	110 × 5	0.5	50	1000	41	8
	S3B	a	2500	210 × 5	—	—	50	1000	50	10
Circular	C1A	b	2500	210 × 5	110 × 5	0.5	35	—	98	65
	C1B	c	2500	210 × 5	110 × 5	0.5	35	—	50	20
	C2A	b	2500	210 × 5	110 × 5	0.5	35	1000	—	39[b]
	C2B	c	2500	210 × 5	110 × 5	0.5	17.2	—	35	12
	C3A	b	2500	210 × 5	110 × 5	0.5	50	1000	91	52
	C3B	b	2500	210 × 5	—	—	50	1000	83	43

[a]TNT-equivalent charge, based on impulse.
[b]LVDT readings were lost for S2B and C2A, residual displacements were manually measured.

5.2.2.2 Material properties

The mechanical properties of the steel tubes were determined from tensile coupons taken from the outer steel tube of a square CFDST specimen in conformance with Chinese Standard GBT228-2010 [43]. The loading increment was $10 \, \mathrm{MPa \, s^{-1}}$ before steel yielding and the pulling chuck was pulled at a rate less than $0.5 \, \mathrm{L \, min^{-1}}$ (where L represents the total length of the specimen) after steel yielding. The average yield strength and ultimate strength of the steel tubes test are 360 MPa and 515 MPa, respectively, with an elongation of 22%. Fig. 5.15 shows a typical stress−strain relationship of the tested steel tubes.

Steel-fiber reinforced self-consolidating concrete with nanoparticles was used as the concrete in all CFDST specimens. The nanoparticle, namely $CaCO_3$, was used as a nanoscale additive to fill up the void existing in concrete as well as to enhance the hydration process. The mixture was produced by mixing silica fume, fine sand, and powder materials, which consisted of cement and nanoparticles, in a laboratory concrete mixer. They were firstly mixed in dry condition for 5 minutes prior to pouring in additives. To fluidize the mix, approximately 70% water was then added and mixed for 3 minutes. Superplasticizer was added followed by the other 30% water. The mixing process was then continued for another 5 minutes and microsteel fibers were added afterward which were manually dispersed and added to the mixer to avoid clumping.

Twenty-nine $100 \, \mathrm{mm} \times 100 \, \mathrm{mm} \times 100 \, \mathrm{mm}$ specimens were made for compressive tests and another twenty-nine $100 \, \mathrm{mm} \times 100 \, \mathrm{mm} \times 400 \, \mathrm{mm}$ specimens were made for flexural bending tests. Prior to the compressive tests, each cube was properly leveled, sanded, polished, cleaned, and dried to attain smooth surfaces. The average cube compressive strength and the flexural tensile strength of the concrete at 28 days were 170 MPa and 33.8 MPa, respectively, which are much higher than the normal strength concrete.
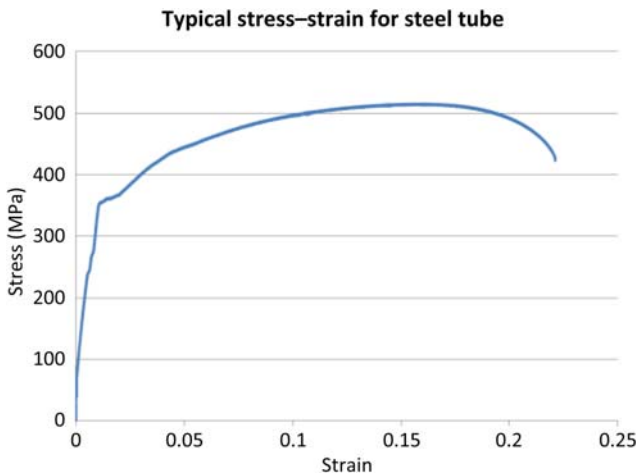
Figure 5.15 A typical stress−strain relationship of steel tube material.

5.2.2.3   Field blast test setup

The same testing facilities as those used in the UHPC column tests were employed
in this study. Three different test setups were used during the blast tests as depicted
in Fig. 5.16. The test pit was designed in such a way that it was as wide as the test
specimens; therefore, as shown in setup (a), when the square specimen was placed
into it, its front side (the side which received the blast load) was leveled with the
ground surface so that neither there would be clearing effect nor would the incident
wave damage the recording apparatus which were placed at the bottom of the pit.
However, the same design cannot be directly applied to circular specimens due to
the location of the pneumatic jack. The geometric center of the pneumatic jack was
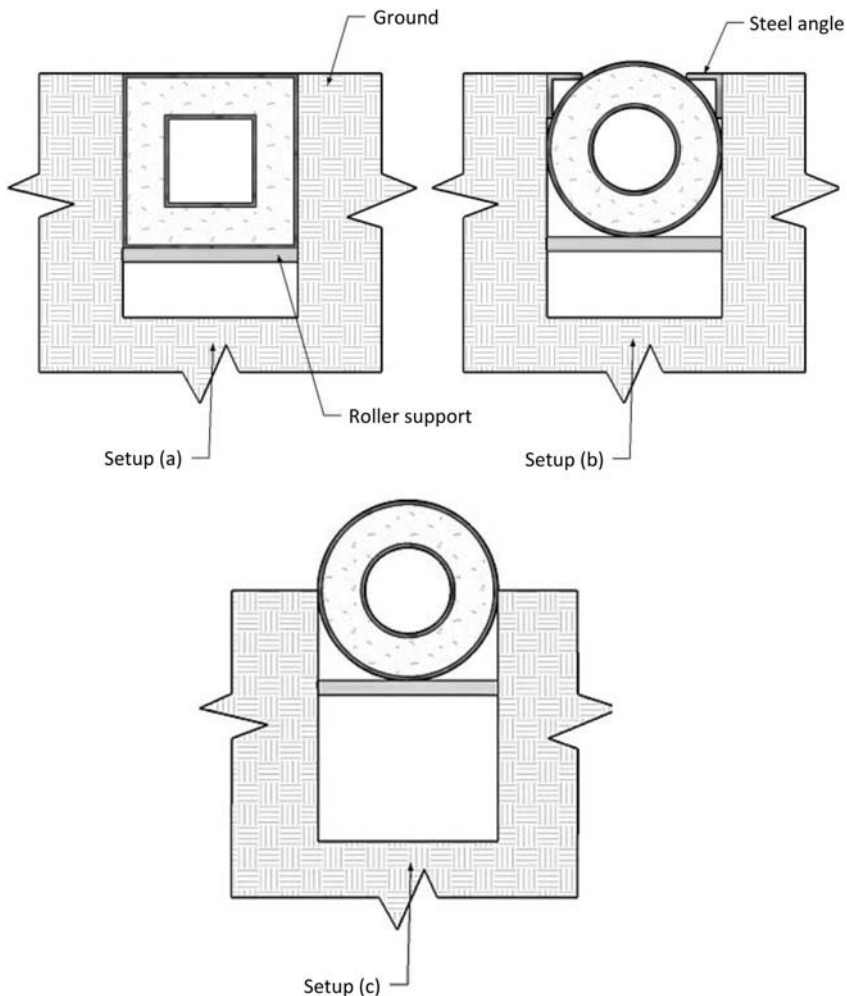
Figure 5.16 Cross-sectional view of the test setups.

aligned with that of the square specimen as shown in setup (a). Because the pneumatic jack cannot be moved upward or downward, setup (b) had to be used for circular specimens if axial load needed to be applied. However, because of the circular cross-sectional shape, the blast wave could now travel into the pit and get reflected and amplified within the narrow space (like a confined blast scenario). Therefore setup (c) was then introduced for these circular specimens without axial load so that the loading condition would not be too complicated to analyze.

In summary, setup (a) was used for square CFDST columns with and without axial load: the specimen was put into the test pit with its top surface level with the ground surface to ensure that the blast wave could not travel into the pit. Setup (b) was used for circular CFDST columns with axial load: almost the entire specimen was placed beneath the ground with steel angles also being used to reduce the blast wave that travels into the pit. Setup (c) was used for circular CFDST columns without axial load: half of the specimen was above the ground surface.

5.2.2.4 Test results

Similar to CFST column tests, ConWep predictions of spherical explosive were used as benchmarks for calculation of the peak reflected pressure and impulse for TNT [44,45]. Table 5.8 lists the comparisons between the measured and ConWep-predicted peak reflected pressures and impulses. Errors between the measured and ConWep-predicted peak reflected pressures and impulses are on average 20% and 18%, respectively, without taking specimen S3B into consideration because it deviates from the average too significantly. Fig. 5.17 compares the measured pressure−time histories to the ConWep-predicted ones of the corresponding TNT equivalents. It is observed that except for Fig. 5.17A,B,F, and G, the measured blast loads are generally in good agreement with the ConWep predictions. Discrepancies are found in measured pressures and impulses between identical blasts, and most measured pressure−time histories have multiple peaks rather than only having one peak pressure as found in the ConWep-predicted cases. In the authors' opinions, these issues are mainly resulted from the following reasons: (1) first of all, when the blast wave travels toward a test specimen, a lot of sand and soil particles travel along with it which inevitably hit on the pressure transducer. As the pressure transducer is highly sensitive, the pressure resulted from the particle collision is therefore also regarded as part of the blast load; (2) secondly, the explosive charge weights used in the blast tests are relatively large; therefore, the accuracy and sensitivity of the pressure transducer can deteriorate over time. It is found that it is more likely to obtain more accurate results every time when a new pressure transducer is put to use specimens such as S2A and C3A; (3) finally, the size of a 70 kg emulsion explosive may be too large that the chemical reactions within the explosive compound were unthorough and incomplete at the initial detonation.

Fig. 5.18 reports two of the typical displacement−time histories of the test specimens. All three LVDTs were aligned along the centerline of the member. LVDT1 was installed right below the center of the specimen and LVDT2 and LVDT3 were installed 360 mm and 720 mm away from LVDT1, respectively. None of the

Table 5.8 **Comparison between measured and ConWep-predicted pressures and impulses**

Specimen no.	Emulsion explosive (kg)	TNT equivalent (kg)	Standoff distance (mm)	Peak reflected pressure (MPa)			Peak reflected impulse (MPa ms)		
				Measured	ConWep	Error (%)	Measured	ConWep	Error (%)
S1A	48	35	1500	18.7	24.5	−24	3.07	3.76	−18
S1B	70	50	1500	18.6	32.2	−42	4.20	4.98	−16
S2A	48	35	1500	18.2	24.5	−26	2.50	3.76	−34
S2A	1.4	1	1500	1.05	1.2	−13	0.29	0.28	+4
S2B	70	50	1500	37.3	32.2	+16	6.54	4.98	+31
S3A	70	50	1500	18.6	32.2	−42	3.50	4.98	−30
S3B	70	50	1500	90.3	32.2	+180	24.0	4.98	+382
C2A	48	35	1500	23.4	24.5	−4	3.85	3.76	+2
C2B	24	17.2	1500	15.4	14.0	+10	2.36	2.18	+8
C3A	70	50	1500	37.4	32.2	+16	5.90	4.98	+18
C3B	70	50	1500	33.3	32.2	+3	3.80	4.98	−24
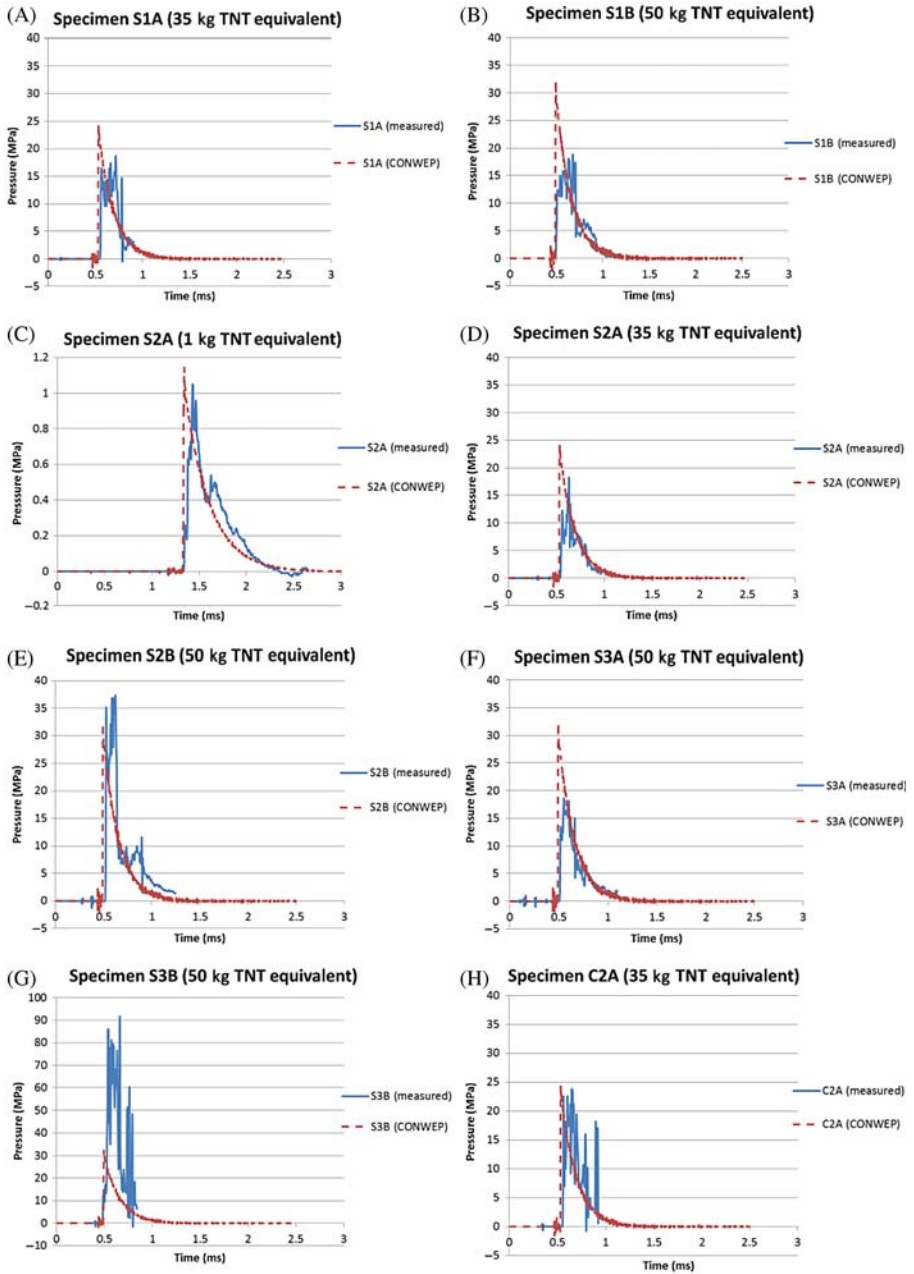
Figure 5.17 Pressure–time histories for tested specimens (A) S1A 35 kg, (B) S1B 50 kg, (C) S2A 1 kg, (D) S2A 35 kg, (E) S2B 50 kg, (F) S3A 50 kg, (G) S3B 50 kg, (H) C2A 35 kg, (I) C2B 17.2 kg, (J) C3A 50 kg and (K) C3B 50 kg.
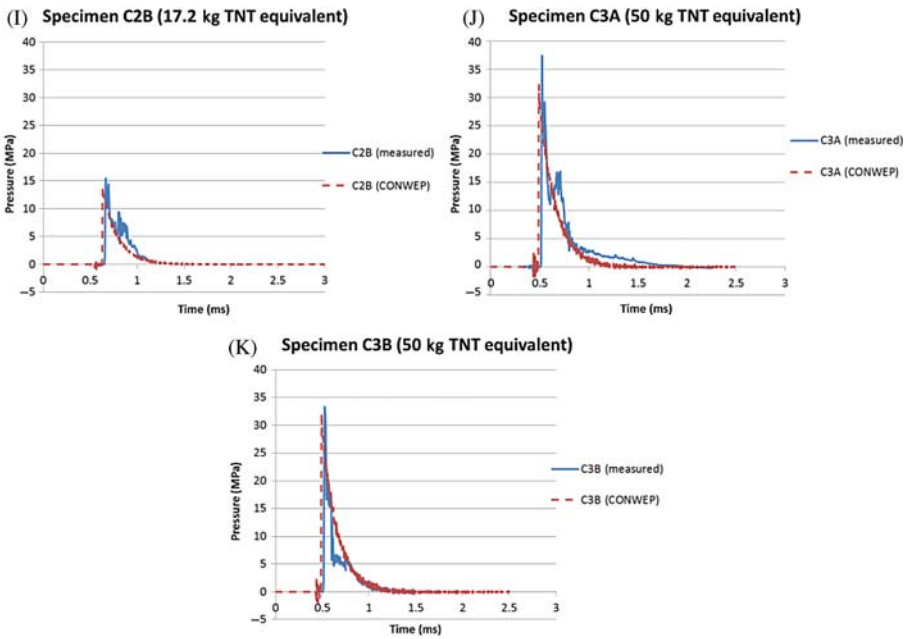
Figure 5.17 (Continued)

displacement measurements reached the LVDT measuring range (120 mm). The mid-span residual displacements of the tested specimens were measured manually posttesting and they were also found to be in good agreement with the LVDT readings.

Fig. 5.19 compares the displacement–time histories of CFDST specimens subjected to different blast loads (LVDT1 recording at mid-span only). As expected, larger charge weight yields larger deflection. However, the test results also suggest that the effect of charge weight is more noticeable for the specimens without axial load than the axially loaded ones. The differences between axially loaded specimens S2A and S3A were small in Fig. 5.19B, while for their axial-load–free counterparts in Fig. 5.19A, S1B undergoes 25% larger peak displacement and 50% larger residual deflection than S1A.

The effect of axial load was investigated by applying two different axial loads, namely 0 and 1000 kN, on several identical specimens and then comparing their displacement–time histories under the same blast loads. In both cases shown in Fig. 5.20, the application of 1000 kN axial load results in a reduction in the deflection. Similar results were also observed by Wang et al. [13], who discussed the relationship between the axial load ratio (i.e., applied axial load/nominal axial load capacity) and the peak displacement. It was found that a small axial load ratio (e.g., less than 0.3) can effectively reduce the deflection, while a large axial load ratio (e.g., more than 0.6) was likely to amplify the deflection. In this research, the applied axial load (i.e., 1000 kN) corresponds to approximately an axial load ratio of 0.2.
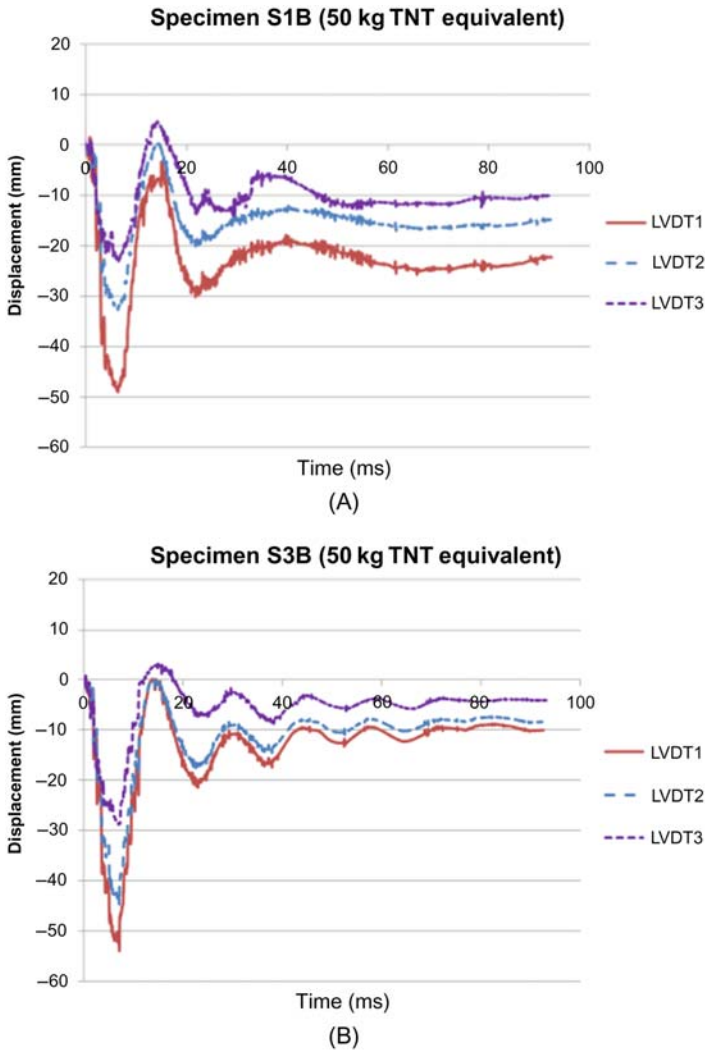
Figure 5.18 Typical displacement−time histories for tested specimens (A) S1B under 50 kg TNT and (B) S3B under 50 kg TNT.

Another possible reason is the membrane effect. In this study, axial loads application provides lateral restrain to the column, and compressive membrane action may occur. Early age deflection may cause a migration of the neutral axis which is accompanied by in-plane expansion of the column at its boundaries. If this expansion is restrained, in this case by the axial load application, the development of arching action enhances the strength of the column. The compressive membrane effects can be accounted for the different column deflections under the same blast loading condition.

As mentioned previously, two different test setups were used on the circular CFDST specimens due to limitations of the pneumatic jack. If the test specimen
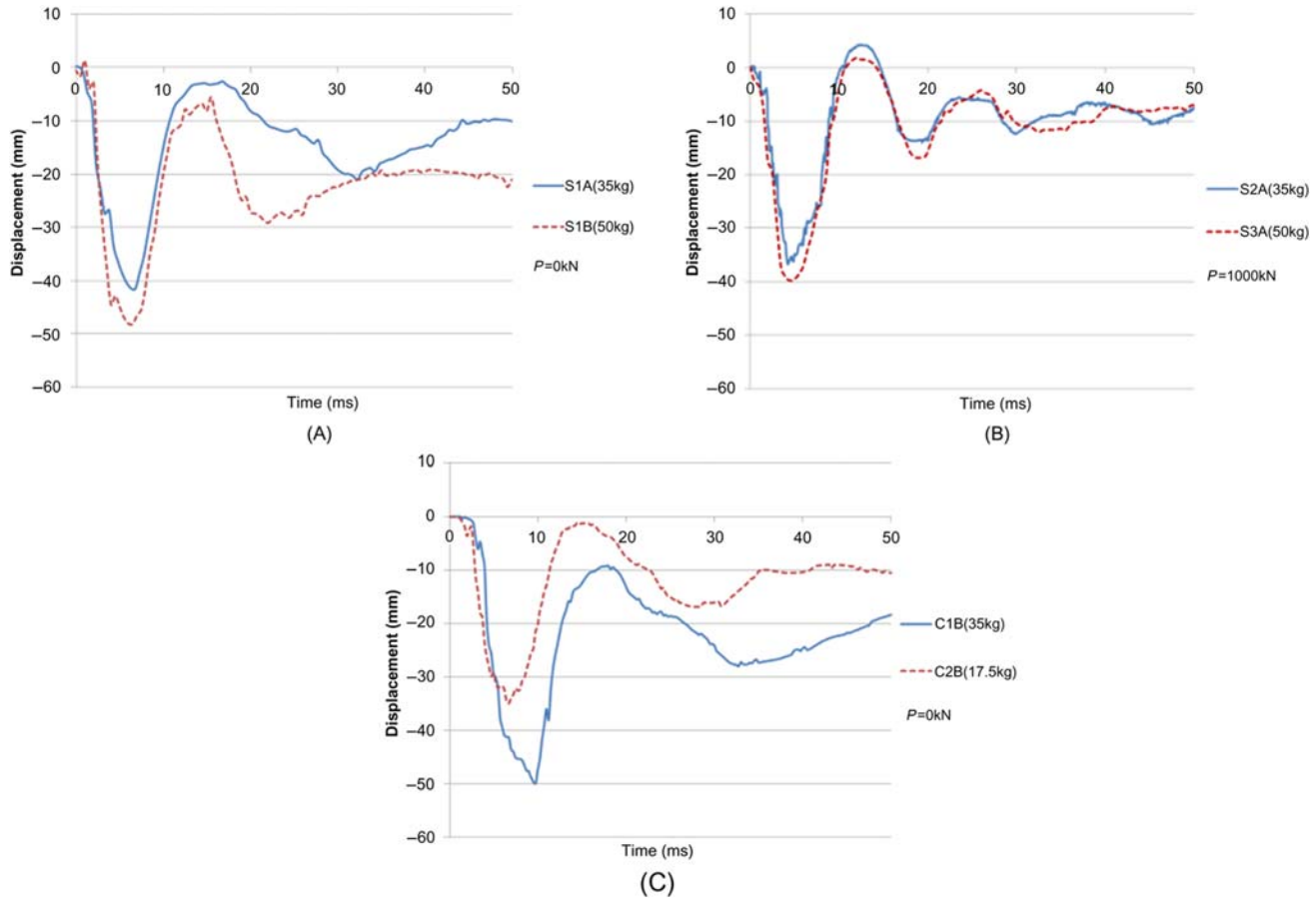
Figure 5.19 Effect of charge weight (A) S1A versus S1B, (B) S2A versus S3A and (C) C1B versus C2B.
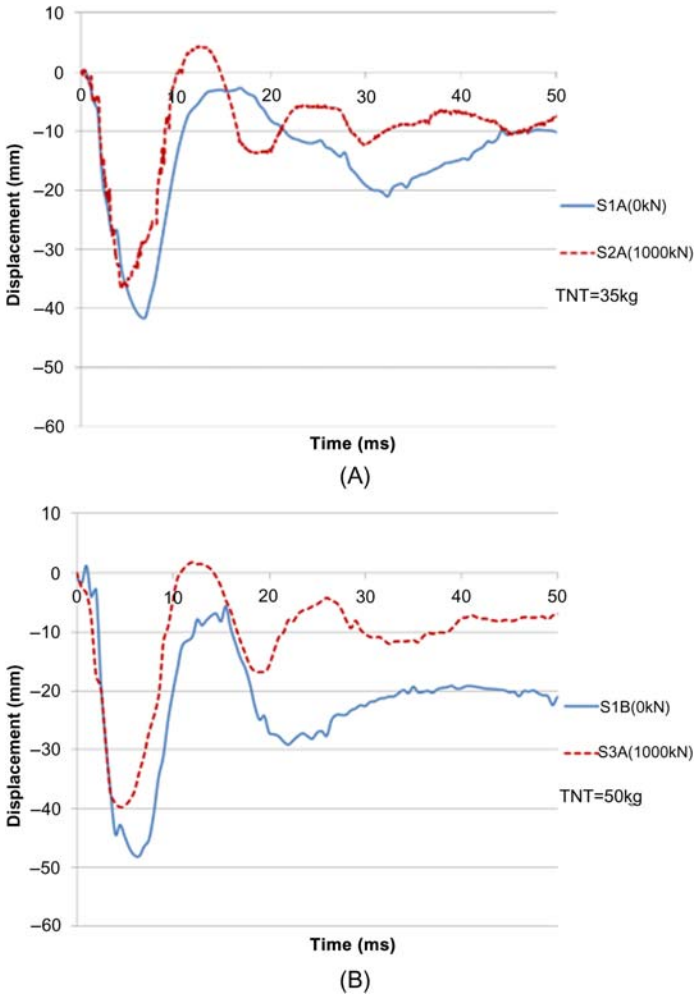
Figure 5.20 Effect of axial load (A) S1A versus S2A and (B) S1B versus S3A.

was to be axially loaded, then setup (b) had to be used because the entire pneumatic jack was buried beneath the ground surface and it could not be moved up or down; otherwise, setup (c) was adopted.

Fig. 5.21 depicts the blast-pressure distributions on CFDST specimens by using the two different setups. Due to the presence of the steel angles, the pressure distribution in setup (b) is similar to the pressure acting on a square specimen: it reaches a peak at the middle and decays very slightly along its width. However, setup (c) exhibits the typical pressure distribution for circular columns: it reaches peak at the middle by the same magnitude as setup (b) and then decreases significantly along its circumference due to its roundness.
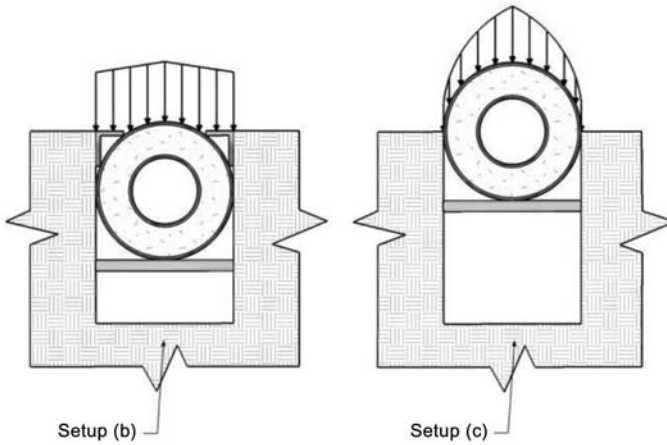
Figure 5.21 Blast load distribution on setups (b) and (c).
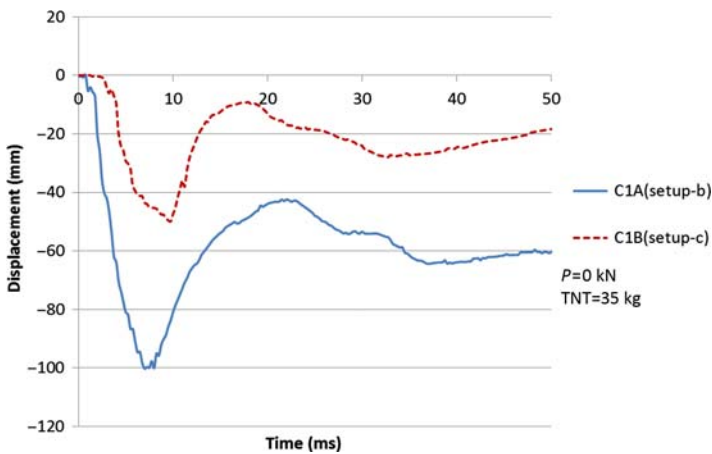
Figure 5.22 Effect of different specimen setups.

Fig. 5.22 compares setup (b) with setup (c) in terms of the displacement−time history. The deflection of the CFDST specimen in setup (b) yielded 100% more maximum deflection and 200% more residual deflection than that of the CFDST specimen in setup (c).

By having a hollow core in this study, the cross-sectional area and self-weight of the specimens (both the circular and square ones) was reduced by 23% relative to fully concrete-filled tubes. In prior research, not much effort has been put into investigating the difference caused by a hollow core versus a fully filled section. Han et al. [21] studied this effect, with the area of hollow core ranging from 0 to 0.77 of the total cross-sectional area, for CFDST specimens under cyclic flexural load. It was then reported that most hollow specimens exhibited a larger flexural

load capacity and ductility than their solid counterparts if the hollow ratio can be kept under a certain value which is dependent on the amount of steel. For specimens with a hollow ratio of 0.77, a very significant decline in the flexural load capacity and ductility was observed.

However, during the blast test, it was found that both CFDST and CFST column specimens behaved in a very similar manner, regardless of the cross-sectional geometry. Despite the difference in the maximum deflection, as shown in Fig. 5.23A and B, the hollow area inside seems to have little effect on the overall structural responses as both types showed similar period of oscillation, maximum, and residual deflection.
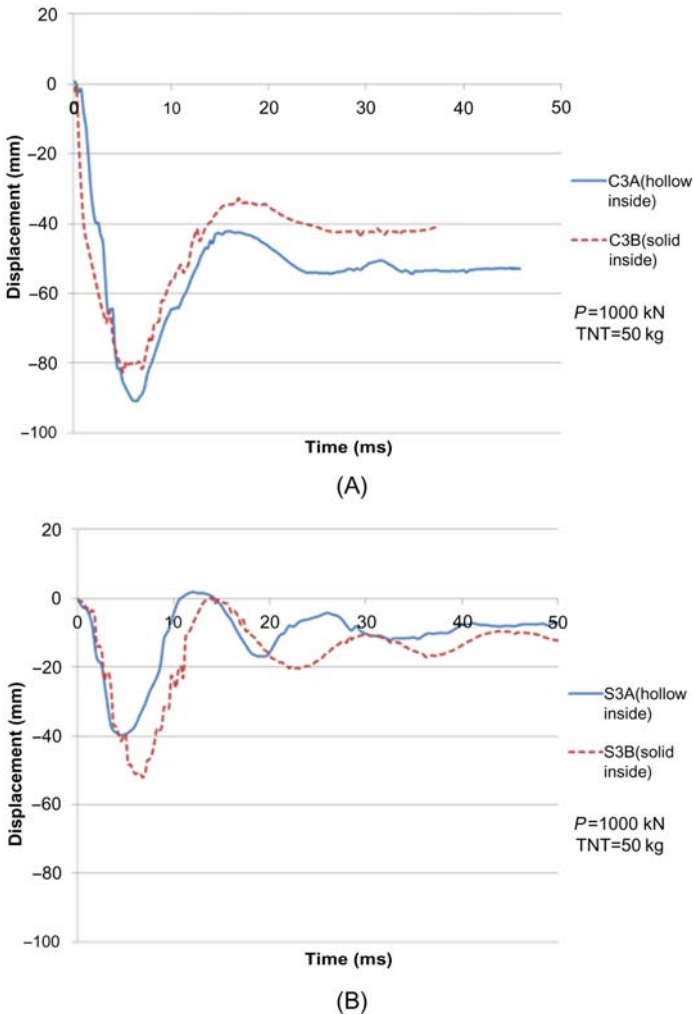
Figure 5.23 Effect of hollowness: S3A and C3A are CFDST and S3B and C3B are CFST (A) C3A versus C3B and (B) S3A versus S3B.

For a CFDST specimen filled with normal strength concrete, its failure under flexural load is mainly due to the crushing of the concrete associated with local buckling of the steel tube, or even rupture, as shown in Fig. 5.24 [46−48].

In this study, the CFDST specimen is filled with steel-fiber reinforced UHPC; therefore its structural response is very different from those filled with normal strength concrete. Fig. 5.25 shows the deformed shapes of specimens S1A and C1A; no steel buckling or localized damage can be observed on both specimens which were subjected to 35 kg TNT equivalent despite specimen C1A yielded the largest maximum (98 mm) and residual deflection (65 mm) of all test specimens. Fig. 5.26 shows the crack propagation in the concrete after removing the outer steel skin from specimens S1A and C1A. There was no obvious sign of concrete
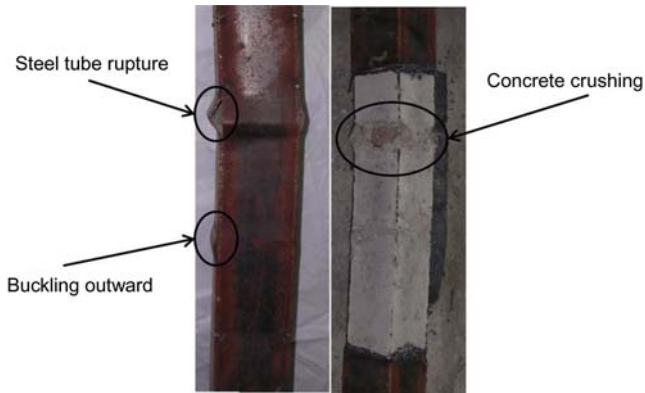
Figure 5.24 Failure of CFDST [21].
Source: Courtesy of Prof. L.H. Han, Tsinghua University, China.

(A)

(B)

Figure 5.25 Deformed shapes of specimens S1A and C1A: (A) S1A and (B) C1A.
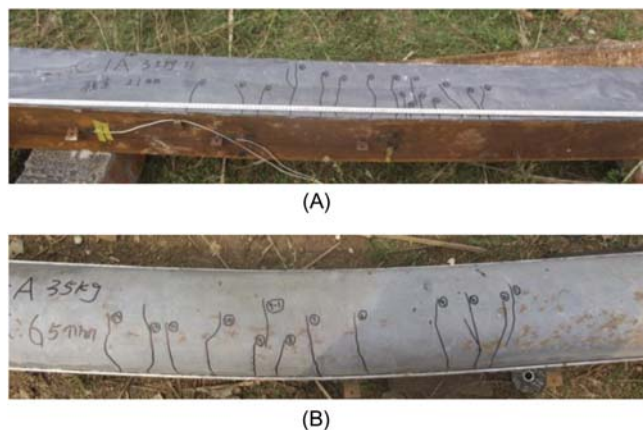
Figure 5.26 Crack propagation in specimens S1A and C1A: (A) S1A and (B) C1A.

crushing on both specimens, only minor flexural cracks of no more than 0.5 mm width on the tensile face of both specimens. Both figures show that the tested CFDST specimens were also able to remain overall global flexural response as opposed to localized structural failure. This is one of the main advantages of using UHPC over conventional concrete in CFST/CFDST members: due to the higher compressive/tensile strength and steel fibers, UHPC is very resistant to crushing or spalling. As mentioned previously, the steel tubes of a CFDST member normally only buckles after the concrete filler at the same location crushes; therefore, compared to conventional concrete, UHPC can more effectively prevent or delay steel buckling.

5.2.3 Conclusions

Based on the experimental study on the CFDST columns under blast loading, the following conclusions can be drawn based on the test results and observations:

1. CFDST columns filled with UHPC can effectively withstand severe blast load without failure. Compared to normal strength concrete-filled CFDST, the UHPC-filled CFDST can better delay/prevent concrete crushing and steel buckling, and thus have an overall global flexural response as opposed to localized structural failure.
2. The peak reflected pressures and impulses measured by the pressure transducer yield 18% and 20% error, respectively, compared to the ConWep predictions.
3. The increase in explosive charge weight caused a larger mid-span deflection, with this effect being more noticeable on axial-load−free specimens rather than axially loaded specimens.
4. The presence of an axial compressive load, corresponding to approximately 20% of the squash load, led to a slight reduction in the peak deflection in two comparative cases.
5. In this study, both CFDST and CFST specimens showed similar behaviors. The hollow area inside seems to have little effect on the overall structural responses as both types had similar period of oscillation, maximum, and residual deflection.

5.3 Residual capacity of ultra-high performance concrete-filled steel tube columns against close-range blasts

5.3.1 Experimental program

5.3.1.1 Phase one: the static test

The axial compression tests and three-point bending tests were carried out to investigate the behaviors of CFDST columns when subjected to axial compressive and transverse loadings, respectively. Those tests were carried out by using the experimental machineries as shown in Fig. 5.27. The test machine was displacement controlled which mainly consisted of two fluid power systems: a horizontal hydraulic loading system for axial loading and a vertical hydraulic loading system for lateral
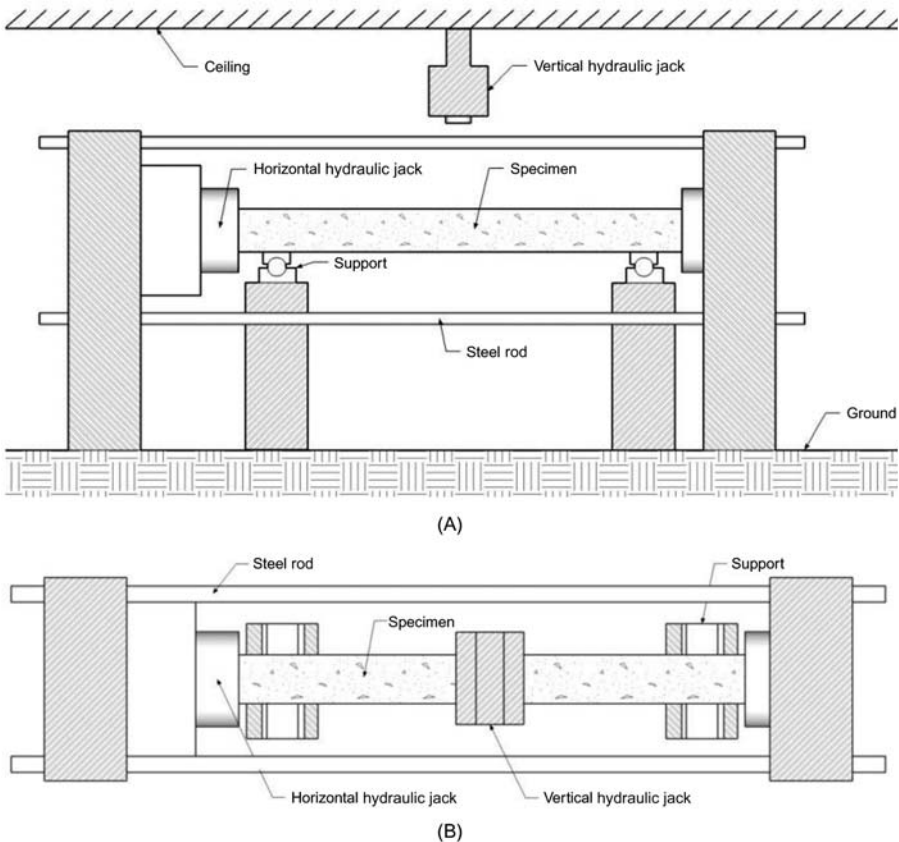
Figure 5.27 The test machineries for the axial load test and three-point bending tests: (A) elevation and (B) top view.

Table 5.9 **Axial compressive test**

Specimen label	Specimen type	Nominal outer dimensions ($D \times t_{so}$)	Nominal inner dimensions ($D \times t_{io}$)	Axial load (kN)
AC_C1	CFDST	210	100	4000
AC_S1	CFDST	210	100	4025

Note: "AC" means axial compression test.

Table 5.10 **Three-point bending test**

Specimen label	Specimen type	Nominal outer dimensions ($D \times t_{so}$)	Nominal inner dimensions ($D \times t_{io}$)	Axial load (kN)	Peak lateral load (kN)
TPB_C1	CFDST	210	100	0	290.54
TPB_C2	CFDST	210	100	1000	484.03
TPB_C3	CFST	210	—	1000	412.52
TPB_S1	CFDST	210	100	1000	660.78
TPB_S2	CFST	210	—	1000	631.12

Note: "TPB" means three-point bending test.

loading. Both hydraulic jacks can carry up to 10,000 kN load and the test specimen length can be from 2000 to 3550 mm with the maximum displacement range of both hydraulic rams being 200 mm. As for support condition, the test specimen was simply supported near both ends and the location of supports can be adjusted accordingly to meet different experiment requirements.

Tables 5.9 and 5.10 summarize the results of the axial compressive tests and three-point bending tests, respectively. For comparison purpose, one circular and one square CFST specimens, namely TPB_C3 and TPB_S2, were also included to check the dissimilarities, in terms of their structural response, when compared with their double-skinned counterparts.

Fig. 5.28 shows the axial load versus axial shortening diagrams from the axial compressive tests. It can be seen that both specimens have similar peak axial load capacity although the specimen with square cross-section has a larger cross-sectional area. This verifies the theory that circular cross-sections often result in better confinement under axial compression, thus larger axial capacity. Fig. 5.29 depicts the lateral load versus lateral displacement diagrams from the three-point bending tests.

Fig. 5.30 compares the axially loaded specimen TPB_C2 to the axial-load−free specimen TPB_C1. It is evident that the applied axial load on specimen TPB_C2 significantly increased the peak lateral load-carrying capacity by 67%, compared to specimen TPB_C1 which was not axially loaded. However, in terms of ductility, specimen TPB_C1 behaved in a more ductile manner under flexural load, while the
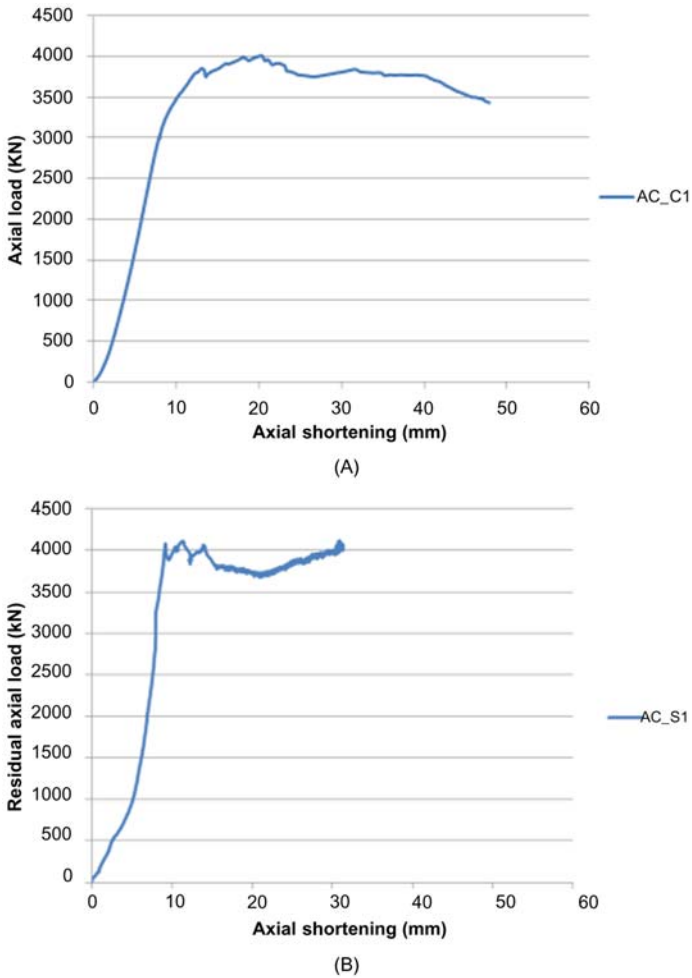
Figure 5.28 Axial compressive load versus axial shortening curve: (A) circular CFDST and (B) square CFDST.

load capacity of specimen TBP_C2 declined immediately after reaching its peak. The increase in the flexural load capacity due to axial loads can be well explained by the schematic moment−load interaction curve depicted in Fig. 5.31, where the moment capacity of a CFDST column can be enhanced by a low level of axial load (i.e., within branch BD). More details can be found in Zhao et al. [12], where an analytical model was also given to calculate the interaction curve for both CFST and CFDST columns.

In addition, the failure mode of axial-load−free specimen TPB_C1 was also found to be different from the rest of the axially loaded specimens. As shown in
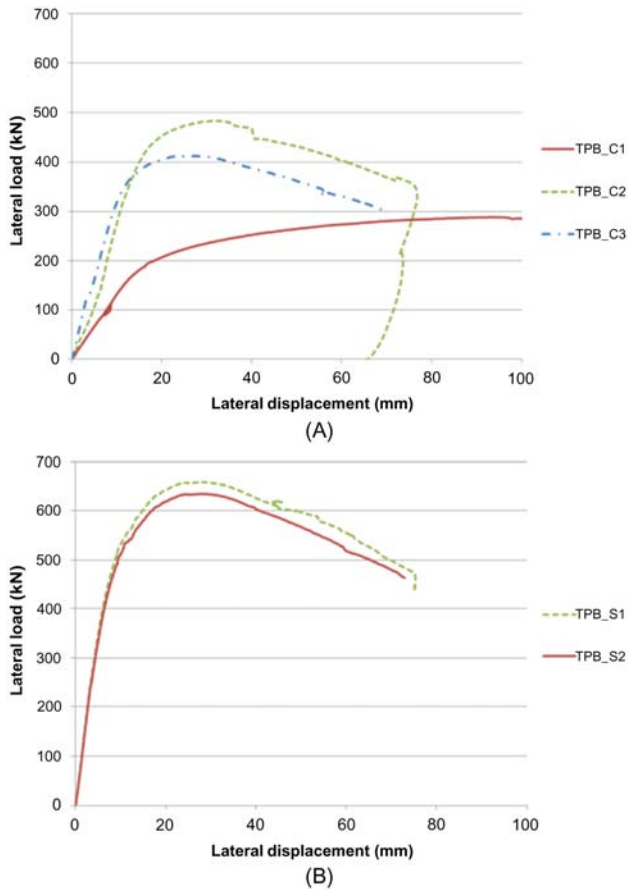
Figure 5.29 Load−displacement histories of three-point bending tests for (A) circular and (B) square CFDST.

Figs. 5.32 and 5.33, the failure mode of the axial-load−free specimen was local buckling of the outer steel tube on the compression zone near the mid-span associated with noticeable outer steel tube crack on the tension zone near the mid-span, whereas the failure mode of the axially loaded specimens was local buckling of the outer steel tube on the compression zone near the mid-span only.

Fig. 5.34 shows the effect of the hollow core on the circular and square cross-sections. It was observed that the presence of the hollow cores in CFDST specimens does not impose a significant effect on the flexural behaviors as both curves showed very similar trend regardless of the cross-sectional type. However, the presence of hollow cores caused a slight increase in the peak lateral load capacity, with this effect being more noticeable on circular specimens (i.e., 17%) rather than square specimens (i.e., 5%).
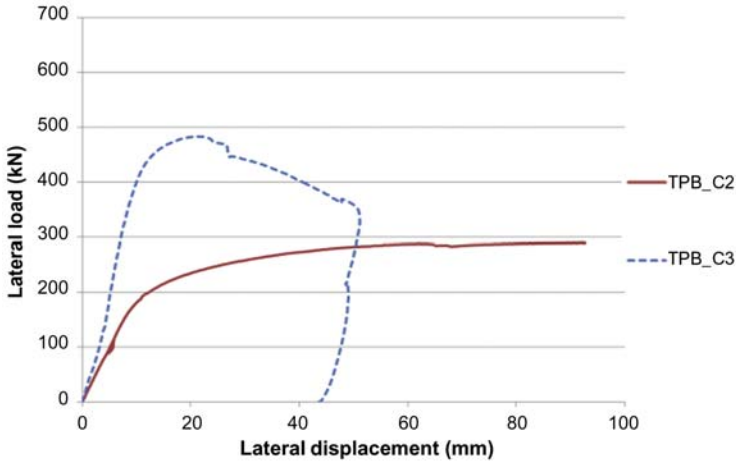
Figure 5.30 Effect of axial load.
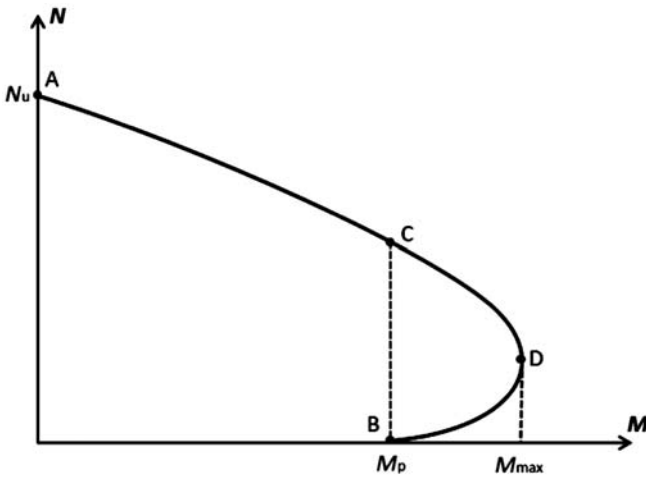
Figure 5.31 Schematic view of $M-N$ interaction diagram for CFST and CFDST [12].
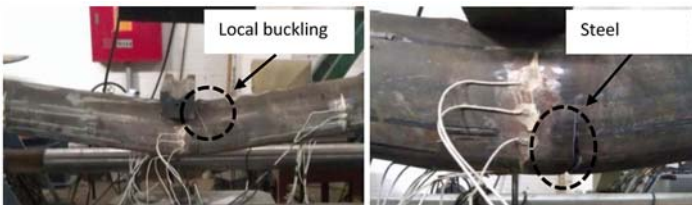
Figure 5.32 Failure mode of TPB_C1.
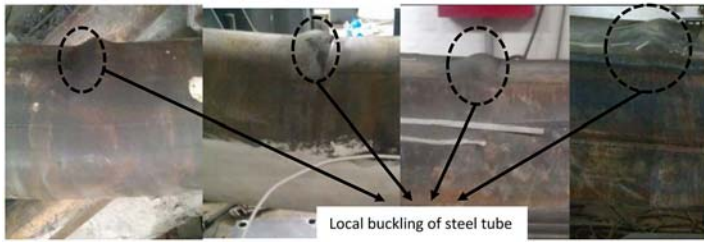
Figure 5.33 Failure mode of other specimens (except TPB_C1).
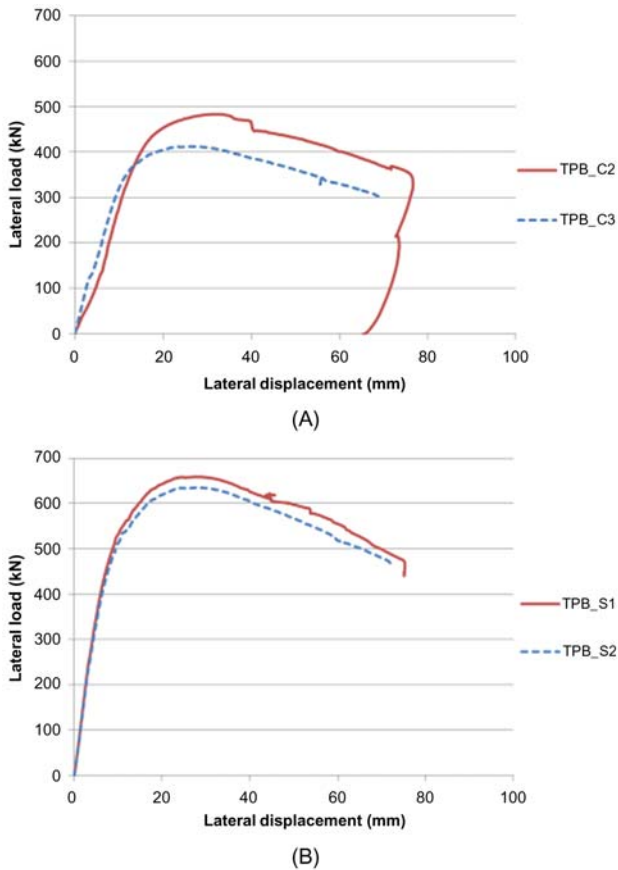
Figure 5.34 Effect of hollow core: (A) circular CFDST and (B) square CFDST.

Fig. 5.35 shows the effect of the cross-sectional geometry on the test specimens. It was shown that, although the overall behaviors of the circular and square specimens followed a similar pattern, the peak flexural load capacities of the square specimens were significantly larger than those of the circular
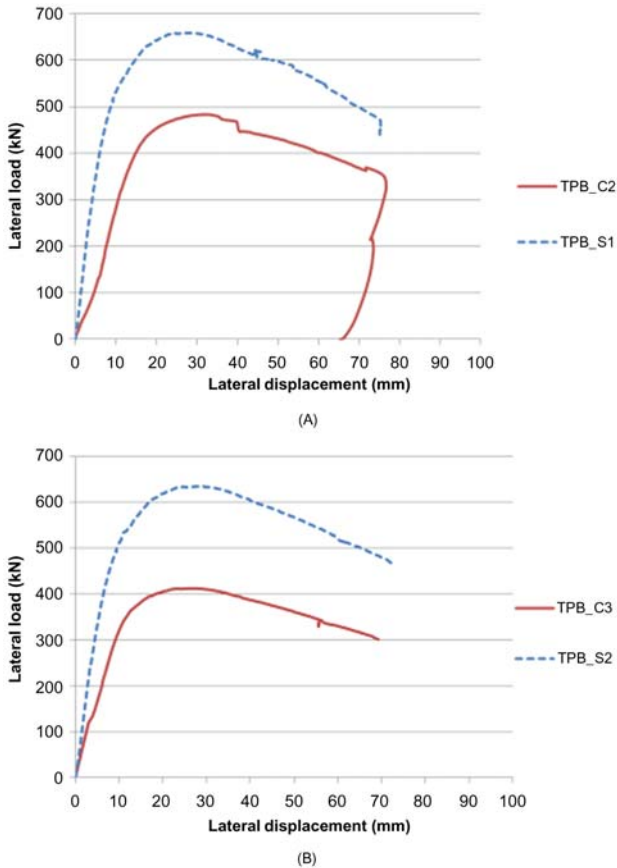
Figure 5.35 Effect of cross-sectional geometry (A) C2 versus S1 and (B) C3 versus S2.

specimens. In addition, the initial stiffness (i.e., the slope of the ascending branch) of the square specimens was also larger than those of the circular specimens. This finding indicates that the better confinement gained by the circular cross-section does not significantly enhance the flexural load capacity as it does to the axial load capacity.

5.3.1.2   Phase two: the blast experiment

Because this study mainly focuses on the residual performance of CFDST columns after blast loading, the blast test itself therefore is not discussed in great detail. The results of the blast test are given in Table 5.11.

To explore the relationship among the residual deflection, the blast load, and the geometry of the specimen, a normalized parameter λ is introduced which is a dimensionless form of the initial kinetic energy of the CFDST specimen [49].

Table 5.11 **Detailed information for each blast test specimen**

Test series	Label	Specimen setup	L (mm)	Nominal outer dimensions ($D \times t_{so}$)	Nominal inner dimensions ($D \times t_{io}$)	TNT (kg)	Axial load (kN)	Maximum $\triangle$ (mm)	Residual $\triangle$ (mm)
Square specimens	S1A	a*	2500	210 × 5	110 × 5	35	—	41	16
	S1B	a	2500	210 × 5	110 × 5	50	—	49	22
	S2A	a	2500	210 × 5	110 × 5	35	1000	36	8
	S2B	a	2500	210 × 5	110 × 5	50	1000	—	14**
	S3A	a	2500	210 × 5	110 × 5	50	1000	41	8
	S3B	a	2500	210 × 5	—	50	1000	50	10
Circular specimens	C1A	b	2500	210 × 5	110 × 5	35	—	98	65
	C1B	c	2500	210 × 5	110 × 5	35	—	50	20
	C2A	b	2500	210 × 5	110 × 5	35	1000	—	39**
	C2B	c	2500	210 × 5	110 × 5	17.2	—	35	12
	C3A	b	2500	210 × 5	110 × 5	50	1000	91	52
	C3B	b	2500	210 × 5	—	50	1000	83	43

*Different experimental setups.
**LVDT readings were lost for S2B and C2A, residual displacements were manually measured.

$$\lambda = \frac{mv_0{}^2 L^2}{M_{\mathrm{u}} H} \tag{5.6}$$

where m is the mass per unit length, v_0 is the initial velocity of the specimen, L is half of the effective length of the specimen, M_{u} is the ultimate moment capacity, and H is the depth of the specimen.

Table 5.12 lists the parameters needed to calculate the value of λ for each CFDST specimen used in the blast experiment. The initial velocity was derived from differentiating the displacement−time history of each specimen. According to Zhao et al. [12], when subjected to flexural loading, the outer steel of a CFDST column behaves in the same way as a CFST column, whereas the inner steel tube behaves in a similar way as an empty steel tube. Therefore the ultimate moment capacity of a CFDST column can be approximately by simply superposing the section capacity of an inner tube and that of an outer tube filled with concrete:

$$M_{\mathrm{CFDST}} = M_{\mathrm{inner\ tube}} + M_{\mathrm{outer\ tube\ with\ concrete}} \tag{5.7}$$

The step-by-step calculations for M_{CFDST} have been demonstrated by Zhao and Choi [50] in detail, thus only the results are given hereafter. It should be mentioned that because UHPFRC is used in this research, its tensile strength shall not be ignored in calculation.

It can be observed that specimens S3B and C3B deviated from the rest of the points quite significantly. This could be due to the fact that both S3B and C3B were CFST specimens (i.e., no hollow section inside) which were structurally different from the rest of the CFDST specimens. Fig. 5.36 also reveals that the residual deflection of a CFDST column increased linearly, regardless of the cross-sectional geometry, and the relationship can be expressed as:

$$\text{Residual deflection} = 13.14\lambda + 1.18 \tag{5.8}$$

5.3.1.3   Phase three: the residual performance test

The residual performance tests were carried out in the Joint Research Centre of Tianjin Chengjian University and The University of Adelaide. The same experiment machineries used for the previous static tests were also used for this test. During the experiment, instead of directly loading specimens to their peak capacities, the loading schematic in Fig. 5.37 was introduced. At first, the specimen was gradually loaded axially to 500 kN, it was then maintained at this load level for 60 s to eliminate any inhomogeneity in the specimen. This procedure was also repeated at 1000 and 2000 kN load levels to achieve the best stability.

5.3.2   Test results

Figs. 5.38 and 5.39 show the residual axial load versus axial shortening diagrams of all test specimens and for comparison purpose, the curves of the undamaged

Table 5.12 **Parameters of each specimen for** λ

Specimen	TNT (kg)	Axial load (kN)	Mass per unit length (kg m^{-1})	Initial velocity (m s^{-1})	Half column length (m)	Ultimate moment capacity (N m)	Cross-sectional depth (m)	Residual deflection (mm)	λ
S1A	35	0	115.3	18.3	1.15	269,200	0.21	16	0.90
S1B	50	0	115.3	28	1.15	269,200	0.21	22	2.11
S2A	35	1000	115.3	13	1.15	269,200	0.21	8	0.46
S2B	50	1000	115.3	—	1.15	269,200	0.21	14	
S3A	50	1000	115.3	22	1.15	269,200	0.21	8	1.31
S3B	50	1000	128	33	1.15	230,400	0.21	10	3.81
C1A	35	0	90.6	43.3	1.15	183,800	0.21	65	5.82
C1B	35	0	90.6	24	1.15	183,800	0.21	20	1.79
C2A	35	1000	90.6	—	1.15	183,800	0.21	39	—
C2B	17.2	0	90.6	16	1.15	183,800	0.21	12	0.79
C3A	50	1000	90.6	36.8	1.15	183,800	0.21	52	4.20
C3B	50	1000	100.5	45.6	1.15	164,000	0.21	43	8.02
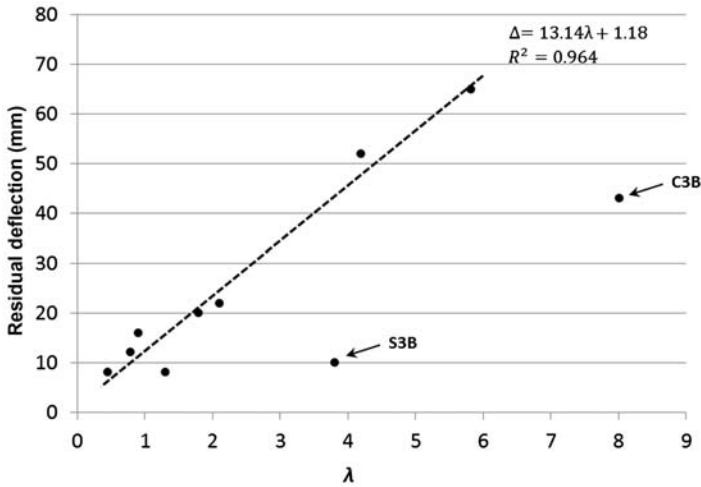
Figure 5.36 Residual deflection versus dimensionless parameter λ.
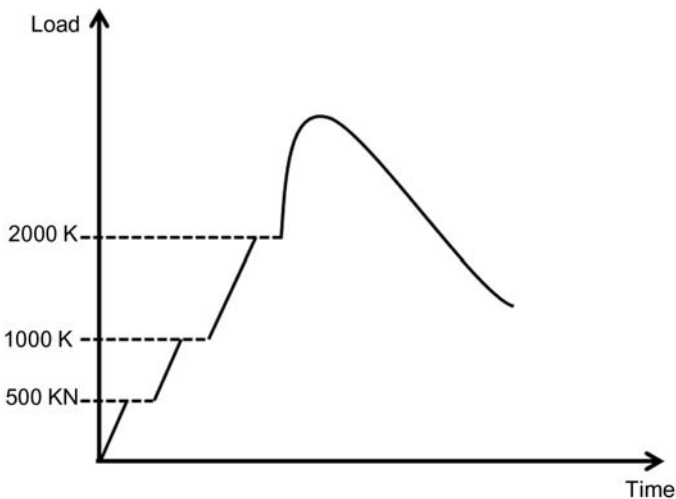
Figure 5.37 The loading schematic for residual capacity test.

specimens were also included. As a result of the damage accumulated during the blast test, none of the test specimens could carry as much axial load as before. In addition, all damaged specimens also behaved in a much less ductile manner under axial compressive load when compared to the undamaged control specimens.

The residual axial load capacities of the test specimens are listed in Table 5.6. The damage criterion is defined as the ratio between the residual axial load capacity
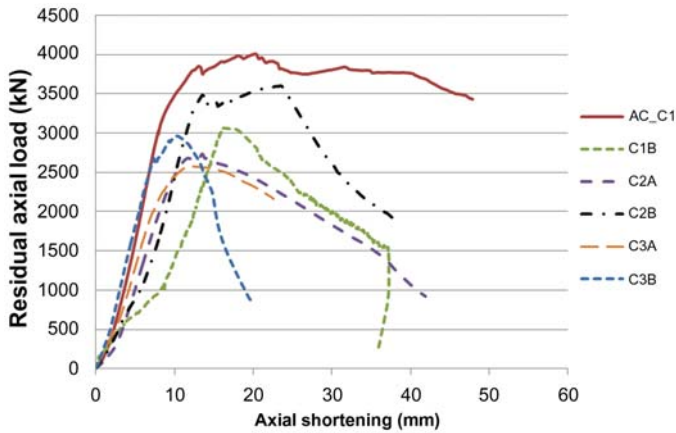
Figure 5.38 The residual axial load versus axial shortening histories for circular specimens.
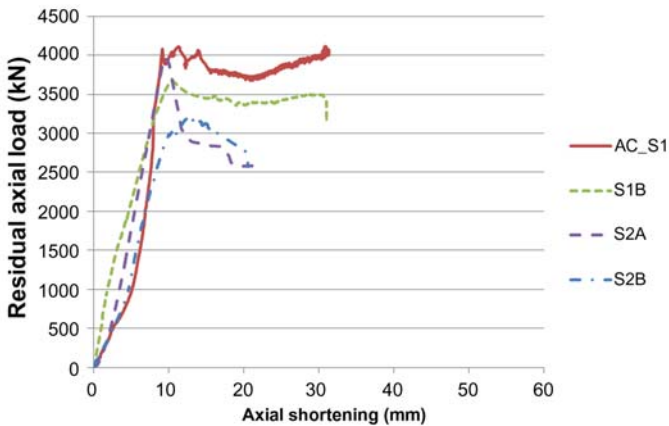
Figure 5.39 The residual axial load versus axial shortening histories for square specimens.

and the designed axial load capacity of an undamaged specimen, known as the damage index D [51]:

$$D = 1 - \frac{P_{N_{\text{residual}}}}{P_{N_{\text{undamaged}}}} \tag{5.9}$$

To calculate the damage index for the CFST specimen C3B, its designed axial load needs to be calculated. It was estimated by simply calculating the extra nominal axial capacity obtained by taking out the inner steel tube and then filling the hollow section by UHPFRC.

Table 5.13 indicates that all damage indices of the test specimens were within 0.4, meaning only minor to moderate damage was done to the specimens during the

Table 5.13 Results of residual performance test

Specimen label	TNT (kg)	Test setup	Applied axial load (kN)	Axial load capacity (kN)	Residual axial load (kN)	Residual deflection (mm)	Max. support rotation (°)	Damage index
S1B	50	a	—	4025	3670	22	2.44	0.09
S2A	35	a	1000	4025	3970	8	1.79	0.01
S2B	50	a	1000	4025	3184	14	—	0.21
C1B	35	c	—	4000	3060	20	2.49	0.24
C2A	35	b	1000	4000	2733	39	—	0.32
C2B	17.2	c	—	4000	3594	12	1.74	0.10
C3A	50	b	1000	4000	2573	52	4.52	0.36
C3B	50	b	1000	4780	2962	43	4.13	0.38
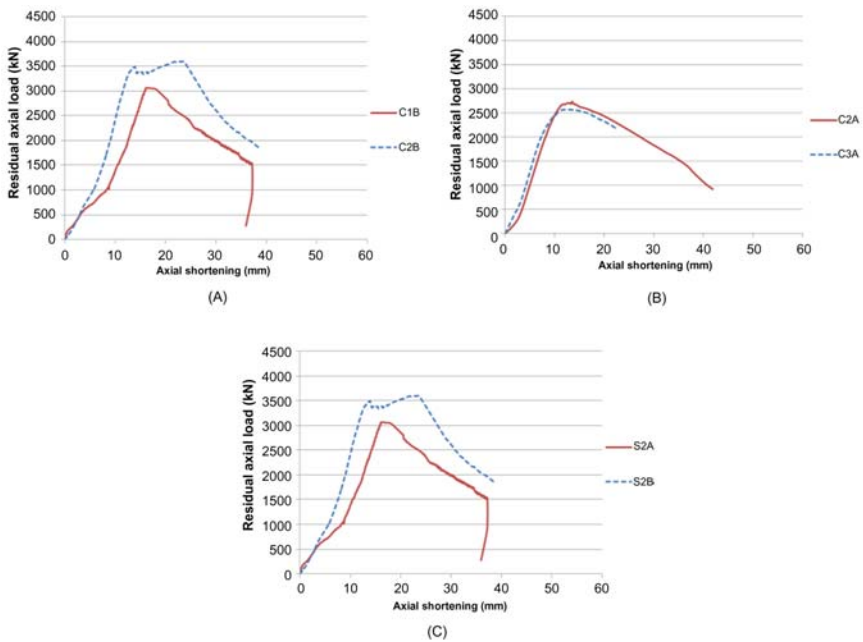
Figure 5.40 Effect of explosive charge weight on residual performance (A) C1B versus C2B, (B) C2A versus C3A and (C) S2A versus S2B.

blast test despite that large TNT-equivalent charge weight was used and placed at a small standoff distance.

5.3.2.1 Effect of the explosive charge weight

Fig. 5.40 shows the effect of explosive charge weight on the residual axial capacity. It is conclusive that, with the same applied axial load, specimens subjected to lesser explosive charge weight can always retain more residual axial capacity regardless of the cross-sectional geometry, thus having a smaller damage index.

5.3.2.2 Effect of the hollow core

From Fig. 5.41, the CFST specimen C3B was able to retain a larger residual axial capacity than the CFDST specimen C3A under the same blast load. However, because specimen C3A had a smaller designed axial load capacity, the damage indices of both specimens were very similar. In addition, specimen C3A seems to have a more ductile behavior over specimen C3B.

5.3.2.3 Effect of the axial load

It can be noticed in the previous section that the axially loaded CFDST column (e.g., S2B) always had a smaller residual deflection than the axial-load−free column (e.g., S1B) under the same blast loads. However, as shown in Fig. 5.42, the
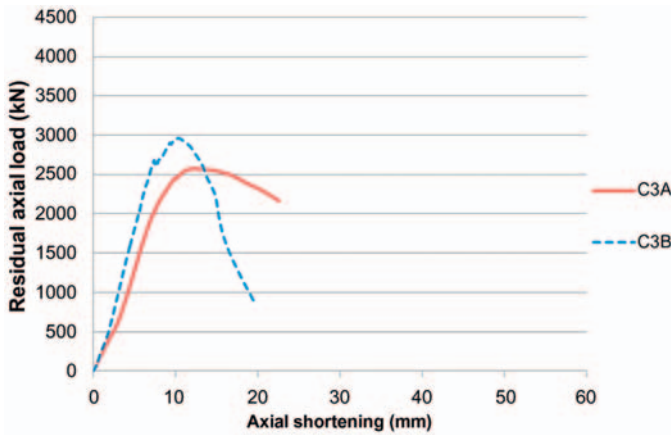
Figure 5.41 Effect of hollow core on residual performance.
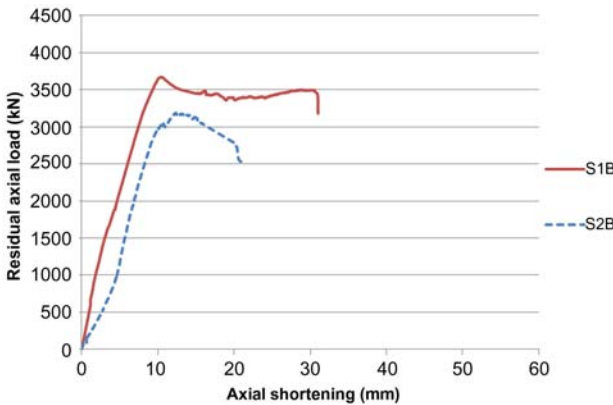
Figure 5.42 Effect of axial load on residual performance.

CFDST specimen (e.g., S1B), which was not previously axially loaded in a blast event, can not only behave in a more ductile manner, but also retain a greater residual axial capacity, thus resulting in a smaller damage index, than an previously axially loaded CFDST specimen (e.g., S2B).

5.3.2.4   Failure mode

Table 5.14 summaries the failure modes of all test specimens and Figs. 5.43 and 5.44 depict the deformed shape of the circular and square specimens, respectively.

For the circular CFDST columns, it was found that if the damage index was less than 0.3, local buckling of steel tube was more likely to happen (i.e., C1B and C2B); otherwise, steel rupture was more likely to happen (i.e., C2A and C3B). The only exception was specimen C3A, whose failure mode was global flexural failure

Table 5.14 Failure modes of all specimens

Label	Failure modes	Damage index
S1B	Local buckling at ends	0.09
S2A	Local buckling at mid-span	0.01
S2B	Local buckling at mid-span and ends	0.21
C1B	Local buckling at mid-span and ends	0.23
C2A	Outer steel rupture at mid-span	0.32
C2B	Local buckling at mid-span	0.10
C3A	Global flexural failure	0.36
C3B	Outer steel rupture at mid-span	0.38

(A)

(B)   (C)

(D)

(E)

Figure 5.43 Failure modes of circular specimens: (A) C1A, (B) C2A, (C) C2B, (D) C3A, and (E) C3B.
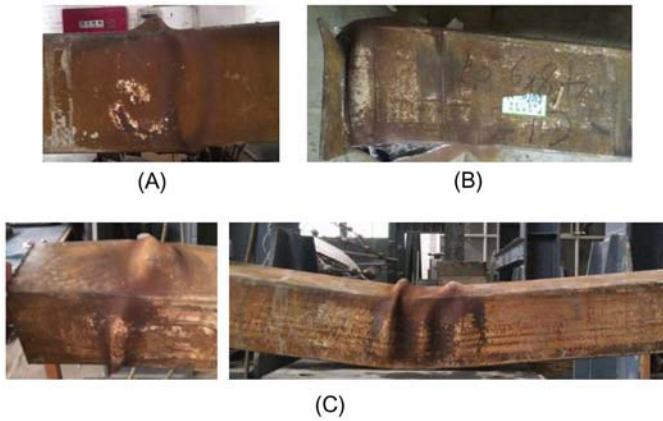
Figure 5.44 Failure modes of square specimens: (A) S1B, (B) S2A, and (C) S2B.

despite having a damage index of 0.36. However, it can be found in Fig. 5.43 that the displacement curve of specimen C3A was very similar to that of specimen C2A (the latter was subjected to a lesser blast load during the blast test with the rest of the parameters being the same) except that the loading somehow stopped when its axial shortening reached 23 mm, whereas the rest of the circular specimens were normally loaded until column instability was observed; also, no obvious sign of local buckling of steel was seen on specimen C3A either. It is then reasonable to speculate that if specimen C3A was further loaded until failure, it would fail due to mid-span rupture just like C2A. Elchalakani et al. [52] also reported a similar phenomenon (i.e., rupture of steel tube near mid-span) on CFST columns under large deformation cyclic loading.

However, for square specimens, local buckling at mid-span and/or column ends was the main failure mode with no signs of steel rupture. This type of local damage mode was also observed by Zhao et al. [53] where they subjected square CFST columns to cyclic axial loading.

5.3.3 Conclusion

This study has presented an experimental study on the static, dynamic, and residual performance of concrete-filled double-skin steel tube (CFDST) columns filled with UHPFRC after close-range blast loading. The following conclusions can be drawn based on the test results and observations:

1. The axial load capacities of undamaged circular and square CFDST specimens were very similar, which were 4000 and 4025 kN, respectively, although square specimens had larger nominal cross-sectional area. This is probably due to better confinement provided by the circular cross-section.
2. Under static lateral load, the flexural load capacity of a square CFDST specimen was larger than its circular counterpart; also, an axially loaded CFDST specimen, with about

25% of its axial capacity, yielded a larger flexural load capacity than an axial-load—free counterpart; however, this also led to a reduction in the ductility.
3. A dimensionless parameter λ was introduced to describe the relationship among the residual deflection, the blast load, and the geometric dimension of the CFDST specimens. It was found that the residual deflection almost increased linearly with λ and the equation describing this linear relationship was also derived.
4. A damage index was used to assess the residual performance of CFDST specimens after blast loading and it was found that the damage indices of all CFDST specimens were less than 0.4, indicating that the CFDST specimens were able to retain more than 60% of its axial load capacity even after severe blast loading.
5. During the residual axial capacity tests after close-range blast loading, localized buckling failure of the outer steel tubes at mid-span and/or column ends always occurred for square CFDST, whereas for circular CFDST, localized buckling failure occurred when the damage level was low and steel rupture happened when the damage level was high. The failure modes were similar to those of CFST members subjected to damage caused by large deformation cyclic loading.

5.4 Numerical simulation of concrete-filled steel square columns against blasts

5.4.1 Finite element analysis of concrete-filled steel tube members

The finite element model was developed using steel and concrete elements in LS-DYNA [54]. To ensure the simulating accuracy and efficiency, the steel tube and the concrete were simulated by eight-node solid elements with single-point integration algorithm. In this study, LS-DYNA/Implicit Solver was used for the static analysis (i.e., the three-point bending test) and LS-DYNA/Explicit Solver was used for the dynamic analysis (i.e., the blast test). Viscos-type hourglass control was activated during the blast test simulation to prevent element distortion and zero energy modes.

5.4.1.1 Concrete model

The K&C concrete model (MAT CONCRETE DAMAGE REL3) was used herein because it is able to model the behaviors of concrete member subjected to active/passive confining stress and high strain rate effect which is particularly suitable for the simulation of blast experiment [55]. A number of previous studies have already demonstrated the ability of the K&C concrete model to provide a robust representation of the complex behaviors of concrete structures under blast load [51,56—58]. The material model provides a parameter self-generation function where the entire set of material properties is generated based on the unconfined compressive strength of the concrete. However, according to the recently released validation studies [55,59], the K&C material model is mesh-size sensitive, especially for concrete under little to moderate confinement, where the default generated parameters are only valid for mesh size around 25.4 mm (1 inch). To achieve an accurate representation of

concrete element with, on average, 8 mm mesh size in this study, necessary modifications have to be made to three parameters namely $B1$, $B2$, and Omega which governs the compressive damage evolution, tensile damage evolution, and volume expansion, respectively. The equations for calculating $B1$ and $B2$ are provided by Wu et al. [59]:

$$B1 = 0.34 \times h + 0.79 \tag{5.10a}$$

$$B2 = \left(0.09 \times w_{lz}^2 - 0.98 \times w_{lz} + 3.06\right) \times (1 - 0.004 \times f_c'^2 + 0.097 \times f_c' - 0.484) \tag{5.10b}$$

where h is the characteristic length of the element in the unit of inch; w_{lz} is the aggregate size in the unit of inch and w_{lz} must be set to smaller than the element regardless of the actual aggregate size; f_c' is the unconfined compressive strength in the unit of ksi.

Additionally, Omega, which controls the volume expansion, is suggested to be 0.75 for a case without confinement and 0.9 for a confined case. Table 5.15 summarizes the key parameters of the K&C material model used in this study.

It is well known that under high strain rate impact, the strength of concrete can significantly increase, by more than 100% for concrete in compression and by more than 600% for concrete in tension [56]. The dynamic increase factor (DIF) is usually used to represent the increase of the compressive and tensile strengths of concrete under blast loading. For concrete in compression, the CEB Code [60], which has been widely used by most researchers as an accurate representation of actual behavior, is adopted.

5.4.1.2   Steel model

Material model 24, namely MAT PIECEWISE LINEAR PLASTICITY, is used to represent the steel tube. It should be noted that an elasto-plastic stress−strain relationship for steel is assumed and the strain rate effect on the steel tube is incorporated by the Cowper and Symonds law which multiplies the yield stress by a factor.

Because the test required to obtain the exact values for parameters C and P is beyond this research scope, the test results from a series of steel tube crush tests

Table 5.15 Key inputs for Material 72

Model parameter	Value
f_c'	40 MPa
f_t	3.5 MPa
Poisson's ratio	0.19
$B1$	0.92 (default $= 1.6$)
$B2$	2.68 (default $= 1.35$)
Omega	0.9 (default $= 0.5$)

conducted in the past were directly adopted without modifications which suggested $C = 808$ s^{-1} and $P = 3.585$ are most suitable [61].

5.4.2 Experimental program

Detailed experimental tests on CFST columns under static and dynamic loads are presented in Section 5.2.1 and only key information is presented here.

5.4.2.1 Static tests

In total, four CFST columns were tested including two square CFST columns and two circular CFST columns; however, due to mechanical failure, the data of CFST column S1 were not recorded. Table 5.16 summarizes the results of the three-point bending tests. It is evident that the tested square specimen S2 exhibited a larger lateral load capacity than the circular specimen C2; moreover, the axially loaded specimen C2 also showed a slightly larger lateral load capacity than its axial-load−free counterpart C1.

5.4.2.2 Blast tests

During the blast test on specimen S3, the blast wave propagating into the test pit and several recording apparatus were destroyed. Consequently, the deflection−time histories of specimen S3 were not recorded successfully and only the residual deflection was measured manually afterward. Table 5.17 summaries the results of the blast test.

5.4.3 Finite element model validation

5.4.3.1 Validation of three-point bending tests

The corresponding LS-DYNA numerical model of the three-point bending test is presented in Fig. 5.45. The cross-sectional geometries and meshing for the CFST

Table 5.16 **Results of the three-point bending tests**

Column no.	Cross-section	Applied axial load (kN)	Maximum lateral load (kN)		Error (%)
			Test	LS-DYNA	
S1	Square (200 mm × 200 mm × 2.8 mm)	0	—	—	—
S2	Square (200 mm × 200 mm × 2.8 mm)	504	168	178	6
C1	Circular (194 mm Dia. × 2.8 mm)	0	88	87	0
C2	Circular (194 mm Dia. × 2.8 mm)	414	95	103	8.4

Table 5.17 **Results of the blast test**

Column no.	Cross-section	Tube thickness (mm)	TNT equivalence (kg)	Maximum deflection (mm)		Residual deflection (mm)	
				Test	LS-DYNA	Test	LS-DYNA
C3	Circular	3.8	25	20	23	4	5
S3		2.8	17.5	–	17	5	3
S4[a]	Square	2.8	35	60	46	34	38
S5		3.8	35	37	32	8	12

[a]For specimen S4, the recording of LVDT1 was missing thus the value of LVDT2, which is 380 mm from LVDT1, was used instead.
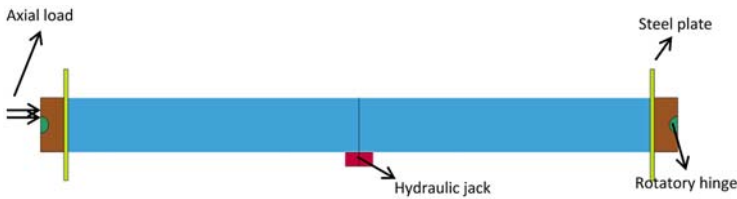
Figure 5.45 The numerical model for three-point bending test.
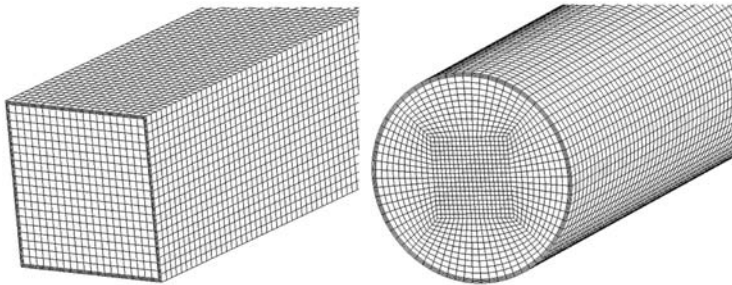
Figure 5.46 Element division of the numerical model.

members are shown in Fig. 5.46. In this research, the average mesh size was 8 mm and a mesh-size convergence study was also performed which suggested that further refining the mesh can only marginally improve the performance but greatly increase the computational burden. The interface between the steel tube and the concrete was merged to assume a perfect bonding between them because no research has mentioned noticeable debonding issue during their experiments. The model was simply supported at both ends and the axial load was applied on the rotatory hinge. It should be noted that the numerical model was analyzed by using the implicit solver in LS-DYNA to simulate the static loading condition.
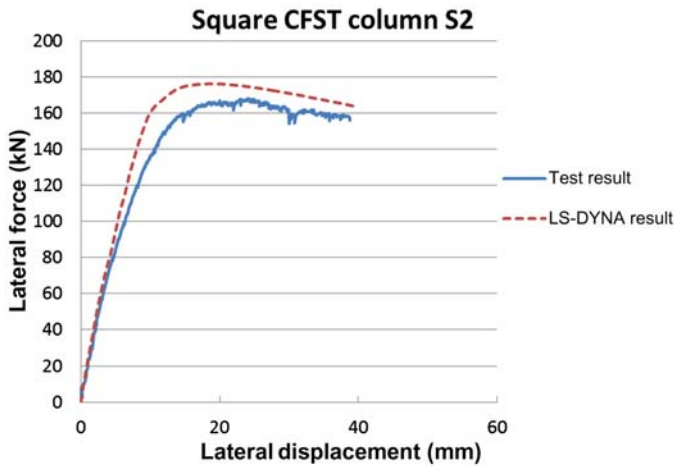
Figure 5.47 Comparison between the numerical results and test results for column S2.
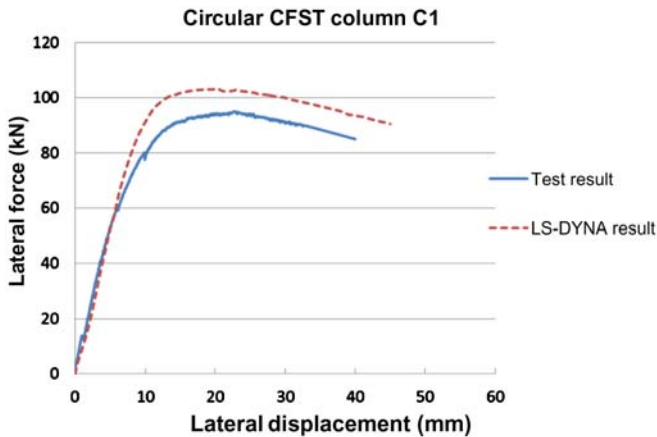
Figure 5.48 Comparison between the numerical results and test results for column C1.

Figs. 5.47−5.49 compare the force−displacement histories obtained from the laboratory tests and the numerical simulations. It is evident that the proposed numerical model can not only provide accurate predictions of the maximum lateral load bearing capacities of the tested CFST specimens with no more than 10% error, it can also correctly predict the lateral displacement at which the tested CFST columns reach their peaks along with the corresponding descending branches.

By comparing specimens C1 and C2, it is clear that the applied axial load increased the maximum flexural load capacity while sacrificing the specimen's ductility. To further demonstrate the influence of axial load on the flexural load capacity and the ductility, another numerical simulation was conducted on a circular
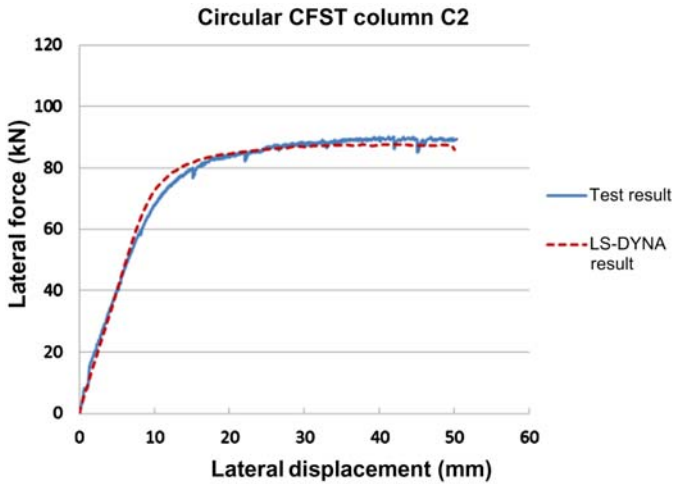
Figure 5.49 Comparison between the numerical results and test results for column C2.
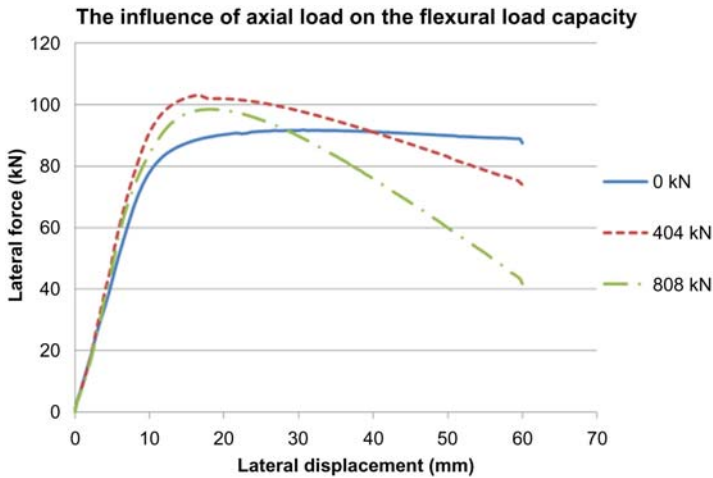
Figure 5.50 The influence of axial load on the flexural load capacity.

CFST specimen with an axial load of 808 kN, around 40% of the ultimate axial load capacity. Fig. 5.50 compares the force−displacement histories of circular CFST specimens with three axial load levels, namely 0%, 20%, and 40% of their ultimate capacity. It is evident that the ductility of a circular CFST specimen decreased significantly with the increase in the applied axial load; however, the flexural load capacity does not always increase with the increase in the applied axial load: the specimen with 404 kN axial load actually resulted in a greater flexural load capacity than the one with 808 kN axial load.

5.4.3.2 Validation of the blast tests

Fig. 5.51 shows the numerical model corresponding to the blast tests mentioned previously. The column was 2500 mm in length which was simply supported by four rollers—two at each ends and all rollers were fully fixed against motions in all directions. A thick steel plate was also placed in between the roller and the column to avoid stress concentration. A head and a footing were included in the numerical model for the purpose of applying axial load.

In blast effects analysis of columns, it is often necessary to use several phases to apply the loading to avoid undesired oscillation [55]. In this study, two loading phases, as shown in Fig. 5.52, were used and these included: (1) to apply the axial load to the column prior to the detonation of the explosive. This was done by
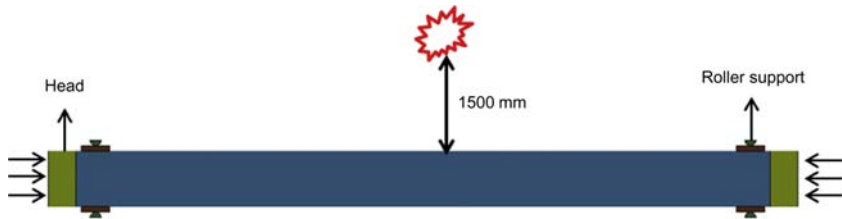
Figure 5.51 The numerical model for the blast test.
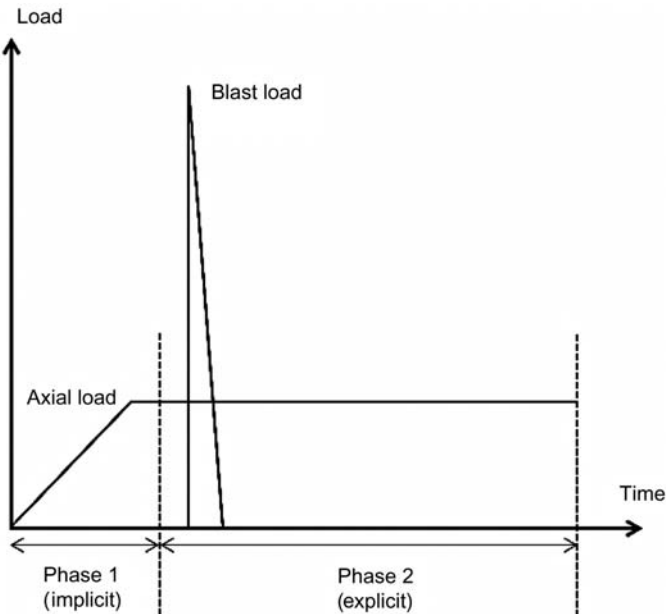
Figure 5.52 Two loading phases (not to scale).

applying a gradually increased axial quasistatic load to the top of the column implicitly to avoid too much oscillation in the way of wave propagation and (2) to apply the blast load while keeping the axial load unchanged and at this stage, the computational algorithm was switched from implicit to explicit to allow for dynamic analysis of the CFST specimens.

In LS-DYNA, one approach to simulate a blast event is to build an air domain which contains the explosive and target structure inside. However, to capture the realistic blast physics such as wave propagation within the air, a very high grid resolution is required which is too computationally expensive especially for a large standoff distance.

An alternative way is to use the ConWep air blast model [44] which was derived empirically from a large number of well-designed blast experiments. It is a built-in function, namely Load Blast Enhanced, in LS-DYNA which only requires simple inputs such as equivalent TNT charge weight and charge location [62]. The blast load acts on a set of user-predefined receptor segments (normally the area that faces the explosive) and the magnitude of pressure p that acts on each segment is calculated by

$$p = p_i \times \left(1 + \cos\theta - 2\cos^2\theta\right) + p_r \times \cos^2\theta \tag{5.11}$$

where p_i and p_r are the incident pressure and reflected pressure, respectively, and θ is the angle of incidence of the pressure wave.

ConWep air blast model has been widely adopted to investigate the structural response under blast load and it has shown a high level of accuracy with a reasonable computational cost compared to other techniques [63–65]. However, it should be noted that ConWep is only applicable to situations where there is no offset or superposition of blast waves and the explosive must be either spherical or hemispherical. In this research, ConWep air blast model was utilized due to the fact that (1) the method of building an air domain returned unrealistic computational time and (2) there was no obstacle between the explosive and the column so that ConWep was actually practicable.

5.4.3.2.1   Conversion between emulsion explosives and TNT explosives

Emulsion explosives were used in this study during the blast test. Simoens et al. [33] discovered that emulsion explosives generated blast wave that has peak pressures of the same magnitude as an identical mass of TNT and for impulse; however, a mass of emulsion explosives equals about 70% of that mass in TNT. It should be noted that Simoens et al. [33] only tested on a relatively small amount of emulsion explosives (i.e., up to 4.8 kg), therefore if the conversion factors still hold once much larger charge weight is used needs to be examined. In addition, according to Wu et al. [66], the shape of the explosive also plays a significant role in the pressure–time history. In this study, the applied charge weight is up to 50 kg which is too large to be made spherical; therefore the explosive is more cylindrical rather than
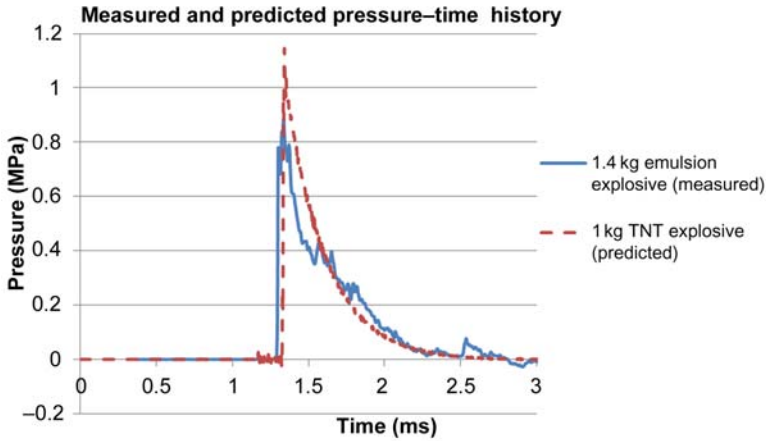
Figure 5.53 Comparison between 1.4 kg emulsion explosive and 1 kg TNT explosive.
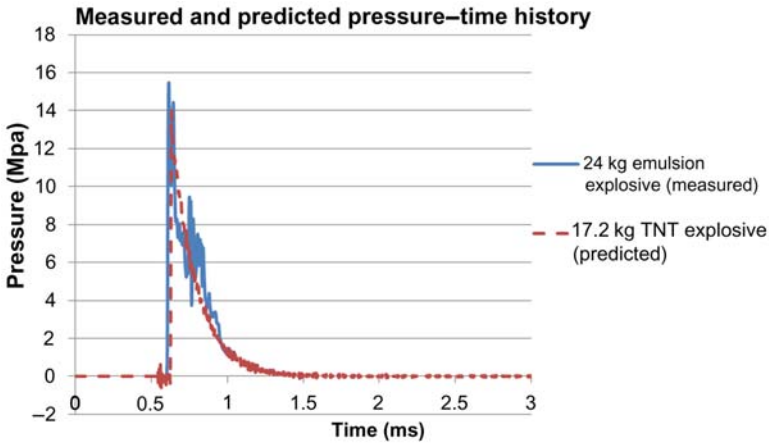
Figure 5.54 Comparison between 24 kg emulsion explosive and 17.2 kg TNT explosive.

spherical which could potentially make a significant difference in the blast pressure−time histories.

To investigate the aforementioned matters, ConWep is used as a benchmark for the peak overpressure and the impulse for TNT [44,45]. It should also be noted that in ConWep, the shape of the explosive is assumed to be spherical. Figs. 5.53−5.56 show the comparison between the measured pressure−time histories and the ConWep-predicted pressure−time histories of the corresponding TNT equivalences. Although the measured reflected pressures were slightly different to the predicted ones by equating 1.4 mass of emulsion explosive to 1 mass of TNT, the predicted
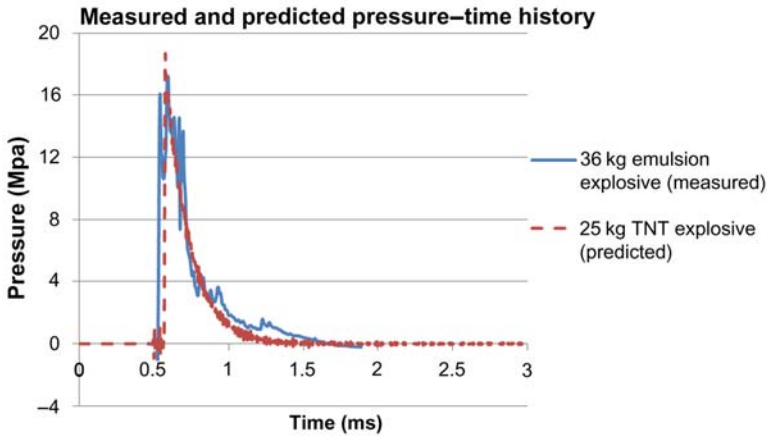
Figure 5.55 Comparison between 36 kg emulsion explosive and 25 kg TNT explosive.
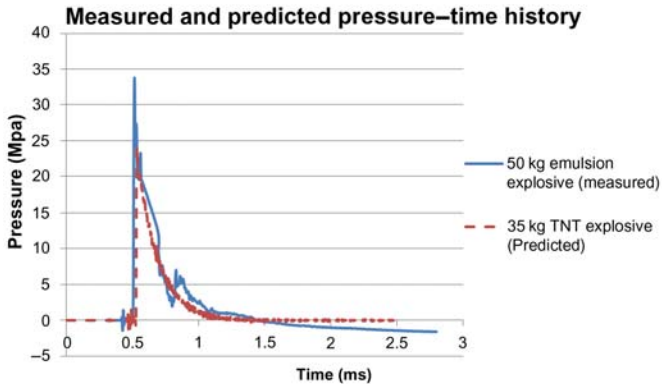
Figure 5.56 Comparison between 50 kg emulsion explosive and 35 kg TNT explosive.

blast impulses (i.e., the area enclosed by the curve) and loading duration agreed with the experiment data very well. Therefore it is of reasonable accuracy to use ConWep to simulate the blast pressure in LS-DYNA and it also makes no significant difference by assuming the explosive charge weight to be spherical although it is closer to be cylindrical in this study.

5.4.3.3 Validation results

Figs. 5.57–5.59 compare the predicted and measured displacement–time histories. The comparisons indicate that the predicted maximum deflection and period of oscillation correspond with the measured curves very well. Although there are
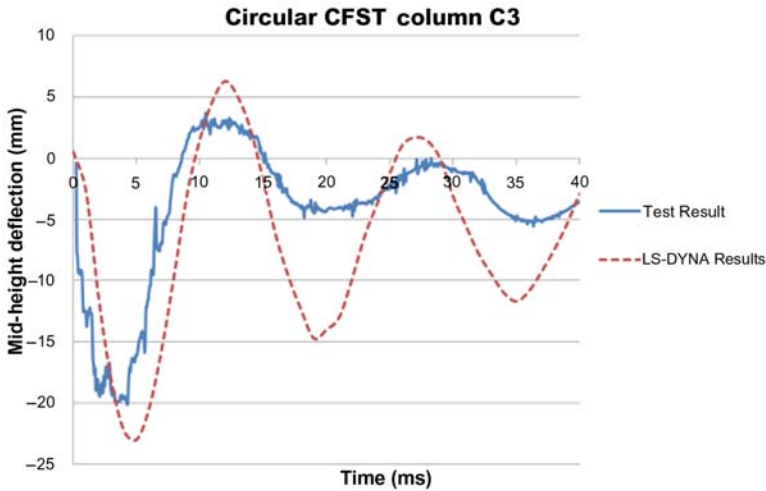
Figure 5.57 Comparison between the numerical results and test results for column C3.
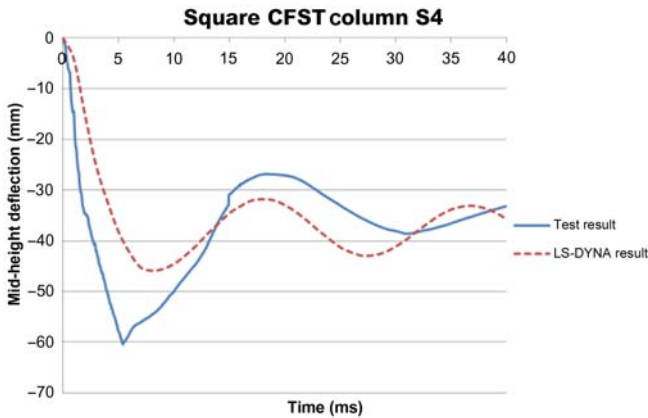
Figure 5.58 Comparison between the numerical results and test results for column S4.

discrepancies in the residual deflections between the test results and the predictions, the difference is no more than 10 mm which was acceptable considering the complexity and uncertainty associated with blast experiments.

It is well known that steel structure is prone to local buckling due to its thinness which can result in the reduction of load capacity. Although the concrete infill can delay the local buckling of the steel tube, it still cannot be prevented especially when subjected to large impact load [13,67]. Fig. 5.60 compares the deformed shape along with the crack formations between the tested specimen S4 and the numerical simulation. Fig. 5.61 evidently demonstrates the ability of the proposed
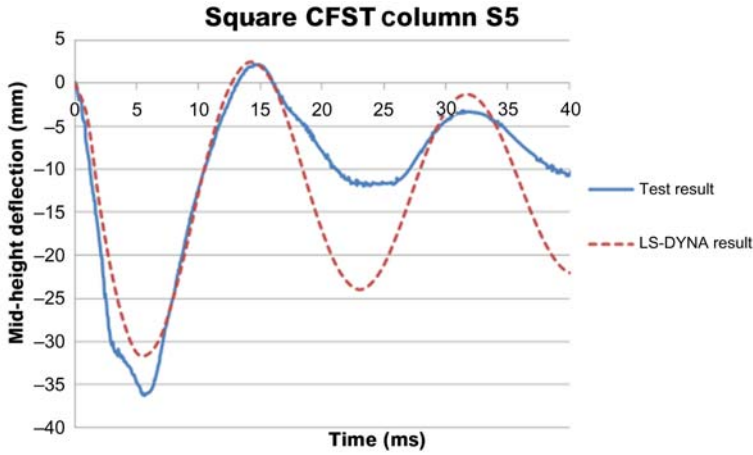
Figure 5.59 Comparison between the numerical results and test results for column S5.
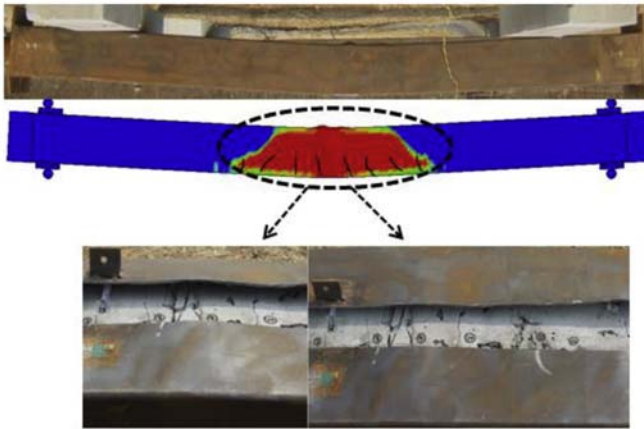
Figure 5.60 Comparison of the deformed shape and cracks from numerical and experimental studies for specimen S4.

numerical model to accurately capture the localized structural responses (i.e., local buckling of steel) during the blast experiment which can be hardly achieved by other analytical methods.

5.4.3.4 Energy absorbed by local and flexural deformation

The energy absorbed by local and flexural deformation was investigated based on the numerical simulation of specimen S4. The local deformation was only found at mid-span and its width was measured to be approximately 95 mm. According to
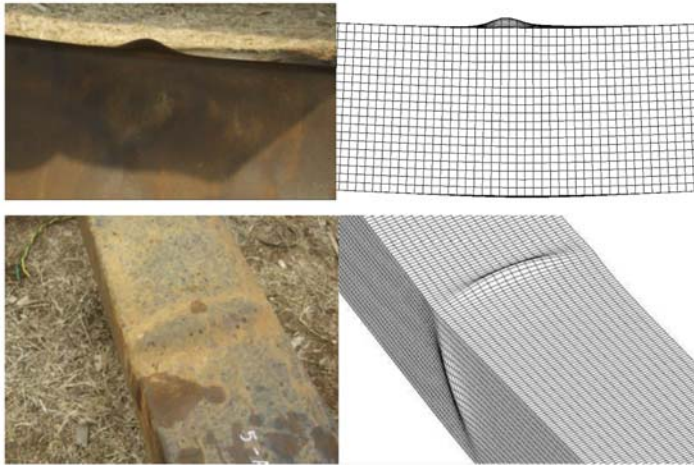
Figure 5.61 The observed local buckling (right) and the predicted local buckling (left) on specimen S4.

Jama et al. [30], the energy absorbed by local deformation can be up to 50% of the total energy absorbed for a steel SHS under transverse blast loads. Under blast loading, the work done by the external force is firstly turned into kinetic energy of the specimen and then the kinetic energy is further absorbed by local and global plastic deformation, which is also known as the internal energy. Fig. 5.62A shows the internal energy of the entirety of specimen S4 after blast loading and Fig. 5.62B shows only the internal energy of specimen S4 where the local deformation occurred. It should be noted that Jama et al. [30] assumed that the local deformation preceded the global deformation; however, it is not the case for CFST specimens in this research. It was observed from the numerical simulation that the specimen began to deform as soon as the blast wave reached (i.e., $t = 0$ ms), whereas the sign of local deformation was only found 3 ms later (i.e., $t = 3$ ms). The global and local deformation continued to develop simultaneously until 6 ms after the time of arrival (i.e., $t = 6$ ms), at which the local deformation was fully developed. The global deformation then continued to develop and reached its peak at $t = 13$ ms. Significant changes in slope of Fig. 5.62B can be noticed at $t = 3$ ms and $t = 6$ ms which indicates that the local deformation does have a notable impact on the energy-absorbing mechanism of CFST columns.

To compare the ratio between the energy absorbed by local and global deformation, it is assumed that between $t = 3$ ms and $t = 6$ ms, all of the energy absorbed in Fig. 5.62B was due to local deformation. It should be mentioned that this assumption overestimates the energy absorbed by local deformation because global deformation also happens between $t = 3$ ms and $t = 6$ ms simultaneously. With the assumption made, the energy absorbed by local deformation of specimen S4 was 2600 J and the energy absorbed by combined local and global deformation was 12,000 J which means that local deformation accounts for 22% of the total energy absorbed.
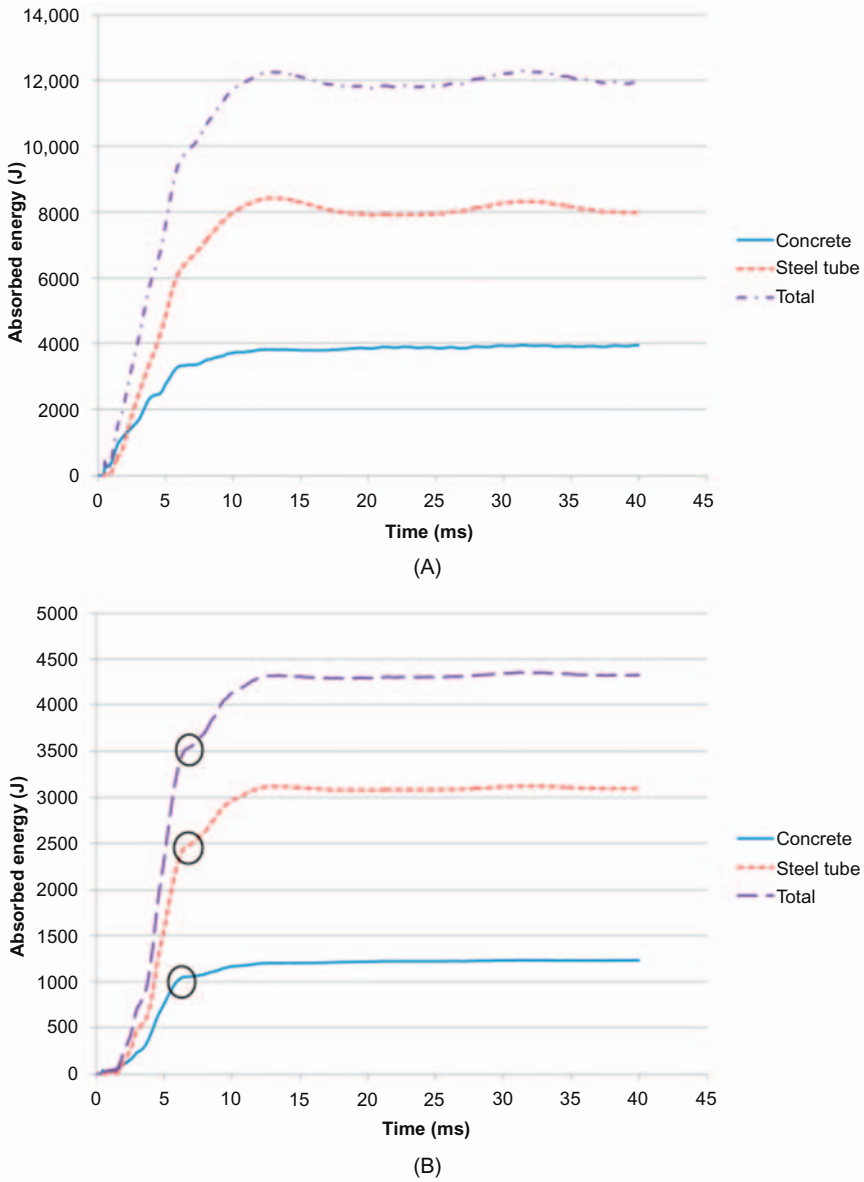
Figure 5.62 The internal energy of (A) the entire specimen S4 and (B) the mid-span part of S4 where local deformation occurred.

5.4.4   Conclusions

This section presented a numerical study of CFST members, with both circular and square cross-sections, under both static and blast loads and the following conclusions can be drawn based on the numerical results presented in this section:

1. The CFST member behaved in a very ductile manner under lateral static load. The applied axial load can slightly increase its flexural load capacity, however, at the cost of reducing the column's ductility at the same time.
2. The numerical model developed in this study can deliver accurate predictions for CFST members under transverse static load. When validated against the blast test, the model still corresponded with test results quite well in terms of the maximum deflection and the period of oscillation. Discrepancies in the residual deflections were found, however considering the complexity and uncertainty associated with a blast experiment, the error is still within the acceptable range.
3. Based on the numerical results, for a CFST member under blast loading, the majority of the energy is absorbed by global deformation due to the fact that local deformation of steel can be effectively prevented by the infilled concrete.

More parametric studies can be made using the developed numerical models in the future to address the key parameters that affect the overall behaviors of CFST members under blast loading.

5.5   Numerical modeling of concrete-filled double-skin steel tubular columns against blasts

5.5.1   Finite element modeling

5.5.1.1   Elements and boundaries

To conduct a parametric study, different model setups are used. However, for comparison purposes, a control specimen is introduced. The circular CFDST control specimen has a 210 mm outer diameter and a 100 mm inner diameter as shown in Fig. 5.63, with a clear span of 2500 mm. Both its inner and outer steel tubes are
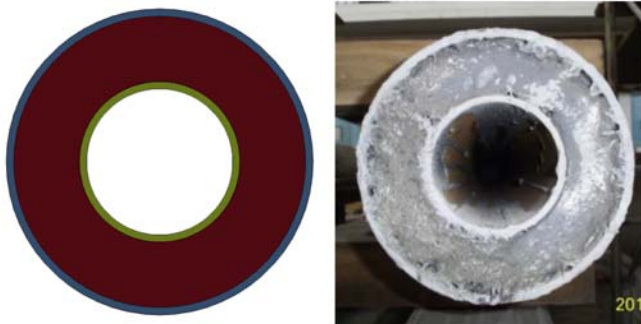
Figure 5.63 Circular cross-section of the numerical model (left) and the actual column (right).
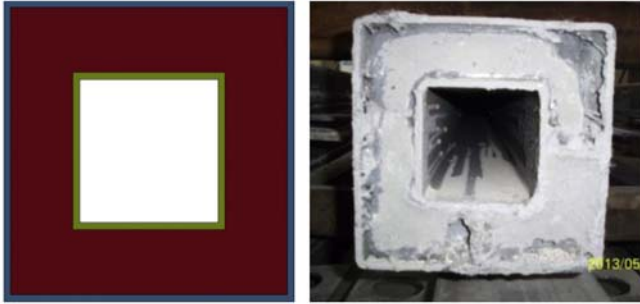
Figure 5.64 Square cross-section of the numerical model (left) and the actual column (right).
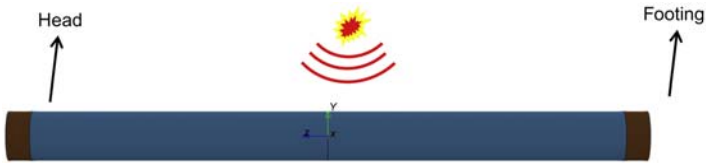
Figure 5.65 Model setup of circular column.

5 mm thick. All elements are built using hexahedrons to achieve the best stability, and solid elements of around 6 mm cube with single-point integration algorithm are used. Mesh-size convergence study suggests that further refinement of the mesh only has a marginal effect on the numerical results but significantly increases the computational effort.

Similarly, Fig. 5.64 depicted the square CFDST control specimen. It has a 210 mm outer side length and 100 mm inner side length. The rest of its parameters are the same as those of the circular column (Fig. 5.65).

As shown in Fig. 5.65, to provide higher fidelity for the column end constraints, a footing and a head are included in the numerical model. The outer face of head and footing are constrained against horizontal motions (i.e., in x and y directions)—both translational or rotational motions [51]. For a structural member with fully fixed-support conditions on both ends, brittle shear failure near the supports could be the potential concern. In circumstances where CFDST or CFT columns are used, hardly any studies but Wang et al. [13], who reported an occurrence of shear failure: it only occurred on the column with an extremely thin outer steel tube (1.7 mm) and there were no signs of shear failure on any other columns with a steel tube thicker than 1.7 mm. In this research, outer and inner steel tubes are both 5 mm thick, thus shear failure near supports is not expected nor considered. Furthermore, almost no researchers except Yu et al. [68] discovered noticeable slip between the concrete and the tube. Therefore, in this study, the nodes at the interface of concrete and steel tubes are merged to assume no debonding conditions.

5.5.1.2 Simulation of blast load

In LS-DYNA, one standard approach to simulate a blast event is to build an air domain that contains the explosive and target structure inside. However, to capture the realistic blast physics in which the wave propagates within the air, a very high grid resolution is required and this is too computationally expensive, especially for a large standoff distance.

An alternative way is to use the conventional weapons (ConWep) air blast model [44], which was derived empirically from a large number of blast experiments. It is a build-in function in LS-DYNA, which only requires simple inputs such as equivalent TNT charge weight and charge location. This model has been widely adopted to investigate the structural response under blast loads and it has shown a high level of accuracy with a reasonable computational cost compared to any other analytical techniques [63−65]. However, it should be noted that this model is only applicable to situations where there is no offset or superposition of blast waves and the explosive must be either spherical or hemispherical.

In this research, the ConWep air blast model is utilized due to the fact that no obstacle is present between the explosive and the column.

5.5.1.3 Validation of the uniaxial compression test

As mentioned previously, confinement effects due to composite action are very important for CFDST members. Therefore the proposed numerical model was validated against the uniaxial compression tests conducted by Fan et al. [69] {Fan, 2010 #55} to demonstrate the capability of the proposed LS-DYNA numerical model to accurately account for the strength enhancement due to confinement.

Two specimens reported by Fan et al. [69] were included in the validation study. They are both 720 mm in height, and one has a 240 mm outer diameter and 80 mm inner diameter and the other one has a 240 mm outer diameter and 120 mm inner diameter. The outer and inner steel tubes for both specimens are 4 mm thick. The elastic modulus of steel E_s is 200,000 MPa, and the modular of concrete E_c is 29,000 MPa. The average yield stress of steel is 280 MPa and the average cylinder strength of concrete is 29 MPa. The loading condition is axial compression applied by using the implicit solver in LS-DYNA to achieve force equilibrium at each time step. Fig. 5.66 shows the comparisons between the test results and the numerical results. In general, the numerical results slightly overestimate the initial stiffness of the tested CFDST specimens; however, the predicted ultimate axial load capacities and the predicted postyield behaviors are in close agreement with the experimentally measured values. With comparison to the ACI [70] design code as shown in Table 5.18, the numerical results only deviate from the experimental results by 8%, while the design code underestimates the axial load capacity by 26% because it does not take into consideration the concrete confinement.
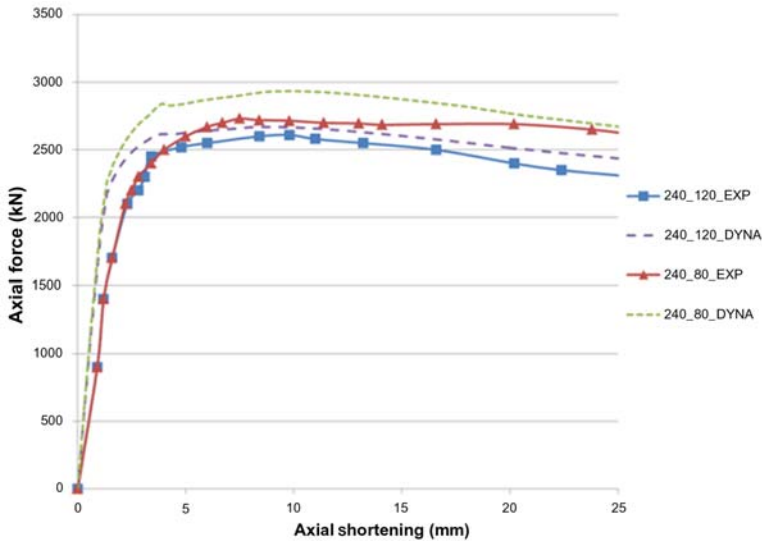
Figure 5.66 Validation results against experiment data [69].

Table 5.18 Values given by numerical model, ACI code, and test results

Column dimension	Experiment result	Numerical result	Num./ exp.	ACI prediction	ACI/ exp.
240×80	2735	2670	0.98	2072	0.76
240×120	2571	2930	1.14	1887	0.73

5.5.2   Parametric studies and discussions

The previously introduced numerically validated model is used to study the influence of different parameters on CFDST columns under blast loads. The parameters investigated in this research include concrete strength, outer and inner tube thicknesses, cross-sectional geometry, hollowness ratio, support condition, and axial load. The concrete strength varies from 30 to 60 MPa; the outer and inner tube thicknesses vary from 2 to 5 mm; the cross-sectional geometry is either circular or square; the hollowness ratio varies from 0 to 0.75; the support is either fixed or pinned, and the axial load ratio varies from 0% to 50% of the ultimate axial load capacity. The gauge point is located on the center of each column to measure the deflection−time history.

5.5.2.1   Concrete strength

To investigate the influence of the concrete strength on CFDST columns under blast loads, three different concrete strengths, namely 30, 45, and 60 MPa, are studied. The applied equivalent TNT charge varies from 20 to 80 kg and the standoff

Table 5.19 **Pressure and impulse values at various scaled distances**

TNT equivalence (kg)	Standoff distance (m)	Scaled distance (m kg$^{-1/3}$)	Pressure (MPa)	Impulse (MPa ms)
20	1.5	0.55	24.6	3.2
40	1.5	0.44	43.7	6.04
60	1.5	0.38	50.5	8.83
80	1.5	0.35	63.2	10.6
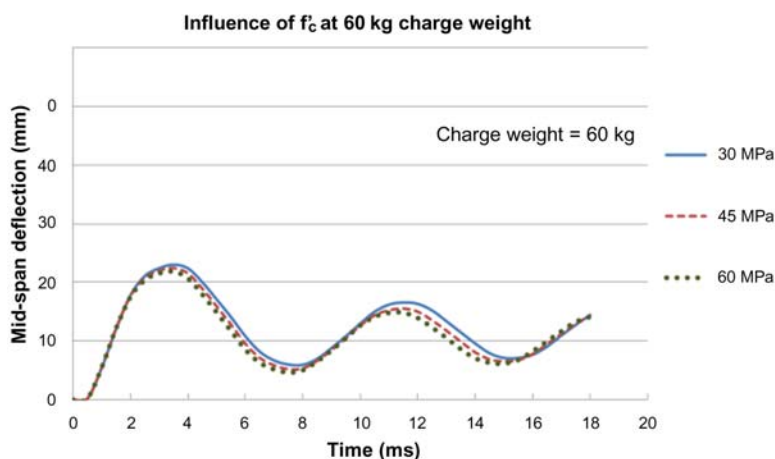
Figure 5.67 Influence of f'_c when charge weight = 60 kg.

distance remains 1500 mm for all cases thus making the scaled distance range from 0.35 to 0.55 m kg$^{-1/3}$. Table 5.19 lists the maximum pressure and impulse values of a blast event at a variety of standoff distances. The column configuration in this section is the same as the circular CFDST control specimen.

Interestingly, Fig. 5.67 shows that varying the concrete strength between 30 and 60 MPa when the column is subjected to 60 kg charge weight has no significant influence on the maximum deflection. It is believed that the steel tubes of a CFDST specimen are the main contributor to the section moment, which makes the concrete strength become insignificant as normal strength concrete is knowingly very weak in tension. Similar results were also reported by other researches on CFT columns as well [71].

Similar trends are also found when subjecting the column to 20, 40, and 80 kg charge weights, which are not further discussed herein.

5.5.2.2 Outer tube thickness

To investigate the influence of outer tube thickness on the response of CFDST columns under blast loads, the outer tube thickness is varied between 2 and 5 mm, while keeping the other parameters the same as the circular CFDST control specimen.

Fig. 5.68 shows the deflection−time histories for CFDST columns under the blast load induced by 60 kg TNT. In general, the column's maximum deflection decreases with increases in outer tube thickness. However, thicker the outer tube, the lower the reduction rate in the maximum deflection that can be achieved by further thickening. For example, by increasing the outer tube thickness from 2 to 3 mm, the maximum deflection can be reduced by 31%, whereas by increasing it from 4 to 5 mm, the reduction in the maximum deflection is only 17%.

Fig. 5.69 shows the maximum deflection versus outer tube thickness of the column under various loading conditions. The slope of these curves becomes steeper
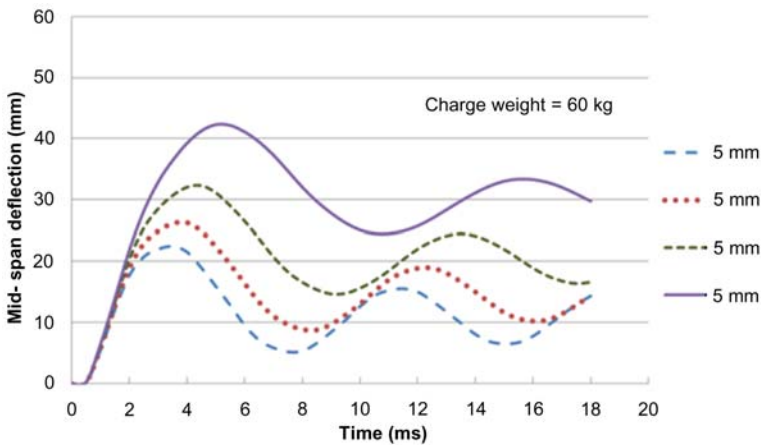
Figure 5.68 Influence of outer tube thickness when charge weight = 60 kg.
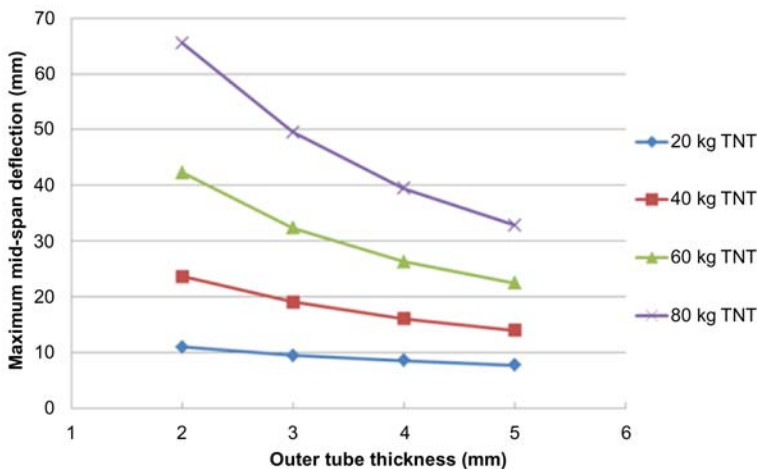
Figure 5.69 Maximum deflection versus outer tube thickness for various blast loads.

as the TNT charge weight increases, suggesting that it is more cost-effective to increase the outer steel tube thickness only when a large blast load is expected.

Moreover, it is also observed that local buckling (bulge on the steel tube) is likely to occur near the fixed ends on a column with a thinner outer tube rather than on one with a thicker outer tube as shown in Fig. 5.70.

5.5.2.3 Inner tube thickness

Similar to the study of outer tube thickness, the influence of inner tube thickness is also investigated in a similar fashion by varying the inner tube thickness from 2 to 5 mm while keeping the remaining parameters the same as for the circular CFDST control specimen.

Figs. 5.71 and 5.72 indicate that increasing the inner tube thickness can also reduce the maximum deflection, but much less significantly compared to increasing the outer tube thickness. This may be due to the fact that because the outer diameter is considerably larger than the inner diameter, increasing the outer tube thickness by 1 can result in a greater increase in the steel ratio than increasing the inner tube
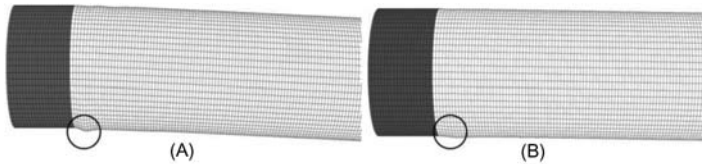
Figure 5.70 Local buckling near column support for (A) 2-mm-thick outer tube and (B) 5-mm-thick outer tube.
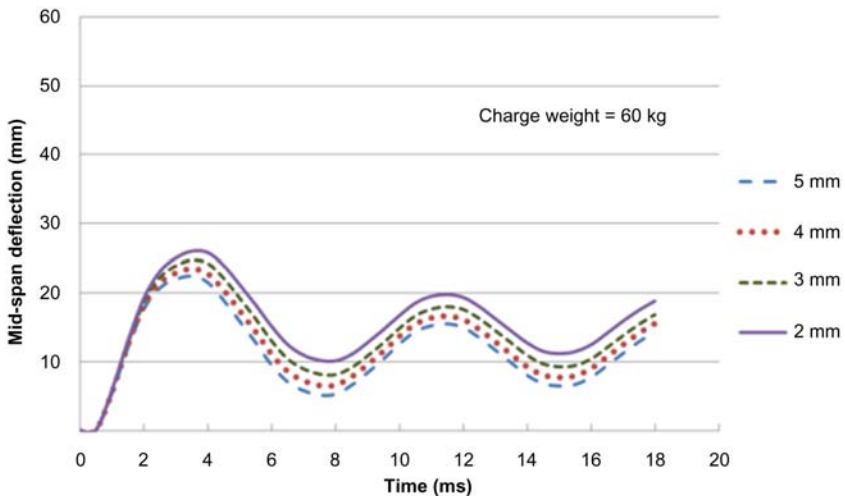
Figure 5.71 Influence of inner tube thickness when charge weight = 60 kg.
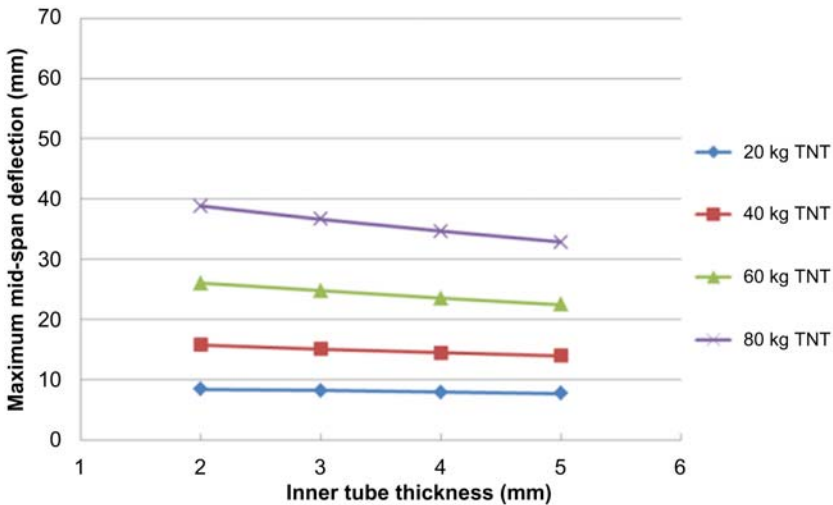
Figure 5.72 Maximum deflection versus inner tube thickness for various blast loads.

thickness by the same amount (e.g., increasing the outer tube thickness from 4 to 5 mm increases the cross-sectional area by 657 mm^2 while doing the same for the inner tube only increases the cross-sectional area by 317 mm^2).

5.5.2.4 Cross-sectional geometry

Two commonly used cross-sectional geometries, namely circular cross-sections and square cross-sections, are investigated in this section. Han et al. [21] suggested that under lateral static loads (i.e., cyclic flexural load), the energy dissipation ability of the CFDST column with a circular cross-section was much higher than those of the specimens with a square cross-section. Similar trends (as shown in Fig. 5.73) are also observed when subjecting CFDST columns to blast loads, but it is only valid when the explosive charge weight is more than 60 kg. However, for a moderate blast load (i.e., less than 40 kg TNT), columns with circular and square cross-sections both yield the similar maximum deflections.

To compare the blast force experienced by both circular and square columns in the numerical analysis, pressure−time histories recorded from 80 kg TNT at three locations on the cross-section of the mid-span are outputted as shown in Figs. 5.74−5.77. Sensor 1 is located right under the explosive, thus receiving the largest blast load. Sensor 3 is located at the edge, thus receiving the smallest blast load. Sensor 2 is located between sensors 1 and 3. The pressure−time histories recorded at sensor 1 are almost identical for both circular and square columns. Once looking at sensors 2 and 3, the maximum pressure on the circular columns declines dramatically, whereas no significant change in the maximum pressure is experienced by the square counterpart, consequently the impulse values for circular columns at locations 2 (6.42 MPa ms) and 3 (1.06 MPa ms) are 40% and 90%
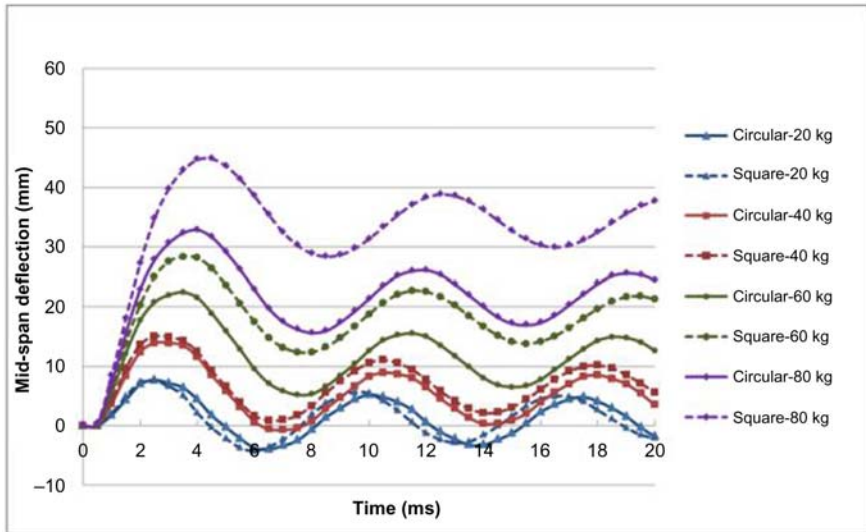
Figure 5.73 Influence of cross-sectional geometry.
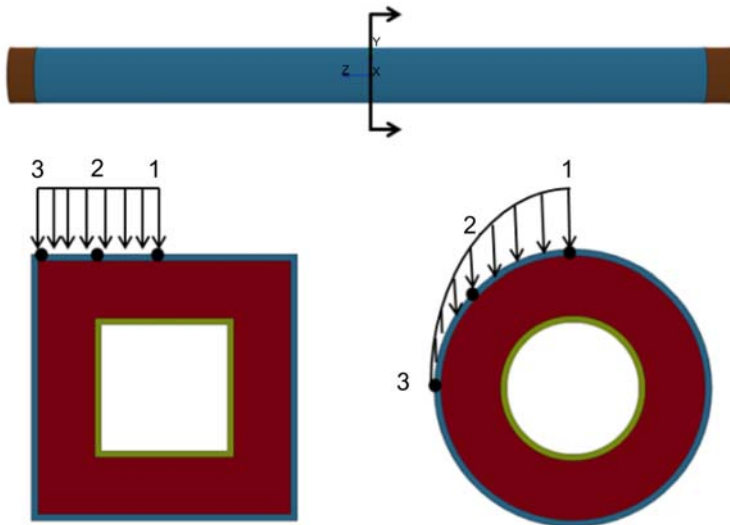
Figure 5.74 Locations of the pressure sensors 1, 2, and 3 and the pressure distribution.

smaller than those for square columns, respectively. The simulated results are some-
what in agreement with the experimental data of Allahverdi [72]. In his experiment,
it was observed that the cross-sectional geometry of an RC column could consider-
ably affect the blast wave propagation pattern. The impulse experienced by a circu-
lar column was, on average, 20% less than that experienced by a square column.
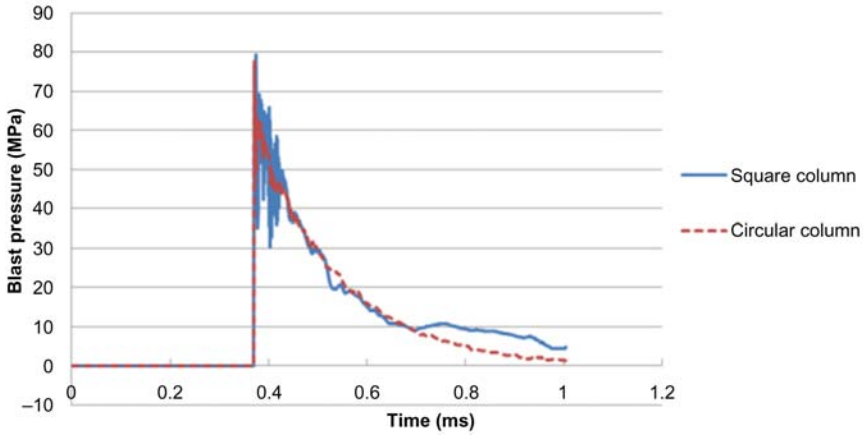
Figure 5.75 Force versus time history at sensor 1 for charge weight = 80 kg.
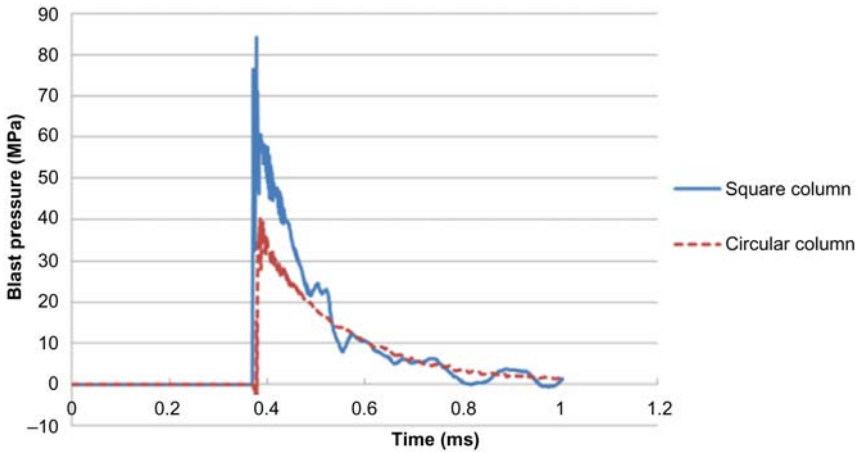
Figure 5.76 Force versus time history at sensor 2 for charge weight = 80 kg.

Another possible reason for square CFDST columns having a larger mid-span deflection than circular CFDST columns might be because the effective confinement area obtained from a square cross-section is much less than that from a circular cross-section [37−39]. The boundaries that identify the effective confinement of a square cross-section are four parabolas intersecting the edges at 45°, while the entire concrete area of a circular cross-section can be effectively confined as shown in Fig. 5.78.

5.5.2.5 Hollowness ratio

Hollowness ratio (χ) is defined as the ratio between the inner diameter D_i and the outer diameter D_o as shown in Fig. 5.79, and $\chi = 0$ indicates a CFT.
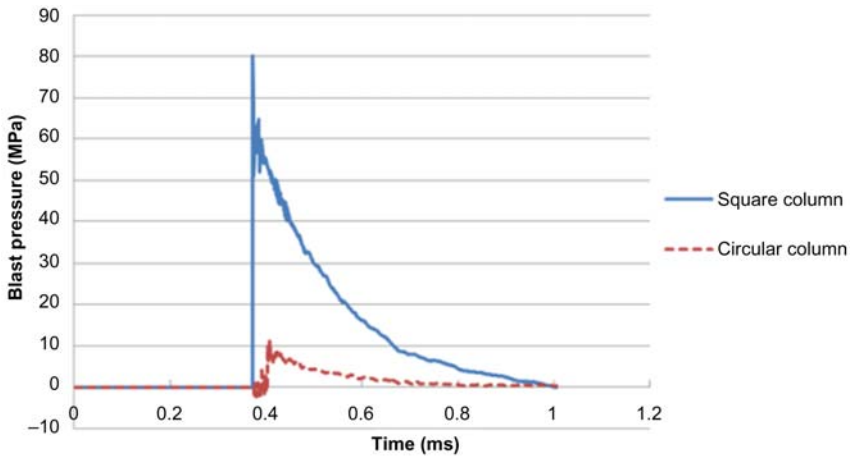
Figure 5.77 Force versus time history at sensor 3 for charge weight $= 80$ kg.
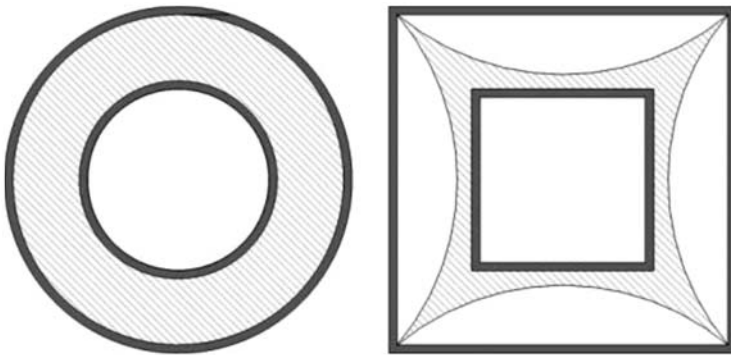
Figure 5.78 Effective confinement area (*shadowed*) for both circular and square cross-section [37].
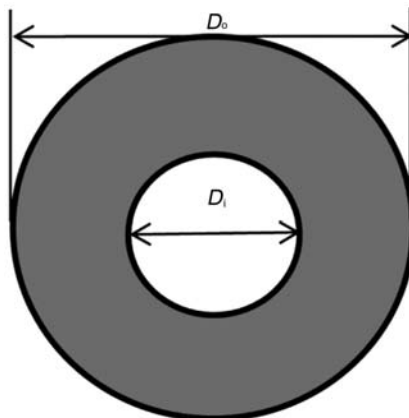
Figure 5.79 Hollowness ratio $\chi = \frac{D_i}{D_o}$.
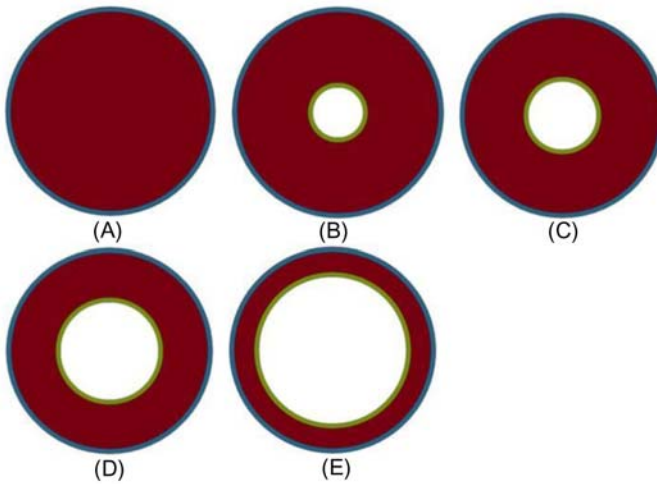
Figure 5.80 Cross-sections of columns with different hollowness ratios (A) $\chi = 0$, (B) $\chi = 0.25$, (C) $\chi = 0.35$, (D) $\chi = 0.5$ and (E) $\chi = 0.75$.
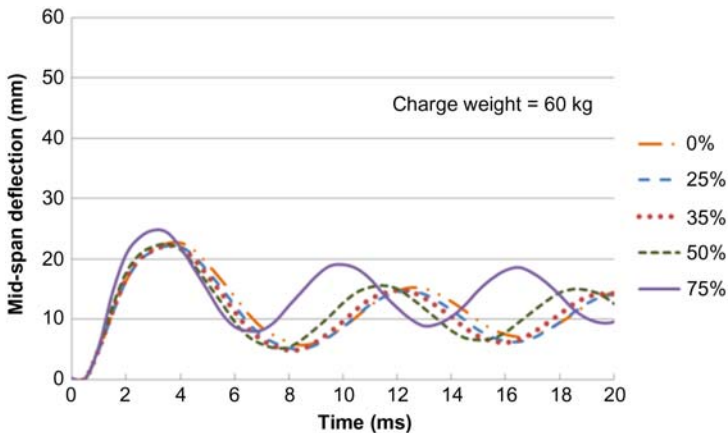
Figure 5.81 Influence of hollowness ratio when charge weight = 60 kg.

Some research [15] suggested that when subjected to axial load, the effectiveness of confinement is inversely proportional to the hollowness ratio; however, the influence of hollowness ratio on CFDST columns under blast loads has not been yet investigated. Therefore, in this study, four different hollowness ratios are studied and compared, namely $\chi = 0$, 0.25, 0.35, 0.5, and 0.75 as shown in Fig. 5.80.

Figs. 5.81 and 5.82 indicate that when χ is less than 0.5, columns with different hollowness ratios behave in a very similar manner, resulting in almost identical deflection−time histories. However, once χ is further increased beyond 0.5 (i.e., to 0.75), a noticeable difference can be observed in the maximum deflection and residual deflection as well as in the period of structural response. More interestingly,
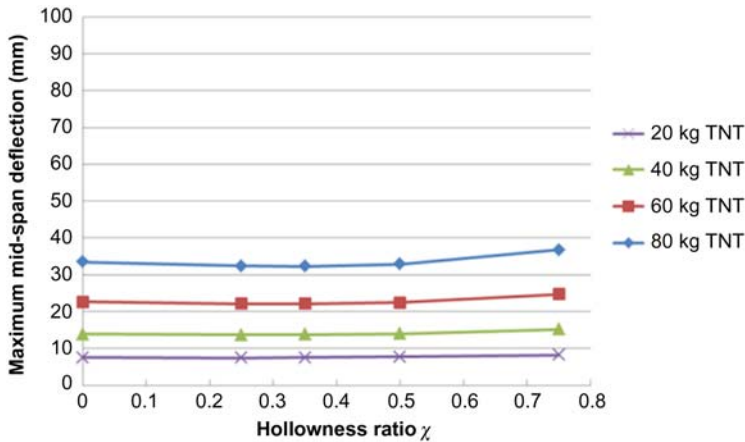
Figure 5.82 Maximum deflection versus hollowness ratio for various blast loads.

when χ is less than 0.5, the differences between a single-skinned column (i.e., CFT) and a double-skinned column (i.e., CFDST) seem insignificant, which again proves the fact that the core concrete contributes more to preventing steel tube buckling rather than to increasing the moment capacity.

5.5.2.6 Axial load

In reality, columns are always loaded by live and dead load prior to a blast incident. Several literatures [63,73] reported that compared to unloaded RC columns, the maximum deflection of axially loaded RC columns under blast loads increases dramatically with increasing axial load. The amplification of deflection is caused by the "P-Δ" effect: when a column deflects due to blast loads, the applied axial load causes a moment at each end that can further increases the deflection; as the deflection increases, the column reaches its plastic limit, transitioning from a gradual strength degradation to a rapid loss of strength due to buckling.

To reflect the influence of axial load on CFDST columns under blast loads, three axial loads, namely 575, 862, and 1150 kN, corresponding to 25%, 37.5%, and 50% of the ultimate axial load capacity, respectively, are applied.

In the blast effects analysis of columns, it is often necessary to use several phases to apply the loading to avoid undesired oscillation [55]. In this study, two loading phases, as shown in Fig. 5.83, are used. These include: (1) applying the axial load to the column prior to the detonation of the explosive. This is done by applying a gradually increased axial quasistatic load to the top of the column implicitly to avoid too much oscillation in the way of wave propagation; (2) applying the blast load while keeping the axial load unchanged; at this stage, the computational algorithm is switched from implicit to explicit to allow for dynamic analysis of the column.
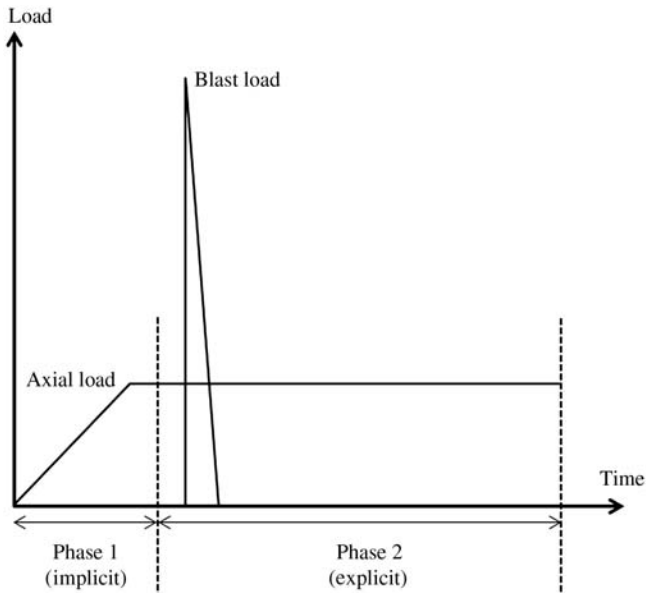
Figure 5.83 Two loading phases (not to scale).
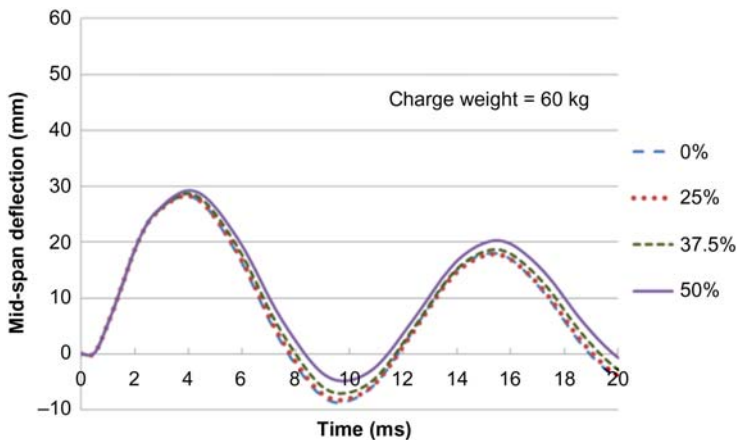
Figure 5.84 Influence of axial load when charge weight = 60 kg.

It can be seen from Figs. 5.84 and 5.85 that the magnitude of axial load ratio does not have a noticeable effect on the maximum deflection, especially when the charge weight is small. This is because the blast-induced deflection is relatively small for these analyzed CFDST columns, thus the moment caused by the P-Δ effect is not large enough to have a significant increase in the maximum deflection.
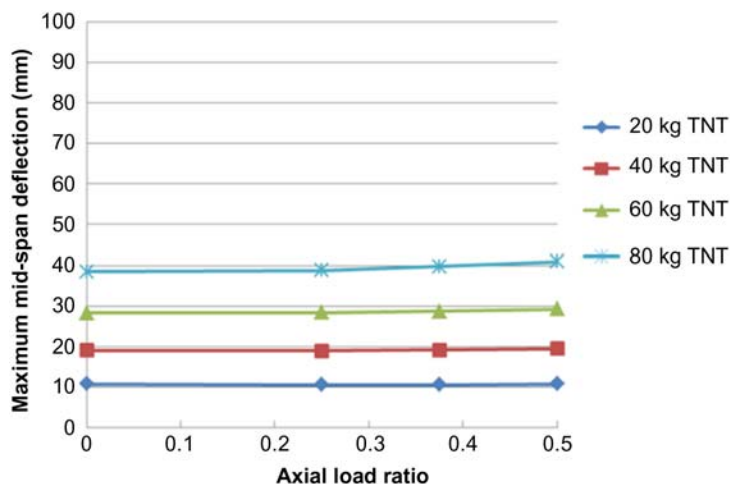
Figure 5.85 Maximum deflection versus axial load ratio of fixed column for various blast loads.

Figure 5.86 Model setup of circular column with pinned support.

5.5.2.7 Support condition

The support condition plays an important role when analyzing structural response and determining structural damage. The numerical results discussed previously were all obtained from CFDST columns with fixed-support conditions. In this study, the influence of support condition is also investigated by changing the fixed−fixed support condition to the pin−pin support condition.

Necessary modifications to the LS-DYNA model are made to account for the change of support condition, and Fig. 5.86 shows the modified model setup. Different axial load ratios are also applied and all results are then compared to the CFDST columns discussed in the previous section.

Figs. 5.87 and 5.88 indicate that under severe blast loads of more than 60 kg TNT charge weight, the maximum deflection of a CFDST column increases dramatically with axial load ratio; however, for moderate blast loads (20 and 40 kg TNT), varying axial load ratio does not have a significant influence.
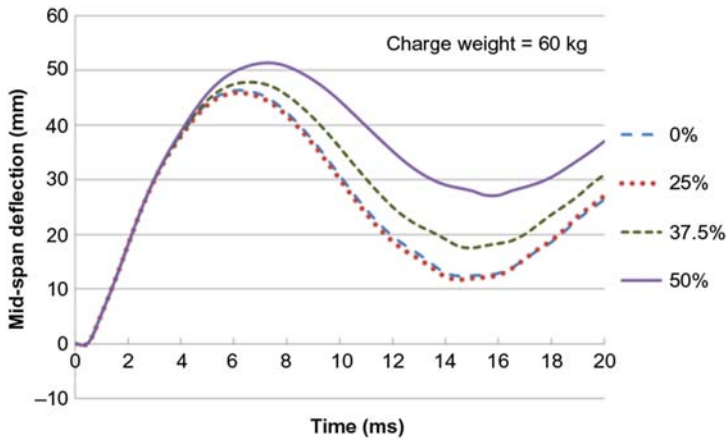
Figure 5.87 Influence of axial load ratio on pinned column.
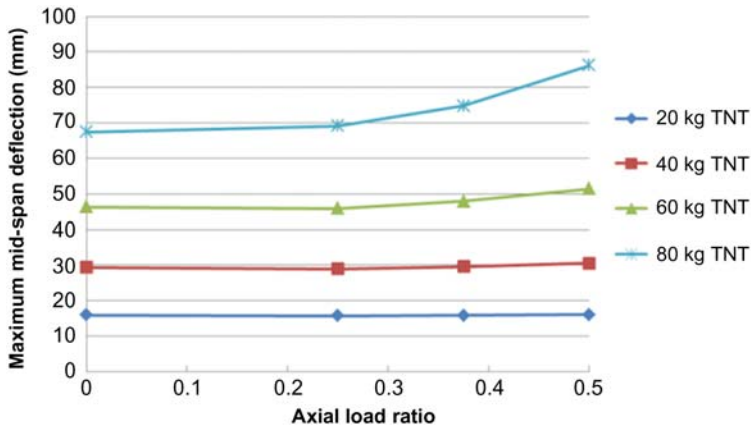
Figure 5.88 Maximum deflection versus axial load ratio of pinned column for various blast loads.

Fig. 5.89 shows the comparison of deflection−time histories between CFDST columns with fixed ends and pinned ends. In general, under the same blast load, columns with pinned ends result in the maximum deflection more significantly than those with fixed ends. The difference in the maximum deflection also increases with the increase in TNT charge weight.

5.5.3 Conclusion

This study numerically evaluates the influence of the concrete strength, outer and inner tube thickness, cross-sectional geometry, hollowness ratio, axial load level,
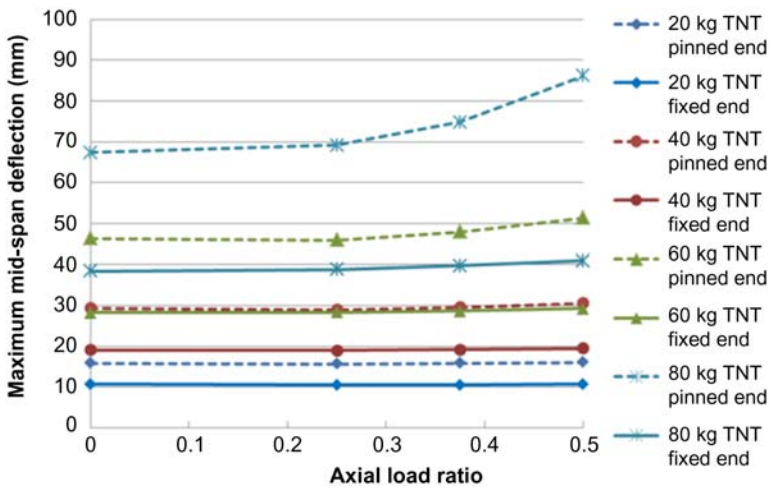
Figure 5.89 Comparison between pinned support and fixed support for various blast loads.

and support condition on the blast load resistance of CFDST columns. The main findings are as follows:

1. Steel tubes are the main contributor to the blast resistance of a CFDST column subjected to blast load, while concrete strength has no significant influence on the mid-span deflection.
2. The outer tube thickness has a significant influence on the mid-span deflection, while the influence of inner tube thickness is much less significant.
3. Under a severe blast event (e.g., greater than 40 kg charge weight), columns with a square cross-section undergo much larger mid-span deflection compared to those with a circular cross-section due to the fact that the roundness of a circular column can effectively reduce the peak pressure and impulse.
4. No significant change in the mid-span deflection can be seen by varying the hollowness ratio between 0 and 0.5. However, once it is increased beyond 0.5, a noticeable increase in the maximum deflection can be observed.
5. The influence of axial load ratio is not noticeable on CFDST columns with fixed supports; however, for CFDST columns with pinned supports, the maximum deflection increases dramatically with axial load ratio.
6. On average, columns with pinned supports yield the maximum deflection more significantly than those with fixed supports under the same blast load.

5.6 Numerical study of blast resistance of square concrete-filled double-skin steel tube columns with steel-fiber reinforced concrete

The results of this experiment have been reported in Section 5.2 [74], hence it is not discussed in detail herein.

5.6.1   Numerical simulation

In this study, finite element models were developed with eight-node solid elements with single-point integration algorithm in LS-DYNA [54]. LS-DYNA/Implicit Solver was used for the static test and LS-DYNA/Explicit Solver was used for the blast test. Viscos-type hourglass control was activated during the blast test simulation to prevent element distortion and zero energy modes.

5.6.1.1   Model calibration

Material model 24, namely MAT_PIECEWISE_LINEAR_PLASTICITY, is used to model the behaviors of the steel tube. The actual stress−strain relationship obtained from tensile coupon test was used as shown in Fig. 5.90.

   As for concrete filler, there are several material models in LS-DYNA that can be used [58,59] and among which, the K&C concrete model (also known as "MAT CONCRETE DAMAGE REL3") is most widely used for its ability to model the behaviors of concrete members under complex loading conditions, including situations involving active/passive confining stress and/or high strain rate effect, with efficiency and accuracy [36,48,51,55]. The K&C concrete model is defined by a number of material parameters, and users can either manually input the values obtained from actual material tests or directly use the default values generated by the program itself. The mechanism behind this constitutive model along with each material input has been thoroughly explained by Mao et al. [75], thus are not further discussed hereafter. However, it should be mentioned that the K&C model was primarily developed based on normal strength concrete, whereas the behaviors of UHPC are significantly different. Therefore the default K&C concrete model, or any other existing models for this matter, should not be directly applied to model the behaviors of UHPC structures without modifications.
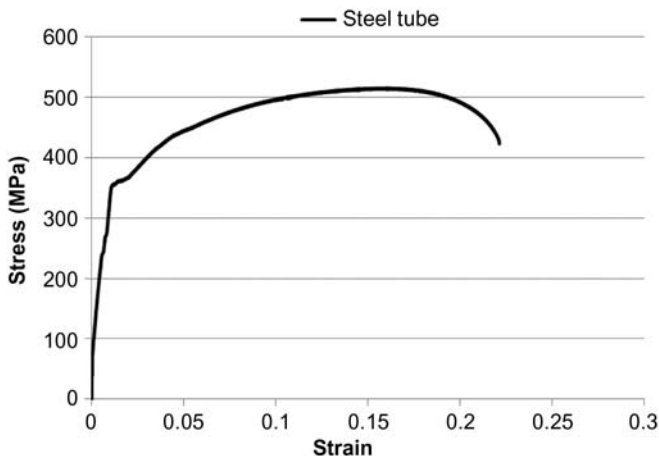
Figure 5.90 Stress−strain relationship for the steel tube.

Table 5.20 Key parameters for K&C concrete model

Model parameter	Value
f_c'	170 MPa
f_t	18 MPa[a]
Poisson's ratio	0.19
$B1$	0.8
w_{lz}	6.00 mm
ω	0.10

[a]f_t is the direct tensile strength, not the flexural tensile strength.
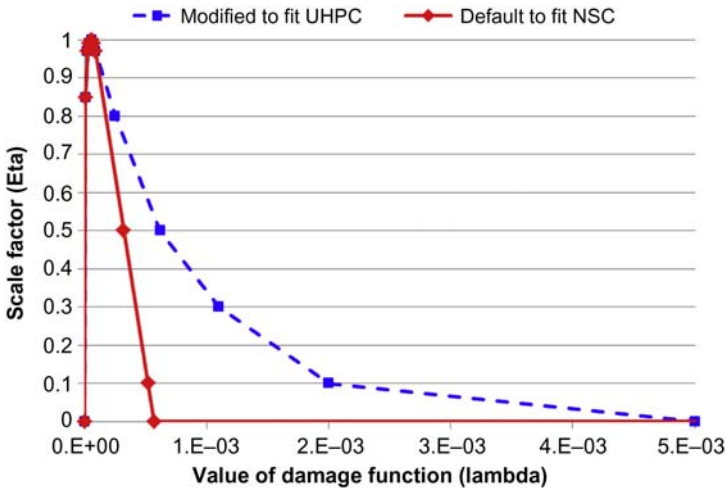
Figure 5.91 λ and η for UHPC and normal strength concrete.

To extend the K&C model to accommodate the behavior of the proposed UHPC material, a number of laboratory tests were conducted for model calibration purpose, the material properties that require calibration were: f_t, which is the uniaxial tensile strength; B_1, which governs the compressive damage and softening behavior; w_{lz}, which governs the fracture energy of each element; ω, which governs the volume expansion; λ and η, which governs the damage function and scale factor, respectively. The key parameters for UHPC material used in this study are listed in Table 5.20 and Fig. 5.91.

5.6.1.2 Uniaxial compression test

As depicted in Fig. 5.92, a numerical model was developed to calibrate material inputs such as B_1, w_{lz}, λ, and η by using the laboratory results of the uniaxial test
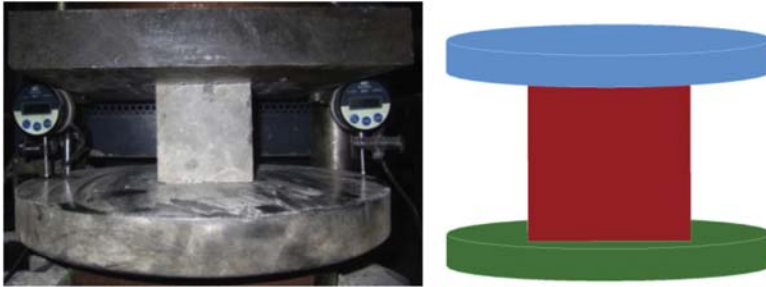
Figure 5.92 Test setup of uniaxial compression test.
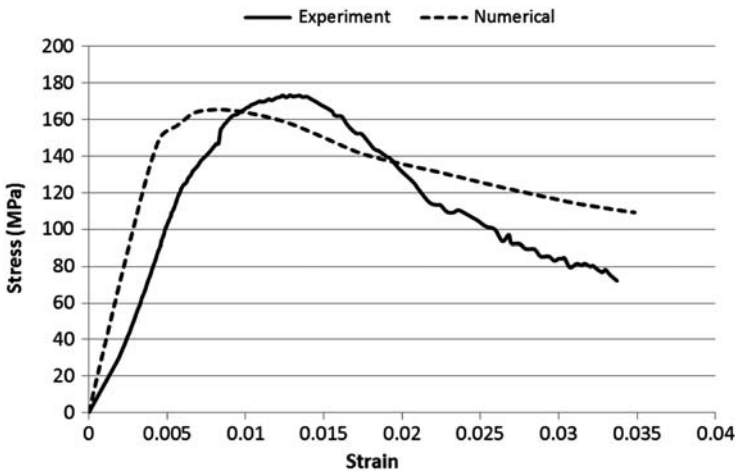
Figure 5.93 Uniaxial compression test results.

on 100 mm $\times$ 100 mm $\times$ 100 mm UHPC specimens. Fig. 5.93 indicated that reasonable agreement was achieved between the numerical and experimental stress−strain curves, demonstrating that the modified material model was able to simulate the ductile postpeak softening phase of UHPC, which was very different from normal strength concrete.

5.6.1.3 Four-point bending test

Fig. 5.94 demonstrates the numerical model of the four-point bending test which was used to calibrate material inputs such as f_t and w_{lz}. It is evident from Figs. 5.95 and 5.96 that not only did the numerical model using modified K&C accurately predicted the load−displacement curve, but it also can correctly simulate the crack formation in the specimen. In the current numerical model, the concrete element eroded when the maximum shear strain reached 0.045.
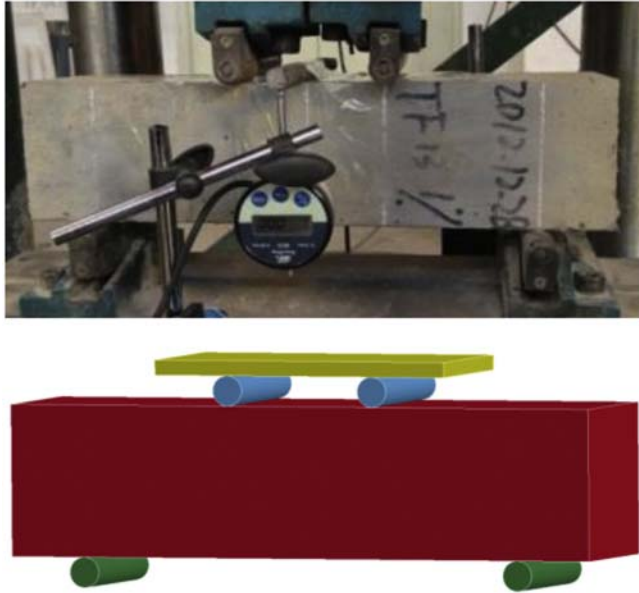
Figure 5.94 Test setup for four-point bending test.
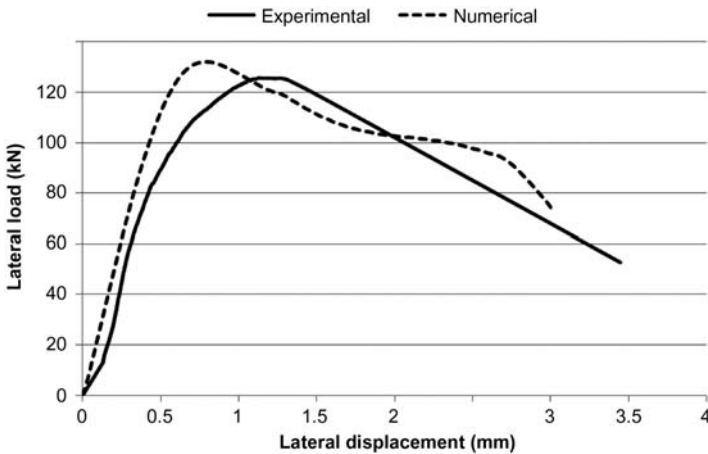
Figure 5.95 Four-point bending test results.

5.6.1.4 Model validation

5.6.1.4.1 Static test

Static test was carried out to study the behaviors of UHPC-filled CFDST specimens when subjected to quasistatic lateral load combined with constant axial load. As shown in Fig. 5.97 that the test equipment consisted of two hydraulic jacks: the vertical hydraulic jack, which was used to apply lateral load, was displacement controlled and the horizontal hydraulic jack, which was used to apply axial load, was force-controlled.
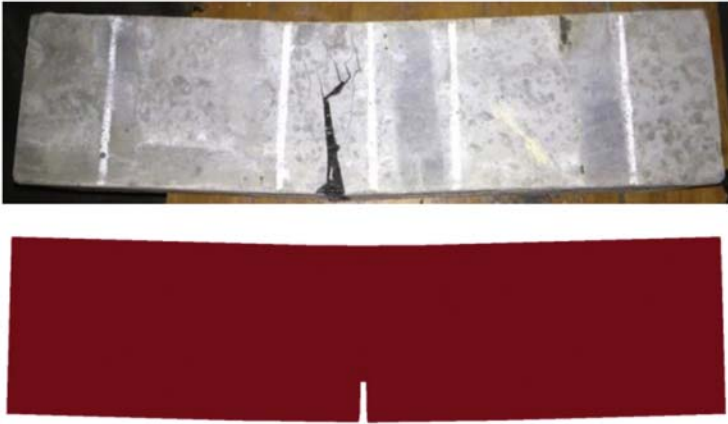
Figure 5.96 Crack formation on UHPC specimen.
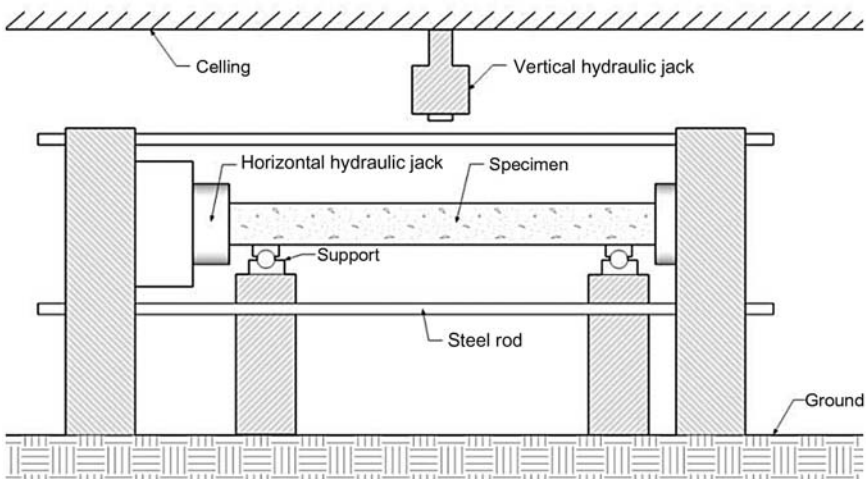
Figure 5.97 Three-point bending test setup.

The specimen was simply supported near both ends by rollers and the axial load was applied by the horizontal hydraulic jack to only one end of the specimen.

Fig. 5.98 illustrates the meshing of the numerical model: the characteristic length of each element ranged from 6.3 to 7.5 mm approximately. Mesh convergence study suggested that by further refining the mesh, only minor improvement can be made, however, with a great increase in the computation time.

Table 5.21 and Fig. 5.99 compare the numerical result to the experimental result of the static test. It can be seen that the initial stiffness of the numerical curve was slightly larger than that of the experimental curve which was similar to what was found in Figs. 5.93 and 5.95. Apart from that the numerical model showed excellent agreement with the experimental observations, yielding only 1.2% error in the maximum loads.
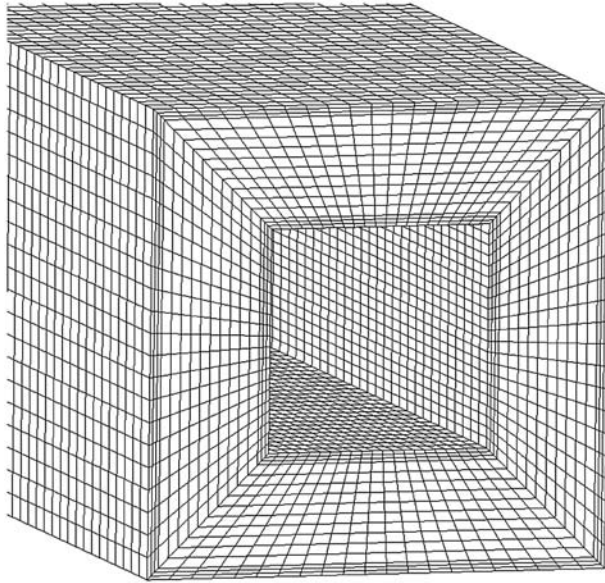
Figure 5.98 Meshing of the numerical model.

Table 5.21 Summary of three-point bending tests

Outer dimensions (mm)	Inner dimensions (mm)	Tube thickness (mm)	Axial load (kN)	Exp. peak load (kN)	LS-DYNA peak load (kN)	Error
210	100	5	1000	660	652	− 1.2%
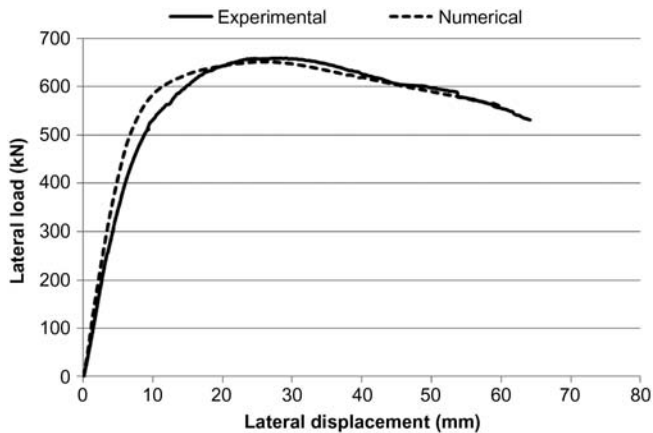
Figure 5.99 Force−displacement histories of three-point bending tests.

These aforementioned results evidently confirmed the practicability and fidelity of numerically modeling UHPC-filled CFDST specimens under static loads. Therefore, in the following section, the behaviors of UHPC-filled CFDST specimens under blast loads were also numerically investigated in a similar manner.

5.6.1.4.2 Blast test

It is well known that under high strain rate impact, the strength of normal concrete increases significantly, by more than 100% for concrete in compression and by more than 600% for concrete in tension and the dynamic increase factor (DIF) for normal strength concrete can be calculated by the CEB Code [60,76]. However, there is very little knowledge on the strain rate behavior of UHPC. Ngo et al. [77] developed DIF model for UHPC with compressive strength up to 160 MPa, it was reported that the strain rate effect on UHPC was significantly smaller than the CEB Code prediction [60,76]. In this research, the dynamic properties of UHPC were studied through Split Hopkinson's Pressure Bar test and the results are depicted in Fig. 5.100 [78]. In comparison to the normal strength concrete, the strain rate of UHPC did not have a significant effect until it reached $200\,\mathrm{s}^{-1}$ for tension and $50\,\mathrm{s}^{-1}$ for compression. The DIF of UHPC at the same strain rate was also much smaller compared to that of the normal strength concrete.

The strain rate effect on the steel tube was incorporated by the Cowper and Symonds law which multiplies the yield stress by a factor given as

$$\text{DIF of steel} = 1 + \left(\frac{\dot{\varepsilon}}{C}\right)^{\frac{1}{P}} \tag{5.12}$$

where $\dot{\varepsilon}$ is the strain rate of steel; C and P are two constants.
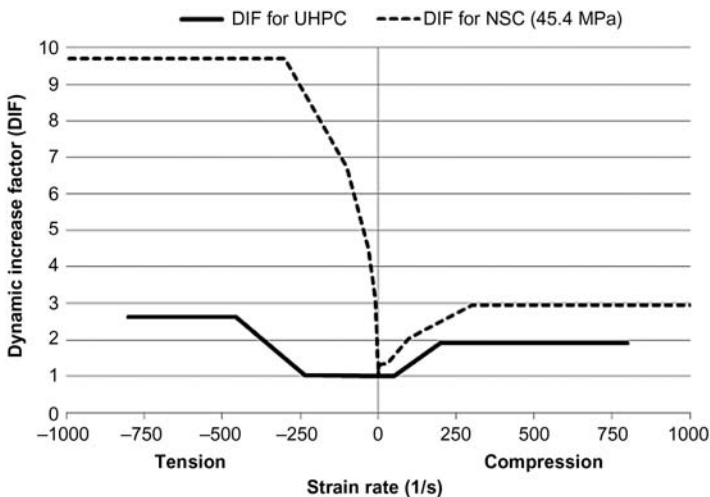
Figure 5.100 DIF for UHPC and NSC.

In this research, $C = 6488$ s^{-1} and $P = 3.91$ were used according to the dynamic axial crushing test on square tubes carried out by Jones [49].

It can be concluded from Table 5.22 and Fig. 5.101 that the proposed numerical model not only accurately predicted the maximum mid-span deflection, with or

Table 5.22 **Summary of blast tests**

Specimen no.	TNT equivalent (kg)	Axial load (kN)	Standoff distance (mm)	Mid-span deflection (mm)		
				Measured	**LS-DYNA**	**Error (%)**
S1B	50	0	1500	49	42.1	−14
S3A	50	1000	1500	41	37.9	−7.5
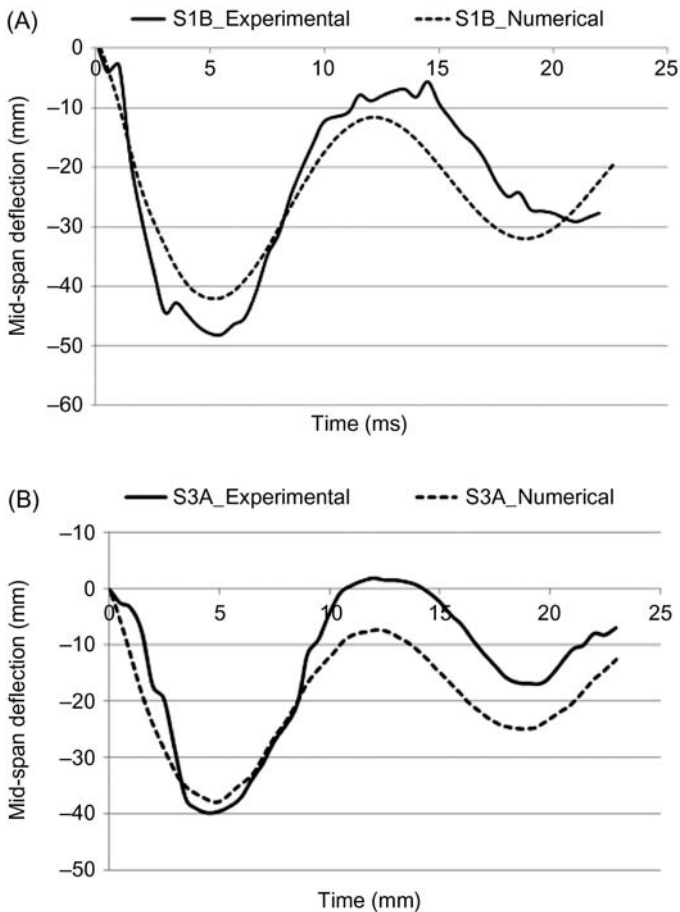
Figure 5.101 Displacement−time histories of blast tests (A) S1B and (B) S3A.

without axial load, the predicted period of oscillation also corresponded with the experimental curve very well. Although some insignificant discrepancies were seen in the residual deflection, the difference was within the acceptable range, considering the complexity and uncertainty associated with blast experiments.

5.6.2   Parametric studies

A total of 33 numerical specimens were designed to investigate the effect of the cross-sectional dimensions and material properties on the behaviors of CFDST columns. Table 5.23 lists the characteristics of the specimens and Fig. 5.102 depicts the specimen setup in the numerical model: both ends of the column used for parametric study were embedded in concrete slabs and the outer faces of both slabs were restrained so that it can only move along the axial direction. The nominal length of all the specimens used in the parametric study was 3500 mm and the nominal yield strength of all steel tubes was 346 MPa.

The specimens were divided into six groups and each group represents one parameter. The first group, namely AR, investigated the effect of axial load ratio under blast loads of three different magnitudes. The second group, namely HR, consisted of five specimens having inner diameter ranging from 0 to 120 mm and a unit outer diameter of 210 mm. The next group, namely CS, focused the influence of concrete strength and the differences between normal strength concrete and UHPC. Groups 4 and 5 examined the impact of inner and outer tube thickness and as a result, all specimens under this category had different inner/outer tube thickness ranging from 3 to 6 mm. The last group compared the behaviors of CFDST specimens having different cross-sectional geometries under the same blast loads. Four cross-sectional combinations were chosen under this category, including CHS inner + CHS outer, CHS inner + SHS outer, SHS outer + CHS inner, and SHS outer + SHS inner.

5.6.2.1   The effect of axial load ratio

Structural columns are under constantly changing live load, therefore it is of great interest to see their behaviors under blast loading with different axial load ratios. Axial load ratio is the ratio between the actual applied axial load and the axial load-carrying capacity of the column. In this research, three blast load levels were used in conjunction with four axial load ratios ranging from 0.016 to 0.5. It is evident from Figs. 5.103 and 5.104 that, within a certain limit (e.g., less than 0.16 in this study), the increase in axial load ratio can result in a smaller deflection regardless of the magnitude of the blast loading. However, if the axial load ratio continued to increase beyond the critical value, a noticeable increase in the deflection or even structural instability can be seen with this effect being more significant when the specimen was subjected to a larger charge weight. This is due to the fact that with an increase in the applied axial load on columns, it resulted in an increase in the moment capacity and the nominal shear strength. However, once this critical axial load ratio was exceeded, the mid-span deflection increased greatly with increasing axial load. When a column undergoes large deflection and plastic hinges formation

Table 5.23 **Characteristics for specimens used for parametric study**

Group	Specimen	Dimensions				Axial load ratio	Charge weight (kg)	Concrete strength	
		W_o (mm)	t_o (mm)	W_i (mm)	t_i (mm)			f'_c (MPa)	f'_t (MPa)
1 (axial load ratio)	AR1	210	5	100	5	0.016	80	170	18
	AR2	210	5	100	5	0.162	80	170	18
	AR3	210	5	100	5	0.325	80	170	18
	AR4	210	5	100	5	0.487	80	170	18
	AR5	210	5	100	5	0.016	120	170	18
	AR6	210	5	100	5	0.162	120	170	18
	AR7	210	5	100	5	0.325	120	170	18
	AR8	210	5	100	5	0.487	120	170	18
	AR9	210	5	100	5	0.016	160	170	18
	AR10	210	5	100	5	0.162	160	170	18
	AR11	210	5	100	5	0.325	160	170	18
	AR12	210	5	100	5	0.487	160	170	18
2 (hollow section ratio)	HR1	210	5	—	—	0.325	120	170	18
	HR2	210	5	40	5	0.325	120	170	18
	HR3	210	5	80	5	0.325	120	170	18
	HR4	210	5	100	5	0.325	120	170	18
	HR5	210	5	120	5	0.325	120	170	18
3 (concrete strength)	CS1	210	5	100	5	0.325	120	30	2.9
	CS2	210	5	100	5	0.325	120	45	3.8
	CS3	210	5	100	5	0.325	120	60	4.6
	CS4	210	5	100	5	0.325	120	170	18

Table 5.23 (**Continued**)

Group	Specimen	Dimensions				Axial load ratio	Charge weight (kg)	Concrete strength	
		W_o (mm)	t_o (mm)	W_i (mm)	t_i (mm)			f'_c (MPa)	f'_t (MPa)
4 (inner tube thickness)	IT1	210	5	100	3	0.325	120	170	18
	IT2	210	5	100	4	0.325	120	170	18
	IT3	210	5	100	5	0.325	120	170	18
	IT4	210	5	100	6	0.325	120	170	18
5 (outer tube thickness)	OT1	210	3	100	5	0.325	120	170	18
	OT2	210	4	100	5	0.325	120	170	18
	OT3	210	5	100	5	0.325	120	170	18
	OT4	210	6	100	5	0.325	120	170	18
6 (cross-section geometry)	CHS + CHS	210	5	100	5	0.325	120	170	18
	CHS + SHS	210	5	100	5	0.325	120	170	18
	SHS + CHS	210	5	100	5	0.325	120	170	18
	SHS + SHS	210	5	100	5	0.325	120	170	18
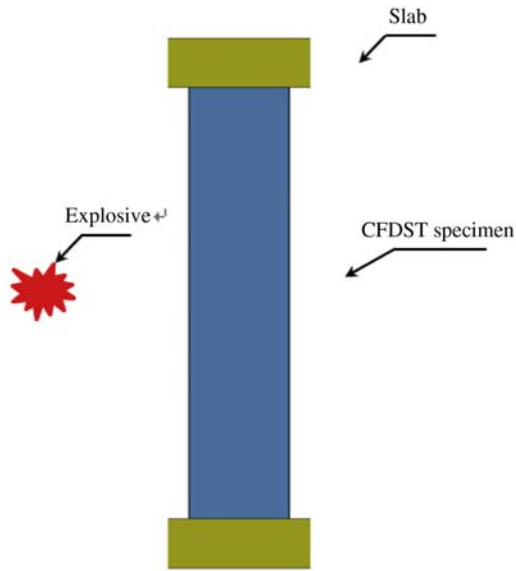
Figure 5.102 Test setup for parametric study.
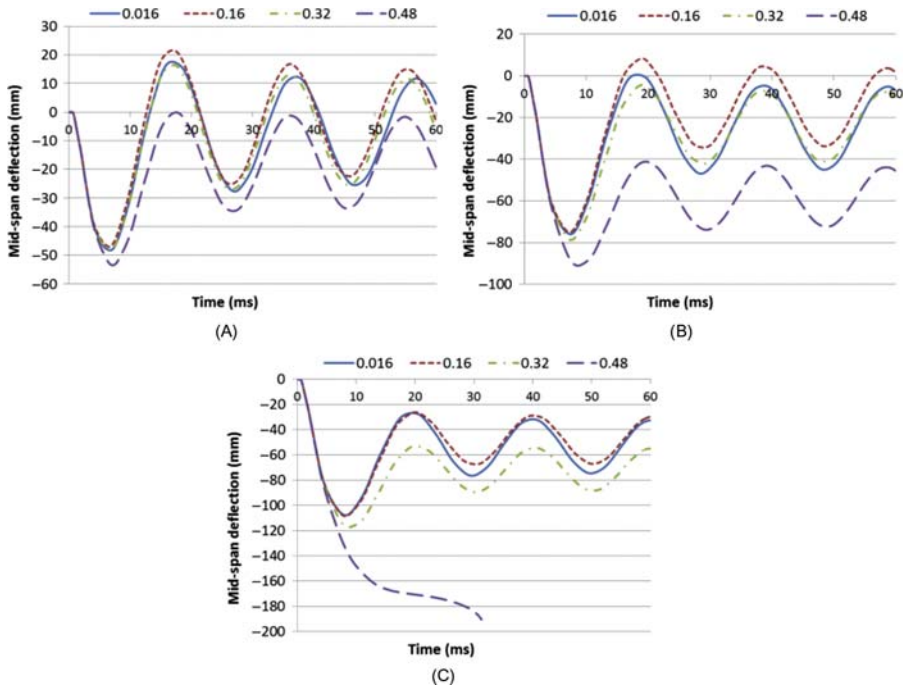
Figure 5.103 Displacement−time histories for different axial load ratios: (A) 80 kg TNT, (B) 120 kg TNT, and (C) 160 kg TNT.
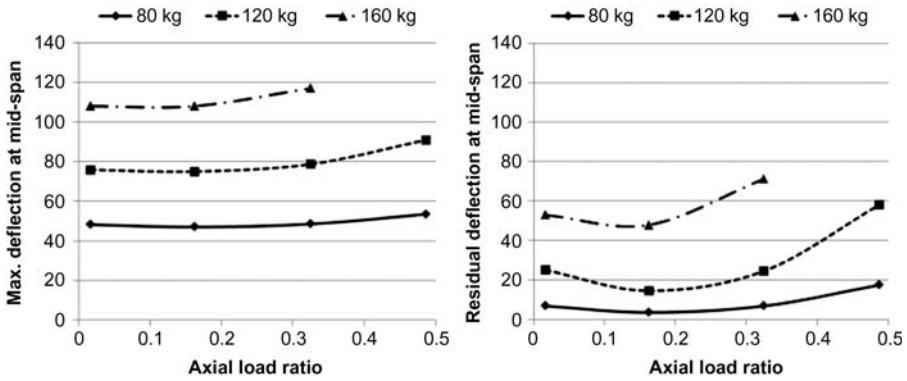
Figure 5.104 The maximum and residual deflections for different axial load ratios.
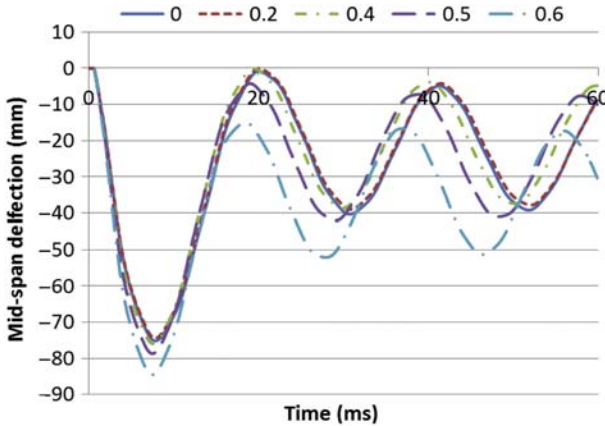
Figure 5.105 Displacement−time histories for different hollow section ratios.

occurs near mid-span and fixed ends, axial loads will amplify the lateral deflection and internal moment due to the P-Δ effect. A number of studies also reported similar findings on other column tests [12,13,48,63].

5.6.2.2   The effect of hollow section ratio

In this section, five hollow section ratios ($\chi = \frac{W_i}{W_o - 2t_{so}}$) were examined as shown in Figs. 5.105 and 5.106. It was concluded that the enlargement of inner width did not demonstrate a significant change in the behaviors of CFDST specimens until the hollow section ratio reached 0.5. From this point onward, the deflection started to increase notably along with a shortening in the period of oscillation. The results also indicated that CFDST specimens can achieve equal blast resistance, however with much less self-weight, when compared to CFST specimens (i.e., when $\chi = 0$).
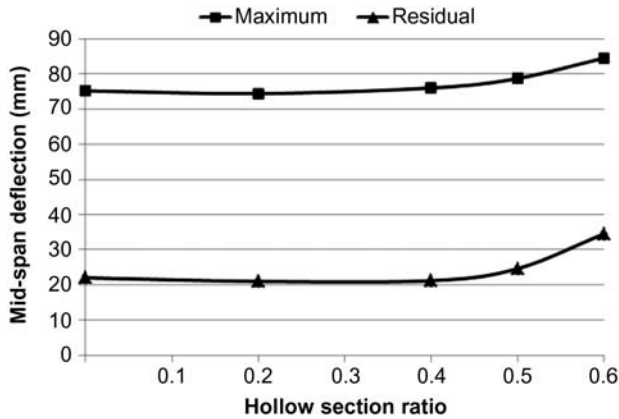
Figure 5.106 The maximum and residual deflections for different hollow section ratios.
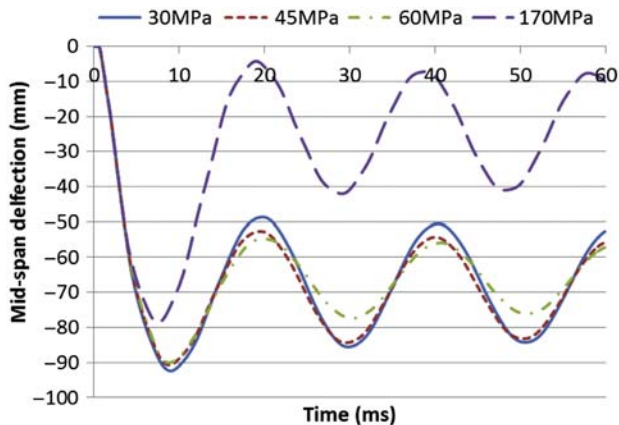
Figure 5.107 Displacement−time histories for different concrete strengths.

5.6.2.3 The effect of concrete strength

Figs. 5.107 and 5.108 demonstrated the differences between CFDST specimens filled with UHPC and those filled with normal strength concrete. It can be concluded that, when only using normal strength concrete, the compressive strength of concrete did not have a significant impact on the structural behavior. However, when UHPC was introduced into the comparison, a remarkable reduction in the residual deflection (up to 62.8%) was achieved, whereas the decrement of the maximum deflection was much smaller in percentage (up to 12.8%). The reason for this is because: (1) the tensile strength of the concrete filler was very small compared to that of the steel tubes, therefore the steel tubes, which were all of the same strength herein, provided a vital contribution in resisting the flexural loads while the concrete filler mainly contributed to the axial load capacity. As a result, there was little
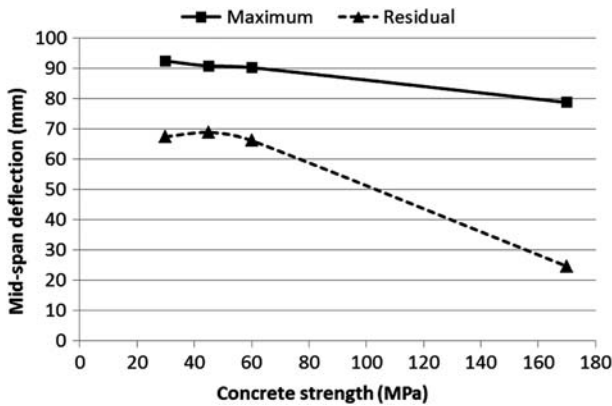
Figure 5.108 Maximum and residual deflections for different concrete strengths.

difference in the maximum deflection although UHPC was much stronger in strength than the normal strength concrete. (2) As for residual deflection, it can be seen in Fig. 5.109 that the CFDST specimen with normal strength concrete filler exhibited clear signs of steel buckling near the end slabs whereas none was observed on the specimen with UHPC filler. Therefore the CFDST specimen with UHPC filler experienced less plastic deformation than that with normal concrete filler.

5.6.2.4   The effect of inner and outer tube thickness

It can be seen in Figs. 5.110 and 5.111 that the increment in the thickness of the inner and outer steel tubes benefited the flexural load capacity, therefore resulting in smaller mid-span deflections. Both the maximum and residual mid-span deflections exhibited linear relationships with steel tube thickness. Nevertheless, the increase in the outer steel tube thickness resulted in a more significant reduction in the mid-span deflection than that in the inner steel tube thickness.

5.6.2.5   The effect of cross-sectional geometry

In this section, four different cross-sectional combinations were examined. It is evident from Figs. 5.112 and 5.113 that the behaviors of CFDST specimens under blast loading were mainly dominated by the shape of the outer steel tube, whereas the inner steel tube geometry did not have a significant impact.

5.6.3   Conclusions

This section has presented an experimental and a numerical study on the behaviors of CFDST columns under blast loading.

   The experimental results indicated that the proposed CFDST columns can withstand severe blast load without failure, while no signs of steel buckling or concrete crushing were found on the test specimens after the tests. The increase in explosive
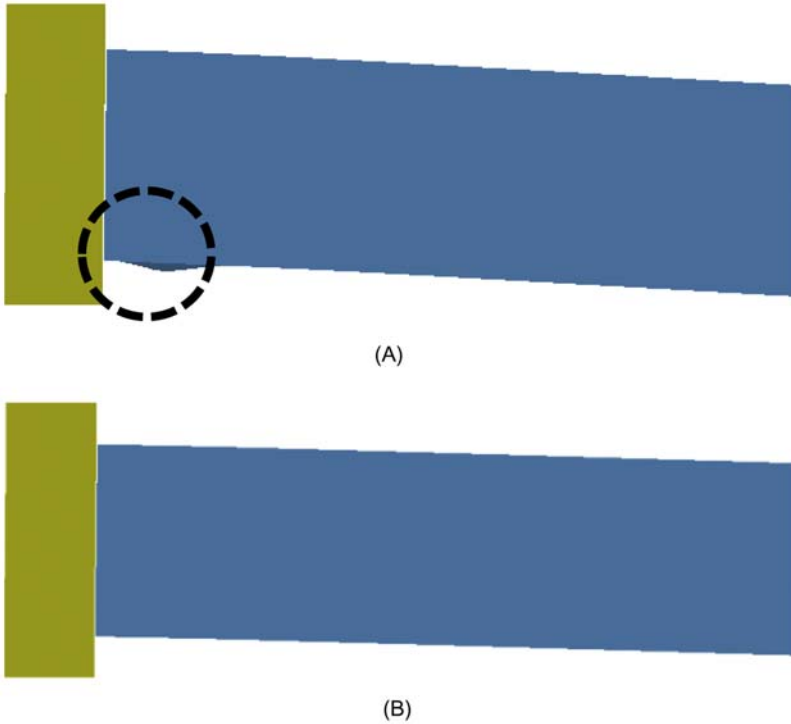
Figure 5.109 Failure mode of the CFDST specimens: (A) deformed shape of CFDST specimen with normal strength concrete filler and (B) deformed shape of CFDST specimen with UHPC filler.
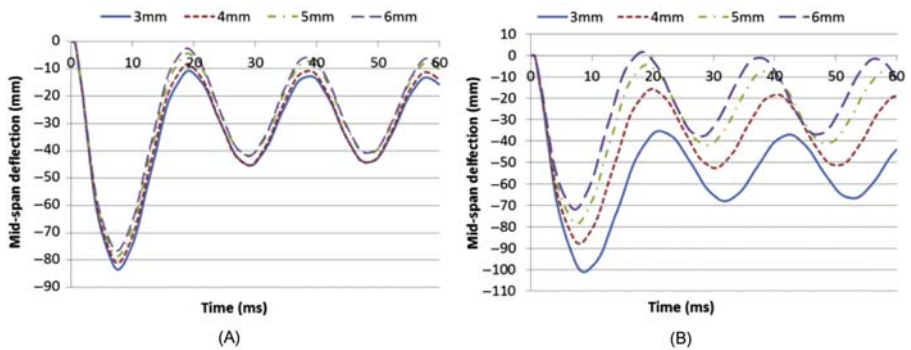
Figure 5.110 Displacement−time histories for different steel tube thickness: (A) inner steel tube and (B) outer steel tube.
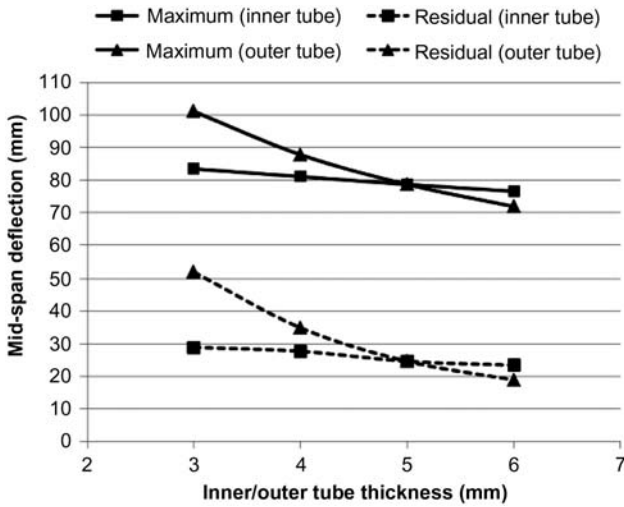
Figure 5.111 Maximum and residual deflections for different steel tube thickness.
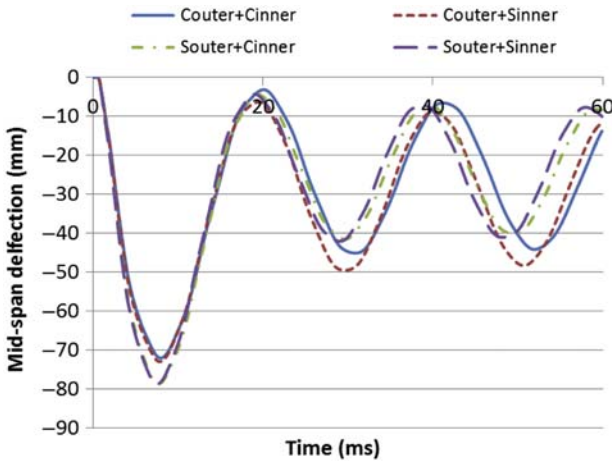
Figure 5.112 Displacement−time histories for different cross-sectional combinations.

charge weight caused a larger mid-span deflection, with this effect being more notice-able on axial-load−free specimens rather than axially loaded specimens. The pres-ence of an axial compressive load, corresponding to 25% of the squash load, led to a slight reduction in the maximum mid-span deflection in two comparative cases.

The numerical model of the proposed CFDST column was carefully calibrated by a series of laboratory test and when validated against the blast tests, good agree-ment was achieved. A number of parametric studies were then carried out numeri-cally to further investigate the behaviors of the CFDST column under blast loading.
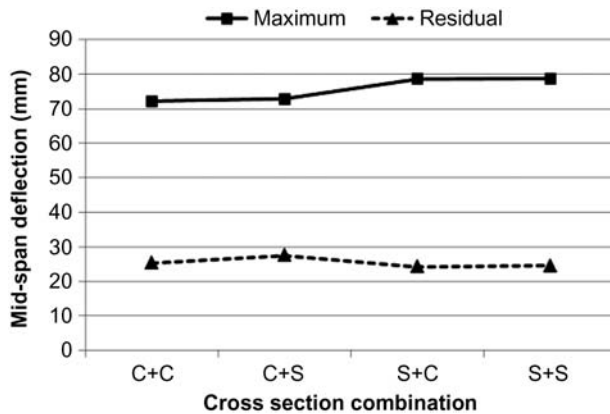
Figure 5.113 The maximum and residual deflections for different cross-sectional combinations.

The following conclusions can be drawn based on the results obtained from this study:

1. Within a certain limit, the increase in the axial load ratio can slightly reduce the mid-span deflection. However, if it increases beyond the limit, a significant increase in the mid-span deflection or even structural instability can be caused.
2. For hollow section ratio up to 0.5, there were no notable differences in the behaviors of the CFDST specimens. Nevertheless, for hollow section ratio greater than 0.5, a significant increase in the deflection was observed along with a notable change in the period of oscillation.
3. Compared to normal strength concrete filler, the use of UHPC filler in the CFDST specimen remarkably reduced the residual deflection, whereas the reduction in the maximum deflection was much less in percentage.
4. The increment in the inner and outer steel tube thickness both resulted in smaller mid-span deflections, however, with this effect being more noticeable on outer steel tube than inner.
5. The behaviors of CFDST specimens under blast loading were mainly dominated by the shape of the outer steel tube, whereas the inner steel tube geometry did not have a notable impact.

5.7 Numerical derivation of pressure−impulse diagrams for square ultra-high performance concrete-filled double-skin tube columns

5.7.1 Numerical modeling

In this section, the commercial software package LS-DYNA was used to investigate the behaviors of UHPCFDST columns under blast loading [54].
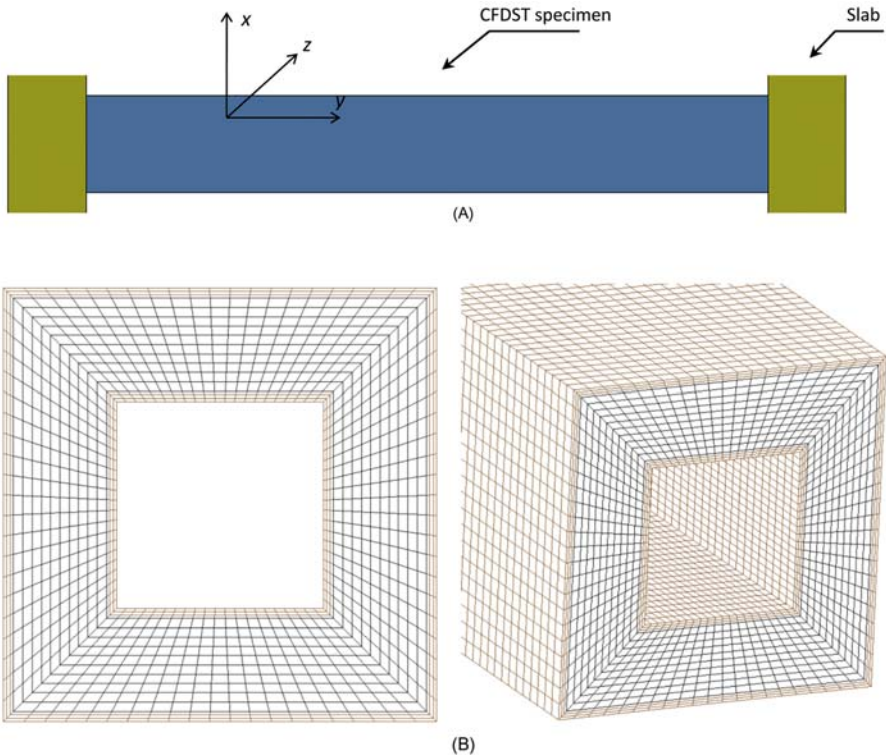
Figure 5.114 Model setup and mesh size (A) overview of test setup and (B) cross-section of the specimen.

5.7.1.1 Meshing and boundaries

The UHPCFDST specimen studied herein is shown in Fig. 5.114. It can be seen from Fig. 5.114A that both ends of the UHPCFDST specimen were fully embedded in concrete slabs and the outer face of both end slabs were restrained against x and z directions so that it can only move along the axial direction. The meshing and element division are shown in Fig. 5.114B. The average characteristic size of the concrete element was 7 mm and the mesh-size convergence study shows that further refinement of the numerical model has little effect on the results but significantly increases the computational burden.

5.7.1.2 Application of the blast loading

Parametric studies were conducted to obtain the pressure-impulse diagrams, and in all the case studies, the idealized triangular shape blast load was adopted in the simulation. In addition, the blast wave was also assumed to be plane wave, therefore the blast load was uniformly distributed on the front face of the UHPCFDST specimen. It should be mentioned that, under circumstances where the explosive is
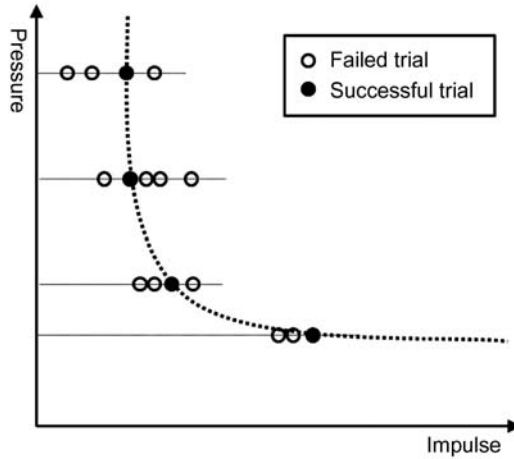
Figure 5.115 The method to generate a pressure−impulse diagram.

placed in close vicinity of the target structure, this assumption could overestimate the blast load and as a result, i.e., overestimate the column damage.

5.7.2 Numerical derivation of pressure−impulse diagram

In this study, the standard procedure of generating a pressure−impulse diagram is shown in Fig. 5.115: (1) choose one pressure and impulse value as the starting point; (2) keep the pressure constant and gradually increase/decrease the impulse (by increasing/decreasing the loading duration) until the structural damage has reached the predetermined level; (3) reduce the pressure and readjust the impulse value until the structural damage has also reached the damage level defined in step 2; (4) repeat steps 1−3 for the rest of the data points until a smooth curve can be drawn (Fig. 5.115).

5.7.2.1 Damage criterion

There are a number of criteria that are commonly used to quantify the damage accumulated in a column. In this research, the damage in an UHPCFDST column caused by the blast loading is quantified by the residual axial load-carrying capacity: the more residual axial load-carrying capacity, the less accumulated blast damage and vice versa. Shi et al. [51] firstly introduced this method to evaluate the damage on RC columns, the advantage of this criterion includes the following: it can be used to evaluate damage accumulated in structural columns from different damage modes; it is straightforward to tell whether a column is severely damaged or not; it is easily obtainable either through numerical simulations or filed tests. The damage index D is defined as

$$D = 1 - \frac{P_{\text{residual}}}{P_{\text{design}}} \tag{5.13}$$
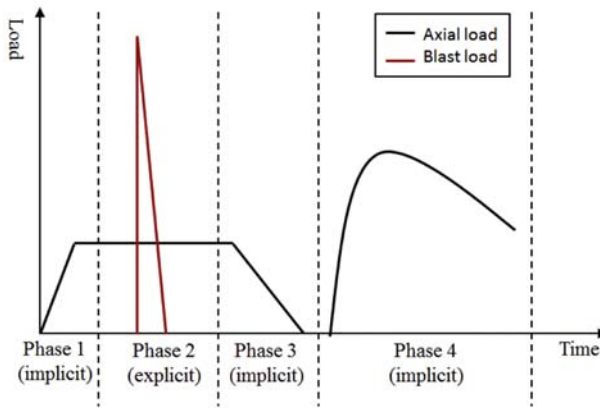
Figure 5.116 Loading schematic (not to scale).

where $P_{residual}$ and P_{design} are the axial load-carrying capacity of the damaged and undamaged UHPCFDST columns, respectively. Both values can be obtained numerically by gradually applying axial load to a damaged/undamaged UHPCFDST specimen until collapse.

In this study, the column is considered failed once its axial load-carrying capacity is halved, in other words when $D = 0.5$, after the explosion. It should be noted that the definition of column failure varies from person to person and case to case. The authors adopted $D = 0.5$ specifically for UHPCFDST columns in this study based on their engineering judgment and experience which may not be valid for other column types. However, this method should be applicable for assessing most structural columns although the definition of the damage degree at failure varies from column to column.

5.7.2.2 Numerical derivation of damage index D

In the numerical simulation, the UHPCFDST column was mainly subjected to two loads, namely the axial load and the transverse blast load. The undamaged axial load-carrying capacity P_{design} was derived straightforwardly by applying a displacement-controlled axial loading until the column fails. However, the residual axial load-carrying capacity, however, was much more complicated.

The method of obtaining damage index D consists of four phases of loading as shown in Fig. 5.116: (1) the first phase is the preloading phase, an axial load, which is roughly 30% of the column axial load-carrying capacity, is applied to the UHPCFDST column to simulate the live load and the self-weight present in the column prior to the explosion. It should be mentioned that the axial load in this phase was applied by using the implicit solver in LS-DYNA to avoid oscillation in the way of wave propagation [55]. This is the ideal method for applying quasistatic load because the stress equilibrium is achieved at the end of every time step. If the

explicit solver is used, even if a very long ramping time is set, the sudden introduction of axial load is still highly likely to cause localized damage near where the axial load is applied; (2) during the second phase, the axial load applied during the first phase is kept constant. The computational algorithm is switched from implicit to explicit right before the blast load is applied to allow for the dynamic analysis; (3) the third phase starts when the free vibration of the column almost stops. The computational algorithm is switched from explicit back to implicit and during which, the velocities of all nodes are set to zero. The axial load applied throughout phases 1 and 2 is slowly unloaded during this phase and the column is kept load-free afterward; (4) the evaluation of the residual axial load-carrying capacity $P_{residual}$ is carried out in the final phase by gradually applying a displacement-controlled axial loading until failure. $P_{residual}$ and P_{design} can be then used to determine the damage index D of the column.

5.7.3 Parametric studies and results

Systematic parametric studies are carried out by using the proposed numerical model to investigate the effect of different parameters on the pressure−impulse diagram of UHPCFDST columns. Analytical formulae for constructing pressure−impulse diagrams for UHPCFDST columns of different configurations are also derived from the results of the parametric study. In total, eight parameters are investigated, namely cross-sectional area, column height, axial load ratio, hollow section ratio, inner and outer tube steel ratios, compressive strength of the concrete and yield strength of the steel tube. Table 5.24 lists the range of each parameter that is investigated in this study. For easy analysis purpose, a control column is introduced; all specimens have the same dimensions as the control specimen during the parametric study unless otherwise specified. The control column is 3500 mm in height, 200 mm in cross-section side length with its axial load ratio being 0.3, hollow section ratio being 0.25, inner tube steel ratio being 0.070, outer tube steel ratio being 0.128, compressive strength of the concrete filler being 170 MPa and steel yield strength being 350 MPa.

5.7.3.1 Side length, b

To investigate the effect of cross-section side length, the pressure−impulse diagrams of four CFDST columns with different cross-section side lengths, i.e., 200, 250, 300, and 400 mm, are generated using the numerical method introduced in the previous section. For easy comparison, Table 5.24 lists the pressure and impulse asymptotes of each pressure−impulse diagram and Fig. 5.117 shows all the numerical points that are used to derive each pressure−impulse diagram along with the fitted curve. It can be seen that both the pressure and impulse asymptotes are increased significantly with the increase in side length. This is because a larger cross-section results in a larger cross-section modulus which increases the flexural and shear resistance of the column.

Table 5.24 Parameters used in the parametric studies

Side (mm)	P_0 (numerical) (MPa)	P_0 (Eq. 5.16) (MPa)	Error (%)	I_0 (numerical) (MPa ms)	I_0 (Eq. 5.17) (MPa ms)	Error (%)
200[a]	1.4	1.37	− 2.00	10.8	10.67	− 1.20
250	2.2	2.35	7.00	14.3	14.31	0.00
300	3.6	3.66	1.70	19	18.16	− 4.40
400	7.4	7.35	− 0.60	26	26.4	1.50
Height (mm)						
2500	3.5	3.49	− 0.40	13.6	14.41	5.90
3500[a]	1.4	1.37	− 2.00	10.8	10.67	− 1.20
4500	0.7	0.68	− 3.00	8.25	8.55	3.60
5500	0.4	0.38	− 4.00	6.5	7.18	10.50
ρ_{axial}						
0.1	1.5	1.51	0.50	10.6	10.65	0.50
0.2	1.5	1.48	− 1.50	11	10.84	− 1.50
0.3[a]	1.4	1.37	− 2.00	10.8	10.67	− 1.20
0.4	1.2	1.19	− 0.60	10.2	10.15	− 0.50
ρ_{hollow}						
0.04	1.2	1.2	0.30	10.6	10.57	− 0.20
0.16	1.3	1.31	1.10	10.9	10.99	0.90
0.25[a]	1.4	1.37	− 2.00	10.8	10.67	− 1.20
0.36	1.4	1.4	0.30	9.5	9.53	0.30
ρ_{inner}						
0.041	1.3	1.29	− 0.50	10.1	10.03	− 0.70
0.055	1.36	1.33	− 2.00	10.4	10.34	− 0.50
0.07[a]	1.4	1.37	− 2.00	10.8	10.67	− 1.20
0.085	1.45	1.41	− 2.70	11.2	11	− 1.80
ρ_{outer}						
0.08	1.1	1.09	− 1.20	8.3	8.26	− 0.50
0.105	1.2	1.23	2.70	9.6	9.49	− 1.10
0.128[a]	1.4	1.37	− 2.00	10.8	10.67	− 1.20
0.151	1.5	1.51	0.30	12	11.8	− 1.70
f'_c						
140	1.3	1.27	− 2.20	10.4	10.4	0.30
170[a]	1.4	1.37	− 2.00	10.8	10.67	− 1.20
200	1.5	1.47	− 1.90	11	11	0.30
f_y						
280	1.2	1.21	0.40	10.2	9.96	− 2.40
350[a]	1.4	1.37	− 2.00	10.8	10.67	− 1.20
420	1.5	1.54	2.50	11.5	11.38	− 1.00
525	1.8	1.79	− 0.70	12.5	12.45	− 0.40

[a]This particular value is used for the control specimen during the parametric study.
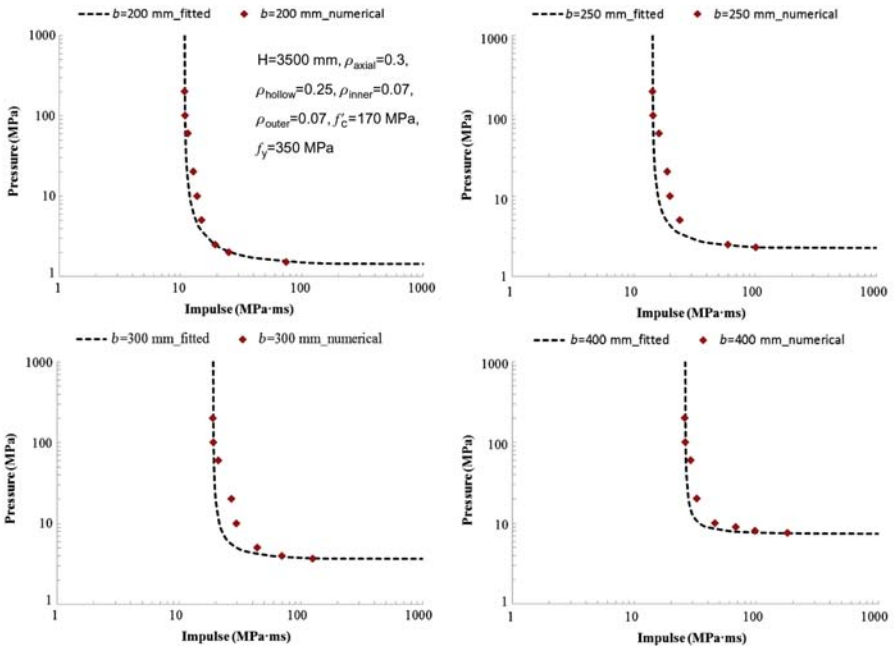
Figure 5.117 Numerically derived pressure and impulse data points for different side lengths.

It should be noted that identical procedures for deriving the numerical points and fitted curves are adopted for all other parameters, therefore Fig. 5.117 serves as an example and similar figures will not be shown hereafter.

5.7.3.2 Column height, H

Four different column heights are studied to investigate the effect on the pressure−impulse diagrams. The numerically derived pressure and impulse asymptotes are summarized in Table 5.24. In general, with all other parameters being constant, the maximum bending moment acting on a longer column is larger than that on a shorter column under the same uniformly distributed load. Therefore it is evident that a higher CFDST column would result in smaller pressure and impulse asymptotes, with this effect being more notable on pressure asymptote than impulse asymptote

5.7.3.3 Axial load ratio, ρ_{axial}

The axial load ratio, ρ_{axial}, is defined as the applied axial load over the design axial load-carrying capacity of the column, $\rho_{axial} = \frac{P_{applied}}{P_{design}}$. In this study, four different axial load ratios ranging from 0.1 to 0.4 are investigated. From Table 5.24, one can see that the values for the pressure and impulse asymptotes peak at $\rho_{axial} = 0.2$ then gradually decreases as the axial load ratio further increases. This is because when

an axial load is applied to a column, it induces two effects: one is the compressive membrane effect that reduces the column deflection and the other one is the P-Δ effect that amplifies the column deflection. In general, when the axial load ratio is small, the compressive membrane effect is more dominant and vice versa [12]. Therefore for CFDST columns studied in this research, when ρ_{axial} is less than 0.2, the compressive membrane effect is more dominant than the P-Δ effect; however, once ρ_{axial} goes beyond 0.2, the P-Δ effect starts to have a larger impact, the pressure and impulse asymptotes therefore become smaller.

5.7.3.4   Hollow section ratio, ρ_{hollow}

The hollow section ratio, ρ_{hollow}, is defined as $\frac{b_{inner}}{b_{outer} - 2t_{outer}}$, where b_{outer} and b_{inner} are the outer and inner side lengths, respectively, and t_{outer} is the thickness of the outer steel tube. In this study, four hollow section area ratios, which are obtained by changing the inner side length while keeping the rest parameters constant, are discussed as shown in Table 5.24. It is evident that the pressure asymptote P_0 is not sensitive with the area of the hollow section. However, the impulse asymptote I_0 is stable until ρ_{hollow} reaches 0.36 which indicates that there is a change in the dynamic behavior of the CFDST column. By examining the failure mode of the numerical model at different ρ_{hollow} values, it can be seen from Fig. 5.118A that when ρ_{hollow} is less than 0.36, flexural failure is the main failure model, whereas signs of both shear and flexural failure are observed when ρ_{hollow} is greater than 0.36. It is well known that for the same structural component, the impulse asymptote is normally smaller for shear failure than flexural failure [79,80].

5.7.3.5   Inner tube steel ratio, ρ_{inner}

The inner tube steel ratio is defined as the cross-sectional area of the inner steel tube over that of the concrete filler, $\rho_{inner} = \frac{A_{inner\ steel}}{A_{concrete}}$. The numerical results from

(A)

(B)

shear failure region
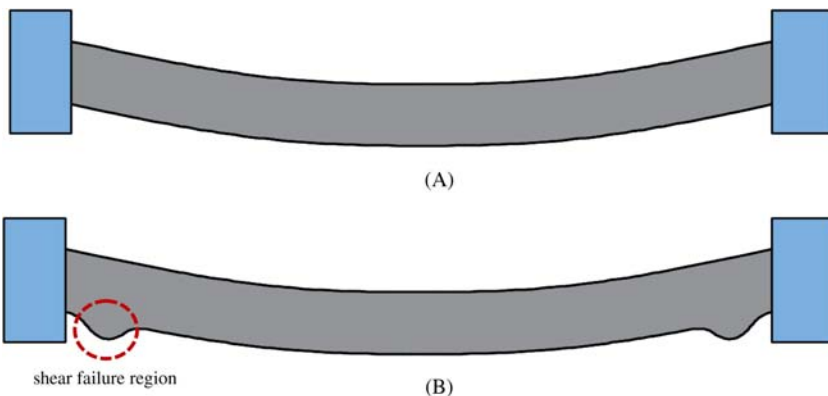
Figure 5.118 Failure modes for different hollow section ratios: (A) typical failure type for $\rho_{hollow} < 0.36$ and (B) typical failure type for $\rho_{hollow} \geq 0.36$.

Table 5.24 suggest that increasing the inner steel tube thickness alone does neither exhibit a significant improvement on the pressure nor impulse asymptotes. This is because, first of all, the inner steel tube is not directly in contact with the blast load; also, the inner steel tube is the innermost part of the UHPCFDST column, the compressive/tensile stress distributed on which is therefore the smallest.

5.7.3.6 Outer tube steel ratio, ρ_{outer}

Similar to the inner tube, the outer tube steel ratio is defined as $\rho_{\text{outer}} = \frac{A_{\text{outer steel}}}{A_{\text{concrete}}}$. One can see from Table 5.24 that, unlike the inner tube, the outer tube is in direct contact with the blast load; therefore it has a more noticeable impact on the pressure and impulse asymptotes, especially on the impulse asymptote. This indicates that increasing the outer tube steel ratio improves the flexural and shear resistance of an UHPCFDST column.

5.7.3.7 Concrete compressive strength, f'_c

CFDST columns with concrete strength of 140, 170, and 200 MPa are considered. The numerical results are presented in Table 5.24. It is clear that increasing the concrete strength does not greatly increase the pressure or impulse asymptotes. This is owing to the fact that the concrete filler in an UHPCFDST column mainly contributes to the axial load-carrying capacity, whereas its effect on the flexural or shear capacity is very limited. Similar results were also reported in other literatures [71,81].

5.7.3.8 Steel yield strength, f_y

In contrast to the concrete strength, the steel yield strength plays a more notable role in the pressure−impulse diagram of an UHPCFDST column as shown in Table 5.24. As expected, higher steel yield strength enhances both the flexural and shear resistance of an UHPCFDST column, therefore resulting in larger pressure and impulse asymptotes.

5.7.4 Normalization of pressure−impulse diagram

To normalize the pressure−impulse diagram of UHPCFDST columns, the simple hyperbolic function recommended by Oswald and Sherkut [82] is used. This method was adopted by Shi et al. [51] for RC columns and [83] for fiber-reinforced polymer-strengthened RC columns, good results were achieved in both cases. The general form of this function can be written as

$$(P - P_0)(I - I_0) = A \left(\frac{P_0}{2} + \frac{I_0}{2} \right)^{\beta} \tag{5.14}$$

where P_0 and I_0 are the pressure and impulse asymptotes of the UHPCFDST column, respectively; coefficients A and β determine the shape of the hyperbola which can be obtained by fitting the numerically derived pressure−impulse points. Based on the numerical results of this study, when A and β equate to 2.2 and 0.8, respectively, the constructed curve can fit through most data points. Therefore Eq. (5.2) can be expressed as

$$(P - P_0)(I - I_0) = 2.2 \left(\frac{P_0}{2} + \frac{I_0}{2} \right)^{0.8} \tag{5.15}$$

By using Eq. (5.3), a pressure−impulse diagram can be easily constructed if the pressure and asymptotes of an UHPCFDST column is given. The analytical formulae to predict the pressure and impulse asymptotes of an UHPCFDST column when the damage index $D = 0.5$ can be derived by using the nonlinear regression analysis in MATLAB. The pressure asymptote P_0 and impulse asymptote I_0 are derived as functions of square side length b, column height H, axial load ratio ρ_{axial}, hollow section ratio ρ_{hollow}, inner tube steel ratio ρ_{inner}, outer tube steel ratio ρ_{outer}, concrete compressive strength f'_c, steel yield strength f_y. The functions are

$$
\begin{aligned}
P_0 = {} & 1.364 \left(\frac{b}{200} \right)^{2.429} + 1.388 \left(\frac{H}{3500} \right)^{-2.75} - 0.333 \left(\frac{\rho_{\text{axial}}}{0.30} \right)^2 \\
& + 0.240 \left(\frac{\rho_{\text{axial}}}{0.30} \right) - 0.105 \left(\frac{\rho_{\text{hollow}}}{0.25} \right)^2 + 0.330 \left(\frac{\rho_{\text{hollow}}}{0.25} \right) + 0.188 \left(\frac{\rho_{\text{inner}}}{0.070} \right) \\
& + 0.763 \left(\frac{\rho_{\text{outer}}}{0.128} \right) + 0.567 \left(\frac{f'_c}{170} \right) + 0.831 \left(\frac{f_y}{350} \right) - 3.863
\end{aligned}
\tag{5.16}
$$

$$
\begin{aligned}
I_0 = {} & 10.972 \left(\frac{b}{200} \right)^{1.283} + 10.113 \left(\frac{H}{3500} \right)^{-0.935} - 1.591 \left(\frac{\rho_{\text{axial}}}{0.30} \right)^2 \\
& + 2.143 \left(\frac{\rho_{\text{axial}}}{0.30} \right) - 2.112 \left(\frac{\rho_{\text{hollow}}}{0.25} \right)^2 + 2.561 \left(\frac{\rho_{\text{hollow}}}{0.25} \right) + 1.564 \left(\frac{\rho_{\text{inner}}}{0.070} \right) \\
& + 6.456 \left(\frac{\rho_{\text{outer}}}{0.128} \right) + 1.700 \left(\frac{f'_c}{170} \right) + 3.562 \left(\frac{f_y}{350} \right) - 24.700
\end{aligned}
\tag{5.17}
$$

As listed in Table 5.24, the error between the P_0 derived numerically and the P_0 predicted by Eq. (5.16) is 2% on average and 7% maximum; the error between the I_0 derived numerically and the I_0 predicted by Eq. (5.17) is also 2% on average but with the maximum error being 10.5%.

For easy comparison, the pressure—impulse curves constructed by using Eq. (5.15) are plotted in Figs. 5.119—5.122 alongside the numerically calculated data points. It is evident that the majority of the numerically derived data points closely follow the fitted curve calculated by the proposed analytical formulae developed in this study.

5.7.5 Conclusion

This section presents a numerical method of investigating UHPCFDST columns under blast loading. The numerical model is calibrated and validated against a series of blast tests carried out by the authors previously and reasonably good agreement was achieved between the experimental and the numerical results.

To quantify the damage accumulated in the UHPCFDST column during blast loading, a damage criterion involving the residual axial load-carrying capacity is used and based on which, pressure—impulse diagrams are derived numerically. Parametric studies are also carried out to investigate the influence of key parameters such as cross-section dimension, column height, axial load ratio, hollow section ratio, inner and outer tube steel ratios, compressive strength of concrete and yield strength of steel tube. The cross-section dimension and column height have the most significant influence on both pressure and impulse asymptotes of the
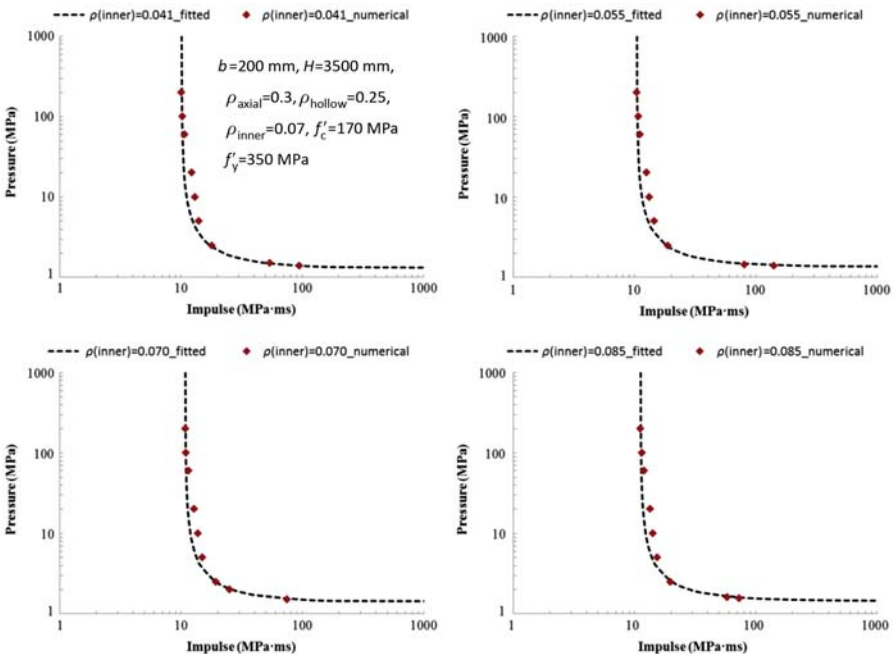
Figure 5.119 Numerically derived pressure and impulse data points for different inner steel ratios.
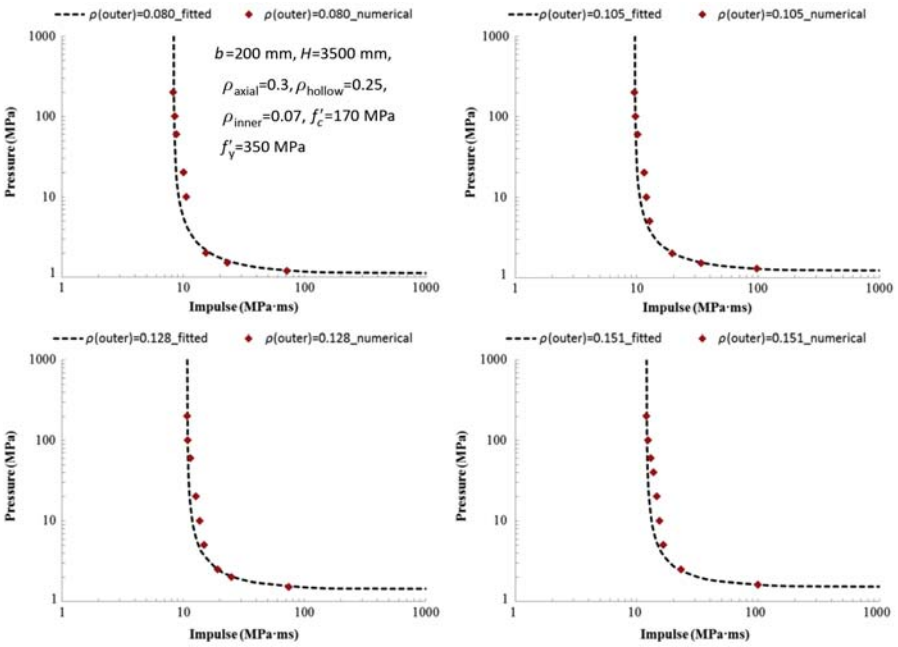
Figure 5.120 Numerically derived pressure and impulse data points for different outer steel ratios.
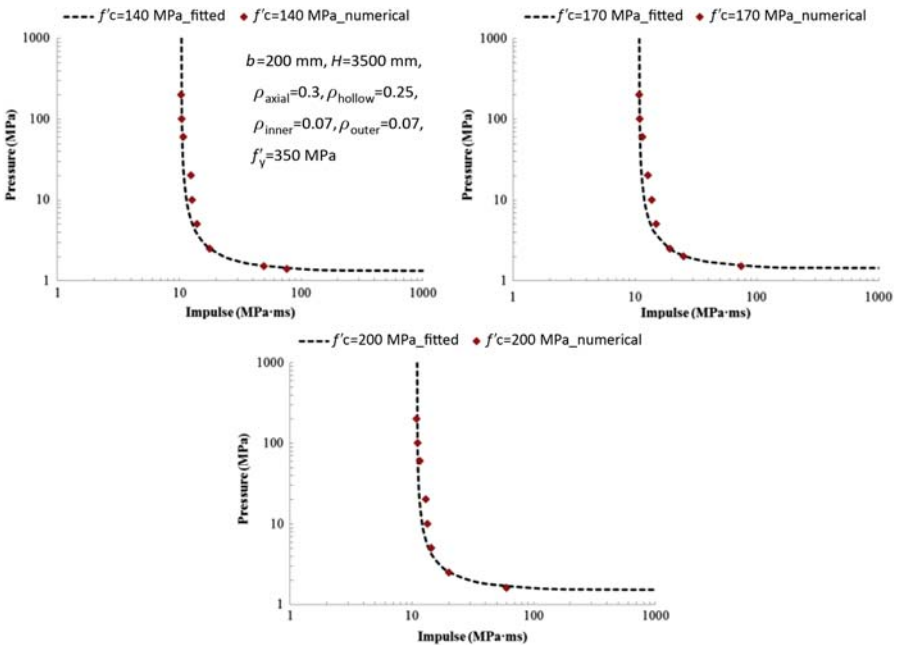
Figure 5.121 Numerically derived pressure and impulse data points for different concrete strengths.
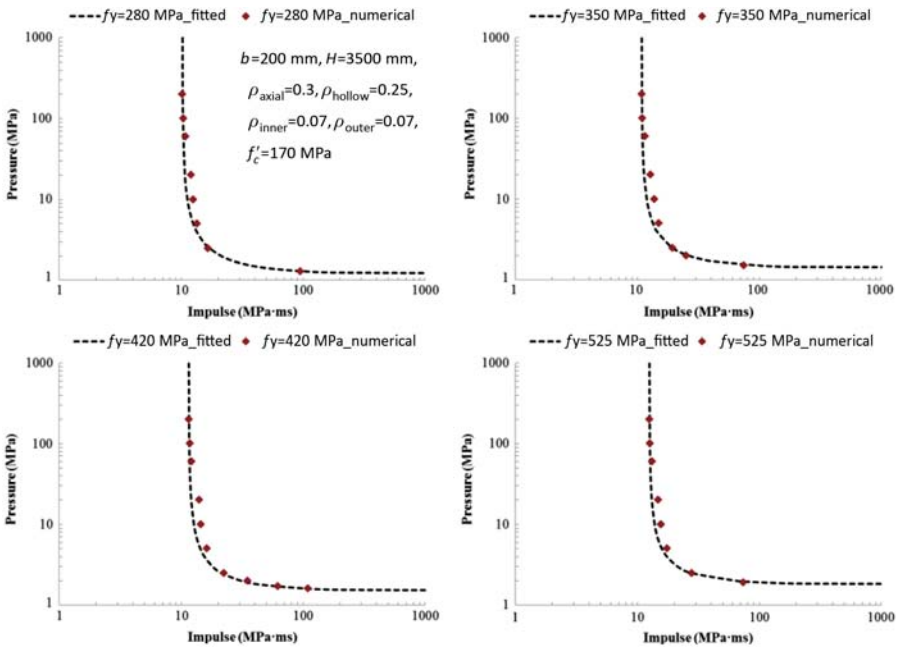
Figure 5.122 Numerically derived pressure and impulse data points for different steel strengths.

pressure−impulse diagram; the values for the pressure and impulse asymptotes peak at axial load ratio = 0.2 and then gradually decreases as it further increases. The hollow section ratio does not exhibit notable impact until it reaches the critical level (i.e., 0.36); the increase in inner and outer tube steel ratios both slightly enhances the pressure and impulse asymptotes with this effect being more noticeable for outer tube; the increase in concrete and steel strength also both limitedly increases the pressure and impulse asymptotes.

Analytical formulae, as functions of column dimension and material properties, are developed which can be used to construct the pressure−impulse diagrams of UHPCFDST columns. The pressure−impulse curves calculated from the proposed analytical formulae are in good agreement with those derived from numerical simulations.

References

[1] C. Wu, L. Huang, D.J. Oehlers, Blast testing of aluminum foam-protected reinforced concrete slabs, J. Perform. Constr. Facil. 25 (2010) 464−474.
[2] G. Ma, Z. Ye, Analysis of foam claddings for blast alleviation, Int. J. Impact Eng. 34 (2007) 60−70.
[3] A. Hanssen, L. Enstock, M. Langseth, Close-range blast loading of aluminium foam panels, Int. J. Impact Eng. 27 (2002) 593−618.

[4] C. Wu, D.J. Oehlers, M. Rebentrost, J. Leach, A.S. Whittaker, Blast testing of ultra-high performance fibre and FRP-retrofitted concrete slabs, Eng. Struct. 31 (2009) 2060−2069.

[5] J. Dragos, C. Wu, M. Haskett, D. Oehlers, Derivation of normalized pressure impulse curves for flexural ultra high performance concrete slabs, J. Struct. Eng. 139 (2012) 875−885.

[6] M. Mirmomeni, A. Heidarpour, X.-L. Zhao, C.R. Hutchinson, J.A. Packer, C. Wu, Mechanical properties of partially damaged structural steel induced by high strain rate loading at elevated temperatures−an experimental investigation, Int. J. Impact Eng. 76 (2015) 178−188.

[7] R. Gerlach, C. Kettenbeil, N. Petrinic, A new split Hopkinson tensile bar design, Int. J. Impact Eng. 50 (2012) 63−67.

[8] S. Morino, M. Uchikoshi, I. Yamaguchi, Concrete-filled steel tube column system-its advantages, Int. J. Steel Struct. 1 (2001) 33−44.

[9] S. Morino, K. Tsuda, Design and construction of concrete-filled steel tube column system in Japan, Earthq. Eng. Eng. Seismol. 4 (2003) 51−73.

[10] S. Wei, S. Mau, C. Vipulanandan, S. Mantrala, Performance of new sandwich tube under axial loading: experiment, J. Struct. Eng. 121 (1995) 1806−1814.

[11] S. Abdalla, F. Abed, M. AlHamaydeh, Behavior of CFSTs and CCFSTs under quasi-static axial compression, J. Constr. Steel Res. 90 (2013) 235−244.

[12] X.-L. Zhao, L.-H. Han, H. Lu, Concrete-Filled Tubular Members and Connections, Spon Press, London, 2010.

[13] R. Wang, L.-H. Han, C.-C. Hou, Behavior of concrete filled steel tubular (CFST) members under lateral impact: experiment and FEA model, J. Constr. Steel Res. 80 (2013) 188−201.

[14] Y. Deng, C.Y. Tuan, Y. Xiao, Flexural behavior of concrete-filled circular steel tubes under high-strain rate impact loading, J. Struct. Eng. 138 (2011) 449−456.

[15] K. Uenaka, H. Kitoh, K. Sonoda, Concrete filled double skin circular stub columns under compression, Thin Wall. Struct. 48 (2010) 19−24.

[16] X.-L. Zhao, L.-W. Tong, X.-Y. Wang, CFDST stub columns subjected to large deformation axial loading, Eng. Struct. 32 (2010) 692−703.

[17] H. Huang, L.-H. Han, Z. Tao, X.-L. Zhao, Analytical behaviour of concrete-filled double skin steel tubular (CFDST) stub columns, J. Constr. Steel Res. 66 (2010) 542−555.

[18] W.-b Yuan, J.-j Yang, Experimental and numerical studies of short concrete-filled double skin composite tube columns under axially compressive loads, J. Const. Steel Res. 80 (2013) 23−31.

[19] M. Pagoulatou, T. Sheehan, X. Dai, D. Lam, Finite element analysis on the capacity of circular concrete-filled double-skin steel tubular (CFDST) stub columns, Eng. Struct. 72 (2014) 102−112.

[20] L.-H. Han, H. Huang, X.-L. Zhao, Analytical behaviour of concrete-filled double skin steel tubular (CFDST) beam-columns under cyclic loading, Thin −Wall. Struct. 47 (2009) 668−680.

[21] L.-H. Han, H. Huang, Z. Tao, X.-L. Zhao, Concrete-filled double skin steel tubular (CFDST) beam-columns subjected to cyclic bending, Eng. Struct. 28 (2006) 1698−1714.

[22] W. Li, L.-H. Han, T.-M. Chan, Tensile behaviour of concrete-filled double-skin steel tubular members, J. Constr. Steel Res. 99 (2014) 35−46.

[23] W. Li, L.-H. Han, T.-M. Chan, Numerical investigation on the performance of concrete-filled double-skin steel tubular members under tension, Thin Wall. Struct. 79 (2014) 108−118.

[24] H. Huang, L.-H. Han, X.-L. Zhao, Investigation on concrete filled double skin steel tubes (CFDSTs) under pure torsion, J. Constr. Steel Res. 90 (2013) 221−234.

[25] H. Lu, X.-L. Zhao, L.-H. Han, Testing of self-consolidating concrete-filled double skin tubular stub columns exposed to fire, J. Constr. Steel Res. 66 (2010) 1069−1080.

[26] W. Li, Q.-X. Ren, L.-H. Han, X.-L. Zhao, Behaviour of tapered concrete-filled double skin steel tubular (CFDST) stub columns, Thin Wall. Struct. 57 (2012) 37−48.

[27] W. Li, L.-H. Han, Q.-X. Ren, X.-L. Zhao, Behavior and calculation of tapered CFDST columns under eccentric compression, J. Constr. Steel Res. 83 (2013) 127−136.

[28] G. Langdon, A. Ozinsky, S.C.K. Yuen, The response of partially confined right circular stainless steel cylinders to internal air-blast loading, Int. J. Impact Eng. 73 (2014) 1−14.

[29] C. Ritchie, J. Packer, M. Seica, X. Zhao, Field blast testing and FE modelling of concrete-filled RHS members, in: Proceedings of the Third International Conference on Protective Structures (ICPS3), Newcastle, NSW, 2015, pp. 478−485.

[30] H. Jama, G. Nurick, M. Bambach, R. Grzebieta, X. Zhao, Steel square hollow sections subjected to transverse blast loads, Thin Wall. Struct. 53 (2012) 109−122.

[31] M. Bambach, X. Zhao, H. Jama, Energy absorbing characteristics of aluminium beams strengthened with CFRP subjected to transverse blast load, Int. J. Impact Eng. 37 (2010) 37−49.

[32] S. Zhong, The Unified Theory for Concrete Filled Steel Tubes, Tsinghua University Press, Beijing, 2006.

[33] B. Simoens, M.H. Lefebvre, F. Minami, Influence of different parameters on the TNT-equivalent,, Cent. Euro. J. Energ. Mater. 8 (2011) 53−67.

[34] L. Stewart, A. Freidenberg, T. Rodriguez-Nikl, M. Oesterle, J. Wolfson, B. Durant, et al., Methodology and validation for blast and shock testing of structures using high-speed hydraulic actuators, Eng. Struct. 70 (2014) 168−180.

[35] L.-H. Han, C.-C. Hou, X.-L. Zhao, K.J. Rasmussen, Behaviour of high-strength concrete filled steel tubes under transverse impact loading, J. Constr. Steel Res. 92 (2014) 25−39.

[36] F. Zhang, C. Wu, X.-L. Zhao, Z.-X. Li, A. Heidarpour, H. Wang, Numerical modeling of concrete-filled double-skin steel square tubular columns under blast loading, J. Perform. Constr. Facil. 29 (2015) 1−12.

[37] J.B. Mander, M.J. Priestley, R. Park, Theoretical stress-strain model for confined concrete, J. Struct. Eng. 114 (1988) 1804−1826.

[38] Y. Idris, T. Ozbakkaloglu, Seismic behavior of high-strength concrete-filled FRP tube columns, J. Compos. Constr. 17 (2013) 04013013.

[39] T. Ozbakkaloglu, M. Saatcioglu, Seismic performance of square high-strength concrete columns in FRP stay-in-place formwork, J. Struct. Eng. 133 (2007) 44−56.

[40] GB/T 8162-2008: Seamless Steel Tubes for Structural Purposes, National Standard of China, 2008.

[41] Australian Standard, 4100:1990: Steel Structures, Standards Australia, Sydney, 1998.

[42] M. Elchalakani, X.-L. Zhao, R. Grzebieta, Concrete-filled circular steel tubes subjected to pure bending, J. Constr. Steel Res. 57 (2001) 1141−1168.

[43] GB/T 228.1-2010: Metallic Materials − Tensile Testing − Part 1: Method of Test at Room Temperature, National Standard of China, 2010.

[44] C.N. Kingery, G. Bulmash, Air Blast Parameters from TNT Spherical Air Burst and Hemispherical Surface Burst, Ballistic Research Laboratories, 1984.

[45] D. Hyde, ConWep, conventional weapons effects program, US Army Engineer Waterways Experiment Station, Vicksburg, 1991.

[46] Z. Tao, L.-H. Han, Behaviour of concrete-filled double skin rectangular steel tubular beam-columns, J. Constr. Steel Res. 62 (2006) 631−646.

[47] X.-L. Zhao, R. Grzebieta, Strength and ductility of concrete filled double skin (SHS inner and SHS outer) tubes, Thin Wall. Struct. 40 (2002) 199−213.

[48] F. Zhang, C. Wu, H. Wang, Y. Zhou, Numerical simulation of concrete filled steel tube columns against BLAST loads, Thin Wall. Struct. 92 (2015) 82−92.

[49] N. Jones, Structural Impact, Cambridge University Press, Cambridge, 2011.

[50] X. Zhao, A. Choi, Moment capacity of concrete filled double skin tubes, in: Tubular Structures XIII-Proceedings of the Thirteenth International Symposium on Tubular Structures, CRC Press/Balkema, 2010, pp. 583−590.

[51] Y. Shi, H. Hao, Z.-X. Li, Numerical derivation of pressure−impulse diagrams for prediction of RC column damage to blast loads, Int. J. Impact Eng. 35 (2008) 1213−1227.

[52] M. Elchalakani, X.-L. Zhao, R. Grzebieta, Concrete-filled steel circular tubes subjected to constant amplitude cyclic pure bending, Eng. Struct. 26 (2004) 2125−2135.

[53] X.-L. Zhao, R. Grzebieta, C. Lee, Void-filled cold-formed rectangular hollow section braces subjected to large deformation cyclic axial loading, J. Struct. Eng. 128 (2002) 746−753.

[54] J.O. Hallquist, LS-DYNA Keyword User's Manual, Livermore Software Technology Corporation, Livermore, CA, 2007.

[55] J. Crawford, Y. Wu, J. Magallanes, S. Lan, Use and Validation of the Release II K&C Concrete Material Model in LS-DYNA, Karagozian & Case, Glendale, CA, 2012.

[56] L.J. Malvar, C.A. Ross, Review of strain rate effects for concrete in tension, ACI Mater. J. 95 (1998) 735−739.

[57] L.J. Malvar, J.E. Crawford, J.W. Wesevich, D. Simons, A plasticity concrete material model for DYNA3D, Int. J. Impact Eng. 19 (1997) 847−873.

[58] Y. Wu, J.E. Crawford, J.M. Magallanes, Performance of LS-DYNA concrete constitutive models, in: Proceedings of the Twelfth International LS-DYNA Users Conference, Karagozian & Case, Burbank, CA, 2012.

[59] Y. Wu, J.E. Crawford, S. Lan, J.M. Magallanes, Validation studies for concrete constitutive models with blast test data, in: Proceedings of the Thirteenth International LS-DYNA Users Conference, Karagozian & Case, Detroit, MI, 2013.

[60] C.E.-I.d. Béton, CEB-FIP Model Code 1990: Design Code, Telford, 1993.

[61] W. Abramowicz, N. Jones, Dynamic progressive buckling of circular and square tubes, Int. J. Impact Eng. 4 (1986) 243−270.

[62] G. Randers-Pehrson, K.A. Bannister, Airblast loading model for DYNA2D and DYNA3D,DTIC Document, 1997.

[63] X. Bao, B. Li, Residual strength of blast damaged reinforced concrete columns, Int. J. Impact Eng. 37 (2010) 295−308.

[64] K. Williams, S. McClennan, R. Durocher, B. St-Jean, J. Tremblay, Validation of a loading model for simulating blast mine effects on armoured vehicles, in: Proceedings of the Seventh International LS-DYNA Users Conference, Detroit, MI, 19−21 May, Livermore Software Technology Corporation, Livermore, CA, 2002, pp. 6−35.

[65] G. Tanapornraweekit, N. Haritos, P. Mendis, T. Ngo, Modelling of a reinforced concrete panel subjected to blast load by explicit non-linear FE code, The Australian Earthquake Engineering Society, 2007.

[66] C. Wu, G. Fattori, A. Whittaker, D.J. Oehlers, Investigation of air-blast effects from spherical-and cylindrical-shaped charges, Int. J. Protect. Struct. 1 (2010) 345−362.

[67] L.-H. Han, Flexural behaviour of concrete-filled steel tubes, J. Constr. Steel Res. 60 (2004) 313−337.

[68] T. Yu, Y. Wong, J. Teng, S. Dong, E. Lam, Flexural behavior of hybrid FRP-concrete-steel double-skin tubular members, J. Compos. Constr. 10 (2006) 443−452.

[69] J. Fan, M. Baig, J. Nie, Test and analysis on double-skin concrete filled tubular columns, Tubular Structures XII: Proceedings of Tubular Structures XII, Shanghai, China, 8−10 October 2008, 2010 pp. 407−411.

[70] C. ACI, Building code requirements for structural concrete (ACI 318-05) and commentary (ACI 318R-05), American Concrete Institute, Farmington Hills, 2005.

[71] J.-C. Xu, C.-Q. Wu, H.-B. Xiang, Y. Su, Z.-X. Li, Q. Fang, et al., Experimental study on the response of ultra-high performance reinforced concrete columns under blast loading, in: Proceedings of the Sixth International Conference on Protection of Structures Against Hazards, 16−17 October, Tianjin, China, 2014.

[72] N.H. Allahverdi, Coupled simulation of loading and response of columns under extreme events (Dissertation), Department of Civil and Environmental Engineering, New Jersey Institute of Technology, New Jersey, 2010, pp. 156.

[73] J. Godinho, A. Montalva, S. Gallant, Analysis of steel columns for air-blast loads, Structure Magazine, 2007, pp. 13−14.

[74] F. Zhang, C. Wu, X.-L. Zhao, H. Xiang, Z.-X. Li, Q. Fang, et al., Experimental study of CFDST columns infilled with UHPC under close-range blast loading, Int. J. Impact Eng. (2016).

[75] L. Mao, S. Barnett, D. Begg, G. Schleyer, G. Wight, Numerical simulation of ultra high performance fibre reinforced concrete panel subjected to blast loading, Int. J. Impact Eng. 64 (2014) 91−100.

[76] L.J. Malvar, J.E. Crawford, Dynamic increase factors for concrete, DTIC Document, 1998.

[77] T. Ngo, P. Mendis, T. Krauthammer, Behavior of ultrahigh-strength prestressed concrete panels subjected to blast loading, J. Struct. Eng. 133 (2007) 1582−1590.

[78] Y. Su, J. Li, C. Wu, P. Wu, Z.-X. Li, Effects of steel fibres on dynamic strength of UHPC, Constr. Build. Mater. 114 (2016) 708−718.

[79] J. Xu, C. Wu, Z.-X. Li, Analysis of direct shear failure mode for RC slabs under external explosive loading, Int. J. Impact Eng. 69 (2014) 136−148.

[80] T. Krauthammer, S. Astarlioglu, J. Blasko, T. Soh, P. Ng, Pressure−impulse diagrams for the behavior assessment of structural components, Int. J. Impact Eng. 35 (2008) 771−783.

[81] F. Zhang, C. Wu, X.-L. Zhao, Z.-X. Li, A. Heidarpour, H. Wang, Numerical modeling of concrete-filled double-skin steel square tubular columns under blast loading, J. Perform. Constr. Facil. 29 (2015) B4015002.

[82] C. Oswald, D. Sherkut, FACEDAP Theory Manual Version 1.2, US Army Corps of Engineers, Omaha, NE, 1994.

[83] A.A. Mutalib, H. Hao, Development of PI diagrams for FRP strengthened RC columns, Int. J. Impact Eng. 38 (2011) 290−304.

This page intentionally left blank

Future work

As reviewed earlier, although ultra-high performance concrete (UHPC) is being utilized in several applications around the world, and increasingly more researches on its static and dynamic performances are carried out recently, it still faces challenges before wider implementation, especially in protective design. The benefits of this innovative material are still not fully understood.

Developing a rational and accurate method for the optimization of UHPC constituents and mixture design to ensure reliable development of UHPC and its wider implementation in the field is deemed necessary. The flexural properties of UHPC are predominantly influenced by the orientation of fibers. Therefore developing a reliable method allowing the effective distribution of fibers in its matrix with desired orientation is required, especially for casting slender elements. The high strength and durability properties of UHPC are highly dependent on thermal treatment. Therefore special arrangements for thermal curing for on-site construction and at precast facilities need to be explored.

In general, the initial material cost of UHPC is higher than that of normal strength concrete and high strength concrete due to its very high cement content and steel fiber addition. However, the application of UHPC can result in more sustainable construction due to possibly better economic, social, and environmental impacts. The overall cost of structures is directly linked with the cross-sectional dimensions of structural elements and foundations. The use of UHPC structural members assists in reducing the cross-sectional dimensions thereby freeing additional useful space in buildings and also reducing the size of foundations. UHPC members require less maintenance cost due to their improved durability characteristics; and hence their life-cycle cost can be reduced while yielding much longer service life. Furthermore, the utilization of by-products such as fly ash/silica fume instead of cement makes UHPC more sustainable and more economic.

Field blast tests demonstrated the advantages of UHPC in blast resistance design. Further study on the dynamic material property may enhance the understanding of UHPC. Numerical model based on both homogeneous and heterogeneous models can yield valuable data for UHPC structures under dynamic loads; however, accurate characterization of the effect of each component such as the steel fiber on the mechanical performance shall be further investigated. Furthermore, an accurate model for predicting the cracking initiation and propagation within UHPC under dynamic loads shall be established.

A prosperous development in material science has been witnessed in recent decades, and a new kind of geopolymers, which are generally synthesized by alkali-activated slag, fly ash, kaolinite clay, and other aluminosilicate materials, has been

developed as promising binders. Emerging concepts of developing UHPC based on geopolymer, rather than the Portland cement, may help enhance the cost-effectiveness of the materials, while maintaining a high level of material performances.

Index

Note: Page numbers followed by "*f*" and "*t*" refer to figures and tables, respectively.

Recent events have promoted the fast development of new construction materials that can be used to enhance the resistance and resilience of buildings and infrastructures against blast loads. As a notable example, ultra-high performance concrete (UHPC) has now been widely investigated by both government agencies and universities. UHPC inherits many positive aspects of ultra-high strength concrete and is equipped with improved ductility as a result of the addition of fiber. These features make it an ideal construction material for bridge decks, storage halls, thin-wall shell structures, and other infrastructure against seismic, impact, and blast loads. Pioneering applications of this material are now being seen world-wide.

This book provides a detailed overview of the development of UHPC and its applications. It also presents key case studies on the novel development of the new generation UHPC with nanoadditives. Field blast test results on reinforced concrete columns made with UHPC as well as the UHPC-filled double-skin tubes columns are presented and analyzed in order to provide an in-depth knowledge of the blast resistance performance of this novel UHPC material.

This book presents a comprehensive overview of the current research practices and the data collected in the blast tests that will serve as an essential reference to protective engineers and researchers. The essential background knowledge and data presented within this book will permit both researchers and engineers to use it in the initial phase of problem solving, and make it the essential companion for anyone interested in this material and its applications in the construction industry.

This book is written by key figures in the field of protective materials used in the construction industry, offering expertise from the prestigious University of Technology Sydney (Australia). Dr. Wu is currently serving as an associate editor of the ASCE Journal of Performance of Constructed Facilities and also as an editorial board member of International Journal of Protective Structures. This book is an amalgamation of the authors' varied expertise and knowledge in this exciting new field.

MATERIALS SCIENCE

ISBN 978-0-08-102495-9

WOODHEAD
PUBLISHING
An imprint of Elsevier
elsevier.com/books-and-journals

ELSEVIER

9 780081 024959